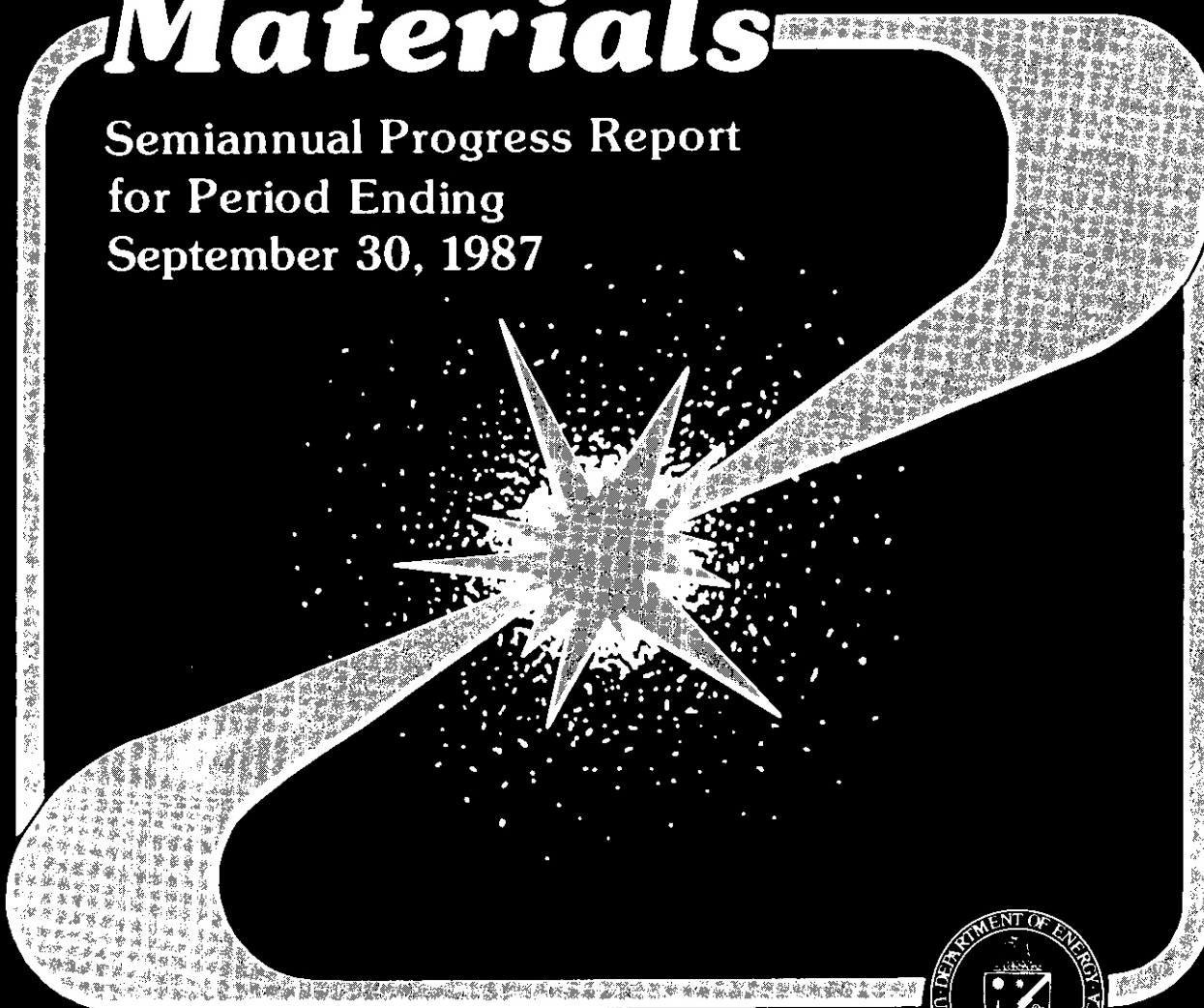


DOE/ER-0313/3

Fusion Reactor Materials

Semiannual Progress Report
for Period Ending
September 30, 1987



U. S. Department of Energy
Office of Fusion Energy



Printed in the United States of America. Available from
National Technical Information Service
U.S. Department of Commerce
5285 Port Royal Road, Springfield, Virginia 22161
NTIS price codes—Printed Copy: A15 Microfiche A01

This report was prepared as an account of work sponsored by an agency of the United States Government. Neither the United States Government nor any agency thereof, nor any of their employees, makes any warranty, express or implied, or assumes any legal liability or responsibility for the accuracy, completeness, or usefulness of any information, apparatus, product, or process disclosed, or represents that its use would not infringe privately owned rights. Reference herein to any specific commercial product, process, or service by trade name, trademark, manufacturer, or otherwise, does not necessarily constitute or imply its endorsement, recommendation, or favoring by the United States Government or any agency thereof. The views and opinions of authors expressed herein do not necessarily state or reflect those of the United States Government or any agency thereof.

**FUSION REACTOR MATERIALS
SEMIANNUAL PROGRESS REPORT
FOR THE PERIOD ENDING SEPTEMBER 30, 1987**

Date Published: March 1988

**Prepared for
DOE Office of Fusion Energy**

**Prepared by
OAK RIDGE NATIONAL LABORATORY
Oak Ridge, Tennessee 37831
operated by
MARTIN MARIETTA ENERGY SYSTEMS, INC.
for the
U.S. DEPARTMENT OF ENERGY
under Contract DE-AC05-84OR21400**

Reports previously issued in this series are as follows:

DOEIER-031311 Period Ending September 30, 1986

DOEIER-031312 Period Ending March 31, 1987

FOREWORD

This is the third in a series of semiannual technical progress reports on fusion reactor materials. This report combines research and development activities which were previously reported separately in the following technical progress reports:

- Alloy Development for Irradiation Performance
- Damage Analysis and Fundamental Studies
- Special Purpose Materials

These activities are concerned principally with the effects of the neutronic and chemical environment on the properties and performance of reactor materials; together they form one element of the overall materials program being conducted in support of the Magnetic Fusion Energy Program of the U.S. Department of Energy. The other major element of the program is concerned with the interactions between reactor materials and the plasma and is reported separately.

The Fusion Reactor Materials Program is a national effort involving several national laboratories, universities, and industries. The purpose of this series of reports is to provide a working technical record for the use of the program participants, and to provide a means of **communicating** the efforts of materials scientists to the rest of the fusion community, both nationally and worldwide.

This report has been **compiled** and edited under the guidance of A. F. Rowcliffe, Oak Ridge National Laboratory, and D. G. Doran, Battelle-Pacific Northwest Laboratory. Their efforts, the work of the publications staff in the Metals and Ceramics Division at ORNL, and the many persons who made technical contributions are gratefully acknowledged. T. C. Reuther, **Reactor** Technologies Branch, has responsibility within DOE for the programs reported on in this document.

G. M. Haas, Chief
Reactor Technologies Branch
Office of Fusion Energy

TABLE OF CONTENTS

FOREWORD		iii
1. IRRADIATION FACILITIES, TEST MATRICES, AND EXPERIMENTAL METHODS		1
1.1 Design and Fabrication of HFIR-MFE RB Spectrally Tailored Irradiation Capsules (Oak Ridge National Laboratory and Midwest Technical, Inc.)		2
	<p><i>Design and fabrication of four HFIR-MFE RB capsules (60, 200, 330, and 400°C) to accommodate MFE specimens preirradiated in spectrally tailored experiments in the ORR is proceeding satisfactorily. These capsule designs incorporate provisions for removal, examination, and reencapsulation of the MFE specimens at intermediate exposure levels en route to a target exposure level of 30 displacements per atom (dpa). With the exception of the 60°C capsule, where the test specimens will be in direct contact with the reactor cooling water, the specimen temperatures (monitored by 21 thermocouples) will be controlled by varying the thermal conductance of a small gap region between the specimen holder and the containment tube. Hafnium sleeves will be used to tailor the neutron spectrum to closely match the helium production-to-atom displacement ratio (14 appm/dpa) expected in a fusion reactor first wall.</i></p> <p><i>Preparation of fabrication drawings for the 330 and 60°C capsules has been completed, and fabrication of parts for both capsules is nearing completion. Fabrication drawings for the 400 and 200°C capsules will be completed in 1988. Operation of the 330 and 60° capsules is scheduled to begin in February 1988, and the other two (400 and 200°C) in October 1989.</i></p>	
1.2 Operation of the U.S./Japan ORR Spectral Tailor'ng Experiments (Oak Ridge National Laboratory)		7
	<p><i>The irradiation of the ORR-MFE-6J and -7J experiments was terminated during the previous reporting period on March 26, 1987, when the ORR was shut down by DOE order. The total accumulated irradiation time is 474.7 full power days (FPD) at 30 MW reactor power. With future operation of the ORR so uncertain, the decision to proceed with encapsulation into KFIR RB capsules was agreed upon by the United States and Japan in June 1987. The capsules were removed from the core on June 29, 1987. Disassembly of the 60°C portion of the MFE-6J was completed August 25, 1987, and the specimens were given to the Metals and Ceramics Division personnel for preparation for reinsertion into the HFIR-MFE-60J-1 capsule. Capsule MFE-7J and the 200°C portion of MFE-6J are in the ORR pool awaiting disassembly.</i></p>	
1.3 Status of the U.S./Japan Collaborative Program Phase II HFIR Target Capsules (Oak Ridge National Laboratory)		8
	<p><i>During this reporting period, a revised matrix for Phase II KFIR target capsules JP-9 through -16 was developed. An extensive thermal analysis for the new designs was completed to support redesign of the capsules, based on the new operating level of 85 MW for the HFIR. These new designs were completed and parts are on hand in preparation for assembly of all eight capsules during the first quarter of FY 1988. All eight capsules will be installed in the KFIR simultaneously beginning with the first full power cycle of the HFIR.</i></p>	
1.4 Fusion Program Research Materials Inventory (Oak Ridge National Laboratory and McDonnell Douglas Astronautics Company - St. Louis Division)		21
	<p><i>A summary of materials in the Fusion Program Research Materials Inventory indicates the nominal diameter of rod or thickness of sheet for product forms of each alloy and also indicates by weight the amount of each alloy in larger sizes available for fabrication to produce other product forms as needed by the program.</i></p>	
1.5 Fusion Program Research Materials Inventory of 12Cr-1Mo Steel (HT-9) (GA Technologies, Inc.)		23
	<p><i>Previously, a 30,000-lb heat of KT-9, 12Cr-1Mo steel made by the argon-oxygen decarburization method (AOD) was procured by GA Technologies, Inc., for the ADIP program. Half of the AOD heat of HT-9 steel was remelted by the electroslag remelting process (ESR). These two heats of KT-9 have been converted to the form of plate and bar stock and then distributed to the DOE Path E fusion reactor materials program users. In September 1987, all the unused KT-9 plates and bars at GA have been shipped to Oak Ridge National Laboratory Material Stockpile.</i></p>	

2. DOSIMETRY, DAMAGE PARAMETERS AND ACTIVATION CALCULATIONS	27
2.1 Neutronics Analysis in Support of the U.S.-Japan Spectral Tailoring Capsules (Oak Ridge National Laboratory)	28
<p><i>The ORR was shut down on March 26, 1987, and the ORR-MFE-63 and -73 capsules were removed. At the time of their removal, scaled fluences from neutronics calculations yielded 62.4 appm He (not including 2.0 appm He from ¹⁹⁸) and 6.92 dpa for type 316 stainless steel in ORR-MFE-63 and 96.8 appm He and 7.97 dps in ORR-MFE-7J. The hafnium shield thickness required to extend the lifetime of the MFE-63 and -7J capsules in a HFIR RB position from 150 full-power days to 275 days at 85% of full power was calculated to be 5.0 mm.</i></p>	
2.2 Dosimetry and Damage Calculations for the JP4, JP5, and JP8 U.S./Japanese Experiments in HFIR (Argonne National Laboratory)	30
<p><i>Results are presented for the JP4, JP5, and JP8 U.S./Japanese experiments in HFIR. All three experiments had similar exposures of about 58,000 MWD resulting in 55 dpa and 3313 appm helium at midplane for 316 stainless steel.</i></p>	
2.3 Enhanced Helium Production in Ferritic Materials (Argonne National Laboratory and Rockwell International Corporation)	33
<p><i>Analyses of iron samples irradiated up to neutron fluences of 10^{22} n/m² in HFIR found more helium than was expected from fast neutron reactions at high fluences. The helium excess increased systematically with neutron exposure, suggesting a transmutation-driven process. The extra helium could be produced in two different ways, either by fast neutron reactions on the transmuted isotopes of iron or by a thermal neutron reaction with the radioactive isotope ⁵⁵Fe. Radiometric and mass spectrometric measurements of the iron isotopes composing the irradiated samples have been used to determine limits on the cross sections for each process. Either of these processes can be used to enhance helium production in ferritic materials during irradiations in mixed-spectrum reactors by isotopically enriching the samples. Further work is needed to clarify the reaction mechanisms and to determine helium-production cross sections. Our measurements determined the thermal neutron total absorption cross section of ⁵⁵Fe to be 13.2 ± 2.1 barns.</i></p>	
2.4 Cross Section Measurements for Long-Lived Isotopes Near 14.8 MeV (Argonne National Laboratory)	39
<p><i>Neutron production cross sections have been measured near 14 MeV following high-fluence irradiations at the RTNS II facility. New results are reported for the production of ⁹³Nb (680y), ⁹³Mo (35900y), and ^{93m}Nb (13.6y) from natural Mo and ⁹⁴Mo enriched targets. Our data suggest that the half-life of ^{93m}Nb may be shorter than previous estimates.</i></p>	
3. MATERIALS ENGINEERING AND DESIGN REQUIREMENTS	43
3.1 Materials Handbook for Fusion Energy Systems (McDonnell Douglas Astronautics Company - St. Louis Division)	44
<p><i>The effort during this reporting period has been directed towards developing the supporting documentation data sheets in preparation for distribution to current handbook holders. The first distribution of the HT-9 data pages was made early in June. A second distribution of the electrical insulator data pages is scheduled for December. The release of these pages constitutes the first step towards establishing a data base of fusion developed experimental data.</i></p>	
3.2 Dimensional Change Correlations for 20% Cold-Worked AISI 316 Stainless Steel for Fusion Applications (University of Missouri - Rolla and Pacific Northwest Laboratory)	45
<p><i>Correlations developed for void swelling and irradiation creep often arise from two separate data bases and sometimes are not well matched, reflecting apparently minor but actually significant differences in environmental history. Previously published correlations are very empirical in nature and reflect prevailing misconceptions about the parametric sensitivity of swelling and irradiation creep. In this study a well-defined data base for swelling of 20% cold-worked AISI 316 is used in conjunction with the latest insights on swelling and creep to develop two matched dimensional change correlations for temperatures in the range of 300 to 550°C. The new creep model, in particular, is much simpler than the complicated empirical correlation published earlier for this steel.</i></p>	

4.	FUNDAMENTAL MECHANICAL BEHAVIOR	53
4.1	Analysis of Cleavage Fracture Behavior in HT-9 with a Statistical Model (University of California, Santa Barbara)	54
	<i>We have investigated the applicability of a statistical model for cleavage fracture to data obtained on a set of HT-9 specimens heat-treated to 25 different conditions, for which prior austenite grain size, lath packet size and carbide size and density varied systematically. The statistical model predictions were in good agreement with observed trends. The results suggest that cleavage in these steels may be dictated by microcrack nucleation and propagation from large boundary carbides.</i>	
4.2	The Tensile Properties of Fe-Cr Binary Alloys Using Miniature Specimens (The Northwest College & University Association for Science – NORCUS and Pacific Northwest Laboratory)	60
	<i>Microtensile specimens of Fe-3, 6, 9, 12, 15 and 18Cr have been tested to provide baseline data for comparison with specimens being irradiated in FPTF. Yield strengths for Fe-6Cr and Fe-9Cr were lower than for the other alloys tested, in agreement with the literature. Impurities in the Fe-3Cr alloy led to increased strength in that alloy. The use of thicker specimens did not significantly reduce experimental uncertainties.</i>	
5.	RADIATION EFFECTS: MECHANISTIC STUDIES, THEORY AND MODELING	65
5.1	Effects of the Neutron Spectrum on Mechanical Property Changes in Low Dose Irradiations (Pacific Northwest Laboratory)	66
	<i>Mechanical property measurements from comparative low dose irradiations of metals and alloys are reviewed. The emphasis is on recent experiments involving miniature tensile specimens irradiated at the Rotating Target Neutron Source II (RTNS-II) at Lawrence Livermore National Laboratory and the Omega West Reactor at Los Alamos National Laboratory. Pure metals, model alloys and structural alloys have been irradiated in RTNS-II from room temperature to 723 K to fluences as high as $8 \times 10^{22} \text{ n/m}^2$. Where temperature effects are apparent, the effect of increasing the irradiation temperature is to delay the onset of irradiation hardening to higher fluences. Companion fission reactor irradiations have been more limited in scope, but comparative information has been obtained on tensile properties at irradiation temperatures of 363 K and 563 K. For most of the materials tested the differences in the neutron energy spectrum can be accounted for by using displacements per atom (DPA) as a correlation parameter. The exceptions are all pure metals: copper, niobium and vanadium. There is also evidence for rate effects in some of the data. The rate effects obscure the spectral effects and prevent examination of dpa as a damage correlation parameter.</i>	
5.2	The Effects of Low Doses of 14 MeV Neutrons on the Tensile Properties of Three Binary Copper Alloys (Pacific Northwest Laboratory)	79
	<i>Miniature tensile specimens of high purity copper and copper alloyed respectively with five atom percent of Al, Mn, and Ni were irradiated with D-T fusion neutrons in the RTNS-II to fluences up to $1.3 \times 10^{22} \text{ n/m}^2$ at 363 K. To compare fission and fusion neutron effects, some specimens were also irradiated at the same temperature to similar damage levels in the Omega West Reactor (OWR). Tensile tests were performed at room temperature, and the radiation-induced changes in tensile properties are compared as functions of displacements per atom (dpa). The irradiation-induced strengthening of Cu5%Mn is greater than that of Cu5%Al and Cu5%Ni, which behave about the same. However, all the alloys sustain less irradiation-induced strengthening by 14 MeV neutrons than pure copper. The effects of fission and fusion neutrons on the yield stress of the copper alloys correlate well on the basis of dpa, in contrast to the behavior of pure copper.</i>	
5.3	Dual-Ion Irradiation of Copper (Oak Ridge National Laboratory)	86
	<i>Simultaneous irradiation of copper with helium and heavy ions produced substantial void formation at a temperature of 440°C. Irradiation at a temperature of 220°C produced small "black-spot" defect clusters. The implanted ions from the heavy ion beam caused a substantial reduction in void swelling at the damage peak for the 440°C irradiation, as determined from a cross-section TEM observation. The void swelling rate was $\sim 0.5\%/dpa$ in regions that were far away from the injected ion peak.</i>	

5.4	Void Swelling and Defect Cluster Formation in Reactor-Irradiated Copper (Oak Ridge National Laboratory)	90
-----	---	----

The **lower** temperature limit for void formation in copper irradiated with moderated fission neutrons at a damage rate of 2×10^{-7} dpa/s lies between 182 and 220°C. At 182°C the clustering of vacancies produces stacking fault tetrahedra instead of voids. The maximum swelling for the 1.3 dpa irradiation is -0.4% at a temperature near 300°C.

5.5	The Distribution of Defect Clusters in Ion Irradiated Ni-10Cu and Ni-50Cu (University of Wisconsin)	94
-----	---	----

The resistance to void formation of concentrated Ni-Cu alloys is confirmed by TEM cross-section observation of the 14 MeV Ni ion irradiated Ni-10Cu and Ni-50Cu alloys with damage levels up to 100 dpa at the peak.

Irradiation produced a substantial number of dislocation loops in both alloys, but the loop size is much smaller and their density is 5-7 times higher in Ni-50Cu than in Ni-10Cu.

Preinjection of 100 ppm oxygen before Ni ion irradiation promotes void formation in Ni-10Cu, but does not show any apparent effect in the case of Ni-50Cu.

Trapping of vacancies and gas atoms by fine-scaled clusters of like atoms is considered the mechanism responsible for the void resistant property of the alloys.

5.6	On Mechanisms Controlling Swelling in Ferritic and Martensitic Alloys (University of California, Santa Barbara)	106
-----	---	-----

Ferritic and martensitic (FM) alloys are highly resistant to swelling in fast reactor irradiations. High self-diffusion rates and low dislocation bias may contribute to their intrinsic swelling resistance. Other factors, such as high sink densities, are metallurgically mediated and may not be permanent. Further, low helium generation rates in FM alloys may contribute significantly to the low swelling observed in fast reactor irradiations. Helium generation is environmentally mediated, and higher levels generated in mixed spectrum reactors increase void swelling. FM alloys also lose their advantageous helium-to-dpa ratio in fusion spectra. The implications of these factors are evaluated with critical bubble-to-void and rate theory swelling models using austenitic alloys as a reference.

5.7	Phase Instabilities in Irradiated Simple Fe-Cr-Mn Low Activation Alloys (Pacific Northwest Laboratory)	115
-----	--	-----

The Fe-Mn system has been proposed to replace the Fe-Ni system in fusion applications to achieve greatly reduced levels of long-term radioactivity. The in-reactor stability of simple Fe-Mn and Fe-Cr-Mn alloys is therefore being studied to determine the nature of the driving forces tending to destabilize these alloys. The results of this study indicate that simple Fe-Cr-Mn alloys exhibit during irradiation a greater level of potential phase instabilities than do comparable Fe-Cr-Ni alloys, requiring careful attention in the development of solute-stabilized alloys.

5.0	Response of Fe-Cr-Mn Austenitic Alloys to Thermal Aging and Neutron Irradiation (Pacific Northwest Laboratory and National Research Institute for Metals - Japan)	123
-----	---	-----

The Fe-Cr-Mn austenitic alloy system is being studied as a replacement of the Fe-Cr-Ni system for fusion applications in which reduced long-term radiactivation is an important consideration. This report describes two aspects of the response of this alloys system to material and environmental variables. First, the neutron-induced void swelling of simple binary and ternary alloys is investigated as a function of composition, thermal-mechanical treatment, temperature (693-873K) and displacement level (976 dpa). The swelling rate of this alloy system approaches $1\%/dpa$ for those conditions which do not favor formation of large levels of ferrite phases. Second, the tendency of the potentially detrimental sigma phase to form during thermal aging is explored at high manganese levels. Variables such as carbon concentration, cold-work level and aging time are shown to influence the distribution and rate of sigma formation.

5.9	Quantitative Analysis of Void Swelling (Pacific Northwest Laboratory and Westinghouse Hanford Company)	131
-----	--	-----

It has been shown that in austenitic alloys void shapes can vary between truncated octahedra and truncated cubes whereas in ferritic alloys the void shapes vary between truncated octahedra, truncated cubes and truncated dodecahedra. In order to provide minimum errors in void swelling measurements, where the degree of truncation varies from void to void in the area of interest, calculations are provided which show that voids

should be measured in $\langle 110 \rangle$ directions for austenitic alloys with cubic and octahedral truncation but for ferritic alloys with cubic and dodecahedral truncation, $\langle 111 \rangle$ and $\langle 110 \rangle$ direction measurements are equivalent provided the correct calibration factor is used.

5.10 Determination of the Bias Factor by the Moments Solution to the Fokker-Planck Equation (University of California, Los Angeles)	137
---	-----

An important parameter in the rate theory of swelling is the dislocation loop bias factor, Z_i^b , which is a measure of the rate of interstitial atom absorption relative to vacancy absorption at interstitial loops. The Fokker-Planck (F-P) equation is used to describe interstitial loop evolution, with a kinetic nucleation current boundary condition at di-interstitial atomic clusters. The majority of loop nucleation is shown to be finished after one milli-dpa, which allows the shape of the loop distribution function to be governed mainly by the drift (F) and dispersion (D) functions in the F-P equation. Since collision cascades contribute significantly to D, their effects must be suppressed by using low-energy ions or high-energy electrons to produce spatially homogeneous atomic displacements. Under these conditions, both F and D are shown to be proportional to the square root of the number of atoms in a loop. The proportionality parameters depend on material and irradiation conditions, and are linearly proportional to Z_i^b . The ratio F/D, can be used in a unique way to determine Z_i^b without the usual complications of uncertainties in material and irradiation conditions. This is shown to constitute an internal variable measurement of the bias factor.

5.11 Binary Collision Monte Carlo Simulations of Cascades in Polyatomic Ceramics (University of California, Los Angeles)	143
--	-----

The binary collision approximation (BCA) is used in a Monte Carlo (MC) study of high-energy collision-cascade creation in SPINEL, the model ceramic insulator. The study focuses on two aspects of cascade generation: cascade morphology and cascade stoichiometry. In the high-energy regime, typical of fusion neutrons, cascades show a tree-like morphology. To a large degree, instantaneous recombination occurs in the "stem" part of the cascade because of the closer separation of vacancy-interstitial pairs. Following this recombination phase, fusion neutron cascades tend to result in Frenkel pairs distributed on the "branches" of the tree in a zone extending over 100 to 200 nm. The stoichiometry of displacements within the cascade is found to be substantially different from bulk stoichiometry, and is dependent upon the energy and type of primary knock-on atom (PKA).

6. DEVELOPMENT OF STRUCTURAL ALLOYS	149
6.1 Ferritic Stainless Steels	150
6.1.1 Effects of Irradiation on Tungsten Stabilized Martensitic Steels (Westinghouse Hanford Company and GA Technologies, Inc.)	150

As part of a program to determine the applicability for a fusion first wall of martensitic stainless steel from which critical elements have been removed in order to assure low retained radioactivity 100 years after decommissioning, two alloys have been designed, fabricated, fast neutron irradiated in FFTF and examined by transmission electron microscopy. The two experimental 7 kg heats of tungsten-stabilized martensitic steels had intended levels of 9 and 11% chromium but contain no intentional additions of niobium, molybdenum and nickel. However, the alloys were found to have deviated somewhat from their intended composition. The actual compositions were 7.5 and 10.2% Cr respectively with 0.02% C in the latter case. Nonetheless, irradiation response is typical of that in ferritic steels. Conditions examined included irradiation temperatures of 365, 420, 520 and 600°C to doses as high as 34 dpa with small amounts of void swelling found at the two lowest temperatures. It is demonstrated that levels of tungsten on the order of 2 wt% do not result in excessive intermetallic precipitation after irradiation to fluences as high as 7.3×10^{22} n/cm² or 34 dpa over the temperature range 365 to 600°C.

6.1.2 The Development of Ferritic Steels for Fast Induced-Radioactivity Decay (Oak Ridge National Laboratory)	161
---	-----

Transmission electron microscopy and X-ray diffraction studies were made on eight heats of normalized-and-tempered chromium-tungsten steel that contained various levels of chromium, tungsten, vanadium, and tantalum. A range of precipitate morphologies and compositions were observed. The types of precipitates

were similar to the precipitates that occur in the *analogous chromium-molybdenum* steels that are presently being considered as candidate structural materials for fusion-reactor applications.

6.1.3 The Influence of Specimen Size on Charpy Impact Testing of Unirradiated HT-9 (University of Missouri – Rolla, Pacific Northwest Laboratory, and Westinghouse Hanford Company) 170

The effect of specimen size on the impact properties of HT-9 has been studied. The data from the precracked and notched-only specimens of HT-9 were used along with previously published data on other steels to develop correlations that predict from subsized specimen data the ductile-brittle transition temperature (DBTT) and upper shelf energy (USE) anticipated for full-size specimens. Each correlation is based on physical insight and can be applied equally well to both precracked and notched-only specimens. The correlation for USE works best for fracture energy in a range characteristic of irradiated materials, while a previously published correlation works better for more ductile materials. The DBTT correlation, however, works well on all materials for which sufficient data have been published.

6.1.4 Temperature Dependence of Young's Modulus of Low-Activation Ferritic Alloys (Auburn University) 178

Measurements of Young's modulus of low-activation ferritic alloys have been performed using a dynamic mechanical technique over the temperature range from -150 to 350°C. The results indicate that the moduli of alloys investigated decrease approximately linearly with test temperature. Also, the constant is independent of chromium content and its corresponding microstructure. Based on a comparison with the literature, good agreement was found between data obtained in this study and those reported by various investigators.

6.2 Austenitic Stainless Steels 181

6.2.1 Irradiation Creep and Swelling of AISI 316 to Exposures of 130 dpa at 385–400°C (Pacific Northwest Laboratory and Argonne National Laboratory) 181

The creep and swelling of AISI 316 stainless steel have been studied at 385 to 400°C in EBR-11 to doses of 130 dpa. Most creep capsules were operated at constant stress and temperature but mid-life changes in these variables were also made. This report concentrates on the behavior of the 20% cold-worked condition but five other conditions were also studied. Swelling at ≤400°C was found to lose the sensitivity to stress exhibited at higher temperatures while the creep rate was found to retain linear dependencies on both stress and swelling rate. The creep coefficients extracted at 400°C agree with those found in other experiments conducted at higher temperatures. In the temperature range of ≤400°C, swelling is in the recombination-dominated regime and the swelling rate falls strongly away from the ~1%/dpa rate observed at higher temperatures. These lower rates of creep and swelling, coupled with the attainment of high damage levels without failure, encourage the use of AISI 316 in the construction of water-cooled fusion first walls operating at temperatures below 400°C.

6.2.2 The Influence of Mo, Si, P, C, Ti, Cr, Zr and Various Trace Elements on the Neutron-Induced Swelling of AISI 316 Stainless Steel (Pacific Northwest Laboratory and Westinghouse Hanford Company) 191

The individual and synergistic influences of seven major and eleven minor solutes on the swelling of 316 stainless steel were investigated in an irradiation experiment conducted in EBR-II. All elements exert their influence on the duration of the transient regime of swelling, through their effect on both vacancy diffusivity and precipitate evolution, often causing a complex response with increasing solute level. On a per atom basis, phosphorus is the most effective and consistent suppressor of swelling. Trace elements were found to have no significant effect. No combination of these elements appears to suppress the tendency of this steel to swell at ~1%/dpa following the transient regime.

6.2.3 Swelling Behavior of Austenitic Stainless Steels in a Spectrally Tailored Reactor Experiment: Implications for Near-Term Fusion Machines (Oak Ridge National Laboratory and Japan Atomic Energy Research Institute on assignment to ORNL) 198

Current designs for engineering test reactors such as the International Thermonuclear Experimental Reactor propose to use an austenitic stainless steel

for the first wall. Most of the available swelling data have been derived from neutron-irradiation experiments in which helium generation rates are very low (fast breeder reactors) or very high (mixed spectrum reactors). Recently a spectrally tailored experiment was concluded in the Oak Ridge Research Reactor in which the helium generation rate and damage rate were maintained at values typical of a fusion reactor operating at $\sim 1 \text{ MW/m}^2$. It was found that the swelling behavior of a titanium-modified stainless steel (PCA) in both the cold-worked and solution-annealed conditions differed significantly from the behavior observed in earlier experiments in which the \dot{H}_e/dpa ratio was either -0.5 or -50. The results suggest that there is a strong dependence of micro-structural evolution on the \dot{H}_e/dpa ratio. The data are shown to be consistent with earlier theoretical predictions of swelling behavior that is a non-monotonic function of the \dot{H}_e/dpa ratio. Finally, both the present data set and a larger collection of low-temperature swelling data are discussed in the context of near-term machines.

6.2.4 Precipitate Identification in Titanium-Modified Austenitic Stainless Steels After Irradiation at 500°C in HFIR to -57 dpa (Japan Atomic Energy Research Institute on assignment to ORNL and Oak Ridge National Laboratory) 206

Irradiation-enhanced and -induced precipitates were identified in the Japanese prime candidate alloy (JPCA) which was irradiated to 57 dpa at 500°C in HFIR. Comparison was made between the solution annealed (SA) and the 20% cold-worked (CW) JPCA. The SA material had higher swelling and also had a higher volume fraction of irradiation-induced precipitates. Precipitation in the SA JPCA was primarily M_6C with small amounts of titanium-rich MC and still smaller amounts of G-phase. By contrast, the CW JPCA contained much more MC and less M_6C .

6.2.5 Swelling Behavior and Microstructural Evolution in Type 316 Stainless Steel Irradiated in HFIR (Oak Ridge National Laboratory and Japan Atomic Energy Research Institute on assignment to ORNL) 212

Swelling behavior and microstructures were investigated in solution-annealed (SA) and 20% cold-worked (CW) type 316 stainless steel irradiated to 30 dpa at 300 to 600°C in the High Flux Isotope Reactor (HFIR). At irradiation temperatures $\leq 400^\circ\text{C}$, a high concentration (2 to $4 \times 10^{23} \text{ m}^{-3}$) of small bubbles (1.5 to 4.5 nm diam) were formed uniformly in the matrix. Swelling was low ($< 0.2\%$) in both SA and CW materials irradiated to 30 dpa. In SA 316, cavity size increased, but the number density decreased with increasing irradiation temperature above 500°C. At 500°C, there was a mixture of bubbles and voids, but at 600°C, most of the cavities were voids. Maximum swelling (-5%) occurred at 500°C. By contrast, cavities in 20%CW specimens were much smaller, with diameters of 6 and 9 nm at 500 and 600°C, respectively, suggesting that they were primarily bubbles. The cavity number density in CW 316 at both 500 and 600°C ($\sim 1 \times 10^{22} \text{ m}^{-3}$) was about one order of magnitude less than at 400°C. Swelling increased slightly as irradiation temperature increased, peaking at 600°C (0.3%). These results indicate that SA 316 swells more than CW 316 at 500 and 600°C, but both SA and CW 316 are resistant to void swelling in HFIR at 400°C and below to 30 dpa.

6.3 Vanadium Alloys 222

6.3.1 Grain Boundary Chemistry of a V-15%Cr-5%Ti Alloy (Pacific Northwest Laboratory) 222

Phosphorus and sulfur grain boundary segregation has been measured in V-15%Cr-5%Ti using a high-resolution (50 nm) Auger electron spectrometer (AES). Surface coverages as high as 0.31 monolayers of phosphorus and 0.13 monolayers of sulfur were observed. A larger titanium concentration on the intergranular surfaces relative to cleavage surfaces could be explained by precipitates of titanium oxide or nitride observed by transmission electron microscopy (TEM). Also, a combined impurity segregation-hydrogen embrittlement was suggested by the percentage of intergranular fracture observed in the hydrogen-charged AES fracture samples.

6.3.2 The Microstructure of Annealed V-15Cr-5Ti (IFF ~ KFA Julich on assignment to ORNL and Oak Ridge National Laboratory) 230

The V-15Cr-5Ti has a bcc structure with a lattice parameter $a_0 = 0.301573 \pm 0.0001071 \text{ nm}$. Numerous small faceted precipitates were observed that are fcc with a composition $Ti_{0.9}V_{0.02}Ni_{0.6}C_{0.4}$. A smaller number of fcc, $M_{23}C_6$ -type, particles were also identified with a composition $(Cr_{0.6}Fe_{0.4})_{23}C_6$.

and $a_0 \approx 1.0621 \text{ nm}$. *Occasionally*, Ti-V phosphides and sulfides [approximate $\text{Ti}_{1.5}\text{V}_{0.25}\text{S}_{0.25}$] were found in the matrix. Some of the particles, especially those containing titanium, may also contain oxygen.

6.3.3 The Tensile Properties of Several Vanadium Alloys After Irradiation to 90 dpa in FFTF (Oak Ridge National Laboratory) 235

The tensile properties of three vanadium alloys have been measured after they were irradiated in the FFTF at 420°C to 90 dpa. The results showed that irradiation hardening saturated in the V-3Ti-1Si alloy after less than 10 dpa and after about 40 dpa for VANSTAR-7 and V-15Cr-5Ti. Implanted helium produced further slight increases in the yield strength after 90 dpa in VANSTAR-7 and V-3Ti-1Si, and caused further embrittlement of V-15Cr-5Ti. The fact that the total elongations for all three alloys were about the same as those measured earlier for 40 dpa was encouraging.

6.3.4 Influence of Neutron Irradiation on the Charpy Impact Properties of V-15Cr-5Ti (Westinghouse Hanford Company and Pacific Northwest Laboratory) 239

Vanadium alloys are being evaluated for fusion reactor first wall end blanket applications to achieve both low neutron activation and operating temperatures above those suitable for ferritic steels. Both pre- and postirradiation impact tests have been completed on miniature Charpy specimens of the alloy V-15Cr-5Ti in the annealed condition (1200°C/1 hr/air cool). Irradiation was conducted in lithium-filled T2M capsules at 365, 404, 520 and 600°C to doses ranging from 6 to 30 dpa. The ductile-to-brittle transition temperature was unexpectedly high in the unirradiated condition, on the order of 130°C. Impact tests demonstrate that irradiation induces a large upward shift in DBTT in this alloy. Fracture occurred primarily by transgranular cleavage in irradiated specimens at test temperatures as high as 240°C.

6.3.5 Strength, Ductility, and Ductile-Brittle Transition Temperature for MFR Candidate Vanadium Alloys (Argonne National Laboratory) 246

The dependence of the yield strength, tensile strength, elongation, and reduction in area on temperature for the V-15Ti-7.5Cr, V-20Ti, V-15Cr-5Ti, V-12Cr-5Ti, V-10Cr-5Ti, and V-3Ti-1Si alloys was determined from tensile tests at temperatures ranging from 25 to 700°C. The strength of the alloys increased with an increase of the combined Cr and Ti concentration. The total elongation for the alloys ranged between 20% and 33%. The reduction in area ranged from 30% to 90%. The ductile-to-brittle transition temperature (DBTT), which was determined from the temperature dependence of the reduction in area, was less than 25°C for the V-15Ti-7.5Cr, V-20Ti, and V-3Ti-1Si alloys. The DBTT for the V-10Cr-5Ti, V-12Cr-5Ti, and V-15Cr-5Ti alloys was also less than 25°C if these alloys were annealed to reduce the hydrogen concentration prior to the tensile test. If these latter alloys were not annealed prior to the tensile test, the DBTT ranged from 40°C to 90°C and the DBTT increased with an increase of the Cr concentration. Alloys with a Cr/Ti concentration ratio of <0.5 were less susceptible to hydrogen embrittlement.

6.4 Copper Alloys 254

6.4.1 Neutron Induced Swelling of Copper Alloys at 98 dpa and 450°C (Westinghouse Hanford Company and Pacific Northwest Laboratory) 254

An irradiation series on copper alloys in FFTF-MOTA at about 450°C has been completed. Four exposure levels were reached with the maximum at 98 dpa. Immersion density measurements of various copper alloys show swelling values ranging from 1 to 64% at 98 dpa. Copper dispersion-hardened with 0.25% Al₂O₃ (designated A125) and the precipitation-strengthened alloy M2C appear to be the most swelling resistant high conductivity alloys.

6.5 Environmental Effects on Structural Alloys 260

6.5.1 Corrosion and Mass Transfer in Lithium 12Cr-1MoVW Steel Systems (University of California - Los Angeles and Oak Ridge National Laboratory) 260

Data from weight change and surface analyses of 12Cr-1MoVW steel exposed to lithium in two modified thermal convection loops (TCLs) showed the importance of chromium depletion and chromium-containing nodule formation over certain temperature ranges. These reactions strongly affected the resulting mass transfer profile and the dependence of such on temperature.

Corrosion data are presented on nonmetallic element transfer and dissolution behavior of several vanadium alloys exposed to flowing lithium at 427, 482, and 538°C. The results indicate that chemical interactions between alloys elements and nitrogen and/or carbon in lithium play an important role in the corrosion behavior of these alloys. The influence of alloy composition and exposure conditions on corrosion of vanadium alloys is discussed.

7. SOLID BREEDING MATERIALS 271

7.1 Beatrix-I Irradiation Experiment (Pacific Northwest Laboratory) 272

A tritium solid breeder irradiation experiment was designed and fabricated to reach a goal exposure of 600 full power days in the fast neutron flux of the EBR-II reactor in order to obtain swelling, tritium retention, and stability data. Lithium ceramic pellets, spheres and single crystals from Europe, Japan and the USA are contained within 19 closed capsules. Burn-up levels from 10 to 30×10^{20} captures/lcc will be obtained during this irradiation at "isothermal" temperatures on 1 cm diameter pellets from approximately 500 to 900°C. Larger diameter pellets (1.6 to 2.3 cm) will produce large temperature gradients and centerline temperatures of over 1200°C. Characterization of these materials provided an assessment of current fabrication capabilities which exist for these materials.

7.2 Solid Breeder Materials Fabrication and Mechanical Properties (Argonne National Laboratory) 277

Samples of lithium orthosilicate were fabricated for mechanical properties tests. Ceramic-grade powder was synthesized from stoichiometric mixtures of lithium carbonate and amorphous silica. Samples were pressed from the powder and sintered in air at temperatures between 950 and 1100°C. Compression tests were conducted at constant cross-head speed in a furnace filled with argon. Temperatures ranged from 750 to 1000°C and strain rates were between 10^{-6} and 10^{-4} s⁻¹. A steady-state stress was obtained as a function of strain rate at each of three temperatures. The stress exponent was found to range from a value of -6.5 at 850°C to -3.3 at 950°C. Two manuscripts were prepared for the Proceedings of the American Ceramic Society Special Symposium on "Fabrication and Properties of Lithium Ceramics." Abstracts have been prepared for the 90th Annual Meeting of the American Ceramic Society, Nuclear Division, to be held in Cincinnati on May 1-5, 1988.

7.3 Adsorption, Dissolution, and Desorption Characteristics of the LiAlO₂-H₂O System (Argonne National Laboratory) 280

Isotherms at 673 and 773 K are presented for surface adsorption of H₂O(g) and for solubility of OH⁻ in LiAlO₂ as a function of H₂O(g) partial pressure. The Freundlich adsorption isotherms for 673 and 773 K, respectively, are:

$$\log(\theta) = (-1.590 \pm 0.691) + (0.497 \pm 0.064) \log(p_{H_2O})$$

and

$$\log(\theta) = (-1.112 \pm 0.061) + (0.497 \pm 0.052) \log(p_{H_2O})$$

where θ is the fraction of surface covered, and p_{H_2O} is the partial pressure H₂O(g) in Pascals. Hydroxide dissolution is exothermic. Depending on conditions, LiAl₂O₃ can be a second phase or a solute to give isotherms with slopes of 0.5 or 0.4, respectively. The hydroxide solubility isotherms for 673 and 773 K, respectively, are:

$$\log(x_{OH^-}) = (-4.667 \pm 0.096) + (0.399 \pm 0.088) \log(p_{H_2O})$$

and

$$\log(x_{OH^-}) = (-4.899 \pm 0.079) + (0.499 \pm 0.063) \log(p_{H_2O})$$

where x_{OH^-} is the mole fraction OH⁻. The rate of H₂O(g) evolution from LiAlO₂ showed the kinetics of the process to be second order in hydroxide with an activation energy of 14.7 ± 1.9 kcal (61.5 ± 7.9 kJ), a value less than that reported for H₂O(g) evolution from Li₂O or from LiOH.

7.4 Modeling of Tritium Transport in Ceramic Breeder Materials (Argonne National Laboratory) . . . 287

A computer model to predict tritium release from a ceramic breeder was developed which considers diffusion and desorption as the rate controlling mechanisms. This model performed much better than a pure diffusion model when predicting the tritium release under pure helium purge gas for Li_2SiO_3 samples from the LISA tritium release experiment. Work is now in progress to develop a more sophisticated model which will also include transport in the gas phase. Plans have also been made to investigate the effects of processes which currently are regarded as secondary in nature. These include grain boundary diffusion, trapping, etc., in order to determine their importance in developing an overall model for tritium transport and release.

8. CERAMICS 291

8.1 Neutron Irradiation Testing of Ceramic-to-Metal Seals (Hittman Materials and Medical Components, Inc., and Los Alamos National Laboratory) 292

Butt-type ceramic-to-metal seals made from (1) niobium bonded to alumina, along spinel, or an alumina/silicon nitride ceramic and (2) MACOR bonded to titanium were irradiated to a dose of 4×10^{23} n/m² at room temperature. The neutron source was the beam stop area of the Los Alamos Meson Physics Facility (LAMPF). Post-irradiation testing showed that hermeticity of all but the MACOR/Ti samples was retained, even after application of 6.9×10^6 Pa (1000 psi) of hydraulic pressure. Pressurization to failure showed that all seals were capable of withstanding much higher pressures without structural failure. All ceramic-to-niobium seals appear qualified for use near the first wall of the Compact Ignition Torus (CIT) for the full lifetime of that machine while MACOR/Ti seals should be usable for lower fluences, or the full fluence where leak tightness is not required.

8.2 Damage to Macor Glass-Ceramic From High-Dose 14 MeV Neutrons (Los Alamos National Laboratory) 294

Eight samples of MACOR machinable glass-ceramic were irradiated at room temperature to fluences between 4 and 10×10^{22} 14 MeV n/m² at RTNS-II. Post-irradiation measurements showed that electrical resistivity was little changed, but that swelling was significant. The latter results are interpreted in terms of differential swelling between the glassy and crystalline phases, implying a possible loss of strength in this dose range. These findings raise a question as to whether MACOR can retain its structural properties at neutron doses characteristic of lifetime exposure at the first wall of the Compact Ignition Torus. Further work on these samples, in progress, will help to answer that question.

8.3 Improved Computation of Dielectric Constants Measured by In-Waveguide Techniques (Los Alamos National Laboratory) 297

Brief details are presented for the derivation of a formula for calculating k from the frequency difference $\Delta f_n = f_{n+1} - f_n$ measured via the channel spectrum ("raw" data) for the transmission loss of a rectangular parallel-piped inserted within waveguide. Comparison is made in terms of the previously used formula adapted from "free-space" theory. Implications for fusion ceramics for "rf" windows are presented.

8.4 Model for Defect Aggregation and Swelling in Neutron-Irradiated Spinel (Los Alamos National Laboratory) 299

Samples of single-crystal spinel ($MgAl_2O_4$) were irradiated to neutron fluences up to 8×10^{22} n/m² [$E \geq 0.1$ MeV] at $\approx 50^\circ C$ in the Omega West Reactor. All the irradiated samples showed continued swelling out of reactor during storage at ambient room temperature. A model based on interstitial clustering has been developed that describes this post-irradiation swelling of spinel.

9. SUPERCONDUCTING MAGNET MATERIALS 305

No contributions received this reporting period

1. IRRADIATION FACILITIES, TEST MATRICES, AND EXPERIMENTAL METHODS

DESIGN AND FABRICATION OF HFIR-MFE RB* SPECTRALLY TAILORED IRRADIATION CAPSULES - A. W. Longest (Oak Ridge National Laboratory), J. E. Corum (Midwest Technical, Inc.), and O. W. Heatherly and K. R. Thoms (Oak Ridge National Laboratory)

OBJECTIVE

The objective of this work is to design and fabricate irradiation capsules for testing magnetic fusion energy (MFE) first-wall materials in the HFIR RB* positions. Japanese and U.S. MFE specimens are being transferred to RB* positions following irradiation to 7.5 dpa at temperatures of 60, 200, 330, and 400°C in ORR experiments ORR-MFE-6J and -7J.

SUMMARY

Design and fabrication of four HFIR-MFE RB* capsules (60, 200, 330, and 400°C) to accommodate MFE specimens preirradiated in spectrally tailored experiments in the ORR is proceeding satisfactorily. These capsule designs incorporate provisions for removal, examination, and reencapsulation of the MFE specimens at intermediate exposure levels en route to a target exposure level of 30 displacements per atom (dpa). With the exception of the 60°C capsule, where the test specimens will be in direct contact with the reactor cooling water, the specimen temperatures (monitored by 21 thermocouples) will be controlled by varying the thermal conductance of a small gap region between the specimen holder and the containment tube. Hafnium sleeves will be used to tailor the neutron spectrum to closely match the helium production-to-atom displacement ratio (14 appm/dpa) expected in a fusion reactor first wall.

Preparation of fabrication drawings for the 330 and 60°C capsules has been completed, and fabrication of parts for both capsules is nearing completion. Fabrication drawings for the 400 and 200°C capsules will be completed in 1988. Operation of the 330 and 60°C capsules is scheduled to begin in February 1988, and the other two (400 and 200°C) in October 1989.

PROGRESS AND STATUS

Introduction

A series of spectrally tailored irradiation capsules are being designed and fabricated as part of the U.S./Japan collaborative program for testing MFE first-wall materials in mixed-spectrum fission reactors. The test specimens (Fig. 1) will be irradiated in the new removable beryllium (RB*) facility¹ of the High Flux Isotope Reactor (HFIR).

The first four HFIR-MFE RB* capsules are designed to accommodate Japanese and U.S. MFE specimens preirradiated to ~7.5 dpa at temperatures of 60, 200, 330, and 400°C in the Oak Ridge Research Reactor (ORR) spectrally tailored experiments ORR-MFE-6J and ORR-MFE-7J. Details of these ORR experiments, including descriptions of the test matrix, mechanical property specimens, and techniques of spectral tailoring, have been reported elsewhere.^{2,3}

Spectral tailoring of the neutron flux to simulate in austenitic stainless steels the expected helium production-to-atom displacement ratio of 14 appm/dpa in the fusion reactor first wall is accomplished by varying the amount of neutron moderator and thermal neutron absorber materials surrounding the capsule. This controls the two-step ⁵⁸Ni thermal neutron reaction producing helium, while fast neutrons are simultaneously producing atomic displacements. In general, the neutron energy spectrum must be hardened as the irradiation progresses; this requires ongoing neutronics analysis support as provided for the ORR experiments.⁴

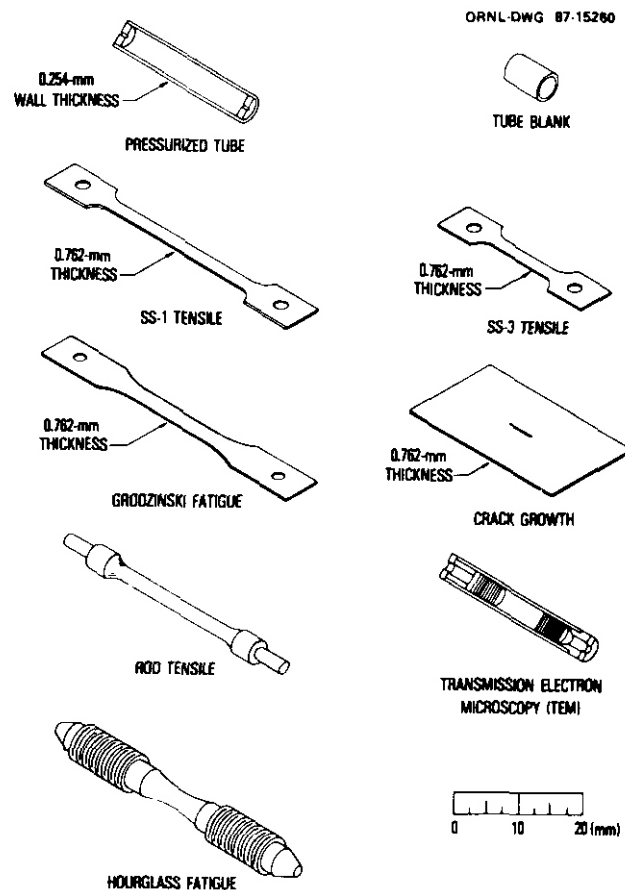


Fig. 1. Magnetic fusion energy materials specimens.

The HFIR-MFE RB* capsules are designed for insertion into any of the eight large-diameter holes (46 mm) of the HFIR RB* facility. Damage rates will increase from about 4 dpa/year in the ORR experiments to 10 dpa/year in the HFIR RB* facility (based on 100-MW HFIR power).

Test specimen loadings for the first four capsules are given in Table 1. Beginning in early 1988, these capsules will be irradiated in pairs (first the 60 and 330°C capsules, then the 200 and 400°C capsules) to a damage level of 20 dpa. After these four irradiations, the test specimens will be removed, examined, and approximately half of them re-encapsulated for irradiation to 30 dpa.

Table 1. Test specimen loadings for the HFIR MFE RB* capsules

Specimen type	Number of specimens in capsule			
	60°C	200°C	330°C	400°C
Pressurized tube	38	26	45	39
Tube blank	9	9	9	9
Transmission electron microscope tube				
Length, mm				
16.5	2	2	0	0
19.1	D	0	4	4
25.4	5	7	6	6
SS-1 tensile	90	83	76	64
SS-3 tensile	54	54	15	15
Grodzinski fatigue	56	24	56	40
Crack growth	30	30	10	10
Rod tensile	0	0	4	0
Hourglass fatigue	0	0	0	5

Facility description

The HFIR RB* capsule irradiation facility allows spectral tailoring of the neutron flux by placement of appropriate sleeves around the in-reactor section of the capsule. Hafnium absorber sleeves (42.2-mm-ID and 4.2-mm-thick) will be used for the first four capsules of the present U.S./Japan collaborative MFE materials testing program to tailor the neutron spectrum to closely match the helium production-to-atom displacement ratio (14 appm/dpa) expected in a fusion reactor first wall. Other new RB* capsule irradiation facility features, which have been incorporated into the capsule designs, include: (1) straight access into any of the eight 46-m-diam positions; (2) standard capsule lead tube design; (3) containment tube design parameters of 6.9 MPa external pressure differential at 93°C; and (4) 180° capsule rotation at the end of each reactor cycle to provide near uniform exposure to all specimens at a given elevation.

Capsule designs

Elevated temperature capsules (200, 330, and 400°C specimen temperatures) - The containment tube (38.1-mm OD) for the elevated temperature capsules is made of 6061-T6 aluminum in the in-reactor region and type 304L stainless steel in the upper region. The upper and lower sections of the containment tube are joined by a special aluminum-to-stainless-steel transition tube. An oxide-dispersion-strengthened aluminum alloy containing 6 to 8 mass % Al_2O_3 was selected for the specimen holders in the higher temperature capsules (330 and 400°C) to provide adequate strength and dimensional stability under the planned irradiation conditions; this alloy also meets requirements of high thermal conductivity (close to that of aluminum) and reasonably low density (2.74 g/cm³). Specimen temperatures (monitored by 21 type K thermocouples) will be controlled by varying the thermal conductance of a small gap region between the specimen holder and the containment tube.

The 330°C capsule (designated HFIR-MFE-330J-1) design is shown in Fig. 2. The general arrangement of the specimens in slots and holes in the solid aluminum alloy specimen holder is similar to that of the ORR-MFE-6J capsule design.⁵ However, gas gaps are generally smaller, and tolerances tighter, in the HFIR-MFE RB* capsules because of the higher gamma heat generation rates in the HFIR. Springs are employed to hold the sheet tensile, fatigue, and crack growth specimens in good contact with the holder. Special fixtures, Fig. 3, have been developed for hot cell assembly and loading of the radioactive specimens, in pairs with a spring in between each pair, into the slots.

The 330°C capsule will be cooled with 49°C reactor coolant water flowing downward at a flow rate of 1.5 L/s; water temperature rise will be ~8°C. The specimen holder temperature will be controlled by adjusting the composition of a flowing mixture of helium and neon (or helium and argon) in the control gas gap between the specimen holder outer sleeve and the containment tube. A purge of helium is maintained through the specimen slots and holes to aid heat removal by conduction from those regions.

The axial temperature gradients caused by curvature in the gamma heating rate profile and end heat losses are minimized by stepping the control gas gap thickness and placing stainless steel spacers at the top and bottom ends of the specimen holder to enhance heat generation at the ends. Another complication in maintaining uniform specimen temperatures is that gamma heat generation measurements⁶ show that the axial distribution changes significantly during the course of a given reactor fuel cycle (Fig. 4). However, calculated temperature distributions in Fig. 5, using the axial gamma heat profiles of Fig. 4, indicate that the temperature of all specimens should be controllable to within ±25°C of 330°C, which satisfies the temperature criterion for these experiments. In these calculations, only the lowermost rod tensile specimen was modeled in detail; the remaining specimens were homogenized with the specimen holder.

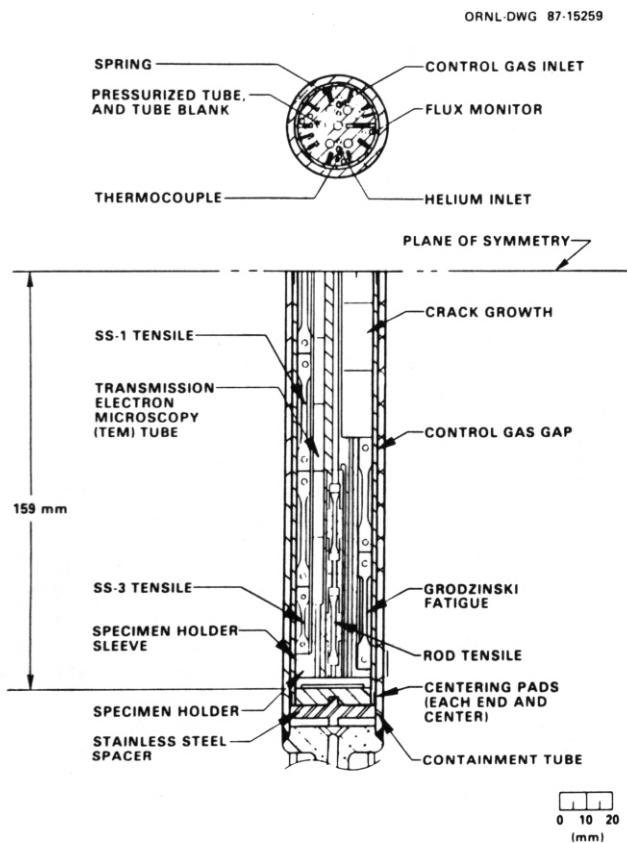


Fig. 2. Lower half of the HFIR-MFE 330J-1 capsule.

The lower temperature at the specimen holder plane of symmetry is caused by centering pads on the specimen holder sleeve surface; other centering pads are located at each end of the sleeve.

The axial fast-neutron-exposure variation over the 0.31-m specimen loading length is predicted to be -30%. Exposure variation across a given capsule diameter will be minimized by rotating the capsule 180° at the end of each 28-day reactor fuel cycle.

Design of the 400°C capsule will be similar to the 330°C capsule.

The 200°C capsule presents a special design problem because it is difficult to remove the large amount of gamma heat generated in the capsule while, at the same time, controlling the operating temperature at 200°C. An aluminum alloy specimen holder with a conventional temperature control gas gap would require a gas gap of ~0.029 mm at operating temperature; a gap this small may be difficult to obtain. Various other possible designs have been considered, one of which is the use of very low density material for the specimen holder, such as 10% dense Duocel (manufactured by Energy Research and Generation, Inc., Oakland, California) aluminum which would generate less heat and permit use of a larger gas gap. Duocel aluminum may have adequate thermal conductance, but it needs to be tested to determine its dimensional stability under the irradiation conditions planned. A test piece of Duocel aluminum will be included in the 330°C capsule at a location above the MFE specimen holder where its temperature will be in the vicinity of 200°C.

YP-4258

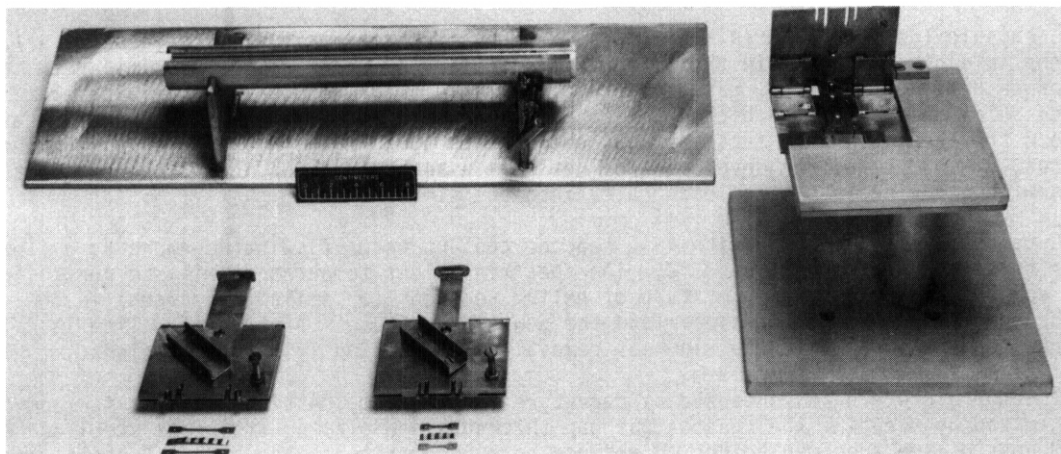


Fig. 3. Hot cell specimen loading fixtures.

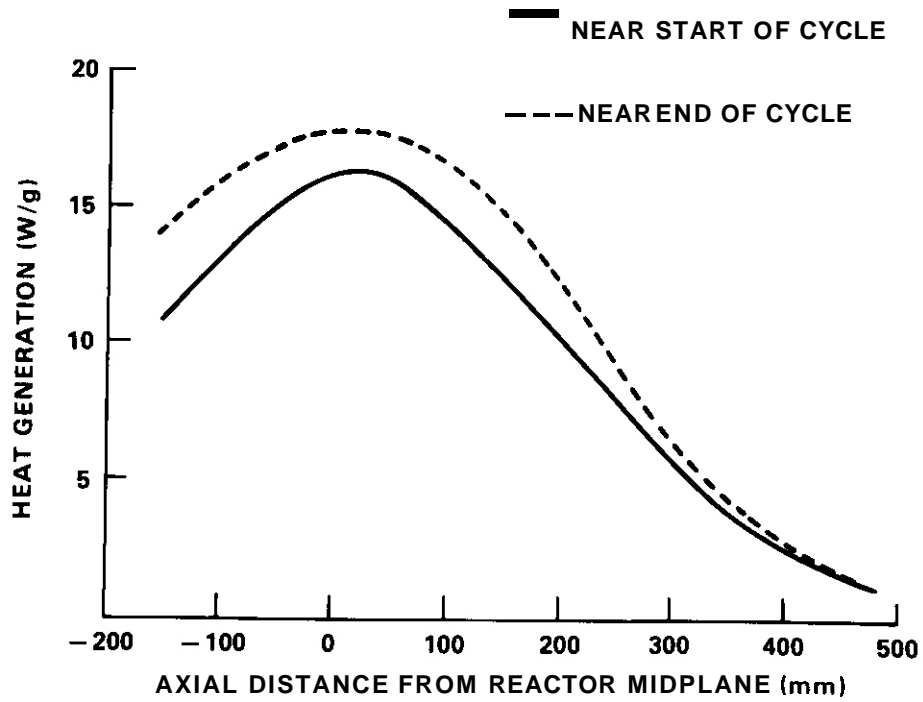


Fig. 4. Measured heat generation in stainless steel in the HFIR RB5 position.

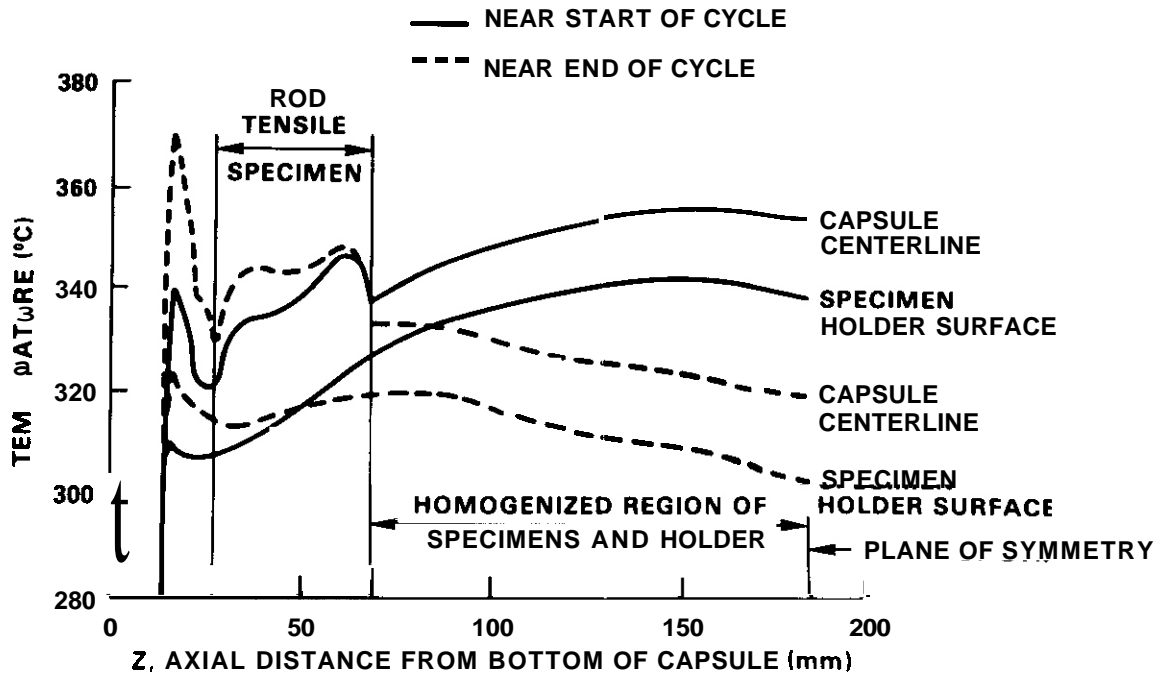


Fig. 5. Calculated temperature profiles for the lower half of the HFIR-MFE-330J-1 capsule.

Also under investigation as a possible design concept for the 200°C capsule is the use of a relatively large temperature control gas gap (4.76 mm) filled with a binary (coarse/fine) mixture of metallic microspheres. In this concept, temperature would be controlled primarily by varying the inert gas pressure (and hence the mean free path of the gas molecules) in the particle bed to change its thermal conductance. Development testing of this design concept is in progress; a decision whether to use it for the 200°C capsule will be made by mid-1988.

A backup design concept for the 200°C capsule is to utilize electrical heaters for temperature control. In this approach, gas gap thicknesses would be reduced to the minimum needed for assembly in the hot cell so that the capsule would operate below 200°C under the condition of no heater power. Disadvantages of this design concept, in addition to added costs of heaters, are the additional temperature gradients induced by the electrical heaters and the possibility that high heater power may be required because of the uncertainties in small-gap thermal conductances and in the gamma heating rate in the new facility.

60°C specimen temperature capsule - The 60°C capsule, designated HFIR-MFE-60J-1, is uninstrumented with the test specimens in contact with the reactor coolant water. A horizontal cross section through this capsule is shown in Fig. 6. Although the general configuration is similar to the elevated temperature capsules, additional coolant flow channels are provided in this design to cool the capsule internally as well as externally. The various coolant passages were designed to permit water flow rates of 0.63 L/s over the capsule surface, 0.51 L/s between the capsule tube and the specimen holder, and 0.063 L/s through each of the five interior specimen holes. Resulting specimen temperatures are predicted to be within $\pm 10^\circ\text{C}$ of 60°C.

Capsule fabrication

All parts for the 330°C capsule have been fabricated with the exception of the complex specimen holder, which is scheduled to be completed in mid-October 1987. Parts for the 60°C capsule are on order and are expected to be received by the end of October 1987. Hafnium sleeves for both capsules are scheduled to be received by the end of 1987. Capsule assembly will begin in early October 1987.

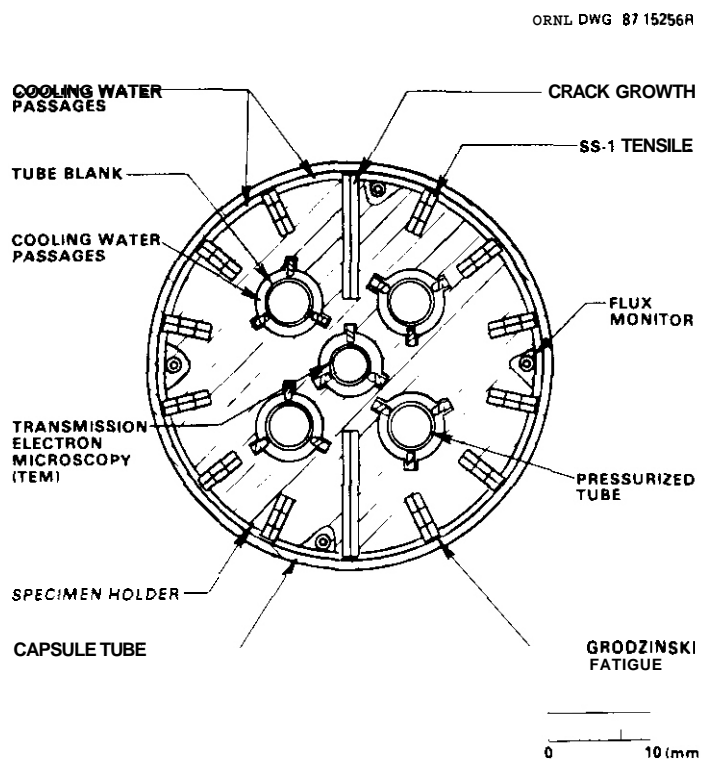


Fig. 6. Horizontal section through the HFIR-MFE-60J-1 capsule.

FUTURE WORK

Design and preparation of fabrication drawings for the 200 and 400°C HFIR-MFE RB* capsules are scheduled to be completed by the end of 1988. Preparation of fabrication drawings for later re-encapsulation of MFE specimens will be an intermittent effort.

Fabrication of parts for the first four HFIR-MFE RB* capsules will continue into 1988 and 1989.

REFERENCES

1. K. R. Thoms et al., "HFIR Irradiation Facilities Improvements -- Completion of the HIFI Project." Proc. Third Intern. Conf. on Fusion Reactor Materials, Karlsruhe, 1987.
2. J. L. Scott et al., pp. 12-20 in ADIP Semiannu. Prog. Rep. March 31, 1985, DOE/ER-0045/14, U.S. DOE, Office of Fusion Energy.
3. J. L. Scott et al., Second Annual Prog. Rep. on United States-Japan Collaborative Testing in the High Flux Isotope Reactor and the Oak Ridge Research Reactor Sept. 30, 1985, ORNL/TM-10102.
4. R. A. Lillie, pp. 36-38 in Fusion Reactor Materials Semiann. Prog. Rep. Sept. 30, 1986, DOE/ER-0313/1, U.S. DOE, Office of Fusion Energy.
5. J. A. Conlin, Irradiation Capsule for Testing Magnetic Fusion Reactor First-Wall Materials at 60 and 200°C, ORNL/TM-9644, Oak Ridge National Laboratory (August 1985).
6. R. L. Senn and W. R. Mixon, Nucl. Technol. 12 (1971) 235.

OPERATION OF THE U.S./JAPAN ORR SPECTRAL TAILORING EXPERIMENTS — I. 1. Siman-Tov (Oak Ridge National Laboratory)

OBJECTIVE

The experiments in the U.S./Japan collaborative testing program in the Oak Ridge Research Reactor (ORR) contain austenitic stainless steel alloys for possible use as first-wall and blanket structural materials in fusion reactors. These alloys will be irradiated with mixed-spectrum neutrons, and with spectral tailoring to achieve the helium-to-displacement-per-atom (He/dpa) ratios predicted for fusion service,

SUMMARY

The irradiation of the ORR-MFE-6J and -7J experiments was terminated during the previous reporting period on March 26, 1987, when the ORR was shut down by DOE order. The total accumulated irradiation time is 474.1 full power days (FPO) at 30 MW reactor power. With future operation of the ORR so uncertain, the decision to proceed with encapsulation into HFIR RB* capsules was agreed upon by the United States and Japan in June 1987. The capsules were removed from the core on June 29, 1987. Disassembly of the 60°C portion of the MFE-6J was completed August 25, 1987, and the specimens were given to the Metals and Ceramics Division personnel for preparation for reinsertion into the HFIR-MFE-60J-1 capsule. Capsule MFE-7J and the 200°C portion of MFE-6J are in the ORR pool awaiting disassembly.

PROGRESS AND STATUS

The details of the U.S./Japan collaborative irradiation program have been described previously.¹⁻⁶

Capsules MFE-6J and -7J were removed from the ORR core on June 29, 1987. This change was the result of the decision to terminate the operation of the ORR. Disassembly of the MFE-6J (60°C) capsule started on August 11, 1987, and was completed on August 25. The specimens were turned over to Metals and Ceramics Division personnel for inspection and preparation for insertion in the HFIR RB* position. The remaining capsules are in the ORR pool. The disassembly of MFE-7J was delayed because of difficulties in procuring a cutter. Now the disassembly is planned for late October 1987 so that the 330°C specimens will be ready for reencapsulation into HFIR-MFE-330J when the HFIR restarts.

REFERENCES

1. J. A. Conlin and J. W. Woods, "Irradiation Experiments for the U.S./Japan Collaborative Testing Program in HFIR and ORR," p. 37 in ADIP Semiannu. Progr. Rep. March 31, 1984, DOE/ER-0045/12, USDOE Office of Fusion Energy.
2. J. A. Conlin and J. W. Woods, "Irradiation Experiments for the U.S./Japan Collaborative Testing Program in HFIR and ORR," pp. 66-67 in ADIP Semiannu. Progr. Rep. Sept. 30, 1984, DOE/ER-0045/13, USDOE Office of Fusion Energy.
3. I. 1. Siman-Tov, J. A. Conlin and J. W. Woods, "Irradiation Experiments for the U.S./Japan Collaborative Testing Program in HFIR and ORR," p. 6 in ADIP Semiannu. Progr. Rep. March 31, 1985, DOE/ER-0045/14, USDOE Office of Fusion Energy.
4. I. I. Siman-Tov, "Assembly and Operation of the U.S./Japan Spectral Tailoring Experiments," p. 41 in ADIP Semiannu. Progr. Rep. Sept. 30, 1985, DOE/ER-0045/15, USDOE Office of Fusion Energy.
5. I. I. Siman-Tov, Fusion Reactor Materials Semiannu. Progr. Rep. Sept. 30, 1986, DOE/ER-0313/1, USDOE Office of Fusion Energy.
6. I. I. Siman-Tov, "Operation of the U.S./Japan ORR Spectral Tailoring Experiments," p. 18 in Fusion Reactor Materials Semiannu. Progr. Rep. March 31, 1987, DOE/ER-0313/2, USDOE Office of Fusion Energy.

STATUS OF U.S./JAPAN COLLABORATIVE PROGRAM PHASE II HFIR TARGET CAPSULES — R. L. Senn (Oak Ridge National Laboratory)

OBJECTIVE

The objective of this program is to determine the response of U.S. and Japanese austenitic stainless steels to the combined effects of displacement damage and helium generation at temperatures in the range of 300 to 600°C. Since a basic understanding is sought in addition to an engineering data base, many advanced alloys and model alloys are included in the program.

SUMMARY

During this reporting period, a revised matrix for Phase II HFIR target capsules JP-9 through -16 was developed. An extensive thermal analysis for the new designs was completed to support redesign of the capsules, based on the new operating level of 85 MW for the HFIR. These new designs were completed and parts are on hand in preparation for assembly of all eight capsules during the first quarter of FY 1988. All eight capsules will be installed in the HFIR simultaneously beginning with the first full power cycle of the HFIR.

PROGRESS AND STATUS

The program for U.S./Japan collaborative testing of the Phase II HFIR target capsules consists of eight capsules, JP-9 through -16. The mutually agreed upon matrix is shown in Fig. 1. This matrix has been somewhat modified from that previously reported,^{1,2} but still retains the space allocations and cost sharing that were shown earlier.

U.S./Japan Phase II HFIR Target Capsules

Introduction

Because of the need to irradiate 25.4-mm-long type SS-3 flat tensile specimens and 45-mm-long welded flat sheet specimens in addition to the previously irradiated TEM, fatigue, and tensile bar specimens, new specimen holders were required and a new experiment matrix was developed.

A complete new thermal analysis was required for the Phase II capsules because of the change in HFIR operating power level from 100 to 85 MW.

Experiment Matrix

The final Phase II experiment matrix is shown in Fig. 1. These experiments incorporate transmission electron microscopy (TEM), tensile bar (TB), hourglass fatigue (F), SS-3 sheet tensile [T(2) and T(4)], and welded sheet (SHEET) specimens. Specimen material, design specimen temperatures, and the location of the various specimen holders are shown on the figure. An attempt was made to maintain the previously used position numbering system (from 1 at the top through 11 at the bottom) by assigning positions 1A, 1B, etc., to the shorter specimens.

Thermal Analysis

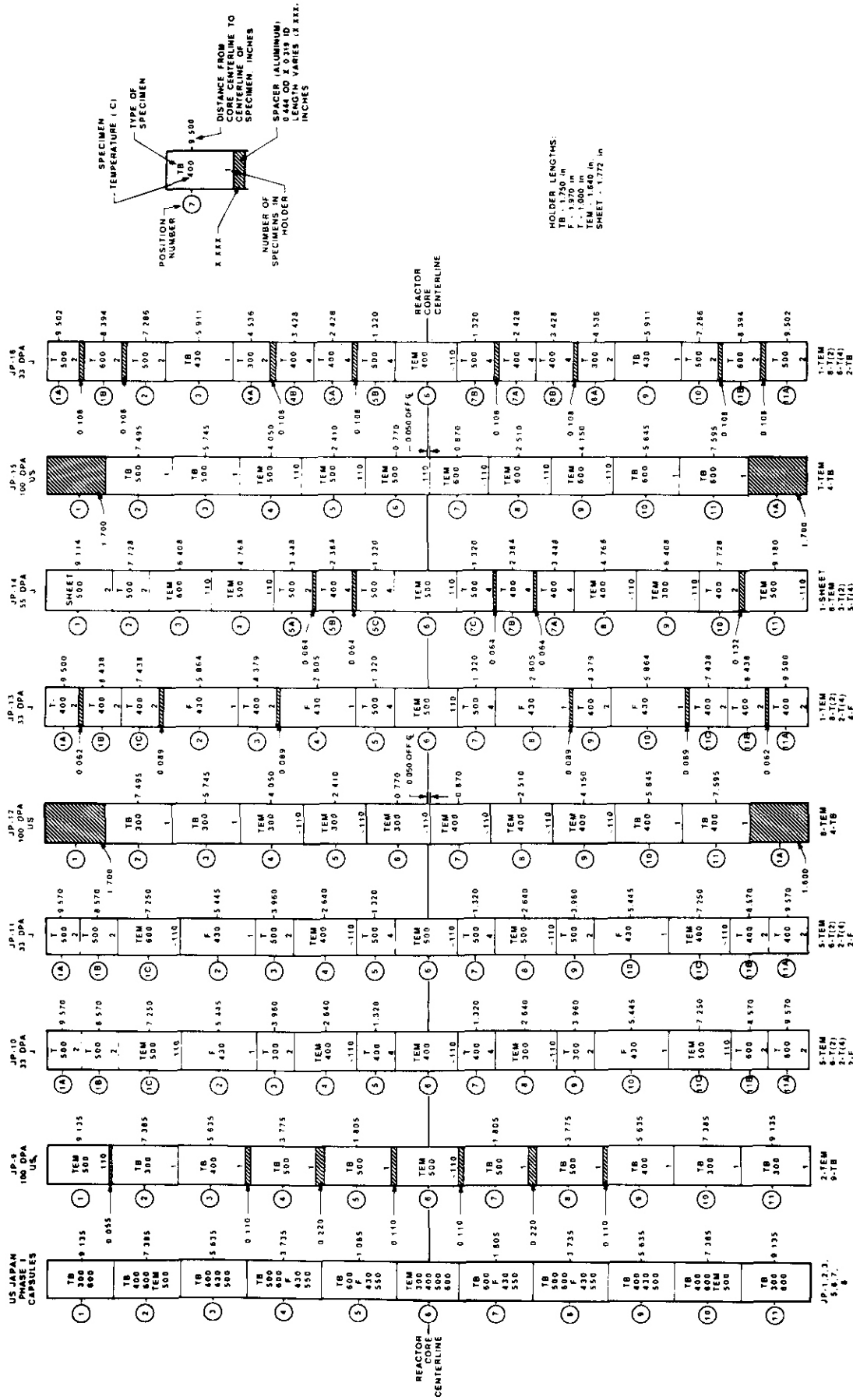
A complete thermal analysis was required for these new capsules because of the change in HFIR operating power level from 100 to 85 MW. New gas gaps required to achieve the specified temperatures were calculated using GENGTC,³ a one-dimensional heat transfer code. Heat generation rates from neutronic heating were assumed to be 85% of those measured in the TTT capsule3 with the same profile. Neutronic heating was assumed to be the same for both aluminum and stainless steel in the HFIR target region for specimen temperature calculations.⁴ The following polynomial, derived from the results of the TTT capsule test,⁵ was used to calculate heat generation rates (HGEN) in the various materials in the capsules:

$$\text{HGEN} = C(0.99768) - (6.19595E - 3*Z) - (6.987997E - 3*Z^2)] \times 54.6 \times 0.85 ,$$

where

Z = specimen distance from reactor horizontal midplane in inches.

The results were checked for the new specimen holder designs with HEATING6,⁶ a three-dimensional heat transfer code. The results from the two methods of calculating the gas gaps and resultant specimen temperatures were in good agreement, providing confidence in the GENGTC calculations used for all of the holders.



US/J PHASE II TARGET CAPSULES

Fig. 1. U.S./Japan collaborative program Phase II HFIR target capsule matrix.

The final gas gaps resulting from the calculations along with the positions, specimen temperatures, and other design information are presented in Tables 1 through 7 for JP-9 through -16.

Table 1. HFIR TARGET CAPSULE JP-0 THERMAL ANALYSIS

POSITION		HEAT GEN.		HEAT GEN. SPECIMEN		CAPSULE JP-9	
NO.	ELEVATION FROM C/L INCHES	HGEN SST W/GM	HGEN AL W/GM	TYPE **	SPECIMEN TEMP. C	COLD GAF IN.	
1	9.135	17.03	17.03	TEM	500	0.0420	
2	7.900	24.10	24.10	TOP	300	0.0098	
	7.385	26.76	26.76	TB		0.0209	
	6.870	29.26	29.26	BOT.		0.0078	
3	6.150	32.46	32.46	TOP	400	0.0113	
	5.635	34.54	34.54	TB		0.0257	
	5.120	36.46	36.46	BOT.		0.0198	
4	4.290	39.19	39.19	TOP	500	0.0132	
	3.775	40.67	40.67	TB		0.0317	
	3.260	41.97	41.97	BOT.		0.0122	
5	2.320	43.92	43.92	TOP	500	0.0116	
	1.805	44.74	44.74	TB		0.0277	
	1.290	45.40	45.40	BOT.		0.0111	
6	0.000	46.30	46.30	TEM	500	0.0199	
7	1.290	45.40	45.40	BOT.	500	0.0111	
	1.805	44.74	44.74	TB		0.0277	
	2.320	43.92	43.92	TOP		0.0116	
8	3.260	41.97	41.97	BOT.	500	0.0122	
	3.775	40.57	40.67	TB		0.0317	
	4.290	39.19	39.19	TOP		0.0132	
9	5.120	36.46	36.46	BOT.	400	0.0198	
	5.635	34.54	34.54	TB		0.0257	
	6.150	32.46	32.46	TOP		0.0113	
10	6.870	29.26	29.26	BOT.	300	0.0078	
	7.385	26.76	26.76	TB		0.0209	
	7.900	24.10	24.10	TOP		0.0098	
11	8.620	20.10	20.10	BOT.	300	0.0122	
	9.135	17.03	17.03	TB		0.0392	
	9.650	13.79	13.79	TOP		0.0188	

** F = FATIGUE SPECIMENS, TEN = TEN DISK SPECIMENS, TB = TENSILE BAR SPECIMENS
 T(2) = TWO SS-3 FLAT TENSILE SPECIMENS/HOLDER, T(4) = FOUR SS-3 FLAT TENSILE SPECIMENS/HOLDER
 ASSUMES 85 MW REACTOR POWER (85% NEUTRONIC HEAT) AND SAME FOR BOTH ALUMINUM AND STAINLESS STEEL.

US CAPSULE, DUG. X2E41517-0025 \123\USJP\JP9THERM R. L. Senn

Table 2. HFIR TARGET CAPSULES JP-10, -11 THERMAL ANALYSIS

POSITION	HEAT GEN.		HEAT GEN.		SPECIMEN TYPE **	CAPSULE JP-10		CAPSULE JP-11		
	NO.	ELEVATION	HGEN	HGEN		SPECIMEN	COLO	SPECIMEN	COLO	SPECIMEN
		FROM C/L INCHES	SST W/GM	AL W/GM			TEMP. C	GAP IN.	TEMP. C	GAP IN.
1A	9.570	14.31	14.31	T(2)	500	0.0188	500	0.0188		
1B	8.570	20.30	20.39	T(2)	500	0.0120	500	0.0120		
1C	7.250	27.43	21.43	TEM	500	0.0227	600	0.0315		
1 2T	5.945	33.31	33.31			0.0070		0.0070		
2	5.445	35.27	35.27	F	430	0.0155	430	0.0155		
2B	4.945	37.07	37.07			0.0070		0.0070		
3	3.960	40.16	40.16	T(2)	300	0.0023	500	0.0059		
4	2.640	43.32	43.32	TEM	400	0.0085	400	0.0085		
5	1.320	45.37	45.37	T(4)	400	0.0034	500	0.0052		
6	0.000	44.30	46.30	TEM	400	0.0078	500	0.0119		
7	1.320	45.31	45.37	T(4)	400	0.0034	500	0.0052		
8	2.640	43.32	43.32	TEM	300	0.0048	500	0.0128		
9	3.960	40.16	40.16	T(2)	300	0.0023	500	0.0059		
10T	4.945	37.07	37.07			0.0070		0.0070		
10	5.445	35.27	35.27	F	430	0.0155	430	0.0155		
10B	5.945	33.31	33.31			0.0070		0.0070		
11C	7.250	27.43	27.43	TEM	500	0.0227	400	0.0152		
11B	8.570	20.39	20.39	T(2)	600	0.0167	400	0.0082		
11A	9.570	14.31	14.31	T(2)	600	0.0260	400	0.0120		

** f = FATIGUE SPECIMENS, TEM = TEM DISK SPECIMENS, TB = TENSILE BAR SPECIMENS. T(2) = TWO SS-3 FLAT TENSILE SPECIMENS/HOLDER, T(4) = FOUR SS-3 FLAT TENSILE SPECIMENS/HOLDER

ASSUES 85 MW REACTOR POWER (85% NEUTRONIC HEAT) AND SAME FOR BOTH ALUMINUM AND SST

J CAPSULES, 33 dpa each. DWG. X2E41517-0026 (JP-10), -0027 (JP-11)

R. L. Senn

Table 3. HFIR TARGET CAPSULE JP-12 THERMAL ANALYSIS

POSITION NO.	HEAT GEN.		HEAT GEN.		SPECIMEN TYPE **	CAPSULE SPECIMEN TEMP. C	JP-12 COLD GAP IN.
	ELEVATION FROM C/L INCHES	HGEN SST W/GM	HGEN AL W/GM	AL W/GM			
1	9.099	17.25	17.25		SPACER		
2 T							0.00%
2	7.495	26.21	26.21		TB	300	0.0215
2 B							0.0060
3 T							0.0070
3	5.745	34.11	34.11		TB	300	0.0150
3 B							0.0060
4 T							
4	4.050	39.90	39.90		TEM	300	0.0055
4 B							
5 T							
5	2.410	43.75	43.75		TEM	300	0.0050
5 B							
6 T							
6	0.770	45.89	45.89		TEM	300	0.0045
6 B							
7 T							
7	0.870	45.81	45.81		TER	400	0.0080
7 B							
8 T							
8	2.510	43.57	43.57		TEM	400	0.0085
8 B							
9 T							
9	4.150	39.61	39.61		TEM	400	0.0095
9 B							
10 B							0.0105
10	5.845	33.71	33.71		TB	400	0.0275
10 T							0.0115
11 B							0.0135
11	7.595	25.70	25.70		TB	400	0.0405
11 T							0.0165
12	9.127	17.08	17.08		SPACER		

** F = FATIGUE SPECIMENS. TEM = TEM DISK SPECIMENS. TB = TENSILE BAR SPECIMENS
T(2) = 2 SS-J FLAT TENSILE SPEC./HOLDER, T(4) = 4 SS-3 FLAT TENSILE SPEC./HOLDER.

ASSUMES 85 MW REACTOR POWER (85% NEUTRONIC HEAT) AND SAME FOR BOTH ALUMINUM AND SST
US CAPSULE, 100 dpa; THERMAL ANALYSIS FROM I. I. Simon-Tov's CTR-57.
\123\USJP\JP12TH Dwg. X2E41517-0044 R. L. Seem

Table 4. HFIR TARGET CAPSULE JP-13 THERMAL ANALYSIS

POSITION	HEAT GEN.	HEAT GEN.	SPECIMEN	CAPSULE	JP-13	
NO	ELEVATION FROM C/L INCHES	HGEN SST W/GM	HGEN AL W/GM	TYPE **	SPECIMEN TEMP. C	COLD 6AP IN.
1A	9.500	14.75	14.75	T(2)	400	0.0116
1B	8.438	21.14	21.14	T(2)	400	0.0078
1C	7.438	26.50	26.50	T(2)	400	0.0061
2T	6.364	31.54	31.54			0.0075
2	5.864	33.64	33.64	F	430	0.0170
2B	5.364	35.57	35.57			0.0075
3	4.379	38.92	38.92	T(2)	400	0.0041
4T	3.105	42.33	42.33			0.0055
4	2.805	42.98	42.98	F	430	0.0125
4B	2.305	43.94	43.94			0.0055
5	1.320	45.37	45.37	T(4)	500	0.0052
6	0.000	46.30	46.30	TEM	500	0.0119
7	1.3211	45.37	45.37	T(4)	500	0.0052
8T	2.305	43.94	43.94			0.0055
8	2.805	42.98	42.98	F	430	0.0125
8B	3.105	42.33	42.33			0.0055
9	4.379	38.92	36.92	T(2)	400	0.0041
10T	5.364	35.57	35.57			0.0075
10	5.864	33.64	33.64	F	430	0.0170
10B	6.364	31.54	31.54			0.0075
11C	7.438	26.50	26.50	T(2)	400	0.0061
11B	8.438	21.14	21.14	T(2)	400	0.0076
11A	9.500	14.75	14.75	T(2)	400	0.0116

** F = FATIGUE SPECIMENS, TEM = TEM DISK SPECIMENS, TB = TENSILE BAR SPECIMENS
T(2) = TWO SS-3 FLAT TENSILE SPECIMENS/HOLDER, T(4) = FOUR SS-3 FLAT TENSILE SPECIMENS/HOLDER.

ASSUMES 85 MW REACTOR POWER (85% NEUTRONIC HEAT) AND SAME FOR BOTH ALUMINUM AND SST

J CAPSULE, 33 dpa DUG. X2E41517-0045 E:\1238\JP13THERM R. L. Senn

Table 5. HFIR TARGET CAPSULE JP-14 THERMAL ANALYSIS

POSITION	HEAT GEN.	HEAT GEN.	SPECIMEN	CAPSULE	JP-14	
NO.	ELEVATION	HGEN	HGEN	SPECIMEN	COLD	
	FROM C/L	SST	AL	**	TEMP.	
	INCHES	W/GM	W/GM		C	
					IN.	
1	9.114	17.16	17.16	SHEET	500	0.0145
2	7.728	25.01	25.01	T(2)	500	0.0097
3	6.408	31.35	31.35	TEM	600	0.0267
4	4.768	37.67	37.67	TEM	500	0.0153
5A	3.448	41.51	41.51	T(2)	500	0.0057
5B	2.384	43.80	43.80	T(4)	400	0.0036
5C	1.320	45.31	45.37	T(4)	500	0.0052
6	0.000	40.30	46.30	TEM	500	0.0119
7c	1.320	45.37	45.37	T(4)	500	0.0052
7B	2.384	43.80	43.80	T(4)	400	0.0036
7A	3.448	41.51	41.51	T(4)	400	0.0038
8	4.768	37.67	31.67	TEM	400	0.0103
9	6.408	31.35	31.35	TEM	300	±1.0075
10	7.728	25.01	25.01	T(2)	400	0.0065
11	9.180	16.75	16.75	TEM	500	0.0426

** F = FATIGUE SPECIMENS, TEM = TEM DISK SPECIMENS, TB = TENSILE BAR SPECIMENS
 1121 = TWO SS-3 FLAT TENSILE SPECIMENS/HOLDER, T(4) = FOUR SS-3 FLAT TENSILE
 SPECIMENS/HOLDER.

ASSUMES 85 MW REACTOR POWER (85% NEUTRONIC HEAT) AND SAUE FOR BOTH ALUMINUM AND SST

J CAPSULE, 55 dpa DWG. X2E41517-0046 \E:\123B\JP14THERM R. L. Senn

Table 7. HFIR TARGET CAPSULE JP-16 THERMAL ANALYSIS

POSITION NO.	HEAT GEN.		HEAT GEN.		SPECIMEN TYPE **	CAPSULE SPECIMEN TEUP. C	JP-16 COLD GAP IN.
	ELEVATION FROM C/L INCHES	HGEN SST W/GM	HGEN AL W/GM	HGEN W/GM			
1A	9.502	14.74	14.74		T(2)	500	0.0174
1B	8.394	21.39	21.39		T(2)	600	0.0158
2	7.286	27.26	27.26		T(2)	500	0.0088
3	6.426	31.27	31.27		TOP	430	0.0133
	5.911	33.45	33.45		TB		0.0312
	5.396	35.45	35.45		BOT		0.0115
4A	4.536	38.43	38.43		T(2)	300	0.0024
4B	3.428	41.56	41.56		T(4)	400	0.0380
5A	2.428	43.72	43.72		T(4)	400	0.0036
5B	1.320	45.37	45.37		T(4)	800	0.0052
6	0.000	46.30	46.30	TEM	TEM	400	0.0078
7B	1.320	45.37	45.37		T(4)	500	0.0052
7A	2.428	43.72	43.72		T(4)	400	0.0036
8B	3.428	41.56	41.56		T(4)	400	0.0038
8A	4.536	38.43	38.43		T(2)	300	0.0024
9	5.396	35.45	35.45		BOT	430	0.0115
	5.911	33.45	33.45		TB		0.0312
	6.426	31.27	31.27		TOP		0.0133
10	1.268	27.35	27.35		T(2)	500	0.0088
11B	8.394	21.39	21.39		T(2)	400	0.0158
11A	9.502	14.74	14.74		T(2)	500	0.0174

** F = FATIGUE SPECIMENS. TEM = TEM DISK SPECIMENS, TB = TENSILE BAR SPECIMENS
T(2) = TWO SS-3 FLAT TENSILE SPECIMENS/HOLDER, T(4) = FOUR SS-3 FLAT TENSILE SPECIMENS/HOLDER.

ASSUMES 85 MW REACTOR POWER (85% NEUTRONIC HEAT) AND SAME FOR BOTH ALUMINUM AND SST

J CAPSULE, 33 dpa. DUG. X2E41417-0048 E:\1238\JP16THER R. L. Senn

New Design Features

New designs were required for specimen holders to contain two and four SS-3 sheet tensile specimens and two welded sheet specimens. Slight modifications were made to the previously used TEM specimen holder designs. Details are discussed below.

T(2) – This specimen holder assembly, shown in Fig. 2, is used to hold two SS-3 sheet specimens back to back in various capsule positions. The filler pieces are made of the same material as the specimen, while the split holder and outer tube are made of HT-9 alloy.

T(4) – This specimen holder assembly, shown in Fig. 3, is used to hold four SS-3 sheet tensile specimens in one assembly in various capsule positions. The design is similar to the T(2) design with the addition of a center post of HT-9 alloy.

SHEET – This specimen holder assembly, shown in Fig. 4, is used to hold two of the rectangular welded sheet specimens and is essentially the same as the T(2) assembly, except longer.

TEM – This assembly, shown in Fig. 5, is the same as that used for previous Phase I capsules except for minor modifications of the centering devices on each end and adjustment of the gas gaps for temperature control. The end cap changes were made to aid in the final assembly.

TB – The tensile bar specimen assembly, shown in Fig. 6, is the same as that used for previous Phase I capsules. The gas gaps were recalculated to achieve the required temperatures for the various locations at the new 85 MW operating level.

F – The hourglass fatigue specimen assembly, shown in Fig. 7, is also the same as that used previously, except for adjusted gas gaps.

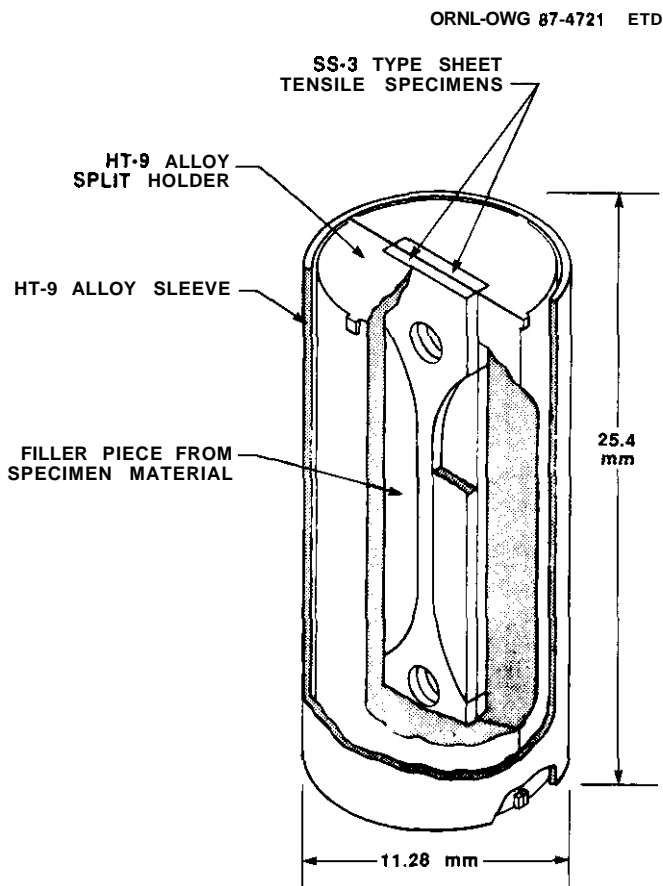


Fig. 2 Typical T(2) specimen holder assembly for U.S./Japan Phase II HFIR target capsules.

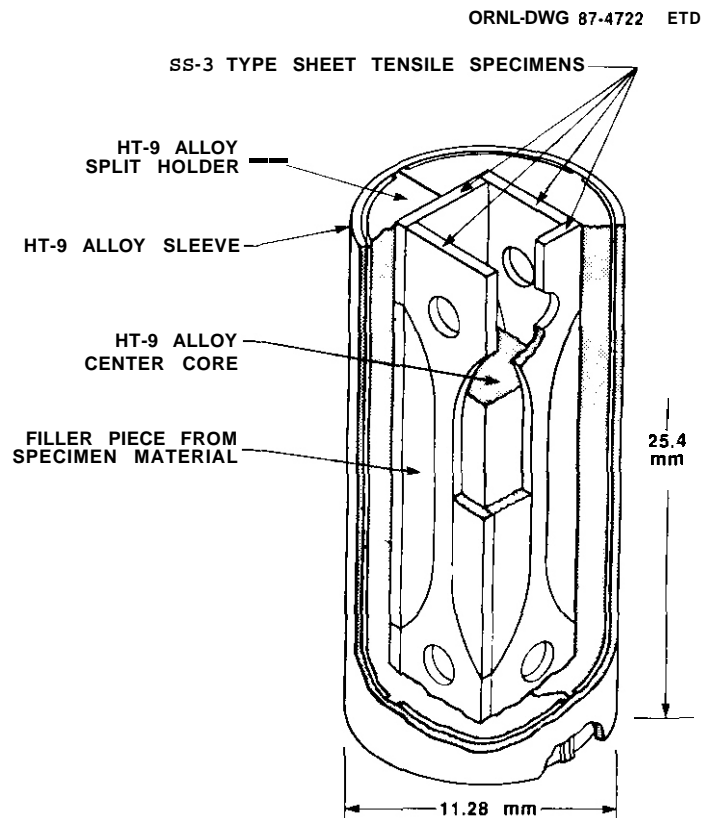


Fig. 3. Typical T(4) specimen holder assembly for U.S./Japan Phase II HFIR target capsules.

ORNL-DWG 87-4723 ETD

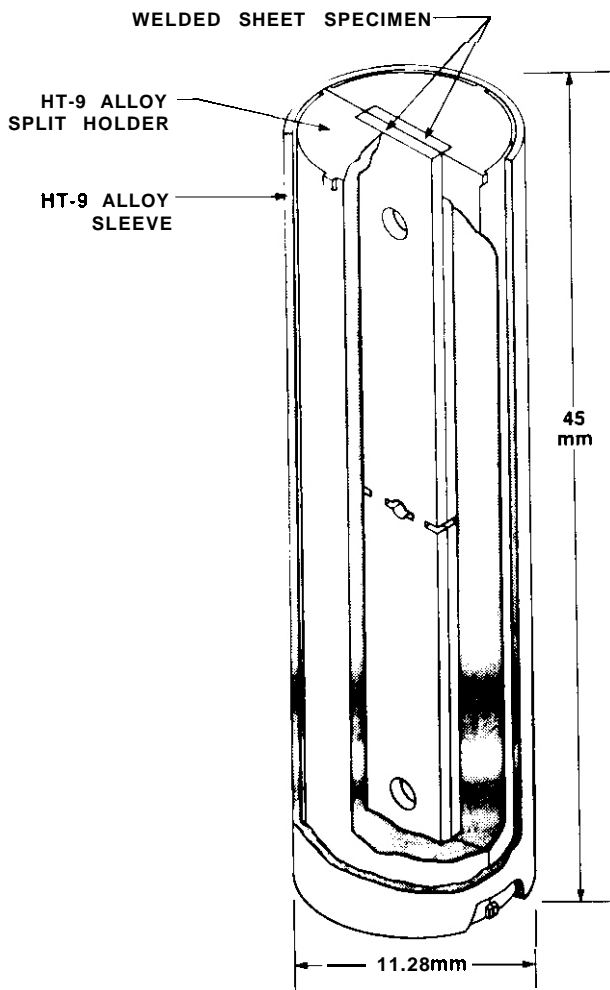


Fig. 4. Welded sheet specimen holder for U.S./Japan Phase II HFIR target capsules.

ORNL-DWG 87-4724 ETD

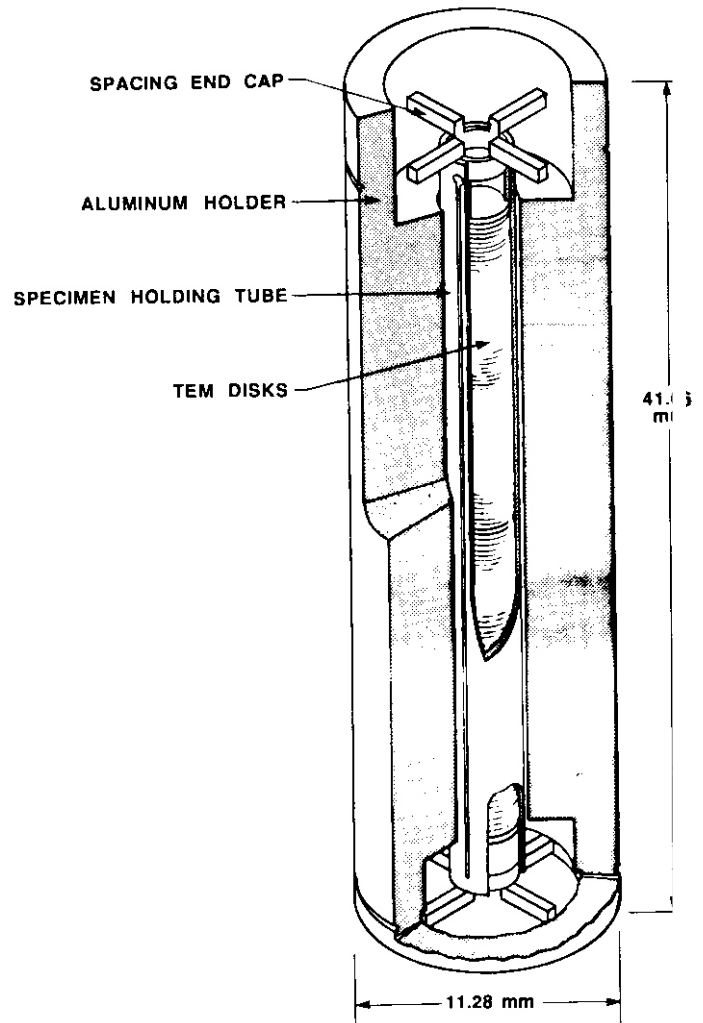


Fig. 5. Typical transmission electron microscopy (TEM) specimen holder for U.S./Japan Phase II HFIR target capsules.

ORNL-DWG 87-4725 ETD

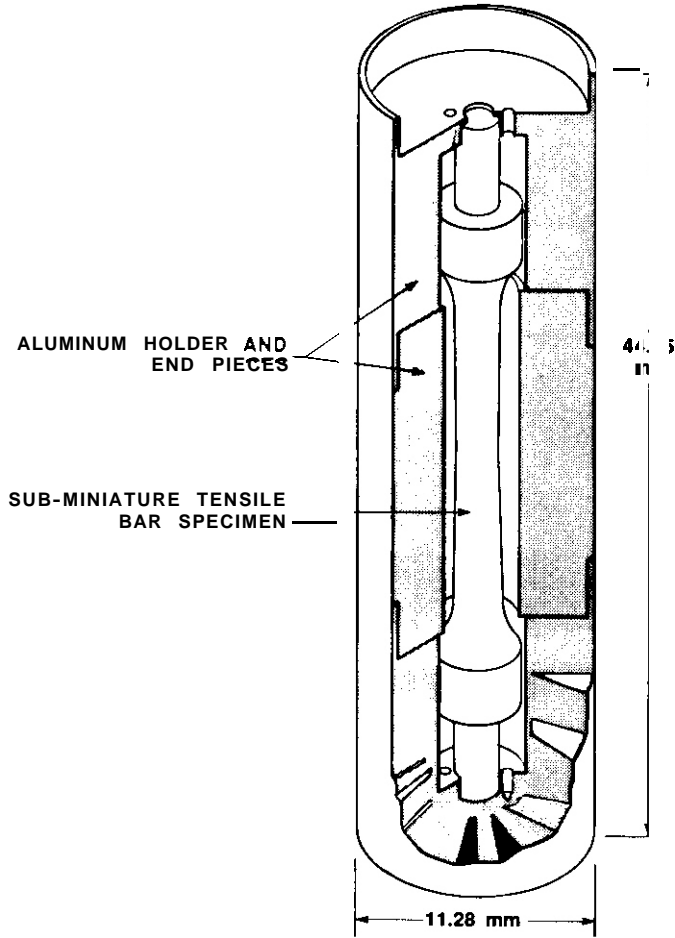


Fig. 6. Typical tensile bar (TB) specimen holder assembly for U.S./Japan Phase II HFIR target capsules.

ORNL-DWG 87-4725 ETD

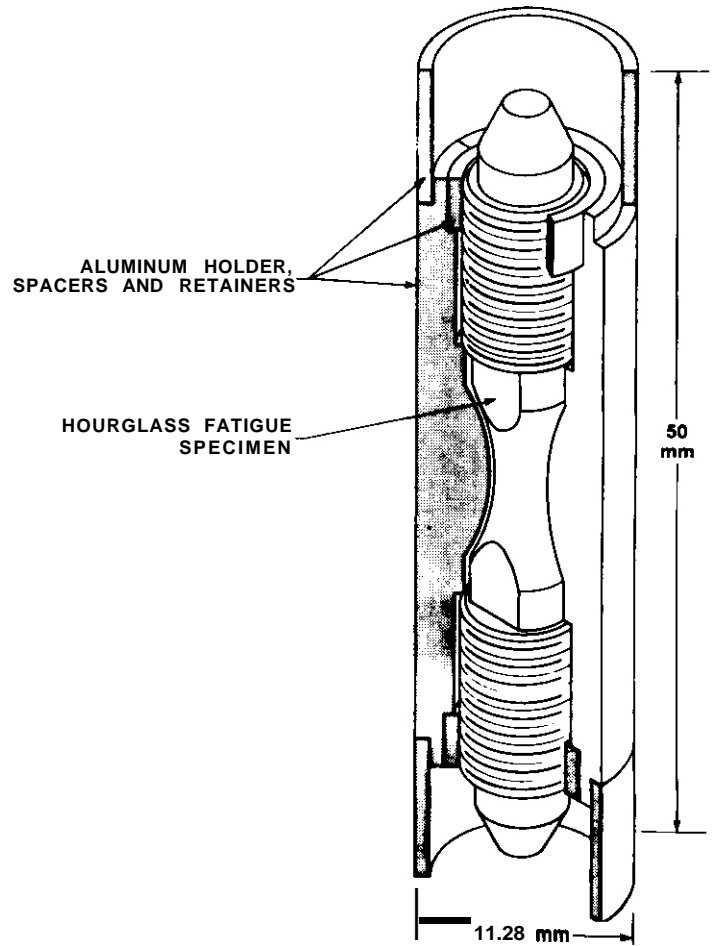


Fig. 7. Typical hourglass fatigue (F) specimen holder assembly for U.S./Japan Phase II HFIR target capsules.

PRESENT STATUS

All parts for the eight new capsules are on hand and the various specimens, flux monitors, and melt-wire temperature monitors are in preparation.

A procedure to accomplish assembly of the capsules has been prepared, approved, and issued.

FUTURE WORK

Assembly of the eight capsules is planned for completion during the first quarter of FY 1988, with installation in the HFIR at the earliest opportunity. Full power operation of the reactor is presently planned for mid-February 1988.

REFERENCES

1. J. L. Scott and M. P. Tanaka, "Status of U.S./Japan Collaborative Testing in HFIR and ORR," pp. 2-28 in Fusion Reactor Materials Semiann. Prog. Rep. Sept. 30, 1986, DOE/ER-0313/1, U.S. DOE, Office of Fusion Energy.
2. J. L. Scott and M. P. Tanaka, "Status of U.S./Japan Collaborative Testing in HFIR and ORR," pp. 19-20 in Fusion Reactor Materials Semiann. Prog. Rep. Mar. 31, 1987, DOE/ER-0313/2, U.S. DOE, Office of Fusion Energy.
3. Hall C. Roland, GENGTC, A One-Dimensional CEIR Computer Program for Capsule Temperature Calculations in Cylindrical Geometry, ORNL-TM-1942 (December 1967).
4. Personal communication with I. I. Siman-Tov, June 1987.
5. I. I. Siman-Tov, "The HFIR Instrumented (JP Type) Target Temperature Test (TTT) Capsule," pp. 10-17 in Fusion Reactor Materials Semiann. Prog. Rep. Mar. 31, 1987, DOE/ER-0313/2, U.S. DOE, Office of Fusion Energy.
6. D. C. Elrod, G. E. Giles, and W. D. Turner, HEATING6, A Multidimensional Heat Conduction Analysis with the Finite-Difference Formulation, PSR-199, RSIC Peripheral Shielding Routing Collection, Radiation Shielding Information Center, July 24, 1985.
7. D. W. Heatherly, "Assembly/Manufacturing Plan for the HFIR-MFE-JP-9 Through JP-16 Irradiation Capsules," ORNL Procedure No. Q-41517-ET-FQ-002 (October 2, 1987).

Alloy	Product Form			Alloy	Product Form		
	Ingot or bar ^a weight (kg)	Rod diameter (mm)	Thickness, mm		Ingot or bar ^a weight (kg)	Rod diameter (mm)	Thickness, mm
Sheet			Thin-wall tubing wall	Sheet			Thin-wall tubing wall
Path D Alloys							
LRO-37 ^e			3.3, 1.6, 0.8				

Path E Alloys

Alloy	Ingot or bar ^a weight (kg)	Rod diameter (mm)	Thickness, mm		
			Sheet	Thin-wall tubing wall thickness	
HT9 (AOD fusion heat) ^f	3400		28.5, 15.8, 9.5	3.1	
HT9 (AOD/ESR fusion heat)	7000	25, 50, 75	28.5, 15.8, 9.5	3.1	
HT9			3.1		
HT9 + 1%Ni			4.5, 18		
HT9 + 2% Ni			4.5, 18		
HT9 + 2% Ni + Cr adjusted			4.5, 18		
T-9 modified ^g			4.5, 18		
T-9 modified + 2% Ni			4.5, 18		
T-9 modified + 2% Ni + Cr adjusted			4.5, 18		
2.25Cr-1Mo					h

^aGreater than 25 mm, minimum dimension. ^bprime candidate alloy.

^cRod and sheet of a USSR stainless steel supplied under the U.S./USSR Fusion Reactor Materials Exchange Program.

^dNONMAGNE 30 is an austenitic steel with base composition Fe-14%Mn-2%Ni-2%Cr. It was supplied to the inventory by the Japanese Atomic Energy Research Institute.

^eLRO-37 is the ordered alloy (Fe,Ni)₃(V,Ti) with composition Fe-39.4%Ni-22.4%V-0.43%Ti.

^fAlloy 12Cr-1MoVW composition equivalent to Sandvik alloy HT9.

^gT-9 modified is the alloy 9Cr-1MoVNb.

^hMaterial is thick-wall pipe, rerolled as necessary to produce sheet or rod.

available for fabrication to produce other product forms as needed by the program. No material was added to the inventory during this reporting period. Table 2 gives the materials distributed from the Inventory.

Alloy compositions and more detail on the alloys and their procurement and/or fabrication are given in this and earlier AOIP and FRM progress reports.

Table 2 Fusion Program Research Materials Inventory Disbursements April 1, 1987, through September 30, 1987

Alloy	Heat	Product form	Dimension ^a (mm)	Quantity (m ²)	Sent to
Path A Alloys - Austenitic Stainless Steels					
316 SS	X-15893	Sheet	1.91	0.014	Rensselaer Polytechnic Institute
Path C Alloys - Reactive and Refractory Alloys					
V-15%Cr-5%Ti	CAM-834	Sheet	1.27	0.064	Grumman Corporation
Path E Alloys - Ferritic Steels					
HT9	AOD/ESR-9607R2	Sheet	3.18	0.014	Rensselaer Polytechnic Institute

^aCharacteristic dimensions: Thickness for plate and sheet, diameter for rod and tubing.

Fusion Program Research Materials Inventory of
12 Cr-1 Mo Steel (HT-9) - Chen-Yih Hsu, GA Technologies Inc.

ADIP Tasks

The Department of Energy (DOE) Office of Fusion Energy (OFE) has cited the need to investigate ferritic steels under the Alloy Development for Irradiation Performance (ADIP) task ferritic steels development (Path E).

Summary

Previously, a 30,000 lb heat of HT-9, 12 Cr - 1 Mo steel made by the argon-oxygen decarburization method (AOD) was procured by GA Technologies Inc. for the ADIP program. Half of the AOD heat of HT-9 steel was remelted by the electroslag remelting process (ESR). These two heats of HT-9 have been converted to the form of plate and bar stock and then distributed to the DOE Path E fusion reactor materials program users. In September 1987, all the unused HT-9 plates and bars at GA have been shipped to Oak Ridge National Laboratory Material Stockpile.

Material History

In 1980 30,000 lb heat of a 12 Cr - 1 Mo steel which meets the specification of Sandvik HT-9 was procured by GA Technologies Inc. from the Electralloy Corporation for the Path E ferritic steel program (1). The 12 Cr -1Mo steel was processed via argon-oxygen decarburization process (AOD) (heat #9607) half of which was converted to plate of thickness 1/8, 3/8, 5/8, and 1-1/8 in. The other half was cast into an electrode for future processing. In 1983, half of the 119607 heat was electroslag remelted (ESR) (heat #9607R2) by Universal Cyclops Corp. in Pittsburgh. The HT-9 steel was then converted to the form of plate with various thickness of 1-1/8", 5/8", 3/8", and 1/8" and also in the bar form with diameter of 1", 2" and 3". The processing of plate and bar stock was detailed previously in ADIP progress report. (2)

Chemical analyses on the ESR heat was performed by International Nickel Co. and the AOD chemistry was provided by Electralloy Corp. The chemical compositions of heats AOD and ESR are given in Table 1. All of the elemental amounts are within the DIN 17175-79 specification, Werkstoff 1.4935, for Sandvik HT-9. The levels of several embrittling elements such as S and P were much lower than those values found in the specification of DIN 1.4935. The mechanical properties of 12 Cr - 1 Mo steel were documented in the previous ADIP progress report. (2)

Current Inventory and Material Movement

GA Technologies Inc. has maintained a central inventory of HT-9 steel to provide a common supply of material for the Path E ferritic steel program. This minimizes unintended material variations and provides for **economy** in procurement. Part of the HT-9 steel has been distributed upon the request of the program participants.

All the unused HT-9 steel plates and bars available at GA Technologies Inc. have been shipped to the Oak Ridge National Laboratory in September 1987. Table 2 lists the HT-9 inventory for shipment to the Oak Ridge National Laboratory. The shipment includes 40 plates of AOD heat #9607 with thickness ranging from 1-1/8" to 1/8", 26 plates of ESR heat #9607R2 with thickness ranging from 1-1/8" to 1/8", 53 bars of ESR heat #9607R2, of the three diameters mentioned, and some scrap plates which are HT-9 steel hut cannot be identified unequivocally by heat without further chemical analysis of key components. All future requests concerning 12 Cr - 1 Mo HT-9 steel shall be directed to the Fusion Program Research Materials Inventory at Oak Ridge National Laboratory.

References

1. Lechtenberg, T. A., et al, ADIP Quarterly Report for the period ending March 31, 1980, DOE/ER-0045/2, page 109.
2. Lechtenberg, T. A., ADIP Semiannual Progress Report for the period ending March 31, 1982, DOE/ER-0045/8, page 363.

TABLE I
A SUMMARY OF CHEMICAL COMPOSITION
FOR HEATS OF HT-9

HEAT	CHEMICAL COMPOSITION LIMITS													
	C	Si	Mn	P	S	Cr	Mo	Ni	V	W	N	Al	Ti	Other (Max.)
DIN SPEC (1.4935)	.17/ .23	.1/ .50	3/ 80	0.035 (max)	0.035 (max)	11.0/ 12.5	0.8/ 1.20	.3/ .80	.25/ .35	.4/ .6				
AOD (9607)	.20	.24	57	0.018	0.007	11.64	1.01	.52	.30	.57	.044	.009	<.01	O ₂ .013, Cb 0.01 Cu .04, Co 0.09, As 0.004 Zr .002, B 0.001. Pb .001, Sn 0.001, Sb trace
ES (9607R2)	.20	.17	57	0.016	0.003	12.1	1.04	.51	.28	.45	.027	.006 .007	.001	Cu .07, Co <0.05, As 0.003 O ₂ .002, B <.001, Bi <.001 Pb <.0001, Sb 0.0005 Sn 0.004, Cb <.001
Breeder (91354)	.17/ .23	.2/ .3	4/ 7	0.020 (max)	0.010 (max)	11.01 12.5	0.8/ 1.2	.3/ .8	.25/ .35	.4/ .6	.010	.050 (max)	.050 (max)	Cu .10, As 0.030, Ta 0.020, Co 0.05, B 0.001

TABLE 2: HT-9 INVENTORY PREPARED FOR SHIPMENT TO OAK RIDGE NATIONAL LABORATORY

PLATE NUMBER	HEAT NUMBER	THICK or DIAM (IN)	LENGTH (IN)	WIDTH (IN)	REMARKS
1.1.3.1	9607	1.125	20.00	4.00	
1.1.4.1	9607	1.125	20.00	4.00	
1.2.2	9607	0.625	32.00	4.00	
1.2.3	9607	0.625	32.00	4.00	
1.2.4	9607	0.625	32.00	4.00	
1.2.5	9607	0.625	16.00	4.00	
1.2.6	9607	0.625	32.00	4.00	
1.2.8	9607	0.625	30.00	4.00	
1.2.10	9607	0.625	32.00	4.00	
1.3.1.F.2	9607	0.625	12.00	4.50	
1.3.1.1.1	9607	0.625	12.00	4.50	
1.3.1.I.2	9607	0.625	12.00	4.50	
1.3.1.K.2	9607	0.625	12.00	4.50	
1.3.2.1	9607	0.625	21.50	4.50	
1.3.11.1	9607	0.625	26.00	4.50	
1.4.3	9607	0.375	52.00	24.00	
1.7.6	9607	0.375	20.00	26.00	
1.9.4	9607	0.375	25.50	25.00	
1.9.5	9607	0.375	25.50	25.00	
1.9.7	9607	0.375	25.50	25.00	
1.12.1	9607	0.125	53.00	26.00	JAGGED EDGE
1.12.2	9607	0.125	51.00	28.00	
1.13.	9607	0.125	52.00	51.00	
1.14.	9607	0.125	52.00	51.00	
1.16.1	9607	0.125	31.00	25.50	
1.16.2	9607	0.125	31.00	25.50	
1.16.3	9607	0.125	30.00	25.50	
1.17.	9607	0.125	59.00	51.00	
1.18.1	9607	0.125	30.00	30.00	
1.18.2	9607	0.125	32.00	21.00	
1.18.3	9607	0.125	30.00	30.00	
1.18.4	9607	0.125	32.00	21.00	
1.19.1	9607	0.125	50.00	30.00	JAGGED EDGE
1.19.2	9607	0.125	50.00	32.00	
1.20.	9607	0.125	60.00	50.50	
1.21.2	9607	0.125	32.00	26.00	
1.21.3	9607	0.125	29.00	26.00	
1.21.4	9607	0.125	32.00	26.00	
1.22.1	9607	0.125	54.00	28.00	
1.22.2	9607	0.125	54.00	29.00	

TABLE 2: CONTINUED
 HT-9 INVENTORY PREPARED FOR SHIPMENT TO OAK RIDGE NATIONAL LABORATORY

PLATE NUMBER	HEAT NUMBER	THICK or DIAM (IN)	LENGTH (IN)	WIDTH (IN)	REMARKS
6.7.3	9607R2	0.625	16.00	2.50	
6.13.1	9607R2	0.375	30.00	18.00	
6.13.3.1	9607R2	0.375	18.00	10.00	
6.13.3.3	9607R2	0.375	18.00	10.00	
6.13.4	9607R2	0.375	30.00	18.00	
6.14.4	9607R2	0.375	20.00	18.00	
6.14.5	9607R2	0.375	20.00	11.00	
6.14.6	9607R2	0.375	20.00	18.00	
6.14.8	9607R2	0.375	20.00	18.00	
6.15.	9607R2	0.375	60.00	36.00	
6.20.2	9607R2	1.125	15.00	14.00	
6.25.	9607R2	1.125	14.00	5.00	
6.28.3	9607R2	0.125	36.00	12.00	
6.28.4	9607R2	0.125	36.00	12.00	
6.28.5	9607R2	0.125	36.00	12.00	
6.28.6	9607R2	0.125	36.00	12.00	
6.28.7	9607R2	0.125	36.00	12.00	
6.28.8	9607R2	0.125	36.00	24.00	
6.29.	9607R2	0.125	96.00	36.00	
6.30.	9607R2	0.125	96.00	36.00	
6.31.	9607R2	0.125	96.00	36.00	
6.32.	9607R2	0.125	96.00	36.00	
6.33.	9607R2	0.125	96.00	36.00	
6.34.	9607R2	0.125	96.00	36.00	
6.35.	9607R2	0.125	96.00	36.00	
6.36.	9607R2	0.125	96.00	36.00	
		0.600	14.00	54.00	SCRAP
		0.625	4.50	26.50	SCRAP
		0.625	4.25	21.00	SCRAP
		0.625	4.20	26.00	SCRAP
		0.625	5.50	21.00	SCRAP
		0.625	5.00	26.50	SCRAP
		0.625	4.50	21.50	SCRAP
		1.000	5.00	19.00	SCRAP
		1.000	4.50	19.00	SCRAP
		1.000	4.25	19.25	SCRAP
		1.000	4.50	20.00	SCRAP
		1.000	4.00	20.00	SCRAP
		1.000	5.50	20.00	SCRAP
		1.000	5.26	20.00	SCRAP
		1.000	5.00	20.00	SCRAP
		1.000	4.00	20.00	SCRAP
		1.000	4.00	20.00	SCRAP
		1.000	4.50	20.00	SCRAP
	9607R2	3.00 DIAM	12.00		QNTY 7 BAR
	9607R2	3.00 DIAM	10.00		QNTY 1 BAR
	9607R2	3.00 D I M	11.00		QNTY 2 BAR
	9607R2	3.00 DIAM	7.00		QNTY 2 BAR
	9607R2	2.00 D I M	10.00		QNTY 7 BAR
	9607R2	1.00 D I M	13.00		QNTY 33 BAR
	9607R2	1.00 DIAM	7.00		QNTY 1 BAR

2 DOSIMETRY, DAMAGE PARAMETERS AND ACTIVATION CALCULATIONS

NEUTRONICS ANALYSIS IN SUPPORT OF THE U.S.-JAPAN SPECTRAL TAILORING CAPSULES — R. A. Lillie (Oak Ridge National Laboratory)

OBJECTIVE

The objective of this work is to provide the neutronic design for materials irradiation experiments in both the Oak Ridge Research Reactor (ORR) and High Flux Isotope Reactor (HFIR). Spectral tailoring to control the fast and thermal fluxes is required to provide the desired displacement damage and helium production rates in alloys containing nickel.

SUMMARY

The ORR was shut down on March 26, 1987, and the ORR-MFE-6J and -7J capsules were removed. At the time of their removal, scaled fluences from neutronics calculations yielded 62.4 appm He (not including 2.0 appm He from ^{10}B) and 6.92 dpa for type 316 stainless steel in ORR-MFE-6J and 96.8 appm He and 7.97 dpa in ORR-MFE-7J. The hafnium shield thickness required to extend the lifetime of the MFE-6J and -7J capsules in a HFIR RB position from 150 full-power days to 275 days at 85% of full power was calculated to be 5.0 mm.

PROGRESS AND STATUS

The operating and current calculated data based on scaling factors obtained from previous comparisons¹ of measured and calculated fluences are summarized in Table 1 for the ORR-MFE-6J and -7J experiments. Since the ORR was permanently shut down on March 26, 1987, the data in Table 1 represent final sets of data for these experiments. At shutdown, both experimental capsules had been exposed to 341,805.8 MWh. On June 8, 1986, the water-aluminum corepiece in the ORR-MFE-7J experiment was replaced with a solid aluminum corepiece. At the time of replacement, the ORR-MFE-7J experiment had been exposed to 280,639.8 MWh and had obtained 76.0 appm He and 6.30 dpa. Before the insertion of the solid aluminum corepiece, the average dpa rate in the ORR-MFE-7J type 316 stainless steel specimens had been 5.91 dpa per full-power year. After insertion of the solid aluminum corepiece, the average dpa rate increased to 7.16 dpa per full-power year.

Table 1. Final Operating and Calculated Data for the ORR-MFE-6J and -7J Experimental Capsules

	ORR-MFE-6J	ORR-MFE-7J
Insertion date	6-28-85	6-28-85
Exposure, MWh	341,805.8	341,805.8
Equivalent full-power days ^a	474.7	474.7
Thermal fluence, n/m ²	7.35×10^{25}	9.47×10^{25}
Total fluence, nm ²	2.46×10^{26}	2.99×10^{26}
dpa	6.92	7.97
Direct helium, appmb	5.42	6.21
Two-step helium, appmb	57.0	90.6
Total helium, appmb	62.4	96.8

^aFull power for the ORR is 30 MW.

^bHelium and dpa values are for type 316 stainless steel.

Calculations were performed to determine the hafnium thickness required to extend the lifetime of the HFIR RB-position, hafnium-shielded experimental capsules from 150 full-power days to 275 (11 cycles) days at 85% of full power. Substantial hafnium shielding is needed to obtain the same helium to dpa ratio in type 316 stainless steel as that expected in a fusion device first wall because of the increased thermal flux in the HFIR. Earlier calculations² predicted hafnium shield thicknesses of 3.0 mm between the 5 and 10 dpa levels and 4.2 mm between the 10 and 30 dpa levels would produce the necessary thermal flux reductions when changed out every 150 full-power days. The present calculations predict that an increase of approximately 30 mils (i.e., increasing the thicker shield from 4.2 to 5.0 mm would maintain the needed flux reduction over 275 days at 85% of full power). However, because of burnup, this increase in thickness and subsequent increase in lifetime produces a thermal flux reduction which drops from an initial 95% to a final 70%, whereas the 4.2 mm shields produced initial and final thermal flux reductions of 91 and 80%, respectively. This more than 25% change in thermal flux over the lifetime of each shield was deemed too great, and the use of thicker shields was discarded. Also, at this time the decision was made to use the thicker 4.2 mm shields between the 5 and 10 dpa levels, since the ORR-MFE-6J and -7J specimens have already obtained approximately 7 and 8 dpa, respectively.

FUTURE WORK

At the present time, the in-house code that has been used to obtain the projected helium and dpa levels in the MFE experimental specimens does not take into account effects spectral changes in the total fluence have on the average cross sections employed in the two-step helium-production equation. To include these effects, which are needed in part because of the drastic change in thermal flux brought about by the use of hafnium shields, the single equation currently in use will have to be discarded in favor of three equations (i.e., separate equations for ^{58}Ni , ^{59}Ni , and helium).

To date, the hafnium shield burnup calculations have been performed employing a simple burnup model which does not take into account changes in the hafnium cross sections which occur during burnup because of transmutations. Normally, the macroscopic cross section for a given material only changes during burnup because of decreasing atom number densities. However, naturally occurring hafnium contains primarily four isotopes, two of which — ^{177}Hf and ^{178}Hf — have large thermal-neutron absorption cross sections and most of the burnup of ^{177}Hf leads to the production of ^{178}Hf . Although ignoring this effect leads to conservative estimates of the thermal flux reduction (i.e., underestimates the thermal flux reduction), it needs to be incorporated into the simple burnup model, and this model should be checked against hafnium-burnup data, if available, and should be validated using more precise and obviously more costly numerical methods. These improvements will allow more credible helium and dpa projections to be made for the HFIR RB irradiations.

REFERENCES

1. R. A. Lillie, "Neutronics Analysis in Support of the U.S.-Japan Spectral Tailoring Capsules," ADIP Semiannu. Prog. Rep. Sept. 30, 1985, DOE/ER-0045/15, U.S. DOE, Office of Fusion Energy.
2. R. A. Lillie, "Neutron Analysis in Support of the U.S.-Japan Spectral Tailoring Capsules," ADIP Semiannu. Prog. Rep. March 31, 1986, DOE/ER-0045/16, U.S. DOE, Office of Fusion Energy.

DOSIMETRY AND DAMAGE CALCULATIONS FOR THE JP4, JP5, AND JP8 US/JAPANESE EXPERIMENTS IN HFIR - L. R. Greenwood and C. A. Seilis (Argonne National Laboratory)

OBJECTIVE

To characterize neutron irradiation facilities and experiments in terms of neutron fluence, spectra, and damage parameters.

SUMMARY

Results are presented for the JP4, JP5, and JP8 US/Japan experiments in HFIR. All three experiments had similar exposures of about 58,000 MWD resulting in 55 dpa and 3313 appm helium at midplane for 316 stainless steel.

PROGRESS AND STATUS

Results are reported for the JP4, JP5, and JP8 US/Japanese experiments in the High Flux Isotopes Reactor (HFIR) at Oak Ridge National Laboratory. These three irradiations were conducted in the target position as follows:

Experiment	Dates	Exposure
JP4	05/01/84 - 04/18/86	57,909 MWD
JP5	09/11/84 - 08/12/86	58,217 MWD
JP8	10/05/84 - 09/07/86	58,214 MWD

Results for the JP1, and JP3¹ and JP2, JP6, and JP7² irradiations were reported previously.

Dosimeters were located at three vertical positions in JP4 and JP8 and at six positions in JP5. The lowest dosimeter from JP5 was damaged during disassembly. All remaining eleven aluminum capsules measured about 0.25" long by 0.05" OD and contained small wires of 0.1% Co-Al, Fe, 80.2% Mn-Cu, and Ti. The Ti samples were totally destroyed in runs JP5 and JP8, presumably due to reactions with gaseous impurities in the helium cover gas. However, the Ti samples from JP4 were all recovered and showed no discoloration. This difference is probably due to the fact that the JP4 specimens were irradiated at 550°C whereas the JP5 and JP8 temperatures were 300-600°C. The Ti could thus be reacting with H, O, or N outgassed from the assemblies.

All of the dosimeters were gamma counted and the corrected activities are listed in Table I. Close comparisons of the data from each run shows only small (1-3%) differences. All of the data are well-described by a simple polynomial, as follows:

$$f(z) = f(o) (1 + bz + cz^2), \quad z = \text{height, cm} \quad (1)$$

where $b \approx 0$ and $c = -8.71 \times 10^{-4}$ for the thermal reactions, and $b = 7.42 \times 10^{-4}$, $c = -9.80 \times 10^{-4}$ for the three fast reactions.

Since the three runs have the same exposure within $\pm 0.3\%$, and the activities at each position agree within $\pm 3\%$, it was decided to report all three runs jointly, with identical neutron fluence and damage parameters.

The neutron energy spectra were determined with the STAY/SL computer code using midplane activities determined from a global fit to the data in Table I using equation (1). The spectral adjustments were small (-10%) and the spectrum is quite similar to previous results.^{1,2} The resultant neutron fluences are given in Table 11.

Damage parameters were calculated with the SPECTER3 computer code and displacements-per-atom (dpa) and helium (at.ppm) are reported in Table III. Thermal effects are included for Ni and Cu, as discussed in recent publications.^{4,5} It should be noted that the recently discovered thermal helium effect in copper produced 9.4 times more helium than expected from fast neutron reactions! For Ni, these irradiations produced about 0.25 at % helium or 3313 appm in 316 S.S. The non-linear gradients for stainless steel are listed in Table IV. Gradients for all other damage parameters (except helium in copper) can be obtained using equation (1) and the midplane values in Table III. All of these results are nearly identical to those reported previously for the JP2 experiment.²

FUTURE WORK

Fifty new aluminum dosimetry capsules have been fabricated for the JP9-16 experiments in HFIR. Fifty additional capsules have also been made for the MFE 330J and 60J experiments in HFIR. These latter two experiments are a continuation of the MFE-6J and 7J irradiations in the Oak Ridge Research Reactor. All dosimeters have been sent to Oak Ridge for planned irradiations starting in January 1988.

References

1. L. R. Greenwood, Damage Analysis and Fundamental Studies, Quarterly Progress Report, DOE/ER/0046/24, pp. 5-9 (February 1986).
2. L. R. Greenwood, Measurements for the JP2, JP6, and JP7 U.S./Japanese Experiments in HFIR, Second Fusion Reactor Materials Semi-Annual Progress Report, DOE/ER-00313/2, in press.
3. L. R. Greenwood and R. K. Smither, ANL/FPP-TM-197, January 1985.
4. L. R. Greenwood, D. W. Kneff, and R. P. Skowronski, J. Nucl. Mater. 122-123, pp. 1002-1010 (1984)
5. D. W. Kneff, L. R. Greenwood, B. M. Oliver, R. P. Skowronski, and E. L. Callis, Rad. Effects 92-96, p. 553-556 (1986).

Table I. Measured Activities for HFIR-JP4, JP5, JP8
(Activities in at/at-5 at 100 MW; +3%)

Height, cm	$^{59}\text{Co}(n,\gamma)^{60}\text{Co}$ ($\times 10^{-8}$)			$^{58}\text{Fe}(n,\gamma)^{59}\text{Fe}$ ($\times 10^{-9}$)		
	JP4	JP5	JP8	JP4	JP5	JP8
25.4	-	3.65	-	-	1.23	-
17.1	5.29	-	-	1.72	-	-
16.5	-	5.31	5.58	-	1.75	1.85
7.1	-	6.19	-	-	-	-
2.1	6.31	6.37	6.29	2.33	2.33	2.40
-12.1	-	5.56	-	-	1.96	-
-19.3	4.69	-	-	1.55	-	-
-21.0	-	-	4.38	-	-	1.40

Height, cm	$^{54}\text{Fe}(n,p)^{54}\text{Mn}$ ($\times 10^{-11}$)			$^{46}\text{Ti}(n,p)^{46}\text{Sc}$ ($\times 10^{-12}$)	$^{55}\text{Mn}(n,2n)^{54}\text{Mn}$ ($\times 10^{-14}$)		
	JP4	JP5	JP8	JP4	JP4	JP5	JP8
25.4	-	2.75	-	-	-	7.91	-
17.1	5.07	-	-	7.34	1.55	-	-
16.5	-	5.21	5.47	-	-	1.66	1.61
7.1	-	-	-	-	-	1.99	-
2.1	6.95	7.39	6.76	9.84	1.98	2.08	1.92
-12.1	-	5.88	-	-	-	1.85	-
-19.3	4.59	-	-	6.14	1.39	-	-
-21.0	-	-	3.84	-	-	-	1.12

Table II. Neutron Fluence for HFIR-JP4, JP5, JP8

Energy	Neutron Fluence ($\times 10^{22}$ n/cm ²)
Total	24.45
Thermal (<0.5eV)*	10.00
0.5eV - 0.1 MeV	7.82
>0.1 MeV	6.63
>1 MeV	3.36

*Total neutrons <0.5 eV; for 2200 m/s value multiply x 0.886.

Table III. Damage Parameters for HFIR-JP4, JP5, JP8
(Values at Midplane; for Gradients use Eq.1)

Element		DPA	He, appm
Al		86.3	41.8
Ti		54.8	28.0
V		61.4	1.41
Cr		54.1	9.60
Mn ^a		59.5	8.46
Fe		47.9	17.1
Co ^a		60.0	8.38
Ni	Fast	51.5	226.2
	⁵⁹ Ni	44.4	<u>25,160.</u>
	Total	95.9	25.386.
Cu	Fast	46.7	12.4
	⁶⁵ Zn	0.2	<u>116.6</u>
	Total	46.9	129.0
Nb		46.3	3.12
Mo		34.5	-
316 SS ^b		55.2	3313.

^aThermal neutron self-shielding may reduce dpa value.

^b316 SS: Fe(0.645), Ni(0.13), Cr(0.18), Mn(0.019), Mo(0.026).

^cCu values reported in Ref. 5.

Table IV. Damage Gradients for 316 SS - HFIR - JP4, JP5, JP8
(DPA includes thermal effect from ⁵⁹Ni)
(Helium includes ⁵⁹Ni and fast reactions)

Height, cm	He, appm	DPA
0	3313	55.2
3	3285	54.7
6	3198	53.2
9	3053	50.7
12	2844	47.2
15	2566	42.7
18	2218	37.2
21	1791	30.7
24	1277	23.1

ENHANCED HELIUM PRODUCTION IN FERRITIC MATERIALS - L. R. Greenwood and D. G. Graczyk (Argonne National Laboratory), D. W. Kneff (Rockwell International Corporation)

OBJECTIVE

To measure gas production rates and to develop new techniques for fusion materials irradiations.

SUMMARY

Analyses of iron samples irradiated up to neutron fluences of 10^{27} n/m² in HFIR found more helium than was expected from fast neutron reactions at high fluences. The helium excess increased systematically with neutron exposure, suggesting a transmutation-driven process. The extra helium could be produced in two different ways, either by fast neutron reactions on the transmuted isotopes of iron or by a thermal neutron reaction with the radioactive isotope ⁵⁵Fe. Radiometric and mass spectrometric measurements of the iron isotopes composing the irradiated samples have been used to determine limits on the cross sections for each process. Either of these processes can be used to enhance helium production in ferritic materials during irradiations in mixed-spectrum reactors by isotopically enriching the samples. Further work is needed to clarify the reaction mechanisms and to determine helium-production cross sections. Our measurements determined the thermal neutron total absorption cross section of ⁵⁵Fe to be 13.2 ± 2.1 barns.

PROGRESS AND STATUS

High-purity (99.99%) iron samples were irradiated at three locations in three separate fusion materials experiments in the Peripheral Target Position of HFIR. These nine iron samples were used for both activation (Argonne) and helium measurements (Rockwell). Other radiometric dosimeters were also included, and the activation measurements were used to determine the neutron energy spectra by spectral adjustment procedures.¹ The iron helium measurements have been reported previously² along with results for other elements, and details of the procedures are reported in that work.

The neutron fluences and measured helium levels are listed in columns 1 and 2 of Table I. Helium production from fast neutrons (column 3 of Table I) can be readily calculated from the adjusted neutron energy spectra using the evaluated helium cross sections given in the ENDFIB-V Gas Production File.³ It is evident from a comparison of the measured and calculated helium that there is a systematic trend with increased neutron exposure, as shown in Table 1 (column 4) and Fig 1 (circles).

The rate of helium production from fast neutrons will change during the course of irradiation due to transmutation of the iron isotopes. We have used two techniques to measure the various iron isotopes in the irradiated samples. Thermal ionization mass spectrometry was performed on three samples to measure the ratios of all iron isotopes, and the results are given in Tables II and III. ⁵⁵Fe was also measured by liquid scintillation spectrometry⁴ and those results are given in Table III. Both types of analyses were performed using dissolutions of the same three samples, and chemical separations were performed to remove the possibility of interferences. Since ⁵⁵Fe decays to ⁵⁵Mn and Mn is more volatile than Fe in the thermal ionization mass spectrometry techniques, Fe-Mn separations were performed within a day of the measurements. All data in Tables II and III have been corrected for decay of ⁵⁵Fe since irradiation.

Table I
Helium Measurements and Fast Neutron Calculations for Iron

Total Fluence (10^{26} n/m ²)	Measured He, appm	ENDF ^a He, appm	C/E ^b	THRESH ^{2c} He, appm	C/E ^b
3.48	2.24	3.38	1.06	2.48	1.11
4.60	2.99	3.14	1.05	3.31	1.11
4.81	3.12	3.25	1.04	3.47	1.11
5.57	3.66	3.68	1.01	4.04	1.10
8.30	5.73	5.64	0.98	6.14	1.07
9.67	6.76	6.39	0.95	7.22	1.07
11.05	8.17	7.64	0.94	8.33	1.02
16.45	12.36	10.99	0.89	12.81	1.04
19.16	14.69	12.95	0.88	15.13	1.03

^aFast helium from ENDF/B-V Gas File 5333 and natural iron

^bCalculated-to-experimental helium ratio

^cFast helium using THRESH28 and ratios of transmuted iron isotopes

Table II
Fe Isotopic Mass Spectrometry Measurements^a
Values are atomic percents
(Calculations based on ENDF/B-V5)

Thermal Fluence (10 ²⁶ n/m ²)	⁵⁴ Fe		⁵⁶ Fe		⁵⁷ Fe		⁵⁸ Fe	
	Exp.	Calc.	Exp.	Calc.	Exp.	Calc.	Exp.	Calc.
6.37	5.02	5.02	78.36	77.81	14.84	15.02	1.28	1.68
3.48	5.33	5.35	83.54	83.80	10.12	9.74	0.70	0.80
3.21	5.41	5.39	84.83	84.37	8.86	9.22	0.59	0.74
Mean(C/E)		0.999		0.997		1.003		1.23

^aUncertainties: ⁵⁴Fe 0.4%, ⁵⁶Fe 0.07%, ⁵⁷Fe 0.3%, ⁵⁸Fe 1.2%

Table III
⁵⁵Fe Measurements and Total Absorption Cross Section
(Values are atomic percents at end of irradiation)

Thermal Fluence (10 ²⁶ n/m ²)	LIQSa	TIMSB	Calc. ^c	C/E ^d
6.37	0.460	0.451	0.463	1.02
3.48	0.317	0.323	0.309	0.97
3.21	0.314	0.302	0.313	1.02
			Mean =	1.00±0.3

- ^a Liquid scintillation measurements (±5%)
^b Thermal ionization mass spectrometry (±4%)
^c ⁵⁵Fe total absorption cross section = 13.2 barns,
⁵⁴Fe capture cross section from ENDF/B-V (Ref. 5)
^d Ratio of calc/exp. (average of LIQS and TIMS)

A computer program was developed to calculate the isotopic ratios and helium production in each sample. These calculations consider all contributing and competing reaction channels, including thermal (n,γ), total absorption, and (n,α) for ⁵⁵Fe. Thermal neutron cross sections were adopted from ENDF/B-V.⁵ An epithermal neutron correction of about 7% was also made based on previous measurements of the neutron energy spectrum in HFIR.1 In all subsequent discussions, references to thermal cross sections will be understood to include this effect. The amount of ⁵⁵Fe in each sample depends on the production from ⁵⁴Fe, losses by radioactive decay, and the burnup of ⁵⁵Fe. The neutron fluence levels were taken from our radiometric dosimetry data, which included measurements of the ⁵⁴Fe(n,p)⁵⁴Mn and ⁵⁸Fe(n,γ)⁵⁹Fe reactions for each sample. As shown in Table II, the ⁵⁴Fe atomic fractions are very well-fit by the data (C/E = 0.999 ± 0.004), thus confirming our calculation of the production of ⁵⁵Fe. The total thermal burnup cross section of ⁵⁵Fe can thus be determined since the decay rate is also well-known (2.73±0.03 years).⁶ A total absorption cross section for ⁵⁵Fe of 13.2±2.1 barns provides an excellent fit to the ⁵⁵Fe data (C/E = 1.00±0.03), as shown in Table III. The only previous estimate of this cross section gave a value less than 170 barns.⁷

Our calculations for the higher-mass isotopes of iron are also given in Table II. As can be seen, the agreement is quite good for ⁵⁶Fe and ⁵⁷Fe (C/E = 0.996 and 1.003, respectively): however, the calculations

overpredict the amount of ^{58}Fe ($C/E = 1.23$). The thermal cross sections and resonance integrals from ENDF/B-V have uncertainties of about 5% for $^{54,56,58}\text{Fe}$ and 12% for ^{57}Fe . In order to fit our iron isotopic data for ^{58}Fe , it is necessary to lower the thermal neutron capture cross section for ^{57}Fe by about 20% from 2.48 ± 0.30 barns (ENDF/B-V)⁵ to about 2.0 barns.

As described above, calculations of helium production from fast neutrons using ENDF/B-V underpredicted the helium at high fluences. A more detailed calculation was then performed using the above transmutation rates. Unfortunately, the energy-dependent helium cross section for each isotope is not well-known. Cross sections were thus calculated for each iron isotope using the THRESH2 computer code.⁸ The abundance-weighted results for iron appear to be in reasonable agreement with the cross section in the ENDF/B-V Gas Production File.³ We also note that the iron isotopic helium cross sections are in reasonable agreement with our published results at 14 MeV. Helium calculations using THRESH2 cross sections and calculated transmutation rates of the iron isotopes are also given in Table I (column 5) and shown in Fig. 1 (triangles).

Although the isotopic helium calculations improve the fit to the data, there is still an increasing deviation with neutron exposure, as shown in Fig. 1 and Table I (column 6). Such a trend is similar to the situation with nickel and copper, where thermal neutrons produce significant amount of helium from transmutants. Consequently, we investigated the thermal, two-step reaction $^{54}\text{Fe}(n,\gamma)^{55}\text{Fe}(n,\alpha)$. It is very unlikely that thermal neutron helium production could be significant for any other isotope in our samples. Thermal helium production is energetically allowed from ^{55}Fe , whose Q-value of +3.58 MeV is much larger than the other iron isotopes. We have also looked at impurities in the iron which might produce helium; however, the only known candidate, boron, is far too low (0.2 appb) in these samples.

As seen in Table I, at the lowest neutron fluences the calculations exceed the measurements. Hence, in order to examine any possible thermal effects, we first readjusted the fast neutron helium cross sections.

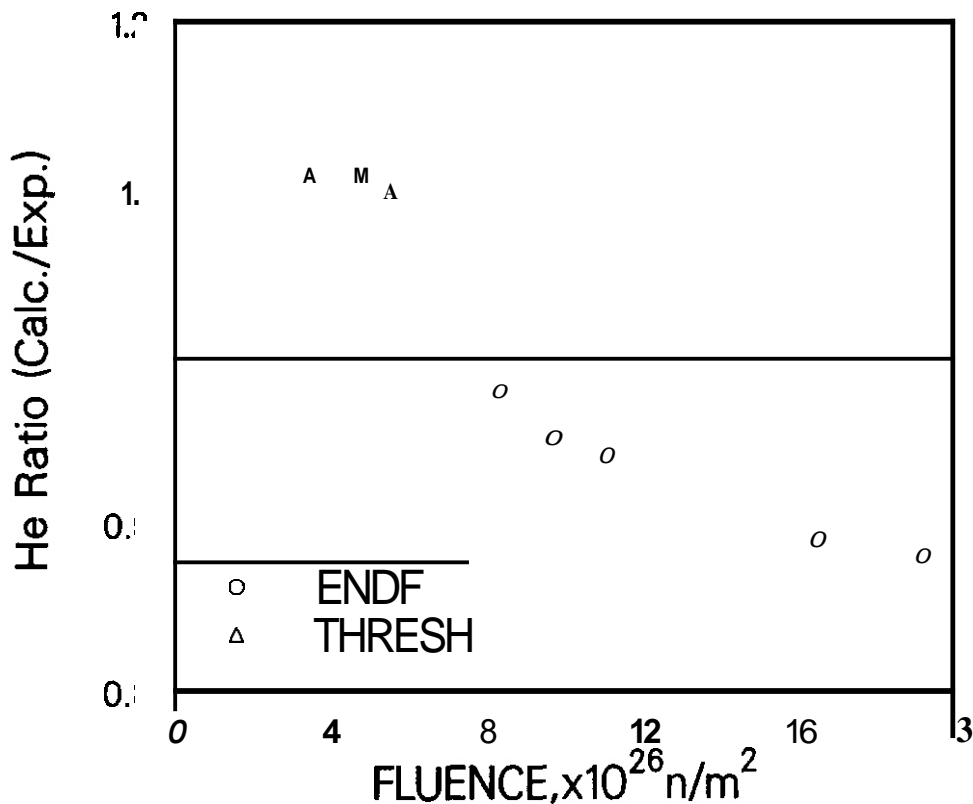


Fig. 1 Ratio of calculated-to-experimental helium production for iron samples in HFIR as a function of total neutron fluence. Calculations are compared for ENDF/B-V (no transmutation) and THRESH2 (with calculated isotopic transmutation).

Based on the data, the calculated fast helium should be reduced by a factor of at least 0.94 (ENDF) or 0.90 (THRESH) simply to fit the measurements at the lowest fluences. Data from iron measurements in other mixed-spectrum reactors at lower fluences give a C/E ratio of 0.92-1.01, and measurements in fast reactors give a value of about 0.84. These differences are compatible with the estimated uncertainties of about 10% in the neutron spectral analyses; however, spectral differences between facilities may also be significant. In the present work, we have assumed that the fast helium production in HFIR must be reduced by a factor between 0.84-0.88.

The data in Table I clearly indicate that the helium levels exceed the fast helium production from natural iron using the ENDF/B-V Gas Production File. If we instead use the isotopic values in THRESH2 for the transmuted iron isotopes, the fit is clearly improved and the difference or excess helium is cut about in half. We are thus faced with three possibilities. Firstly, the THRESH2 helium values with C/E of 1.08 (Table I, column 6) could be improved to 1.00 ± 0.04 if we reduce the fast helium cross sections by 0.92. It is further possible that by varying the isotopic fast (n, α) cross sections we could fit the data more precisely; however, we have not attempted to do this. In this case, there would be no effect from thermal neutrons. Secondly, the THRESH2 values may be entirely misleading and thus should be ignored. In this case, we should use the ENDF values for natural iron and the entire helium excess is due to a thermal neutron effect from ^{55}Fe . Finally, it is possible that the THRESH2 values are about right. In this case, about half the excess is due to fast transmutation and half is due to thermal neutron effects from ^{55}Fe .

If we assume that the calculated helium excess is indeed due to thermal helium production from ^{55}Fe , then we can use the previously described computer code to determine the cross section. Unfortunately, we do not know exactly how to adjust the fast helium calculations. If we use the ENDF fast helium values, reduced by a factor of 0.84-0.88, and assume that the entire helium excess is due to thermal production from ^{55}Fe , then the cross section is 18 ± 3 millibarns. If we instead use the THRESH2 helium production, similarly reduced, then we deduce that the thermal helium production cross section is 9 ± 4 millibarns. The uncertainties are determined from the uncertainties in the helium measurements (1%), neutron fluences (5%), and a sensitivity analysis of the uncertainties in the other parameters. Both cases are illustrated in Fig. 2.

Simulations of fusion reactor damage and gas production in fission reactor irradiations are not generally possible since the low helium rates do not produce the correct helium-to-dpa ratios. This problem has been solved for nickel-bearing materials by using the thermal helium production from ^{59}Ni . However, this Ni trick cannot be used for ferritic alloys, and thus fusion simulations are more difficult.

Based on the present work, increased helium-to-displacement ratios can be readily achieved in iron or ferritic alloys irradiated in mixed-spectrum reactors by isotopic tailoring. If the observed helium excess is due to thermal neutron production from ^{55}Fe , then iron enriched in ^{54}Fe would increase the helium production from 10 appm to 30-60 appm for a 1 year irradiation in HFIR, depending on the thermal cross section. If we further dope the sample with about 30-60% ^{55}Fe , we would produce about 300 appm helium thereby achieving a fusion-like 10:1 helium-to-dpa ratio. It is also interesting to note that, with initial ^{55}Fe doping, the helium-to-dpa ratio for iron does not change very much with neutron fluence and hence is always close to the fusion ratio.

If no thermal effect is operative, then it would not be possible to achieve fusion-like helium-to-dpa ratios. Nevertheless, we note that there are large differences in the isotopic cross sections as predicted by THRESH2. Using samples enriched in ^{54}Fe or ^{57}Fe would increase the helium production by factors of 2 to 3, respectively. Using ^{55}Fe would increase the helium production by a factor of 6. This would be about a factor of five less than fusion; however, the variation might be enough to predict the influence of helium production on materials properties.

FUTURE WORK

Our measurements demonstrate enhanced helium production in iron irradiated in HFIR. Although we are not presently able to determine precisely the reactions responsible for this enhancement, thermal neutron effects from ^{55}Fe could be used to simulate fusion-like helium-to-dpa ratios in irradiations in mixed-spectrum reactors. Obviously, more measurements are needed to determine the reaction modes and hence the usefulness of this effect. Irradiations of isotopically enriched iron isotopes would readily determine both fast and thermal neutron cross sections. An irradiation of a sample enriched in ^{55}Fe would rapidly demonstrate the presence of thermal helium production. Data at lower neutron exposures would more accurately determine the required correction to the fast neutron data.

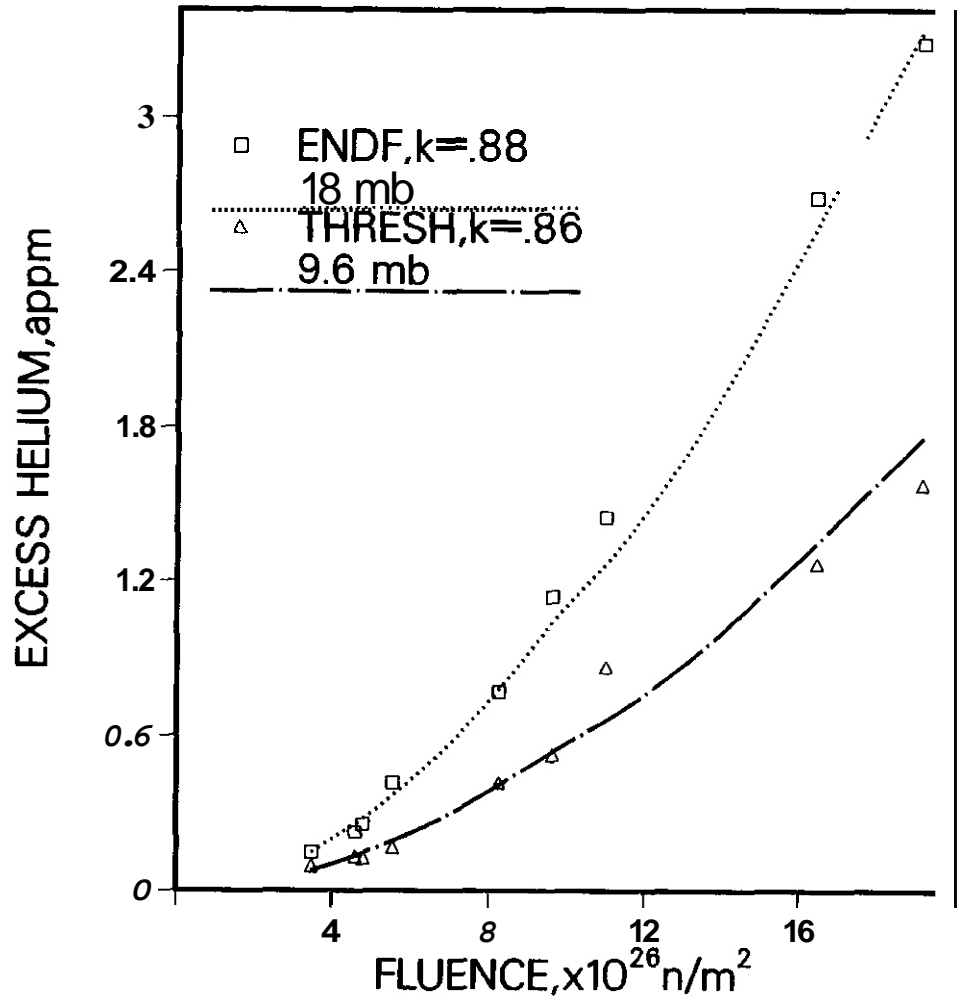


Fig. 2 Excess helium as derived from the difference between measurements and fast neutron calculations with either ENDF/ ^{55}Fe or THRESHZ. These differences are fit assuming thermal neutron helium production from ^{55}Fe with a cross section of about 18 mb (ENDF) or 9 mb (THRESH).

The proposed use of this process to achieve fusion-like helium-to-dpa ratios in iron or ferritic alloys appears to be chemically quite feasible. ^{55}Fe decays by electron capture and only produces low energy x-rays and electrons. Consequently, it does not present handling difficulties. The half-life of 27 years is long enough to allow fabrication and irradiations up to several years. Although the ^{55}Fe will decay to ^{55}Mn , this does not provide a compositional material problem since ^{55}Mn , ^{55}Mn has a high thermal capture cross section to ^{56}Mn , which rapidly decays (2.5 hour) to ^{56}Fe . Furthermore, Mn has been suggested as a suitable replacement for Ni in low-activation alloys for fusion. Finally, ^{55}Fe is available and reasonably cheap, allowing utilization of this technique for fusion materials testing in small specimens. For larger specimens, we note that ^{55}Fe could be produced in quantities from the $^{55}\text{Mn}(p,n)$ reaction without iron isotopic separations.

PUBLICATIONS

This work was presented at the ICFRM3 conference in October, 1987, in Karlsruhe, F. R. Germany. A paper has been accepted for publication in the Journal of Nuclear Materials.

REFERENCES

1. L. R. Greenwood, Damage Analysis and Fundamental Studies Quarterly Progress Report, DOE/ER-0046/21, pp. 9, May 1985.
2. D. W. Kneff, L. R. Greenwood, B. M. Oliver, and R. P. Skowronski, J. Nucl. Mater. 141-143, pp. 824-828 (1986).
3. Evaluated Neutron Data File (ENDF), Gas Production File 533, Brookhaven National Laboratory (1979).
4. D. L. Bowers and L. R. Greenwood, Analysis of Long-Lived Isotopes by Liquid Scintillation Spectrometry, Proc. Int. Conf. Meth. and Applications of Radioanalytical Chemistry, Kona, Hawaii, April 5-10, 1987, to be published in J. Radioanalytical Chem.
5. S. F. Mughabghab, M. Divadeenam, and N. E. Holden, Neutron Cross Sections, Vol. I, Academic Press, New York, 1981.
6. E. Brown and R. B. Firestone, Table of Radioactive Isotopes, V. S. Shirley, Ed., John Wiley, New York 1986.
7. A. Anufriev, Proc. Fifth All-Union Conf. on Neutron Physics, 15-19 September 1980, Kiev, USSR.
8. S. Pearlstein, Nucl. Cross Sections and Technology, Vol. I, NBS Spec. Pub. 425, pp. 332-333 (1975).

CROSS SECTION MEASUREMENTS FOR LONG-LIVED ISOTOPES NEAR 14.8 MeV - L. R. Greenwood and D. L. Bowers (Argonne National Laboratory)

OBJECTIVE

To measure 14 MeV neutron production cross sections for reactions leading to long-lived radioisotopes in fusion reactor materials.

SUMMARY

Neutron production cross sections have been measured near 14 MeV following high-fluence irradiations at the RTNS II facility. New results are reported for the production of ^{91}Nb (680y), ^{93}Mo (35900y), and $^{93\text{m}}\text{Nb}$ (13.6y) from natural Mo and ^{94}Mo enriched targets. Our data suggest that the half-life of ^{91}Nb may be shorter than previous estimates.

PROGRESS AND STATUS

We are engaged in an ongoing effort to measure production cross sections near 14 MeV for long-lived radioisotopes in fusion reactor materials. We have previously published results for ^{26}Al , ^{55}Fe , ^{63}Ni , and ^{94}Nb .¹⁻⁶ These production rates are needed to determine the activity levels in fusion waste materials and the data is also useful for dosimetry, plasma diagnostics, and reactor maintenance applications.

In the present case results are reported for the measurement of ^{91}Nb , ^{93}Mo , and $^{93\text{m}}\text{Nb}$. Natural Mo and enriched ^{94}Mo samples were irradiated at the RTNS II to neutron fluences between 0.5-1.5 $\times 10^{18}$ n/cm². Details concerning fluences were published previously¹ along with our results for the $^{94}\text{Mo}(n,p)^{94}\text{Nb}$ (20,000y) reaction since the same samples were used for both measurements.

After irradiation samples were dissolved in a mixture of HCl and HNO₃. Small aliquots were then flame dried on tantalum discs and covered with a thin layer of tape for x-ray counting. The deposits generally measured about 1 mg of Mo spread over an area of about 0.5 cm². In this way self-absorption corrections were less than 1% for x-rays in the 15-19 keV region. Absolute calibration of the detector was determined with a $^{93\text{m}}\text{Nb}$ x-ray standard (NBS-SRM4267). $^{93\text{m}}\text{Nb}$ has a half-life of 13.6±0.3 years and the K X-ray (16.5-19.1 keV) intensity is 10.57±0.54%. The half-life of ^{93}Mo is 3500±700 years and it has the same x-rays as $^{93\text{m}}\text{Nb}$ except that the intensity is 73.0±2.7%. ^{91}Nb decays with a lifetime of 680±130 years and the K x-rays (15.7-18.1 keV) have an intensity of 63.6±2.2%. All of the above decay data is taken from reference 7.

Since we irradiated both natural Mo and ^{94}Mo -enriched samples, measurements of the K x-ray activity can be used to uniquely determine the fraction of the activity in each sample which is due to either ^{92}Mo or ^{94}Mo . At the long decay times of our measurement (1090 days), there are no other known sources of Nb or Zr K x-rays from the other Mo isotopes, except for very long-lived isotopes such as ^{92}Nb (3.7 $\times 10^6$ y). Four samples were counted (2 natural, 2 enriched, and a simultaneous fit to the data yields the cross section values listed in Table I. In the case of ^{91}Mo , the only known activity with x-rays in this energy region is

Table I. Mo Cross Section Measurements

Reaction	Energy, MeV ^a	σ , mb
$^{92}\text{Mo}(n,2n)^{91}\text{Nb}$	14.7	603±119 ^b
$^{94}\text{Mo}(n,x)^{93}\text{Mo}$	14.7	< 810 ^c
$^{94}\text{Mo}(n,x)^{93\text{m}}\text{Nb}$	14.7	< 26 ^d

^aMean energy: width -0.5 MeV

^bUncert.: Stat. 1%, std. 2.4%, T_{1/2} 19%, fluence 5%, net 20%

^cUncert.: Stat. 1%, std. 2.4%, T_{1/2} 20%, fluence 5%, net 21%

^dUncert.: Stat. 1%, std. 2.4%, T_{1/2} 2.2%, fluence 5%, net 6%

^{91}Nb . The 62 day isomer of $^{91\text{m}}\text{Nb}$ has already decayed away in these samples. ^{91}Nb can be made by several reactions, primarily $^{92}\text{Mo}(n,2n)^{91}\text{Mo}$ which rapidly decays to ^{91}Nb . Although there is an isomer in ^{91}Mo and in ^{91}Nb , all of these reaction products eventually decay to ^{91}Nb . ^{91}Nb can also be made by the $^{92}\text{Mo}(n,d+np+pn)$ reactions. Hence, our cross section value represents the net production of ^{91}Nb from ^{92}Mo .

In the case of ^{94}Mo , we can make ^{93}Mo from the (n,2n) reaction and $^{93\text{m}}\text{Nb}$ from the (n,d+np+pn) reactions. $^{93\text{m}}\text{Nb}$ can also be made from the (n,t+nd+nnp) reactions on ^{95}Mo ; however ^{95}Mo is only 5.18% of the enriched sample and thus can only make a minor contribution (<1%). The situation is further complicated by the fact that ^{93}Mo decays to $^{93\text{m}}\text{Nb}$. We plan to perform a radiochemical separation of Nb and Mo in order to uniquely

determine the cross sections for both species. However, at present we can only place limits on the cross sections for both reactions. The decay of ^{93}Mo to ^{93m}Nb is rather slow due to the long half-life of 3500 Year and we calculate that at least 2% of the present activity must be due to ^{93m}Nb . Hence, we can place upper limits on both cross sections, as is done in Table I. It is, however, most probable that we produced more ^{93}Mo than ^{93m}Nb during the irradiation, as discussed below.

There are no known previous measurements of the $^{94}\text{Mo}(n,2n)^{93g}\text{Mo}$ cross section. The cross section to the 6.9 hr isomeric state of ^{93}Mo is reported to be between 2.4-6.4 mb; however, the reaction proceeds mainly to the ground state of ^{93}Mo and the total cross section should be much larger.

Haight, et al.,⁸ have reported a value of 9 ± 3 mb for the $^{94}\text{Mo}(n,d)$ reaction cross section. This would be quite consistent with our results; however, our measurements also include other possible reaction channels such as $^{94}\text{Mo}(n,np+pn)$.

We have used the THRESH29 semi-empirical computer code to estimate the strength of various reaction cross sections in order to gain some insight concerning the relative importance of unobserved reactions. These calculations predict a relatively flat energy dependence near 14 MeV for the $^{94}\text{Mo}(n,2n)$ reaction with a cross section of about 1 barn. This calculation is close to our maximum value of 810 mb. THRESH also predicts that the ^{94}Mo production cross section for ^{93m}Nb is 51 mb and that the $(n,np+pn)$ cross sections are about equal to the (n,d) value. However, these reaction cross sections are steeply rising near 14 MeV. If we assume that the ratio of the production cross sections from THRESH2 for $^{93}\text{Mo}/^{93m}\text{Nb}$ is roughly correct, then we would estimate that the $^{94}\text{Mo}(n,2n)^{93}\text{Mo}$ cross section is about 280 mb and that for $^{94}\text{Mo}(n,x)^{93m}\text{Nb}$ is about 17 mb. This latter value would agree with the (n,d) measurements assuming equal strength for the $(n,np+pn)$ reactions.

There have been several measurements of the $^{92}\text{Mo}(n,2n)^{91}\text{Mo}$ reaction to both the ground and isomeric states. Unlike the $^{94}\text{Mo}(n,2n)$ reactions, the $^{92}\text{Mo}(n,2n)$ cross section is steeply rising with energy near 14 MeV. Hence, some care must be taken in comparisons with our data since our energy resolution is about 0.4 MeV. Previous measurements give a value of about 200-250 mb in our energy region between 14.5-14.9 MeV. However, our measurements also include the production of ^{91g}Nb by the $^{92}\text{Mo}(n,d,np+pn)$ reactions. Haight, et al.,⁸ measured a value of 22 ± 7 mb for the (n,d) reaction at 14.8 MeV. Using the THRESH2 computer code, we estimate that the $(n,np+pn)$ reaction cross sections sum to about 70 mb. Thus the total production cross section of ^{91g}Nb should be about 300 mb, much less than our measurement of 603 mb.

There are several possible explanations for the discrepancy between our measurements and previous data for the production of ^{91g}Nb from ^{92}Mo . Since our measurement is based on the strength of the Zr K x-rays, it is possible that there are other contributing isotopes. However, due to the long decay time before analysis (1090 days), we are unable to identify any known interferences from other Mo isotopes or impurities in the material. It may also be that the unobserved $^{92}\text{Mo}(n,np+pn)$ reactions have a much larger cross section than predicted by THRESH2; however, this seems highly unlikely since we expect these reactions to be much weaker than the $(n,2n)$ reaction. A more likely explanation is that our measurements could be reconciled with previous data if the half-life of ^{91}Nb were reduced to about 350 years. The present value of 680 \pm 130 years has a rather large uncertainty (19%). Further measurements are needed to resolve this issue.

The present measurements can be used to calculate the production of these radioisotopes in a fusion reactor. Using the STARFIRE reactor design with a lifetime, first-wall irradiation of 21.6 MW-y/m² and 3000 day cooling, we calculate that Mo would produce 243 mCi/cc of ^{91}Nb , <41 mCi/cc of ^{93}Mo , and <140 mCi/cc of ^{93m}Nb .

FUTURE WORK

Further measurements are in progress to chemically separate Mo and Nb, thereby resolving the cross sections for ^{93}Mo and ^{93}Nb . Other reactions are also being studied involving the production of ^{14}C , ^{53}Mn , ^{93}Zr , and ^{92}Nb .

REFERENCES

1. L. R. Greenwood, D. G. Doran, and H. L. Heinisch, Phys. Rev. **34C**, 76-80 (1987).
2. R. K. Smither and L. R. Greenwood, J. Nucl. Mater. **122**, 1071-1077 (1984).
3. R. K. Smither and L. R. Greenwood, Damage Analysis and Fundamental Studies Progress Report DOE/ER-0046/17, 11-13 (1984).
4. L. R. Greenwood, Symp. on Effects of Rad. on Materials, Seattle, June 1986, ASTM-STP 956, in press.
5. R. K. Smither, L. R. Greenwood, and H. Hendel, Rev. Sci. Instrum. **56**, 1078-1080 (1985).

6. L. R. Greenwood and D. L. Bowers, Proc. Sixth ASTM-EURATOM Symp. on Reactor Oosimetry. Jackson, WY, June 1987, in press.
7. E. Browne and R. B. Firestone. Table Of Radioactive Isotopes, V.S. Shirley, Ed., John Wiley. New York (1986).
8. R. C. Haight, S. M. Grimes, R. G. Johnson, and H. H. Barschall, Phys. Rev. C23,700 (1981).
9. S. Pearlstein, Nucl. Cross Sections for Technology. NBS-SP425, 332 (1975).

PUBLICATIONS

These measurements were presented at the Third International Conference on Fusion Reactor Materials in Karlsruhe, F. R. Germany, October 1987, and they will be published in the Journal of Nuclear Materials.

3. MATERIALS ENGINEERING AND DESIGN REQUIREMENTS

MATERIALS HANDBOOK FOR FUSION ENERGY SYSTEMS - J. W. Davis (McDonnell Douglas Astronautics Company - St. Louis Division)

OBJECTIVE

To provide a consistent and authoritative source of material property data for use by the fusion community in concept evaluation, design, and performance/verification studies of the various fusion energy systems. A second objective is the early identification of areas in the materials data base where insufficient information or voids exist.

SUMMARY

The effort during this reporting period has been directed towards developing the supporting documentation data sheets in preparation for distribution to current handbook holders. The first distribution of the HT-9 data pages was made early in June. A second distribution of the electrical insulator data pages is scheduled for December. The release of these pages constitutes the first step towards establishing a data base of fusion developed experimental data.

PROGRESS AND STATUS

The materials handbook has now been expanded to two volumes. Volume 1, Engineering Design Data, is intended for use by designers, structural analysts, and material scientists, who participate in reactor design studies. It contains engineering curves of data, extrapolations of data, comparisons of properties of various materials, information with regard to the treatment of data, and recommendations as to the application of these materials and their operational limitations. Volume 2, Supporting Documentation, is designed primarily for the material scientist and contains the experimental data used to develop the data curves found in Volume 1. scatter plots of the data with the predictive curves, a bibliography of where the data was obtained, and a discussion of the relevancy of the particular data sets. The effort for this period has been directed towards the Supporting Documentation volume of the handbook. More than 60 data pages on the ferritic steel alloy HT-9 were distributed to authorized handbook holders June, another 50 data pages on lithium and magnet insulators is currently in work and should be distributed in December. This will leave a backlog of roughly 200 data pages awaiting publication in Volume 2.

During the summer, at a meeting in Washington, it was agreed that where possible, the handbook would be the source of material's property information for the Compact Ignition Tokamak (CIT). To help facilitate this, the CIT project requested 30 additional handbooks to be distributed to the System Managers. The additional handbooks were mailed to these individuals in August together with a letter requesting them to identify their material needs and the response time required. The first of these questionnaires has been received, requesting information on diagnostics.

FUTURE WORK

Anticipating the type of information that will be needed on the CIT work is in progress to prepare new data pages that would be of interest to them. The data pages that are in work will cover magnet case materials, electrical insulators, and high heat flux materials. It is anticipated that the first of these data pages will be available for review in the first quarter of 1988.

DIMENSIONAL CHANGE CORRELATIONS FOR 20% COLD-WORKED AISI 316 STAINLESS STEEL FOR FUSION APPLICATIONS -
R. W. Clark and A.S. Kumar (University of Missouri-Rolla) and F. A. Garner (Pacific Northwest Laboratory)

OBJECTIVE

The object of this effort is to provide documentation for design correlations included in the Fusion Materials Handbook.

SUMMARY

Correlations developed for void swelling and irradiation creep often arise from two separate data bases and sometimes are not well-matched, reflecting apparently minor but actually significant differences in environmental history. Previously published correlations are very empirical in nature and reflect prevailing misconceptions about the parametric sensitivity of swelling and irradiation creep. In this study a well-defined data base for swelling of 20% cold-worked AISI 316 is used in conjunction with the latest insights on swelling and creep to develop two matched dimensional change correlations for temperatures in the range of 300 to 650°C. The new creep model, in particular, is much simpler than the complicated empirical correlation published earlier for this steel.

PROGRESS AND STATUS

Introduction

Dimensional changes of fusion reactor components are expected to occur as a consequence of neutron-induced void swelling, irradiation creep and phase-related density changes. Dimensional change correlations are therefore required for design studies to predict the anticipated stresses and strains that will arise from these processes. Since there are no high flux devices available at the present time that possess the required fusion neutron spectra, such correlations must be developed using fission reactor data. Fast reactors, such as EBR-II and FFTF, operate at displacement rates comparable to those anticipated in fusion devices, but have neutron spectra that are significantly softer in energy. If one assumes that the concept of displacements per atom (dpa) and its current method of calculation adequately define the exposure damage parameter, then dimensional change correlations can be developed, providing sane account is taken of the possible influence of neutron spectra on transmutation.

Another aspect of correlation development involves the necessity of extrapolating beyond the range of available data. Such extrapolations require that the perception of the parametric dependency of the individual strain components be formulated in some model. With respect to void swelling and irradiation creep, however, the perception of these processes has changed strongly in the last decade. Whereas swelling in austenitic steels was previously thought to possess a steady-state swelling rate that was quite sensitive to an extensive range of material and environmental variables, (1) it is now known that this parameter is relatively insensitive to these variables over a wide range of temperatures. (2) The sensitivity of swelling has been found to reside primarily in the duration of the transient regime that precedes the onset of steady-state swelling. Subsequent to the transient the steady-state swelling rate is approximately 1%/dpa.

Another recently developed insight was that the irradiation creep rate of austenitic steels could be described largely by the sum of two terms, one of which is relatively insensitive to temperature and swelling, and another which is proportional to the instantaneous swelling rate, (2,3,4) at least for levels of swelling below approximately 10%. (When swelling is greater than 10% the irradiation creep at 550°C appears to vanish; the cause of this disappearance has not yet been determined. (5,6) Since the largest component of the creep rate is proportional to the swelling rate, irradiation creep should exhibit the same parametric sensitivities as those of swelling.

This anticipated similarity in sensitivity is fortunate because irradiation creep experiments are more difficult and expensive to conduct compared to those of swelling, and usually lag behind in accumulated exposure. Swelling and creep of austenitic steels have also been shown to be very responsive to variations in displacement rate and temperature history. (2) This is important because creep and swelling correlations are usually developed from separate data bases, and it is highly unlikely that both sets of experiments would have experienced exactly the same history.

Since AISI 316 is often proposed as a candidate material for construction of fusion reactor components, a set of matched swelling and creep correlations for 20% cold-worked AISI 316 was developed using only swelling data. The simple swelling-based creep correlation derived in this study was then compared with an older and more complicated empirical creep correlation developed from lower fluence data than is currently available for swelling.

Correlation Approach

The available fast reactor data base on swelling of AISI 316 was reviewed in this study, and much of these data are compiled in References 2 and 7. The major barrier to development of a swelling correlation is the demonstrated strong variability of the transient regime of swelling of this steel in response to environmental variables such as displacement rate, temperature history and stress, as well as to material variables such as composition, interpass annealing temperatures, cold-working schedule and level, and even furnace feed-through rates.

In order to minimize this problem, it was decided to develop a correlation for stress-free swelling at one displacement rate (1×10^6 dpa/sec) and for isothermal irradiation, using data on one reproducible group of steels irradiated in one well-characterized experiment. The steels employed were four heats of 20% cold-worked tubing used for the first core of the FFTF fast reactor located in Richland, Washington. These four heats yielded very reproducible swelling behavior and such behavior could presumably be reproduced for fusion applications by using the same specifications to which these steels were made.

The experiment was designated the Reference Swelling Experiment #1 (RS-1) and involved the irradiation of these four heats plus eight others in a typical B-7 irradiation capsule in Row 2 of the EBR-II reactor. The experiment and all of the data used to develop the swelling correlation are described in detail in Reference 7. The target temperatures were obtained by the use of gamma heating and by providing a gas gap between the subcapsules and the B-7 outer capsule. All data at any one temperature were obtained from one capsule and position in the core, and were therefore developed at the same neutron flux and displacement rate. The specimens were periodically discharged for density measurement and then reincapsulated into new subcapsules for further irradiation. This procedure tends to minimize the influence of reactor history, specimen-to-specimen variability, and temperature changes arising from neutron-induced differential swelling of the capsule and subcapsule.

Irradiation proceeded at nine target temperatures between 370 and 650°C, and data were extracted at peak fluences of 5, 9, 14, and 17 x 10^{22} n/cm² (E > 0.1 MeV). The neutron spectra across this irradiation vehicle produces 5.0 dpa (±5%) for each 10^{22} n/cm² (E > 0.1 MeV). (7) Swelling levels as large as 35% were observed at the highest fluence levels. (7)

The temperatures were found by later analysis to have been overestimated and to have fallen slowly throughout the long history of this experiment due to the progressive insertion of other non-fueled experiments in Row 2. This displaced some of the power generation and the associated gamma heating rate toward the outer rows, and gradually lowered the temperature experienced in each subcapsule. These temperatures were recalculated in this study for each reactor run by making detailed analyses of the run-to-run gamma heating levels as reported by the EBR-II operating staff. The full swelling data base is reported in reference 7 and the details of the temperature recalculations are described in reference 8.

The swelling data were then fit to the "bilinear" equation" shown in Fig. 1 using linear regression analysis after specifying that the steady-state swelling rate R would be 1.0%/dpa at all temperatures over the range of interest. Thus the incubation parameter τ_0 and the curvature parameter α were required to absorb the temperature dependence of swelling. The incubation parameter will be expanded later to incorporate the influence of spectrum-related variables such as He/dpa ratio and solid transmutants, as well as operational variables such as displacement rate, applied stress and temperature history. All input parameters are expressed in terms of dpa rather than neutron fluence.

Results: Swelling

Figs. 2 and 3 show the derived values of τ_0 and α , respectively, with the width of the horizontal bar at each target temperature showing the actual temperature range over which that particular subcapsule fell during the duration of the experiment. It is important to note, however, that much of the temperature decrease occurred after the onset of swelling. Based on previous studies it is known that deliberate and abrupt changes in temperature have very little effect on swelling if the transient regime is over or almost over when the change is made, (9) while similar changes occurring prior to the onset of accelerated swelling can have a very large influence (10,11). Thus the goal of developing an isothermal swelling equation is not thought to have been compromised. Figs. 4 and 5 show the predictions of this equation for stress-free isothermal irradiation.

Results: Irradiation Creep

Ehrlich (3) has compiled the results of published creep studies on austenitic steels using the formulation of Foster and coworkers (11) where:

$$\dot{\epsilon}/\sigma = B_0 + D\dot{S}$$

which states that the strain rate per unit stress equals the sum of the creep compliance B_0 and a term proportional to the swelling rate \dot{S} . Thermal creep is not included in this formulation. Ehrlich has shown

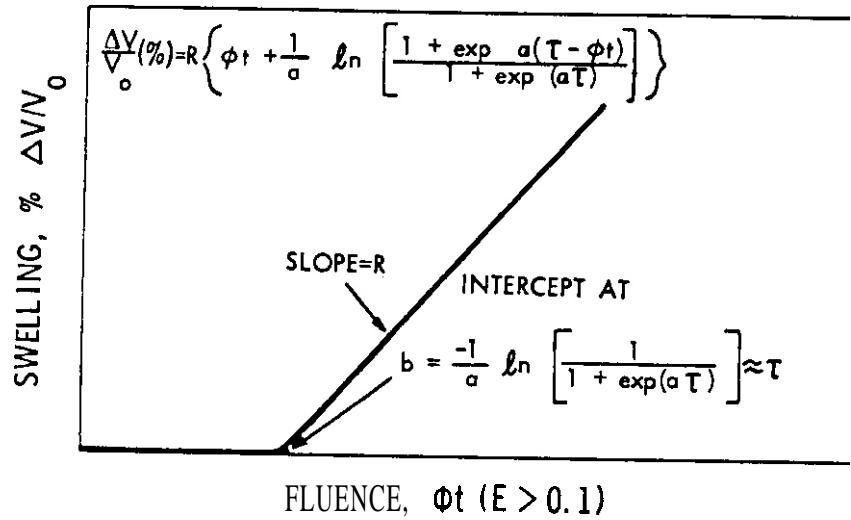


Fig. 1. Bilinear swelling equation as used for neutron-induced swelling. (1) In this study the neutron fluence Φt is replaced by the damage expressed in dpa.

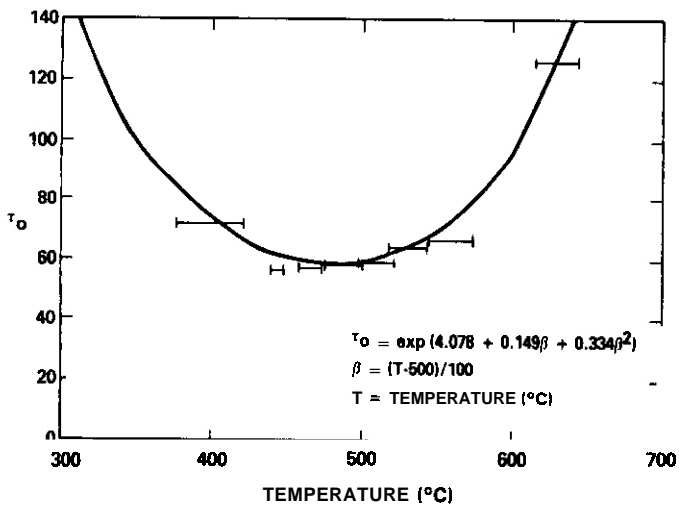


Fig. 2. Derived correlation for the stress-free incubation parameter τ_0 .

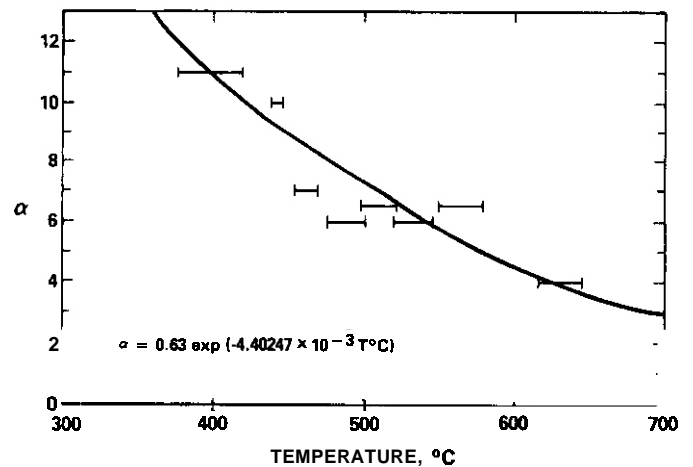


Fig. 3. Derived correlation for the curvature parameter α .

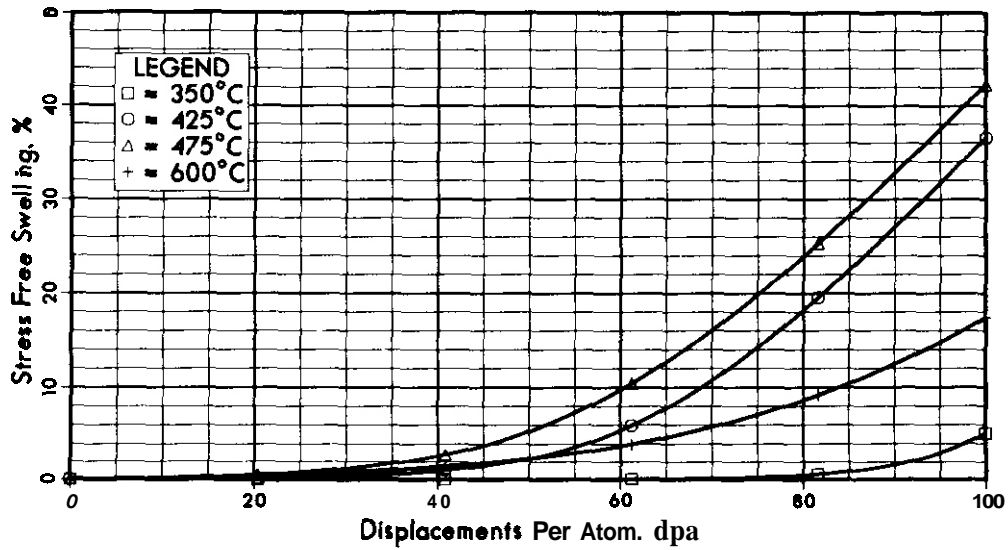


Fig. 4. Predicted stress-free swelling of 20% cold-worked AISI 316 stainless steel, showing approach to steady-state swelling.

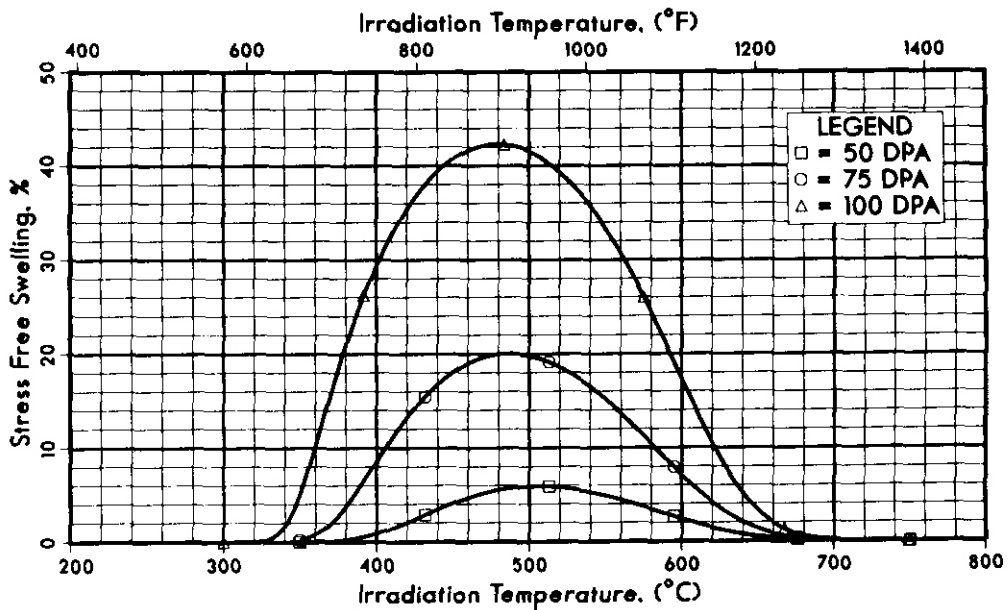


Fig. 5. Predicted stress-free swelling of 20% cold-worked AISI 316 stainless steel for several displacement levels.

that $B_0 = 10^{-6} \text{ Mpa}^{-1} \text{ dpa}^{-1}$ and $D = 10^{-2} \text{ Mpa}^{-1}$ for a wide range of materials and conditions. Similar conclusions were reached in other studies. (4,12) If we accept these values for the current study we can predict irradiation creep rates by noting that:

$$S = R \left\{ 1 - \left[\frac{\exp(-\gamma_c \text{dpa})}{1 + \exp(-\gamma_c \text{dpa})} \right] \right\}$$

where R , α and γ_c have previously been defined.

In the unstabilized cold-worked steels irradiated in the U.S. Breeder Reactor Program there is usually a short transient in the creep rate that accompanies the initial radiation-induced relaxation of the high dislocation density that is characteristic of cold-worked material. Therefore, the creep correlation has been modified to include this process.

$$\dot{\epsilon}/\sigma = B_0 + DS + A_1 (1 - \exp(-3(\text{dpa})))$$

where $A = 134 \exp(-9461/T)$ for biaxial loading and $A_1 = 268 \exp(-9461/T)$ for bending and $T =$ temperature in Kelvin. This formulation was borrowed from the "prompt jump" term of the more complicated empirical creep correlation developed by Puigh, Gilbert and Chin. (13)

Fig. 6 shows a comparison of the simple creep equation derived in this study compared to that of Puigh and coworkers. (13) This comparison was performed as a check of the reasonableness of the swelling-derived Correlation, particularly in areas where creep data are available. Some differences in the two predictions were anticipated. At lower temperatures the empirical creep correlation did not anticipate the higher rates of swelling and creep found in later studies. At temperatures approaching 600°C thermal creep begins to overtake irradiation creep. Remember that thermal creep was not included in this correlation since fusion applications of this steel do not anticipate temperatures above 600°C . Within the range where Puigh and coworkers have published creep data, the two correlations give approximately the same creep rate, indicating that the simple swelling-based correlation is reasonable. This provides confidence that a creep correlation could be developed for another steel using only swelling data.

Discussion and Conclusions

The two correlations developed in this study provide a matched set of consistent correlations for 20% cold-worked AISI 316 which can be used to conduct design studies in the range 300 to 600°C . They will not predict, however, the small negative strains which arise from precipitation of carbides very early in the irradiation (14) or the larger positive strains that arise from formation of intermetallic phases. (15) These strains must be superimposed on those of swelling and irradiation creep. Unlike swelling, the precipitate-related strains are anisotropic in nature. In the range of 600 to 650°C the creep correlation will underpredict the total strain due to the absence of thermal creep in this analysis. These strains can be estimated from Reference 15, however.

The influence of other variables relevant to fusion applications can be included in an expansion of the incubation parameter γ such that

$$\begin{aligned} \gamma = & \gamma_0(T_i) + q_1 f(\text{stress}) + q_2 f(\text{dpa rate}) \\ & + q_3 f(\text{He/dpa}) + q_4 f(T_f/T_i) + \dots \end{aligned}$$

where q_i are constants possibly dependent on temperature, and T_i and T_f are initial and final temperatures for time dependent temperature histories. Each of these functions needs to be evaluated separately and synergisms have been found to exist between some of these variables. (4,16) An earlier study addressed the effect of stress, utilizing the assumption that the hydrostatic component of the stress state was the operating variable. Thus, tensile stresses accelerated the onset of swelling (as was observed) and compressive stresses were assumed to delay swelling. (17) Recently this assumption has proved to be incorrect in that compressive stress states were found to be equally effective in accelerating swelling. (18) Thus, the influence on the incubation parameter of stress and other variables such as displacement rate or helium requires further study. A summary of the known behavior of swelling in response to these variables is listed in References 2 and 7.

It is important to remember that the correlations developed in this study apply only to a specification of steel demonstrated to be reproducible in its behavior. The use of this correlation for other specifications will lead to mispredictions of the swelling behavior, arising primarily in the duration of the transient regime. The user of these correlations should also remember that the transient regime has been shown to be sensitive to many reactor-specific variables. Since some of these have yet to be explored for fusion-relevant devices (e.g., pulsed rather than steady-state operation), additional uncertainty in the predictions will therefore arise.

FUTURE WORK

This effort is complete.

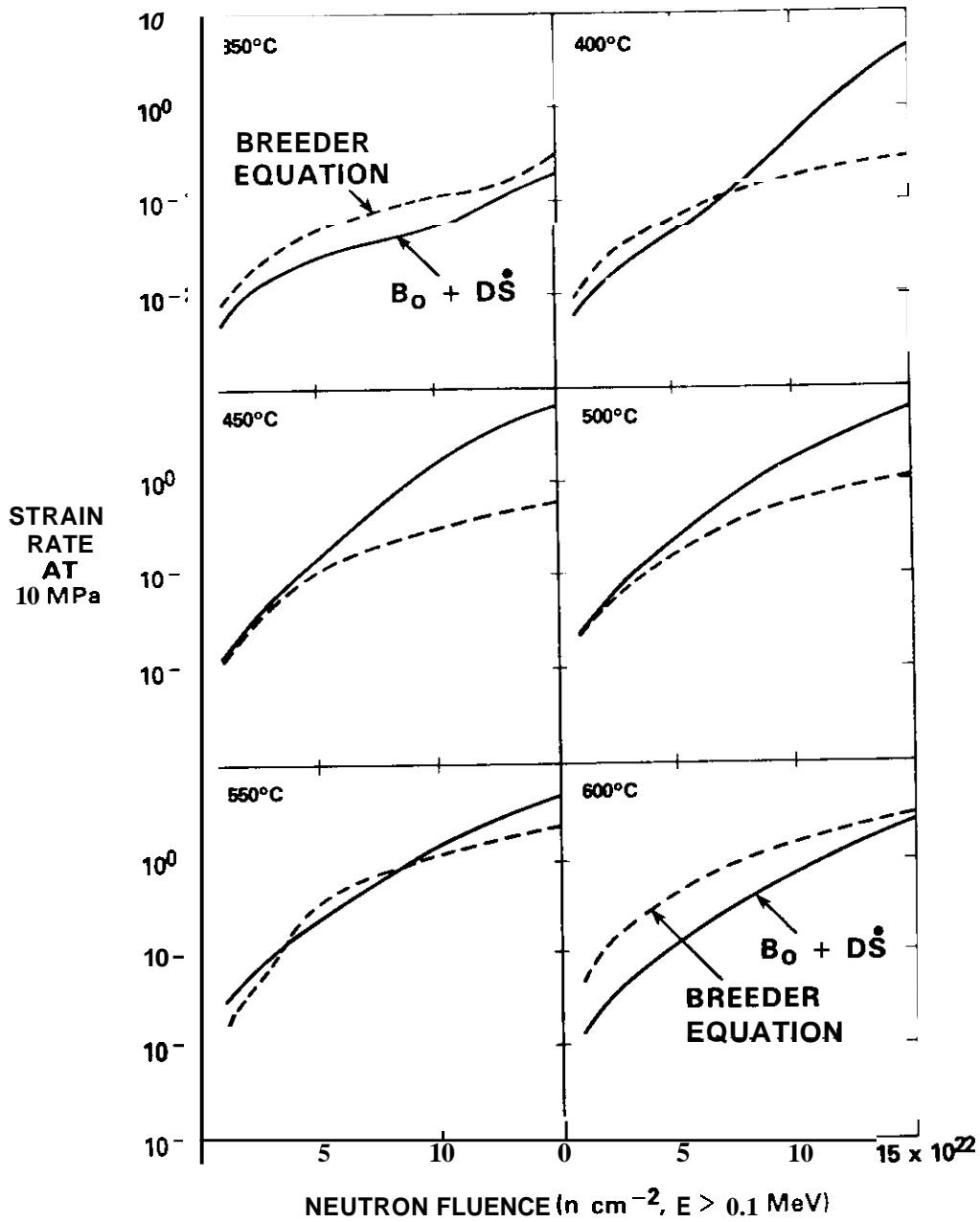


Fig. 6. Comparison of empirical breeder creep correlation with the simpler correlation developed in this study. The strain rate is in units of % per $10^{22} n \text{ cm}^{-2}$ ($E > 0.1 \text{ MeV}$) using a conversion factor of $5 \text{ dpa} = 10^{22} n \text{ cm}^{-2}$.

References

1. F. A. Garner, J. J. Laidler and G. L. Guthrie in Irradiation Effects on the Microstructure and Properties of Metals, ASTM STP 611, ed. F.R. Shober (American Society for Testing and Materials, Philadelphia, PA, 1976) p. 208.
2. F.A. Garner. J. Nucl. Mater., 122 & 123 (1984) 459.
3. K. Ehrlich. J. Nucl. Mater., 100 (1981) 149.
4. F. A. Garner and D. L. Porter. this semiannual report.
5. F. A. Garner, D. L. Porter and B. J. Makenas. J. Nucl. Mater., 148 (1987) 279.
6. D. L. Porter and F. A. Garner in Influence of Radiation on Material Properties, ASTM STP 956, eds. F.A. Garner, CH. Henager, Jr., and N. Igata (American Society for Testing and Materials, Philadelphia, PA 1987) 11.
7. F. A. Garner in Optimizing Materials for Nuclear Applications, eds. F.A. Garner, D. S. Gelles and F.W. Wiffen (TMS-AIME, Warrendale, PA, 1985) 111.
8. R. W. Clark. Dimensional Change Correlations for 20% Cold-Worked AISI 316 Stainless Steel for Fusion Applications (Masters Thesis). University of Missouri-Rolla. 1986.
9. W. J. S. Yang and F. A. Garner in Effects of Radiation on Materials: Proceedings of the 11th International Symposium, ASTM STP 782, eds. H. R. Brager and J. S. Perrin (American Society for Testing and Materials, Philadelphia, PA, 1982) 186.
10. F. A. Garner, E. R. Gilbert, D. S. Gelles and J. P. Foster. in Effects of Radiation on Materials, Proceedings of the 10th International Symposium, ASTM STP 725, eds. D. Kramer, H. R. Brager and J. S. Perrin (American Society for Testing and Materials, Philadelphia, PA, 1980) 698.
11. J. P. Foster, W. G. Wolfer, A. Biancheria and A. Boltax. Proceedings BNES Conference on Irradiation Embrittlement and Creep in Fuel Cladding and Core Components, London (1972) 273.
12. J. L. Boutard, Y. Carteret, R. Cauvin, Y. Guerin and A. Maillard. Proceedings Conference on Dimensional Stability and Mechanical Behavior of Irradiated Metals and Alloys, Brighton, England (1983) Vol I, 109.
13. R. J. Puigh, E. R. Gilbert and B. A. Chin. in Reference 9, p. 108.
14. F. A. Garner, W. V. Cummings, J. F. Bates and E. R. Gilbert. HEDL-TME 78-9, Hanford Engineering Development Laboratory. June 1978.
15. R. J. Puigh, A. J. Lovell and F. A. Garner. J. Nucl. Mater., 122 and 123 (1984) 242.
16. D. L. Porter and F. A. Garner in Effects of Radiation on Materials: Thirteenth International Symposium, ASTM STP 870, eds. F. A. Garner and J. S. Perrin (American Society for Testing and Materials, Philadelphia, PA, 1985) 212.
17. F. A. Garner, E. R. Gilbert and D. L. Porter in Reference 10, p. 680.
18. T. Lauritzen, S. W. Vaidyanathan, W. L. Bell and W. J. S. Yang in Radiation-Induced Changes in Microstructure, ASTM STP 955, eds. F. A. Garner, N. H. Packan and A. S. Kumar (American Society of Testing and Materials, Philadelphia, PA, 1987) 101.

4. FUNDAMENTAL MECHANICAL BEHAVIOR

ANALYSIS OF CLEAVAGE FRACTURE BEHAVIOR IN HT-9 WITH A STATISTICAL MODEL

- G. E. Lucas, H. Yih, G. R. Odette (University of California, Santa Barbara)

OBJECTIVE

To establish a fundamental understanding of the mechanism of cleavage fracture as an essential step in developing ferritic/martensitic steels for fusion reactor structural applications.

SUMMARY

We have investigated the applicability of a statistical model for cleavage fracture to data obtained on a set of HT-9 specimens heat-treated to 25 different conditions, for which prior austenite grain size, lath packet size and carbide size and density varied systematically. The statistical model predictions were in good agreement with observed trends. The results suggest that cleavage in these steels may be dictated by microcrack nucleation and propagation from large boundary carbides.

PROGRESS AND STATUS

The interest in ferritic/martensitic steels for fusion reactor structures is somewhat tempered by their exhibition of a brittle cleavage mode of fracture at low temperature and by a potential increase with neutron irradiation in the transition temperature delineating the ductile and brittle fracture regimes. However, we have previously suggested that operation in the cleavage fracture temperature regime may be possible providing that 1) irradiation and other environmental factors do not degrade the lower shelf toughness, 2) fracture occurs at stresses associated with general yield, and 3) sufficient ductility is retained [1-4]. Demonstration of this requires in part understanding the basic mechanism of cleavage fracture and identifying the pertinent microstructure-property relations.

To this end we have investigated the applicability of the Ritchie-Knott-Rice (RKR) model [5] to various heat treatments of HT-9 [3,6-8]. The RKR model postulates that cleavage fracture occurs when the applied stress ahead of a sharp crack exceeds a critical value σ_f^* over a microstructurally significant distance ℓ^* . Work previous to ours suggested that in lath bainitic/martensitic structures $\sigma_f^* \propto \frac{1}{\sqrt{d_p}}$, where d_p = lath packet size, and that ℓ^* may be a small multiple of the prior austenite grain size. While we were successful in applying this approach to one heat of HT-9 [3], we have found that in HT-9 heat treated to a wide range of microstructures, these microstructural dependencies are not entirely observed. One possible reason for this is that the statistical nature of cleavage fracture is not completely captured by a simple critical stress - critical distance criteria for the steels previously examined. Consequently, it was the objective of this study to re-examine the data in terms of a statistical model for cleavage fracture.

STATISTICAL MODELS

The current understanding of the cleavage fracture process in ferrous steels indicates that cleavage microcracks must both initiate and propagate [cf. 9]. Microcrack nucleation most likely occurs at grain boundaries where large dislocation pileups can provide sufficient stress intensity to initiate the crack. However, dislocation generation within pure ferrite occurs readily down to relatively low temperatures. Since this would blunt the microcrack and render it inactive, it is generally felt that at temperatures above about ~ 73K microcracks nucleate in hard particles, such as carbides or inclusions, at grain boundaries. But microcrack nucleation alone is insufficient to initiate cleavage. The applied stress must also be sufficient to propagate the microcrack out of the hard particle, into the matrix and through at least one highly misoriented crystal (grain, lath, lath packet ...) boundary; otherwise the microcrack can arrest, providing sufficient opportunity for dislocation generation to blunt and deactivate it. Once running, the microcrack tip may advance too rapidly for dislocation generation to blunt it. As reported elsewhere [3,8], we have obtained microstructural evidence in HT-9 which supports the association of microcracks with grain boundary carbides and microcrack arrest at grain boundaries.

Consequently, the cleavage initiation event is associated with an applied stress large enough to nucleate and propagate a microcrack, with propagation being the limiting step. The critical stress for a given carbide (i.e., carbide "strength") is determined by the stress needed to propagate a carbide-sized crack into the surrounding matrix; and based on a Griffith energy approach [10], it is of the form

$$S = \left[\frac{\pi \gamma E}{(1 - \nu^2) d_c} \right]^{\frac{1}{2}}$$

where E = elastic modulus, ν = Poisson ratio, d_c = carbide size, and γ represents a fracture surface energy. Hence, large particles require the smallest applied stress to initiate cleavage. However, ahead of a blunt notch or a sharp crack the stress field is not uniform. Moreover, the carbides are not uniform in size or spatial distribution. Hence, beginning with Curry and Knott [11], a number of authors [12-14] have argued that cleavage in notched or cracked specimens/structures is statistical in nature and occurs when some carbide ahead of the crack/notch is stressed beyond its critical value. The various models developed to describe this statistical sampling of carbides/particles [11-14] have differed in 1) the description of particle size distribution, 2) the description of the stress fields ahead of the crack, and 3) the volume of material considered ahead of the crack. We apply here one of these – the model of Evans [12] as modified by Lin *et al.* [15] – to the data we have obtained to date on HT-9.

A Weibull distribution of carbides is assumed such that

$$G(\sigma) = 1 - \exp \left[- \left(\frac{\sigma - S_u}{S_o} \right)^m \right] \quad (2)$$

where $G(\sigma)$ = fraction of particles with strength $S \leq \sigma$, S_u is the strength of the largest particle, and m and S_o are shape and scale parameters of the carbide distribution. Using both Hutchinson-Rice-Rosengren (HRR) [16,17] and elastic stress field solutions, Lin *et al.* derive a function describing the probability that in the material ahead of the crack tip a critical condition is achieved. Calibrating against experimental data, they define the fracture toughness as the stress intensity when the probability exceeds 50%. For the HRR field, the equation is of the form

$$K_{IC}^{HRR} = \left\{ \frac{\xi n 2}{\eta f N_o b} \right\}^{\frac{1}{4}} \left\{ \frac{S_o}{S_u} \right\}^{\frac{m}{4}} S_u^{\frac{(1+n)}{2}} \sigma_o^{\left(\frac{1-n}{2}\right)}$$

where

ξ	–	an integral of the HRR field = $\xi(n)$
		$\int (x-1)^m x^{-(2n+3)} dx$
σ_o	–	yield stress
F	–	maximum ratio of applied stress to yield stress ahead of the crack tip
n	=	work hardening exponent $\frac{d \ln \epsilon}{\log \sigma}$
N_o	–	carbide number density
f	=	fraction of microcrack nuclei which participate in the cleavage process
b	–	characteristic dimension along the crack front

For the elastic field, the solution is

$$K_{IC}^{el} = \left\{ \frac{\xi n 2}{1.35 \eta f N_o b} \right\}^{\frac{1}{4}} \left(\frac{S_o}{S_u} \right)^{\frac{m}{4}} S_u \quad (4)$$

The elastic solution dominates at low temperature (lower shelf) whereas the HRR-field-based solution dominates in the transition region where the plastic zone becomes large. The net behavior can be simply modeled by taking

$$K_{IC} = \max (K_{IC}^{el}, K_{IC}^{HRR}) \quad (5)$$

APPLICATION

We have previously reported microstructural and mechanical property data for HT-9 heat treated to 25 different combinations of austenitization temperature ($T!$: 950°C, 1000, 1050, 1100, 1200°C) and tempering condition (650°C, 1h; 650°C, 56h; 715°C, 1h; 735°C, .5h; 780°C, 1h) [6,7]. Briefly, the prior austenite grain size was found to increase from 25 to 325 μm and the lath packet size from 8 to 100 μm as T_γ increased from 950 to 1200°C. Massive grain boundary carbides were observed in the $T_\gamma = 950^\circ C$ material, but they diminished in size and number as T_γ increased. Beyond 1050°C they were no longer apparent, although other carbide populations were present.

To supplement the microstructural information previously obtained and reported, we determined carbide size distributions from carbide extraction replicas for purposes of applying eqs. (1)-(5). Carbide sizes were converted to strengths using eq. (1) and a fracture surface energy of $\gamma = 14\text{J/m}^2$. Values of S_u , S_o and m were then determined by fitting eq. (2) to the data. The three-parameter Weibull distribution did a reasonable job of describing the carbide distribution. It should be noted, however, that while the value of S_u plays a dominant role in determining K_{IC} , it is very difficult to determine accurately. The number density of carbides of a particular size class decreases with increasing carbide size, so that S_u becomes an extrapolation of a function strongly determined by smaller carbides. While for this study we have used all carbide sizes to determine the Weibull parameters, alternate ways of determining S_u more accurately (such as weighting the large carbide fraction more heavily) will be examined in the future.

The variation of S_u with austenitization temperature and tempering condition is shown in Fig. 1. S_u shows a peak at $T_\gamma = 1050^\circ\text{C}$ which corresponds to the disappearance of the massive grain boundary carbides described earlier. The lines drawn through the data are not least squares fits. The uncertainties on S_u were relatively high, and direct fits to the data consequently produced confounding results. Instead it was noted that data at all tempering conditions showed a systematic increase in S_u with T_γ to 1050°C , and a subsequent decrease with higher T_γ . The variation of S_u with T_γ between 1050°C and 1200°C was similar to the observed variations with T_γ (i.e., same slope) of measured values of the critical cleavage fracture stress σ_f^* [7], which is mechanically related to (but not numerically equivalent to) S_u . Consequently, the shape of the S_u vs. T_γ curve was estimated from a consideration of all the data, and the curves themselves were then scaled to the data for the various tempering conditions. Carbide populations (and hence values of S_u) were quite similar for the tempering conditions: 650°C , 56h; 715°C , 1h; 735°C , 0.5h. These all have the same value of the tempering parameter $P_T = T(^{\circ}\text{K})(\log t(\text{h}) + 20) = 20 \times 10^3$. Hence, the data points used in constructing the middle curve Fig. 3 were taken as averages of the data obtained from these conditions. Finally, while the variation in S_u from condition to condition was large and systematic, variations of S_o and m were modest and not as systematic. S_o had values largely in the range 3000-4500 MPa, and m 1.5-2.0.

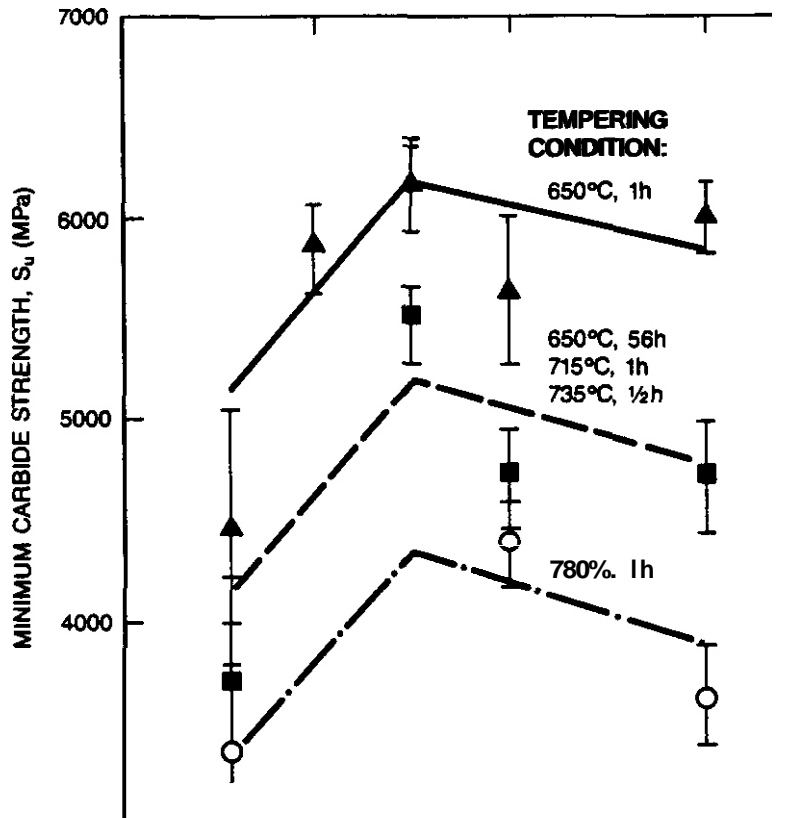


Figure 1. Variation in the value of S_u with austenitization temperature and tempering condition

Carbide density was also determined from the extraction replicas; only prior austenite grain (PAG) boundary carbides were counted, although other carbide densities (lath, matrix, lath packet boundary) appeared to scale with the PAG boundary density. Yield strengths as a function of temperature were taken from ref. 7, and values of $\xi(n)$ taken from ref. 18. The value of the work hardening exponent n was assumed to be ~ 6 from tensile data obtained on several materials. The product fb was just taken as a fit parameter. It was determined by fitting the elastic solution (eq. 5) to lower shelf toughness data for one condition ($T_\gamma = 1050^\circ\text{C}$; 650°C , 1h).

Using the values so obtained, K_{IC} as a function of temperature was calculated for each of the twenty-five materials. Unfortunately, full experimental fracture toughness curves are not available for each material, but some static toughness data were obtained at two temperatures for several heat treatments, and dynamic toughness data were obtained for all conditions from instrumented pre-cracked Charpy specimen tests at 161K. Comparison of the calculated curves to the static data are shown in Fig. 2, and comparisons of calculated values to dynamic data are shown in Fig. 3. In both instances the agreement between calculated values and data is good, although the goodness of fit is in part a reflection of the smoothness in variation of S_u with T_γ assumed in the construction of Fig. 1. More importantly, the correct trends are predicted; namely, 1) the lower shelf toughness does not appear to vary dramatically among materials, even though large scale microstructural parameters vary significantly from material to material (eg., prior austenite grain size and lath packet size change by a factor of 10 from $T_\gamma = 950$ to 1200°C); 2) increasing tempering and increasing austenitizing temperature tend to shift the curves to lower temperatures; 3) dynamic testing reduces the toughness to near lower shelf values.

DISCUSSION

The insensitivity of the lower shelf toughness (K_{IC}^{ls}) to heat treatment can be understood with the aid of eqs. (1) and (4). Recalling the small variation of S_o and m among materials and substituting eq. (1) into eq. (4), the result can be approximately written as

$$K_{IC}^{ls} \sim (d_c^{max} N_o)^{-\frac{1}{4}} \quad (6)$$

where d_c^{max} is the size of the largest carbide. Hence, the sensitivity of the lower shelf toughness to microstructural variations for the conditions investigated is primarily manifest in a dependence on carbide density and the maximum carbide size. This sensitivity is relatively small. Moreover, for many condition-to-condition variations, d_c^{max} and N_o varied inversely; for instance, as austenitization temperature increased from 1050°C to 1200°C , d_c^{max} increased while N_o decreased. Hence, these changes offset one another in their effect on K_{IC}^{ls} . It might also be noted that for a fixed volume fraction of carbides, d_c^{max} would be proportional to $N_o^{-\frac{1}{3}}$. In such an instance, eq. (6) can be rewritten as

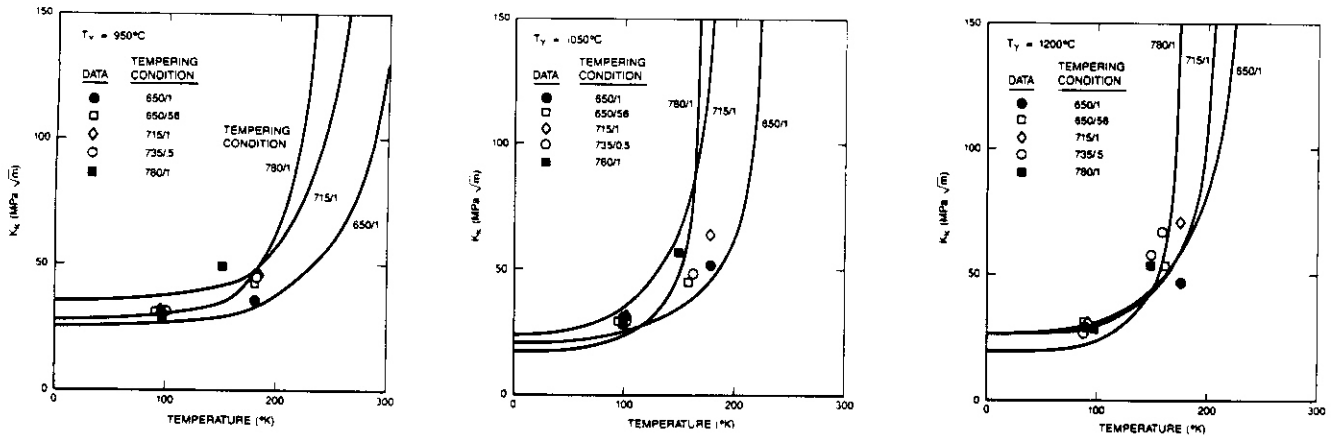


Figure 2. Comparison of calculated toughness curves with static toughness data for three austenitization temperatures.

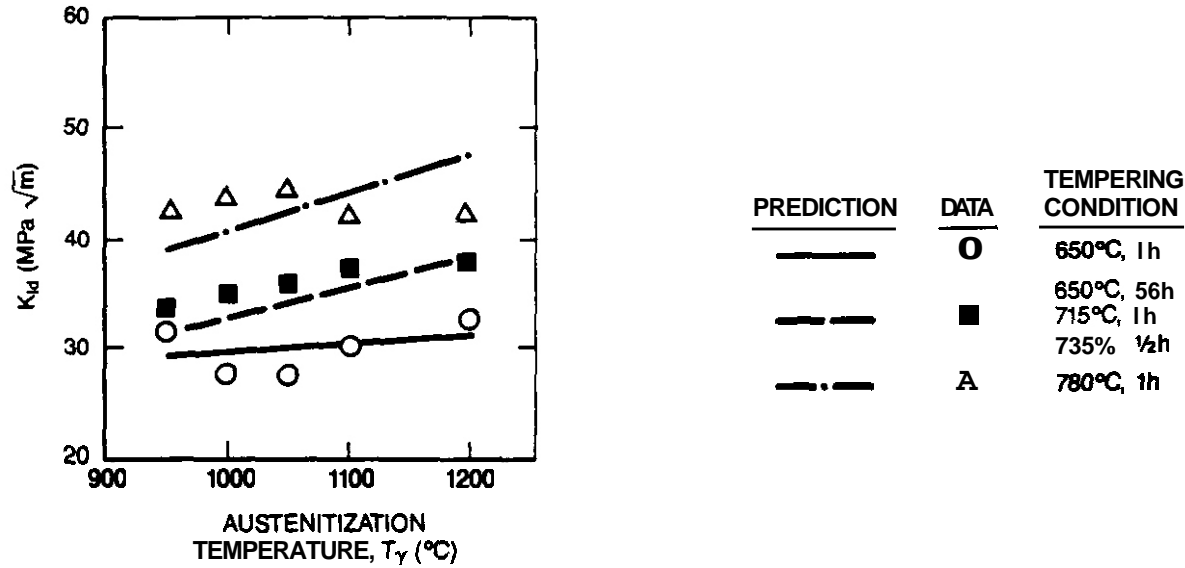


Figure 3. Comparison of calculated dynamic toughness with data for all twenty-five materials. Data for similar tempering conditions (600°C, 50h; 715°C, 1h; 735°C, 0.15h) have been averaged.

$$K_{IC}^{\ell_s} \sim (N_o)^{-\frac{1}{6}} \quad (7)$$

Thus, the dependence of $K_{IC}^{\ell_s}$ on N_o would be very weak indeed

Transition behavior is largely dictated by the upper limit of the integral defining η in eq. (3). That is, when $F\sigma_o/S_u$ approaches 1, η approaches 0 and K_{IC} approaches infinity. As reported earlier [7], σ_o had a dependence on heat treatment similar to that found for S_u . That is, maximum yield stresses were found for austenitization temperatures of 1050°C and σ_o was reduced by increasing tempering time/temperature. However, magnitudes of σ_o and S_u were such that the ratio of σ_o/S_u (at any given test temperature) tended to decrease with increasing T_γ and increasing tempering parameter, thus giving rise to the trends indicated in predicted transition behavior. Smaller observed values of dynamic versus static toughness are simply manifestations of high transition temperatures in the dynamic case, effected by a strain-rate sensitive increase in σ_o .

The good agreement between the predicted and observed trends suggests the statistical model may be a good description of the dominant processes involved in cleavage fracture in HT-9. The statistical model is not inconsistent with the **RKR** model. For instance, for a mild steel where the plastic zone was quite large compared to the grain size, the statistical model we have used has been shown to be equivalent to the **RKR** model [19]. Curry [20] has also shown that his statistical approach is equivalent to the **RKR** model, but only when the plastic zone ahead of the crack is larger than the critical distance. Since this was not the case for a number of the conditions we examined, it may not be surprising that the **RKR** model was not found to be in agreement with observed trends.

The implications of these results to alloy development are as follows. Since eq. (6) suggests that lower shelf toughness may depend mainly on the product of d_c^{max} and N_o , increases in $K_{IC}^{\ell_s}$ might be anticipated in steels with a small density of fine carbides at grain boundaries. Moreover, implied in eq. (6) is a dependence of $K_{IC}^{\ell_s}$ on γ , the fracture surface energy. We have noted previously the appearance of tear ridges on cleavage fracture surfaces of the HT-9 specimens examined here [8]. These appear to be associated with prior austenite grain and lath packet boundaries, and suggest that ductile tearing is required when the cleavage crack traverses these boundaries. An increased density of these tear ridges appears to increase γ , hence increases in γ , by increasing the amount of plastic tearing required during cleavage crack propagation, may also improve $K_{IC}^{\ell_s}$. Since knee and transition behavior are largely dictated by the ratio σ_o/S_u , improvements in behavior would be largely obtained by reductions in yield strength, or increases in S_u (again by minimizing carbide size).

Irradiation may alter the lower shelf toughness by changing the size/distribution of grain boundary carbides, or by introducing additional brittle obstacles (eg. intermetallics) at grain boundaries. This remains to be examined experimentally. Irradiation is already known to increase the transition temperature in ferritic/martensitic steels, and increases can generally be correlated with strength/hardness increases [21,22]. Hence, improved transition behavior might be expected in alloys resistant to irradiation hardening. Further advances in understanding the effects of irradiation on cleavage fracture behavior will require additional irradiation testing. Since the microstructural and hence mechanical responses are sensitive to the character of the irradiation environment, future tests should be conducted at near-service conditions.

CONCLUSIONS

We have investigated the applicability of a statistical model for cleavage fracture to data obtained on a set of HT-9 specimens heat treated to 25 different combinations of austenitization temperature and tempering treatment. The statistical model predictions were in good agreement with observed trends. While the comparison is not conclusive, the agreement lends validity to the model assumption that cleavage is dictated by microcrack nucleation and propagation from large boundary carbides. The results suggest that improved toughness in ferritic/martensitic steels might be obtained through reductions in carbide size and number density and increases in fracture surface energy, perhaps by increasing the amount of plastic tearing required at grain and packet boundaries.

FUTURE WORK

We will continue to investigate the applicability of statistical models, and we will attempt to combine the models with calculated stress fields ahead of crack tips to improve them.

REFERENCES

1. G. R. Odette and G. E. Lucas, *J. Nucl. Mater.*, **117** (1983) 264.
2. G. R. Odette and G. E. Lucas, *J. Nucl. Mater.*, **117** (1983) 276.
3. G. R. Odette, G. E. Lucas, R. Maiti, J. W. Sheckherd, *J. Nucl. Mater.*, **122/123** (1984) 442.
4. G. R. Odette, G. E. Lucas, R. Maiti, J. W. Sheckherd, *J. Nucl. Mater.*, **133/134** (1985) 849.
5. R. O. Ritchie, J. F. Knott, J. R. Rice, *J. Mech. Phys. Solids*, **21** (1973) 395.
6. C. Elliott, R. Maiti, G. E. Lucas, G. R. Odette, *J. Nucl. Mater.*, **141/143** (1986) 439.
7. R. Maiti, G. E. Lucas, G. R. Odette, J. W. Sheckherd, *J. Nucl. Mater.*, **141/143** (1986) 527.
8. G. R. Odette, G. E. Lucas, R. Maiti, *J. Nucl. Mater.*, **148** (1987) 22.
9. G. T. Hahn, *Met. Trans.*, **15A** (1984) 947.
10. A. A. Griffith, Proc. 1st Int'l Cong. Appl. Mech., Delft, Holland (1979) 55.
11. D. A. Curry and J. F. Knott, *Met. Sci.*, **10** (1976) 341.
12. A. G. Evans, *Met. Trans.*, **14A** (1983) 1349.
13. F. M. Beremin, *Met. Trans.*, **14A** (1983) 2277.
14. K. Wallin, T. Saario, K. Torronen, *Met. Sci.* (1984) 13.
15. T. Lin, A. G. Evans, O. Ritchie, *J. Mech. Phys. Solids* (in press).
16. J. R. Rice and G. F. Rosengren, *J. Mech. Phys. Solids*, **16** (1968) 1.
17. J. W. Hutchinson, *J. Mech. Phys. Solids*, **16** (1968) 13.
18. T. Lin, Ph.D Thesis, Engineering, University of California, Berkeley, 1986.
19. T. Lin, A. G. Evans, R. O. Ritchie, *Acta Met* (in press).
20. D. A. Curry, *Met. Sci.*, **19** (1980) 78.
21. G. E. Lucas and D. S. Gelles, "The Effects of Neutron Irradiation on Fracture and Impact Properties of Fusion Reactor Materials," *J. Nucl. Mat.* (in press).
22. G. E. Lucas and G. R. Odette, *ASTM-STP-956* (in press)

THE TENSILE PROPERTIES OF FE-CR BINARY ALLOYS USING MINIATURE SPECIMENS - M.F. Maxson (The Northwest College & University Association for Science, NORCUS), H.L. Heinisch and D.S. Gelles (Pacific Northwest Laboratory)

OBJECTIVE

The ultimate objective of this work is to determine the effect of fast neutron induced void swelling on the mechanical properties of ferritic alloys. The immediate objective is to provide baseline measurements on an altered specimen geometry for later comparison with irradiated specimen results.

SUMMARY

Microtensile specimens of Fe-3, 6, 9, 12, 15 and 18Cr have been tested to provide baseline data for comparison with specimens being irradiated in FFTF. Yield strengths for Fe-6Cr and Fe-9Cr were lower than for the other alloys tested, in agreement with the literature. Impurities in the Fe-3Cr alloy led to increased strength in that alloy. The use of thicker specimens did not significantly reduce experimental uncertainties.

PROGRESS AND STATUS

Introduction

It has been suggested that void swelling in ferritic alloys may promote ductility loss due to channel fracture¹. Examination of the effect of void swelling on ductility in ferritic alloys is generally difficult because such alloys are inherently resistant to swelling. However, it has been shown that reasonable levels of void swelling can be developed in simple Fe-Cr binary alloys¹⁻³. Based on these results, an experiment has been initiated to examine the likelihood that channel fracture could control ductility in ferritic alloys. Specimens of Fe-3, 6, 9, 12, 15 and 18Cr were fabricated into miniature sheet tensile specimens and were irradiated starting in MOTA 1E at 365, 420, 520 and 600°C. Sufficient numbers of specimens are being irradiated to provide three levels of dose with six specimens to be available at each condition.

The present effort is intended to provide baseline data for the irradiated specimens. Therefore, the present study was initiated to determine the 0.2% offset yield strength, ultimate tensile strength, and uniform elongation for Fe-Cr binary alloys as a function of chromium content. The study and the results obtained from it will be used to: 1) establish a reliable tensile testing procedure for miniature, sheet-type, ferritic specimens, 2) determine the reliability of the data as compared to that obtained from previous studies¹⁻³ on the same test apparatus, but using specimens with twice the thickness of the usual miniature tensile specimens, and 3) establish a control group data base for similar alloys currently being irradiated in the Fast Flux Test Facility at 365, 420, 520, and 600°C.

Experimental Procedure

1. Materials

Miniature, sheet-type specimens of Fe-Cr binary alloys over the composition range 3 to 18%Cr at intervals of 3 Cr were punched from sheets previously rolled to 0.508 mm thickness (0.635 mm for Fe-12Cr). These materials were identical to those used in previous irradiation effects studies¹⁻² and it has been shown that the Fe-3Cr alloy was impure. The specimens were 12.7 x 2.54 x 0.508 mm overall with a gauge section dimension of 5.10 x 1.03 x 0.508 mm, except 12Cr which had a thickness of 0.635 mm. The usual specimen thickness for this specimen configuration has been 0.2-0.3 mm. After punching, the specimens were polished by hand to remove any burrs, laser engraved with identification codes, and heat-treated as follows:

$$1040^{\circ}\text{C}/ 1\text{h}/ \text{AC} + 760^{\circ}\text{C}/ 2\text{h}/ \text{AC}.$$

The minimum width and minimum thickness of the gauge section of each specimen was measured with a micrometer prior to tensile testing.

2. Tensile Testing

Tensile tests were conducted at room temperature using a tensile testing machine specifically designed for miniature specimens⁴. All tests were conducted at a constant cross-head speed of 2.5×10^{-6} m/s. The load and displacement values were collected in both analog and digital form. The 0.2% offset yield strength, ultimate tensile strength, and uniform elongation were determined through a graphical analysis of the analog data.

3. Metallography

One tensile specimen of each alloy was prepared for metallographic examination in order to determine the minimum number of grains across the specimen thickness. The specimens were prepared by making a transverse cut through the center of the gauge section and then mounting one-half of each specimen. Photomicrographs were taken of each specimen at a measured magnification of 99.5x and the minimum number of grains was determined.

Results

Tensile tests were conducted in two stages. First, testing was performed on nine specimens of the Fe-9Cr alloy to allow for operator familiarization with the equipment and to determine measurement repeatability. Then three or more specimens of the remaining Fe-Cr binary alloys were tested. The values obtained for 0.2% offset yield strength, ultimate tensile strength, and uniform elongation are listed in Table 1. In all cases the standard deviation of the data refer to one sigma values.

Table 1. Fe-Cr binary alloy analog tensile test data.

Alloy	0.2% Offset Yield strength (MPa)	Ultimate Strength (MPa)	Uniform Elongation (%)
Fe-3Cr	217	319	21
	221	319	21
	<u>209</u>	<u>317</u>	<u>20</u>
	mean 216 ± 6	318 ± 1	21 ± 1
Fe-6Cr	120	268	19
	121	264	19
	<u>131</u>	<u>287</u>	<u>13</u>
	mean 124 ± 6	273 ± 12	17 ± 3
Fe-9Cr	120	278	17
	119	272	16
	125	285	16
	120	272	15
	116	281	15
	107	270	15
	133	292	15
	126	292	19
	<u>123</u>	<u>293</u>	<u>21</u>
	123	297	22
	125	299	20
	mean 117 ± 6	285 ± 10	17 ± 3
Fe-12Cr	171	340	20
	169	339	21
	<u>168</u>	<u>332</u>	<u>22</u>
	mean 169 ± 2	337 ± 4	21 ± 1
Fe-15Cr	170	271	17
	171	312	19
	166	279	16
	<u>166</u>	<u>301</u>	<u>21</u>
	mean 168 ± 3	291 ± 19	18 ± 2
Fe-18Cr	176	236	17
	180	266	21
	<u>178</u>	<u>242</u>	<u>12</u>
	mean 178 ± 2	248 ± 16	17 ± 5

The yield strength as a function of chromium content is shown in Figure 1. The value for the Fe-3Cr alloy is highest and two distinct levels of strength are found for the other five alloys. The ultimate strength as a function of chromium content is shown in Figure 2. These observations will be discussed more fully later.

Shown in Figure 3 are photomicrographs of the gauge section of a specimen of each alloy. These photomicrographs are representative of the specimen geometry produced by the punching and deburring process used in specimen fabrication and show that the specimens have a slight curvature resulting from the punching process. The average number of grains across the specimen thickness (minimum dimension) was determined for each alloy from a representative photomicrograph. The minimum number was found in the Fe-18Cr alloy which had an average of 1.5 grains across the specimen thickness. The other five alloys all had at least an average of 4 grains across the specimen thickness with the thickest specimen condition, Fe-12Cr, having an average of 10 grains across the specimen thickness.

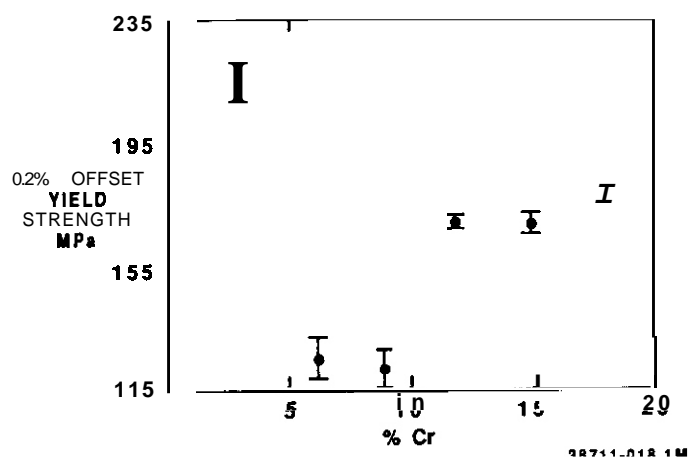


Figure 1. The 0.2% Offset Yield Strength as a Function of Chromium Content.

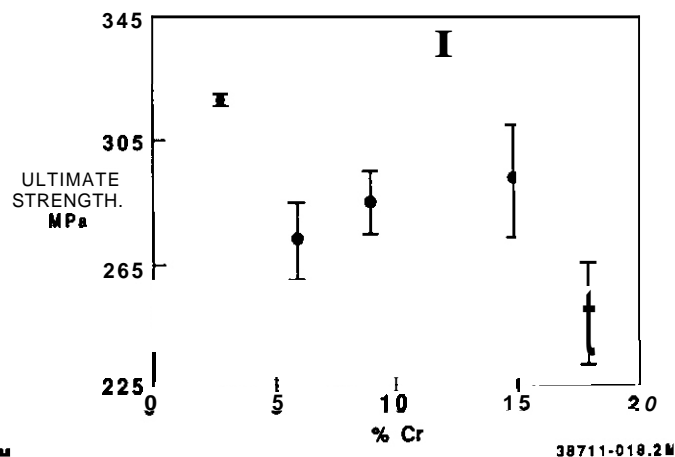


Figure 2. The Ultimate Strength as a Function of Chromium Content.

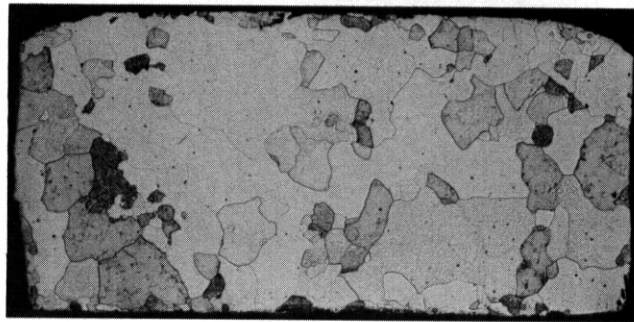
Discussion

The 3Cr alloy was significantly stronger than the other five alloys. The trends in the remainder of the test matrix and the results of previous studies⁶⁻⁹ would suggest that it should be weaker. However, it has been demonstrated that the Fe-3Cr alloy contained high levels of impurity^{1,2}. Therefore, the high yield strength value for the Fe-3Cr alloy is probably a consequence of these impurities and it should be disregarded in any analysis of the effect of chromium content on yield strength.

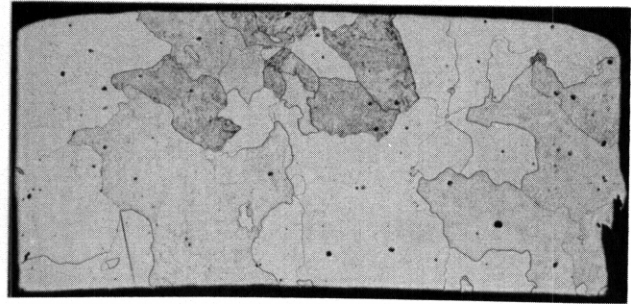
Earlier measurements of yield stresses for Fe-Cr binary alloys⁶⁻¹¹ covered chromium concentrations up to only about 9%, or involved single crystals⁷. Yield stresses in the range of 140 - 150 MPa are reported for 6%Cr, compared to 124 MPa in the present study. The effects of chromium concentration on the yield stresses in the earlier studies are mixed, apparently influenced by interstitial impurities⁶. The effects in the concentration range of interest are fairly small, being within about 25%. The data show there are two distinct levels of yield strength values in the group of alloys tested. The Fe-6Cr and Fe-9Cr alloys both exhibited yield strengths of approximately 125 MPa while the Fe-12Cr, 15Cr, and 18Cr alloys all exhibited yield strengths of approximately 170 MPa. In past studies^{6,7,9}, the yield strength of pure Fe was found to be approximately 100 MPa. Thus additions of 6 to 18%Cr strengthen pure Fe. In present work miniature tensile specimens have been used, so any effects of the specimen size must also be considered when comparing the present results with earlier measurements. Using the photomicrographs in Fig. 3, the average number of grains across the specimen thickness was determined for each alloy. When the test results were plotted as a function of this "relative grain size," the yield stress measurements showed no sensitivity to this parameter. However, as shown in Fig. 4, the ultimate tensile strength values increased with decreasing relative grain size. Thus, effects of the chromium concentration are obscured by the grain size differences. The uniform elongation is insensitive to the chromium content (Table 1) or to the relative grain size as shown in Fig. 5. Note in Fig. 5 that the uncertainty in the measurement of the uniform elongation decreases with increasing number of grains across the specimen thickness.

Microstructural studies provide no immediate explanation for the occurrence of the two distinct levels of yield strength. The grain sizes are nearly the same for the different alloys except that the Fe-15Cr and Fe-18Cr alloys having slightly larger grains. The larger grain size in the higher chromium alloys is due to phase stability. Since these compositions are completely within the ferrite region, no grain refinement due to a phase change will occur on cooling and larger grains result. One possible explanation for differences in strength as a function of chromium content as was suggested in an earlier study⁶ is a change in the yield mechanism as the chromium content is increased. Small chromium additions may lower the twinning stress so that yielding occurs by twinning rather than slip. However, no evidence of load drops due to twinning were identified in stress strain curves.

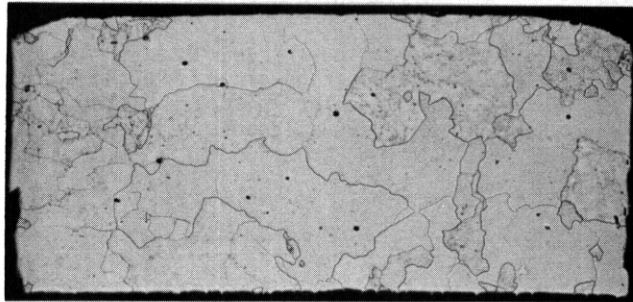
Even though the present results cannot be directly compared to earlier results because of grain size and impurity effects, they still form a useful data set for the most important objective of this study. The prime objective of the study was to establish a control group data base for the mechanical properties of these alloys. Specimens fabricated from the same sheet stock as the alloys tested here are currently being irradiated in the Fast Flux Test Facility and will be tested to determine their mechanical properties upon removal from reactor. Thus the effects of irradiation on the mechanical properties of these alloys can be determined.



Fe-3Cr



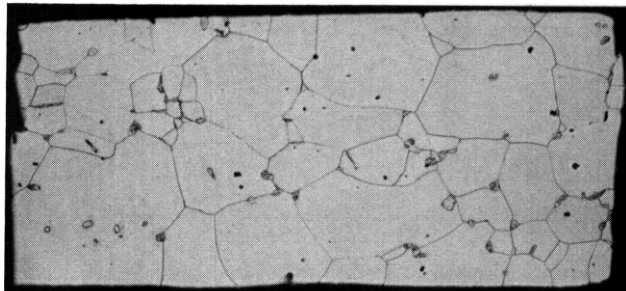
Fe-6Cr



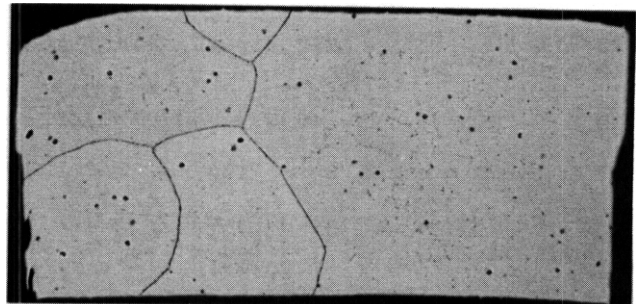
Fe-9Cr



Fe-12Cr



Fe-15Cr



Fe-18Cr

Figure 3. Photomicrographs of the Gauge Cross-Section of a Specimen of Each Alloy. Note the Specimen Curvature Produced by the Punching Process Used for Fabrication.

The thicker specimens used in this study in comparison to the earlier studies ^{4,5}, did not significantly decrease the uncertainty in measurements of the mechanical properties. However, in the case of the thickest specimens used, the 0.635 mm Fe-12Cr specimens, highly consistent results were obtained (1% uncertainty for yield and ultimate strengths and 5% uncertainty for uniform elongation). This may be simply a result of the increased thickness or, more likely, a result of the increased number of grains across the specimen thickness.

CONCLUSIONS

1. The mini-tensile testing frame can be used to test 0.508 mm thick specimens with consistent results.
2. There are two distinct levels of yield strength exhibited by the alloys tested in this study. low strengthening up to about 10% Cr and higher strengthening above about 10%Cr, which are possibly the result of two different yield mechanisms. A separate study to determine the nature of these mechanisms may be useful.
3. The thicker specimens used in this study did not significantly reduce uncertainty in the yield stress results obtained. Ultimate strength values and total elongation uncertainties were affected by the grain size relative to specimen thickness.

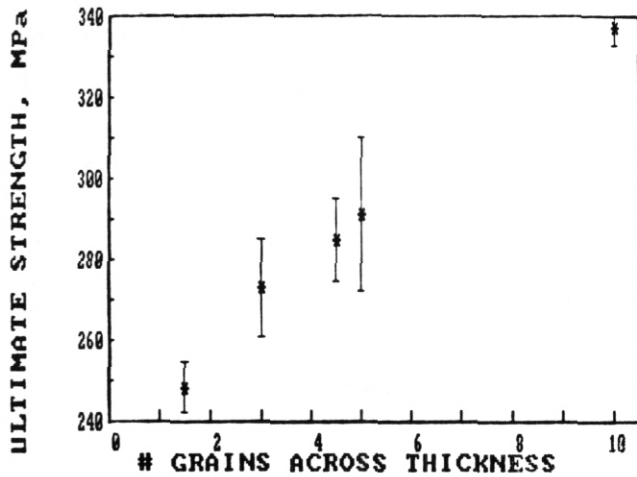


Fig. 4. Ultimate strength in MPa of Fe-Cr Alloys Plotted as a Function of the Average Number of Grains across the Thickness of the Gauge Section of the Tensile Specimens. The number of grains across the Thickness is assumed to be the Same for all Specimens of a Given Alloy.

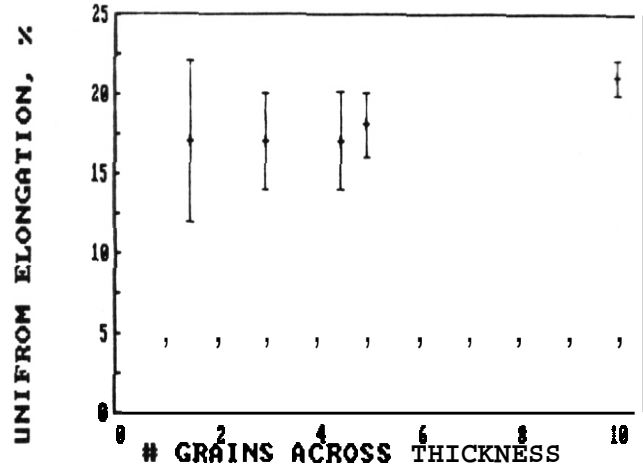


Fig. 5. Uniform Elongation in Percent of Fe-Cr Alloys Plotted as a Function of the Average Number of Grains across the Thickness of the Gauge Section of the Tensile Specimens.

FUTURE WORK

This work will be continued when irradiated specimens are available for testing.

REFERENCES

- [1] D.S. Gelles, Damage Analysis and Fundamental Studies Quarterly Progress Report. October-December 1985, DOE/ER-0046/24, p. 43.
- [2] D.S. Gelles, *J. Nucl. Mater.*, 108&109 (1982) 515-526.
- [3] E.A. Little and D.A. Stow, *Met. Sci.* (1980), 89.
- [4] N.F. Panayotou, S.D. Atkin, and R.J. Puigh, Proc. ASTM Symp. on Use of Nonstandard, Subsize Specimens for Irradiation Testing, Albuquerque, NM, September 23, 1983, ASTM STP 888 (1986).
- [5] H.L. Heinisch, S.D. Atkin, and C. Martinez, 2nd Int. Conf. on Fusion Reactor Materials, Chicago, IL, April 13-17, 1986, *J. Nucl. Mater.* 141-143 (1986).
- [6] M.J. Kelley and N.S. Stoloff: *Met. Trans.* 1976, vol. 7a, pg 332.
- [7] G.T. Horne, R.B. Roy, and H.W. Paxton: *J. Iron Steel Inst.* 1963, vol. 201, pg 161.
- [8] E. Anderson and J. Spreadborough: *J. Iron Steel Inst.*, 1968, vol. 206, pg 1223.
- [9] W.P. Rees, B.E. Hopkins, and H.R. Tipler: *J. Iron Steel Inst.*, 1954. vol. 177, pg 93.
- [10] W.O. Binder and Howard R. Spindelov, Jr. : *Trans. ASM*, 1951, 43, 759-777.
- [11] S.I. Bulat, et al : *Fizika: Khim Obrabot. Mat.*, April 1969. (2), 122-130.

5. RADIATION EFFECTS: MECHANISTIC STUDIES, THEORY AND MODELING

EFFECTS OF THE NEUTRON SPECTRUM ON MECHANICAL PROPERTY CHANGES IN LOW DOSE IRRADIATIONS - H. L. Heinisch
(Pacific Northwest Laboratory)

OBJECTIVE

The objective of this work is to determine the effect of the neutron spectrum on radiation-induced changes in mechanical properties for metals irradiated with fission and fusion neutrons.

SUMMARY

Mechanical property measurements from comparative low dose irradiations of metals and alloys are reviewed. The emphasis is on recent experiments involving miniature tensile specimens irradiated at the Rotating Target Neutron Source II (RTNS-II) at Lawrence Livermore National Laboratory and the Omega West Reactor at Los Alamos National Laboratory. Pure metals, model alloys and structural alloys have been irradiated in RTNS-II from room temperature to 723°K to fluences as high as $8 \times 10^{22} \text{ n/m}^2$. Where temperature effects are apparent, the effect of increasing the irradiation temperature is to delay the onset of irradiation hardening to higher fluences. Companion fission reactor irradiations have been more limited in scope, but comparative information has been obtained on tensile properties at irradiation temperatures of 363 K and 563 K. For most of the materials tested the differences in the neutron energy spectrum can be accounted for by using displacements per atom (DPA) as a correlation parameter. The exceptions are all pure metals: copper, niobium and vanadium. There is also evidence for rate effects in some of the data. The rate effects obscure the spectral effects and prevent examination of dpa as a damage correlation parameter.

PROGRESS AND STATUS

Introduction

The success of structural materials for fusion reactor power plants depends on their being able to endure extraordinary environmental conditions, among which neutron irradiation stands as one of the most formidable. The biggest challenge in designing and testing these materials is having to proceed in the absence of a relevant neutron environment. Irradiation facilities in fission reactors can easily achieve lifetime fusion reactor doses in the time frame available for materials development, but they do not contain the large component of 14 MeV neutrons produced in the d-t fusion reaction. There are two important features of fusion reactor neutron irradiation that are missing in fission reactors: the high energy displacement cascades and the large amounts of helium produced by 14 MeV neutrons.

Experiments in fission reactors utilizing isotopic tailoring of materials, neutron spectrum tailoring and helium injection methods are expected to produce about the right amounts of helium and (fission reactor neutron) irradiation damage in many materials. However, without an appropriately intense source of d-t fusion neutrons, we cannot directly test for the effects of high energy displacement cascades. For this we are relying on theory and modeling, along with very low flux, accelerator-based d-t fusion neutron sources, such as the Rotating Target Neutron Source-I (RTNS-II) at Lawrence Livermore National Laboratory, the most intense source of controlled d-t fusion neutrons that has existed.

D-t neutron sources such as RTNS-II permit direct investigation of the differences between effects of 14 MeV fusion neutrons and fission reactor neutrons. Examinations of defect production and microstructural features reveal the effects of neutron energy on the initial damage state in the material, providing insight for modeling and interpretation of tests done in fission reactors. Comparative studies of mechanical property changes allow us to determine and evaluate damage correlation parameters with which to correlate the effects of fission and fusion neutron irradiation damage.

There have been few direct comparisons of D-T fusion and fission reactor neutron damage effects on mechanical property changes. Table 1 contains a list (not necessarily complete) of such direct comparisons. The list will undoubtedly be enlarged by contributions to the present conference. The availability of the unique RTNS-II facility under a joint US/Japan operating agreement has produced a large quantity of specimens irradiated by 14 MeV neutrons. Companion low fluence fission reactor irradiations at controlled temperatures are difficult to perform, and they have been much slower in coming.

This report offers a brief review of fission-fusion comparisons and a more detailed description of a recent set of experiments utilizing the RTNS-II and the Omega West Reactor at Los Alamos National Laboratory. The emphasis in this report is on correlation of tensile data.

TABLE 1

Direct Comparisons of Fission and Fusion Neutron
Effects on Tensile Properties

<u>Material</u>	<u>Fusion source^a / T</u>	<u>Fission source^b / T</u>	
Cu, Nb	RTNS / 300,438 K	LPTR / 338,438 K	Mitchell et al. [5]
Nb-1%Zr V	RTNS / 300°K	LPTR / 338 K	Mitchell et al. 161
316 SS	RTNS / 300 K	LPTR / 333 K	VanderVoort et al. C71
Fe	RTNS-XI / 300 K	KUR / 350 K	Matsui et al. [8]
V	RTNS-XI / 300 K	KUR / 350 K	Matsui et al. [9]
cu 316 SS A3029 PV ^c	RTNS-XI / 363,563 K	OWR / 363,563 K	Heinisch et al [10]
Cu-5%Al Cu-5%Mn Cu-5%Ni	RTNS-XI / 363 K	OWR / 363 K	Heinisch [11]
CuAgPd CuNiBe MZC Cu-Al ₂ O ₃	RTNS-XI / 363,563 K	OWR / 363,563 K	Heinisch et al [12]

- a RTNS and RTNS-XI are the original and upgraded Rotating Target Neutron Sources at Lawrence Livermore National Laboratory.
- b LPTR (Livermore Pool Type Reactor)
KUR (Kyoto University Reactor)
OWR (Omega West Reactor. Los Alamos National Laboratory)
- c A3029 pressure vessel steel
- d See Ref. 13 for compositions of these solution-strengthened, precipitate-strengthened and dispersion-strengthened copper alloys.

1. Fission-Fusion Correlations of Mechanical Property Changes

Damage Correlation Parameters

Comparing mechanical property changes of materials irradiated in different neutron environments requires a damage correlation parameter that accounts for the effects of the neutron energy spectrum in the material being irradiated. The **practice** of quoting fluences of neutrons having energy greater than a threshold energy (e.g. $E > 1$ MeV) is an attempt to incorporate some spectral sensitivity, but this does not take into account important details of how neutrons interact with materials.

Property changes in materials due to neutron-induced displacement damage are a function of neutron energy, neutron flux and temperature, as well as the material properties that determine **how** neutrons interact with atoms and **how** defects interact within the material. Clearly a damage correlation parameter need not account for all these **variables**, but **it** should factor out the direct influence of the neutron energy spectrum in any comparison.

Displacements per atom (**dpa**) is in wide use as an exposure index and a damage correlation parameter. **It** is a measure of the average number of times an atom of the material can be **displaced** from its lattice site during an irradiation. For neutron **irradiations**, dpa is based on the neutron spectrum and a neutron energy-dependent displacement cross section for the material. Calculation of the displacement cross section **requires** a set of **reaction** cross sections, a model of the kinematics of the **reactions** that produce primary atomic **recoils**, a model for the dissipation of the primary recoil energy as electronic **excitation** and damage energy, and a model for the conversion of damage energy into dpa.

For neutron irradiations of metals, the calculation of damage energy is a standardized procedure [11]. For calculating dpa, a modification of the Kinchin and Pease model by Norgett et al. [2] is used, in which the number of displacements $\nu(T)$ is proportional to the damage energy, T , above a threshold energy, E_d , depending on the material.

$$\nu(T) = 0.8 T / 2 E_d \quad (1)$$

It is very important to remember the distinction between dpa and residual defects. The number of residual defects created during a specified time is a function of the temperature and the material, as well as the neutron fluence. Dpa was originally intended as a measure of the number of stable defects created at low temperatures (below Stage I), but in general it is not a measure of even that. Resistivity measurements C31 at low temperatures have shown that the ratio of observed defects to calculated dpa is a function of pka energy. Modeling C41 indicates that even at low temperatures there is spontaneous recombination within displacement cascades that is a function of cascade energy.

Some researchers, in attempting to incorporate this information into a damage correlation parameter, have reported dpa values that were calculated using an additional energy dependent "efficiency" factor, $\epsilon(T)$, to more nearly reflect the production of residual defects, i.e.,

$$\nu(T) = \epsilon(T) T / 2 E_d \quad (2)$$

It is this author's opinion that the term "dpa" should maintain its original definition, i.e., using eq. 1. Other damage correlation parameters, reflecting more realistic residual defect production, should be clearly defined and distinguished from dpa. Researchers should always be careful to define the damage correlation parameters used in their reports.

Fission- on

The first mechanical property measurements from comparative low dose d-t and fission irradiations C5-71 were done using RTNS, the lower-flux predecessor to RTNS-II. Mitchell, et al. investigated pure copper and pure niobium [5] and Nb-1%Zr alloy [6], while VanderVoort et al. [7], investigated annealed AISI 316 stainless steel. Tensile specimens approximately 0.5 mm thick by 25 mm overall length were irradiated. Fission irradiations for both studies were conducted in the Livermore Pool Type Reactor (LPTR) at Lawrence Livermore National Laboratory. RTNS irradiations were performed at room temperature, while the LPTR irradiations were performed at 338 K. In room temperature tensile tests it was found that the fusion neutrons on average are 20 times more effective at hardening than fission neutrons. When compared on the basis of damage energy, specimens of Cu irradiated at LPTR required a dose with 2.3 times the calculated damage energy of those irradiated at RTNS to produce the same change in yield stress C51. Failure to correlate with respect to damage energy was also observed in Nb with a factor of 1.6. Tensile data for vanadium irradiated in RTNS and LPTR was reported as a function of fluence by Mitchell [6], but correlation with respect to damage energy was not reported. Based on the ratio of displacement cross sections for vanadium in RTNS and LPTR, we conclude that damage energy also does not correlate the yield stress changes in vanadium. The 40°K difference in irradiation temperatures in LPTR and RTNS is unlikely to account for these differences (in fig. 1 note the temperature sensitivity of copper irradiated in RTNS-II). The limited data on Cu and Nb in LPTR and RTNS at 483°K also demonstrated the failure of damage energy as a correlation parameter for yield stress changes at that temperature. In the Nb-1%Zr alloy [6] and 316 SS C71 (with the same irradiation temperature differences) the changes in yield stress due to fission and fusion neutrons were reasonably well-correlated when compared as a function of damage energy.

Observations of the microstructures of fission and fusion neutron irradiated copper by Mitchell et al. [5] indicated that in both spectra the damage structure consists of vacancy and interstitial clusters and loops, but that the number densities, sizes and spatial distributions of the defects were significantly different. In particular, the inhomogeneous distribution of interstitial defects in fission neutron irradiated copper suggest they are formed by diffusional processes. In the fusion neutron irradiations, the defects are more homogeneously distributed, suggesting for example, the possibility of spontaneous creation of vacancy clusters in high energy cascades.

Matsui and co-workers irradiated zone-refined iron [8] and vanadium [9] in RTNS-II at room temperature and in the Kyoto University Reactor (KUR) at 350 K. Although tensile test were done on specimens from both RTNS-II and KUR, there was no attempt made to directly correlate the radiation strengthening. Investigation of the microstructure led to the conclusion that radiation strengthening in both Fe and V depends on defects not visible by TEM. In Fe the difference between RTNS-II and KUR, demonstrated in the dependence of the yield stress on test temperature, was interpreted in terms of the relative densities of weak and strong obstacles.

2. RTNS-II/OWR Spectral Effects Experiment

The RTNS-II/OWR Spectral Effects Experiment [10] is being conducted to determine any differences in the effects of RTNS-II and fission reactor neutrons on the changes in tensile properties and microstructure of metals irradiated to low exposures (<0.03 dpa). The earlier RTNS and LPTR irradiations [5-7] were performed at different temperatures, respectively, and the fluences were very low (<0.001 dpa). The goals

of the present experiment are to extend the investigation of spectral differences to higher fluences, maintaining the same irradiation temperature in each spectrum, and to provide data on tensile properties and microstructures for a systematic study of metals and alloys.

Miniature tensile specimens were irradiated to fluences of 1×10^{21} to 9×10^{22} n/m^2 (0.0003 to 0.03 dpa in copper) in RTNS-II and to comparable dpa levels in the Omega West Reactor (OWR) at Los Alamos National Laboratory. Irradiations have been performed at 300, 363, 473, 563, and 723 K with RTNS-II and at 363 and 563 K in OWR. Details of the irradiations, the material compositions and the testing procedures are reported in an earlier publication [10]. Results, including new data, of tensile tests on solution annealed AISI 316 stainless steel, as received A302B pressure vessel steel plate and annealed high purity (99.999%) copper will be presented here.

Results

Tensile tests were performed at room temperature, and the 0.2% offset yield stress values were determined. Ultimate tensile strength and uniform and total elongations were also determined. Discussion will be confined to the changes in yield stress, i.e., the difference between the yield stresses of the irradiated and unirradiated material, because they reveal the temperature and spectral effects most effectively. The other test data will be presented in a future publication.

Fluence Dependence and Temperature Effects

Fig. 1 shows the change in yield stress as a function of 14 MeV neutron fluence at four temperatures in copper. In all the figures each point is the result of a single test. The bars on selected points in some figures indicate the estimated precision of 5% in the measurement of the absolute yield stress of the irradiated specimens. The bars are used only when an indication of the potential scatter in the data is important to the interpretation. Fluences are known to within about 5%.

The fluence dependence of the yield stress change is qualitatively the same at each irradiation temperature. The effect of increasing the temperature is to delay the onset of significant strengthening. The curves in Fig. 1 are determined by least squares fitting to the expression

$$\Delta\sigma_y = a + b(\phi t)^{1/4}, \quad (3)$$

where $\Delta\sigma_y$ is the yield stress change, ϕt is the neutron fluence, and a and b are constants. In many cases the curves were fitted to only the data lying above an apparent "transition" fluence, demarking the onset of significant strengthening. The transition fluences in copper are temperature dependent and are estimated to range from 5×10^{19} to 5×10^{21} n/m^2 for irradiations at 300 K to 473 K. The specimens irradiated at 563-K did not reach a post-transition fluence; the transition fluence is estimated to be about 5×10^{22} n/m^2 .

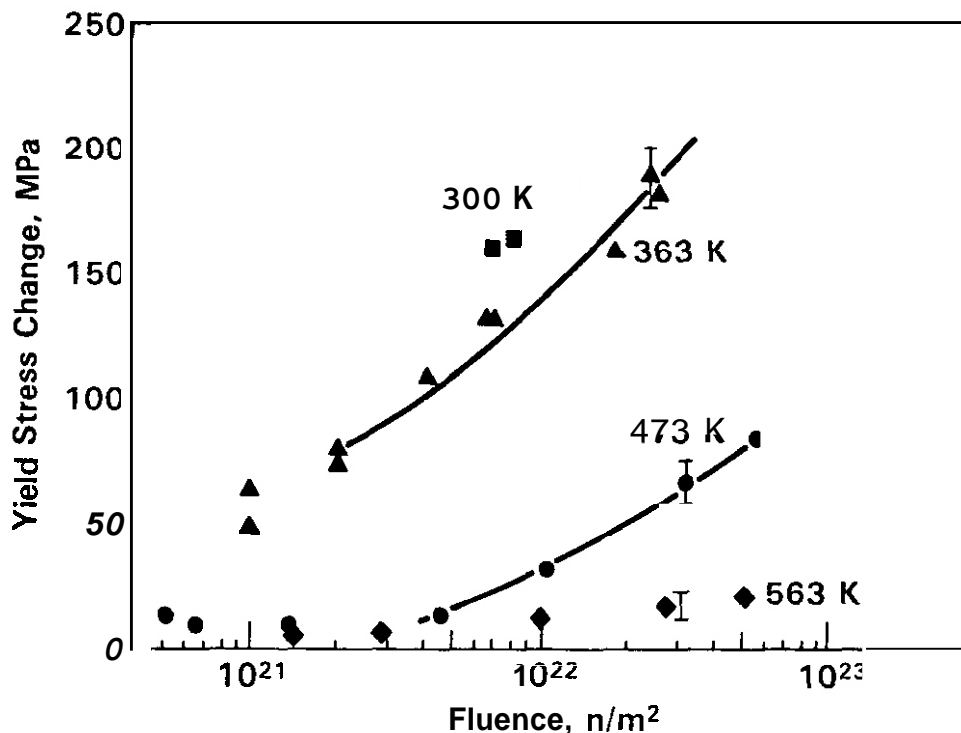


Fig. 1. Changes in 0.2% Offset Yield Stress as a Function of Neutron Fluence for Copper Irradiated in RTNS-II at Temperatures of 300-563 K. The curves are fits of eq. 1 to the data. Error bars represent the 5% estimated precision in the absolute yield stress measurements.

Fig. 2 shows yield stress changes for solution annealed AISI 316 stainless steel (316 SS) irradiated under the same conditions as the copper above. The 316 SS is less affected by temperature than is copper in this temperature range. The room temperature data cannot be distinguished from the 363 K data, and the 563 K data show significant radiation-induced strengthening. The curves in fig. 2 were determined by fitting eq. 3 to only the data lying clearly above the transition fluences, which were estimated to range from 2×10^{20} to 2×10^{21} n/m² for 300–563 K. The 316 SS data for all temperatures are fit almost as well by expressions linear in the square root of fluence, with no transition fluences.

A302B exhibits similar temperature dependence of irradiation strengthening in RTNS-II. Transition temperatures are in the range $2-5 \times 10^{21}$ n/m² for 363 K to 563 K. The scatter in the data appears large at 563 K (see fig. 12), because the irradiation strengthening is small relative to the high yield stress of A302B. At the highest fluence the strengthening in A302B is about 50% of the unirradiated yield stress, compared to factors of 2–3 for 316 SS and copper.

Damage Rates

In RTNS-II irradiations, a range of fluences are achieved during the same time interval by utilizing the fact that the neutron intensity decreases with the distance of the specimen from the source, approximately as $1/R^2$. Thus the damage rates are different at each dose level in RTNS-II, varying from about 3×10^{-11} to 3×10^{-9} dpa/s. In OWR all specimens were exposed at the damage rate of 5×10^{-8} dpa/s. The specimens reported on here for 363 K, 473 K and 563 K (Figs. 1 and 2) were exposed in RTNS-II irradiations of the same duration; thus, all specimens with the same dose were irradiated at about the same damage rate. The few specimens irradiated at room temperature were exposed at a damage rate about six times higher at each dose than the other RTNS-II specimens.

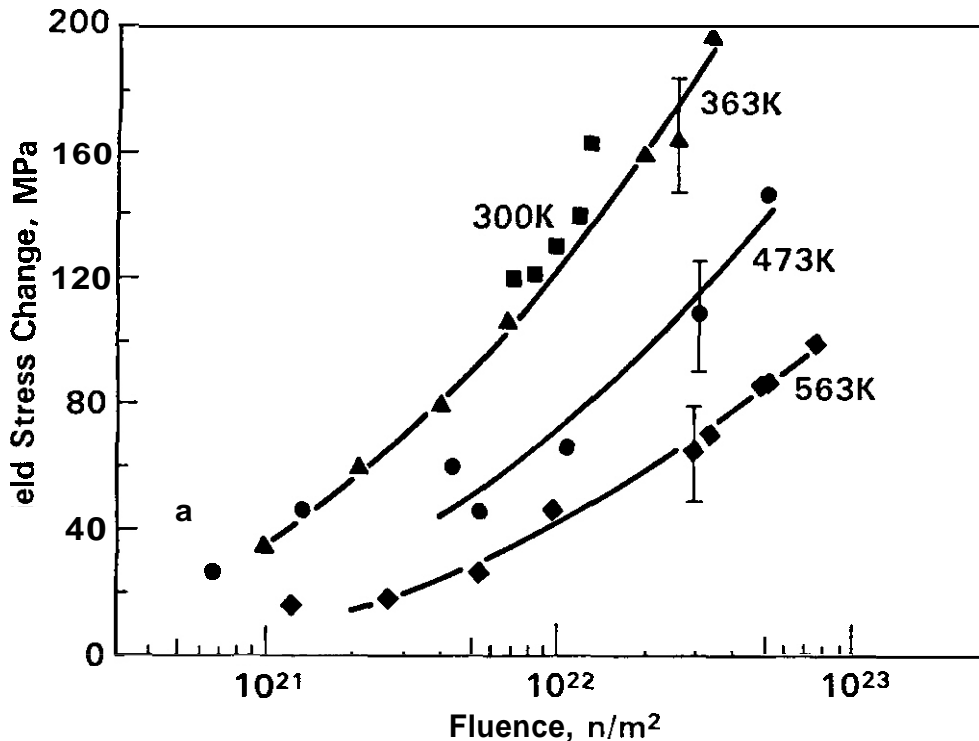


Fig. 2. Changes in 0.2% Offset Yield Stress as a Function of Neutron Fluence for AISI 316 Stainless Steel Irradiated in RTNS-II at Temperatures of 300–563 K. The curves are fits of eq. 1 to the data. Error bars represent the 5% estimated precision in the absolute yield stress measurements.

Comparison of RTNS-II and OWR

Fig. 3 compares the yield stress changes as a function of total neutron fluence for high purity copper irradiated at 363 K in RTNS-II and OWR. The curves are least squares fits of eq. 3. When only fast neutrons ($E > 1$ MeV) are considered, as in Fig. 4, the OWR data are still clearly separated from RTNS-II data. In OWR about 16% of the total neutrons have energy greater than 1 MeV.

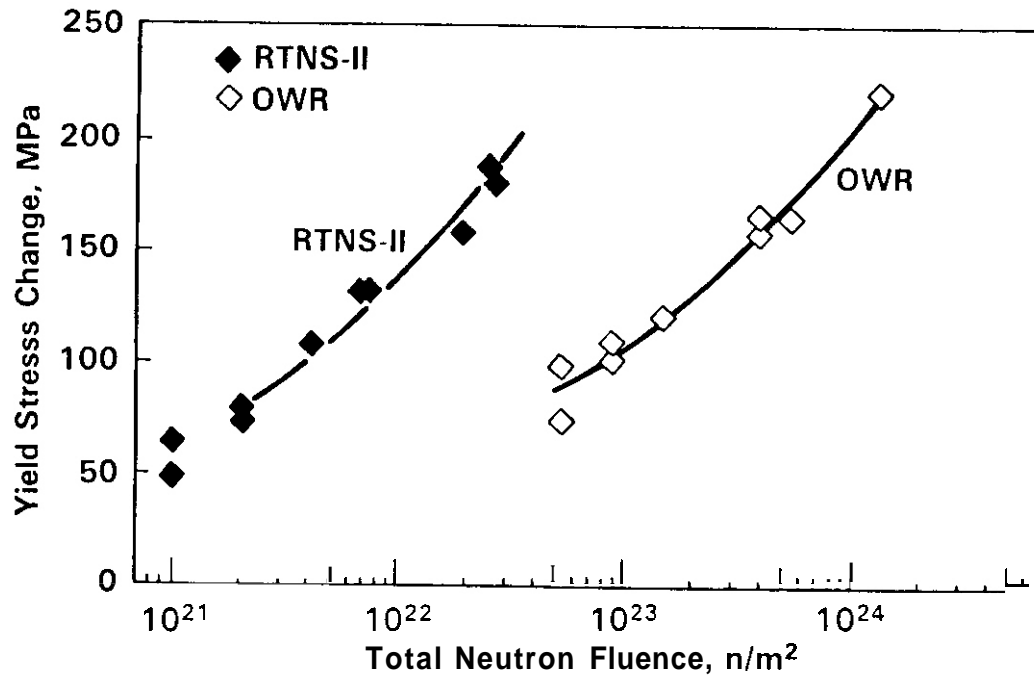


Fig. 3. Changes in 0.2% Offset Yield Stress as a Function of Neutron Fluence for Copper Irradiated in RTNS- II and OWR at 363 K The curves are fits of eq. 1 to the data.

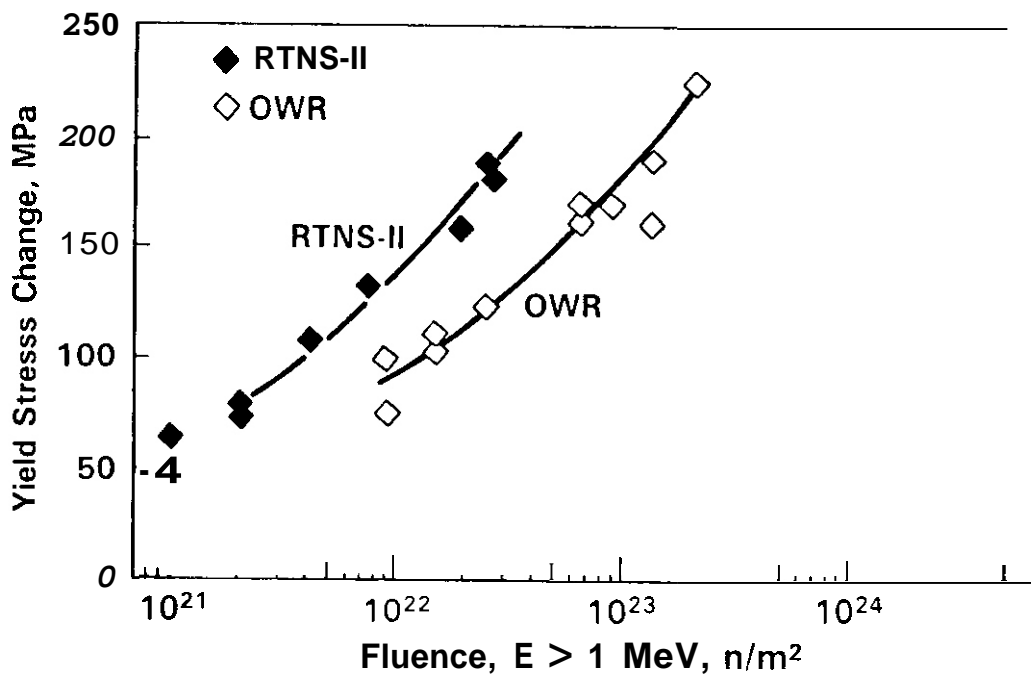


Fig. 4. Changes in 0.2% Offset Yield Stress as a Function of Fast Neutron Fluence ($E > 1$ MeV) for Copper Irradiated in RTNS-II and OWR at 363 K. The curves are fits of eq. 1 to the data.

Figs. 5 and 6 compare the yield stress changes as a function of total neutron fluence for annealed 316 SS and A302B pressure vessel steel, respectively, for irradiations at 363 K in RTNS-II and OWR. When plotted as a function of fast neutron fluence (not shown), the RTNS-II and OWR data sets are not correlated for 316 SS or A302B.

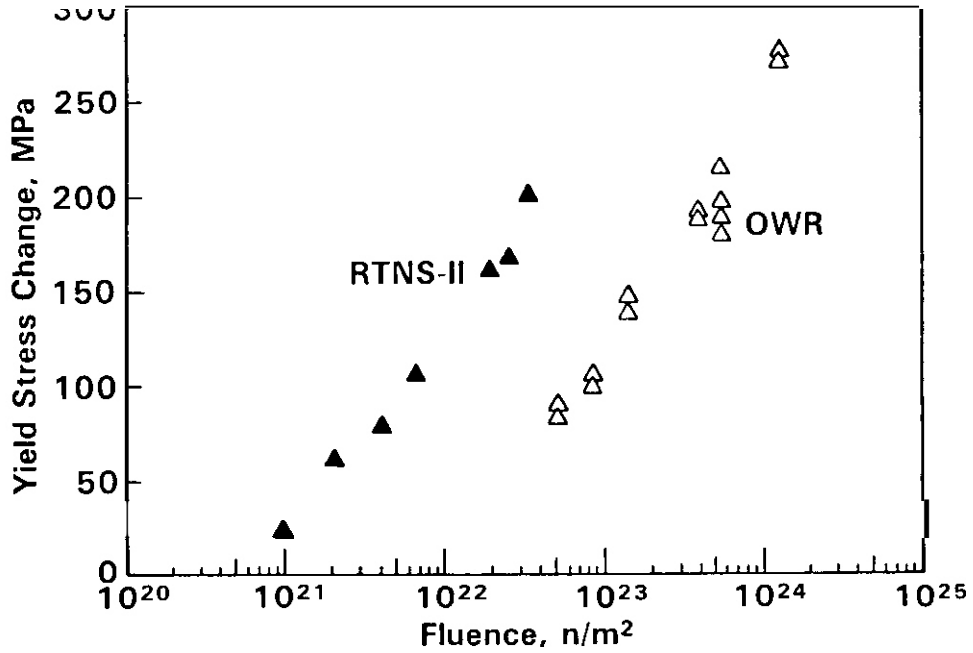


Fig. 5. Changes in 0.2% Offset Yield Stress as a Function of Neutron Fluence for AISI 316 Stainless Steel Irradiated in RTNS-II and OWR at 363°K.

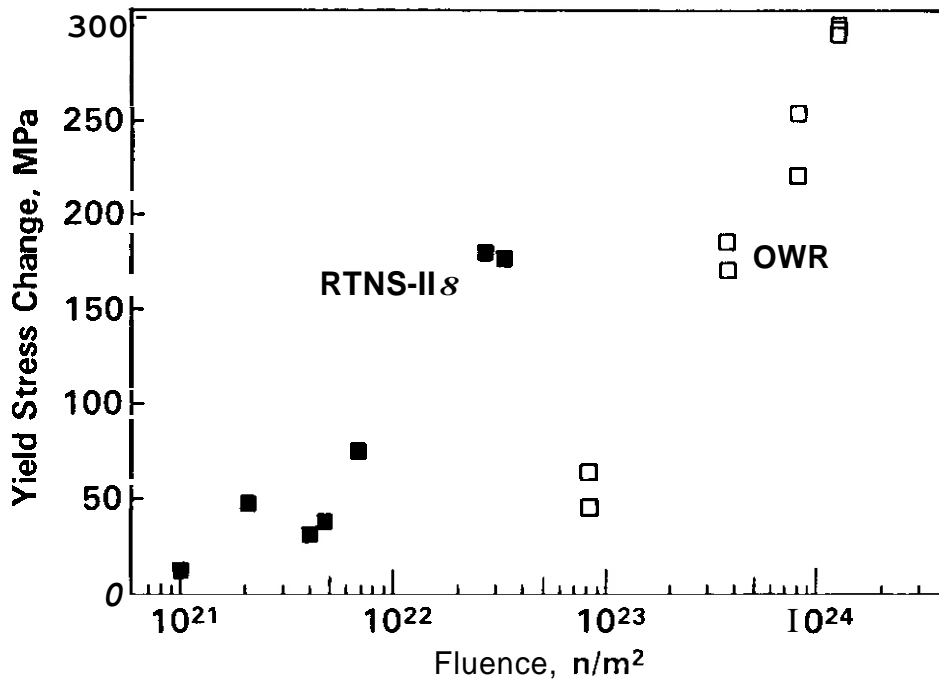


Fig. 6. Changes in 0.2% Offset Yield Stress as a Function of Neutron Fluence for A302B Pressure Vessel Steel Irradiated in RTNS-II and OWR at 363 K.

In Figs. 7, 8 and 9, yield stress changes are plotted as a function of dpa for copper, 316 SS and A302B pressure vessel steel, respectively, for irradiations at 363 K in RTNS-II and OWR. Dpa values were determined on the basis of total neutrons, using spectral averaged displacement cross sections calculated using the NJOY [11] nuclear data code. Eq. 1 was used, with displacement energies of 29 eV for copper and 40 eV for 316 SS and A302B. For copper the spectral averaged displacement cross sections are 293 b and 3699 b for OWR and RTNS-II, respectively. For 316 SS the cross sections are 230 b and 2782 b, and for A302B they are 222 b and 2810 b for OWR and RTNS-II, respectively. The curves in each figure are determined from least squares fits of the data to eq. 3, modified for dpa rather than fluence.

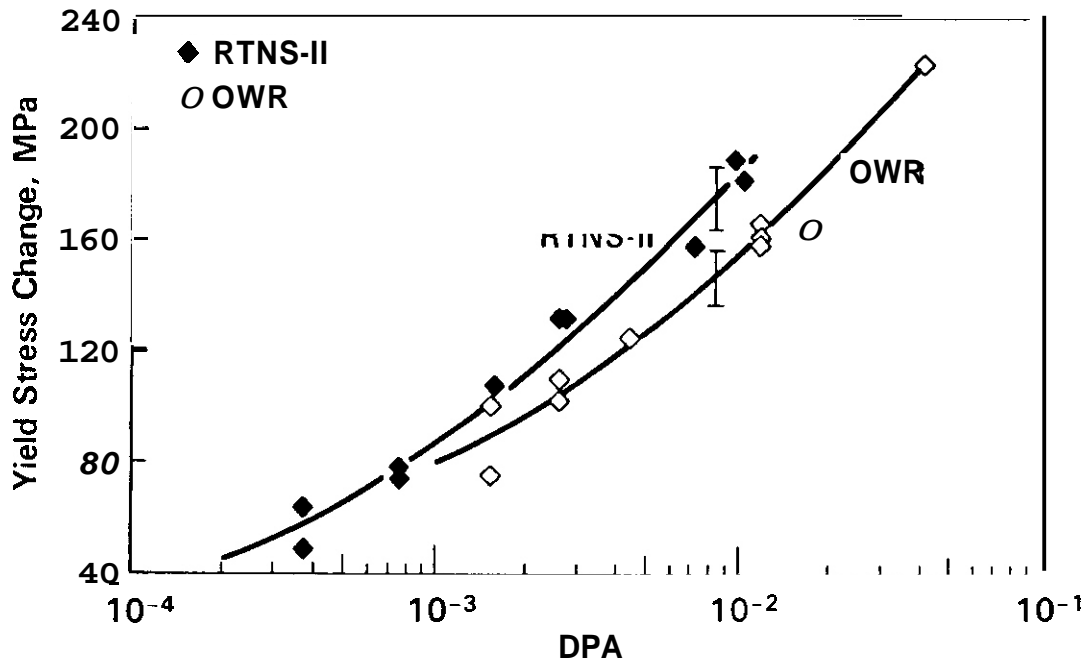


Fig. 7. Changes in 0.2% Offset Yield Stress as a Function of OPA for Copper Irradiated in RTNS-II at 363 K. The curves are fits of eq. 1 to the data. Error bars represent the 5% estimated precision in the absolute yield stress measurements.

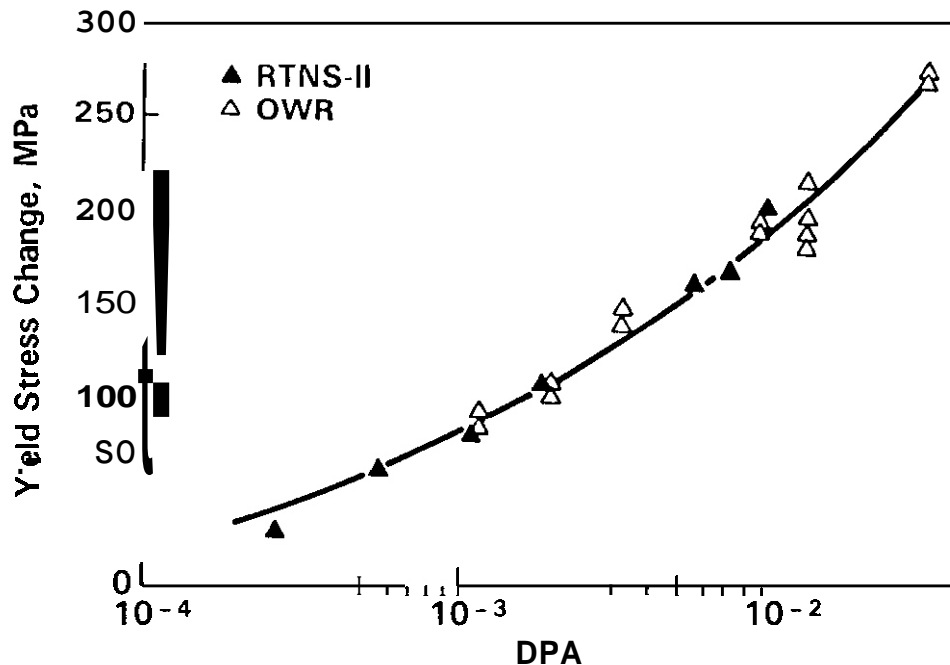


Fig. 8. Changes in 0.2% Offset Yield Stress as a Function of OPA for AISI 316 Stainless Steel Irradiated in RTNS-II at 363 K. The curve is a fit of eq. 1 to the data.

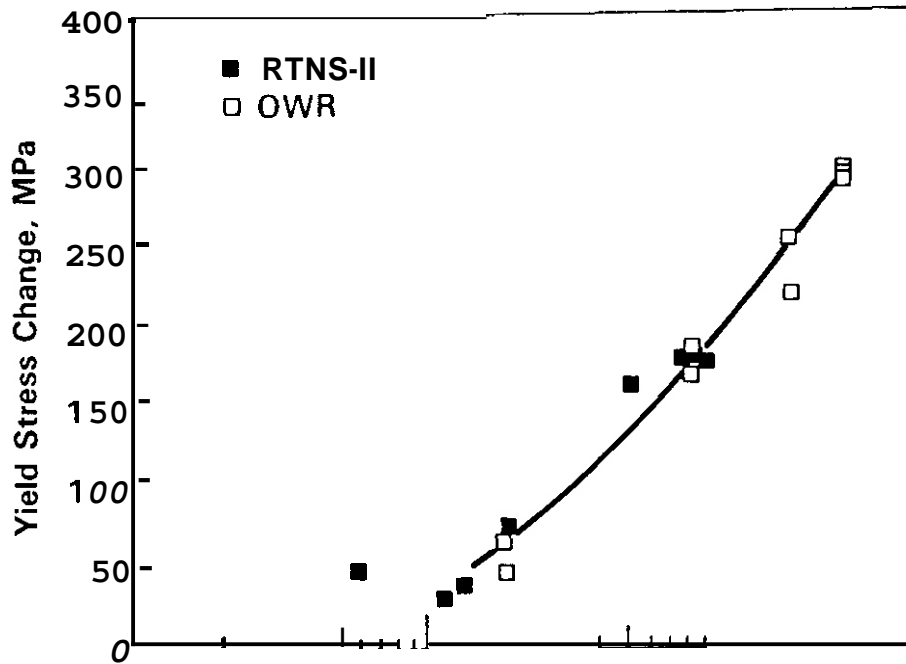


Fig. 9. Changes in 0.2% Offset Yield Stress as a Function of DPA for A302B Pressure Vessel Steel Irradiated in RTNS-II at 363 K. The curve is a fit of eq. 1 to the data.

The yield stress changes of copper in RTNS-II and OWR do not correlate on the basis of dpa. In the range of 0.01 dpa, about 2.1 times more dpa are required in OWR to produce the same yield stress change as in RTNS-II. The OWR and RTNS-II data for 316 SS and A302B at 363 K are well-correlated on the basis of dpa. Opa also correlates the yield stress changes in three binary copper alloys 1121 and in several high-strength commercial copper alloys 1131 tested in adjunct RTNS-II/OWR experiments.

An earlier report on this experiment [10] showed a lack of correlation with respect to dpa for A302B at low fluences. Several of the early irradiation capsules at the lower fluences in OWR developed leaks, allowing reactor coolant water to contact the specimens (which should have been sealed in a high purity helium environment). The specimens, although suspect, were tested, and they appeared to give reasonable, reproducible results. The OWR irradiations were successfully redone in that fluence range, and the results for A302B at 363 K were found to correlate with the RTNS-II results with respect to dpa (fig. 9). The yield stress changes in copper and 316 SS were apparently unaffected by the leaks, since data from both sets of irradiations coincide for each material.

In Figs. 10, 11 and 12 the yield stress changes for irradiations at 563 K in RTNS-II and OWR are plotted as a function of dpa for copper, 316 SS and A302B pressure vessel steel, respectively. At 563 K in copper, even the highest fluence in OWR is barely beyond the "transition" fluence (if, indeed, there is one). Within the 5% precision estimate, the RTNS-II and OWR yield stress changes in copper can be said to correlate on the basis of dpa. This conclusion does not preclude the possible failure to correlate at fluences higher than we have obtained.

In A302B irradiated at 563 K the yield stress changes also appear to correlate on the basis of dpa, at least within the 5% precision estimate. The higher fluence data give a hint that strengthening of A302B in RTNS-II may be increasing more slowly than in OWR, but higher fluence data are needed to investigate this trend.

Annealed 316 SS behaves quite differently at 563 K than at 363 K. The OWR produces more strengthening per dpa than RTNS-II at 563 K. The curves are fits of eq. 3 to the data; the resulting slopes differ by a factor of 2.5. At the highest fluence achieved in RTNS-II about 2.5 times more dpa are required in RTNS-II to achieve the same yield strength change as OWR.

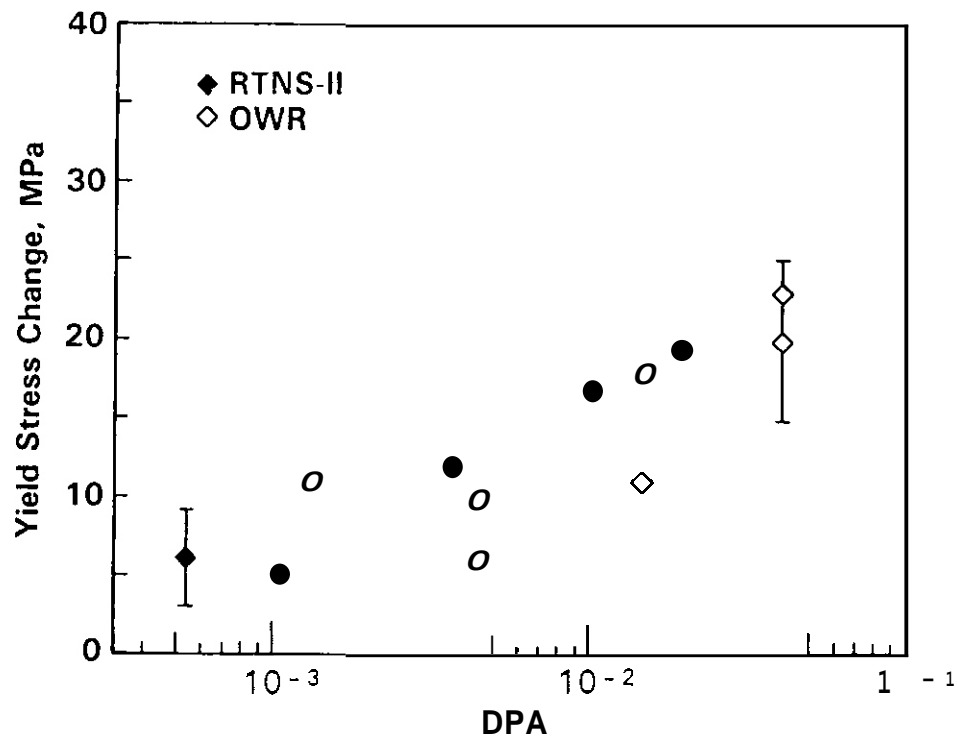


Fig. 10. Changes In 0.2% Offset Yield Stress as a Function of DPA for Copper Irradiated in RTNS-II at 563 K. Error bars represent the 5% estimated precision in the absolute yield stress measurements.

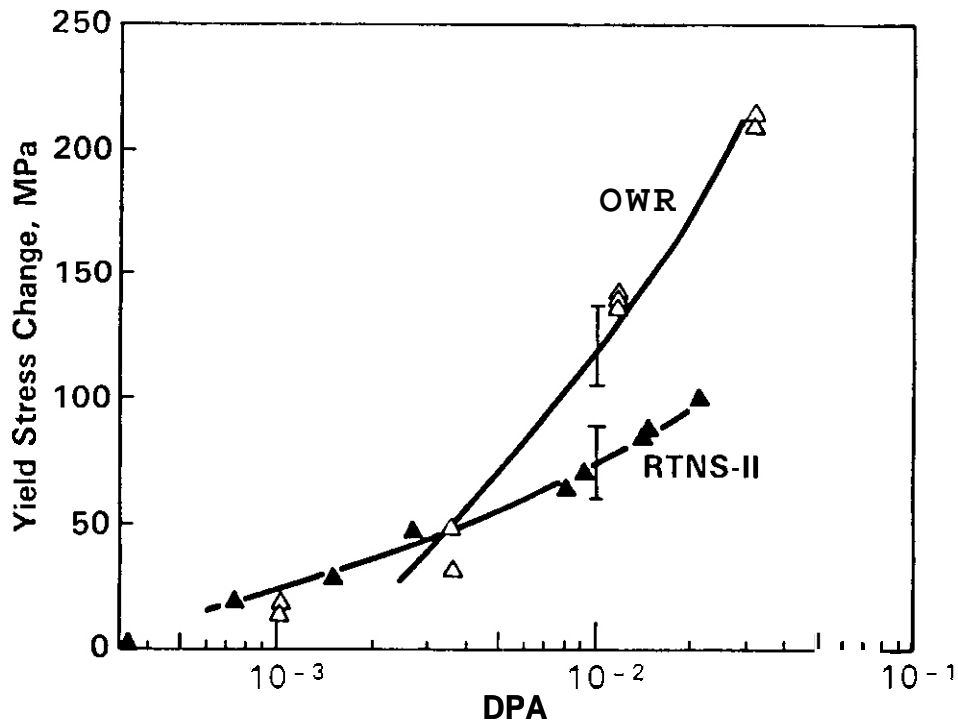


Fig. 11. Changes in 0.2% Offset Yield Stress as a Function of DPA for AISI 316 Stainless Steel Irradiated in RTNS-II at 563 K. The curves are fits of eq. 1 to the data. Error bars represent the 5% estimated precision in the absolute yield stress measurements.

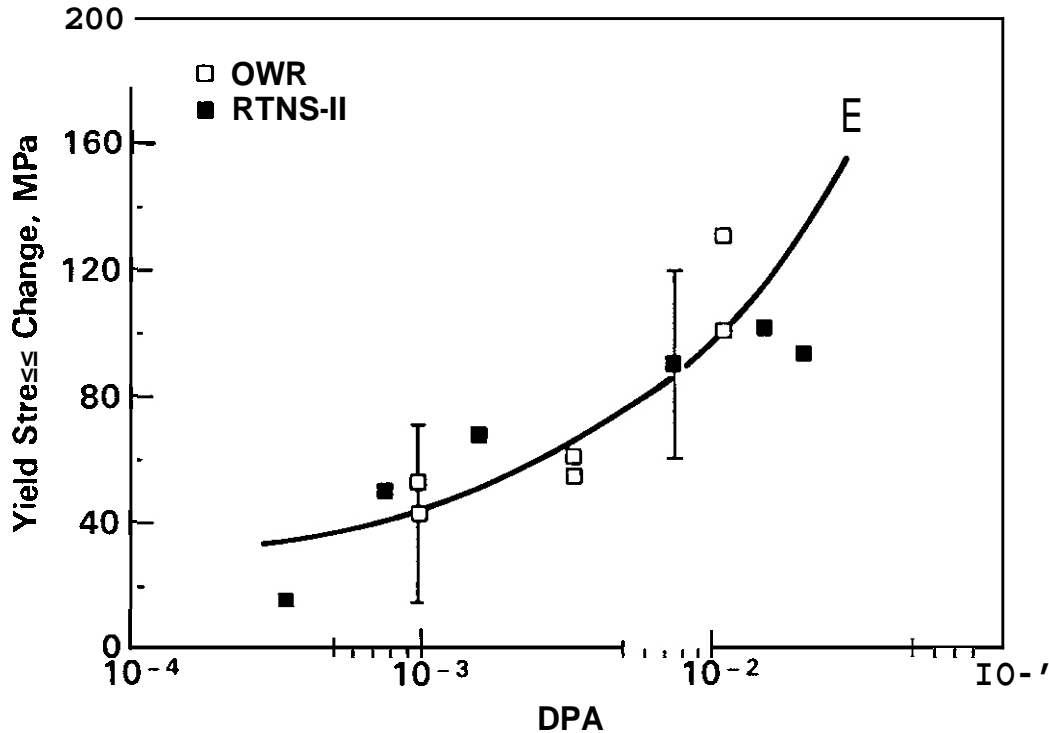


Fig. 12. Changes in 0.2% Offset Yield Stress as a Function of DPA for A302B Pressure Vessel Steel Irradiated in RTNS-II at 563 K. The curve is a fit of eq. 1 to the data. Error bars represent the 5% estimated precision in the absolute yield stress measurements.

3. Discussion

Equation 3, relating the change in yield stress linearly to the fourth root of the fluence (or dpa), provides a good description of all the sets of data discussed here when coupled with the concept of a "transition" fluence. An expression linear in the square root of the fluence was also fitted to the data, and in many cases it fit equally well, especially when evidence of a transition fluence was lacking. The selection of one equation over the other was not compelling for any set of data.

According to the familiar dispersed barrier model [14], strengthening is proportional to the factor $(Nd)^{1/2}$, where N is the number density of strengthening obstacles of size d. If the size distribution of the obstacles remains constant, then the fluence dependence of irradiation strengthening resides in N. N increases linearly with fluence, a common reasonable assumption for low fluences, then the strengthening goes as the square root of fluence. Zinkle [15] has re-examined defect cluster densities and radiation hardening data for fcc metals and alloys in low fluence irradiations with fission and fusion neutrons reported by many experimenters. He concludes that in all cases the visible cluster density, after a short transition period, is proportional to the square root of the fluence. Also, the radiation hardening data can be consistently described by fourth root fluence dependence for a variety of fcc metals from 100-400°K.

Fourth root fluence dependence of strengthening is consistent with a model in which strengthening centers nucleate, reach critical size, and then grow [16]. The existence of an incubation fluence is also consistent with a nucleation and growth model. Correlation of the strengthening with the TEM-visible microstructure indicated by Zinkle [15] implies that large obstacles, possibly achieved by growth, are important for strengthening. On the other hand, one may postulate that defects too small to be visible, proportional in number to the visible objects, may also play a role in strengthening.

The irradiation temperature dependence of yield stress changes observed in the RTNS-II irradiations of copper and 316 SS is manifested by an increase in the transition fluence. This could be interpreted as a delay in the development of critical-size strengthening centers. However, the slopes of the straight lines of eq. 1 fitted to the data also vary with temperature by about a factor of 2, indicating perhaps a more complicated effect of temperature.

The lack of significant strengthening of copper at 563 K is probably due to the instability of defect clusters at this temperature. This temperature is within Stage V of resistivity recovery experiments, which is attributed to dissolution of vacancy clusters [17].

In direct comparisons of yield stress changes due to fission reactor and 14 MeV neutron irradiations **dpa** has been found to be an effective correlation parameter in most of the materials tested so far (Table 1). The exceptions within the cases examined here are pure copper, pure vanadium and pure niobium at temperatures below about **500°K** and 316 stainless steel at **563°K**.

Damage rate effects should be examined as an explanation for the **apparent** failure to correlate with respect to **dpa**. It is very likely that a rate effect is responsible for **the** behavior of 316 SS at 563 K. The highest dose in OWR was achieved in about 200 hours, while the RTNS-II irradiation **took** about 6 months. At 563 K vacancy clusters in 316 SS become relatively unstable, thus causing some annealing over the long duration of the low rate RTNS-II irradiation. At 363 K clusters are more stable and strengthening correlates with respect to **dpa**, independent of damage rate. Insensitivity to rate at lower temperatures is also demonstrated in a comparison of data on yield stress changes of annealed 316 SS irradiated at temperatures of 363 K or less in several fission reactors. OWR, LPTR C71 and HFR in Petten, Holland [18]. There is no evidence for a damage rate effect, although there is an order of magnitude difference in damage rates.

In copper, vanadium and niobium the fission reactors produce less strengthening per dpa than in RTNS-II. Thus, the rate effect argument above does not apply. However, different rate-related mechanisms can be postulated for the pure metals at the lower temperatures. For example: at the higher rate, the average density of **newly-formed** interstitials is higher, increasing the probability of formation of more small, stable clusters at the expense of growth of the large clusters important for strengthening.

Damage rate effects are sensitive to temperature, fluence, damage rate, neutron energy, and materials variables. They are essentially determined by the relationship between the newly created defects and the evolving microstructure. Damage rate is a difficult variable to control in fission-fusion neutron irradiation comparisons.

In the pure metals, the failure of dpa to correlate yield stress changes at low temperatures might **also** be explained as a spectral effect related to the nature of high energy cascades. In high energy cascades vacancy clusters and loops form **spontaneously** from collapsed depleted zones. For fusion neutrons the Occurrence of damage regions having enough energy to spontaneously produce defects is very infrequent compared to fission neutrons. At temperatures where clusters dissociate rapidly, the differences between fission and fusion neutron damage should be much less, e.g. in copper at 563 K (fig. 10).

The number of subcascades per atom capable of producing strengthening obstacles, obtained from computer modeling [19,20], shows promise for correlating strengthening by neutrons in pure metals. Further work is needed to investigate why cascade effects are evident only in pure metals. Solute atoms may affect the nature of the initial damage distribution. Diffusional processes may be altered by defect-solute interactions.

Continuing work is needed to investigate the effects reported in this paper. Electron microscopy and positron annihilation studies are beginning on specimens from the RTNS-II/OWR experiment. Information from other RTNS-II experiments continues to be reported, and companion reactor experiments are beginning to yield results. Resolution of the role of rate effects in low fluence irradiations is a critical need, to be attacked by a few well chosen experiments and increased efforts in modeling and analysis.

4. Conclusions

Recent experiments in RTNS-II have significantly increased the amount of information on irradiation strengthening by 14 MeV neutrons. For comparative studies, more reactor data at the same temperatures and damage levels are needed.

For the **low** dose fission-fusion comparisons reviewed in this report, dpa has been found to be an effective correlation parameter for yield stress changes. Exceptions **occur** in the pure metals copper, niobium and vanadium, from 300-500 K, where additional neutron spectral effects may be contributing.

The yield stress changes in 316 SS at 563 K are evidently strongly affected by the differences in damage rates of the fission and fusion neutron irradiations. Damage rate effects may dominate neutron **spectral** effects under some conditions, thus, mitigation of rate effects in spectral effects experiments must be pursued.

ACKNOWLEDGEMENTS

The assistance of Carlos Martinez, Jeff Pintler, Ruby Ermi and the staffs of RTNS-II and OWR is **greatly** appreciated. Calculations of displacement cross sections by R. L. Simons and his helpful comments are gratefully acknowledged. The OWR dosimetry was performed by L. R. Greenwood. RTNS-II irradiations were performed as part of the US-Japan Collaboration Program for Operation and Utilization of the RTNS-XI.

REFERENCES

1. D. G. Doran and N. J. Graves. "Displacement Cross-Sections and PKA Spectra: Tables and Applications," HEOL-TME 76-70 (1976).
2. N. J. Norgett, M. T. Robinson and I. M. Torrens. Nucl. Eng. & Des. **33** (1975) 50.
3. R. S. Averback, R. Eenedek and K. L. Merkle. Phys. Rev. **B18** (1978) 4156.
4. M. W. Guinan and J. H. Kinney, J. Nucl. Mater. **103 & 104** (1981) 1319.
5. J. B. Mitchell, R. A. VanKonynenburg, C. J. Echer and D. M. Parkin, Proc. Int. Conf. on Radiation Effects and Tritium Technology for Fusion Reactors, Gatlinburg, TN, Oct 1-3, 1975, Vol II, 172.
6. J. E. Mitchell, Univ. of California, Lawrence Livermore National Laboratory Rept. UCRL-52388 (1978).
7. R. R. VanderVoort, E.L. Raymond and C. J. Echer, Rad. Eff. **45** (1980) 191.
8. H. Matsui and O. Yoshinari, J. Nucl. Mater. **141-143** (1986) 851.
9. H. Matsui, O. Yoshinari and K. Abe, J. Nucl. Mater. **141-143** (1986) 855.
10. H. L. Heinisch, S. D. Atkin and C. Martinez, J. Nucl. Mater. **141-143** (1986) 807.
11. R. E. MacFarlane, R. J. Barret, D. W. Muir and R. E. Boccourt, The NJOY Nuclear Data Processing System, Vol. I: Users Manual, LA-7584-M, Los Alamos National Laboratory (1978).
12. H. L. Heinisch. Proc. of The Third International Conference on Fusion Reactor Materials, Karlsruhe, October 4-9, 1987.
13. H. L. Heinisch and C. Martinez. J. Nucl. Mater. **141-143** (1986) 883.
14. J. Diehl, Int. Conf. on Vacancies and Interstitials in Metals, Ed. A. Seeger et al. (1970) 739.
15. S. J. Zinkle. J. Nucl. Mater.. in press.
16. R. L. Simons. Proc. of ASTM Thirteenth International Symposium on Effects of Radiation on Materials, Seattle, June 23-35. 1986.
17. W. Schilling, P. Erhart and K. Sonnenberg, Proc. Int. Conf. on Fundamental Aspects of Radiation Damage in Metals, Gatlinburg, TN, Oct., 1975, eds., M. T. Robinson and F. W. Young, USEROA CONF-751006 (1976) 470.
18. H. R. Higgy and F. H. Hammad, J. Nucl. Mater. **55** (1975) 177.
19. H. L. Heinisch and R. L. Simons, DAFS Quarterly Progress Report, Jan-March 1982, DOE/ER-0046/9 (1982) 147.
20. T. Muroga, M. Eguchi, N. Yoshida, N. Tsukuda and K. Kitajima. J. Nucl. Mater. **141-143** (1986) 865.

THE EFFECTS OF LOW DOSES OF 14 MeV NEUTRONS ON THE TENSILE PROPERTIES OF THREE BINARY COPPER ALLOYS -
 HL Heinisch (Pacific Northwest Laboratories)

OBJECTIVE

The objective of this experiment is to determine the effects of 14 MeV neutrons on radiation-induced changes in tensile properties of three alloys of copper, and to compare the effects of 14 MeV and fission reactor neutrons.

SUMMARY

Miniature tensile specimens of high purity copper and copper alloyed respectively with five atom percent of Al, Mn, and Ni were irradiated with D-T fusion neutrons in the RTNS-II to fluences up to 1.3×10^{22} n/m² at 363 K. To compare fission and fusion neutron effects, some specimens were also irradiated at the same temperature to similar damage levels in the Omega West Reactor (OWR). Tensile tests were performed at room temperature, and the radiation-induced changes in tensile properties are compared as functions of displacements per atom (dpa). The irradiation-induced strengthening of Cu5%Mn is greater than that of Cu5%Al and Cu5%Ni, which behave about the same. However, all the alloys sustain less irradiation-induced strengthening by 14 MeV neutrons than pure copper. The effects of fission and fusion neutrons on the yield stress of the copper alloys correlate well on the basis of dpa, in contrast to the behavior of pure copper.

PROGRESS AND STATUS

Introduction

The most powerful source of d-t fusion neutrons, the Rotating Target Neutron Source - II (RTNS-II) at Lawrence Livermore National Laboratory, is limited to practical maximum doses of less than 1×10^{23} n/m². Thus, direct comparisons of materials irradiated with fission and fusion neutrons are limited to doses orders of magnitude smaller than typical fusion reactor first wall doses. However, for the purpose of investigating fundamental differences between fission and fusion neutron displacement damage, the low dose region is preferred.

Low dose fission-fusion neutron comparisons of the irradiation-induced changes in yield stress of pure copper have shown that the widely applied neutron spectral correlation parameter, displacements per atom (dpa), is not effective for fission reactor and d-t neutrons in pure copper [1,2]. The present experiment was conducted to determine if similar behavior would be observed in simple binary alloys of copper.

Brager, et al. [3], produced stock of three binary copper alloys having, respectively, five atom percent aluminum, manganese and nickel. The alloys and pure copper were irradiated at room temperature in RTNS-II to fluences ranging from 7.6×10^{20} to 7.5×10^{21} n/m². Brager, et al., examined the microstructures by transmission electron microscopy (TEM) and determined irradiation hardening by diamond pyramid hardness tests, with the objective of investigating the visibility and survivability of defect clusters. They concluded that a significant fraction of the defects responsible for hardening both pure copper and the alloys were not visible in their TEM.

The same binary copper alloys were supplied to Zinkle [4-6], who also irradiated them at room temperature in RTNS-II from 1×10^{20} to 2×10^{21} n/m². They performed TEM, resistivity and low-load microhardness measurements on the alloys, and analyzed hardening and defect survivability using simple models. Zinkle [6] determined that the hardening of the alloys increases linearly with the fourth root of the fluence after a "transition" fluence has been reached.

In both these earlier studies the radiation-induced changes in yield stress of copper and the copper alloys were examined as a function of 14 MeV neutron fluence and compared with an earlier study of 14 MeV neutron-irradiated copper [2]. The yield stress changes were obtained indirectly from the hardness measurements by applying a simple empirical correlation derived for copper [7].

In the present work the yield stress changes of pure copper and the copper alloys were measured directly in tensile tests of irradiated sheet-type miniature tensile specimens punched from the same sheet stock used in the earlier studies. Irradiations were carried out with both 14 MeV neutrons and fission reactor neutrons to determine the effects on fission-fusion correlation caused by the substitution of larger and smaller atoms into pure copper.

Experimental Procedure

Miniature sheet-type tensile specimens were prepared from pure (Marz grade) copper and three binary copper alloys of five atomic percent aluminum, manganese and nickel, respectively. The specimens were punched from 0.25 mm sheet stock, de-burred, laser engraved, then annealed using the same heat treatment for the

alloys described in the earlier work of both Brager and Zinkle: 750 C for 30 minutes in an argon atmosphere. The pure copper was annealed at 1000 C for 15 minutes in argon.

Five tensile specimens of each alloy were irradiated with 14 MeV neutrons at 90 C in the RTNS-II to fluences of $1.9 - 13 \times 10^{21} \text{ n/m}^2$. The pure copper tensile specimens received doses of $1.0 - 26.5 \times 10^{21} \text{ n/m}^2$. The specimens were included in a joint US/Japan elevated temperature irradiation utilizing a dual temperature vacuum furnace. Companion irradiations to similar dpa levels at 90 C were performed in helium-filled capsules at the Omega West Reactor (OWR) at Los Alamos National Laboratory.

Tensile tests were performed at room temperature on five to eight specimens of each alloy from each neutron environment. The pure copper specimens were irradiated and tested as part of the larger spectral effects experiment reported elsewhere [1,2], where more details of the irradiations and tensile testing are discussed.

Tensile tests and diamond pyramid hardness measurements were made on unirradiated samples in order to compare with the characterization of the materials in the earlier alloy studies.

Results

Results of the hardness and tensile tests on the unirradiated materials are compared in Table 1 with the hardness measurements of Brager et al. C31 and Zinkle and Kulcinski C41 on the same materials. The yield stress of the Cu5%Mn alloy is 1/3 larger than that of the other alloys and pure copper, indicating a measurable effect of solute hardening for this alloy. The hardness measurements of Brager and the present work also show significantly increased hardening for Cu5%Mn and slightly increased hardening for Cu5%Al. Zinkle's microhardness measurements were made with 10 and 5 g loads, while Brager's and the present measurements were made with 50 g loads. The low-load microhardness evidently measures a different property of the material, probably related to strain hardening near the surface.

TABLE 1

Yield Stress and Diamond Pyramid Hardness (DPH)
of Unirradiated Copper and Copper Alloys.

	σ_y (MPa)	DPH (50g) (kg/mm ²)	DPH (50g) ^a (kg/mm ²)	DPH (10g) ^b (kg/mm ²)
cu	49 ± 5	54 ± 5	56	57 ± 4
Cu5%Al	50 ± 6	62 ± 4	66	54 ± 1
Cu5%Mn	66 ± 2	79 ± 6	73	53 ± 3
Cu5%Ni	50 ± 4	59 ± 2	58	53 ± 3

a Brager et al. C31

b Zinkle and Kulcinski C41

Fig. 1 shows the change in 0.2% offset yield stress as a function of 14 MeV neutron fluence for pure copper and the copper alloys. Curves of the form

$$\Delta\sigma_y = a + b (\phi t)^{1/4} \quad (1)$$

are fitted to the data, where $\Delta\sigma_y$ is the change in yield stress and ϕt is the 14 MeV neutron fluence. Curves linear in the square root of the fluence were also fitted to the data. Curves with square root and fourth root fluence dependence fit the alloys equally well. Fourth root fluence dependence was clearly better than square root dependence for the pure copper data, however the evidence for fourth root fluence dependence is not compelling. The minimum fluences were higher than the "transition" fluences noted by Zinkle [6], and the data showed no evidence of that behavior.

The pure copper hardens more than the alloys in the fluence range investigated. The behavior of Cu5%Mn is different from that of the other two alloys, the slope being more nearly like that of pure copper.

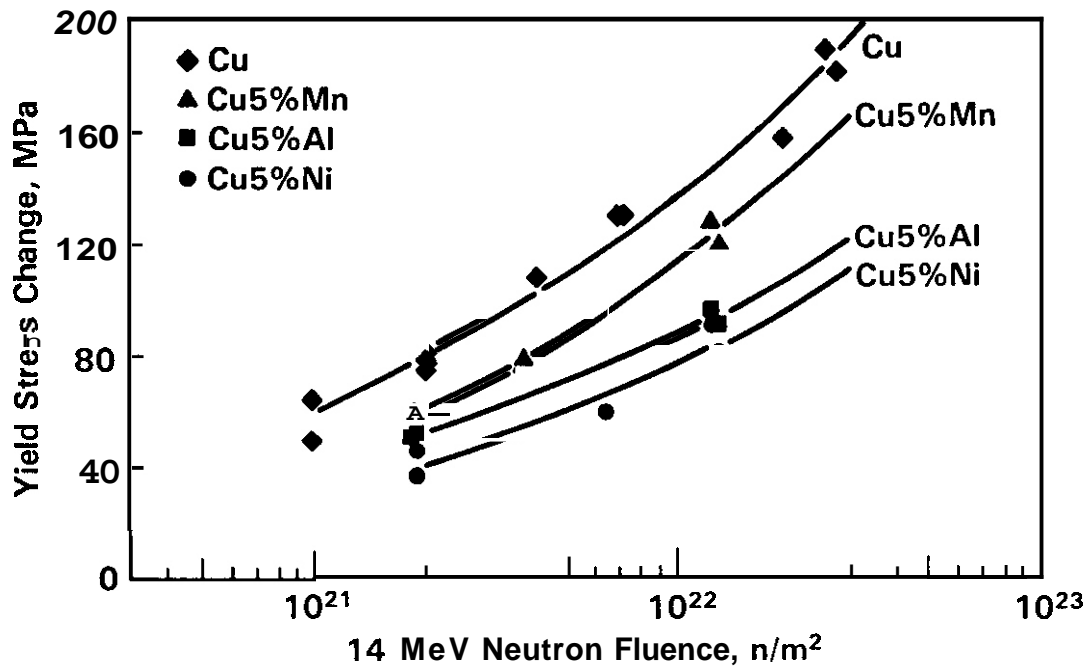


Fig. 1. Changes in 0.2% Offset Yield Stress as a Function of Neutron Fluence for Cu, Cu5%Al, Cu5%Mn and Cu5%Ni Irradiated in RTNS-II at 363 K. The curves are fits of eq. 1 to the data.

Fig. 2 shows the yield stress changes for pure copper irradiated in both RTNS-II and OWR as a function of total neutron fluence. The curves are fittings of eq. (1) to the data. Plotting the data against the fluence of only high energy neutrons (in OWR 31% have $E > 0.1$ MeV) would shift the OWR data somewhat to the left in Fig. 2, but it would still fall short of the RTNS-II data.

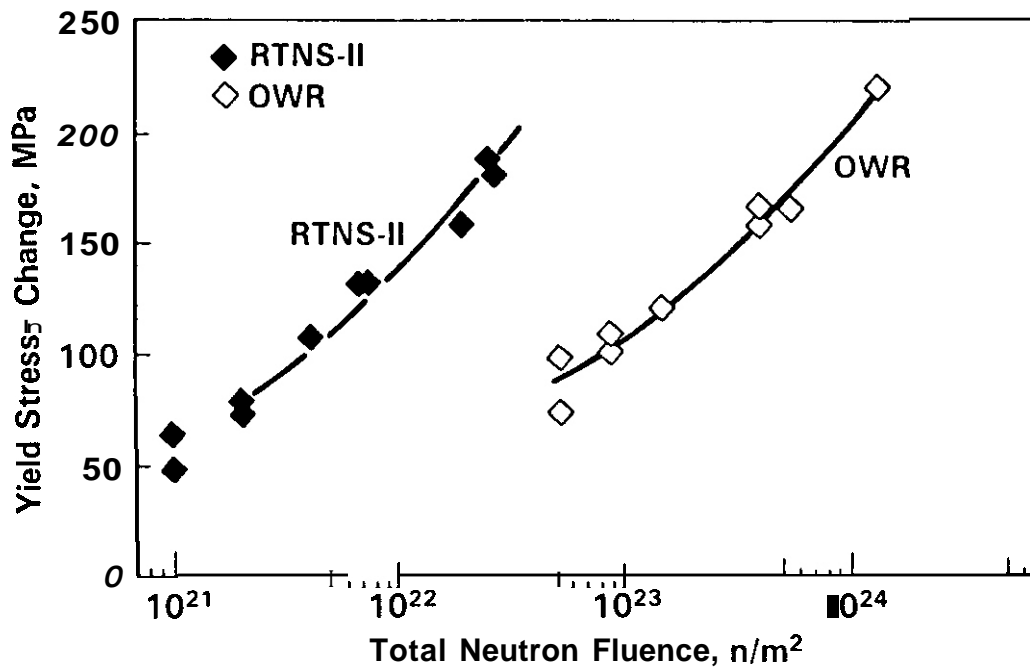


Fig. 2. Changes in 0.2% Offset Yield Stress as a Function of Total Neutron Fluence for Pure Copper Irradiated in RTNS-II and the Omega West Reactor at 363 K. Curves are fits of eq. 1 to the data.

Yield stress changes from the two irradiation sources were compared using displacements per atom (dpa) as a damage parameter. The spectral averaged displacement cross sections used for copper in RTNS-II and OWR are 3699 b and 293 b, respectively [1]. Fig. 3 shows the change in yield stress for copper plotted as a function of dpa. About twice as many dpa are required in OWR to produce the same yield stress change obtained in RTNS-II. Earlier investigations [1,2] have also shown that dpa does not correlate the yield stress changes in copper from RTNS-II and OWR.

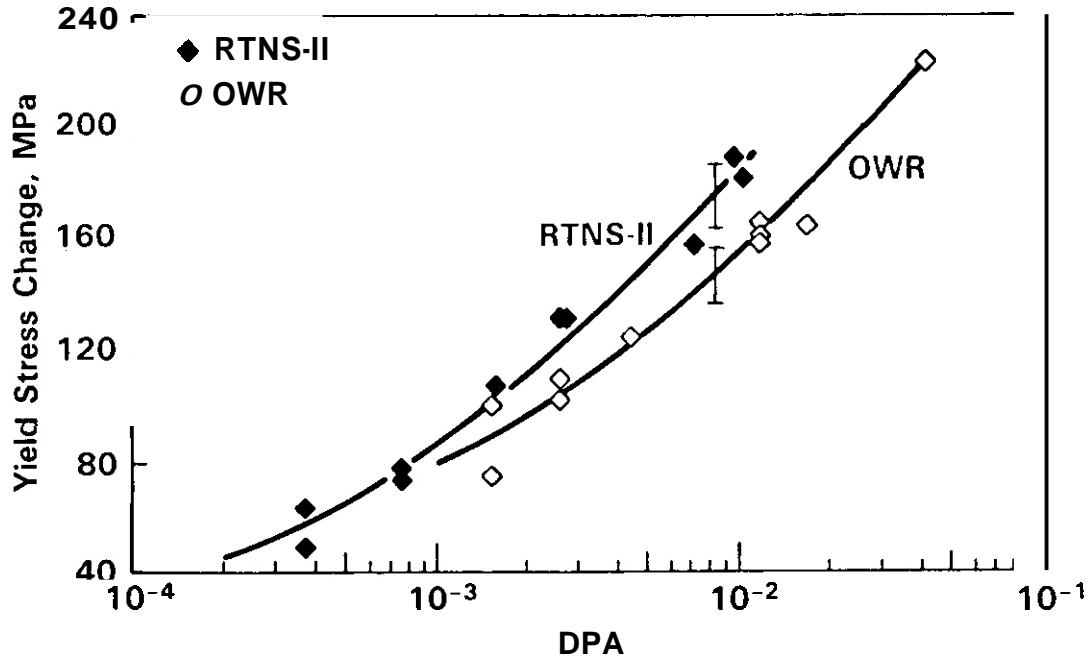


Fig. 3. Changes on 0.2% Offset Yield Stress as a Function of Displacements Per Atom (DPA) for Pure Copper Irradiated in RTNS-II and the Omega West Reactor at 363 K. Curves are fits of eq. 1, using DPA in place of fluence.

Figs. 4-6 compare the yield stress changes from RTNS-II and OWR as a function of dpa for Cu5%A1, Cu5%Mn and Cu5%Ni, respectively. Dpa is an effective correlation parameter in all three alloys at the temperature and fluence range investigated.

Cu5%A1 and Cu5%Mn irradiated in OWR display a trend toward saturation in yield stress change at the highest fluence levels. The trend appears more dramatically when the data are plotted versus the fourth (or second) root of dpa. Because of their marked deviation from linearity, the two highest fluence data points in each case were ignored when fitting eq. (1). This behavior was observed in pure copper at the same fluence. It is difficult to determine if Cu5%Ni behaves as the other alloys because the OWR data for Cu5%Ni show much more scatter than the other sets of data.

Discussion

Results of the present investigation cannot be compared directly with the extensive studies of these alloys by Zinkle [4-6], since the irradiation temperatures were different and the fluence ranges barely overlap. Nevertheless, keeping those differences in mind, comparisons can be made.

The fourth root fluence dependence of the yield stress changes is consistent with Zinkle's results that hardness changes are linear in the fourth root of the fluence. Simple models of dislocation pinning lead to the criterion that σ_y varies as $(Nd)^{1/2}$, where N is the density of obstacles of average size d . Zinkle finds that the average visible cluster size is independent of fluence and visible cluster density varies with the square root of fluence. Hence, if visible clusters are responsible for hardening, the change in yield stress is proportional to the fourth root of the fluence. Zinkle observes a "transition" fluence before the fourth root fluence dependence begins. The lowest fluences in the present work were much higher than the "transition" region, so this phenomenon could not be investigated through tensile testing. Zinkle attributes the fluence dependence of the visible cluster density to uncorrelated recombination of interstitials, that is, recombination of interstitials with vacancies or vacancy clusters in other cascades. Thus, as damage builds, there are more vacancy clusters, hence increased annihilations per defect produced in the cascade.

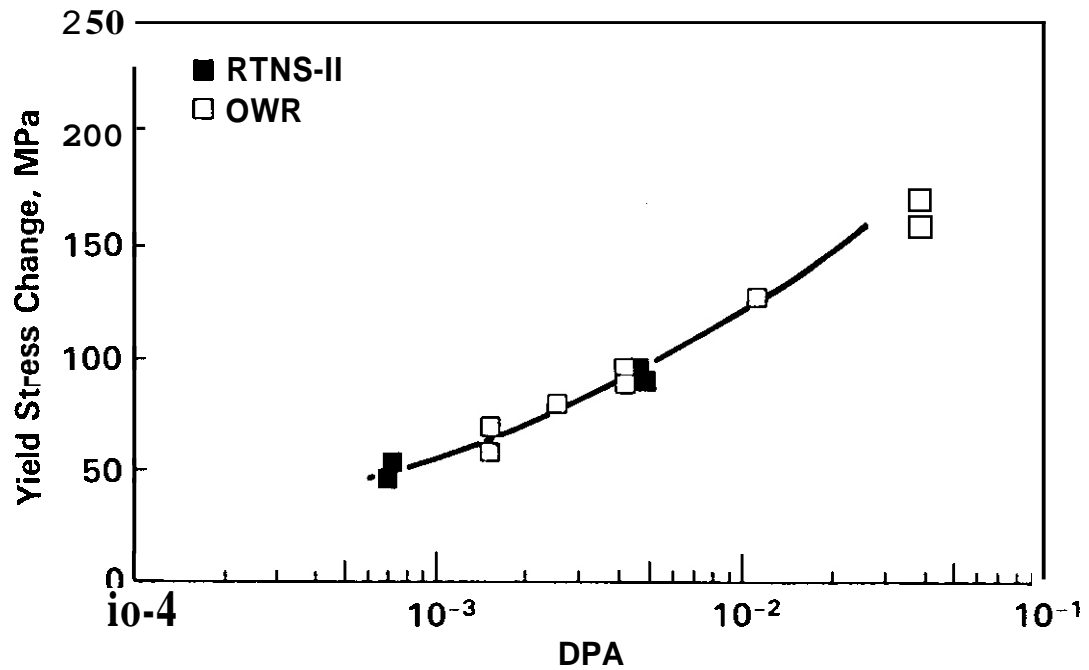


Fig. 4. Changes in 0.2% Offset Yield Stress as a Function of DPA for Cu5%Al Irradiated in RTNS-II and the Omega West Reactor at 363 K. The curve is a fit of eq. 1, using DPA in place of fluence.

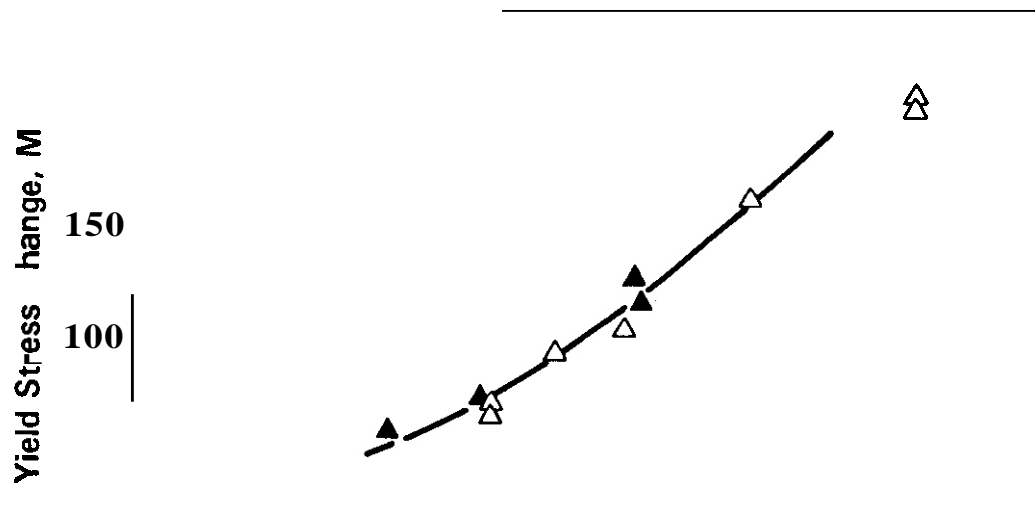


Fig. 5. Changes in 0.2% Offset Yield Stress as a Function of DPA for Cu5%Mn Irradiated in RTNS-II and the Omega West Reactor at 363 K. The curve is a fit of eq. 1, using DPA in place of fluence.

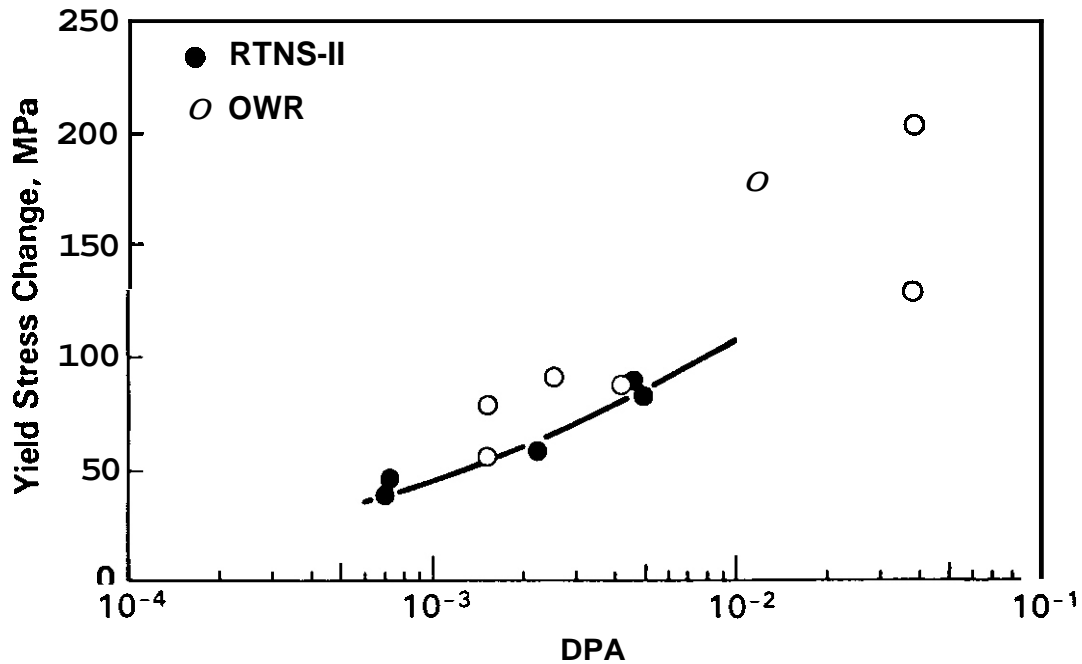


Fig. 6. Changes in 0.2% Offset Yield Stress as a Function of DPA for Cu5%Ni Irradiated in RTNS-II and the Omega West Reactor at 363 K. The curve is a fit of eq. 1 to the RTNS-II data, using DPA in place of fluence.

In the present experiment at 363 K pure copper is hardened by 14 MeV neutrons significantly more than are the alloys. From two to six times higher fluences are needed in the alloys to produce the same yield stress change as pure copper. Zinkle's measured visible defect densities in pure copper and the alloys vary by about a factor of two (i.e., about twice the fluence is needed in the alloys to get the same visible defect density as in pure copper). The smaller variation with respect to defect density is consistent with the model that yield stress change varies as the square root of the defect cluster density.

Zinkle points out that in the alloys a smaller fraction of the visible defects are observed to be stacking fault tetrahedra, which are stronger obstacles than loops. This may be related to the reduced hardening in the alloys, but the relationship is not straightforward. Data on the influence of stacking fault energy, primary knock-on atom (pka) energy and irradiation temperature on formation of stacking fault tetrahedra in copper and copper alloys present an ambiguous picture [6].

It is also possible that defects not visible in the microscope play a role in the hardening. Solute-defect interactions may diminish clustering (of both visible and invisible clusters) in the alloys, resulting in less hardening.

For RTNS-II irradiations both Zinkle and Brager measured defect densities in Cu5%Al that are somewhat larger than in Cu5%Mn and Cu5%Ni, which are about the same. In contrast, the yield stress changes (and Zinkle's hardness changes) are larger for Cu5%Mn than for Cu5%Al and Cu5%Ni, which are about the same. This is additional evidence that, at least in RTNS-II, hardening may depend on something more than the visible microstructure.

The departure of the yield stress changes from the fourth root fluence dependence in the highest fluence OWR irradiations is probably an indication of cascade overlap. However, this occurs only in the alloys and not in pure copper.

When comparing RTNS-II and OWR irradiations, dpa was found to correlate the yield stress changes very well in the alloys, although dpa does not correlate the yield stress changes in pure copper. A possible explanation for the difference in behavior of the pure copper and the alloys may be the differences in how displacement cascades are produced.

Computer modeling of **displacement** cascades in copper [8] has shown that cascades **from** pkas having hundreds of **keV** in damage energy, such as produced in **RTNS-II**, consist of a collection of mostly connected damage regions (depleted zones), each having the characteristics of cascades of about 5-30 **keV**. In the **OWR** **only** a small fraction of the pkas have energies above 30 **keV**. If depleted zones with minimum energy of about 30 **keV** collapse to form loops, stacking fault tetrahedra, etc., then 14 **MeV** neutrons will form more obstacles per **dpa** than fission reactor neutrons. Hence, the hardening, dominated by obstacles directly produced by collapsing depleted zones, will not correlate on the basis of **dpa**.

On the other hand, in the copper alloys, replacement collision sequences have difficulty propagating because of the mass and size differences of the solute **atoms**, **resulting** in less separation of the vacancy and interstitial populations. This leads to more recombination and fewer collapsing depleted zones. Thus, with many fewer obstacles formed directly by collapse, the 14 **MeV** and **fission** reactor neutron cascades could have about the same **number** of obstacles per **dpa**.

This may also explain why the alloys are subject to cascade overlap at lower fluences than pure copper. With vacancies and interstitials more closely intermingled, the energy of a nearby or overlapping cascade can more easily promote recombinations.

FUTURE WORK

The microstructures of the irradiated copper and copper alloys will be examined by TEM.

REFERENCES

1. H. L. Heinisch, S. D. Atkin and C. Martinez. *J. Nucl. Mater.*, 141-143 (1986) 807-815.
2. J. B. Mitchell, R. A. VanKonynenburg, C. J. Echer and D. M. Parkin. In Radiation Effects and Tritium Technology for Fusion Reactors, eds. J. S. Watson and W. D. Wiffen. Gatlinburg, TN, (1975), 172.
3. H. R. Brager, F. A. Garner and N. F. Panayotou. *J. Nucl. Mater.*, 103 & 104, (1981) 955.
4. S. J. Zinkle and G. L. Kulcinski. in The Use of Small-Scale Specimens for Testing Irradiated Material, Eds. W. R. Corwin and G. E. Lucas. Albuquerque, NM, Sep, 1983. ASTM-STP 888 (1986).
5. S. J. Zinkle. Fusion Reactor Materials Semiann. Prog. Report. Mar., 1987, DOE/ER-0313/2, in press.
6. S. J. Zinkle. *J. Nucl. Mater.*, in press.
7. N. F. Panayotou, *J. Nucl. Mater.*, 108 & 109, (1982), 456.
8. H. L. Heinisch. *J. Nucl. Mater.*, 103 & 104, (1981) 1325.

DUAL-ION IRRADIATION OF COPPER — S. J. Zinkle (Oak Ridge National Laboratory)

OBJECTIVE

The objective of this study is to investigate the effects of simultaneous irradiation of copper with helium and heavy ion beams.

SUMMARY

Simultaneous irradiation of copper with helium and heavy ions produced substantial void formation at a temperature of **440°C**. Irradiation at a temperature of **220°C** produced small "black-spot" defect clusters. The implanted ions from the heavy ion beam caused a substantial reduction in void swelling at the damage peak for the **440°C** irradiation, as determined from a cross-section TEM observation. The void swelling rate was **~0.5%/dpa** in regions that were far away from the injected ion peak.

PROGRESS AND STATUS

Introduction

There have been relatively few systematic high-dose studies of copper at conditions relevant for fusion reactor applications. A high-dose **self-ion** irradiation study² on high-purity oxygen-free copper has shown that void formation does not occur at temperatures from 100 to **500°C**. On the other hand, neutron irradiation studies have observed substantial void swelling over a wide range of **conditions**.^{1,3,4} The **most** likely cause of these differences in void swelling behavior is helium effects. In the present study, ion-irradiated copper that has been simultaneously injected with helium at a rate appropriate for first-wall fusion reactor conditions is investigated.

Experimental procedures

High-purity (99.999%) polycrystalline copper was obtained from Johnson-Mathey in the form of **1 mm** foil. The foils were cold rolled to achieve a 50% reduction in thickness, and TEM disks of 3 mm diameter were punched from the foils. The disks were mechanically **polished** and then **electropolished** at **-40°C** using a solution of **33% HNO₃/67% CH₃OH** with an applied **potential** of 5 V. A thermocouple wire was spot welded to the back of the TEM disks to monitor the irradiation temperature.

The irradiation was performed using the Oak Ridge dual-beam Van de Graaff irradiation facility.⁵ The helium beam energy was ramped sinusoidally between 0.2 and 0.4 MeV at **0.025 Hz** during the irradiation to provide a uniform helium implantation (48 appm) at depths of 0.5 to **1.1 μm**. A 4-MeV **Fe⁺⁺** ion beam was used to produce the displacement damage. The disks were irradiated to a peak damage level of 16 dpa (**9.5 × 10¹⁹ ions/m²**), which occurred at a depth of **0.8 μm** according to an EDEP-1 calculation. The peak damage rate was **~6 × 10⁻³ dpa/s**. Specimen arrays consisting of nine TEM disks were irradiated at temperatures of 220 and **440°C**. The pressure was **<2 × 10⁻⁷ torr** for both irradiations.

The surfaces of the specimens were examined optically following the irradiation and then selected TEM disks were prepared for cross-sectional examination. The preparation of the cross-section specimens was similar to that described in detail **elsewhere**,⁶ with the following exceptions: (1) a magnetic stirring bar was used for agitation instead of an argon gas bubbling system, and (2) the electroplating was performed without removing any of the original irradiated surface (**i.e.**, there was no electropolishing or strike treatment prior to the electroplating).

The TEM disks were jet-thinned using a lacquer painting technique⁶ designed to force the perforation to occur near the irradiated foil-plating interface. A solution of **25% H₃PO₄/75% H₂O** (by volume) was used in a Tenupol jet-polishing unit. The polishing conditions were **0°C** and **6 V dc (160 mA)**. TEM examination was performed using a JEOL **2000FX** electron microscope. The foil thickness was determined using thickness fringes.

Results

Optical examination of the TEM disks irradiated at **440°C** showed that they had recrystallized during the 45-min irradiation. The surfaces of these specimens were also covered by an unusual array of small conical projections. As shown in Fig. 1, the occurrence of these features depended on the crystallographic orientation of the surface grains. Examination in a scanning electron microscope revealed that the base of the cones was nearly square in cross section with an edge length of **~1 μm**. The height of the

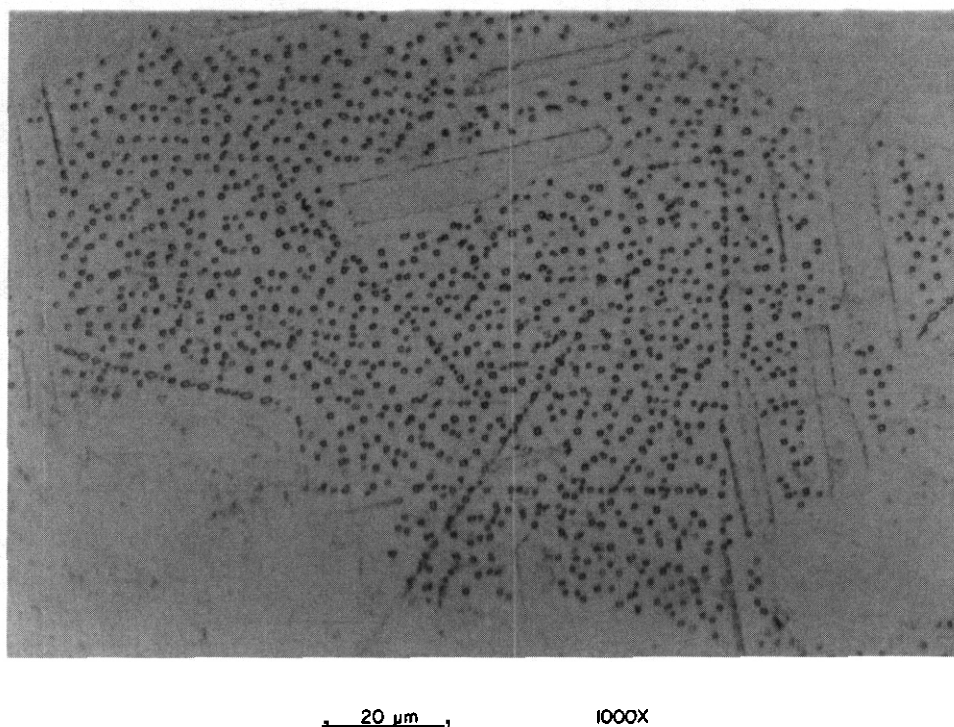


Fig. 1. Optical micrograph of the surface of copper following dual beam irradiation at 440°C showing the presence of cones.

cones was $-0.2 \mu\text{m}$. There was no evidence of cone formation in the specimens irradiated at 220°C. Conical features have been frequently observed on ion-bombarded copper surfaces.⁷

The microstructure of the specimens irradiated at 220°C consisted of a high density ($\sim 2 \times 10^{23}/\text{m}^3$) of small "black spot" defect clusters. A preliminary through-focus examination did not detect the presence of any helium bubbles, but a detailed high-resolution analysis has not yet been performed. The size and density of the defect clusters were essentially constant over the entire ion damage region.

Substantial void formation was observed in the specimens irradiated at 440°C. Figure 2 shows a cross-sectional view of the irradiated microstructure. Void formation occurred from the surface to a depth of $\sim 1.3 \mu\text{m}$, in good agreement with the damage range predicted by the EDEP-1 calculation. The depth-dependent void swelling parameters are given in Fig. 3 along with the calculated displacement damage profile. There was no significant void-denuded zone at the specimen surface. The amount of void swelling was strongly suppressed in regions near the damage peak, where the injected ions come to rest. As shown in Fig. 3, both the void density (nucleation) and size (growth) were affected for depths between 0.5 to $1.1 \mu\text{m}$.

Discussion

Theoretical calculations have predicted that the injected ions associated with ion irradiation can have a substantial effect on both void growth⁸ and nucleation.⁹ It is also possible under some conditions for implanted helium to cause a suppression of void nucleation.¹⁰ The present result is the first known direct observation of an injected ion effect in ion-irradiated copper. The void swelling rate at a depth of $\sim 0.3 \mu\text{m}$ is approximately 0.5%/dpa (assuming that there is no appreciable incubation dose for void swelling in copper). This swelling rate is in agreement with several recent high-dose neutron irradiation studies on copper.^{4,11} It is believed that void swelling at a depth of $0.3 \mu\text{m}$ should be relatively unaffected by the injected ions for the irradiation conditions of this study. The present results indicate that cross-sectional analysis should be used to evaluate void swelling in ion-irradiated copper and simple copper alloys in order to separate out the effects of injected ions.

ACKNOWLEDGMENTS

The author would like to thank M. B. Lewis and S. W. Cook for performing the ion irradiations, and Frances Scarboro for manuscript preparation.

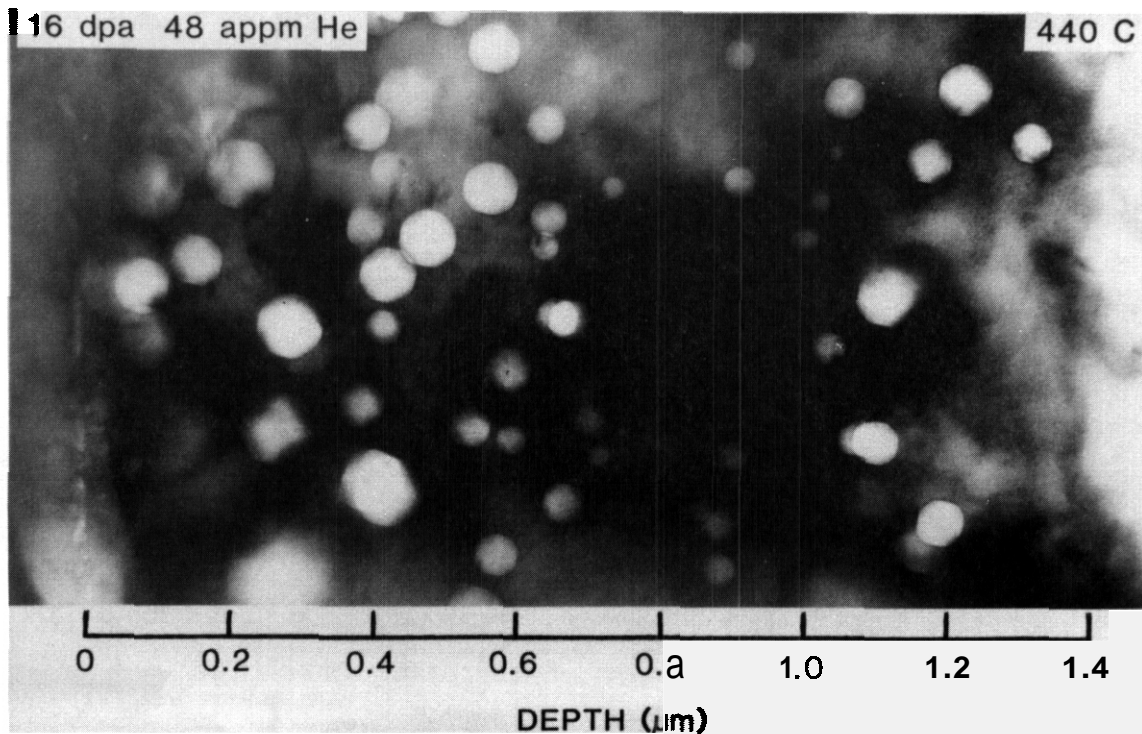


Fig. 2 Depth-dependent void microstructure of irradiated copper.

REFERENCES

1. S. J. Zinkle and R. W. Knoll. A Literature Review of Radiation Damage Data for Copper and Copper Alloys, University of Wisconsin Fuslon Technology Inst. Report UWFD-578 (1984).
2. S. J. Zinkle, G. L. Kulcinski, and R. W. Knoll, J. Nucl. Mater. 138 (1986) 46.
3. H. R. Brager, J. Nucl. Mater. **141-143** (1973) 86.
4. R. J. Livak et al., J. Nucl. Mater. 141-143 (1986) 160.
5. M. B. Lewis, N. H. Packan, G. E. Wells, and R. A. Buhl, Nucl. Instr. Meth. 167 (1979) 233.
6. S. J. Zinkle and R. L. Sindelar, Nucl. Instr. Meth. 816 (1986) 154.
7. R. Kelly and O. Auciello, Sur. Sci. 100 (1980) 135.
8. L. K. Mansur, Nucl. Technol. **40** (1978) 5
9. B. Badger, Jr., et al., p. 297 in Effects of Radiation on Materials: 12th Inter. Symp., ASTM STP 870, eds., F. A. Garner and J. S. Perrin (1985).
10. A. S. Kumar and E. A. Garner, p. 493 in Effects of Radiation on Materials: 12th Inter. Symp., ASTM STP 870, eds., F. A. Garner and J. S. Perrin (ASTM 1985).
11. E. A. Garner, personal communication on void swelling results for copper irradiated to 98 dpa at 450°C in FFTF (swelling rate = 0.5%/dpa).

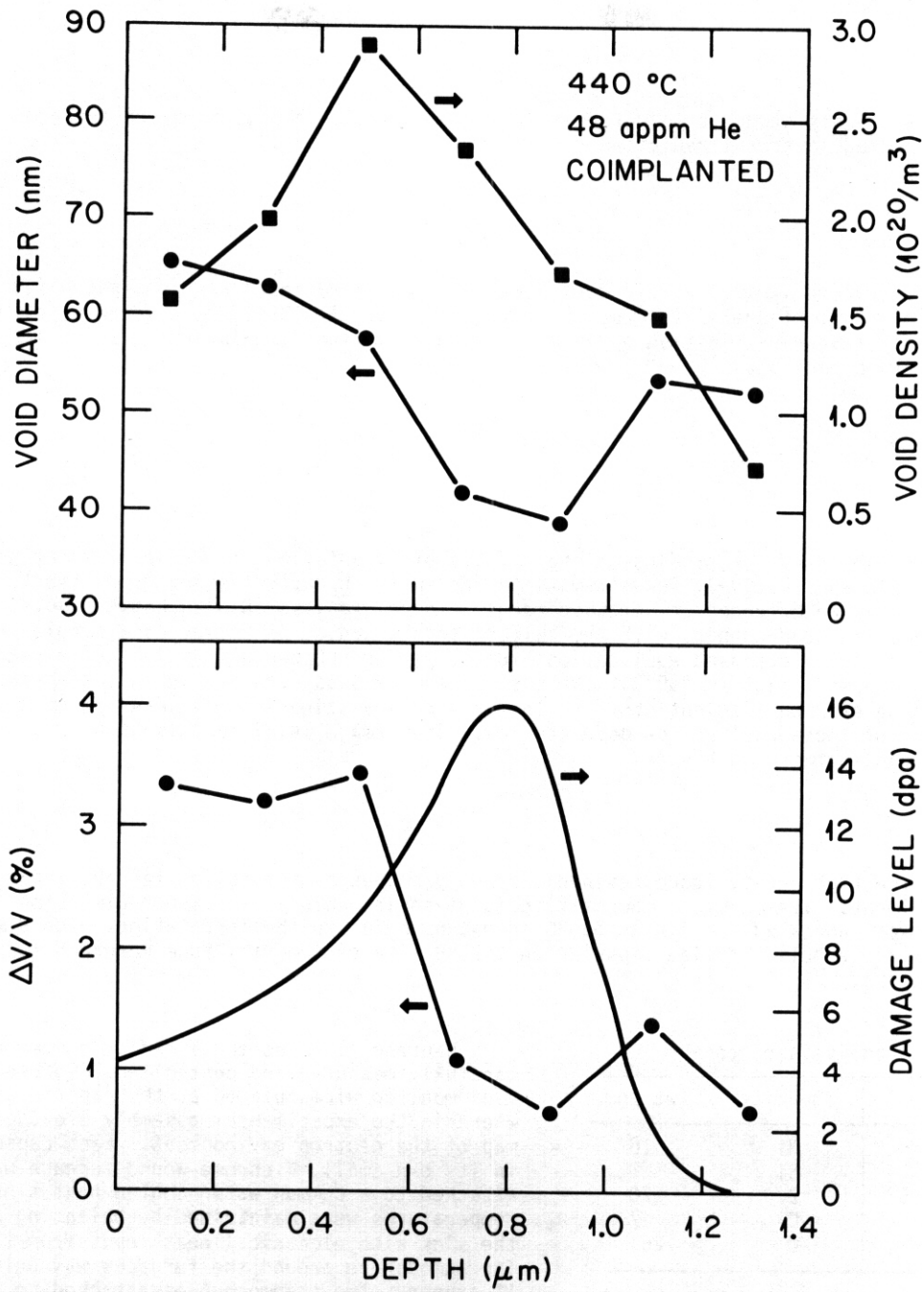


Fig. 3. Measured void swelling parameters and calculated damage level versus implantation depth for ion-irradiated copper.



VOID SWELLING AND DEFECT CLUSTER FORMATION IN REACTOR-IRRADIATED COPPER — K. Farrell and S. J. Zinkle (Oak Ridge National Laboratory)

OBJECTIVE

The objective of this study is to determine the void swelling behavior of copper under carefully controlled and measured neutron irradiation conditions.

SUMMARY

The lower temperature limit for void formation in copper irradiated with moderated fission neutrons at a damage rate of 2×10^{-7} dpa/s lies between 182 and 220°C. At 182°C the clustering of vacancies produces stacking fault tetrahedra instead of voids. The maximum swelling for the 13 dpa irradiation is ~0.4% at a temperature near 300°C.

PROGRESS AND STATUS

Introduction

There have been hundreds of studies on the effects of irradiation on copper over the past 30 years. However, there have been relatively few attempts to carefully characterize the microstructure of neutron-irradiated copper over an extended temperature range. There are less than 20 known studies of void formation in neutron-irradiated copper, with the bulk of these studies performed at a single irradiation temperature.¹ Most of the proposed applications for copper and copper alloys in fusion reactors involve irradiation temperatures of 100 to 400°C. The most extensive study to date in this temperature range was performed by a group of French scientists.²⁻⁴ The present investigation was intended to confirm and extend the results of these earlier low-dose studies. The damage level in this study was about a factor of 2 higher than in the French work.

Experimental procedures

Polycrystalline high-purity (zone-refined) copper produced by the Solid State Division at ORNL was used in the experiment. Its chemical composition is given in Table 1. Disks of dimensions 32 mm diam by 0.28 mm thick were annealed for 1 h at 550°C in vacuum prior to the irradiation. The disks were irradiated in nine separate helium-filled capsules in the B8 site of the Oak Ridge Research (ORR) reactor for a period of ~14 weeks.

Table 1. Chemical analysis of copper

Impurity	(wt ppm)	Impurity	(wt ppm)
Ag	50	Ni	10
Al	1	Si	1
B	<0.5	Zr	70
Cr	5	C	7
Fe	10	O	261

Neutron fluences and irradiation temperatures were carefully measured and controlled: Fourteen packages of flux monitor wires placed at the capsule sites and elsewhere in the experimental assembly provided a thorough map of the neutron environment. Each capsule was housed in its own small, Nichrome-wound furnace which was attached to a common water-cooled heat sink. Irradiation temperatures were maintained by balancing heat loss to the sink with electrical heat input from the furnaces. The atmosphere around the furnaces was helium containing 1% oxygen. Two thermocouples attached to each capsule measured the temperatures and controlled the furnace input. Temperatures were recorded continuously on disk

charts; the measured values remained within $\pm 5^\circ\text{C}$ of the targeted nominal values. The lowest temperature of 182°C was the minimum controllable temperature attainable with this arrangement. The irradiation temperatures ranged from 182 to 350°C, and the damage level was about 13 dpa. A summary of the irradiation parameters is given in Table 2. The irradiation generated a calculated⁵ gas concentration of ~0.3 appm He and ~15 appm H in the disks.

Table 2 Irradiation data for copper specimens

Temperature (°C)	Neutron fluence (10^{25} n/m ²)			Damage Level (dpa)
	Total	Thermal	>0.1 MeV	
182	3.6	1.2	1.1	1.3
220	36	1.2	1.1	1.3
250	43	1.2	1.2	15
275	40	1.2	1.3	14
300	3.6	1.1	1.0	1.3
350	37	1.2	1.2	1.3

Results

Irradiation at 182°C resulted in uniform "black-spot" formation, with no evidence of voids or helium bubbles. Figure 1 shows the defect microstructure for this irradiation condition. About half of the visible clusters were resolvable as stacking fault tetrahedra (SFT), seen as triangular clusters in Fig. 1. The cluster density was $1.7 \times 10^{23}/\text{m}^3$ and the mean diameter was 25 nm. Further details are given elsewhere.⁶

ORNL-PHOTO-7858-87



Fig. 1 Weak-beam dark-field (g , $3g$) microstructure of copper irradiated at 182°C. The foil normal is near $[110]$ and $g = \langle 002 \rangle$.

Loop and void formation was observed in copper irradiated at 220 to 350°C. The void parameters are given in Table 3. A network dislocation density of about $2 \times 10^{12}/\text{m}^2$ was found for all of the irradiation conditions. The small loops produced by the irradiation increased in size as the irradiation temperature increased, changing from a mean diameter of 25 nm at 182°C to ~10 nm at 300°C. The loop density was not accurately measured, but a decrease was observed above 250°C.

The voids exhibited faceting consistent with that of truncated octahedra bounded by $\{111\}$ planes, in agreement with previous observations.¹⁻⁴ The void microstructure in copper following irradiation at 300°C is shown in Fig. 2. Some small dislocation loops are also visible in this picture. A void denuded zone was observed along grain and incoherent twin boundaries. The width of this denuded zone varied from ~0.3 μm at 250°C to ~0.7 μm at 350°C. Figure 3 shows the void microstructure adjacent to a grain boundary in copper irradiated at 350°C. Adamson et al.⁷ have reported a denuded zone width of ~0.7 μm for copper irradiated at 327°C.

Table 3. Void parameters for irradiated copper

Temperature (°C)	Void Density ($10^{18}/\text{m}^3$)	Mean Void Diameter (nm)	$\Delta V/V$ (%)
182			0
220	146	19	0.06
250	155	28	0.23
275	66	46	0.38
300	65	45	0.37
350	38	49	0.35

ORNL-PHOTO-7859-87

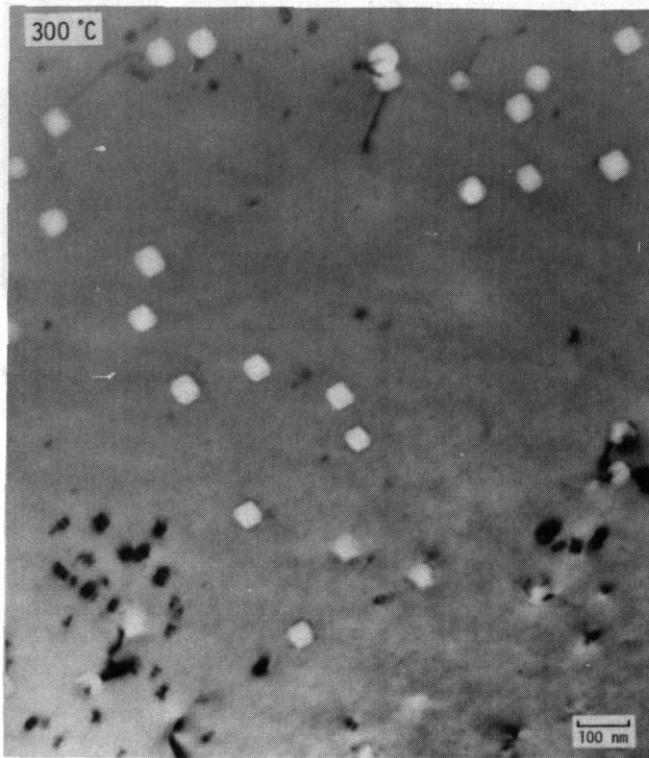


Fig. 2. Microstructure of copper irradiated at 300°C.

the void swelling is reduced compared to that at 215 to 350°C. Therefore, the swelling peak for the present study shows a rather broad maximum that is centered at $\sim 300^\circ\text{C}$ ($0.42 T_m$).

From a practical standpoint, the present results suggest that void swelling will not be of concern for copper exposed to moderate neutron doses at temperatures below 180°C. At these low irradiation temperatures, the vacancies combine to form SFTs and small faulted loops. These findings on the temperature-dependent vacancy cluster geometry are in agreement with a simple theory on the relative stability of voids and SFT in irradiated metals.⁹ Irradiation of copper at temperatures between 220 and 400°C may cause substantial void swelling. Further work may be needed to develop copper alloys that are resistant to void swelling in this temperature range.

CONCLUSIONS

Substantial void formation occurs in copper following neutron irradiation to ~ 1.3 dpa at temperatures from 220 to 350°C. There was no evidence of void formation at 182°C; instead, stacking fault tetrahedra

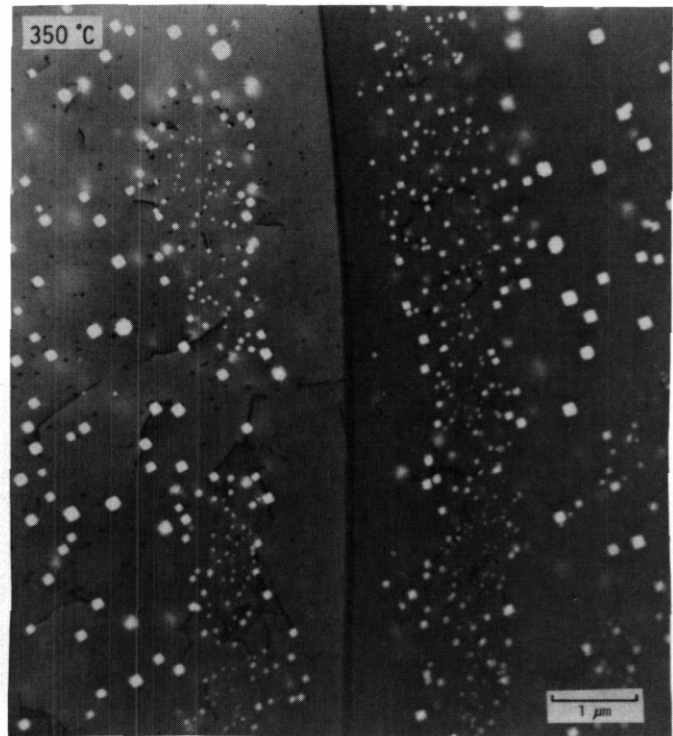


Fig. 3. Void-denuded zone along a grain boundary in copper irradiated at 350°C.

Discussion

Previous neutron irradiation studies on copper have found that the lower limit for void formation in copper is $< 220^\circ\text{C}$.¹⁻⁴ The present investigation confirms this, showing that substantial void formation occurs at a measured irradiation temperature of 220°C whereas there is no void formation at 182°C for the damage rate employed in this study. Wolfenden⁸ found that voids did not form in copper irradiated with neutrons to a damage level of 10 dpa at $175 \pm 25^\circ\text{C}$. The peak void swelling temperature of copper has been found to occur at 300 to 350°C.¹⁻⁴ We have examined the microstructure of copper specimens irradiated above 400°C in a companion experiment and found that

were observed. The maximum void swelling in copper irradiated at a damage rate of 1.7×10^{-7} dpa/s occurs at $\sim 300^\circ\text{C}$, and the lower temperature limit for void formation lies between 182 and 220°C .

REFERENCES

1. S. J. Zinkle and R. W. Knoll, A Literature Review of Radiation Damage Data for Copper and Copper Alloys, University of Wisconsin Fusion Technology Inst. Report UWFD-578 (1984).
2. Y. Adda, Radiation-Induced Voids in Metals, ed., J. W. Corbett and L. C. Ianniello, AEC Symposium Series No. 26, CONF-710601 (1972), pp. 31-81.
3. M. Labbe and J. P. Poirier, J. Nucl. Mater. **46** (1973) 86.
4. M. Labbe, G. Brebec, and J. P. Poirier, J. Nucl. Mater. 49 (1973) 232.
5. T. A. Gabriel, B. L. Bishop, and F. W. Wiffen, Oak Ridge National Laboratory report, ORNL/TM-6361 (August 1979).
6. S. J. Zinkle and R. L. Sindelar, "Defect Microstructures in Neutron-Irradiated Copper and Stainless Steel," Third International Conference on Fusion Reactor Materials, Karlsruhe, FRG (October 1987); to be published in Journal of Nuclear Materials.
7. R. B. Adamson, W. L. Bell, and P. C. Kelly, J. Nucl. Mater. 92 (1980) 149.
8. A. Wolfenden, Rad. Effects 15 (1972) 255.
9. S. J. Zinkle et al., Phil. Mag. A 55 (1987) 127.

THE DISTRIBUTION OF DEFECT CLUSTERS IN ION IRRADIATED Ni-10Cu AND Ni-50Cu - LM. Wang, R.A. Oodd and G.L. Kulcinski (University of Wisconsin)

OBJECTIVE

To investigate the oxygen effect on the void resistance of Ni-Cu alloys.

SUMMARY

The resistance to void formation of concentrated Ni-Cu alloys is confirmed by TEM cross-section observation of the 14 MeV Ni ion irradiated Ni-10Cu and Ni-50Cu alloys with damage levels up to 100 dpa at the peak.

Irradiation produced a substantial number of dislocation loops in both alloys, but the loop size is much smaller and their density is 5-7 times higher in Ni-50Cu than in Ni-10Cu.

Preinjection of 100 appm oxygen before Ni ion irradiation promotes void formation in Ni-10Cu, but does not show any apparent effect in the case of Ni-50Cu.

Trapping of vacancies and gas atoms by fine-scaled clusters of like atoms is considered the mechanism responsible for the void resistant property of the alloys.

PROGRESS AND STATUS

Introduction

The Ni-Cu system is one of the few simple alloy systems which form a complete solid solution over the entire composition range. While voids can easily be produced in both pure Ni and pure Cu by irradiation, the concentrated Ni-Cu alloys have been shown to be very resistant to void formation under neutron,¹ ion²⁻⁴ and electron⁵ irradiations. However, the database for the irradiation of Ni-Cu is still quite small, and the cause of the suppressed void formation in the alloy remains uncertain.⁶ Although Ni-Cu alloys are unlikely to be used as structural materials in future fusion reactors, the response of such a system to irradiation merits more detailed study in the view of the considerable importance attached to the understanding and control of void formation.

In the present study, we have investigated the effects of 14 MeV Ni ion irradiation on two Ni-Cu alloys, Ni-10Cu (atomic %) and Ni-50Cu, using the cross-section technique⁷ which allows the entire ion damage region to be viewed at once by transmission electron microscopy (TEM). The effect of oxygen in the alloys was also investigated since oxygen has been shown to promote void formation in Cu and Ni both theoretically and experimentally.⁸⁻¹²

Experimental Procedure

The two Ni-Cu alloys, Ni-10Cu and Ni-50Cu, were fabricated from Marz grade Ni (99.995 wt.% pure) and Cu (99.999 wt.% pure) in an arc melter. Before melting, the chamber of the melter was evacuated to 2.6 Pa then flushed with Ar gas five times. A Ti getter was used to absorb active gases during melting. The ingots were inverted and remelted for several times after the original melting, and then treated in flowing Ar at 1000°C for 24 hours to assure homogeneity. Analyses performed by Los Alamos National Laboratory, using a vacuum fusion technique, indicated the oxygen content in the alloys is about 100 appm. The ingots of the alloys were cold rolled with intermittent annealing in flowing Ar at 800°C to 0.5 mm thick foils. The foil samples were then mechanically polished with 0.3 μm alumina abrasive.

Three samples of each alloy were irradiated with 14 MeV Ni³⁺ ions at the University of Wisconsin Heavy-Ion Irradiation Facility with a flux of 3×10^{16} Ni³⁺/m²s at a homologous temperature of $T/T_m = 0.45$, i.e. 485°C for Ni-10Cu and 425°C for Ni-50Cu. The fluences were chosen according to a Monte Carlo calculation¹³ to give peak damage levels of 20, 40 and 100 dpa. The samples with peak damage levels of 20 and 40 dpa were preinjected with 5 MeV oxygen at room temperature to an average concentration of 100 appm in the region 1.3-2.0 μm below the surface. The distribution of the injected 5 MeV oxygen and 14 MeV Ni ions as well as the displacement damage caused by 14 MeV Ni ions in the Ni-10Cu alloy calculated by a Monte Carlo code, TAMIX, is shown in Fig. 1. One Ni sample irradiated earlier¹⁴ with 14 MeV Ni ions to a peak damage of 15 dpa at 500°C, which is also 0.45 T_m , is also included in this study for comparison. The Ni sample had a bulk oxygen concentration of 75 appm and contains an additional 75 appm injected oxygen in the first ~ 1.2 μm region. After irradiation, all of the samples were prepared in cross-section for TEM observation and analyzed under a JEOL TEMSCAN-200CX electron microscope.

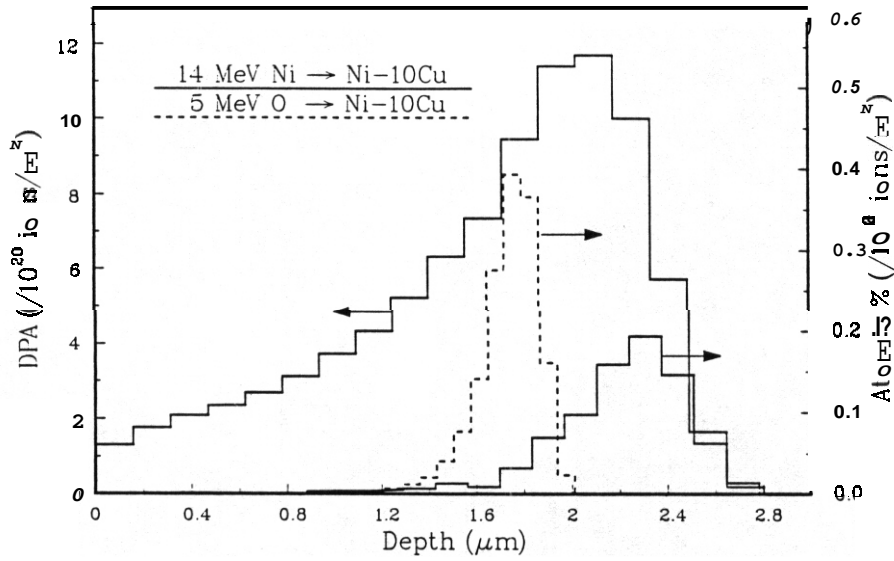


Fig. 1. Displacement damage (by 14 MeV N ions only) and injected ion distribution (14 MeV N ions and 5 MeV oxygen ions) in Ni-10Cu calculated by using the TAMIX code.¹³

Table 1. Defect characteristics of 14 MeV N ion irradiated Ni-Cu alloys.

No.	Material	Oxygen pre-injected (appm)	dpa (peak)	dpa (1.5 μm)	Voids*		Dislocation loops* density (m ⁻³)
					density (m ⁻³)	average size (nm)	
(1)	Ni	75	15	7	~1x10 ²¹	29	—
(2)	Ni-10Cu	100	20	10	~7x10 ¹⁹	12	~1x10 ²¹
(3)	Ni-10Cu	100	40	20	~1x10 ²⁰	5(90%) 53(10%)	~1x10 ²¹
(4)	Ni-10Cu	none	100	50	not observed	nt 1.5 μm	~1x10 ²¹
					~9x10 ¹⁹	14 (peak damage region)	
(5)	Ni-50Cu	100	20	10	not observed		~7x10 ²¹
(6)	Ni-50Cu	100	40	20	not observed		~5x10 ²¹
(7)	Ni-50Cu	none	100	50	not observed		~5x10 ²¹

* Counted in a region of 1.5(1.3~1.8) μm from the irradiated surface unless noted.

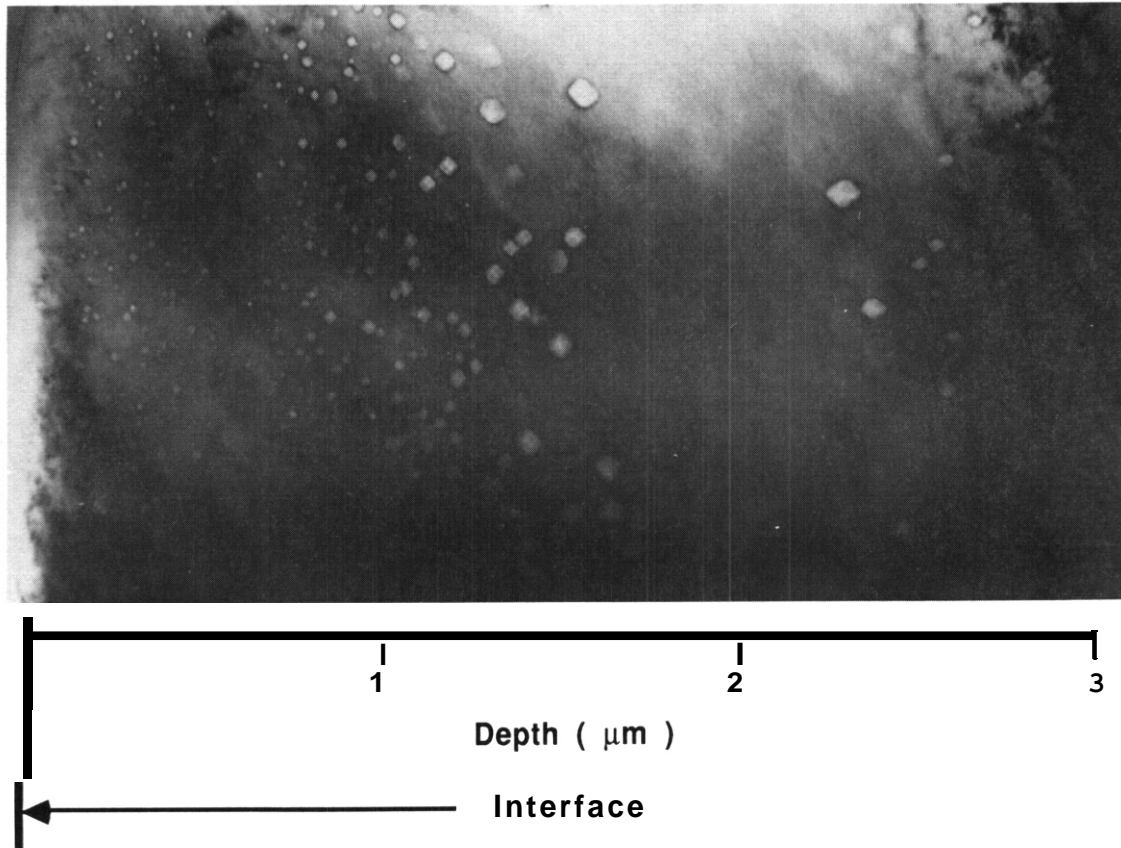


Fig. 2. TEM cross-section micrograph showing void distribution in 14 MeV Ni ion irradiated Ni. Damage level at peak damage depth ($\sim 2 \mu\text{m}$) is 15 dpa. 75 appn oxygen was preinjected in the first $1.3 \mu\text{m}$ region. Since about $0.3 \mu\text{m}$ was removed from the original surface, the actual distance from the original irradiated surface should be the distance from the interface plus $0.3 \mu\text{m}$.

Results

The defect characteristics of all seven irradiated samples are summarized in Table 1. The void density, void size and dislocation loop density listed are all counted from the region of about $1.5 (1.3-1.8) \mu\text{m}$ from the irradiated surface unless noted in the table. This is the region where the injected oxygen ions come to rest and the effect of the injected Ni interstitials¹⁴ would not be significant. It should be noticed that the dpa level at that depth is about half the peak level.

Voids are the only significant kind of the defect cluster observed in the irradiated Ni sample. The void distribution in the entire irradiated region in the sample is shown in Fig. 2. The high density of smaller voids in the first $\sim 1.2 \mu\text{m}$ region, which contains 75 appn injected oxygen, gives strong evidence of the effect of oxygen in promoting void formation.

Figures 3 and 4 show the entire damage region of the two Ni-Cu alloys irradiated to the peak damage level of 20 dpa. In the Ni-10Cu sample, most defect clusters are dislocation loops (Fig. 3(a)), although some voids are also observed by tilting the loops out of contrast (Fig. 3(b)). The voids are mainly located in the oxygen implanted region, with only a few voids with an average diameter of 8 nm occurring at the peak damage depth. In the Ni-50Cu sample, dislocation loops with much smaller size and much higher density are observed (Fig. 4(a)), and no voids were found when the loops were tilted out of contrast (Fig. 4(b)). The latter fact remains true even after a careful examination for all the three irradiated Ni-50Cu samples at a magnification of 100,000x.

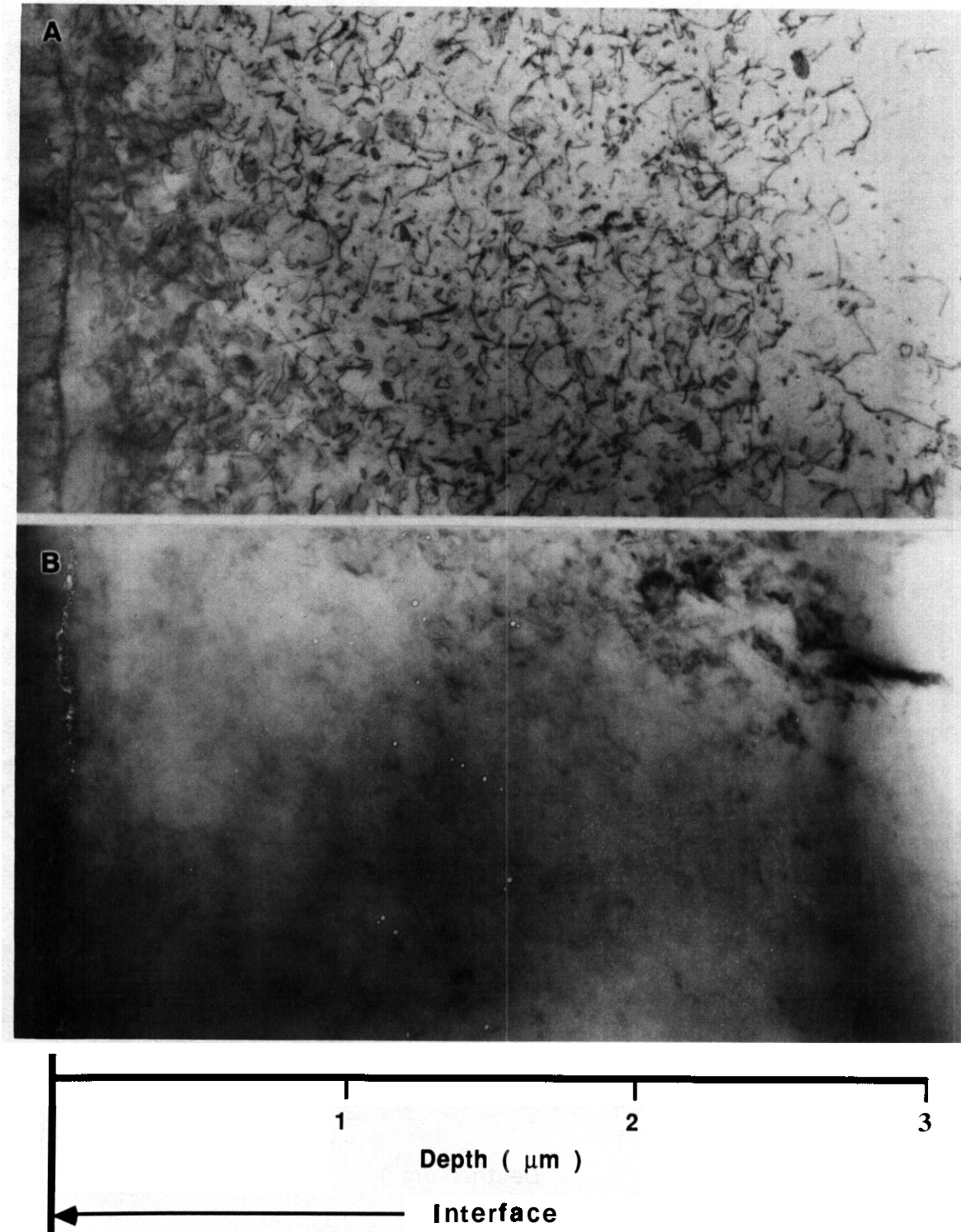


Fig. 3. TEM cross-section micrographs showing (a) dislocation loop and (b) void distribution in a Ni-10Cu sample with 100 appn oxygen preinjection and a peak damage level of 20 dpa. (b) was taken by tilting the dislocation loops out of contrast.

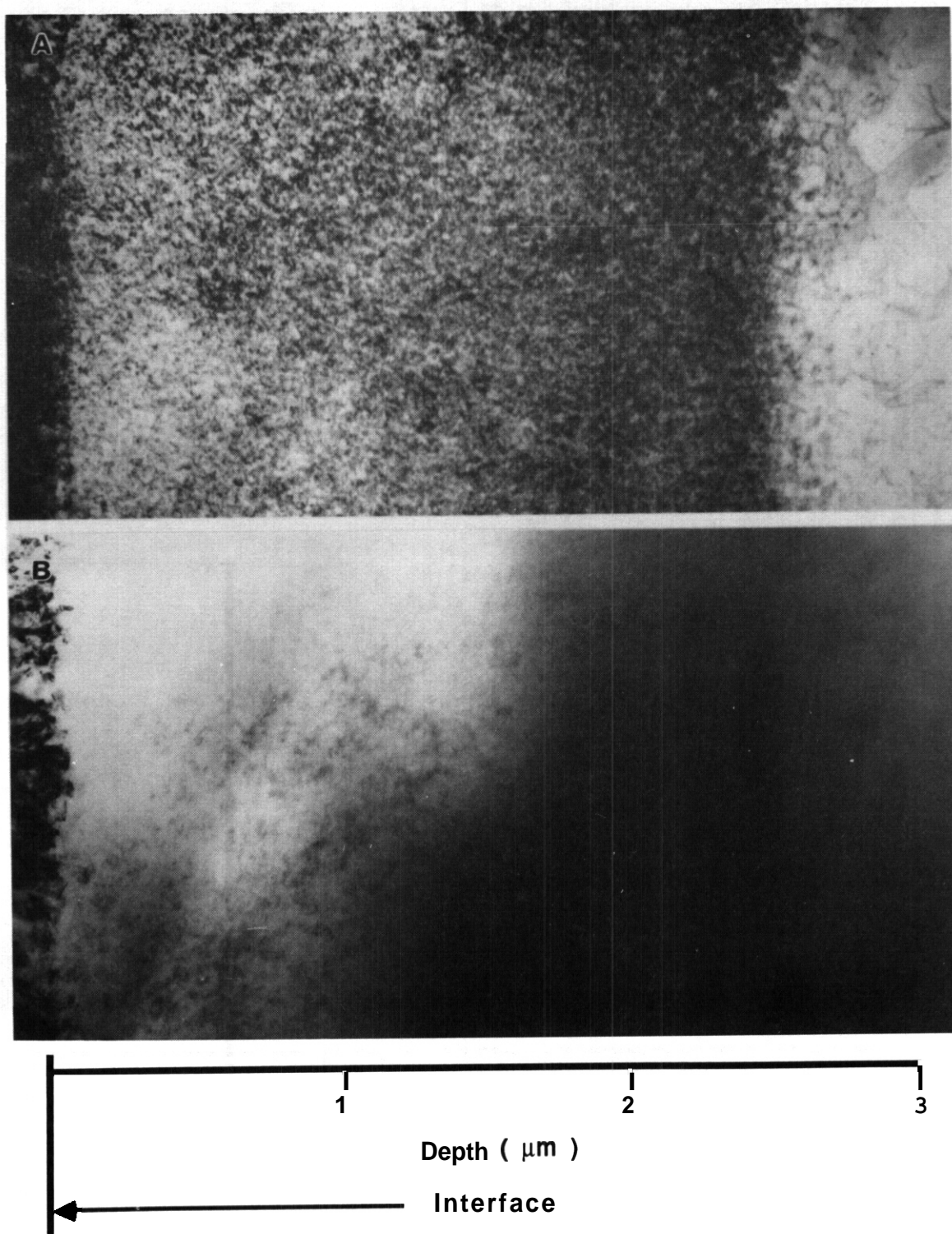


Fig. 4. TEM cross-section micrographs obtained from a Ni-50Cu sample with 100 appm oxygen preinjection and a peak damage level of 20 dpa. (a) dislocation loop distribution; (b) loops tilted out of contrast showing absence of voids.

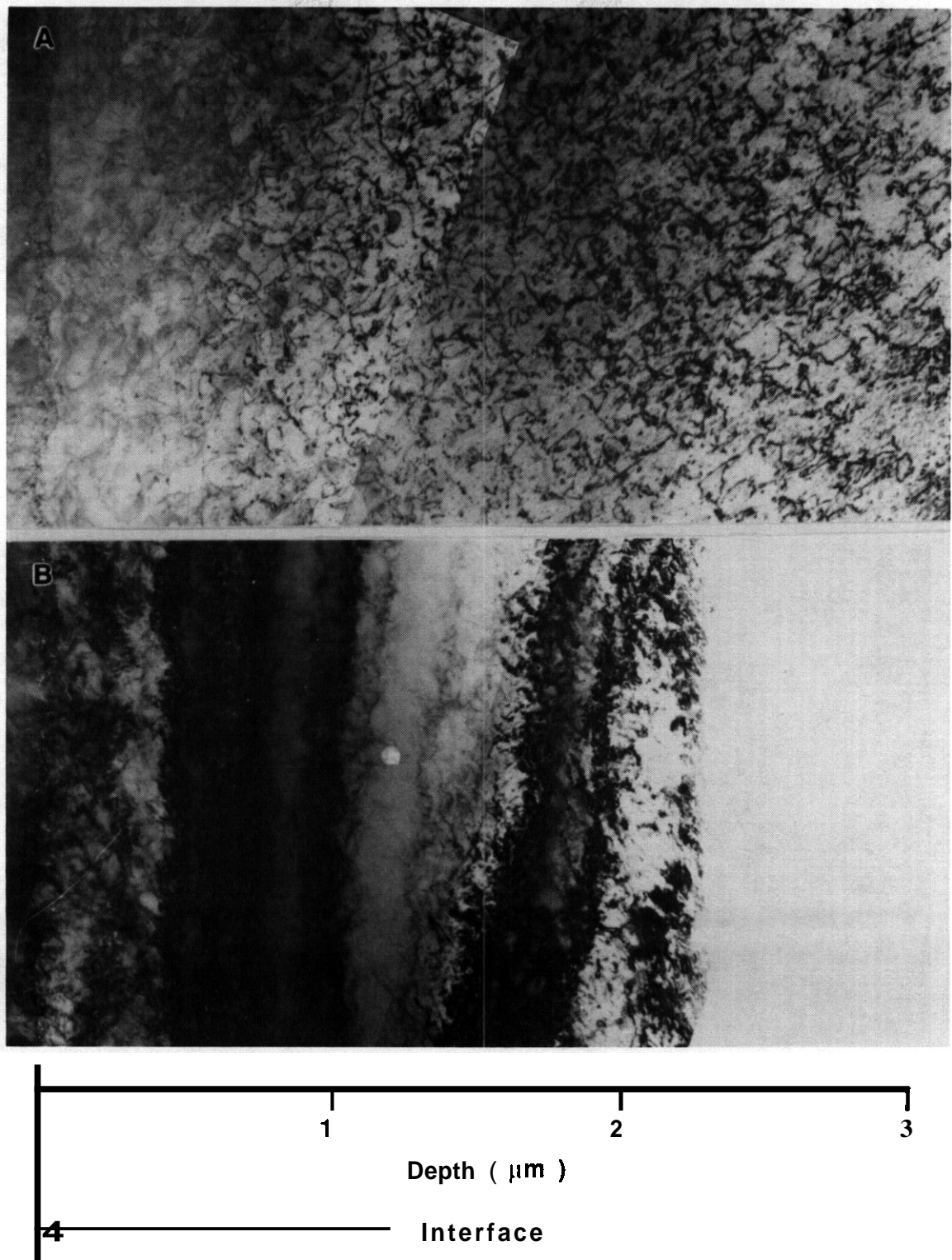


Fig. 5. TEM cross-section micrographs showing (a) dislocation loop and (b) void distribution in a Ni-IOCu sample with 100 appm oxygen preinjection and a peak damage level of 40 dpa. (b) was taken by tilting the dislocation loops out of contrast.

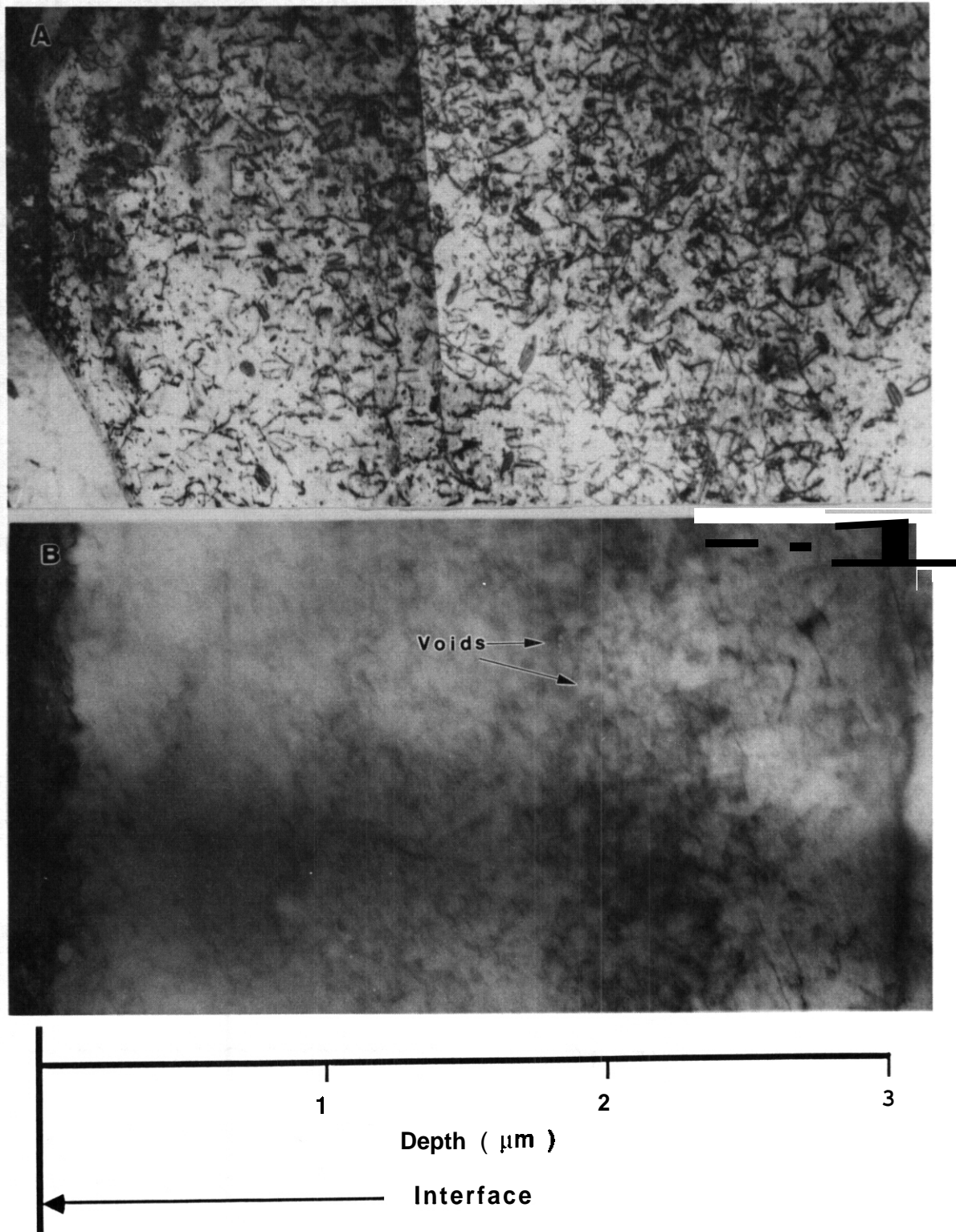


Fig. 6. TEM cross-section micrographs showing (a) dislocation loop and (b) void distribution in a Ni-10Cu sample with a peak damage level of 100 dpa. (b) was taken by tilting the dislocation loops out of contrast.

The distribution of defect clusters in the other two **Ni-10Cu** samples are shown in Figs. 5 and 6. In the **Ni-10Cu** sample irradiated to 40 dpa at the peak, the void distribution was rather heterogeneous. Some larger voids (~ 50 nm in diameter) surrounded by many smaller voids (~ 5 nm in diameter) were observed in the oxygen implanted region, which implies the agglomeration of smaller voids during the continuous irradiation. Only one larger void (125 nm in diameter) was found at the damage peak region. Some voids were also found in the **Ni-10Cu** sample irradiated to 100 dpa at the peak without oxygen preinjection, but they were all located in the peak damage depth (~ 2.2 μm from the original surface). In Fig. 7 the void structures in the irradiated Ni and **Ni-10Cu** samples are compared.

It should be mentioned that a surface layer of ~ 0.3 μm thick was removed from all samples during the process of cross-section specimen preparation to assure good bonding at the interface, so the actual depth from the irradiated surface is 0.3 μm more than the depth from the interface indicated in the cross-section micrographs (Figs. 2-6). Also, the injected oxygen region in the Ni sample is 0.8-1.0 μm closer to the interface than in the alloys because of a special operation after the preinjection.¹¹

Figure 8 gives a comparison of the dislocation structures in the **Ni-10Cu** alloy with various irradiation conditions, and Fig. 9 gives that comparison for the **Ni-50Cu** alloys. In Fig. 10, the distributions of the dislocation loop size in the six Ni-Cu alloy samples are compared. Through the above comparisons, it is quite clear that higher doses generally produce larger loops in both alloys, and that the loop density in the **Ni-50Cu** alloy is 5-7 times higher than that in the **Ni-10Cu** alloy under the same irradiation conditions, while the loop size is much larger in the latter.

Discussion

The results of this study support the previous findings that voids are increasingly more difficult to form with increasing Cu content for the Ni-based Ni-Cu alloys.^{2,5} The reason for the void suppression is of great interest. Brimhall and Kissinger¹ have excluded the possibility of void suppression in Ni-Cu alloys due to a stacking fault energy effect or differences in diffusion between the alloys and the pure metals, because the stacking fault energy is 50% higher in **Ni-50Cu** as compared to pure Cu,¹⁵ and the effective migration energies of point defects in the alloys change monotonically and continuously between values for pure Ni and pure Cu.¹⁶ However, their explanation based on trapping of point defects by single solute atoms in the solution due to the size difference breaks down for the **Ni-50Cu** alloy. Mazey and Menzinger² proposed the possibility of trapping of vacancies and interstitials at the boundaries of fine-scaled clusters having compositions different from the matrix. Their explanation seems more plausible, but they did not give further elaboration of the mechanism.

More information has now become available in the literature which seems to be strong evidence suggesting that clustering takes place in Ni-Cu alloys during irradiation.¹⁷⁻¹⁹ The clustering in the alloy is also justified by thermodynamic considerations. A miscibility gap has been included in the Cu-Ni phase diagram²⁰ based on a calculation of Elford et al.,²¹ although it could not be experimentally verified because of the low temperature.²² In addition, the positive value of the heat of mixing of the Ni-Cu system²³ suggests a repulsive interaction between unlike atoms based on a regular solution assumption.²⁴ In this case, it means $E_{\text{Cu-Ni}} > 1/2(E_{\text{Cu-Cu}} + E_{\text{Ni-Ni}})$ where E is the near-neighbor bonding energy. Thus, there is a tendency for clustering of like atoms to occur in Ni-Cu alloys, as long as the entropy change due to clustering is not important, which is true at lower temperatures.²⁴ The boundaries of clusters might trap vacancies and gas atoms to reduce the high bonding energy as well as the strain energy. The traps can operate as nucleation sites for vacancy clusters. When a high density of this kind of trap is present, the arrival rate of irradiation produced vacancies at each site will be low, so the small vacancy clusters will not grow fast enough to reach the critical size of the void embryo before collapsing into dislocation loops. This inhibits void formation in the alloys. Although the vacancy/interstitial nature of the dislocation loops observed in this study has not been determined by experimental work at this stage, it seems to be reasonable to assume that at least most of the smaller loops are vacancy type by comparing with the work of Leister.³ On the other hand, it is apparent that **Ni-50Cu** will contain more fine-scaled clusters of like atoms than **Ni-10Cu**; in other words, more vacancy traps are present in **Ni-50Cu** than in **Ni-10Cu**. Therefore, the higher resistance to void formation and the higher density of dislocation loops observed in the **Ni-50Cu** can be explained.

CONCLUSIONS

The resistance to void formation of concentrated Ni-Cu alloys is confirmed by 14 MeV Ni ion irradiation on **Ni-10Cu** and **Ni-50Cu**.

Irradiation produced smaller dislocation loops with higher density in **Ni-50Cu** than in **Ni-10Cu**.

100 appm oxygen preinjection promotes void formation in **Ni-10Cu**, but showed little effect on **Ni-50Cu**.

Void resistance in the alloys appears to be the result of trapping of vacancies and gas atoms by fine-scaled clusters.

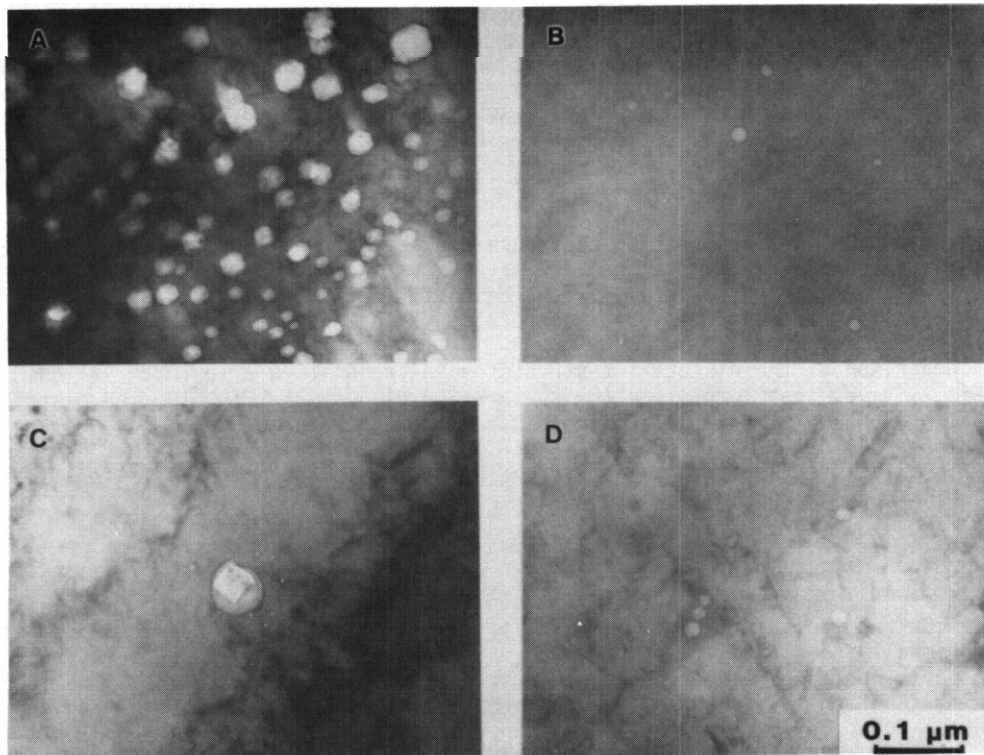


Fig. 7. Comparison of the void structures in irradiated Ni and Ni-10Cu samples. (a) Ni, 7 dpa, ~ 75 appn oxygen; (b) Ni-10Cu, 10 dpa, 100 appn oxygen; (c) Ni-10Cu, 20 dpa, 100 appn oxygen; (d) Ni-10Cu, 100 dpa. (a), (b) and (c) were taken at a 1.3-1.8 μm depth from samples (1), (2) and (3) respectively, and (d) was taken from the peak damage region of sample (4).

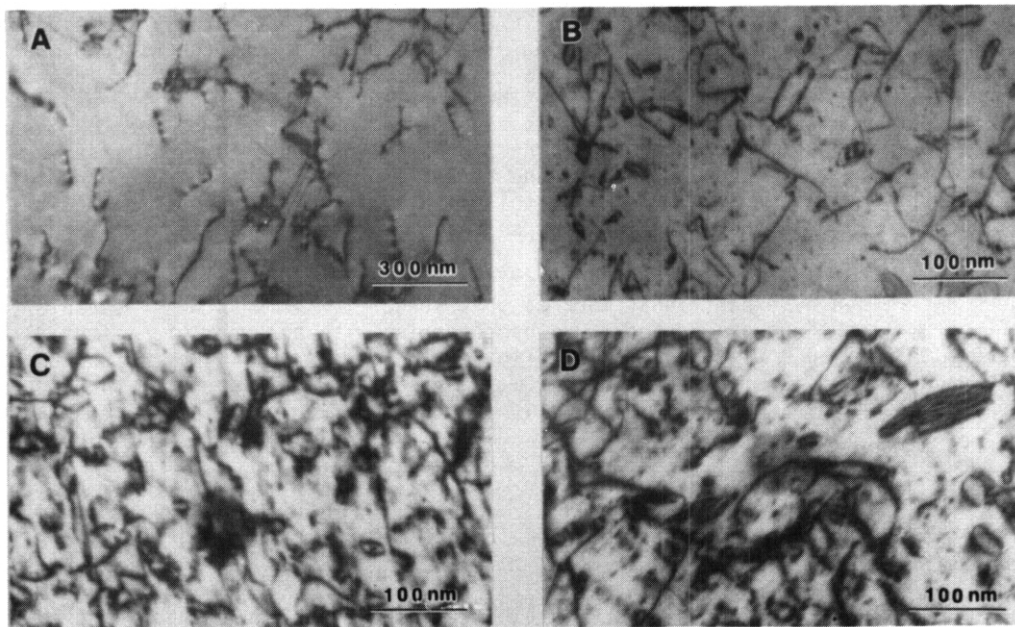


Fig. 8. Comparison of the dislocation structures in Ni-10Cu with various irradiation conditions. (a) Control region; (b) 10 dpa, 100 appn oxygen; (c) 20 dpa, 100 appn oxygen; (d) 50 dpa. (b), (c) and (d) were taken at a 1.3-1.8 μm depth from samples (2), (3) and (4) respectively.

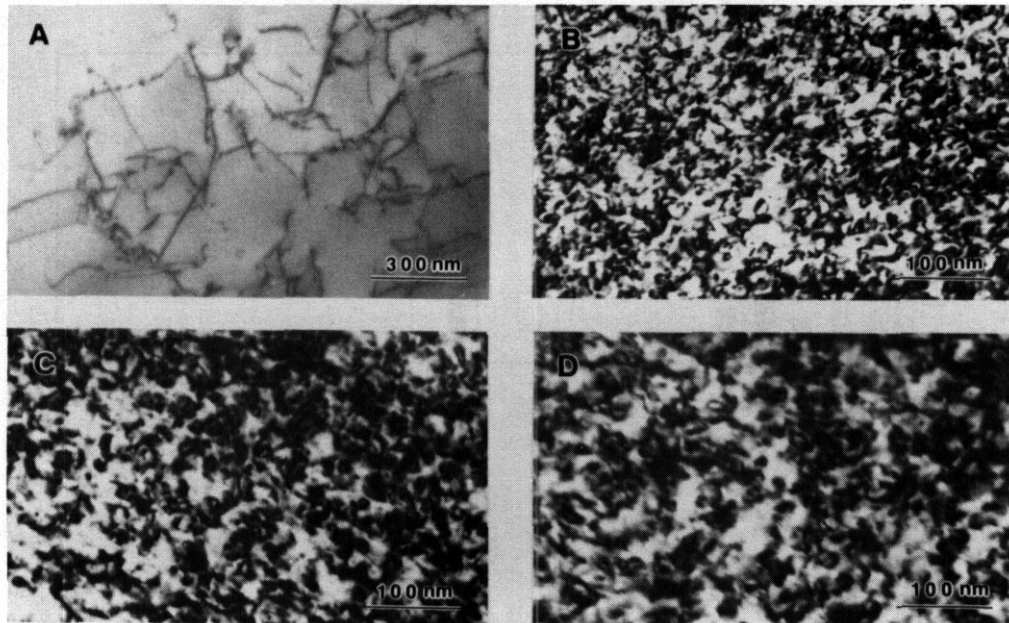


Fig. 9 Comparison of the dislocation structures in Ni-50Cu with various irradiation conditions. (a) Control region; (b) 10 dpa, 100 appn oxygen; (c) 20 dpa, 100 appn oxygen; (d) 50 dpa. (b), (c) and (d) were taken at a 1.3-1.8 μm depth from samples (5), (6) and (7) respectively.

ACKNOWLEDGMENT

The authors wish to thank S. Han for calculating the dpa and injected ion distributions using his new computer code, and Pat Caliva for preparing the manuscript. This research is supported by the U.S. Department of Energy, Office of Fusion Energy.

REFERENCES

1. J.L. Brimhall and H.E. Kissinger. *Rad. Eff.* 15 (1972) 259.
2. D.J. Mazey and F. Menringer, *J. Nucl. Mater.* 48 (1973) 15.
3. K-H. Leister, PhD Thesis, *Kernforschungszentrum Karlsruhe* (May, 1983).
4. P. Dauben and R.P. Wahi, Progress Report No. 2 (1981-1984), Reports of Hahn-Meitner-Institute.
5. P. Barlow, PhD Thesis, University of Sussex (April, 1977).
6. S.J. Zinkle, R.A. Oodd, G.L. Kulcinski and K. Farrell. *J. Nucl. Mater.* 117 (1983) 213.
7. S.J. Zinkle and R.L. Sindelar. *Nucl. Instr. and Meth.* B16 (1986) 154.
8. L.D. Glowinski and C. Fiche, *J. Nucl. Mater.* 61 (1976) 29.
9. S.J. Zinkle, W.G. Wolfer, G.L. Kulcinski and L.E. Seitzman, *Phil. Mag.* A55 (1987) 127.
10. S.J. Zinkle, PhD Thesis, University of Wisconsin (May, 1985).
11. L.E. Seitzman, L.M. Wang, G.L. Kulcinski and R.A. Dodd. *J. Nucl. Mater.* 141-143 (1986) 738.

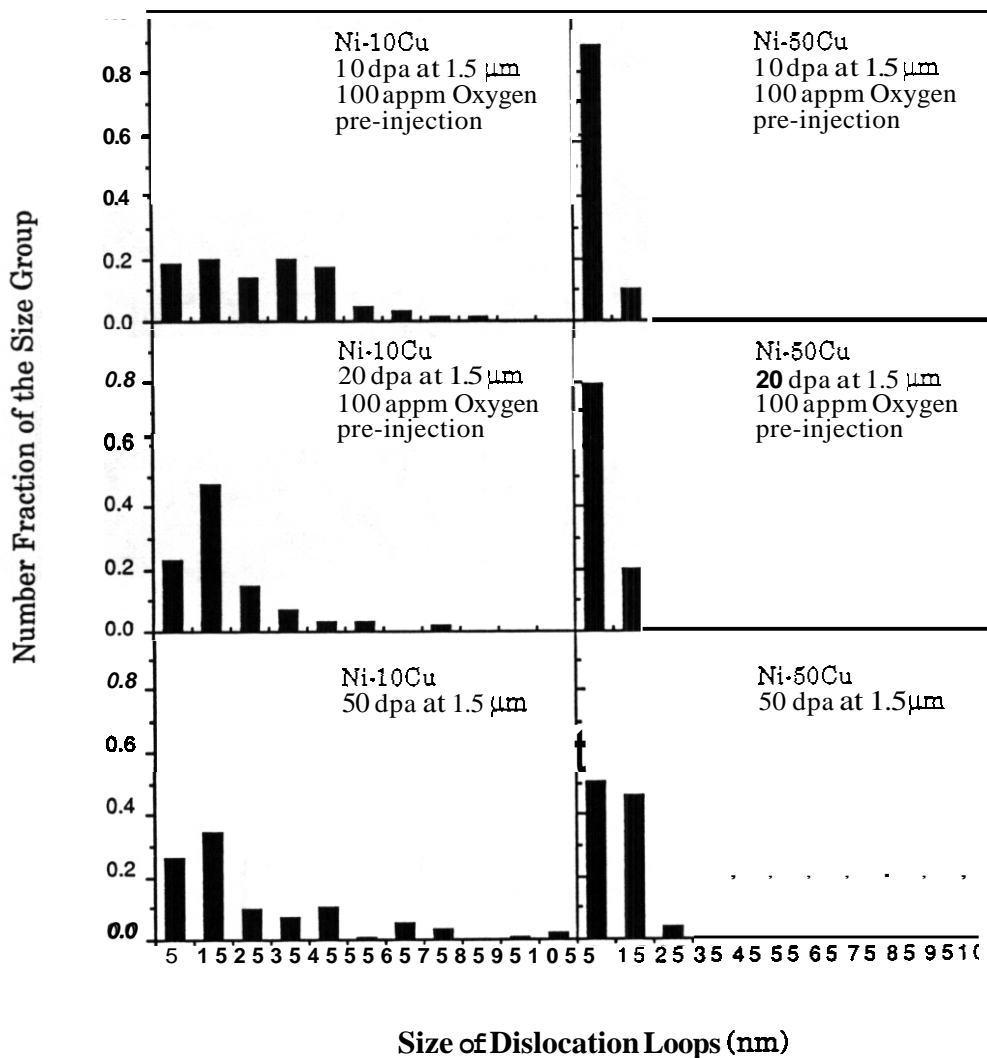


Fig. 10. Comparison of the dislocation loop size distribution in the six irradiated Ni-Cu alloy samples (data were obtained by counting the region at a depth of 1.3-1.8 μm from the irradiated surface).

12. L.M. Wang, RA Odd and GL Kulcinski, *J. Nucl. Mater.* 141-143 (1986) 713.
13. S. Han and GL Kulcinski. Fusion Reactor Materials, 00E/ER-0313/2, 105.
14. S. Badger, Jr., DL Plumton, S.J. Zinkle, RL Sindelar. GL Kulcinski. RA Dodd and WG Wolfer, *ASTM STP 870* (1985) p. 297.
15. P.C.J. Gallagher, *Met. Trans.* 1 (1970) 2429.
16. F. Lihl and H. Wildhack, *Z. Metallk.* 62 (1971) 143.
17. W. Schule, P. Spindler and E. Lang, *Z. Metallk.* 66 (1975) 50.
18. R. Poerschke and H. Wollenberger, *Thin Solid Films* 25 (1975) 50.

19. R. Poerschke and H. Wollenberger, *Rad. Effects* 49 (1980) 225.
20. *Metals Handbook*, 8th edition (American Society for Metals), Vol. 8 (1973) p. 294.
21. L. Elford, F. Muller and O. Kubaschewski, *Ber Bunsenges Physik Chem.* 73 (1969) 601.
22. M. Hansen, *Constitution of Binary Alloys*, 2nd edition (McGraw-Hill, 1958).
23. *INCRA Monograph on the Metallurgy of Copper*, I. Selected Thermodynamic Values and Phase Diagrams for Copper and Some of Its Binary Alloys (International Copper Research Association, Inc., 1971, Eds. R. Hultgren and P.O. Desai) p. 126.
24. R.A. Swalin, *Thermodynamics of Solids* (John Wiley & Sons, New York, 1972) p. 146.

ON MECHANISMS CONTROLLING SWELLING IN FERRITIC AND MARTENSITIC ALLOYS

.G. R. Odette (University of California, Santa Barbara)

OBJECTIVE

The objective of this work is to evaluate the mechanisms which control swelling in ferritic-martensitic alloys for fusion structures.

SUMMARY

Ferritic and martensitic (FM) alloys are highly resistant to swelling in fast reactor irradiations. High self-diffusion rates and low dislocation bias may contribute to their intrinsic swelling resistance. Other factors, such as high sink densities, are metallurgically mediated and may not be permanent. Further, low helium generation rates in FM alloys may contribute significantly to the low swelling observed in fast reactor irradiations. Helium generation is environmentally mediated, and higher levels are generated in mixed spectrum reactors increase void swelling. FM alloys also lose their advantageous helium-to-dpa ratio in fusion spectra. The implications of these factors are evaluated with critical bubble-to-void and rate theory swelling models using austenitic alloys as a reference.

PROGRESS AND STATUS

Introduction

Ferritic and martensitic (FM) *steels* are highly resistant to void swelling in fast reactor environments up to exposure levels of over **100** displacements per atom (dpa) [1-12]. Hence, they are leading candidates for fusion reactor structural applications. Therefore, it is important to understand the factors which control swelling in these alloys in order to predict their behavior in fusion environments and to guide alloy development efforts. This paper will assess some potential mechanisms controlling swelling in FM alloys and evaluate their implications to dimensional stability in fusion environments at high damage levels.

Summary of Microstructural Trends in Ferritic Alloys

The data base on microstructural evolution in FM alloys is much more limited than that for austenitic alloys. Fast [1-12] and mixed spectrum [13-16] reactor and charged particle [17-23] irradiations suggest the following trends.

- 1) Void formation and swelling occurs in both simple model and more complex commercial FM alloys over a relatively narrow temperature range around 400 to 425°C for neutron irradiations [1-16], and **about 100 to 150°C** higher for charged particle irradiations [19]. However, swelling levels are generally low and swelling rates are less than about 0.1%/dpa.
- 2) Void formation and swelling is promoted by higher levels of helium generated in mixed spectrum reactors or by implantation in charged particle experiments [13-19]. In particular, higher helium levels enhance the larger component of a bimodal cavity distributions composed of small bubbles and larger voids, This implies has driven cavity growth and a critical bubble-to-void conversion process governing incubation exposures prior to rapid void swelling [18,24-28].
- 3) Commercial martensitic alloys typically have high dislocation densities and a fine scale subgrain microstructure [20], associated with lath boundaries. The subgrain structure may coarsen under irradiation [16], but at lower irradiation temperatures high dislocation densities are often maintained [2,5]. In contrast, simple model ferritic alloys are coarser grained and have low dislocation densities [6,12].
- 4) A variety of phase instabilities and evolutions occur under irradiation, including radiation induced or modified precipitates [6,7,16].

Irradiation microstructures in FM alloys are dependent on the combination of metallurgical and environmental variables. However, the qualitative characteristics of the microstructures of commercial alloys under irradiation are often similar to those observed for cold-worked austenitic alloys [28]. Therefore, it is useful to use austenitics as a base for assessing the swelling behavior of FM alloys.

Hypotheses on the Swelling Resistant of Martensitic Alloys

A number of hypotheses have been proposed to explain the swelling resistance of FM steels. While they are plausible and may contribute to such behavior, none appear to completely explain experimental observations.

- 1) Sniegowski and Wolfer [29] have proposed that dislocation bias for interstitials is lower in body centered cubic crystal structures due to a smaller relaxation volume of point defects. This intrinsic factor would effect both the incubation and steady state swelling regimes.
- 2) Bullough and coworkers [30,31] have proposed that swelling is reduced by the $\alpha\langle 100 \rangle$ dislocation loops found in FM alloys. They postulate that partitioning of excess interstitials to the $\alpha\langle 100 \rangle$ loops and vacancies to the $\alpha/2\langle 111 \rangle$ loops or dislocation line segments reduces net vacancy fluxes available for swelling. However, if less biased or neutral sinks, such as cavities, are present, excess vacancies would be partitioned to them. Further, swelling is also low in temperature regimes where loops are not observed.
- 3) Little [12] and others [32] have proposed that defect solute trapping leads to increased recombination. However, high vacancy mobility and high sink densities in commercial alloys at low temperatures, and detrapping at higher temperatures, suggest that recombination effects might be small.
- 4) Maziasz [16] and Ayrault [17] suggest that the fine scale subgrain structure retards swelling. A high density of point defect sinks would increase incubation exposures and decrease void swelling rates. This is supported by observations of retarded void formation in small subgrains and near subgrain boundaries [16]. Further, subgrain sinks would also trap helium, increasing incubation exposures. However, subgrain structures are not always stable under irradiation and relatively low swelling is also observed in coarse grained ferritic alloys [6,12]. Further, subgrain structures in commercial martensitic alloys are qualitatively similar to those found in cold-worked austenitic alloys. Hence, the subgrain structure offers only a partial explanation of the swelling resistance of FM alloys.
- 5) Horton and Mansur [18] have suggested that the void dominated microstructures they found in a charged particle study of a model Fe-Cr alloy could be responsible for low swelling rates. This results from an imbalance between biased dislocation and neutral void sinks. In contrast, a dislocation dominated microstructure may be more characteristic of commercial alloys, when long incubation times result in low void densities. Further, detailed swelling rate calculations must consider the effect of other sinks, such as bubbles, cascade clusters and boundaries.
- 6) Gelles has observed systematic swelling variations with solute additions to model Fe-10Cr alloys which he correlates with misfit strain [33]. The dislocation structures and void shape are also effected . Based on these observations he proposes that solute segregation is an important factor in the swelling of FM alloys. While he does not specify a mechanism, segregated solutes could effect surface energies or dislocation bias.

There are two other mechanisms which would appear to have a direct impact. First, the intrinsic self-diffusion rates are higher in ferritic compared to austenitic alloys. This would be expected to retard swelling by extending the incubation exposure, particularly at higher temperatures. Figure 1 plots diffusion coefficients for high purity α and γ -iron taken from the literature [34,35]. Extrapolated diffusion rates in pure Fe-Cr-Ni austenitic alloys [36] are slightly lower than for the γ -iron. The self-diffusion coefficient in α -iron is about 30 times higher than in γ -iron in the temperature regime for swelling (far below the Curie temperature). Generally, impurity and alloying effects would be expected to increase diffusion coefficients in both systems [37]. Unfortunately, there is insufficient data to quantify these effects. However, it is reasonable to assume that the higher intrinsic diffusivity in FM alloys relative to austenitic alloys would be maintained.

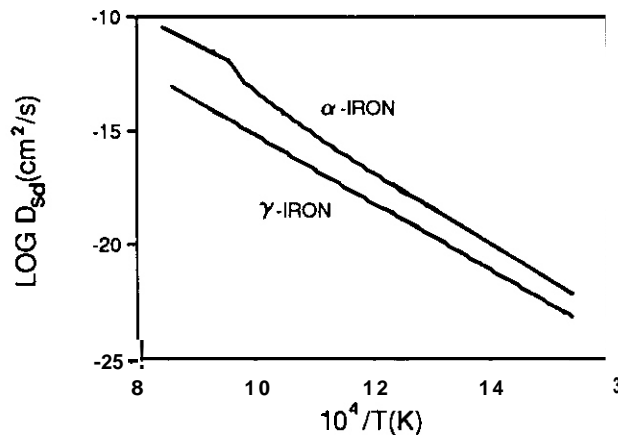


Figure 1. Self-diffusion coefficients as a function of temperature for α and γ -iron

Second, helium generation rates in FM alloys are about a factor of 3 to 4 times lower than in 316 series austenitic steels in fast reactor irradiations. Austenitic alloys generate more helium in fast reactors because they contain nickel which has a much higher average cross section for threshold n, α reactions than iron or chromium. Hence, FM alloys would be expected to have high incubation exposures in fast reactor irradiations. This advantage is not maintained in fusion environments. Precise values of the He/dpa ratios depend on the neutron spectrum and alloy composition. Using cross sections compiled from the literature [38] typical $\text{He}(\text{appm})/\text{dpa}$ are: austenitic/fast reactor - 0.48; FM/fast reactor - 0.12; FM/fusion first wall - 12.

Model Calculations

Some of the concepts outlined in the previous section were evaluated using a simplified version of a semi-empirical model of swelling developed for cold-worked austenitic alloys that has been described in detail elsewhere [24-28]. This model is based on rate theory and a critical helium bubble-to-void size criteria. In applying the model to ferritic alloys the following assumptions were made.

- 1) The dislocation is unaltered
- 2) The cascade cluster sink strength is unaltered. Vacancy loops and stacking fault tetrahedra typically found in FCC alloys have not been observed in iron. There is, however, limited evidence of the formation of compact vacancy clusters (*i.e.* microvoids or depleted zones) from positron annihilation [39], small angle neutron scattering [40,41], and electron microscopy [41] studies. Kuramoto et al. [23] have suggested that such clusters lead to the reduction of swelling at low temperatures.
- 3) Precipitate sinks and precipitate-assisted void formation are neglected (this restricts the calculations to temperatures below about 500°C). The subgrain size (λ) is varied parametrically. Because of the high sink strengths, recombination is neglected.
- 4) The void and bubble density in FM alloys are reduced by a factor of 2 relative to austenitics in fast-reactor environments environments to reflect differences in the He/dpa ratio based on a square root scaling law. The void and bubble density is increased in ferritics by a factor of 10 in the fusion versus fast-reactor environments, again to reflect the differences in the He/dpa ratio.
- 5) The surface energy and cascade efficiency parameters are unaltered. The self-diffusion coefficient (D_{sd}) and dislocation bias (B) are treated parametrically.
- 6) The terminal void density is taken as 0.1 the bubble density consistent with behavior in austenitics [25]. Helium is permanently partitioned into the subgrain structure and bubbles, including the fraction (0.1) which convert to voids. Bubbles are often observed on dislocation lines which act as helium traps and collectors, transporting helium to attached bubbles by rapid pipe diffusion [42]. Hence, the fraction of helium which is partitioned into void precursor bubbles by dislocations is

$$F_{He} = \frac{0.1L_d}{(L_d + L_{sgb})} \quad (1)$$

where the L_d and L_{sgb} are the dislocation and subgrain boundary sink strengths.

- 7) First-order interactive models are used to calculate sink strengths [43].

The model parameters were taken from reference [25] except for the modifications shown in Table 1. The swelling rate \dot{S} is

$$\dot{S} = D_{sd}L_v \left\{ \phi - \exp \left[\left(\frac{2\gamma}{r_v} - P_g \right) \frac{\Omega}{kT} \right] \right\} \quad (2)$$

where L_v , r_v and N_v are the void sink strength, radius and number density, P_g the internal gas pressure, γ the surface tension, and Ω the atomic volume. The effective vacancy supersaturation is

$$\phi = \frac{(D_v C_v - D_i C_i)}{D_{sd}} \quad (3)$$

where $D_{v,i} C_{v,i}$ are the vacancy/interstitial diffusivity concentration products which are calculated from the steady-state

Table 1
Model Parameters

<u>Term</u>	<u>Expression</u>
bubble sink strength (cm^{-2})	$3.9 \times 10^{15} \exp(-0.0153T)$
cascade cluster sink strength (cm^{-2})	$7 \times 10^9 \exp(30150/T)$
void density (cm^{-3})	$\sqrt{\frac{He/dpa}{0.48}} 1.33 \times 10^{22} \exp(-0.023T)$
subgrain dimension (cm)	$= C_1 10^{-4}$ (C_1 variable parameter)
self-diffusion coefficient (cm^2/s)	$C_2 0.8 \exp(-33745/T)$
dislocation bias	variable parameter
helium-to-displacements per atom (appm)	FM fast reactor = 0.12 FM fusion = 12 Austenitic fast reactor = 0.48

defect balance equations [39]. The critical number of helium atoms per cavity m^* is

$$m^* = \frac{4\pi}{3} \left(\frac{\gamma}{kT} \right)^3 \left(\frac{\Omega}{\ell n \phi} \right)^2 f_1(\phi) \quad (4)$$

where the function corrects f_1 for non-ideal gas behavior [27]. The incubation exposure is defined as

$$\tau_i = \frac{\Omega N_v}{\left\{ m^* \left(\frac{He}{dpa} \right) F_{He} \right\}} \quad (5)$$

Swelling as a function of time can be computed by integration of Equation 2.

Figure 2a shows the calculated incubation exposures for austenitics in fast reactors for temperatures from 375 to 475°C (648 to 748K). **These** exposures range from about 30 to 60 dpa, reasonably **consistent** with **the experimental trend band** [44]. Figure 2b shows calculated swelling rates at 400 and 475°C as a function of swelling compared to a recent compilation of data for a similar temperature range [44]. Agreement is quite good, although the calculated rates are somewhat higher than observed at low swelling, particularly at low temperatures. This may be due partly to the assumption that the full terminal void population is formed immediately at the incubation time.

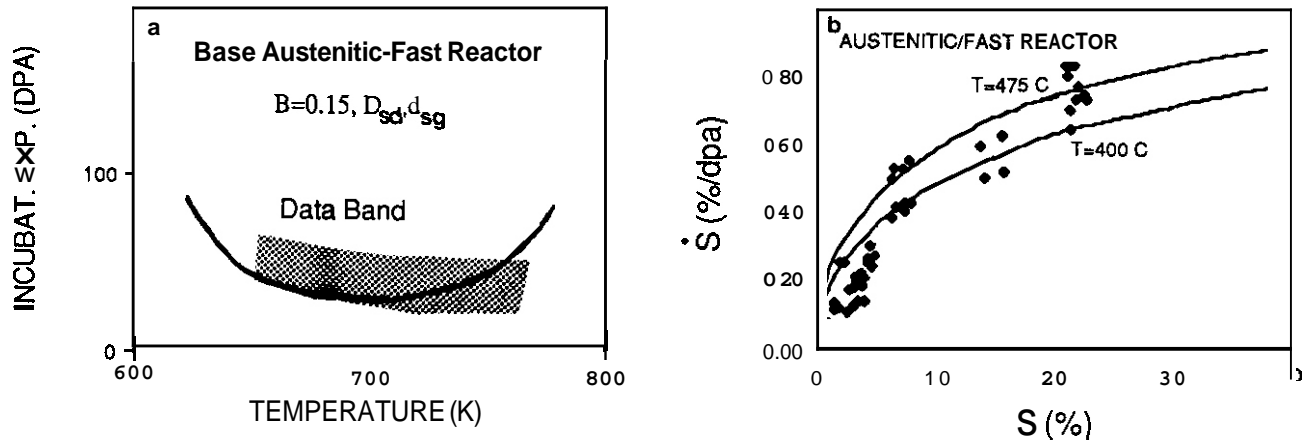


Figure 2. Comparison of base austenitic model predictions to data trends for a) incubation exposures versus temperature; and b) swelling rate versus swelling.

These results demonstrate the semi-quantitative consistency between the model predictions in the transition and steady state swelling regimes. Both the data and calculations show that, as in FM alloys, swelling rates are low in austenitics at low levels of swelling.

Figure 3 shows calculated fast-reactor incubation exposures for FM alloys for various choices of the self-diffusion coefficient (D_{sd}), the subgrain dimension (d_{sg}) and bias (B). The results are presented as ratios to the austenitic base case, since this normalization is expected to be less sensitive to model assumptions and parameters than absolute values. The effect of the lower helium generation rate in FM alloys is partially compensated by the lower cavity density, with a net effect of doubling the incubation exposures, Incubation exposures are further increased by modest increases in D_{sd} (by factors of 2 and 5, Figure 3a), and decreases in B (by factors of 3 and 5, Figure 3b) and d_{sg} (by a factor of 2 to 4, Figure 3c). Combinations of decreased B and increased D_{sd} have a strong effect (Figure 3d). Clearly, the high incubation exposures found in FM alloys can be readily explained by these factors taken singly or in combination. Further, these results suggest that swelling occurs in FM alloys irradiated in fast-reactors only at temperatures below 450°C, consistent with observation.

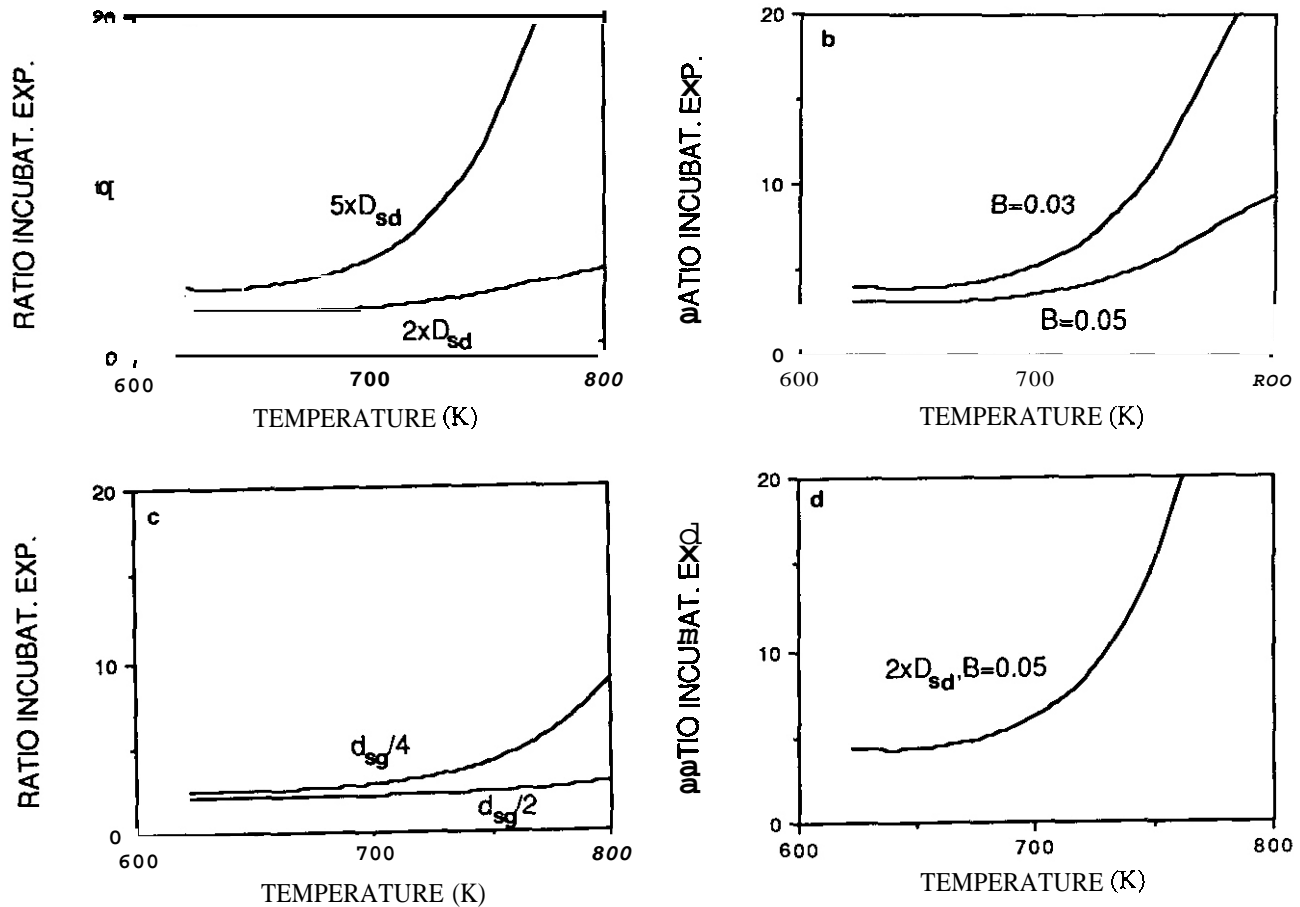


Figure 3. Calculated ratios of incubation exposures versus temperature: FM(fast reactor)/base austenitic(fast reactor).

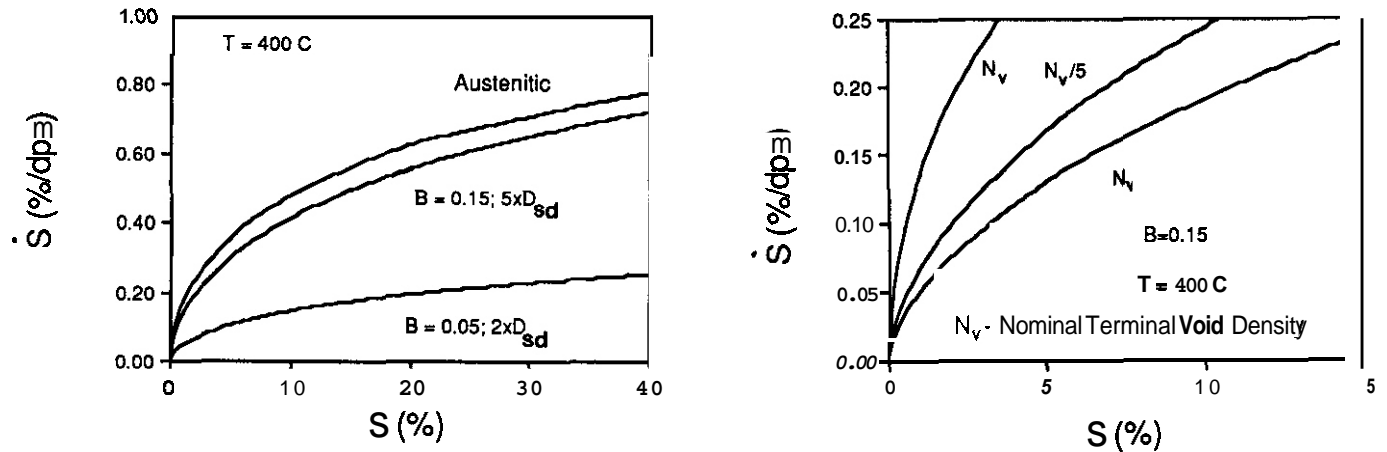


Figure 4. Calculated swelling rates versus swelling in FM alloys irradiated in fast reactors a) as a function of bias; and b) void density. The austenitic base case is also shown for comparison.

Figure 4a shows calculated fast-reactor swelling rates versus swelling at 400°C for FM alloys for two combinations of modified D_{sd} and B , which are consistent with observed incubation exposures. The effect of D_{sd} is small and the swelling rates scale approximately as B . Even with low biases ($B = 0.05$) the eventual swelling rates are significant and rates are similar to austenitic alloys if normal biases ($B = 0.15$) are used. The assumption that all the voids are formed at precisely the incubation exposure is obviously an oversimplification. Hence, a possible reason for low swelling rates is that, due to high incubation exposures, voids have not reached terminal densities in the fast reactor experiments. The effect of lower void densities is illustrated in Figure 4b where swelling rates for nominal biases are computed for decreases by factors of 5 and 10. Even with this high bias, at the reduced void densities swelling rates are less than 0.15%/dpa below 5% swelling.

Figure 5 shows the ratio of calculated incubation exposures for FM alloys in fusion environments to austenitics in fast-reactor environments for the same choices of D_{sd} , B and d_{sg} as in Figure 3. In general, the ratios are small at lower temperatures. For parameters consistent with behavior observed in fast and mixed spectrum reactors, modest incubation exposures in fusion environments up to about 450°C are predicted. The higher void density expected in fusion environments also slightly increases the swelling rate as shown in Figure 6. The effect is even stronger if full terminal void densities occur in fusion spectra but are lower in fast reactor environments (*i.e.*, Figure 6 versus Figure 4b). Even for low biases ($B = 0.05$) eventual swelling rates of about 0.2%/dpa are predicted. Coupled with relatively low incubation exposures, this suggests that there may be significant swelling in FM alloys in fusion environments at exposures below lifetime goals.

The model calculations provide guidance on qualitative trends, rather than reliable quantitative predictions. The model is consistent with the narrow temperature range of swelling (around 400°C), high incubation exposures and low swelling rates in fast reactor irradiations. Low swelling rates may be due to both small swelling levels and void densities below terminal values as well as low bias. The high incubation exposures in FM alloys due to high diffusion rates and low bias are largely intrinsic. In contrast, microstructural factors may not be persistent, and environmentally mediated mechanisms, may result in lower incubation exposures and higher swelling rates in FM alloys in fusion environments.

Modeling is useful for planning and analyzing experiments. Clearly, the results indicate the value of comprehensive microstructural and microchemical characterization. Joint experiments between Oak Ridge National Laboratory (ORNL), Battelle Pacific Northwest Laboratories (BPNL) and the University of California at Santa Barbara (UCSB) using isotopically tailored alloys are planned for the High Flux Isotope Reactor (HFIR). These experiments will permit controlled single variable studies of the effect of He/dpa ratio over a range characteristic of fusion to fast reactor environments [45].

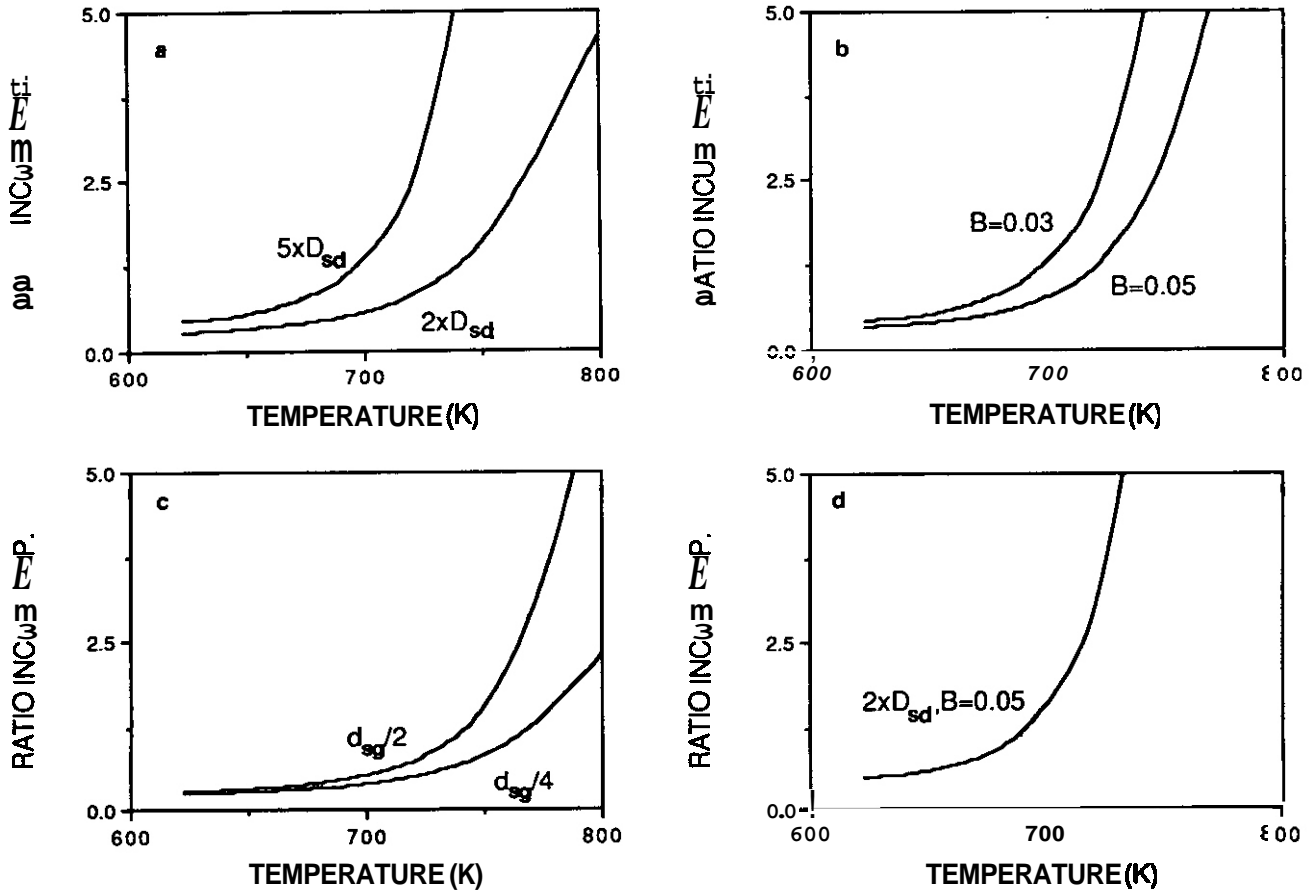


Figure 5. Calculated ratios of incubation exposures as a function of temperature: FM(fusion)/base austenitic(fast reactor).

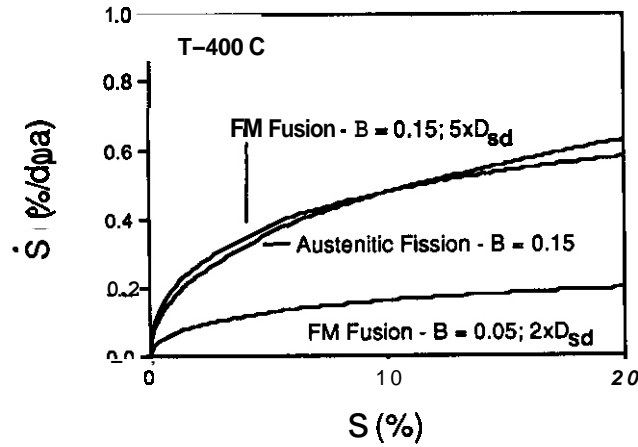


Figure 6. Calculated swelling rates versus swelling for FM alloys as a function of bias. The austenitic base case is also shown for comparison.

Summary and Conclusions

A critical bubble/rate theory swelling model is used to assess some possible mechanisms controlling the swelling resistance of FM alloys. The analysis suggested that low bias, high self-diffusion and low helium generation rates, possibly coupled with high subgrain boundary sink strengths, explains most swelling trends observed to date. While the self-diffusion and bias effects are largely intrinsic, the He/dpa ratio is environmentally mediated. Hence, incubation exposures may be much lower and swelling rates higher in fusion relative to fast-reactor environments. These results point to the importance of additional experimental efforts on FM alloys to comprehensively characterize microstructural evolution, to conduct single variable He/dpa experiments and to evaluate ways of improving radiation stability in high helium environments.

FUTURE WORK

The models will be further developed as more experimental information becomes available. Particular emphasis will be placed on the analysis of the results of isotopic tailoring experiments which are planned.

REFERENCES

1. D. S. Gelles, *J. Nucl. Mater.* **122 & 123** (1984) 207.
2. D. S. Gelles, *J. Nucl. Mater.* **103 & 104** (1981) 975.
3. D. S. Gelles, "ADIP Semiannual Progress Report," *DOE/ER-0045/16* (1986) 123.
4. D. S. Gelles and R. J. Puigh, "Effects of Radiation on Materials," *ASTM-STP-870*, ASTM (1985) 19
5. D. S. Gelles and L. E. Thomas, "Proceedings of Topical Conference on Ferritic Alloys of Use in Nuclear Energy Technologies," AIME (1984) 559.
6. D. S. Gelles and R. L. Meinecke, "ADIP Semiannual Progress Report," *DOE/ER-0045/11* (1984) 103
7. E. A. Little and D. A. Stow, *Met. Sci.* (1980) 89.
8. L. L. Horton and J. Bentley, *ibid* 5, 569
9. F. A. Smidt, Jr., P. R. Malonberg, J. A. Sprague, and J. E. Westmoreland, "Irradiation Effects on the Microstructure and Properties of Metals," *ASTM-STP-711*, ASTM (1976) 227.
10. E. A. Little, *Phys. Stat. Sol. (a)* **87** (1985) 441.
11. L. P. Stoter and E. A. Little, "Proc. Advances in Physical Metallurgy and Applications of Steels," TMS-London, (1981) 369.
12. E. A. Little and D. Stow, *J. Nucl. Mater.* **87** (1979) 25.
13. J. M. Vitek and R. L. Klueh, *ibid* 5, 551.
14. D. S. Gelles, "ADIP Semiannual Progress Report," *DOE/ER-0045/14* (1985) 129.
15. J. M. Vitek and R. L. Klueh, *J. Nucl. Mater.* **122 & 123** (1984) 254.
16. P. J. Maziasz, R. L. Klueh and J. M. Vitek, *J. Nucl. Mater.* **141-143** (1986) 929.
17. G. Ayrault, *J. Nucl. Mater.* **114** (1983) 34.
18. L. L. Horton and L. K. Mansur, *ibid* 4, 344.
19. K. Farrell and E. Lee, *ibid* 4, 383.
20. D. J. Mazey, et al., "Radiation Damage Simulation Studies of Selected Austenitic and Ferritic/Martensitic Alloys for Fusion Reactor Structural Applications," *AERE Harwell Report 11710* (1985).
21. W. G. Johnston, T. Lauritzen, J. W. Rosolowski and A. M. Turkalo, "Effects of Radiation on Materials," *ASTM-STP-782*, ASTM (1982) 809.
22. L. Horton, J. Bentley and K. Farrell, *J. Nucl. Mater.* **108 & 109** (1982) 222.
23. E. Kuramoto, N. Yoshida, N. Tsukuda, K. Kirajima, N. Packan, M. Lewis and L. Mansur, *J. Nucl. Mater.* **103 & 104** (1981) 1091.
24. G. R. Odette, P. J. Maziasz and J. A. Spitznagel, *J. Nucl. Mater.* **103 & 104** (1981) 999.
25. R. E. Stoller and G. R. Odette, "Effects of Irradiation on Materials," *ASTM-STP-782*, ASTM (1982) 275.

26. G. R. Odette and R. E. Stoller, *J. Nucl. Mater.* **122 & 123** (1984) 514.
27. R. E. Stoller and G. R. Odette, *J. Nucl. Mater.* **131** (1985) 118.
28. R. E. Stoller and G. R. Odette, "Effects of Irradiation on Materials," *ASTM-STP-955*, ASTM (1987) 871.
29. J. J. Sniegowski and W. G. Wolfer, *ibid* **5**, 579.
30. R. Bullough, H. M. Wood, and E. A. Little, "Effects of Irradiation on Materials," *ASTM-STP-725*, ASTM (1981) 593.
31. E. A. Little, R. Bullough, and H. M. Wood, *Proc. Royal Soc.* **A372** (1980) 565.
32. M. R. Hayns and T. M. Williams, *J. Nucl. Mater.* **74** (1978) 151.
33. D. S. Gelles, "Fusion Reactor Materials Semiannual Progress Report," *DOE/ER-0313/1* (1987) 145.
34. G. Hettech, H. Mehrer and K. Maier, *Scripta Met* **11** (1977) 795.
35. A. M. Brown and M. F. Ashby, *Acta Met* **28** (1980) 1035.
36. S. J. Rothman, L. J. Nowicki and G. F. Murch, *J. Phys. F Met. Phys.* **10** (1980) 383.
37. A. LeClaire, *J. Nucl. Mater.* **69-70** (1978) 70.
38. G. R. Odette, "DAFS Quarterly Progress Report," *DOE/ER-0046/21* (1985) 19.
39. P. Havtojärvi, L. Pöllänen, A. Vehanen, and J. Yli-Kauppila, *J. Nucl. Mat.* **114** (1983) 250.
40. F. Frisius, R. Kampmann, P. Beaven and R. Wagner, *Proc. BNES Conf. Dimensional Stability and Mechanical Behavior of Irradiated Metals and Alloys*, **1** (1983) 171.
41. G. R. Odette and G. E. Lucas, "Radiation Embrittlement of Pressure Vessel Steels: An International Review," *ASTM STP 909*, ASTM (1986) 206.
42. J. Spitznagel, S. Wood, N. Doyle, W. Choyke, J. McGruer, J. Townsend, R. Irwin, *J. Nucl. Mater.* **103-104** (1981) 1463.
43. L. K. Mansur, *Nucl. Tech.* **40** (1978) 5.
44. R. E. Stoller, *ibid* **33**, 171.
45. G. R. Odette, *J. Nucl. Mater.* **141-143** (1986) 1011.

PHASE INSTABILITIES IN IRRADIATED SIMPLE Fe-Cr-Mn LOW ACTIVATION ALLOYS - J. M. McCarthy and F. A. Garner (Pacific Northwest Laboratory)

OBJECTIVE

The object of this effort is to determine the nature of the driving forces which tend to destabilize alloys in the Fe-Cr-Mn system during neutron irradiation.

SUMMARY

The Fe-Mn system has been proposed to replace the Fe-Ni system in fusion applications to achieve greatly reduced levels of long-term radioactivity. The in-reactor stability of simple Fe-Mn and Fe-Cr-Mn alloys is therefore being studied to determine the nature of the driving forces tending to destabilize these alloys. The results of this study indicate that simple Fe-Cr-Mn alloys exhibit during irradiation a greater level of potential phase instabilities than do comparable Fe-Cr-Ni alloys, requiring careful attention in the development of solute-stabilized alloys.

PROGRESS AND STATUS

Introduction

The Fe-Cr-Mn alloy system has been proposed to replace the Fe-Cr-Ni system in the construction of components for fusion energy devices. (1-5) This change is directed toward the attainment of greatly reduced levels of long-term radioactivity. Manganese is a much more reactive element than nickel, however, and there is concern that reduced activation will be achieved at the expense of phase stability, corrosion resistance, and other properties. There is also some indication that the radiation-induced phase evolution is more complex in simple Fe-Cr-Mn alloys than it is in simple Fe-Cr-Ni alloys. (6)

In the absence of radiation there are other indications of phase instability in Fe-Cr-Mn alloys. The simple Fe-Mn system differs from the Fe-Ni system primarily in its propensity toward mechanical twinning and the associated transformation to hcp epsilon martensite and bcc alpha martensite. (7-9) Aging of cold-worked Fe-Cr-Mn steels has also been shown to yield the potentially detrimental sigma phase. (10) Additional complexities have been observed in solute-modified steels. (11-12)

In this study, the evolution of simple binary Fe-Mn and ternary Fe-Cr-Mn alloys during irradiation was examined to determine the nature of the driving forces tending to destabilize these alloys and to guide the development of solute-stabilized alloys.

Experimental Details

Three binary Fe-Mn and six ternary Fe-Cr-Mn alloys with low levels of solute elements (see Table 1) were prepared as microscopy disks 3000 μm in diameter by 250 μm thick and annealed at 1030°C for 0.5 hr and then air cooled. They were irradiated in static sodium in the Fast Flux Test Facility (FFTF) at 3×10^{-6} dpa sec^{-1} using the Material Open Test Assembly (MOTA) which controls the temperature to within $\pm 5^\circ\text{C}$. The displacement levels range from 9 dpa at 420°C to 14 dpa at 520 and 600°C. The neutron spectrum in this experiment produces 5 dpa for each 1.0×10^{22} n cm^{-2} ($E > 0.1$ MeV).

The bulk swelling level was measured first using an immersion density technique for both these 9-14 dpa specimens and those at higher displacement levels. These data are reported elsewhere. (1,2,6) The microstructure of these low dose specimens was then examined using conventional methods of specimen preparation, microscopy and energy dispersive X-ray microanalysis techniques.

TABLE 1

Composition of Simple Fe-Cr-Mn Alloys (Wt%)

	Fe	Cr	Mn		Fe	Cr	Mn
R66	80	5	15	R71	75	0	25
R67	70	15	15	R72	70	0	30
R68	80	0	20	R73	65	5	30
R69	70	10	20	R74	60	10	30
R70	65	15	20	R75	65	0	35

Results

The approach taken in this short paper is to summarize in general terms the trends observed in radiation-induced phase evolution, rather than present a detailed report of each of the 21 combinations of alloy and irradiation condition. Illustration of the various phase instabilities observed will be made only for representative examples.

As can be seen in the phase diagram shown in Fig. 1, at the lower manganese levels investigated, Fe-Mn alloys fall into the two phase regime, particularly at lower temperatures. (13) At lower chromium levels in Fe-Cr-Mn alloys similar two-phase behavior is also expected. Indeed, the greatest level of phase instability was observed in the Fe-5Cr-15Mn alloy irradiated at 420°C to 9 dpa, with a combination of two-phase decomposition and radiation-induced segregation within each of the two phases.

Fig. 2a shows that the alloy prior to irradiation consisted only of austenite grains containing many stacking faults; but after irradiation a massive decomposition had occurred, yielding large lenticular grains of alpha martensite interspersed with grains of retained austenite (Fig. 2b). Both the lenticular shape of the alpha grains and the near-identical bulk compositions of the alpha and austenite grains suggested that the decomposition proceeded via a martensitic transformation. (At higher irradiation temperatures diffusion-driven processes can alter the local composition substantially and the decomposition proceeds in a different manner, as will be discussed shortly.

Within the alpha grains are a moderate density (10^{15} cm^{-3} , 30-50 nm in diameter) of manganese-rich precipitates of the bcc Chi phase with polygonal cross-sections. The shape and distribution of these suggest that they form as a result of relatively short-range radiation-induced segregation, possibly on dislocation loops formed during irradiation. These precipitates were vigorously and selectively attacked during foil preparation by electropolishing, giving an initially erroneous impression that substantial void swelling had occurred in the alpha phase. Fig. 2b and 2c show those precipitates which have not yet been attacked and the regular void-like cavities that remain after attack. Also seen in Fig. 2b and 2c is a relatively high density of hcp epsilon martensite plates formed in the austenite grains. These exist at higher densities than that of the stacking faults shown in Fig. 2a. Small voids were also observed at sizes less than 30 nm and it appeared that they might have some sort of shells on their surface, but this could not be confirmed. No voids were observed in the alpha grains.

The tendency toward massive decomposition at 420°C disappeared as either the chromium or manganese level was increased. The tendency, at all temperatures studied, toward formation of epsilon martensite also decreased as the manganese level was increased. However, further increases in manganese above 20% yielded a progressive radiation-induced densification, reaching an astounding 2.2% increase in density at Fe-35Mn. The choice of astounding as a descriptor reflects the finding that microscopy examination did not yield any type of precipitation or large-scale gradients in composition. The microstructure consisted only of a high density of small dislocation loops and a higher density of small (<8 nm) voids. Such microstructures are typical of Fe-Ni and Fe-Cr-Ni alloys irradiated at this temperature and displacement level. (6)

The bcc Chi phase was again observed as a chromium-rich precipitate, increasing as the chromium level was increased. It was observed both within austenite grains and at larger sizes and higher densities at boundaries separating austenite grains, as shown in Fig. 3.

Some of the most striking phase instabilities observed concerned the formation of ferrite phases. Whereas the decomposition of Fe-5Cr-15Mn at 420°C appeared to proceed without significant levels of long-range radiation-induced segregation, the increased levels of diffusion at 520 and 600°C caused long stick-like ferrite precipitates to form. These were essentially pure iron (>95%) and the matrix was correspondingly enriched in manganese.

During electropolishing the manganese-rich matrix was preferentially attacked. Figs. 4a and 4b show that the ferrite precipitates protrude from the edge and surfaces of the thinned foil. The voids are also encased in iron-rich shells which likewise resist electropolishing.

The tendency for ferrite to form first decreases quickly with increasing manganese levels, but reasserts itself again at 35% manganese. Although Fig. 1 shows that this alloy is securely in the austenite regime at 520°C, stick-like precipitates of essentially pure iron and iron-rich void shells were again observed in Fe-35Mn, particularly at the foil edge where they protrude from the preferentially-etched manganese-rich austenite matrix. (6)

As shown in Fig. 5, in Fe-35Mn at 600°C and 14 dpa, large voids dominate the microstructure and have iron-rich shells which resist electropolishing. No ferrite precipitates were observed at 600°C. At both 520 and 600°C the void shells were not sufficiently enriched in iron to undergo a transformation to ferrite. Fig. 6 shows that the segregation of iron at void surfaces in Fe-10Cr-30Mn is balanced by a comparable decrease in manganese. Chromium does not appear to participate in the segregation process.

The segregation of iron in this alloy system during irradiation appears to be a rather general phenomenon. Note in Fig. 5 that grain boundaries also resist electropolishing, reflecting their enrichment in iron. A similar tendency toward preservation of grain boundaries at foil edges was observed in

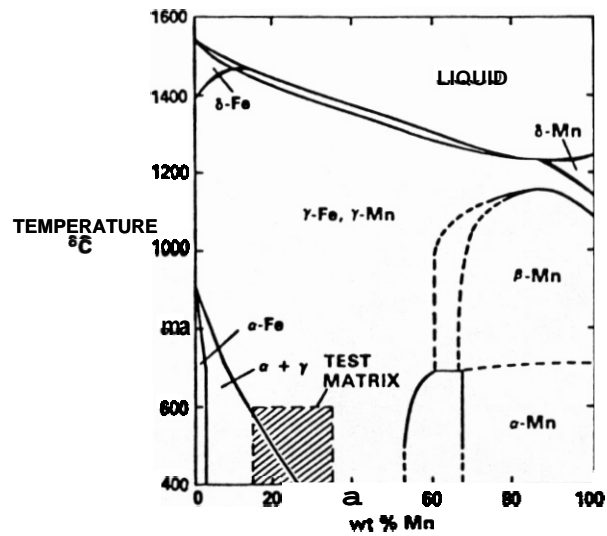


Fig 1: Phase diagram for the Fe-Mn system (13) showing range of manganese levels and irradiation temperatures explored in this experiment.

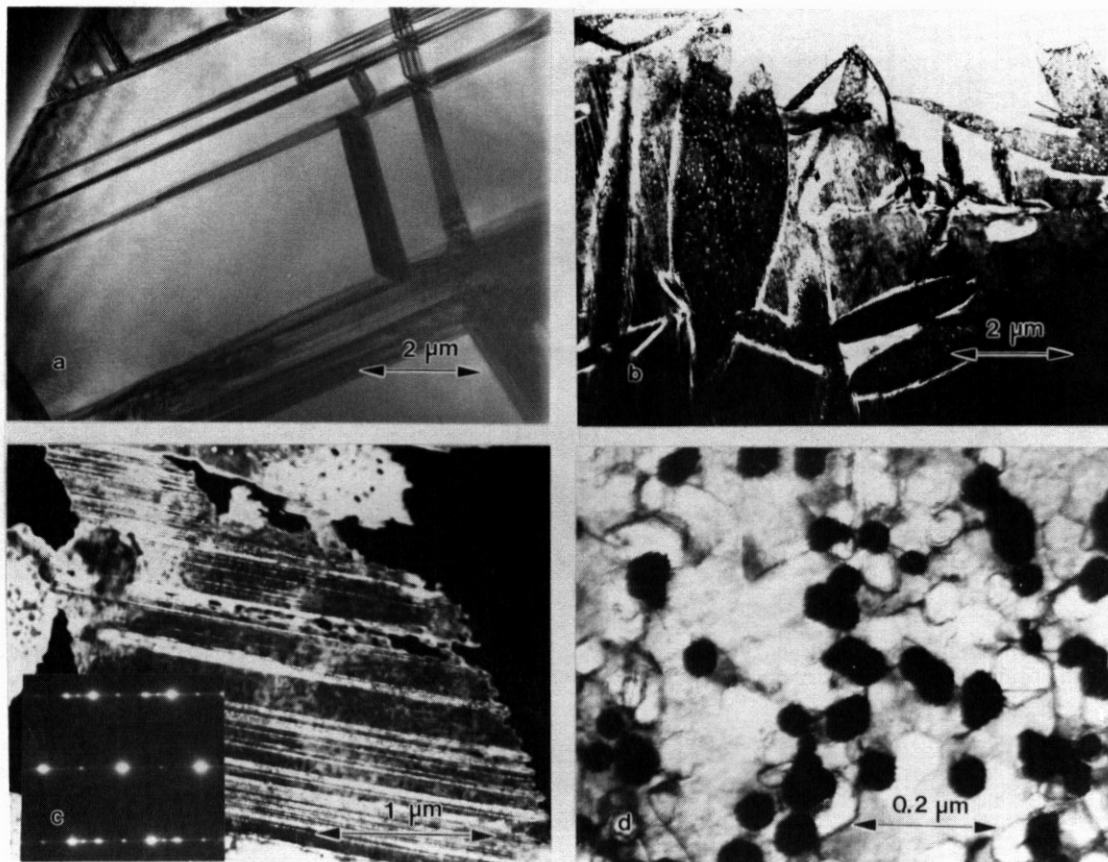


Fig 2: Fe-5Cr-15Mn in the (a) annealed and unirradiated condition. (b) after 9 dpa at 420°C, (c) dark field micrograph showing epsilon plates in the austenite. (d) Chi phase precipitates in the process of being attacked.

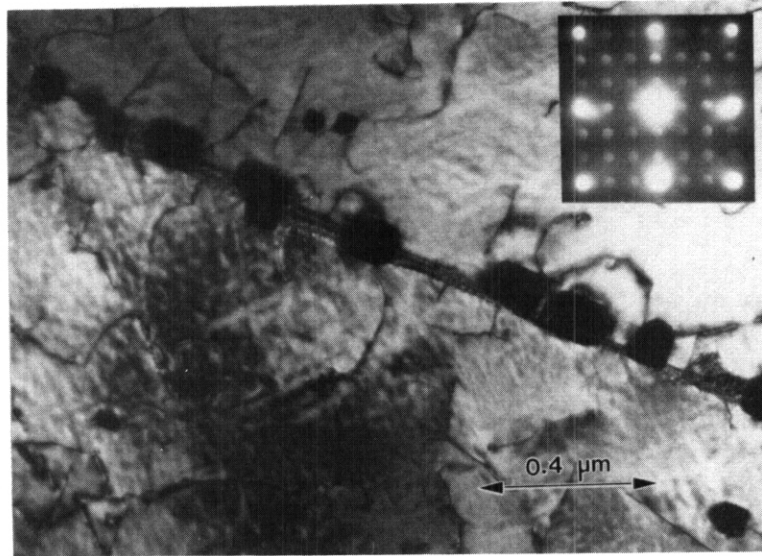


Fig 3: Chromium-rich Chi phase precipitates in Fe-15Cr-20Mn at 9 dpa and 420°C.

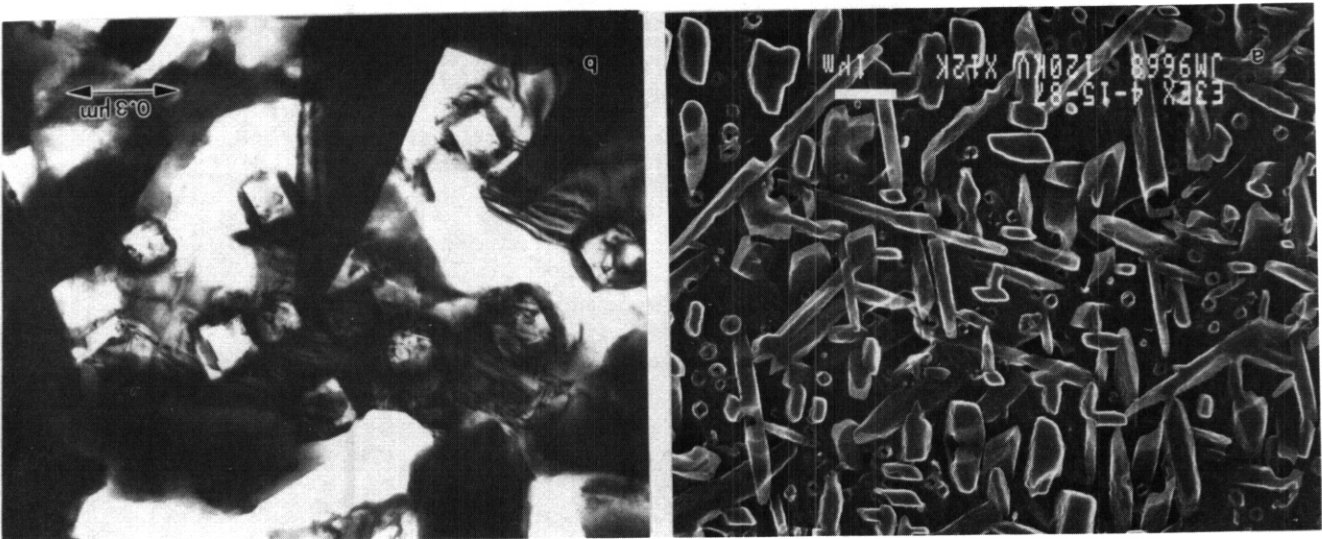


Fig 4: Fe-5Cr-15Mn at 14 dpa and 600°C, showing (a) scanning micrograph of foil surface and (b) bright field transmission micrograph near foil edge.

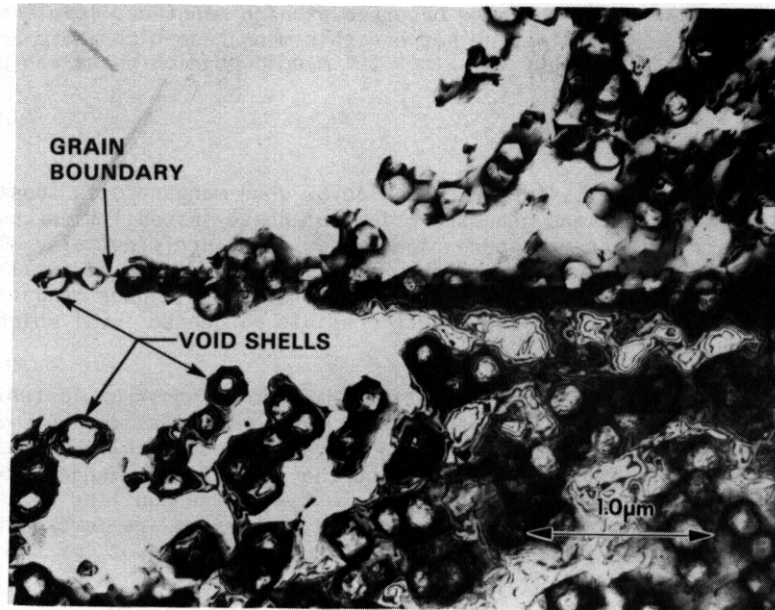


Fig 5: Fe-35Mn at 14 dpa and 600°C showing relative resistance of void shells and grain boundaries to electropolishing.

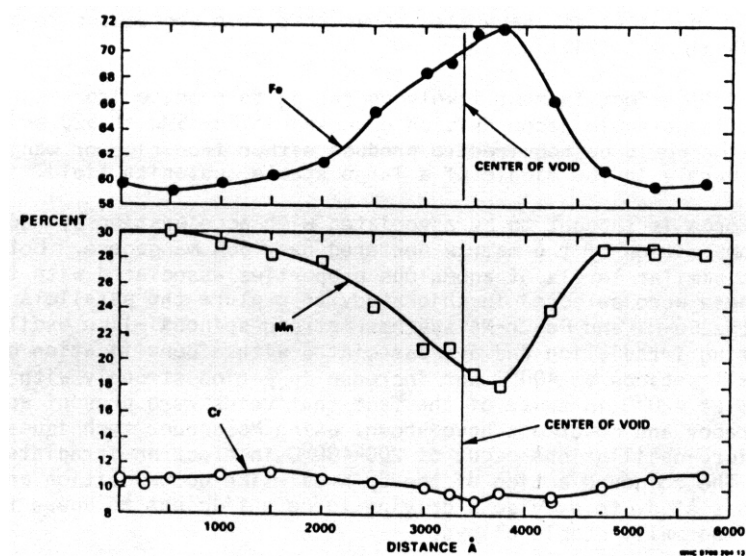


Fig 6: Profiles of composition across a void in Fe-10Cr-30Mn at 14 dpa and 600°C.

Fe-35Ni and Fe-7Cr-35Ni, but in these cases the relative resistance toward electrochemical attack was a result of the tendency for nickel rather than iron to segregate at microstructural sinks. (14-15)

A manganese-rich bcc stick-like phase was also observed at high manganese levels and higher temperatures, such as in Fe-10Cr-30Mn at 520°C. A distinction between this manganese-rich phase and that of the iron-rich phase was not noted in an earlier paper (6) since the manganese-rich phase was preferentially attacked, leaving mostly holes in the foil.

Discussion

The general increase in chemical activity of these alloys, when manganese is substituted for nickel, is demonstrated first by the higher level and greater variety of phase instabilities, but also by the persistent tendency of both fcc and bcc manganese-rich phases to be preferentially attacked during electropolishing. This sensitivity, coupled with the relative independence of swelling on manganese content (1,2,6,16) and also with the greater rate of liquid metal corrosion at higher manganese levels (17), signals that manganese substitution is best kept at the lowest possible manganese level which can be successfully stabilized with solute addition.

The tendency of Fe-Cr-Mn alloys to undergo sequential transformations from austenite to hcp epsilon and then bcc alpha martensite does not appear to be suppressed during irradiation, but may be shifted in compositional space in response to long-range diffusion-driven compositional changes. The formation of iron-rich ferrite across a wide range of compositions and the formation of manganese-rich ferrite phases at higher manganese levels can be considered to be consistent with the equilibrium phase diagram in Fig. 1 only if some rather powerful radiation-induced segregation mechanisms are invoked to make large changes in local composition. Simple radiation-enhanced diffusion could not account for the striking breakdown at higher manganese levels.

It is obvious, however, that iron segregation at a variety of microstructural sinks is a very general process during irradiation. While voids and grain boundaries segregate iron, it is suspected that the stick-like ferrite precipitates nucleate on dislocations. The absence of stick-like precipitates in Fe-35Mn at 600°C might be considered to be consistent with the well-known decrease in dislocation density with irradiation temperature at low displacement levels.

Fe-Cr-Ni alloys tend to segregate nickel at sinks, thereby ensuring that ferrite phases are not nucleated. Instead a variety of radiation-stabilized nickel-rich phases are formed with relatively small consequences on the stability of the austenite matrix. (18-20) Segregation in each of the two alloy systems is thought to be the result of the inverse-Kirkendall mechanism, whereby the slowest diffusing elements segregate by default at the base of vacancy gradients developed at various microstructural sinks. Okawa has shown that iron indeed diffuses slower than manganese and chromium in both fcc and bcc iron-based alloys (21) and there is a large amount of data showing that nickel is the slowest diffusing element in Fe-Cr-Ni alloys. (22,23) Takahashi et al. have also shown that iron segregates to grain boundaries in electron irradiated Fe-Cr-Mn alloys. (24)

While the inverse-Kirkendall effect is most likely operating to produce iron segregation, another driving force may help to cause the large-scale decomposition observed in Fe-35Mn at 520 and 600°C. Note in Fig. 1 that substantial segregation would be required to produce either iron-rich or manganese-rich ferrite phases. This alloy sits squarely in the middle of a large stable austenite field.

The additional driving force is thought to be associated with acceleration by radiation of an ordinarily sluggish spinodal-like decomposition of the matrix centered near 35% manganese. Both Fe-XNi and Fe-XMn alloys are known to exhibit similar levels of anomalous properties associated with the "invar" regime, and the higher levels of manganese were selected in this study to explore the parallels between invar anomalies and void swelling. (1) In the Fe-Ni and Fe-Cr-Ni systems, strong spinodal-like oscillations in composition develop in invar alloys during irradiation and are associated with a densification of ~1%. (14, 15, 25) These oscillations have small periods at 400°C but increase in period strongly with temperature. Remember that Fe-35Hn densified 2.2% at 420°C in spite of the fact that voids were present and no obvious precipitation had occurred. Mekhrabov and coworkers have shown, using Mossbauer techniques, that small scale pronounced compositional micro-oscillations occur at 200-400°C in electron-irradiated alloys in this compositional range. (26) The compound action of the spinodal-like decomposition and the inverse-Kirkendall effect are postulated in this study to provide a driving force sufficient to cause the observed large-scale decomposition of otherwise thermally stable alloys.

The addition of chromium to these alloys leads to formation of chi phase, most likely with the assistance of radiation-assisted segregation. This phase is known to be brittle and should be avoided in development of a solute-stabilized alloy. Sigma phase is also brittle and the potential exists for its formation, as seen in thermal annealing studies where sigma formed in cold-worked steels but not in annealed steels. (10) The absence of sigma phase formation in this study reflects the use of annealed specimens.

The formation of various low-swelling bcc phases is also thought to explain why Fe-Cr-Mn alloys initially swell at the $\sim 1\%/dpa$ rate characteristic of iron-based austenite alloys (2), but then exhibit a progressive reduction in swelling rate with increasing exposure. (2,6,10) The lower density of the bcc phases also contributes to the measured changes in density.

CONCLUSIONS

The simple Fe-Cr-Mn alloy system at 420-600°C is subject to a variety of phase instabilities during irradiation. These range from diffusionless martensitic transformation, radiation-driven formation of several phases which would not be thermally stable, and a radiation-accelerated version of an ordinarily sluggish spinodal-like decomposition in the invar compositional regime. Only the latter has been observed in simple Fe-Cr-Ni alloys irradiated at comparable conditions. The larger level of phase instabilities in the Fe-Cr-Mn system must be addressed in the development of a low activation solute-stabilized austenitic alloy.

FUTURE WORK

This effort will continue concentrating on Fe-Cr-Mn-Ni quaternary alloys and commercial alloys.

REFERENCES

1. H.R. Brager, F.A. Garner, O.S. Gelles and M.L. Hamilton, *J. Nucl. Mater.* 133 and 134 (1985), 907.
2. F.A. Garner and H. R. Brager. in Radiation-induced Changes in Microstructure, ASTM STP 955. Eds., F.A. Garner, N.H. Packan and A.S. Kumar (American Society for Testing and Materials, Philadelphia, 1986), p. 195.
3. R.L. Kleuh and E.E. Bloom. in Optimizing Materials for Nuclear Applications, Eds., F.A. Garner, D.S. Gelles and F.W. Wiffen, (The Metallurgical Society, AIME, Warrendale, PA, 1985) p. 73.
4. A.H. Bott, F.B. Pickering and G.J. Butterworth, *J. Nucl. Mater.*, 141-143 (1986), 294.
5. M. Snykers and E. Ruedl. *J. Nucl. Mater.* 103 and 104 (1981), 1075.
6. F.A. Garner, H.R. Brager, D.S. Gelles and J.M. McCarthy, *J. Nucl. Mater.* 148 (1987), 294.
7. E. Garstein and A. Rabinkin, *Acta Met.* 27 (1979) 1053.
8. Y. Tomota, M. Strum and J.W. Morris, Jr., *Met. Trans. A*, 17A (1986) 537; 18A (1987) 1073.
9. R. Scholz, W. Schule, E. Lang and A. Panzarasa. Fusion Technology and Safety Programme Progress Report. J.R.C. ISPRA Establishment. June 1984, 57.
10. F.A. Garner, F. Abe and T. Noda. this conference.
11. E. Ruedl and T. Sasaki. *J. Nucl. Mater.* 122 and 123 (1984) 794.
12. E. Ruedl, V. Couer, T. Sasaka and H. Koibe, *J. Nucl. Mater.* 122 and 123 (1984) 1247.
13. *Constitution of Binary Alloys*. Ed. M. Hansen (McGraw-Hill, New York, 1958).
14. F.A. Garner, H.R. Brager and J.M. McCarthy, In ref. 2, 775.
15. R.A. Dodd, F.A. Garner, J.-J. Kai, T. Lauritzen and W.G. Johnston. in ref. 2, 788.
16. O.S. Gelles and F.A. Garner, *J. Nucl. Mater.* 133 and 134 (1985) 521.
17. P.F. Tortorelli and J.H. DeVan, *J. Nucl. Mater.* 141-143 (1986) 579.
18. H.R. Brager and F.A. Garner, *J. Nucl. Mater.* 73 (1978) 9.
19. H.R. Brager and F.A. Garner, *J. Nucl. Mater.* 116 (1983) 267.
20. F.A. Garner In Phase Stability During Radiation. Eds. J.R. Holland, L.K. Mansur and D.I. Potter. The Metallurgical Society of AIME (1981) 165.
21. H. Oikawa, Technology Reports, Tohoku University, 47 (1982) 251; 48 (1983) 7.

REFERENCES - Continued

22. E. Esmailzadeh and **A.S.** Kumar, in Effects of Radiation on Materials: Twelfth International Symposium. ASTM STP 870, Eds. F.A. Garner and J.S. Perrin (1985) 468.
23. F.A. Garner and A.S. Kumar. in ref. 2, 289.
24. H. Takahashi. F.A. Garner, H. Itoh. E. Hu and S. Ohnuki. in ref. 2, 268.
25. F.A. Garner and H. R. Brager, R.A. Dodd and T. Lauritzen. Nucl. Inst. Meth. in Phys. Res. B16 (1986) 244.
26. A.O. Mekhrabov, K. G. Binnatov, **Andulla** O. Mekhrabov and T.A. Shukyurov, in ref. 2, 741.

RESPONSE OF Fe-Cr-Mn AUSTENITIC ALLOYS TO THERMAL AGING AND NEUTRON IRRADIATION - E. A. Garner (Pacific Northwest Laboratory) and F. Abe and T. Noda (National Research Institute for Metals, Japan)

OBJECTIVE

The object of this effort is to determine the suitability of Fe-Cr-Mn austenitic alloys for fusion reactor candidates.

SUMMARY

The Fe-Cr-Mn austenitic alloy system is being studied as a replacement of the Fe-Cr-Ni system for fusion applications in which reduced long-term radioactivation is an important consideration. This paper describes two aspects of the response of this alloy system to material and environmental variables. First, the neutron-induced void swelling of simple binary and ternary alloys is investigated as a function of composition, thermal-mechanical treatment, temperature (693-873K) and displacement level (9-76 dpa). The swelling rate of this alloy system approaches 1%/dpa for those conditions which do not favor formation of large levels of ferrite phases. Second, the tendency of the potentially detrimental sigma phase to form during thermal aging is explored at high manganese levels. Variables such as carbon concentration, cold-work level and aging time are shown to influence the distribution and rate of sigma formation.

PROGRESS AND STATUS

Introduction

Manganese-stabilized austenitic steels are of current interest as a possible replacement for conventional Fe-Cr-Ni stainless steels.¹⁻⁴ The motivation for this substitution arises from the desire to strongly reduce the level of long-term radioactivation associated with waste disposal considerations.^{5,6} At present, however, little is known about the phase stability of Fe-Cr-Mn austenite during high temperature exposure and neutron irradiation. Based on numerous studies of the Fe-Cr-Ni system, it is anticipated that neutron-induced changes in mechanical properties, as well as dimensional changes arising from void swelling and irradiation creep, will depend on the phase evolution that occurs at high temperature prior to and during irradiation.

Neutron-induced swelling data have been accumulating on a variety of simple binary Fe-Mn and Fe-Cr-Mn alloys, as well as a number of solute-modified and commercial alloys. These have been reported for low to moderate displacement levels^{1,7-9} and have been shown to be related to the phase evolution that occurs at relatively low displacement levels.^{9,10} In this paper, the swelling of simple Fe-Cr-Mn alloys is reported to displacement levels as large as 75 dpa over the range 693 to 873K, as a function of composition and thermal-mechanical treatment. The data on solute-modified and commercial alloys are still being collected at these high displacement levels and will be reported elsewhere.

Also included in this paper are the results of thermal aging studies on two Fe-10Cr-30Mn alloys, one without carbon addition and one with a high carbon level. The major concern of this effort is the possibility that austenite stabilized with manganese might be more susceptible to formation of sigma phase than austenite stabilized with nickel.

Experimental details

The irradiation portion of this experiment is a continuation of work reported earlier at lower displacement levels.^{1,7-10} The irradiations were essentially isothermal ($\pm 5^\circ\text{C}$) and were conducted at -3×10^{-6} dpa sec^{-1} in the Materials Open Test Assembly (MOTA) located in the Fast Flux Test Facility (FFTF) in Richland, WA. The nine alloys irradiated were primarily in the solution-annealed condition (1300K/0.5 h/AC) and were irradiated as standard 3 mm diameter microscopy disks in static sodium. Two of these alloys (Fe-15Cr-15Mn and Fe-30Mn) were also irradiated in the 20% cold-worked condition and in the 20% cold-worked and aged (923K/1 h/AC) condition. The neutron-induced swelling was determined by measurement of density change using an immersion technique.

Two steels were employed in the aging study, with their compositions given in Table 1. Steel A contained a low level of carbon and steel B had a high level (0.546 wt%). The specimens were prepared by vacuum melting in a high frequency induction furnace to produce ingots weighing 17 kg, followed by homogenization at 1423K for 24 h and hot forging to 13 x 13 mm square rods. The steels were solution annealed for 3.6 ks at 1273K for steel A and at 1423K for steel B; both steels were then quenched in water. The average grain size in these steels following the heat treatment was about 50 μm . Portions of each rod were cold-rolled 10, 30, 60 or 80% at room temperature. Aging of each of these conditions proceeded at 923K for times between 3.6 and 3600 ks.

Microstructural observations were performed using a 200 kV transmission electron microscope, selected area diffraction and energy dispersive X-ray (EDX) analysis. The identification of the precipitates also employed X-ray diffraction using filtered $\text{Cu K}\alpha$ ($\lambda = 1.5405 \text{ \AA}$) radiation at 30 kV and 30 mA. The details of the X-ray procedure are described elsewhere."

Table 1. Composition (wt%) of Steels Employed in Aging Studies

	C	Cr	Mn	Si	S	P	O	N
Steel A	0.003	10.09	28.40	0.46	0.010	0.002	0.006	0.005
Steel B	0.546	9.92	30.77	0.46	0.010	0.002	0.002	0.002

Results of irradiation studies

The swelling levels of the simple binary and ternary alloys in the solution annealed condition are shown in Fig. 1 for irradiation at 793 and 873K. Note that the swelling rate at 873K approaches 1%/dpa for most alloys. At 793K many of the higher swelling alloys also appear to be approaching a swelling rate of 1%/dpa but a down-turn in swelling rate appears to be developing in the lower swelling alloys. At 693K (Fig. 2), the swelling rate is clearly declining, both with decreasing temperature and increasing displacement level, especially for those alloys which densified prior to the onset of measurable swelling. In recognition that the density change has negative components, the data in Fig. 2 are reported as changes in density ($\Delta\rho/\rho_0$) rather than void swelling ($\Delta V/V_0$) where $\Delta V/V_0 = [\Delta\rho/\rho_0 / (1 - \Delta\rho/\rho_0)]$. Note that many of the curves in Fig. 1 appear to extrapolate to a value of 2 to 3% "swelling" at zero displacements, implying that other non-void components of density change have occurred. Formation of ferrite phases in these alloys would give rise to a decrease in density that would mimic void swelling.

Fig. 3 shows that cold-working in general reduces swelling but the effect of subsequent aging at 923K varies with alloy composition and irradiation temperature.

Results of aging studies

Precipitation of sigma phase was found to occur in steels A and B only in cold-worked specimens and not in the annealed condition. No other intermetallic compounds were observed. Fig. 4 shows the microstructural changes that occur in steel A aged in the 30% cold-worked condition. At 3.6 ks a recrystallized grain having a size of several microns had grown from prior grain boundaries. Few of these recrystallized grains were observed at this time, indicating that the nucleation stage of recrystallization is in progress. As shown by the arrows in Fig. 4a, sigma precipitates on the order of 0.5 to 1.0 microns in size have developed at the recrystallization interfaces. With increasing time the interfaces advanced into the deformed matrix, increasing the number of sigma precipitates without increasing the size of those precipitates formed at earlier positions of the interface. Sigma phase was not observed to form in deformed grains prior to the advancement of the interface through that volume. Fig. 5 shows schematic illustrations of the sigma formation process.

At the lower level of 10% cold-work, recrystallization was not observed in steel A during aging to 3600 ks and the sigma phase formed infrequently and only at triple points of grain boundaries. For cold-work levels larger than 30%, the rates of recrystallization and precipitation increased during aging and the number density of sigma precipitates increased at the expense of their mean size.

The composition of the sigma phase was determined in-situ by EDX analysis to be 15 to 23%Cr, 47 to 50%Fe, 30%Mn and 1%Si in the 30% cold-worked specimen aged for 3600 ks. Thus, sigma phase forms via segregation of chromium from the matrix and by the partial rejection of iron.

In the high carbon steel B only M_{23}C_6 carbides were observed to form in the annealed condition, precipitating preferentially at grain boundaries. A composition of $(\text{Cr}_{13}\text{Mn}_6\text{Fe}_4)\text{C}_6$ was determined for these precipitates using EDX analysis of electrolytically extracted residues. Both M_{23}C_6 and sigma were found in cold-worked specimens but the addition of carbon suppressed the rate of sigma formation relative to that of the low carbon steel.

Fig. 6 shows the microstructures that develop during aging of steel B in the 30% cold-worked condition. The M_{23}C_6 precipitates form preferentially on deformation bands produced during cold-rolling, suppressing recrystallization and thereby suppressing sigma formation. At higher cold-work levels, recrystallization occurs more readily as shown in Fig. 7 for steel B in the 80% cold-worked condition. Sigma formation developed in steel B as a consequence of recrystallization yielded precipitates that were very small and at higher densities than those observed in steel A, indicating that carbon additions lead to a refinement of sigma phase.

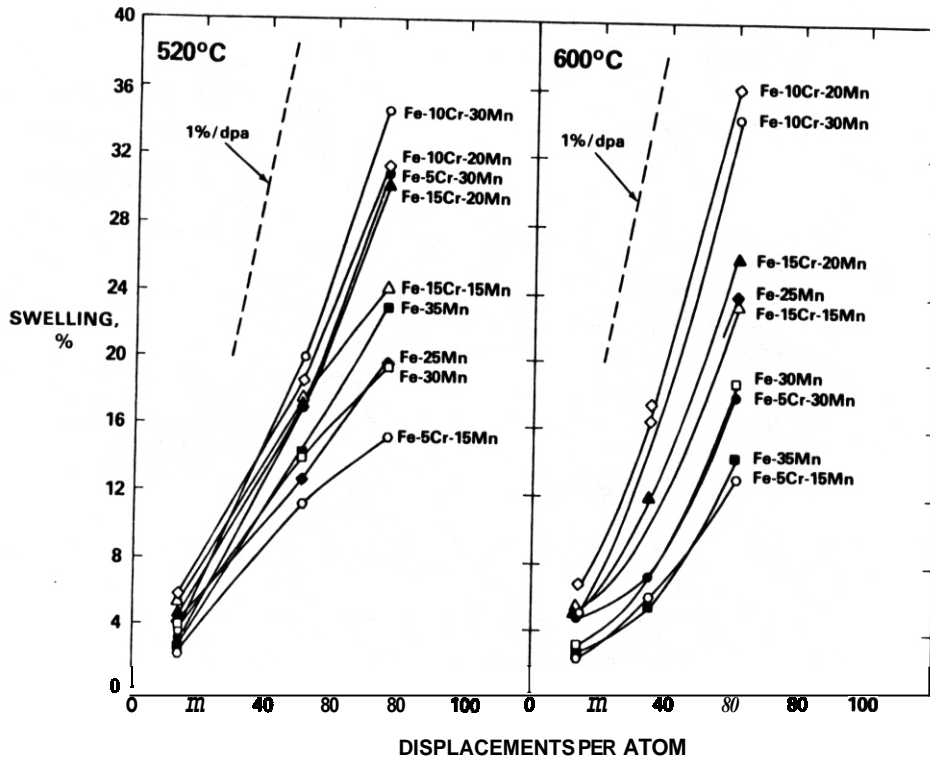


Fig. 1 Neutron-Induced Swelling of Fe-Cr-Mn Alloys at 793 and 873K (520 and 600°C)

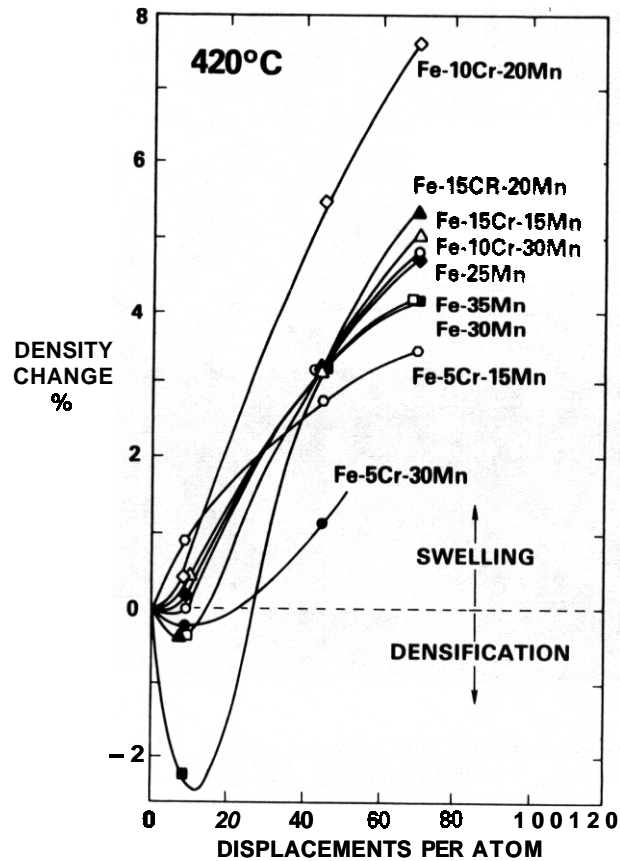


Fig. 2 Neutron-Induced Density Changes of Fe-Cr-Mn Alloys at 693K (420°C)

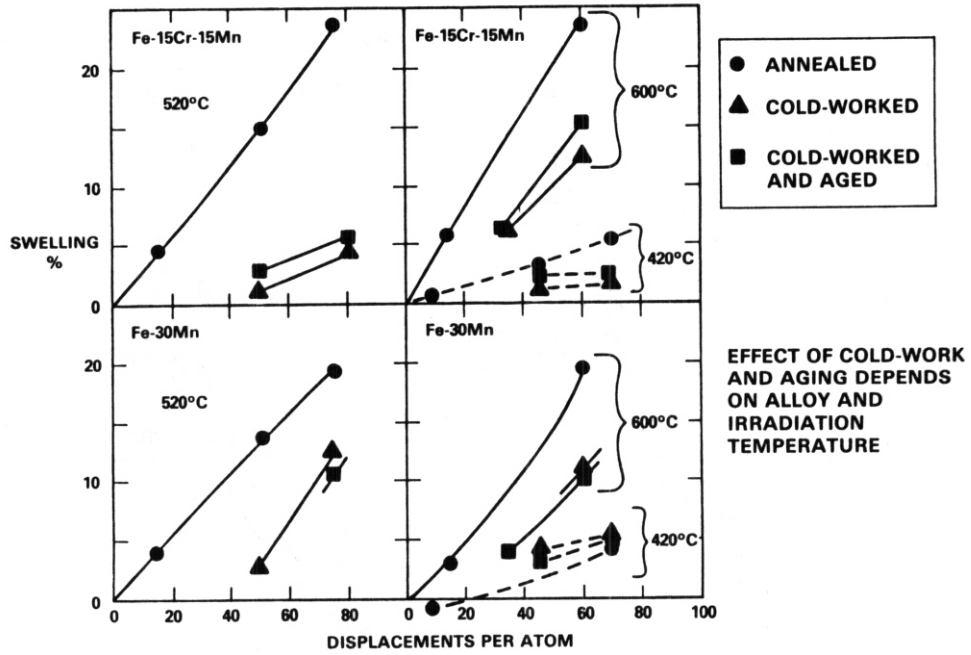


Fig. 3. The Influence of 20% Cold Work and Cold Work and Aging on the Swelling of Fe-15Cr-15Mn and Fe-30Mn

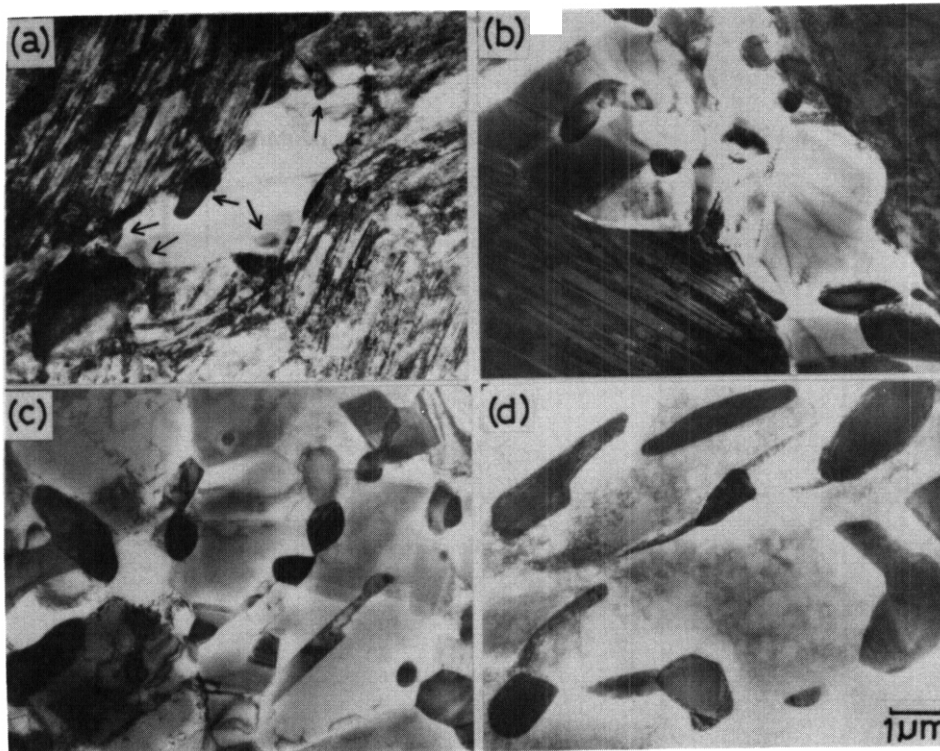


Fig. 4. Microstructural Changes Observed During Aging at 923K in Steel A in the 30% Cold-Worked Condition for Times of (a) 3.6, (b) 36, (c) 360, and (d) 3600 Kiloseconds

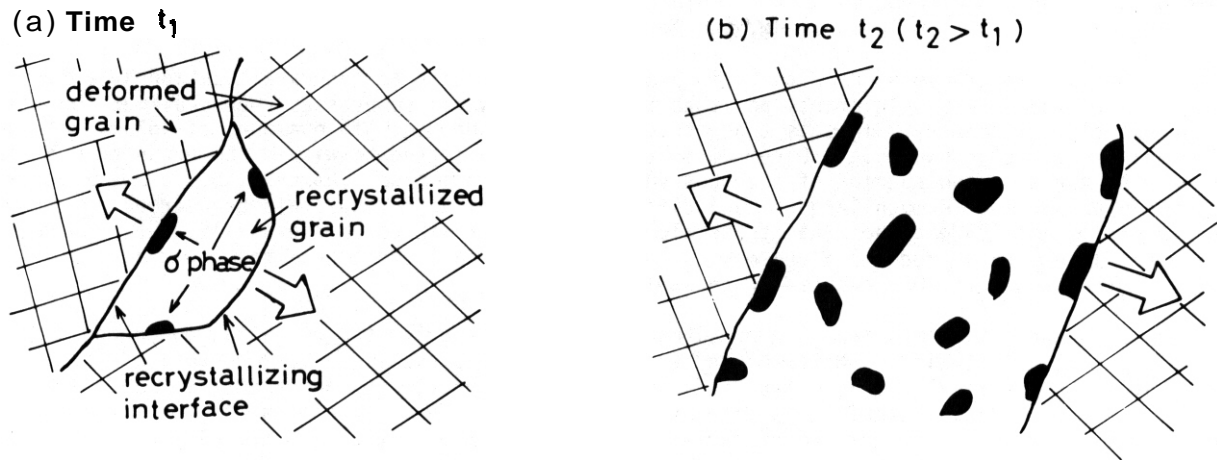


Fig. 5. Schematic Representation of the Formation of Sigma Phase at the Advancing Boundaries of Recrystallization

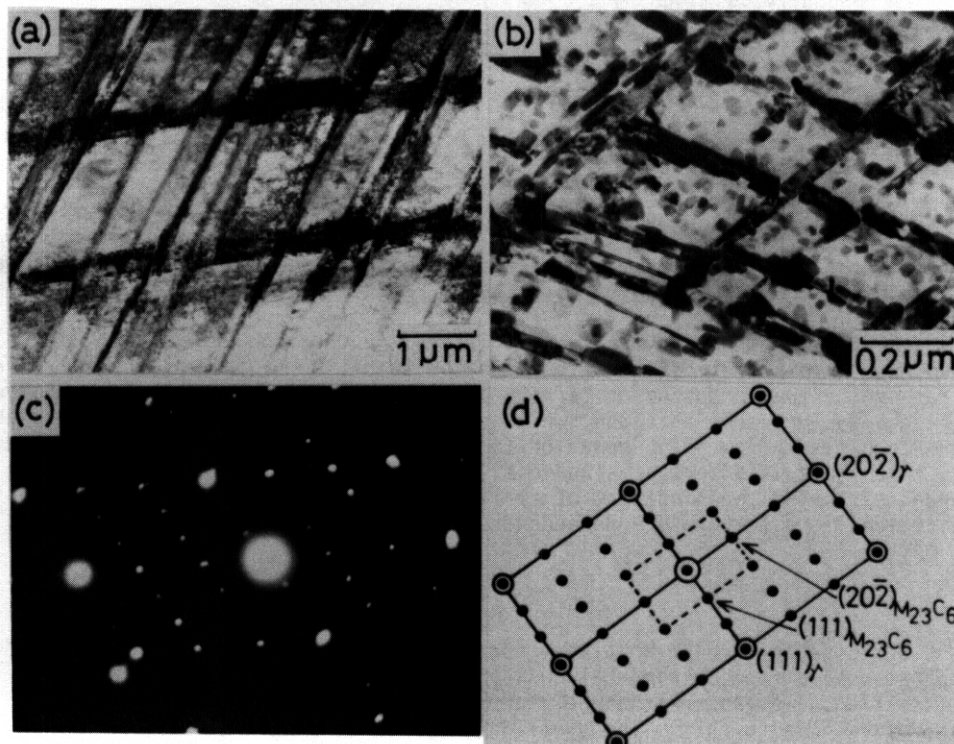


Fig. 6. Microstructural Changes Observed During Aging at 923K in Steel B in the 30% Cold-Worked Condition, (a) as Cold-Rolled, (b) after 36 Kiloseconds at 923K, (c,d) Selected Area Diffraction of (b)

Discussion

In steel B the initial composition of the austenite matrix differs from that of the total alloy due to precipitation of the chromium-rich carbides. Assuming that all carbon precipitates as carbides, the matrix composition prior to sigma formation was calculated to be 5.6% Cr, 31.4% Mn and 61.9% Fe. This implies that sigma phase, even though rich in chromium, can form at 30% manganese with chromium levels as low as 5%.

It is obvious from these studies that sigma phase can form only at recrystallization interfaces or occasional grain boundary triple points and that any variable which suppresses recrystallization will likewise suppress sigma formation. This is thought to arise from the negligible amount of volume diffusion at 923K for aging times of <3600 ks.¹² Chromium is thus unable to segregate within the grain on a scale commensurate with the size and spacing of the observed sigma precipitation. However, diffusion along stationary grain boundaries is much larger¹² and diffusion rates along moving grain boundaries are known to be several orders of magnitude higher than those along stationary grain boundaries.^{13,14} Furthermore, solute atoms are not likely to be reduced along moving boundaries, since in this case the boundaries advance toward the untransformed and therefore supersaturated solid solution.

It has been suggested that the rate of sigma formation is accelerated by radiation-enhanced diffusion in AISI 316 and 316+Ti steels.¹⁵ McCarthy and Garner did not observe sigma to form during irradiation in either Fe-10Cr-30Mn or similar alloys but their studies were conducted on annealed alloys.¹⁰ The possibility of accelerated sigma formation in deformed and irradiated Fe-Cr-Mn alloys has yet to be studied. It is known, however, that in the absence of radiation, the sigma phase requires unusually long times to form in solution-treated steels.¹⁶

Looking at the Fe-Cr-Mn phase diagram (Fig. 8) at 923K¹⁷ one can see that the $\gamma/(\gamma+\sigma)$ boundary lies at ~15% Cr, well above the chromium level of steel A and steel B (both before or after carbide formation). This apparent discrepancy was addressed using the d-electron theory of Morinaga et al. which has been reported to describe well the $\gamma/(\gamma+\sigma)$ boundary in the Fe-Ni-Cr system.¹⁸ According to this theory, a critical value of the d-electron parameter \bar{M}_d describes the energy level of d-electrons beyond which phase decomposition will occur in a terminal solid solution, and is given by

$$\bar{M}_d = 0.858 x_{Fe} + 1.142 x_{Cr} + 0.957 x_{Mn}$$

where x_{Fe} , x_{Cr} and x_{Mn} are the atomic fractions. The \bar{M}_d parameter has units of eV. The temperature dependence of \bar{M}_d at the phase boundary is given by

$$\bar{M}_d = 6.25 \times 10^{-5} T + 0.834,$$

where T is the absolute temperature. Using these equations the predicted $\gamma/(\gamma+\sigma)$ boundary is shown in Fig. 8. Note that this prediction shows a shift of the boundary from ~15% Cr to ~2% Cr at 30% manganese. in line with the observation of this study that sigma forms to a level of at least 5% Cr.

Not only might the sigma phase cause significant degradation in mechanical properties, but the combined loss of chromium to both sigma and carbide phases will reduce the matrix chromium level to only several percent, leading to a degradation of corrosion resistance. Other chromium-rich phases such as chi-phase have also been found to form during neutron irradiation of Fe-Cr-Mn alloys.¹⁰

While chromium reduction does not have a large impact on neutron-induced swelling in this alloy system;^{1,7,8} it does have a relatively strong effect on the stability of the alloy matrix during radiation, particularly with respect to the formation of ferrite phases.¹⁰ Since ferrite is known to swell at a lesser rate than austenite, one would expect that the swelling rate would decline as the volume fraction of ferrite increases. When one compares the swelling behavior in Figs. 1 to 3 with the tendency toward ferrite formation, it is obvious that there is some correspondence. At 600°C all alloys attempt to swell at ~1%/dpa but as the temperature decreases the swelling rate of ferrite-prone alloys falls away from this value, in agreement with the compositional and temperature dependence of ferrite formation.

CONCLUSIONS

The development of austenitic Fe-Cr-Mn alloys for fusion service must overcome the tendency of this system at high temperatures to form detrimental phases such as ferrite and chi during irradiation and sigma in the absence of radiation. It appears that solute modification by carbon and perhaps other elements may preclude the tendency for sigma to form. The swelling of Fe-Cr-Mn alloys seems to be influenced by the phase instabilities that also occur during irradiation.

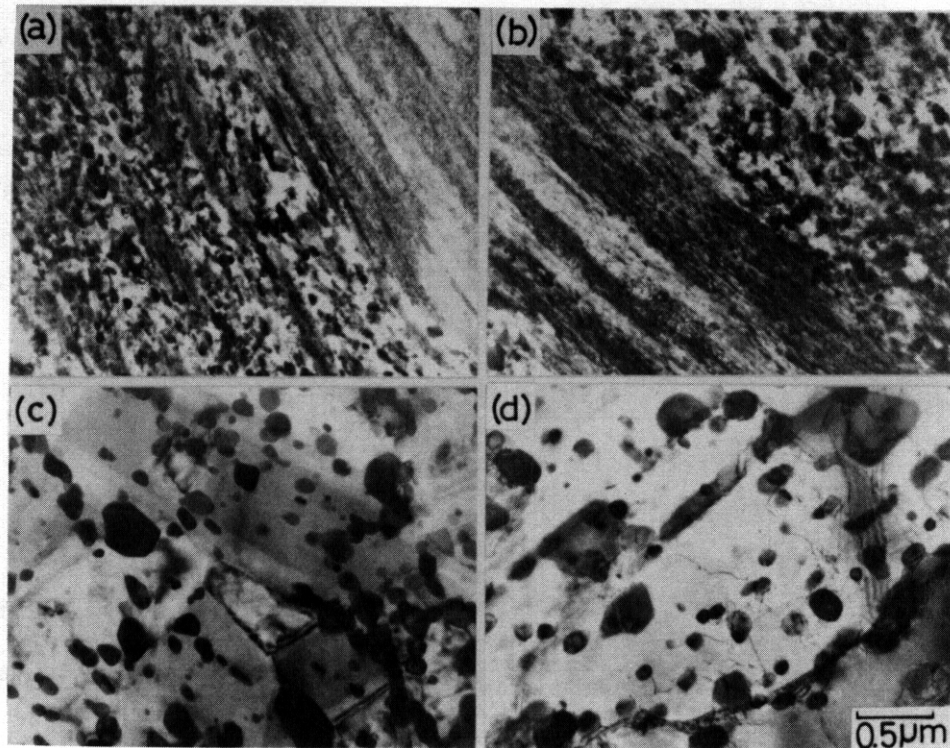


Fig. 7. Microstructural Changes Observed During Aging at 923K in Steel B in the 80% Cold-Worked Condition after Times of (a) 36, (b) 36, (c) 360, and (d) 3600 Kiloseconds

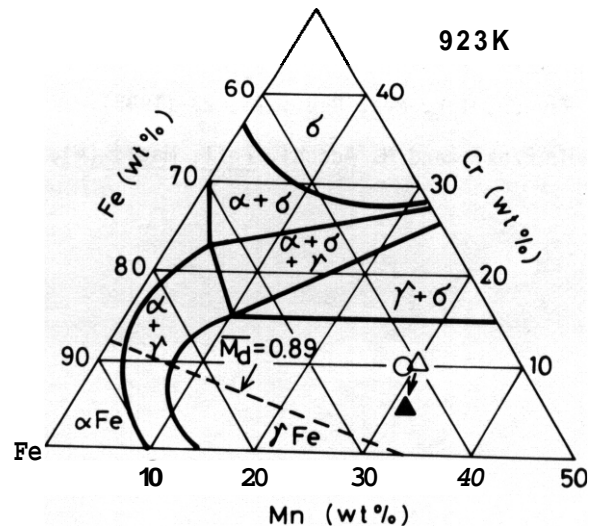


Fig. 8 Fe-Cr-Mn Ternary Phase Diagram at 923K.¹⁷ The circle and the triangles represent the composition of alloys A and B, before and after carbide precipitation. Also shown is the $\gamma/(\gamma+\sigma)$ boundary evaluated using the d-electron theory.

FUTURE WORK

This effort will continue, concentrating on the thermal stability of Fe-Cr-Mn ternary alloys. The binary and ternary alloys from MOTA IE will probably not be measured since their swelling levels will be very large.

REFERENCES

1. H. R. Brager, F. A. Garner, D. S. Gelles, and M. L. Hamilton, J. Nucl. Mater., 133&134, 907 (1985).
2. R. L. Kleuh and E. E. Bloom, p. 73-85 in Optimizing Materials for Nuclear Applications, Eds. F. A. Garner, D. S. Gelles, and F. W. Wiffen, (TMS-AIME, Warrendale, PA, 1985).
3. A. H. Bott, F. B. Pickering, and G. J. Butterworth, J. Nucl. Mater., 141-143, 294 (1986).
4. M. Snykers and E. Ruedl, J. Nucl. Mater., 103&104, 1075 (1981).
5. D. G. Doran, H. L. Heinisch and F. M. Mann, J. Nucl. Mater., 133&134, 892 (1985).
6. F. M. Mann, Fusion Technology 6, 273 (1984).
7. F. A. Garner and H. R. Brager in Ref. 2, pp. 87-109.
8. F. A. Garner and H. R. Brager, pp. 195-206. in Radiation-Induced Changes in Microstructure. ASTM STP 955, Eds. F. A. Garner, N. H. Packan and A. S. Kumar (1987).
9. F. A. Garner, H. R. Brager, D. S. Gelles, and J. M. McCarthy, J. Nucl. Mater., 148, 294 (1987).
10. J. M. McCarthy and F. A. Garner, this semiannual report.
11. F. Abe, H. Araki and T. Noda, Report of the Japan Society for the Promotion of Science. 123rd Committee 28, 169 (1987).
12. W. Hume-Rothery, The Structure of Alloys of Iron, Pergamon Press Limited, England, (1966).
13. M. Hillert and G. R. Purdy, Acta Met., 26, 333 (1978).
14. K. Smidoda, C. Gottschalk and H. Glieter, Met. Sci., 13, 146 (1979).
15. E. H. Lee, P. J. Maziasz and A. F. Rowcliffe, p. 191 in Phase Stability During Irradiation, Ed., J. R. Holland, L. K. Mansur, and D. I. Potter, (TMS-AIME, Warrendale, PA, 1981).
16. J. K. L. Lai, Mat. Sci. Eng., 58, 191 (1983).
17. V. G. Rivilin and G. V. Raynor, Int. Met. Rev., 28, 23 (1983).
18. M. Morinaga, N. Yukawa, H. Ezaki, and H. Adachi, Phil. Mag., (A), 51, 223 (1985).

QUANTITATIVE ANALYSIS OF VOID SWELLING - D. S. Gelles, R. M. Claudson* and L. E. Thomas (Pacific Northwest Laboratory. and * Inquiry-into-Science-Student, Westinghouse Hanford Company)

OBJECTIVE

The **objective** of this work is to optimize procedures for the measurement of void swelling based on transmission electron microscopy.

SUMMARY

It has been shown that in austenitic alloys void shapes can vary between truncated octahedra and truncated cubes whereas in ferritic alloys the void shapes vary between truncated octahedra, truncated cubes and truncated dodecahedra. In order to provide minimum errors in void swelling measurements, where the degree of truncation varies from void to void in the area of interest, calculations are provided which show that voids should be measured in $\langle 110 \rangle$ directions for austenitic alloys with cubic and octahedral truncation but for ferritic alloys with cubic and dodecahedral truncation. $\langle 111 \rangle$ and $\langle 110 \rangle$ direction measurements are equivalent provided the correct calibration factor is used.

PROGRESS AND STATUS

Introduction

Swelling determination from transmission electron micrographs involves physically measuring the total void volume contained within a given sample volume. Despite the apparent **directness** of this method, void image measurements and volume calculations readily produce uncertainties of over 100% in swelling and swelling rate when measurements are based on circle approximations of the void size. The problem arises because voids in irradiated metals are polyhedral, crystallographically-oriented features. In austenitic stainless steels and other face-centered-cubic (fcc) alloys, voids range in shape from octahedra with $\{111\}$ faces to cubes with $\{100\}$ faces, and exhibit all intermediate (truncated) forms. ¹ In ferritic steels, voids range in shape from cubes with $\{100\}$ faces to dodecahedra with $\{110\}$ faces, with all intermediate truncations, but octahedra with $\{111\}$ faces are also found. ² In both cases, the degree of truncation can vary significantly even within a given field of view. In addition, well-defined parameters for size measurement, such as crystallographic **directions**, are difficult to find in random crystal orientations, and their relationship to the void volume is seldom known.

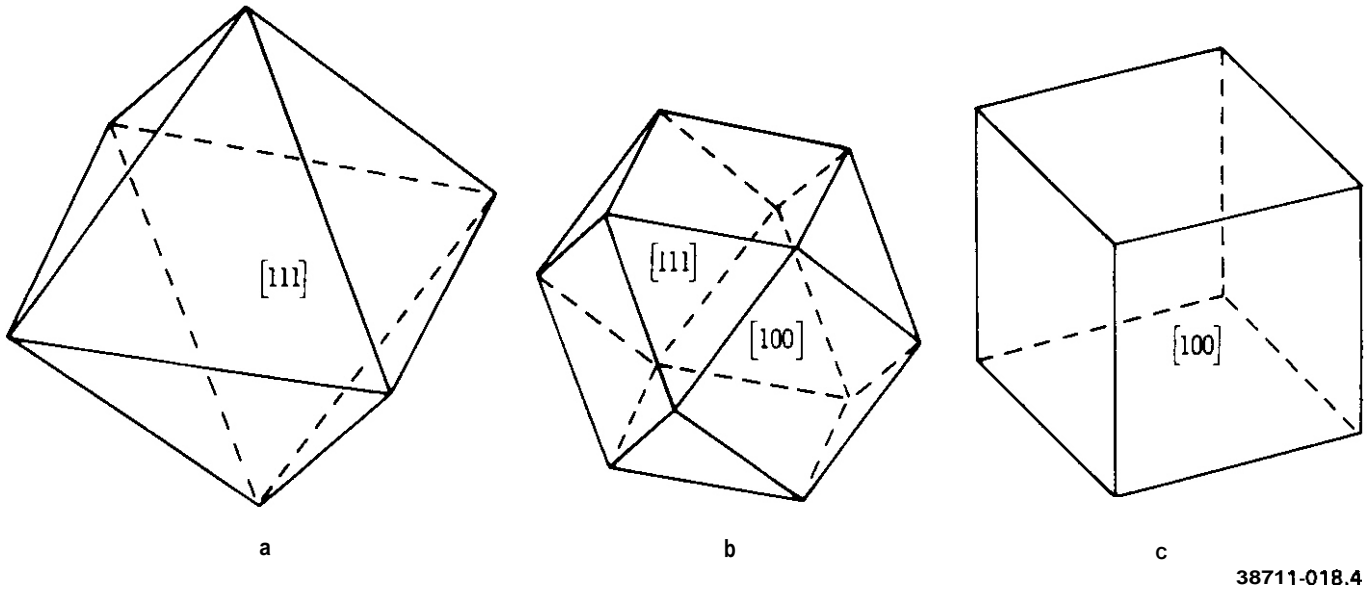
The relationship between void shape (as seen on electron micrographs) and void volume has therefore been studied with the aim of developing more accurate swelling determination procedures without sacrificing the efficiency of measuring a single size parameter for each void. Void volumes were determined as a function of a shape parameter and related to the various parameters available for measurement in different crystal orientations. Procedures were then defined in order to minimize the **error** in swelling measurement. For the case of fcc alloys, these procedures have been in place at our laboratory for over a decade. Much more recently, the case of body-centered-cubic (bcc) alloys has been considered and has just been implemented. This paper is intended to review the case for fcc alloys and provide comparison with the case for bcc alloys. The **optimum** procedures for the two cases are found to be different.

Void shapes in fcc alloys

Figure 1 provides examples of void shape variation in fcc alloys showing a) an octahedral void, b) a void containing equal octahedral and cubic truncations and c) a cubic void. In order to emphasize the consequences of void shape and **truncation** on apparent appearance, Figure 2 provides comparison of four views of cubic and octahedral voids with small truncation. The orientations shown are $[112]$, $[110]$, $[100]$ and $[111]$. Of particular note is the fact that for a $[100]$ orientation, cubic and octahedral voids with zero truncation will look identical except for a 45° rotation. Also included in figure 2 is the definition of the parameters which were used for volume calculation. W is defined as the void dimension in the $\langle 100 \rangle$ direction, X is defined as the void dimension in the $\langle 110 \rangle$ direction and Z is defined as the void dimension in the $\langle 111 \rangle$ direction and U, V and Y define the degree of truncation in the $\langle 110 \rangle$ for the various views shown.

Void volumes in fcc alloys

Void volumes (V) for voids in fcc materials over the full range of observed truncation have been calculated and compared with volumes computed from the three major directions cubed: V/W^3 , V/X^3 and V/Z^3 . These values are plotted in figure 3 which shows the volume factor as a function of truncation parameter where 0 truncation corresponds to cubic truncation and 1.0 to octahedral truncation. Also shown is the value $\pi/6$, which corresponds to the volume factor for a spherical void. The zero truncation values shown agree with published values. ³⁻⁵ From figure 3, it can be seen that if one measures the apparent void size in the $\langle 100 \rangle$ direction, W, and uses the cubed value as the void volume, the volume estimated for cubic voids would be very large and the volume estimated for octahedral voids very small compared with that for a spherical void. Only at a truncation factor of 0.65 would the **correct** volume be obtained.



38711-018.4

Figure 1. Void Shapes in Face Centered Cubic Alloys a) Octohedron, b) Tetrakaldecahedron, and c) Cube.

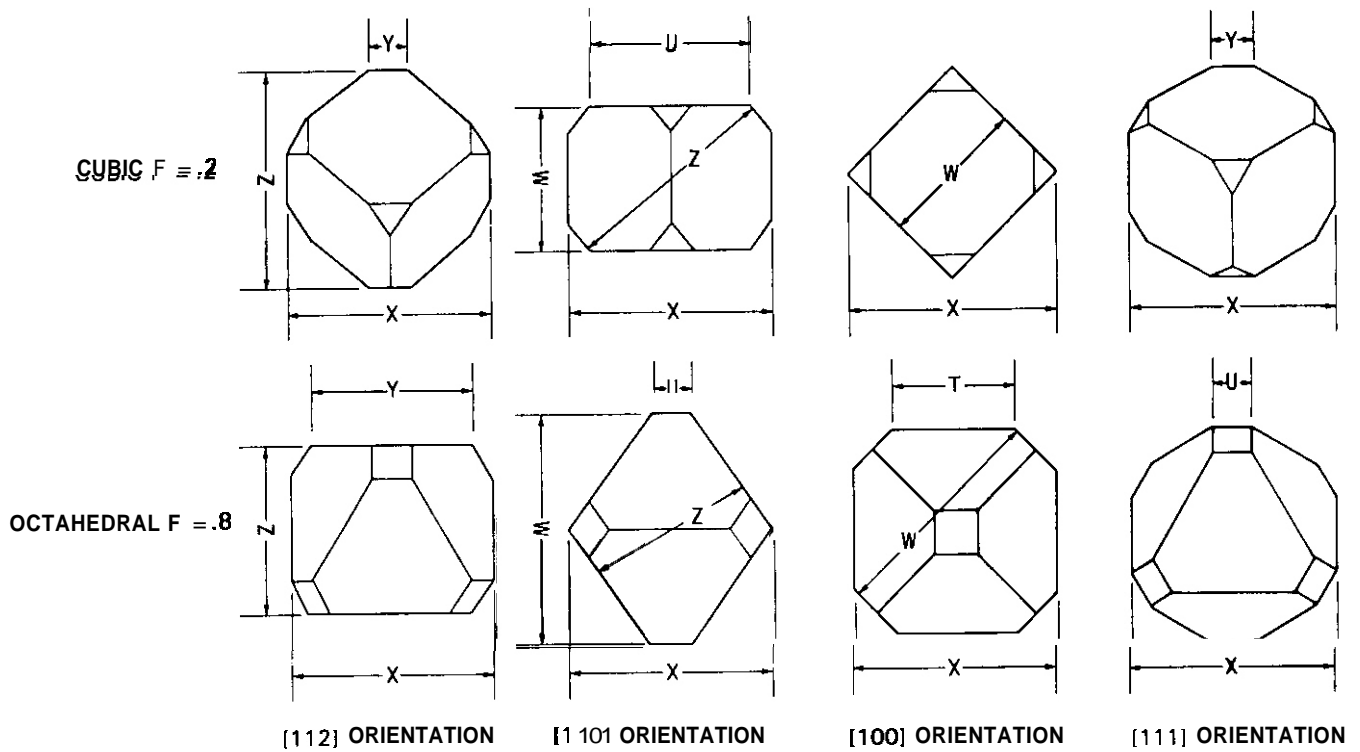


Figure 2. Apparent Shape in Truncated Cubic and Octahedral Voids for Various Crystal Orientations: [112], [110], [100] and [111].

Similarly, if one measures the apparent void size in the $\langle 111 \rangle$ direction, Z , and uses as the void volume, the cubed value, the volume estimate for octahedral voids will be very large and the volume estimate for cubic voids would be very small. Volume determinations based on $\langle 110 \rangle$ measurements, X , provide the smallest variation in volume factor over the full range of possible truncations. Therefore, the most accurate procedure for measuring voids in fcc alloys which cover a wide range of truncation parameters is to use $\langle 110 \rangle$ measurements cubed and multiplied by an average volume factor covering the range of truncation observed.

Void shapes in ferritic alloys

The case for voids in ferritic alloys is more complicated because three basic void shapes have been identified: octahedral, cubic and dodecahedral. Figure 4 provides comparison of these void shapes. The upper figures show cube, octahedron and dodecahedron respectively and the lower figures show those morphologies respectively with dodecahedral, cubic and cubic truncations. For the case of octahedral/cubic truncation, the above analysis for voids in fcc alloys applies. The case of cubic/dodecahedral truncation represents an unexplored situation however. The effect of truncation on void shape for the cube/dodecahedron case is shown in Figure 5 giving $[112]$, $[110]$, $[100]$ and $C1111$ void orientations. This figure has been constructed to provide a direct comparison with Figure 2. Surprising similarities are found between these two cases. Note for example that voids with octahedral and dodecahedral shapes are effectively indistinguishable for a $[100]$ orientation and a rotational error will cause great consternation for a $[111]$ orientation. The most effective orientations for assessing the void shape and degree of truncation are the $[112]$ and $[110]$ morphologies.

Void volumes in bcc alloys

Void volumes have been determined over the full range of truncations for the case of cubic/dodecahedral voids and the results ratioed to the cube of the measured void in the three major directions, as was done for the cubic/octahedral case. The results are given in figure 6. Again, the zero truncation values agree with published calculations.³⁻⁵ Large variations in the ratio are again found for measurements in the $\langle 100 \rangle$ direction but in this case measurement in the $\langle 111 \rangle$ direction provides similar variation in volume factor as a function of truncation as does the $\langle 110 \rangle$ case but at a lower volume factor. In both cases, there is a factor of two between the extreme cases and the same functional dependence applies. Therefore the most accurate procedure for measuring voids in ferritic alloys with cubic/dodecahedral truncation which cover a wide range of truncation is to select the more convenient measurement direction of either $\langle 110 \rangle$ or $\langle 111 \rangle$ and use the cube of that value multiplied by an average of the appropriate volume factor covering the range of observed truncation.

Choice of crystal orientation

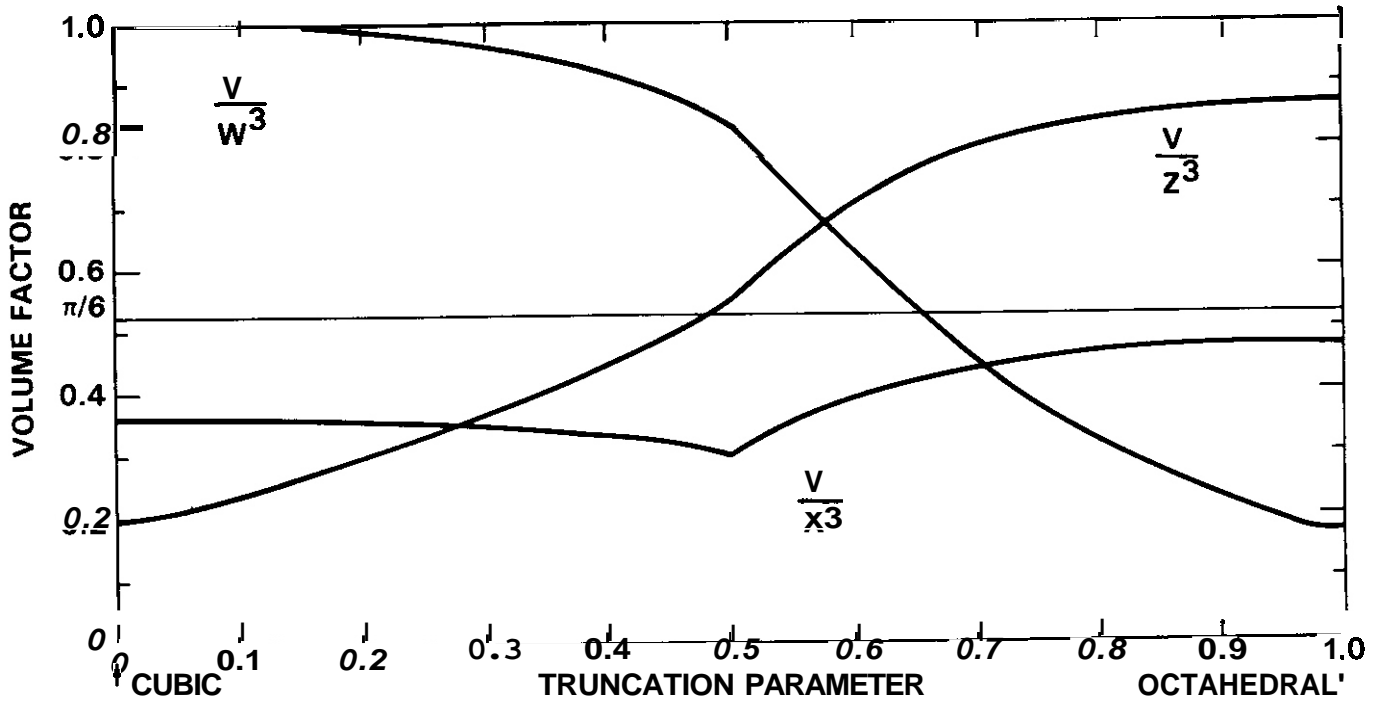
Comparison of Figures 2 and 5 reveals that for voids in $[100]$ orientation, morphology (dodecahedral versus octahedral) is very difficult to assess. Also, if the cube directions are not well known, differentiation between cubic and dodecahedral or octahedral morphology is difficult to determine. Similar problems arise for voids in $C1111$ orientation when the $\langle 110 \rangle$ direction is not well known. However, there is sufficient variation in void shape as a function of morphology or either $[112]$ or $[110]$ orientations. Therefore, optimized measurement procedures should encourage void imaging within 10 degrees of $[112]$ or $[110]$ orientations.

Recommended measurement procedure

The recommended procedure for swelling determination from transmission electron micrographs can be summarized as follows. Choose a crystal orientation within 10 degrees of either $[112]$ or $[110]$. Determine the void morphology and the range of variation in truncation by visual inspection. Figures 7 and 8 have been prepared in order to simplify this procedure. Select an appropriate measurement direction, most likely $\langle 110 \rangle$, and determine a suitable average volume factor. Compute the void volume as the cube of the measurement times the average volume factor. Report the void diameter as the equivalent sphere diameter (cube root of void volume divided by $\pi/6$). This procedure can be simplified if the truncated shape is known whereupon a wide range of crystal orientations is available for measuring well-defined size parameters. In practice, a single average shape parameter usually gives uncertainties of $<20\%$ in void volume determinations, and this uncertainty can be reduced arbitrarily by considering the voids by groups with different shapes.

CONCLUSIONS

A study of the relationship between void shape as seen on electron micrographs and void volume has been made in order to develop more accurate swelling determination procedures without sacrificing the efficiency of measuring a single parameter for each void. Volume factors have been determined as a function of degree of truncation both for octahedral/cubic truncation, pertinent to austenitic and ferritic alloys, and for dodecahedral/cubic truncation pertinent to ferritic alloys. It is shown that when a range of truncation occurs in a group of voids of interest, the accuracy in volume determination can be improved by measuring the voids in the $\langle 110 \rangle$ direction and using the appropriate average volume factor for the range of truncation encountered. For ferritic alloys with dodecahedral/cubic truncation, measurement in the $\langle 111 \rangle$ direction provides equivalent accuracy.



38711-018.3

Figure 3. Volume Factor Parameter as a Function of Truncation Parameter for Cubic/Octahedral Voids. The Parameters W, X and Z are Defined in Figure 2.

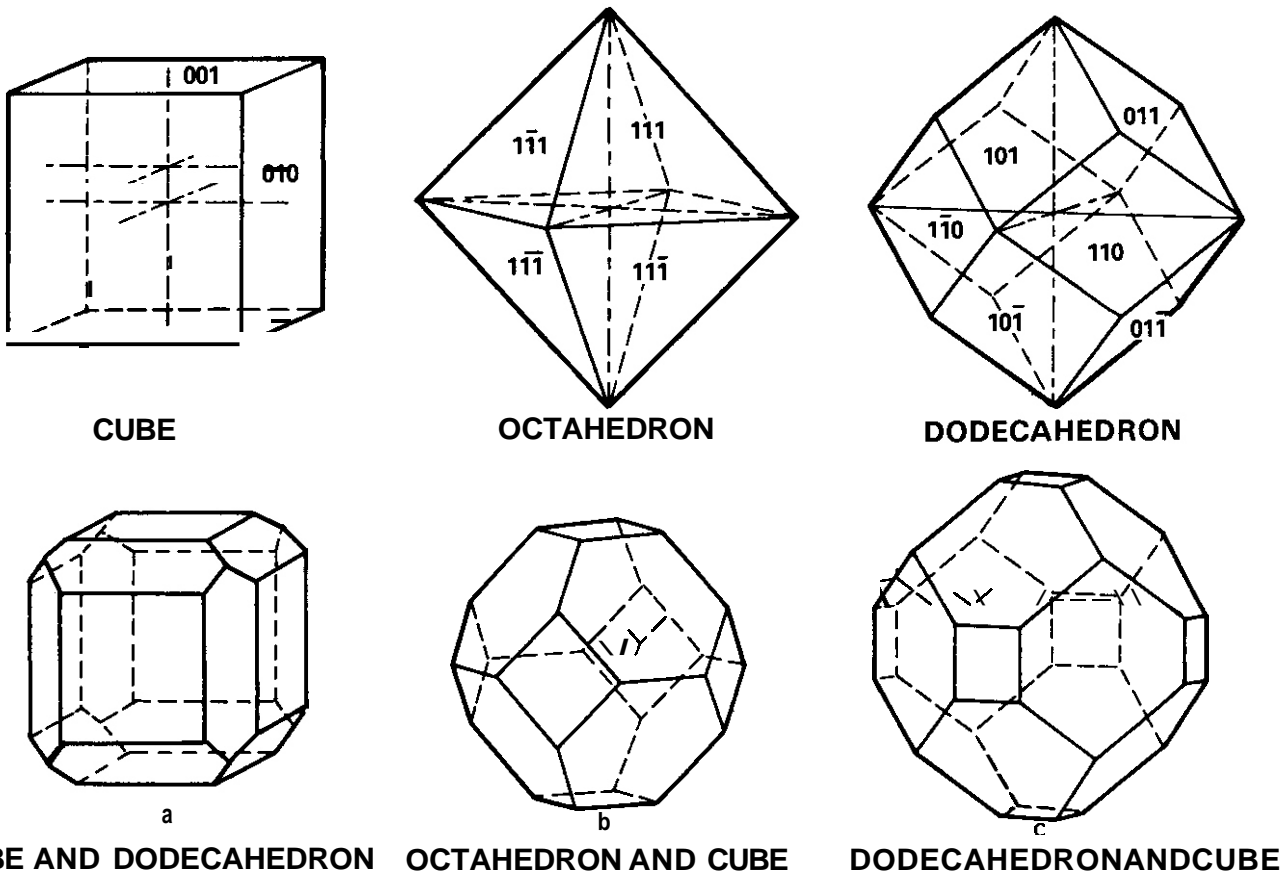
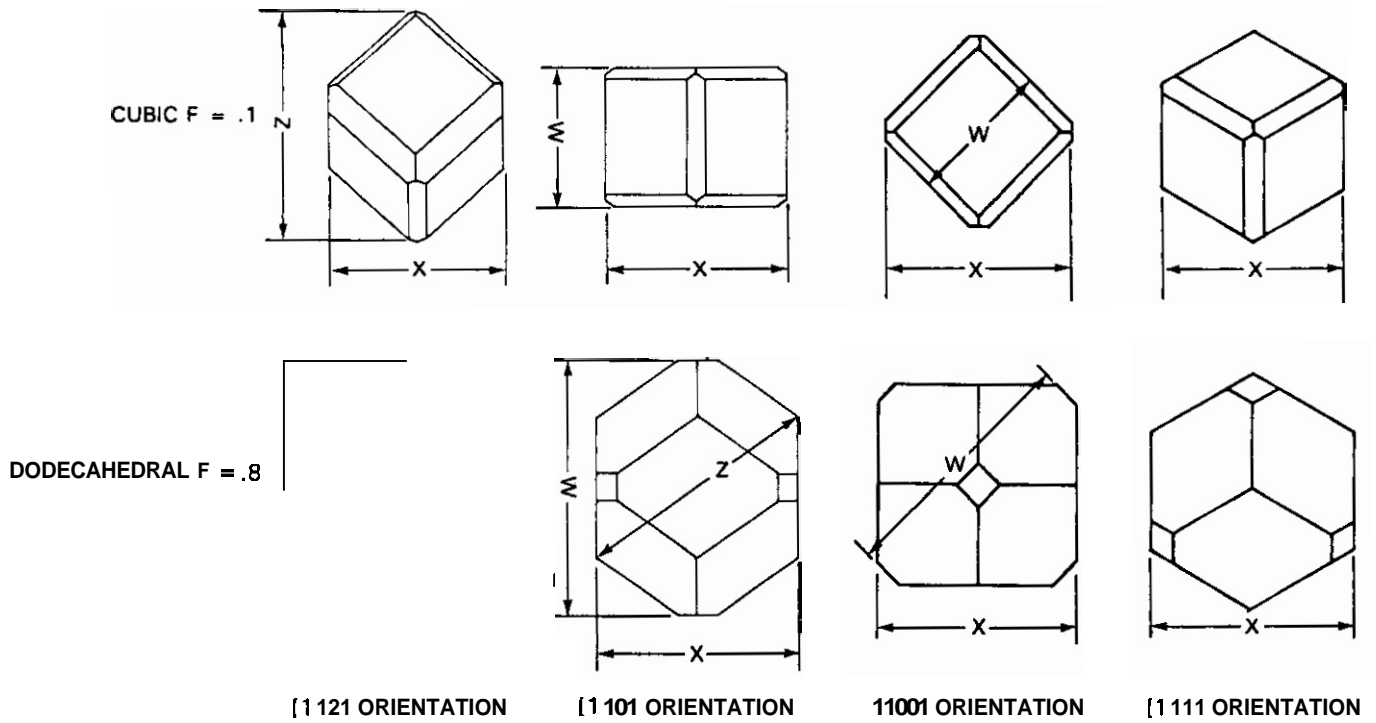
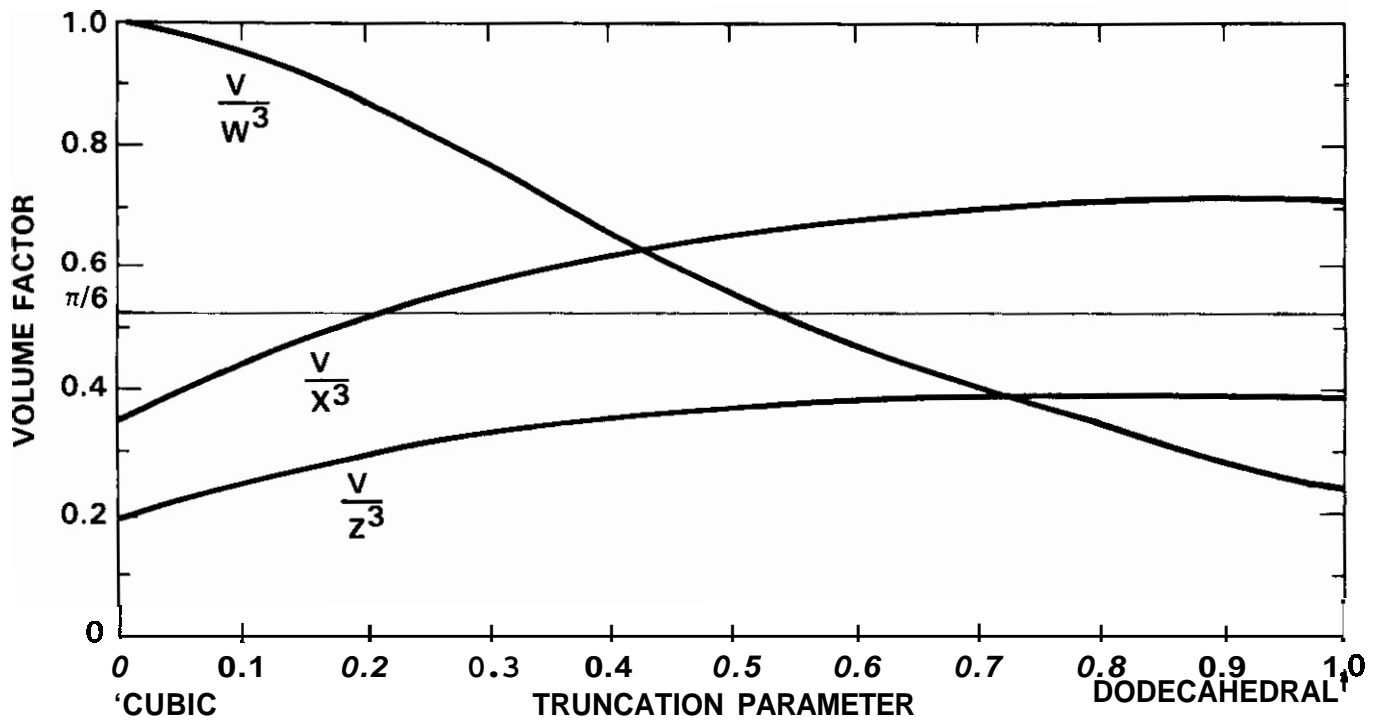


Figure 4. Void Shapes in Ferritic Alloys: a) Cube. b) Octahedron and c) Dodecahedron both Untruncated and Truncated.



38711-018.6

Figure 5. Apparent Shape in Truncated Cubic and Dodecahedral Voids for Various Crystal Orientations: [112], [110], [100] and [111].



38711-018.7

Figure 6. Volume Factor Parameter as a Function of Truncation Parameter for Cubic/Dodecahedral Voids. The Parameters W, X and Z are Defined in Figure 5.

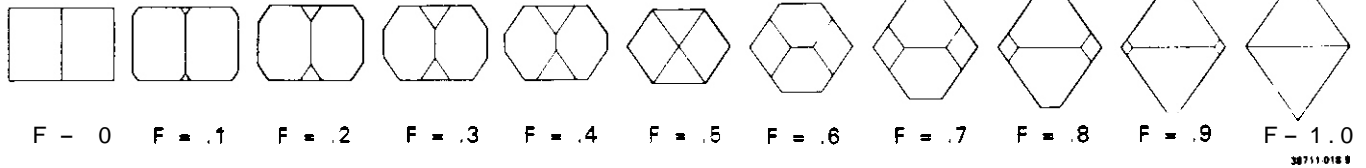
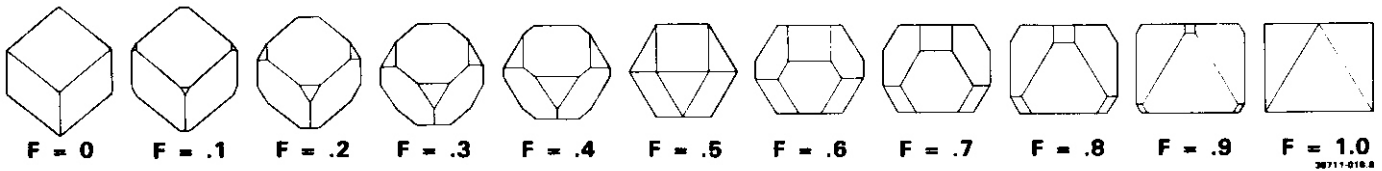
CUBIC VOIDS 11101 ORIENTATION**OCTAHEDRAL VOIDS [1 101] ORIENTATION****CUBIC VOIDS 11121 ORIENTATION****OCTAHEDRAL VOIDS 11121 ORIENTATION**

Figure 7. Examples of Cubic/Octahedral Voids in [110] and [112] Orientation as a Function of Truncation Parameter.

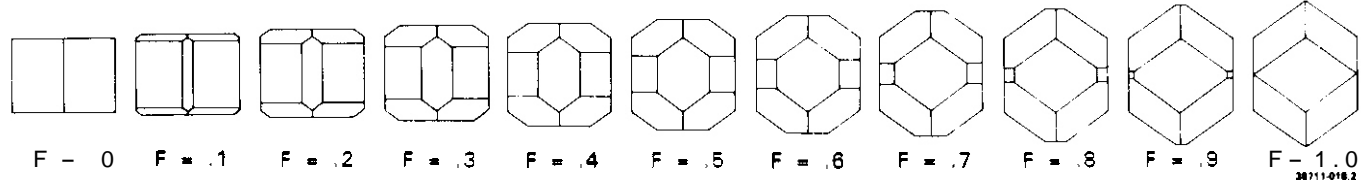
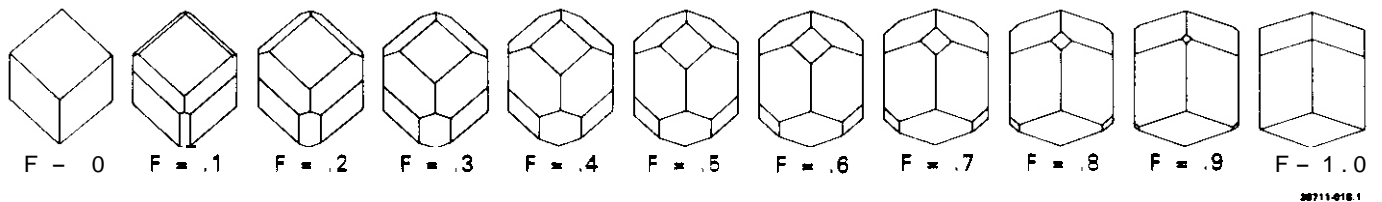
CUBIC VOIDS [1 101] ORIENTATION**DODECAHEDRAL VOIDS [1 101] ORIENTATION****CUBIC VOIDS [1 121] ORIENTATION****DODECAHEDRAL VOIDS [1 121] ORIENTATION**

Figure 8. Examples of Cubic/Dodecahedral Voids in [110] and [112] Orientation as a Function of Truncation Parameter.

FUTURE WORK

No further work is planned.

REFERENCES

1. See for example J.L. Brimhall, H.E. Kissinger and G.L. Kulcinski. "The Effect of Temperature on Void Formation in Irradiated Pure and Impure Metals." in Radiation-Induced Voids in Metals J.W. Corbett and L.C. Ianniello. eds., CONF-710601 (1972) p. 338 and D.S. Gelles. "Solute segregation to Point-Defect Sinks in Neutron Irradiated Nimonic PE16," J. Nucl. Mater. V. 83 (1979) p. 200.
2. D.S. Gelles, "Effects of Substitutional Alloying Elements on Microstructural Evolution in Neutron Irradiated Fe-10Cr," Fusion Reactor Materials Semiannual Progress Report for the Period Ending September 30, 1986, DOE/ER-0313/1, p. 144.
3. H.F. Kaiser, "The Estimation of Inter-granular Surfaces and Volumes in Metals." Metals & Alloys, 9 (1938) p. 23.
4. E.E. Underwood, "Surface Area and Length in Volume," in Quantitative Microscopy, R.T. DeHoff and F.N. Rhines, eds., (McGraw Hill Book Company. N.Y.) p. 77.
5. E.E. Underwood, Quantitative Stereology, (Addison-Wesley Publishing Company. Reading, MA) p. 80.

DETERMINATION OF THE BIAS FACTOR BY THE MOMENTS SOLUTION TO THE FOKKER-PLANCK EQUATION
N. M. Ghoniem (University of California, Los Angeles)

OBJECTIVE

The objective of this work is to develop a theoretically based experimental technique for a direct determination of the interstitial loop bias factor.

SUMMARY

An important parameter in the rate theory of swelling is the dislocation loop bias factor, Z_i^d , which is a measure of the rate of interstitial atom absorption relative to vacancy absorption at interstitial loops. The Fokker-Planck (F-P) equation is used to describe interstitial loop evolution, with a kinetic nucleation current boundary condition at di-interstitial atomic clusters. The majority of loop nucleation is shown to be finished after one milli-dpa, which allows the shape of the loop distribution function to be governed mainly by the drift (F) and dispersion (D) functions in the F-P equation. Since collision cascades contribute significantly to D, their effects must be suppressed by using low-energy ions or high-energy electrons to produce spatially homogeneous atomic displacements. Under these conditions, both F and D are shown to be proportional to the square root of the number of atoms in a loop. The proportionality parameters depend on material and irradiation conditions, and are linearly proportional to Z_i^d . The ratio F/D, can be used in a unique way to determine Z_i^d without the usual complications of uncertainties in material and irradiation conditions. This is shown to constitute an internal variable measurement of the bias factor.

PROGRESS AND STATUS

Introduction

Interstitial loops form by atomic clustering of self-interstitials during irradiation. Once a small cluster of a few interstitial atoms form, a strain field is set around the atomic cluster. The strain field results in a preferential attraction of interstitials over vacancies. Swelling by vacancy agglomeration into cavities is a consequence of this biasing effect of interstitial loops. Of course, other factors control the magnitude of swelling rate, such as the presence of gas atoms, point-defect recombination centers, and other microstructural features (e.g., dislocation network and precipitates). However, dislocation loop bias towards interstitials remains as an important ingredient determining the swelling rate.

Important as it is, no experimental method has ever been proposed to measure the loop bias factor in a direct way. Rate theory has been pursued during the past two decades to predict the swelling rates of various metals and alloys.¹⁻³ The large number of parameters used in the theory of swelling makes the unique determination of each one uncertain. It is sometimes possible, as is shown in this paper, to discover an experimental method that allows the unique determination of a specific parameter. The method is based on the analysis of the interstitial loop microstructure evolution using a moments solution to the F-P equation.

Systems of non-linear ordinary differential equations have been used (e.g., Ghoniem⁴) to represent the concentrations of hierarchies of atomic clusters of increasing size. Solutions of these systems of equations are not possible without mathematical or numerical approximations. For example, grouping methods, where a group of equations are assigned the same reaction rate, have been introduced by Kiritani⁵ and Hayns.⁶ In the study of multi-state kinetic transitions, the hierarchy of rate equations is replaced by an equivalent parabolic partial differential equation. The resulting continuum equation is of the F-P type, and it describes a process of particle diffusion in a general drift field. This approach was used to describe vacancy and interstitial atom clustering by Sprague, Russell and Choi,⁷ Wolfer, Mansur and Sprague,⁸ and also by Hall.⁹

Recent efforts by Gurol,¹⁰ Clement and Wood,¹¹ Trinkaus,¹² Kitajima and co-workers,¹³⁻¹⁶ and by Ghoniem¹⁷ have considered an interpretation of atomic clustering within the framework of statistical mechanics. The F-P equation resulting from Taylor series expansion of rate equations⁷⁻⁹ is a representation of stochastic size fluctuations produced by single atomic additions. When collision cascades are to be considered, size fluctuations in atomic clusters are dramatically influenced by direct cascade collisions as well as by point-defect arrival produced from random cascades.

An equation for the nucleation of interstitial loops is developed in Section 2 which is used as one of the kinetic boundary conditions necessary for the solution of the F-P equation. A moments solution to the one-dimensional (1-D) interstitial-loop F-P equation for general drift

and diffusion functions is given in Section 3. This is followed by a specific example illustrating a suggested procedure for determining the loop bias factor.

Theory and moments solution

The concentrations of single vacancies, C_v , and single self-interstitial atoms, C_i , are given by^{4,17}

$$\frac{dC_v}{dt} = \epsilon P - \alpha C_v C_i - \lambda_v C_v \quad , \quad (1)$$

$$\frac{dC_i}{dt} = \epsilon P + K_v(2) C_v C_{2i} + 2\delta C_{2i} - 2K_i(1) C_i^2 - \alpha C_v C_i - K_i(2) C_i C_{2i} - \lambda_i C_i \quad , \quad (2)$$

where P is the point-defect generation rate, ϵ the cascade survival efficiency, α the recombination rate, δ the di-interstitial dissociation rate, and $K_a^D(x)$ is the reaction rate constant between a mobile specie (a) and an immobile specie (b) containing x atoms. The parameters λ_i and λ_v represent effective loss rates to homogeneous microstructural sinks. Equations for λ_i and λ_v and details of all equations in this paper are given by Choniem.¹⁷ In Eqs. (1) and (2), vacancy clustering is assumed to be negligible during the early phase of loop formation, and a trapping model is used to describe the effective migration of self-interstitials.

The formation of di-interstitial clusters is governed by the following rate equation for their concentration, C_{2i} :

$$\frac{dC_{2i}}{dt} = J_1 - J_2 \quad (3)$$

The di-interstitial cluster is assumed to be mobile with a homogeneous absorption rate λ_{2i} . J_1 is the net rate of transformation of single interstitial atoms to di-interstitial clusters and J_2 is the net rate of transformation to tri- or tetra-clusters. These are given by

$$J_1 = K_i(1) C_i^2 - \delta C_{2i} - \lambda_{2i} C_{2i} \quad , \quad (4)$$

$$J_2 = K_i(2) C_i C_{2i} + 2 K_{2i}(2) C_{2i}^2 \quad . \quad (5)$$

When the di-interstitial binding energy is large ($E_{2i}^b \approx 1$ eV), the backward reaction rates of clusters with $x \geq 2$ are negligibly small.¹⁸ The di-interstitial cluster can then be assumed to be the critical nucleus and transformations to tri- or tetra-clusters are therefore nearly irreversible. With this simplification, Eq. (3) can be written as

$$\frac{\partial C^*}{\partial t} \approx \frac{\partial}{\partial x} J^* \quad ,$$

Eq. (6) is coincident with the F-P equation for any size, x , given by

$$\frac{\partial C}{\partial t} + \vec{v} \cdot \vec{J} = 0 \quad , \quad (7)$$

where the operator $\vec{v} = \partial/\partial x$ in this case, and the current \vec{J} is only the 1-D component:

$$\vec{J} = J_x = FC \cdot \frac{\partial}{\partial x} (DC) \quad , \quad (8)$$

where F is a drift function and D a dispersion function. F and D can be estimated to include size fluctuations caused by single atomic transitions, and fluctuations due to cascades (e.g., Kitajima.^{13,15})

The zeroeth moment of Eq. (7) is obtained by direct integration over the distribution function, $C(x)$, between x^* and the maximum loop size. Therefore

$$\frac{dN}{dt} = J^* \quad , \quad (9)$$

where
$$N(t) = \int_{x^*}^{\infty} C(x) dx \quad , \quad (10)$$

N is the total loop density. The boundary and initial conditions for the unique solution of Eq. (7) are given by

$$\left. \begin{aligned} C(\infty, t) &= 0 \\ C(x^*, t) &= C_{2i}(t) = C^*(t) \\ C(x, 0) &= 0 \end{aligned} \right\} \quad (11)$$

$$M_r = (x \cdot \langle x \rangle)^r \quad (13)$$

where the symbol $\langle \rangle$ is used for averaging **over** the distribution function we obtain

$$\frac{d\langle x \rangle}{dt} = F\langle x \rangle + \sum_{k=2}^{\infty} \frac{M_k}{k!} \frac{d^k}{dx^k} (F\langle x \rangle) \Big|_{\langle x \rangle} + \frac{D^* C^*}{N} - (\langle x \rangle - x^*) \frac{d}{dt} (\ln N) \quad (14)$$

Performing similar manipulations, and starting from Eq. (13), we obtain the following equation for the r th moment:

$$\begin{aligned} \frac{dM_r}{dt} &= r(r-1) \left\{ \delta_{r2} D\langle x \rangle + \sum_{k=2}^{\infty} \frac{M_k}{k!} \frac{d^k}{dx^k} \left[(x - \langle x \rangle)^{r-2} D \right] \Big|_{\langle x \rangle} \right\} \\ &- r \left\{ \delta_{r1} F\langle x \rangle + \sum_{k=2}^{\infty} \frac{M_k}{k!} \frac{d^k}{dx^k} \left[(x - \langle x \rangle)^{r-1} F \right] \Big|_{\langle x \rangle} \right. \\ &\left. - M_{r-1} \left[F\langle x \rangle + \sum_{k=2}^{\infty} \frac{M_k}{k!} \frac{d^k}{dx^k} F \Big|_{\langle x \rangle} \right] \right\} \\ &+ r \frac{D^* C^*}{N} \left\{ \left[(x^* - \langle x \rangle)^{r-1} - M_{r-1} \right] + \frac{d}{dt} (\ln N) \right. \\ &\left. \times \left[(x^* - \langle x \rangle)^r - M_r - r M_{r-1} (x^* - \langle x \rangle) \right] \right\}, \quad r=2,3,4, \end{aligned} \quad (15)$$

δ_{rM} is the usual Dirac-Delta function. The terms enclosed by the first pair of brackets are ascribed to the effects of the dependence of D on x ; those enclosed by the second pair represent distortions in the distribution functions caused by $F(x)$; the third pair give the effects of continuous nucleation on the distribution function. **The** distribution function, $C(x, t)$, can be formally reconstructed, albeit not uniquely, from the infinite set of moments.

Determination of the loop bias factor

The F-P equation for loops is linear, hence the distribution function can be represented by a small set of moment equations. For the purposes of this paper, the moments above the **second** are assumed to be zero. If experimental conditions are such that cascade-induced size fluctuations are negligible, the functions F and D can be ~~shown~~ to be of the form

$$F(x) = \frac{4}{3} \left(\frac{3}{\pi} \right)^{1/4} [\alpha Z_1^{\ell} C_i + \gamma - \beta C_v] x^{1/2} = g_1 x^{1/2}, \quad (16)$$

$$D = D_s(x) = \frac{2}{3} \left(\frac{3}{\pi} \right)^{1/4} [\alpha Z_1^{\ell} C_i + \gamma + \beta C_v] x^{1/2} = g_2 x^{1/2}, \quad (17)$$

where γ is the vacancy emission rate from the loop, α and β are impingement frequencies for interstitials and vacancies, respectively, and Z_1^{ℓ} is the interstitial loop bias factor.

Detailed numerical computations, presented in Section 4, show that nucleation effects on the moments are small and that quasi-static conditions are quickly established. Inserting $F(x)$ and $D(x)$ given by Eqs. (16) and (17) into the truncated series [Eqs. (14) and (15)] gives

$$\frac{d\langle x \rangle}{dM_2} = \frac{g_1[1 - (\lambda/2)]}{2g_2\{1 - \lambda[1 - (2g_1/g_2)]\}} \quad (18)$$

where $A = M_2/(2\langle x \rangle)^2 \ll 1$ and $g_1/g_2 \ll 1$. At temperatures where vacancy emission is negligible, an approximate quasi-static relationship can be obtained from Eq. (18), i.e.,

$$\frac{d\langle x \rangle}{dM_2} = \frac{Z_1^l - Z}{Z_1^l + Z} = S \quad (19)$$

Eq. (19) indicates that eventually the rate of increase of the average loop size will be proportional to the rate of increase of the second moment. The proportionality constant, S , is thus an internal variable and is independent of all material and irradiation conditions. It should, in principle, be insensitive to defect parameters and can therefore be used to determine Z_1^l . The bias factor for straight dislocations, Z , is close to unity. Hence, once S is experimentally measured, Z_1^l is given by

$$Z_1^l = \frac{1 + S}{1 - S} \quad (20)$$

The bias factor Z_1^l has been assumed to be size-independent for simplicity. However, its functional dependence on x can be introduced without loss of generality.

To apply Eq. (20), the loop size distribution must be experimentally determined at various irradiation doses. Since the set of equations [Eqs. (14) and (15)] is truncated beyond the second moment, it can be shown¹⁷ that the size distribution is approximately given by a propagating Gaussian function of the form

$$C(x, t) \approx \frac{N}{(2\pi M_2)^{1/2}} \exp\left[-\frac{(x - \langle x \rangle)^2}{2 M_2}\right] \quad (21)$$

The loop number density, N , is shown by many experiments to be nearly independent of the irradiation dose after an initial short transient period. The experimental procedure is to fit the data to Eq. (21), thus determining $\langle x \rangle$ and M_2 as functions of dpa. Taking an average value of S can thus uniquely determine Z_1^l without having to know any of the defect parameters!

Numerical application of the theory

It seems unlikely that the exact experimental conditions prescribed in this paper have been attempted. Therefore, the theory is applied to available experiments where cascade fluctuations exist. Comparisons between theory and existing experiments are made through parametric variations of defect properties. Hall and Potter¹⁹ carried out a series of experiments where 3 MeV N^{58+} ions were used to bombard Ni-Si samples at 465°C. Their calculated peak displacement rate is 3×10^{-4} dpa/s. Eqs. (1) through (3), (9), and (14) through (15) were numerically integrated, assuming that all moments higher than the second are approximately zero. A standard set of defect parameters was used throughout the calculations¹⁹ only the effective migration energy of interstitials (E_i^m), the di-interstitial binding energy (E_{2i}^b), the interstitial loop bias factor (Z_1^l), and the ratio of cascade to single transition dispersion functions (D_c/D_s) were treated as free parameters.

An increase in Z_1^l results in a corresponding increase in the average loop diameter (Fig. 1); however, the total loop density is insensitive to variations in the bias factor (Fig. 2). This interesting feature can be used in determining groups of defect parameters by comparison to kinetic data on loop densities. When E_{2i}^b is increased, the loop density increases dramatically (Fig. 3) while the average loop size decreases because of the near-conservation of total number of atoms in loops. Variations in E_i^m produce opposite effects on the loop density and average size.

Comparison with the experimental data of Hall and Potter¹⁹ shows that single-atom transitions may be an underestimation of the magnitude of stochastic fluctuations, and that collision cascade effects must be included. For statistically uncorrelated events, we take $D = D_c + D_s$, where D_c is for cascade fluctuations, and D_s for single-atom transitions. By a parametric increase of D_c/D_s , a closer comparison with experiments is obtained, as shown in Fig. 4. The effects of collision cascades on the re-solution of loops and on point-defect concentrations can be calculated in a manner similar to that done by Kitajima¹³⁻¹⁶ and Chou and Ghoniem.^{20,21}

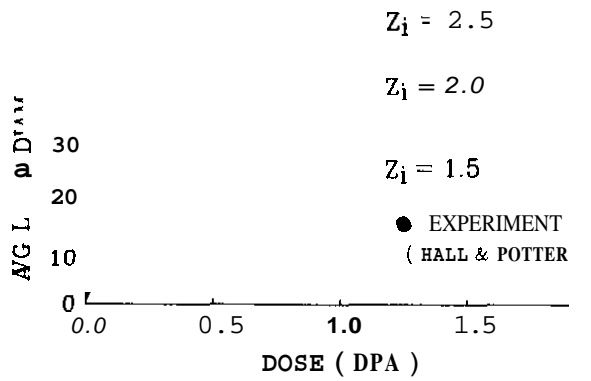


Fig. 1. Effect of Z_i^a on the avg diam of interstitial loops [theory=—; experiment=•].

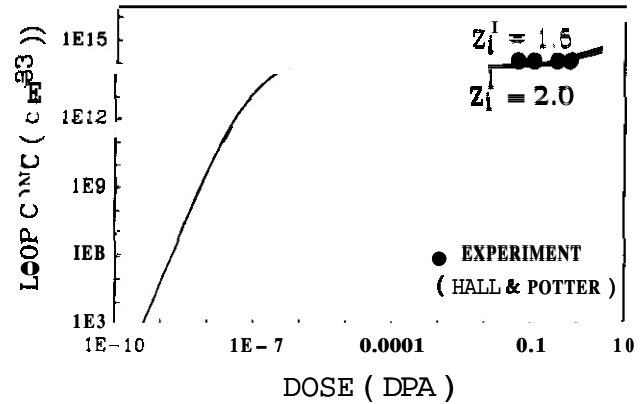


Fig. 2. Effect of Z_i^e on the interstitial loop density [theory=—; experiment=•].

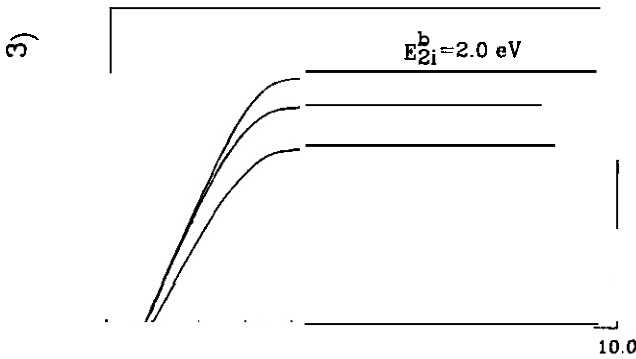


Fig. 3. Effect of E_{2i}^b on the interstitial loop density [theory=—; experiment=•].

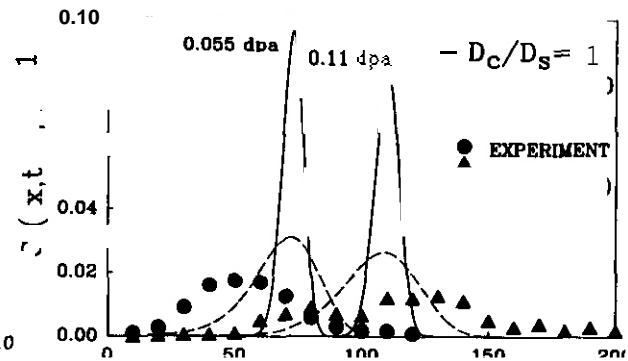


Fig. 4. Effect of cascade-induced fluctuations on the loop distribution function (Hall and Potter).

Conclusions

The moments solution to the F-P equation, with transient nucleation conditions, can be effectively used to measure the interstitial loop bias factor Z_i^l . To take advantage of this solution, a number of experimental conditions must be satisfied. These conditions are: (1) Irradiation doses beyond a short transient period of ~ 0.001 dpa and before loop unfauling at several dpa's; (2) Sample temperatures low enough such that vacancy emission from loops does not significantly contribute to their growth (i.e., below $450^\circ\text{--}500^\circ\text{C}$ for Ni at a dose rate of $\geq 10^{-4}$ dps/s); (3) The use of low energy ions or high energy electrons to minimize the effects of collision cascades on the fluctuations in loop sizes during their growth.

Comparison between the current theory and experiments show that a combination of the parameters Z_i^l , E_{2i}^b , E_{1i}^M , and D_c/D_s can produce all observed features of interstitial loop evolution in ion-irradiated nickel. The best set of these parameters is found to be $Z_i^l = 2$, $E_{2i}^b = 1.19$ eV, $E_{1i}^M = 0.55$ eV, and $D_c/D_s = 60$.

Acknowledgement

This work was supported by the U. S. Department of Energy, Office of Fusion Energy. Grant #DE-FG03-84ER52110, with UCLA.

References

1. R. Bulough, B. Eyre, and R. Krlshan, Proc. Roy. Soc. London **A346** (1975) 81.
N. M. Ghoniem and G. L. Kulcinski, Radiat. Eff. **41** (1979) 81.
L. K. Mansur, Nucl. Technol. **40** (1978) 5.
4. N. M. Ghoniem, J. Nucl. Mater. **89** (2&3) (1980) 359.
5. M. Kiritani, J. Phys. Soc. Jpn. **35** (1973) 95.
6. M. R. Hayns, J. Nucl. Mater. **36** (1975) 267.
7. J. A. Sprague, K. C. Russell, and Y. H. Choi, in: Proc. Conf. on Fundamental Aspects of Radiation Damage in Metals, Eds. M. T. Robinson and F. W. Young. CONF-751006-P2 (Nat. Tech. Info. Serv., Springfield, VA 1975) p. 1181.
8. W. G. Wolfer, L. K. Mansur, and J. A. Sprague, in: Radiation Effects in Breeder Reactor Structural Materials, Eds. M. Blisberg and J. W. Bennet, (AIME. NY, 1977) p. 841.
9. B. O. Hall, J. Nucl. Mater. **91** (1980) 63.
10. H. Guröl, Trans. Am. Nucl. Soc. **27** (1977) 264.
11. C. F. Clement and M. H. Wood, J. Nucl. Mater. **89** (1980) 1.
12. H. Trinkaus, Phys. Rev. **B27** (1983) 7372.
13. K. Kitajima, N. Yoshida, and E. Kuramoto, J. Nucl. Mater. **103&104** (1981) 1355.
14. K. Kitajima, E. Kuramoto, and N. Yoshida, J. Nucl. Mater. **108&109** (1982) 267.
15. K. Kitajima, J. Nucl. Mater. **133&134** (1985) 64.
16. K. Kitajima, Y. Akashi, and E. Kuramoto, J. Nucl. Mater. **133&134** (1985) 486.
17. N. M. Ghoniem, "Stochastic Theory of Diffusional Planar Atomic Clustering," University of California, Los Angeles Report **UCLA-ENG-8730/PPG-1093** (1987).
18. N. M. Ghoniem and D. D. Cho, Phys. Status Solidi **A54** (1979) 171.
19. B. O. Hall and D. I. Potter, in: Effects of Radiation on structural Materials, Eds. J. A. Sprague and D. Kramer. ASTM-STP-683 (American Society for Testing and Materials. Philadelphia, 1979) p. 32.
20. S. P. Chou and N. M. Ghoniem, Nucl. Inst. Meth. **B9** (1985) 209.
21. S. P. Chou and N. M. Ghoniem, J. Nucl. Mater. **117** (1983) 55

FUTURE WORK

Future efforts will be directed towards an investigation of the effects of higher order moment truncation on the obtained results.

BINARY COLLISION MONTE CARLO SIMULATIONS OF CASCADES IN POLYATOMIC CERAMICS - N. M. Ghoniem and S. P. Chou (University of California, Los Angeles)

OBJECTIVE

The objective of this work is to examine two aspects of fusion neutron cascades in polyatomic ceramic materials, cascade morphology and cascade stoichiometry relative to the matrix stoichiometry. These aspects are applied to SPINEL ($MgAl_2O_4$).

SUMMARY

The binary collision approximation (BCA) is used in a Monte Carlo (MC) study of high-energy collision-cascade creation in SPINEL, the model ceramic insulator. The study focuses on two aspects of cascade generation: cascade morphology and cascade stoichiometry. In the high-energy regime, typical of fusion neutrons, cascades show a tree-like morphology. To a large degree, instantaneous recombination occurs in the "stem" part of the cascade because of the closer separation of vacancy-interstitial pairs. Following this recombination phase, fusion neutron cascades tend to result in Frenkel pairs distributed on the "branches" of the tree in a zone extending over 100 to 200 nm. The stoichiometry of displacements within the cascade is found to be substantially different from bulk stoichiometry, and is dependent upon the energy and type of primary knock-on atom (PKA).

PROGRESS AND STATUS

Introduction

Polyatomic ceramic insulators are proposed for a variety of applications in fusion reactors (e.g., waveguides and dielectric windows). They must be used to insulate between conductor turns in normal magnet designs. In some designs, such as the reversed field pinch concept, insulating materials are used as part of the design of the conducting shell (or first wall), and also in the breeding blanket of the system. The use in this case stems from the need to reduce toroidally continuous eddy currents that are detrimental to plasma stability. The magnetohydrodynamic (MHD) force opposing liquid-metal fluid flow in self-cooled liquid-metal blankets is by far the most serious design problem in these types of blankets. Without insulated walls, the MHD force can be more than an order of magnitude larger than the same design with wall insulation. Ceramic insulators are therefore proposed in applications ranging from low neutron flux/low temperature conditions to locations near the first wall where both the neutron flux and temperature are high,

SPINEL, $MgAl_2O_4$, appears to be a primary candidate for these applications. Irradiation to 2×10^{26} n/m² at 1100 K produced no void swelling of single-crystal $MgAl_2O_4$.² Low swelling rates of SPINEL have also been observed by a number of investigators.^{3,4} The strength of SPINEL has been observed to be enhanced by neutron irradiation.⁵ The lack of significant swelling under irradiation has been attributed to the nature of generation, recombination, and agglomeration of defects.⁵ In particular, the lack of helium bubble nuclei and the absence of dislocation loops which are precursors to swelling were proposed as reasons for swelling resistance. In an experimental study by Buckley,⁶ 1-MeV electron irradiation of SPINEL samples preimplanted with 1000 ppm helium atoms resulted in no observable loops or voids after 10 to 30 dpa. Coghlan et al.⁷ presented results of swelling saturation for relatively low neutron fluences ($\approx 2 \times 10^{22}$ n/m², $E > 0.1$ MeV) at 50°C. They attributed the swelling saturation to interstitial-type defects leading to point-defect recombination and swelling saturation.

To understand the nature of displacement damage in SPINEL, the primary damage state must be carefully analyzed. The complex crystal structure of the material renders simple extrapolations from metallic alloys unreliable. Using a continuous slowing-down theory of collision cascades, Parkin and Coulter⁸⁻¹⁰ showed that the structure of cascades in polyatomic materials is quite complex, and that cascade stoichiometry generally differs from that of the bulk material. Itoh and Tanimura¹¹ indicated that in addition to the production of Frenkel pairs by the atomic displacement process, stable point defects can be produced from self-trapped excitons in certain materials.

In a fusion neutron environment, PKAs may be initiated with kinetic energies of several MeV. A molecular dynamics (MD) simulation of cascades generated by such high energy PKAs is still not achievable. On the other hand, analytical approximations of cascade behavior may not accurately represent important details. In this paper, we present results of cascade simulations using the BCA, and we illustrate the nature of the primary damage generation by a study of cascade morphology and stoichiometry in SPINEL.

Monte Carlo Model

The Monte Carlo transport code, TRIPOS, (Transport of Ions in Polyatomic Multi-Layer Solids) has been developed for the analysis of bulk and surface primary damage.^{12,13} The code is based on the binary collision approximation for an amorphous solid. The free path between collisions, and the nuclear energy transfer and scattering angle are accurately calculated by using the power-law cross sections and a new method for general interatomic potentials.¹⁴

The free path between collisions is estimated from the probability of interaction using the total Scattering cross section. In the BCA, a moving atom can interact with only one medium atom at a time. The total interaction cross section is first calculated as a linear stoichiometric sum of individual atomic cross sections. The type of recoil is determined randomly from the ratio of an atomic cross section to the total cross section. The mass and energy dependence of cross sections dictate, therefore, the stoichiometry of recoils within the cascade.

Recoils travel between these discrete collisions losing part of their energy continuously to electrons. In one version of the code, TRIPOS-E,¹⁵ energy transfers to electrons are discretely treated and distributions of electron-hole (e-h) pairs along ion tracks are calculated. Nevertheless, we do not include here the effects of exciton relaxation on stable Frenkel-pair generation as proposed by Itoh and Tanimura.¹¹ Approximately 10 keV of electronic energy deposition is required for the production of a Frenkel pair through this mechanism, which indicates that the contributions of these events to total displacements are negligible in a fusion environment. Therefore, the results presented here are limited by the validity of the BCA, and no attempt is made to include mechanisms of low energy dissipation. The basic problem we confront is that the size of a fusion collision cascade results in computational irreducibility if a direct MD approach is used, particularly when electronic excitational energy transfers are simulated. The BCA is deemed to give a reasonable description of the general features of collision cascades. The contributions of low-energy correlated-collision sequences were observed in several MD calculations.^{16,17} However, Hou and Todorov¹⁸ noted the similarity of cascade simulation results between BCA and MD approaches.

The value of the minimum displacement threshold, E_d , of individual atoms in a polyatomic material has an important influence on cascade properties. This value is difficult to measure, and a wide range is reported in the literature. Crawford¹⁹ used the values of 86 eV for Mg, 77 eV for Al, and 130 eV for O. Summers et al.²⁰ reported a value of 59 eV for O, while Matzke²¹ used a similar value of 56 eV for O. Itoh and Tanimura¹¹ indicated that E_d for Al and Mg is in the range 18 to 30 eV. In view of these uncertainties, we show the effects of displacement threshold energy by studying two illustrative conditions.

Discussion of results

Near the first wall of a fusion reactor, the majority of neutrons will have energies in the range of 14 MeV. These neutrons generate PKAs with average energy on the order of several MeV. Fig. 1 shows a three-dimensional simulation of anion and cation interstitials, before instantaneous recombination, in a collision cascade initiated by a 2-MeV-oxygen PKA. The cascade exhibits a "tree-like" morphology, with a relatively long "stem" and self-similar "branches" towards the top. When instantaneous recombination is allowed within a recombination radius of 1.0 nm, the stem portion undergoes more complete recombination events than the branches (Fig. 2). Coulombic energy transfers tend to favor recoils with small energies, thus resulting in point defects at close separation. As the PKA slows down, large-angle collisions occur with higher probabilities and point defects are produced at larger separations.

Cascade stoichiometry is described by the chemical composition of a molecular displacement. At the end of the cascade propagation phase, the cascade is said to be stoichiometric if atoms are displaced at the ratios 1:2:4 for Mg, Al, and O, respectively. A non-stoichiometric cascade is represented by the formula $MgAl_{2+x}O_{4+y}$, where x is the excess aluminum displacements and y is the excess oxygen displacements, as normalized to Mg displacements. The first set of calculations are performed for equal E_d ; 56 eV for Al, Mg, and O. Fig. 3 shows the dependence of the excess stoichiometry, x , on the PKA energy, where cascades are initiated with O, Mg, or AP PKAs. At high PKA energies, cascade mixing eliminates the dependence of y on the PKA type. At lower energies, however, PKAs distribute their energy preferentially to the corresponding lattice atoms. This x is positive for AP PKA and negative for both O and Mg PKAs. It is to be noted here that even with a species-independent displacement threshold, differences in mass and charge appear in the interaction cross sections. Energy partitioning favors displacement of higher mass atoms.

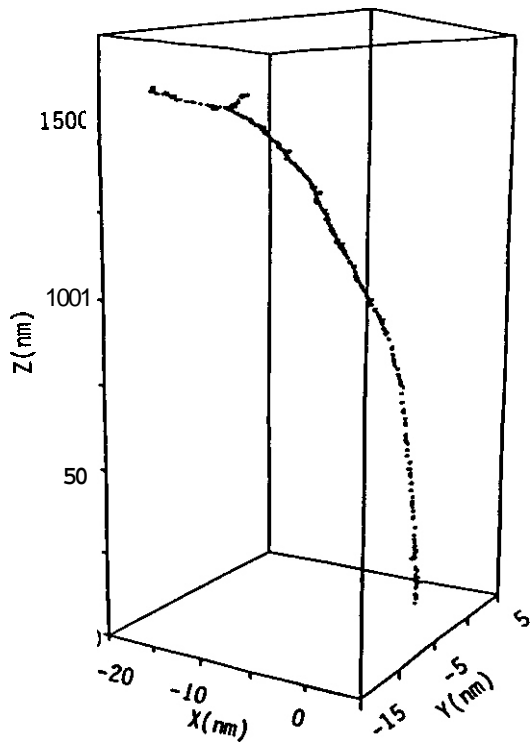


Fig. 1. Fusion neutron cascade simulation (3-D) in SPINEL (PKA=0, 2-MeV energy).

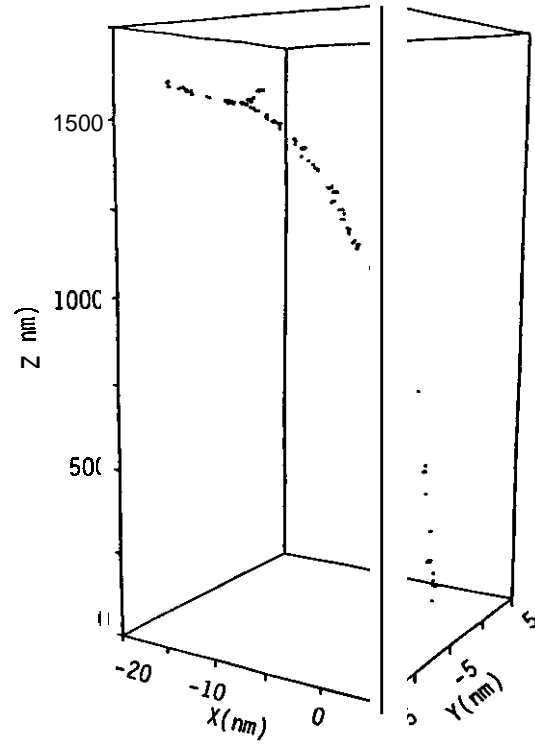


Fig. 2. Cascade simulation (3-D) in SPINEL allowing for instantaneous recombination (PKA=0, 2-MeV energy).

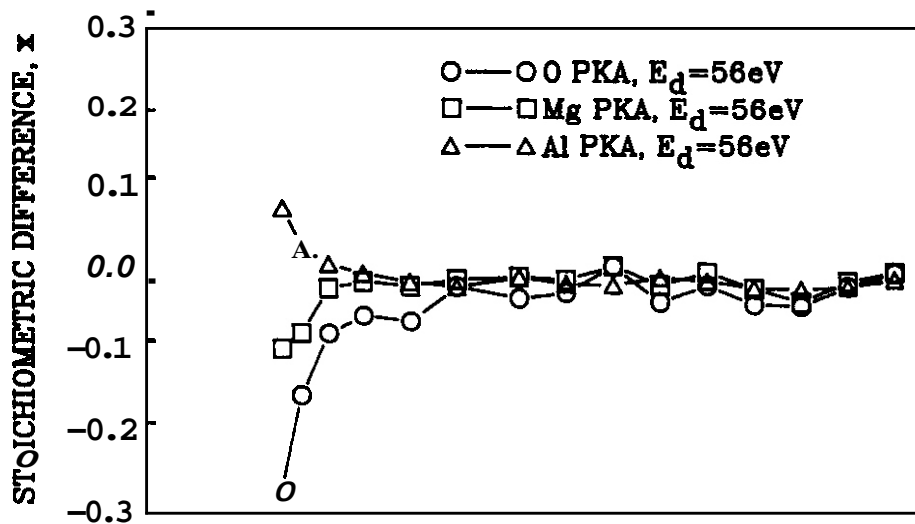


Fig. 4 shows the total number of displacements per PKA as a function of the PKA energy. The solid lines with heavy dots result from analytical calculations based on Lindhard's theory for comparison. The displacement threshold is taken as 56 eV for the three elements. It is interesting to note that over a wide range of PKA energies, the number of displacements per PKA is independent of the PKA type. This behavior extends up to PKA energies in the range of 30 to 100 keV. Above this range, electronic energy loss is PKA dependent. Larger PKA masses tend to produce more displacements, as is well known from simple analytical cascade theories.

The next set of calculations are performed for displacement threshold energies that are energy dependent. E_d is taken as 56 eV for oxygen, and it is assumed to be 18 eV for both Al and Mg. Fig. 5 shows the stoichiometric excess (or deficiency), y , as a function of the PKA energy. The higher oxygen displacement threshold results in a dramatic decrease in y over the entire PKA energy range. In the lower range of PKA energies, a significant fraction of recoils is generated with energies close to the oxygen displacement threshold. Cascades propagate entirely on the cation sublattices, when PKAs are initiated with a few hundred eV.

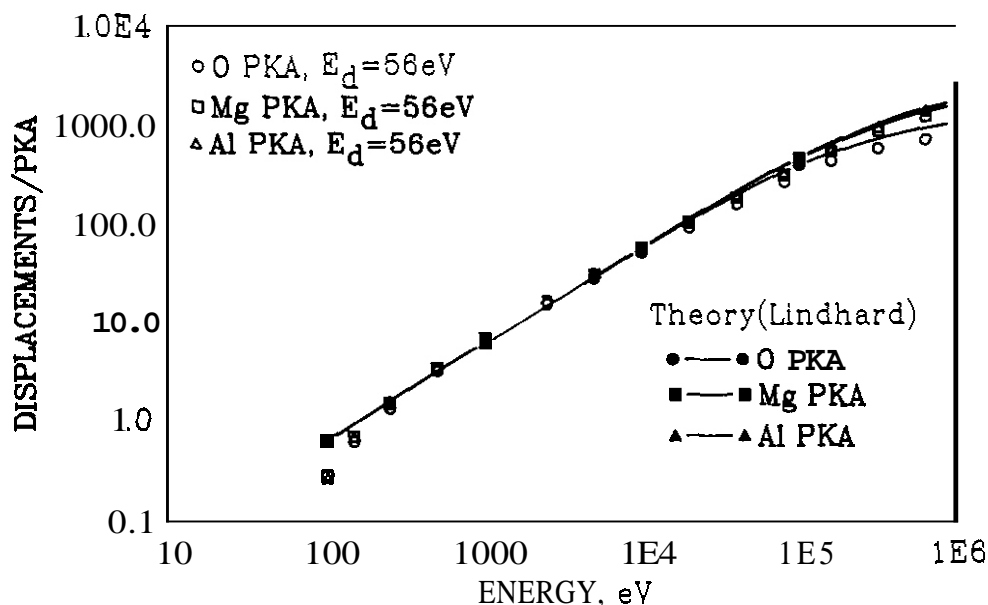


Fig. 4. Comparison between TRIPOS results and Lindhard's theory for the total no. of displacements per PKA.

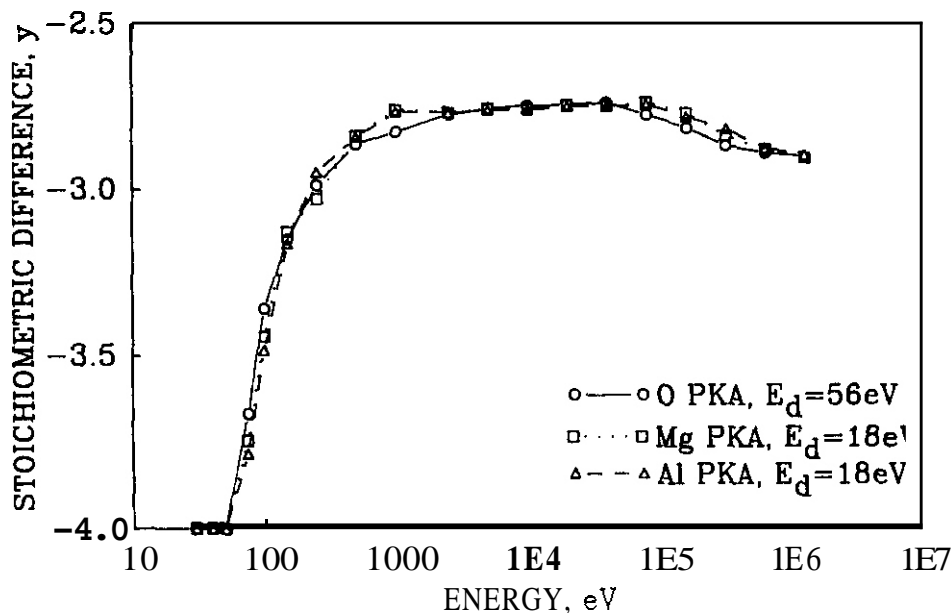


Fig. 5. Oxygen stoichiometric excess (y) in SPINEL as a function of various PKA energies.

Since the mass difference between Al and Mg is not very large, and since they both have the same displacement threshold, the magnitude of x is much smaller than y . Our calculations indicate that the dependence on PKA type is not significant, particularly at high PKA energies. In the low energy regime, however, a slight preferential energy coupling with Mg is noticed: hence negative values of x are observed. For the same conditions, the number of displacements per PKA is shown as a function of the PKA energy in Fig. 6. Calculations using Lindhard's theory with an effective displacement threshold are also shown for comparison with Monte Carlo results. The major fraction of knock-ons have low energies, close to the displacement threshold. Our analytical theory of cascade slowing down in an infinite medium indicates that the number of knock-ons, N , is energy dependent in the form^{2,3}

$$N(E) \sim \frac{1}{E^{5/2}} \quad (1)$$

Eq. (1) is based on a hard-sphere scattering cross section which usually overestimates low energy transfers. Empirically, an effective value of the displacement threshold is therefore suggested as

$$E_d^e = \left[\sum_i s_i E_{d,i}^{-n} \right]^{-1/n} \quad (2)$$

where E_d^e is the effective displacement threshold and s_i is the stoichiometry of the element with a displacement threshold $E_{d,i}$. Application of Lindhard's theory, together with Eq. (2), shows good agreement with MC calculations for $n = 1$ (Fig. 6). In all MC calculations, the relative uncertainty in y is $<3\%$. For x , however, the absolute uncertainty is <0.005 for high energy cases and is <0.02 for low energy cases.

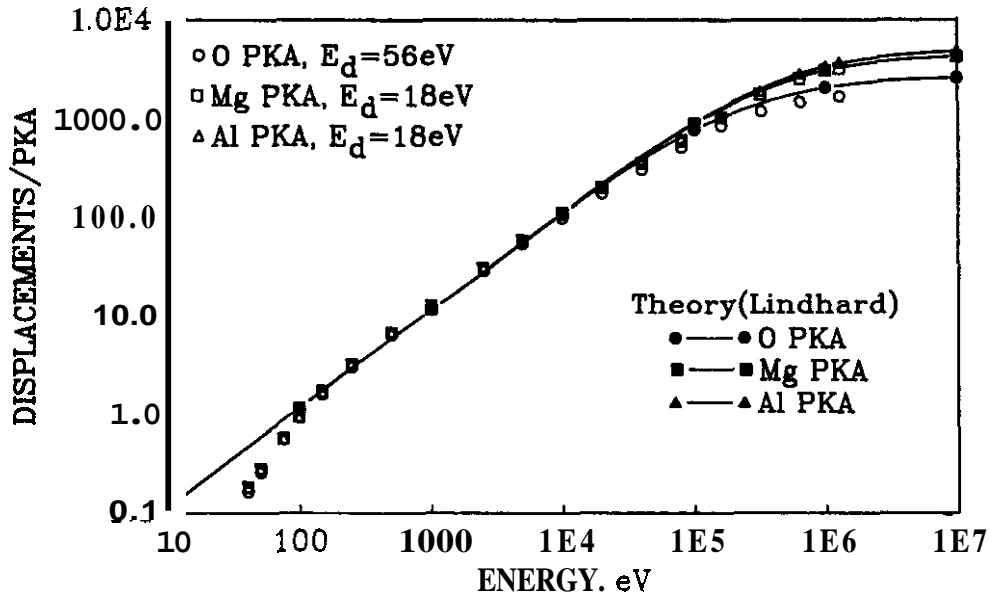


Fig. 6. Comparison between TRIPOS results and Lindhard's theory for the total no. of displacements (E_d weighting is used).

Conclusions

Displacement cascade morphology in polyatomic ionic solids in a fusion environment is similar to previous simulations of cascades in a metallic structure. The BCA shows large cascade dimensions (on the order of 100 to 200 nm). Cascades resulting from high energy neutrons show a tree-like morphology with more instantaneous recombination occurring in the stem part of the cascade. The stoichiometry of cascades in SPINEL shows a large oxygen deficiency. This oxygen displacement deficiency is even more dramatic if a higher O displacement threshold is used. Cascade mixing eliminates the dependence of this deficiency on the type of PKA for high energy. Low energy PKAs tend to favor coupling with like atoms, thus introducing O displacement deficiency when AP or Mg PKAs are used for the case of equal displacement thresholds. If it is experimentally confirmed that the displacement threshold for O is higher than for Al and Mg, experimental simulation with ions, electrons, or fission neutrons may therefore be inaccurate representations of fusion neutron cascades. The total number of displacements in a ceramic can be calculated by Lindhard's theory, provided that an effective displacement threshold is used. This effective value is obtained by applying the suggested Eq. (2).

Acknowledgements

The authors would like to acknowledge the support of the U.S. Department of Energy, Office of Fusion Energy, Grant #DE-FC03-84ER52110, with UCIA.

References

1. F. Najmabadi et al., "The Titan Reversed-Field Pinch Fusion Reactor Study," Scoping Phase Report. University of California, Los Angeles Report No. UCLA-PPG-1100 (1987).
2. F. W. Clinard, Jr., G. F. Hurley and L. W. Hobbs, J. Nucl. Mater. **108&109** (1982) 655.
3. G. F. Hurley, J. C. Kennedy, F. W. Clinard, Jr., R. A. Youngman and W. R. McDonell, J. Nucl. Mater. **103&104** (1981) 761.
4. F. W. Clinard, Jr., G. F. Hurley, R. A. Youngman and L. W. Hobbs, J. Nucl. Mater. **133&134** (1985) 701.
5. L. W. Hobbs and F. W. Clinard, Jr., J. de Phys. **41** (1980) C6-232.
6. S. N. Buckley, J. Nucl. Mater. **141-143** (1986) 387.
7. W. A. Coghlan, F. W. Clinard, Jr., N. Itoh and L. R. Greenwood, J. Nucl. Mater. **141-143** (1986) 382.
8. D. M. Parkin and C. A. Coulter, J. Nucl. Mater. **101** (1981) 261.
9. C. A. Coulter and D. M. Parkin, J. Nucl. Mater. **85&86** (1979) 611.
10. D. M. Parkin and C. A. Coulter, J. Nucl. Mater. **103&104** (1981) 1315.
11. N. Itoh and K. Tanimura, Radiat. Eff. **98** (1986) 269.
12. P. Chou and N. Ghoniem, J. Nucl. Mater. **117** (1983) 55.
13. P. Chou and N. Ghoniem, Nucl. Instru. and Meth. **328** (1987) 175.
14. J. Blanchard, P. Chou and N. Ghoniem, J. Appl. Phys. **61** (1987) 3120.
15. R. C. Martin and N. M. Ghoniem, "Monte Carlo Simulation of Coupled Ion-Electron Transport in Semiconductors," Phys. Status Solidi. **A104**(2) (1987).
16. J. B. Gibson, A. N. Goland, M. Milgram and G. H. Vineyard, Phys. Rev. **120** (1960) 1229.
17. C. Erginsoy, G. H. Vineyard and A. Englert, Phys. Rev. **A133** (1965) 535.
18. M. Hou and S. Todorov, Phys. Lett. **A91** (1982) 461.
19. J. H. Crawford, Jr., Adv. Phys. **17** (1968) 93.
20. G. P. Summers, G. S. White, K. H. Lee and J. H. Crawford, Phys. Rev. **321** (1980) 2575.
21. H. Matzke, Radiat. Eff. **64** (1982) 3.
22. J. Lindhard, V. Nielsen, M. Scharff and P. V. Thomsen, K. Dan. Vidensk. Selsk. Mat. Fys. Medd. **33**, 10 (1963).
23. P. S. Chou and N. M. Ghoniem, Nucl. Instru. and Meth. **B9** (1985) 209.

FUTURE WORK

Future work will focus on the investigation of the cascade structure at low energies

6. DEVELOPMENT OF STRUCTURAL ALLOYS

6.1 Ferritic Stainless Steels

EFFECTS OF IRRADIATION ON TUNGSTEN STABILIZED MARTENSITIC STEELS - D. S. Gelles (Westinghouse Hanford Company), C. Y. Hsu and T. A. Lechtenberg (G A Technologies, Inc.)

OBJECTIVE

The objective of this work is to determine the applicability of low activation ferritic alloys as fusion reactor structural materials.

SUMMARY

As part of a program to determine the applicability for a fusion first wall of martensitic stainless steel from which critical elements have been removed in order to assure low retained radioactivity 100 years after decommissioning, two alloys have been designed, fabricated, fast neutron irradiated in FFTF and examined by transmission electron microscopy. The two experimental 7 kg heats of tungsten-stabilized martensitic steels had intended levels of 9 and 11% chromium but contain no intentional additions of niobium, molybdenum and nickel. However, the alloys were found to have deviated somewhat from their intended composition. The actual compositions were 1.5 and 10.2 % Cr respectively with 0.02 % C in the latter case. Nonetheless, irradiation response is typical of that in ferritic steels. Conditions examined included irradiation temperatures of 365, 420, 520 and 600°C to doses as high as 34 dpa with small amounts of void swelling found at the two lowest temperatures. It is demonstrated that levels of tungsten on the order of 2 wt% do not result in excessive intermetallic precipitation after irradiation to fluences as high as 7.3×10^{22} n/cm² or 34 dpa over the temperature range 365 to 600°C.

PROGRESS AND STATUS

Introduction

As a part of the U.S. Fusion Structural Materials Program, tungsten stabilized martensitic steels are being developed as potential low activation structural materials¹. Low activation alloys may be defined as alloys from which critical elements have been removed in order to assure low retained radioactivity 100 years after reactor decommissioning. The critical elements for steel are niobium, molybdenum and nickel. The tungsten stabilized martensitic steel design effort has involved what may be termed three different paths: low, intermediate and higher levels of tungsten additions. The present effort examines alloys with nominal tungsten contents of 2.5% the higher level. (All compositions are given in weight percent unless noted.)

There is considerable international interest in tungsten stabilized martensitic steels as low activation structural materials. In the United Kingdom, a large series of alloys is being examined which considers tungsten levels to as high as 3%, carbon levels generally in the range 0.16%, manganese at 0.8%, and chromium varying between 9 and 12%². All but the highest levels of chromium and tungsten are found to be fully martensitic and although the alloy class appears to be somewhat weaker than its commercial alloy counterpart, many of the alloys are serviceable. In Japan, two independent programs are underway. At the National Research Institute for Metals, two series of alloys are being studied, one varying chromium from 2 to 15% at 2% W and 0.1% C and the other varying tungsten to as high as 4% at 9%Cr and 0.1% C³. Dual phase structures were found for the 12 and 15%Cr and for the 4% W alloys. All fully martensitic alloys gave satisfactory tempering and impact fracture response. At Nippon Kokan K.K., a fully martensitic alloy of composition Fe-0.1C-8Cr-2W-0.2V has been developed which provides properties as good as commercial counterparts⁴.

One of the important issues regarding the use of tungsten stabilized martensitic steels for a fusion reactor first wall concerns phase instability and its effect on mechanical properties. In question is what is the optimum level of tungsten? At too high a level of tungsten, precipitation occurs which degrades mechanical properties such as impact resistance. At too low a level, insufficient high temperature strength is obtained. Laves phase forms in tungsten stabilized steels and chi phase has been shown in Fe-Cr-W alloys⁵. The facts that chi phase forms in Fe-Cr-Mo steels following irradiation⁶ and that tungsten-containing chi phase apparently has significantly less tungsten than does the molybdenum-containing chi phase contain molybdenum⁵, suggests that chi phase formation may be detrimental in tungsten stabilized steels used in irradiation environments. Therefore, an examination of the effect of irradiation on the microstructure of tungsten stabilized martensitic steels with high tungsten contents is appropriate.

As part of the US Department of Energy MIP effort, two tungsten stabilized martensitic steels were designed and melted at GA Technologies with nominal tungsten levels at 2.5%, chromium levels at 9 or 11%, carbon at 0.15% and vanadium at 0.3%. Unfortunately, the laboratory heats did not reach the proposed nominal composition. Table 1. The tungsten levels were less than 2% and one of the alloys contained only 0.02% C, making it a duplex delta ferrite and martensite structure rather than a fully martensitic alloy. However, it was felt that an examination of the effect of irradiation on phase stability in these alloys would provide worthwhile insights into the behavior of tungsten stabilized steels as low activation structural steels.

Table 1. The nominal and actual chemical compositions of reduced activation steels in the GA program.

Heat Number		Composition (w/o)					
		C	Cr	W	V	Mn	S
GA3X	nominal	0.15	9	2.5	0.3	--	--
	actual	0.165	7.5	1.95	0.015	0.002	0.005
GA4X	nominal	0.15	11	2.5	0.3	--	--
	actual	0.02	10.2	1.7	0.3	0.011	<0.003

Experimental Procedure

Three 7 kg (15 lb) ingots of two experimental compositions and one control composition of 12Cr-1MoWV were melted and cast in a GCA vacuum induction furnace. The nominal and actual compositions of the experimental tungsten-stabilized low activation alloys are given in Table 1. Following a homogenization treatment of 1100°C for 24 h, the alloys were warm rolled at about 700°C to 0.25 mm sheet. The rolled sheet was heat treated 1 h at 1000°C, water quenched and tempered at 700°C for 1 h. Disk specimens 3 mm in diameter were punched from the thin sheet, each specimen was engraved with a four digit code and specimens were loaded into TEM packets for irradiation beginning with the MOTA 1C test in FFTF. The TEM packets were irradiated in one below-core and three in-core positions, intended to provide irradiation temperatures of 365, 420, 520 and 600°C. The specimen engraving codes and corresponding irradiation conditions are provided in Table 2. Details regarding the 12Cr-1MoWV control alloy specimens, including post irradiation examination, have been reported in reference 8 and experimental procedures used for the present work were identical to those described in reference 8. The microstructure of alloy GA3X has previously been described in references 9 and 10.

Table 2. Irradiation conditions for the GA experimental tungsten-stabilized martensitic steels in MOTA 1C.

Engraving code		Irradiation	Neutron	Displacement
GA3X	GA4X	Temperature	Fluence	Damage
			(n/cm ²)*	
KX07	KX99	365°C	3.03x10 ²²	11.3 dpa
K107	K199	426°C	7.27x10 ²²	33.5 dpa
K407	K499	520°C	7.32x10 ²²	33.8 dpa
Kb07	K699	600°C	7.32x10 ²²	33.8 dpa

• E > 0.1 MeV

Results

Microstructural Examination

The microstructures of GA3X and GA4X were confirmed to be as previously described^{9,10}. In the fully heat treated condition (1000°C/1h/WQ ± 700°C/1h/AC), GA3X was fully martensitic whereas GA4X contained primarily delta ferrite with only a few regions of martensite found. In both cases, grain boundaries and martensite lath boundaries were decorated with M₂₃C₆. Examples of these microstructures as shown by optical metallography using Vilella's etch are given in Fig. 1. Figs. 1a and b show GA3X at low and intermediate magnification respectively, and Figs. 1c and d show similar views of GA4X. Fig. 1c provides a montage showing the variation in microstructure from the edge of a TEM disk to the center. It is apparent that in the center of the disk, the volume fraction of martensite is on the order of 10% whereas at the disk edge the martensite volume fraction increases to about 30%. Heat treatment appears to have resulted in

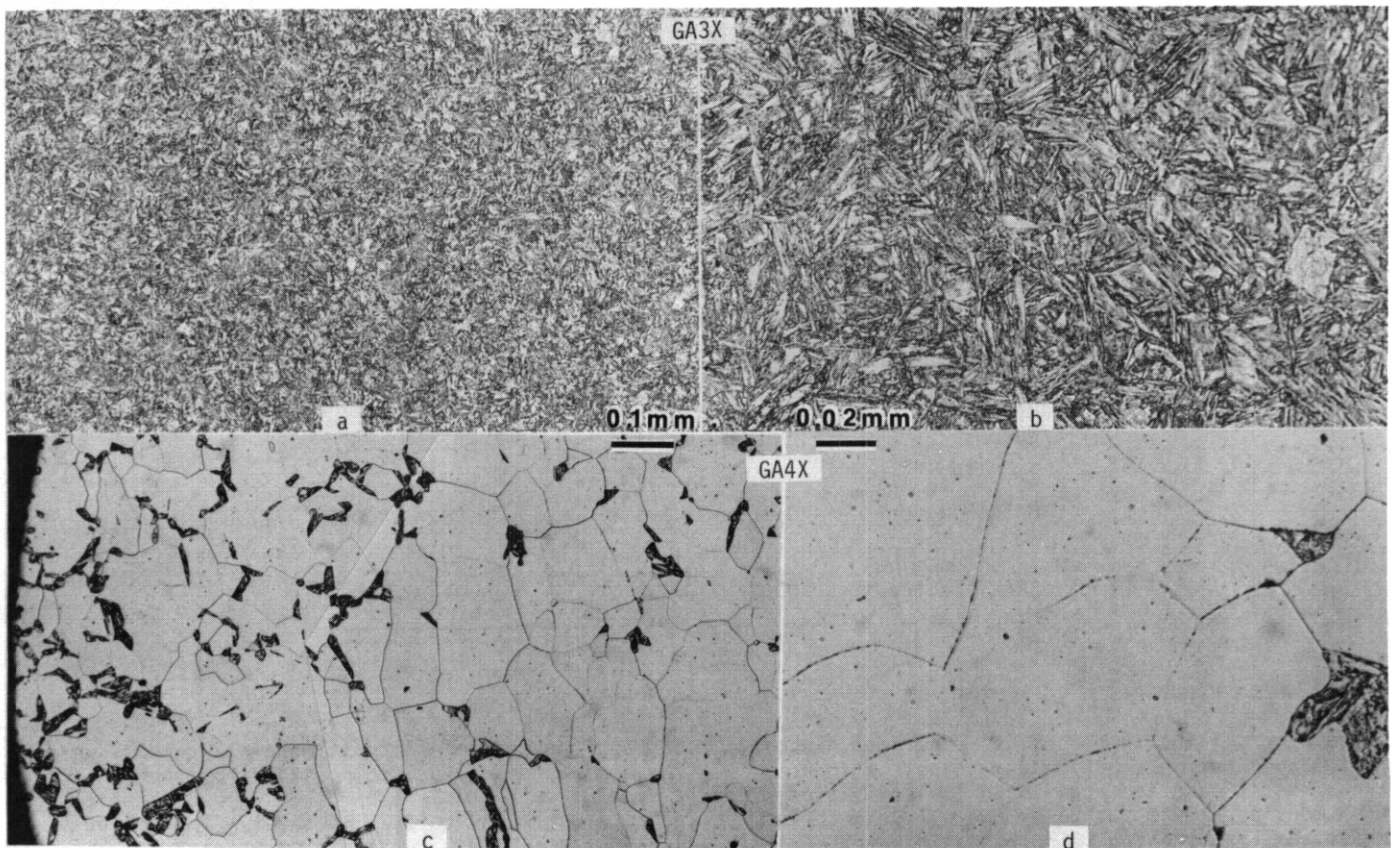


Fig. 1. Microstructures of GMX and GA4X as shown by optical metallography at low and intermediate magnifications.

surface carburization of the specimen. This inhomogeneity is not expected to affect microstructural results on the effect of irradiation on tungsten stabilized martensitic steels because all TEM examinations are restricted to the central portion of the specimen disk, but analytical measurements on carbide particles are based on extraction replicas taken near the surface and are expected to be more representative of a higher carbon containing alloy.

Fig. 2 provides low and intermediate magnification examples using transmission electron microscopy of the preirradiation microstructures of GNX and GA4X. The structures are typical of martensitic and ferritic steels, respectively.

Effects on microstructure due to irradiation were apparent in all specimen conditions examined. Following irradiation at 365 and 420°C, dislocation evolution was found and in each case, at least a few irradiation induced voids were observed. Following irradiation at 520°C, void and dislocation evolution was observed in GA4X and precipitate coarsening was found in GNX. Finally, following irradiation at 600°C, coarsening of both precipitate and martensite lath structures could be demonstrated.

Examples of these microstructures at low magnification are shown in Figs. 3 and 4. Figure 3 provides low magnification comparisons of GNX following irradiation at 365, 420, 520 and 600°C. The martensite lath structure is found to be maintained during irradiation to temperatures as high as 520°C but both the lath and the carbide structures have coarsened following irradiation at 600°C. Fig. 4 shows similar response in GA4X but void development is apparent following irradiation at 420 and 520°C.

The microstructures generated by irradiation at 365°C are shown at higher magnification in Figs. 5 and 6. Fig. 5 gives several imaging conditions for the same area in GMX specimen KX07, (a) in void contrast and (b) through (d) in various dislocation imaging conditions. Fig. 5a shows very few cavities (two or three 13 nm cavities were found in a typical martensite lath) but equiaxed precipitate particles 10 nm in diameter can also be identified. Comparison of the images in T10 and 002 contrast in Figs. 5b and d demonstrates the presence of both $a\langle 100 \rangle$ and $a/2 \langle 111 \rangle$ dislocation loops. Fig. 6 allows comparison of two areas in GA4X specimen KX99. Figs. 6a and b show an area containing both martensite and ferrite with the larger martensite region on the right and the ferrite at the lower left. The martensite contains no voids whereas a moderate density of voids can be identified in the ferrite. The dislocation structure in the martensite includes loops and a tangled dislocation network. In both phases.



Fig. 2. Microstructures of unirradiated GA3X and GA4X as shown by transmission of electron microscopy at low and intermediate magnifications.

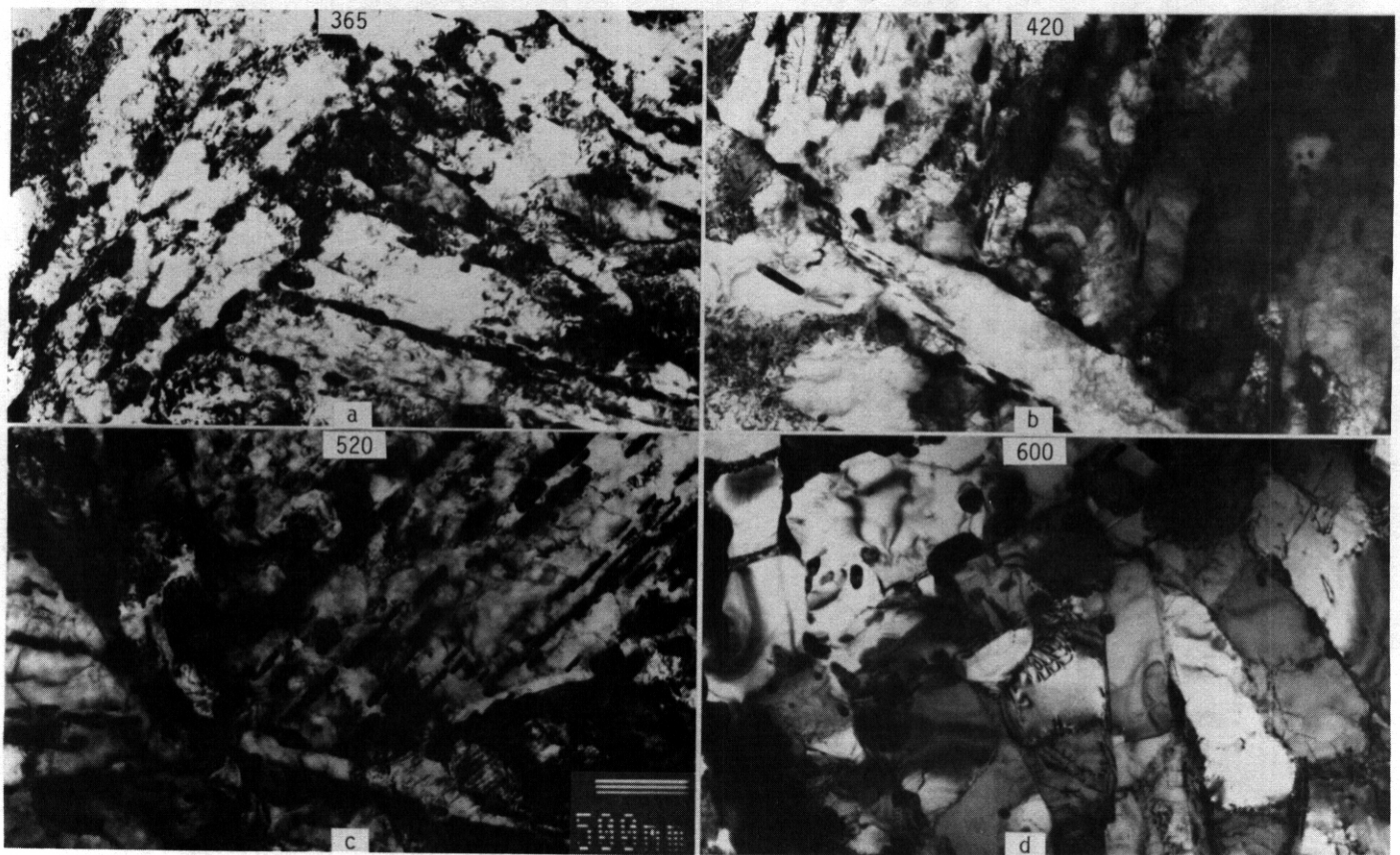


Fig. 3. Effects of irradiation on microstructure as a function of temperature in GA3X.

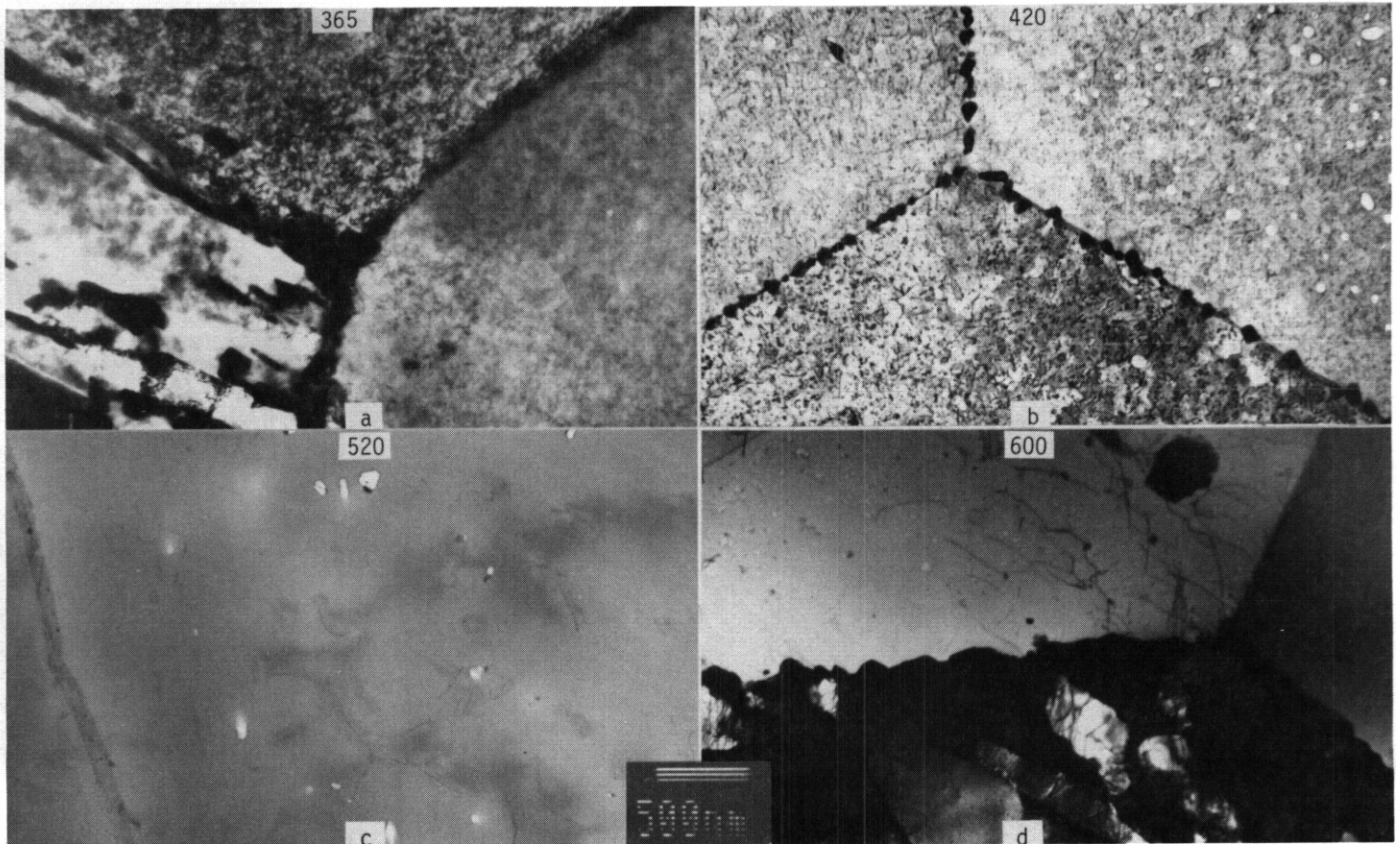


Fig. 4. Effects of irradiation on microstructure as a function of temperature in GA4X.

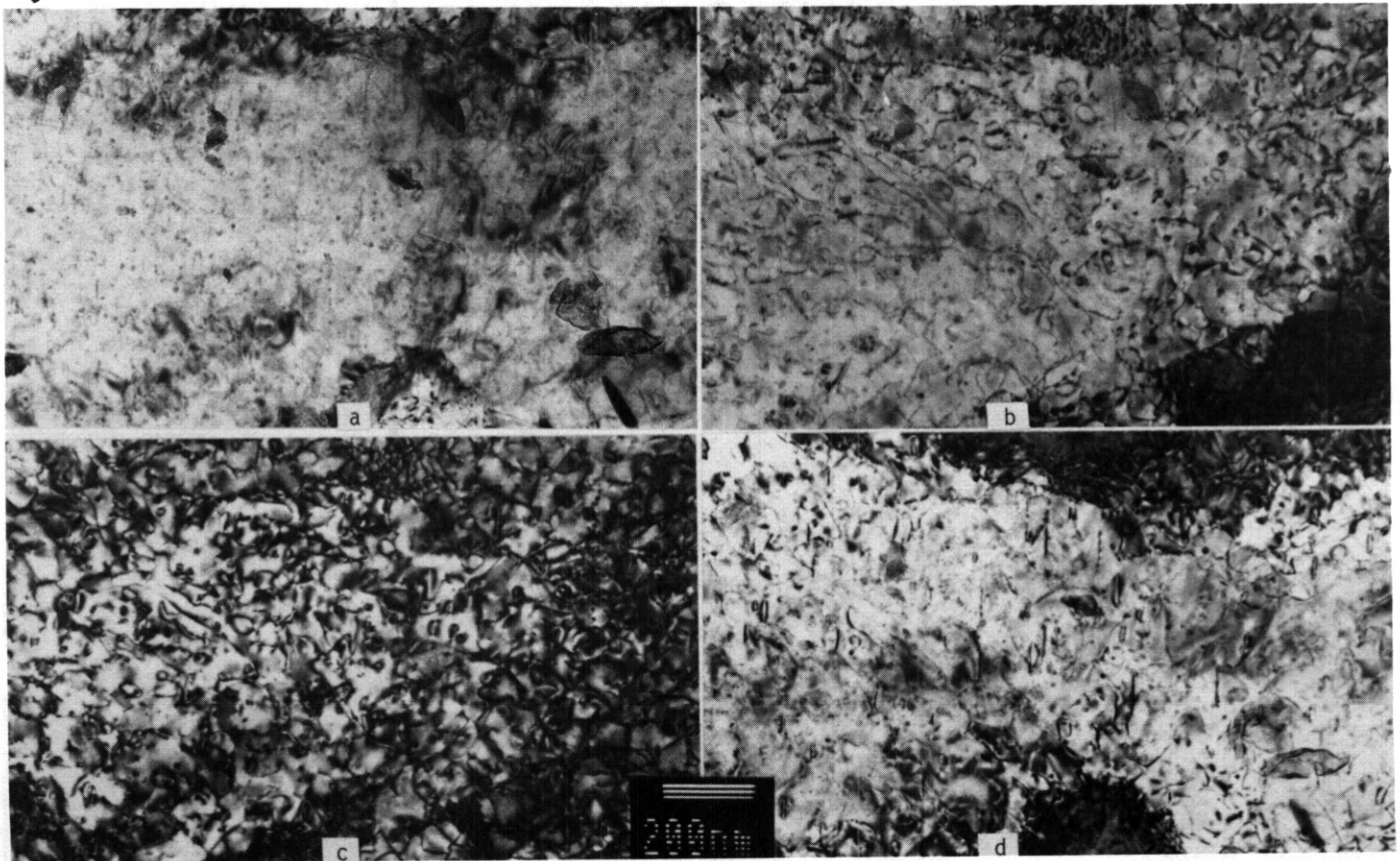


Fig. 5. The microstructure of GA3X following irradiation at 365°C to 11.3 dpa showing the same area in a) void contrast, b) $\bar{1}10$ dislocation contrast, c) strong $\bar{1}10$ dislocation contrast, and d) 002 dislocation contrast.

equiaxed precipitate particle images can be identified. Figs. 6c and d compare a ferrite region in void and dislocation contrast. Voids are as large as 45 nm and are often aligned in rows indicating that voids preferentially nucleated on dislocations. The dislocation structure is loop dominated with some loops as large as 75 nm, but a few network dislocations are present. In summary, martensite regions contain a higher density of network dislocations and subgrain boundaries whereas void development is much more advanced in ferrite. Etch pit artifacts resulting from specimen preparation can be identified in Fig. 6d and should be ignored.

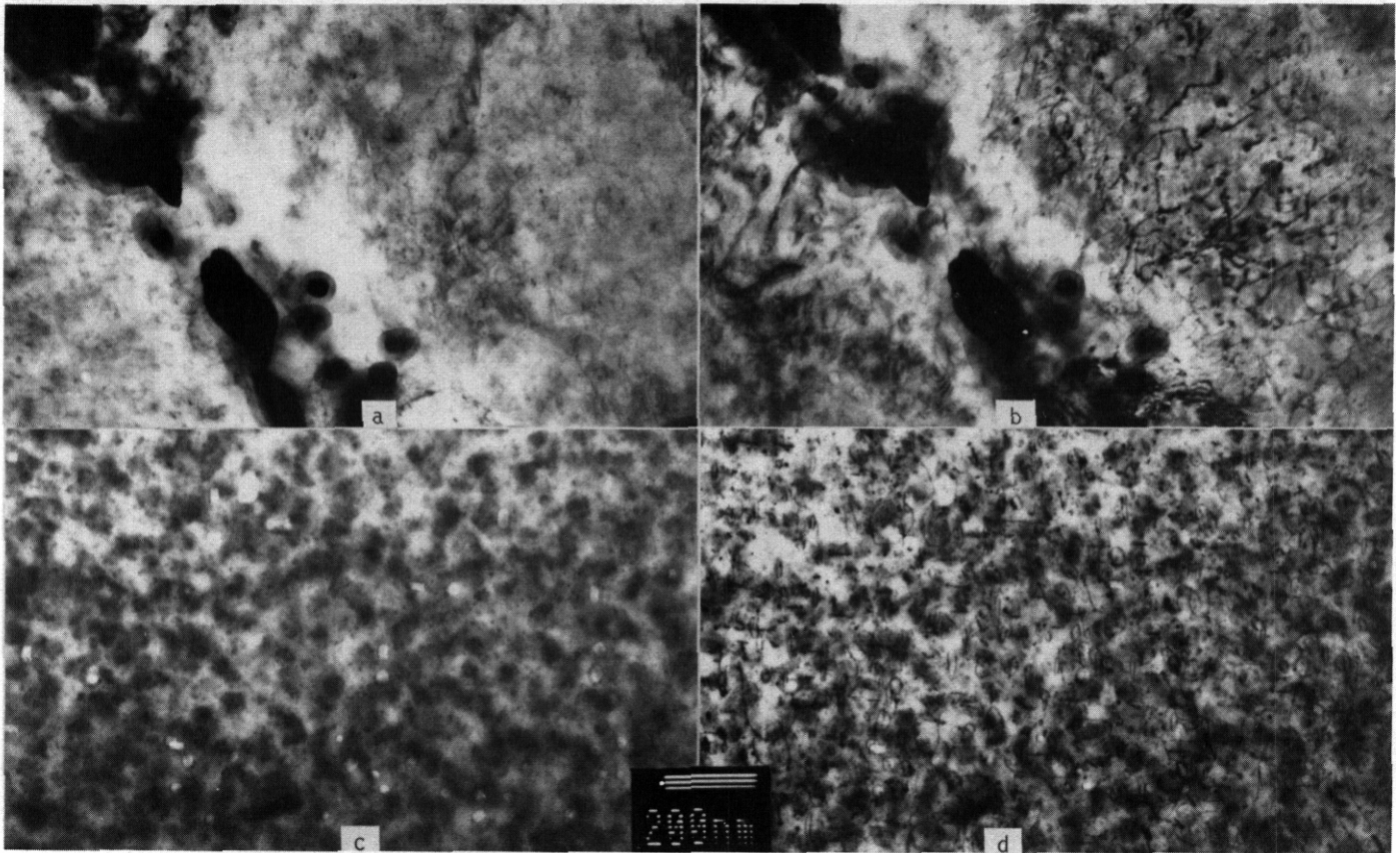


Fig. 6. The microstructure of GA4X following irradiation at 365°C to 11.3 dpa showing a martensite region in a) void and b) dislocation contrast and a ferrite region in c) void and d) dislocation contrast.

The microstructures generated by irradiation at 426°C are shown at higher magnification in Figs. 7 and 8. Fig. 7 provides examples of void swelling and dislocation development in GA3X specimen K107. Voids are as large as 40 nm but the void distribution is very non-uniform, typical of a material in the incubation regime of void development. The dislocation structure consists of a dislocation tangle with only a few individual loops identifiable. Fig. 8 shows void and dislocation development in GA4X specimen K199. Fig. 8a shows an unusual example of void development near a grain boundary. The voids near the boundary in a band 750 nm wide and 250 nm from the boundary have an average size of 35 nm whereas voids away from the boundary are larger with an average size of 55 nm and are more typical of the bulk of the material. Both sides of this grain boundary contained similar void arrays. An example of a void associated with a rod shaped precipitate particle can be seen in Fig. 8a but such associations were not found to be common. Fig. 8b shows the dislocation structure near a more typical grain boundary. The structure contains both loop and network dislocations.

Figs. 9 and 10 provide higher magnification examples of microstructures generated by irradiation at 520°C. GA3X specimen K409 is shown in Fig. 9 with a typical example of grain boundary and matrix structure in absorption contrast provided in Fig. 9a. The grain boundary precipitate particles are somewhat larger than those in the unirradiated condition, but it is apparent that they remain discrete indicating that grain boundary embrittlement is unlikely. The dislocation structure, as shown in Fig. 9b, consists of both subgrain boundary configurations and a loose tangle of network dislocations. No void swelling was found. GA4X specimen K499 is shown in Fig. 10. Voids are shown both on a grain boundary in Fig. 10a and in a band 1000 nm from a grain boundary and 2000 nm wide in Fig. 10b. Precipitate particles decorate the voids in the matrix and several of the voids are extended into rod like shapes. This extended shape was

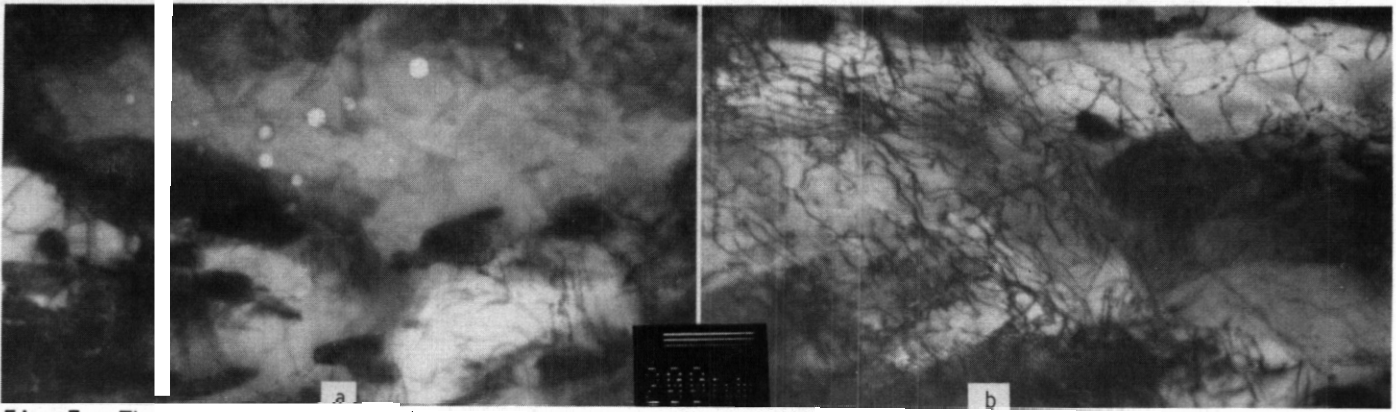


Fig. 7. The microstructure of GA3X following irradiation at 426°C in a) void and b) dislocation contrast.

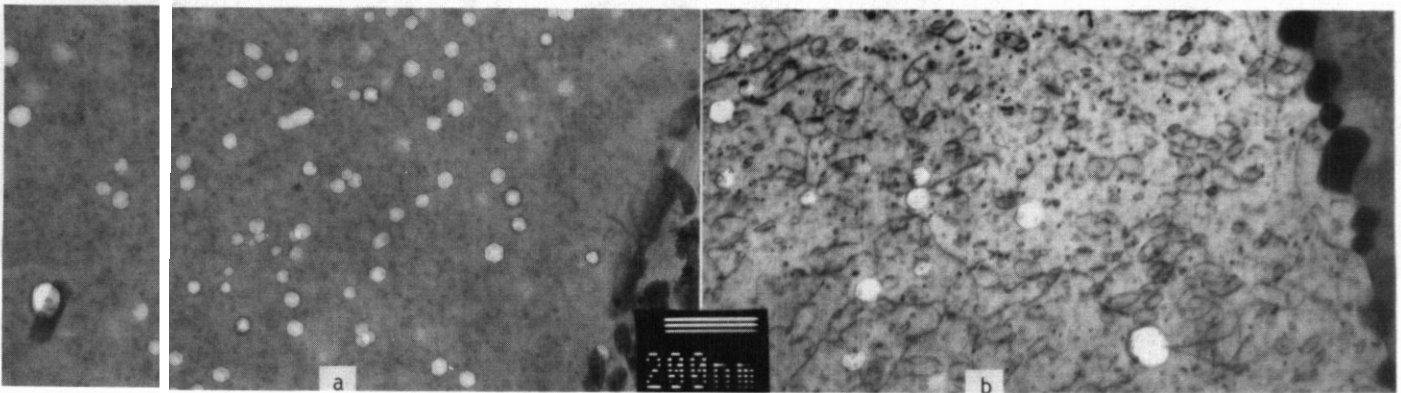


Fig. 8. The microstructure of GA4X following irradiation at 426°C in a) void and b) dislocation contrast.

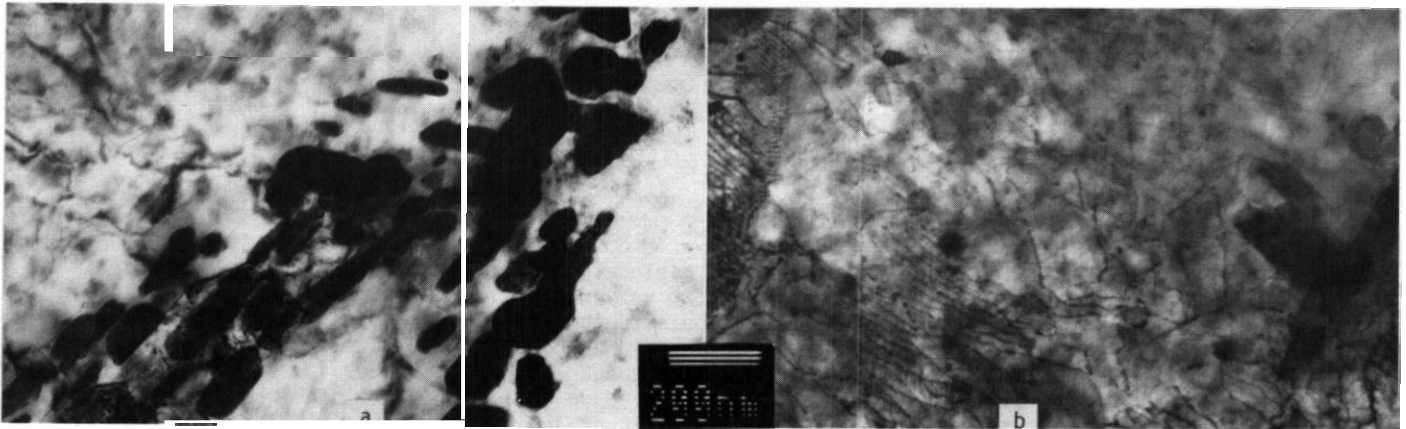


Fig. 9. The microstructure of GA3X following irradiation at 520°C in a) absorption and b) dislocation contrast.

typical for voids in high swelling regions near grain boundaries. The dislocation structure consists of a loose tangle with several examples of dislocations coupled to voids. Well away from grain boundaries, the dislocation tangle was present but voids and precipitate decorations on voids were much smaller.

Fig. 11 provides comparison of GA3X and GA4X dislocation structure following irradiation at 600°C. In both cases, the dislocation structure is confined to subgrain boundaries in martensite lath regions. Few matrix dislocations were observed.

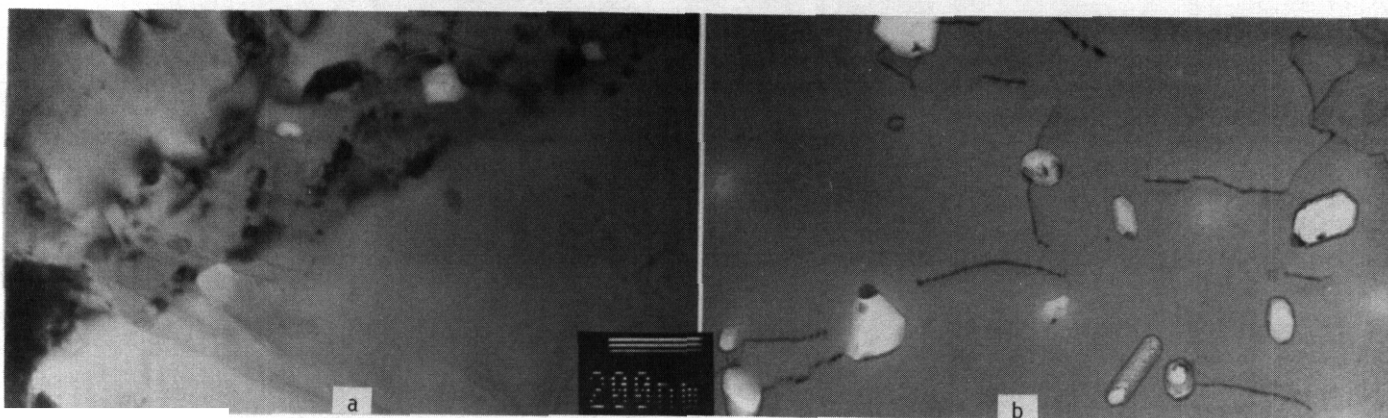


Fig. 10. The microstructure of GA4X following irradiation at 520°C in a) a grain boundary and b) voids and dislocations adjacent to a boundary.

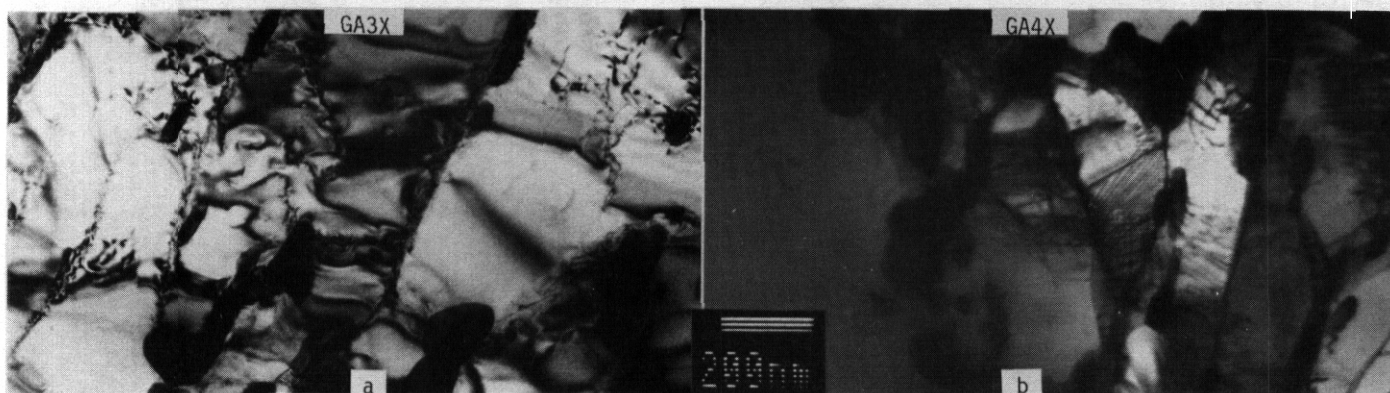


Fig. 11. The microstructures of a) GA3X and b) GA4X following irradiation at 600°C. The mean size comparison for specimen K199 is misleading because a number of small voids were present in the region which was analyzed.

Microstructural Analysis

Quantitative measurements of radiation induced void microstructures were made in a high swelling region of GA3X following irradiation at 426°C and of radiation induced void and dislocation microstructures in ferrite for GA4X following irradiation at 365, 426 and 520°C. Results are provided in Table 3. From Table 3 it can be shown that void swelling remains low for fluences on the order of 30 dpa and that peak swelling for ferrite in GMX is at 426°C. The enhanced void nucleation near a grain boundary in specimen K199 is found to result in a four fold increase in void density but only a modest increase in swelling.

Table 3. Quantitative measurements for void and dislocation microstructure in tungsten stabilized martensitic stainless steels.

Specimen Alloy	Irradiation condition		Fluence (%)	Void Swelling (cm ⁻³)	Disloc. Density		Density
	Temp. (°C)	(dpa)			Size (nm)	(cm ⁻²)	
GA3X	K107	426	33.5	0.075	9.1x10 ¹³	25.5	
GA4X	KX99	365	11.3	0.047	2.7x10 ¹⁴	16.7	4.2x10 ¹⁰
	K199	426	33.5	0.27	9.4x10 ¹³	36.3	3.6x10 ¹⁰
		520	33.5	0.35*	3.5x10 ¹⁴ *	30.3	
	K499	520	33.8	0.12	1.4x10 ¹³ *	56.3*	9.4x10 ⁸ *

* For a region with enhanced void density near a grain boundary.

Composition analysis of individual particles on precipitate extraction replicas was determined for all specimen conditions of Interest. Examples of the extraction replica microstructures are given in Fig. 12. The results are given in Table 4. From Table 4, it is apparent that in the control conditions and following irradiation at 365, 426 and 520°C, $M_{23}C_6$ remains the major extracted phase whereas after 600°C, 30 to 50% of the particles are rich in tungsten and are probably Laves. Several unusual compositions were found on an individual basis, but positive identifications have not yet been made. Also of note was the observation of titanium in large particles in both alloys. Apparently, titanium was an impurity from the melting process.

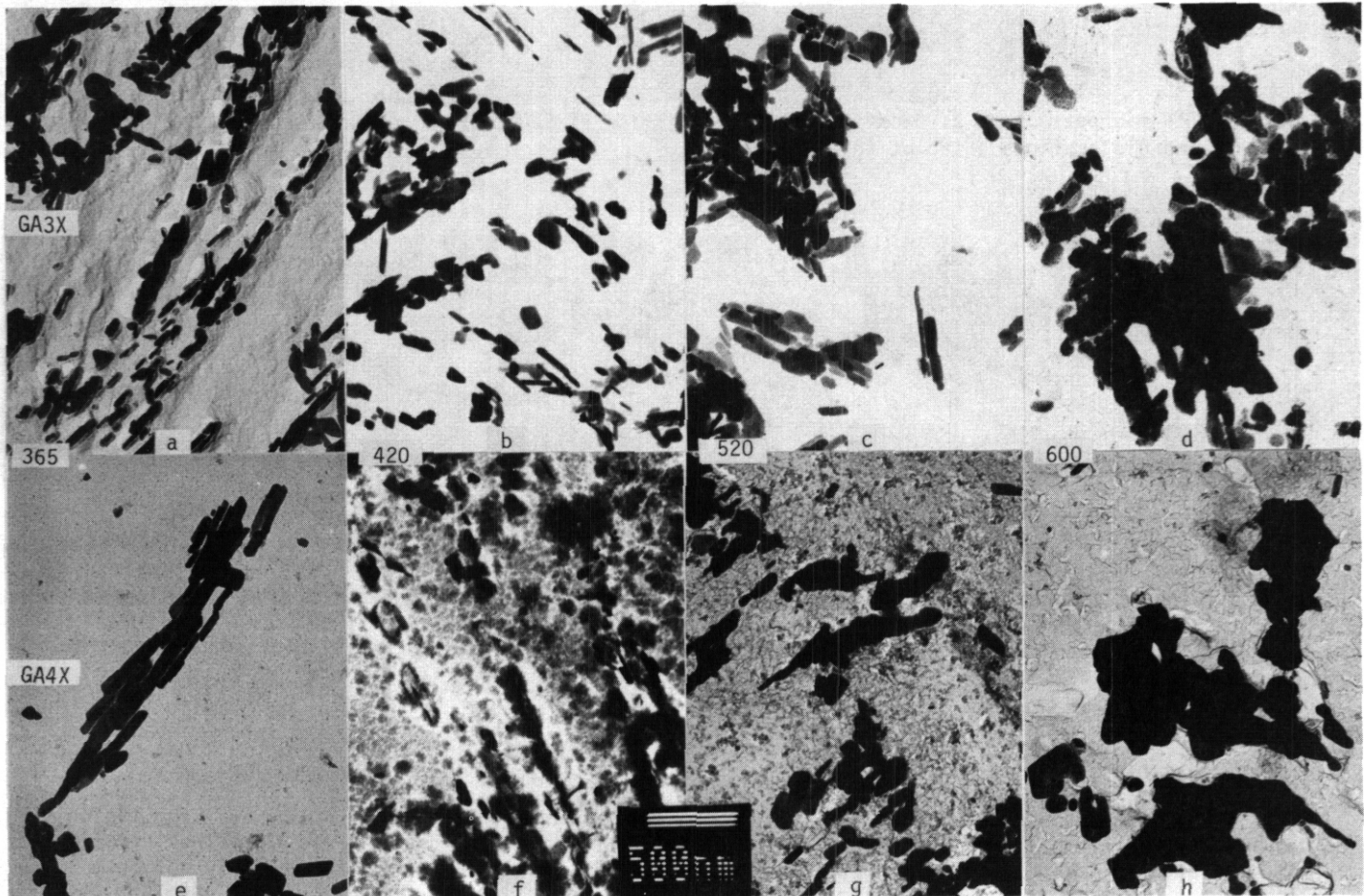


Fig. 12. Examples of extraction replica precipitate structures as a function of irradiation temperature in specimens of GA3X (a-d) and GA4X (e-h).

Discussion

The intent of this work was to determine the appropriate limit of tungsten additions to tungsten stabilized martensitic stainless steel for fusion reactor applications. The alloys examined contained tungsten levels of 2%. The experimental results demonstrate two effects resulting from the tungsten additions: precipitate formation and unusual swelling response. This section will therefore center on a discussion of these effects.

Precipitate particles which contained high concentrations of tungsten were found following irradiations at 426 and 600°C in GA3X and following irradiation at all temperatures in GA4X. These observations indicate that tungsten additions on the order of 2% do lead to precipitation of tungsten rich phases. The composition analyses indicated that both Laves and chi phases can form. However, microstructural examination does not indicate excessive precipitation at grain boundaries so that crack nucleation within a particle will not significantly weaken the boundary. Nor does composition analysis of $M_{23}C_6$ indicate significant change in tungsten level. Therefore, precipitation of tungsten rich phases are not expected to significantly degrade properties (unless solid solution hardening is adversely affected). This has been confirmed by recent results on miniature Charpy impact test specimens of GA3X irradiated at 365°C to 10.5 dpa¹¹. The results showed that GA3X gave the smallest shift in ductile to brittle transition

Table 4. **Precipitate** compositions in weight percent for tungsten stabilized martensitic stainless steels as determined by analytical electron microscopy of precipitate extraction replicas.

Specimen Condition	Code	Composition				#	tentative I.D.
		Fe	Cr	W	Other		
GA3X	07	28.1-34.1 30.4	42.6-51.2 36.8	18.9-26.1 32.8		11 1	M ₂₃ C ₆
@ 365°C	KX07	25.7-31.1	49.1-53.3	18.8-21.3		18	M ₂₃ C ₆
@ 426°C	K107	18.9-30.2 16.8-24.6	50.6-61.2 33.1-49.4	13.1-26.6 31.0-50.1		12 3	M ₂₃ C ₆ Chi ?
@ 520°C	K407	16.9-28.1 6.0 15.7	51.1-61.6 14.3 36.5	19.1-27.2 7.0 21.9	72.7 Ti 25.9 Ti	14 1 1	M ₂₃ C ₆
@ 620°C	K607	15.4-23.1 33.0-39.9	54.2-62.4 10.9-23.9	21.0-25.1 43.0-53.6		10 6	M ₂₃ C ₆ Laves 7
GA4X	99	not available					
@ 365°C	KX99	20.7-28.5 -	55.6-58.1 28.9	13.8-23.7 60.2	0-0.8 V 10.9 Ti	9 1	M ₂₃ C ₆
@ 426°C	K199	24.3-30.5 27.1 49.0 45.5	56.5-61.6 30.3 51.0 36.2	12.1-16.5 42.7 -	0-0.6 V -	13 1 1 1	M ₂₃ C ₆ , ,
@ 520°C	K499	16.0-25.5 0-5.5 15.3	55.3-64.5 20.1-26.6 58.4	14.1-28.7 69.1-78.4 45.9	0-1.1 V 0-5.2 V	14 4 1	M ₂₃ C ₆
@ 620°C	K699	17.8-23.3 33.7-38.0 22.3	60.4-64.3 11.4-14.3 42.5	15.7-21.6 47.7-53.5 35.2		5 6 1	M ₂₃ C ₆ Laves 7 mix 7

temperature of all the alloys studied (24°C). Unfortunately, tensile specimens have not been irradiated, and good higher fluence Charpy behavior remains to be demonstrated.

Swelling was found to be unusual in GA4X following irradiation both at 426 and at 520°C. Following irradiation at 426°C the grain boundary shown in Fig. 8a was found which developed a higher density of smaller voids than in the neighboring matrix. Both sides of the boundary were similarly decorated. In comparison, all other boundaries observable in the specimen contained more normal adjacent regions denuded of voids. Following irradiation at 520°C, all grain boundaries examined were found to contain adjacent regions with enhanced swelling whereas away from these regions, the swelling was much lower.

Also of note was the shape of voids in these enhanced swelling regions; the voids were highly elongated and often associated with precipitate particles. The swelling behavior following irradiation at 520°C was unexpected because irradiation induced voids had not been seen in ferritic alloys irradiated at such a high temperature. For both irradiation temperatures, swelling behavior near grain boundaries was affected. The most likely cause is from the tungsten additions. Effects due to the low carbon content can probably be discounted based on microstructural development in Fe-12Cr-1Mo where no unusual swelling response was found.¹² However, it is not yet clear whether the effects observed were a result of composition gradients which promoted precipitation or which promoted dislocation evolution.

CONCLUSIONS

Tungsten stabilized martensitic and ferritic steels have been examined by transmission electron microscopy following irradiation in the FFTF to fluences as high as 34 dpa over the temperature range 365 to 600°C. The martensitic steel was found to have developed void and dislocation evolution at 365 and 426°C and precipitate coarsening at 600°C. The ferritic steel was found to have developed void and dislocation evolution over the temperature range 365 to 520°C with peak swelling of 0.3% at 426°C to 34 dpa and significant precipitate coarsening at 600°C. Unusual swelling response was observed near grain boundaries in the ferritic steel. Composition analysis of extracted precipitates demonstrated formation of tungsten

rich intermetallic phases but microstructural examinations indicate that at fluences on the order of 35 dpa, mechanical properties are not expected to be degraded. Intermetallic formation was most pronounced at 600°C.

FUTURE WORK

This work will be continued when similar specimens have been irradiated to approximately 100 dpa.

REFERENCES

1. R.L. Klueh, D.S. Gelles and T.A. Lechtenberg. "Development of Ferritic Steels for Reduced Activation: The US Program." J. Nucl. Mater., V141-143 (1986), p. 1081.
2. D. Dufeu, T.W. Tupholme and G.J. Butterworth. "Development of Low-Activation Stainless Steels," IBID p. 1097.
3. T. Noda, F. Abe, H. Araki and M. Okada, "Development of Low Activation Ferritic Steels." IBID p. 1102.
4. M. Tamura, H. Hayakawa, M. Tanimura, A. Hishinuma and T. Kondo, "Development of Potential Low Activation Ferritic and Austenitic Steels," IBID p. 1067.
5. H.J. Goldschmidt, "Discussion on Interstitial Compounds," J. Inst. Metals V. 97 (1969) p. 173.
6. for example. D.S. Gelles.
7. T.A. Lechtenberg. "Melting and Fabrication of Low Activation Ferritic Alloys for FFTF Irradiations." Alloy Development for Irradiation Performance Semiannual Progress Report for the Period Ending March 31, 1985, DOE/ER-0045/14, p. 117.
8. C.Y. Hsu, D.S. Gelles and T.A. Lechtenberg. "Microstructural Examination of 12%Cr Martensitic Stainless Steel After Irradiation at Elevated Temperatures in FFTF," in Radiation Induced Changes in Microstructure, ASTM STP 955, FA. Garner, NH. Packan and A.S. Kumar. eds., In press. Also see IBID reference 2, DOE/ER-0045/16, March 1986, p. 150.
9. C.Y. Hsu and T.A. Lechtenberg. "Preliminary Evaluation of Microstructure and Mechanical Properties on Low Activation Ferritic Steels," IBID Reference 2, p. 120.
10. C.Y. Hsu and T.A. Lechtenberg. "Microstructure and Mechanical Properties of Unirradiated Low Activation Ferritic Steel." IBID Reference 1, p. 518.
11. NS. Cannon, WL. Hu and D.S. Gelles, "Charpy Impact Test Results for Low Activation Ferritic Alloys," in Fusion Reactor Materials Semiannual Progress Report for the Period Ending September 30, 1986, DOE/ER-0313/1, in press. (HEDL-7659, May 1987)
12. D.S. Gelles, J. Nucl. Mater. 108 & 109 (1982), 515.

THE DEVELOPMENT OF FERRITIC STEELS FOR FAST INDUCED-RADIOACTIVITY DECAY ** R. L. Klueh and P. J. Maziasz
(Oak Ridge National Laboratory)

OBJECTIVE

Induced radioactivity in the first-wall and blanket-structure materials of fusion reactors will make these components highly radioactive after their service lifetime, leading to difficult radioactive waste-management problems. One way to minimize the disposal problem is to use structural materials in which the radioactive isotopes induced by irradiation decay quickly to levels that allow simplified disposal techniques. We are assessing the feasibility of developing such ferritic steels.

SUMMARY

Transmission electron microscopy and x-ray diffraction studies were made on eight heats of normalized-and-tempered chromium-tungsten steel that contained various levels of chromium, tungsten, vanadium, and tantalum. A range of precipitate morphologies and compositions were observed. The types of precipitates were similar to the precipitates that occur in the analogous chromium-molybdenum steels that are presently being considered as candidate structural materials for fusion-reactor applications.

PROGRESS AND STATUS

Introduction

We have continued studies to characterize eight heats of ferritic steel designed for fast induced-radioactivity decay (FIRD).¹ These steels were patterned on the chromium-molybdenum steels that are of interest for fusion-reactor applications -- namely, 2 1/4Cr-1Mo, 9Cr-1MoVNb, and 12Cr-1MoVW steels. The major changes for the chromium-molybdenum steels involve the replacement of molybdenum by tungsten, the use of vanadium in a 2 1/4%-Cr steel, and the replacement of niobium in the 9%-Cr steel by tantalum. The composition of the eight heats and their designations are given in Table 1. The results of optical microscopy, tempering behavior, and tensile properties of the eight steels have previously been presented. In this report, information on the microstructures and precipitate identification obtained by transmission electron microscopy (TEM) and x-ray analysis will be presented.

Table 1. Chemical composition of fast induced-radioactivity decay (FIRD) ferritic steels

Alloy	Chemical composition, ^a wt %						
	Cr	W	V	Ta	C	Mn	Si
2 1/4CrV	2.36		0.25		0.11	0.40	0.17
2 1/4Cr-1WV	2.30	0.93	0.25		0.10	0.34	0.13
2 1/4Cr-2W	2.48	1.99	0.009		0.11	0.39	0.15
2 1/4Cr-2WV	2.42	1.98	0.24		0.11	0.42	0.20
5Cr-2WV	5.00	2.07	0.25		0.13	0.47	0.25
9Cr-2WV	8.73	2.09	0.24		0.12	0.51	0.25
9Cr-2WVTa	8.72	2.09	0.23	0.075	0.10	0.43	0.23
12Cr-2WV	11.49	2.12	0.23		0.10	0.46	0.24

^aP = 0.014-0.016, S = 0.005-0.106, Ni < 0.01, Mb < 0.01, Nb < 0.01, Ti < 0.01, Co = 0.005-0.888, Cu = 0.02-0.03, Al = 0.02-0.03, B < 0.001, bal Fe.

Experimental procedure

Details on the preparation of the eight heats of steel were previously provided.^{2,3} The steels are projected to be used in a normalized-and-tempered condition. Depending on the composition of the steel, this treatment will produce either a tempered bainite or a tempered martensite microstructure. For the present study, all but the 2 1/4Cr-2W steel were normalized by austenitizing 1 h at 1050°C and then air cooling; the 2 1/4Cr-2W steel was austenitized 1 h at 900°C and air cooled. The 2 1/4CrV and 2 1/4Cr-2W were tempered 1 h at 700°C, the 2 1/4Cr-1WV was tempered 1 h at 725°C, and the other five alloys were tempered 1 h at 750°C.

The microstructures of the steels were studied by analytical electron microscopy on specimens that were cut from 159-mm plate. Both extraction replicas and foil specimens

were examined. Electron microscopy was performed on a JEOL 100C transmission electron microscope and on a Philips 400 transmission electron microscope. The Philips 400 microscope was equipped with an X-ray energy-dispersive spectrometer (XEDS) that was modified for analytical work. Extraction replicas on carbon-coated copper grids were used for precipitate analysis to avoid matrix effects in obtaining XEOS spectra. Precipitates were identified by a combination of electron diffraction and XEOS analysis.

Electrolytic carbide extractions were produced from samples with an approximate mass of 0.3 g in a solution of 10% HCl-90% methanol at 1.5 V for 5 h. These solutions ensured selective removal of the matrix without any dissolution of carbides. The precipitates were weighed in air, and the weights were converted to weight in vacuum to correct for atmospheric variations. The accuracy of the extraction results was determined by a series of multiple measurements on similar material. A value of $2\sigma = 0.2$ wt % was found for the range of 0 to 4 wt % precipitate.

Results

1. Transmission Electron Microscopy

To examine the carbide structure of the normalized-and-tempered 15.9-mm-thick plate, carbide extraction replicas were used. Figures 1 to 7 show the different types of microstructures that were observed.

The 2 $\frac{1}{4}$ CrV and 2 $\frac{1}{4}$ Cr-1WV steels (Fig. 1) showed the most diverse microstructures. Both steels contained fibrous precipitates, interphase precipitates, and large blocky precipitates. The fibrous precipitates are quite obvious in the micrographs of Figs. 1 and 2. The 2 $\frac{1}{4}$ CrV contained two types of fibers: the fine fibers that are illustrated in Figs. 1 and 2(a) and, in addition, coarser fibers or "ribbons," as seen in Fig. 2(b). A morphological characteristic of the interphase precipitation is that it generally consists of rows of fine precipitates [Fig. 2(b)]. Large precipitates [Fig. 2(c)] appeared in two regions: along prior austenite grain boundaries and within regions of the matrix in which there were no fibrous or interphase precipitates.

Fibrous and interphase precipitates are known to form during the austenite-to-ferrite transformation.⁴ These morphologies are present in large quantities in the 2 $\frac{1}{4}$ CrV and 2 $\frac{1}{4}$ Cr-1WV steels because they contained large amounts of polygonal ferrite. The fibrous precipitate in the 2 $\frac{1}{4}$ Cr-1WV was finer than that present in the 2 $\frac{1}{4}$ CrV steel. The rows in the interphase precipitate in the 2 $\frac{1}{4}$ CrV steel were usually quite easily recognized, although in some instances the high density of precipitates made such recognition difficult. This difficulty in recognizing rows of precipitates was especially true for the 2 $\frac{1}{4}$ Cr-1WV steel, where the precipitate was somewhat finer than that formed in the 2 $\frac{1}{4}$ CrV steel.

The large blocky types of precipitate in the matrix were in the bainitic regions of the steels. As demonstrated in Fig. 2(c), the large precipitates appeared in various shapes. On the average, the large precipitates were smaller in the 2 $\frac{1}{4}$ Cr-1WV steel than in the 2 $\frac{1}{4}$ CrV steel. Also, the regions that contained large precipitates generally also contained a distribution of finer precipitate particles, although these particles were generally not as small and were not present in the number density as were the particles where interphase precipitation occurred. The 2 $\frac{1}{4}$ Cr-1WV steel contained a higher density of these finer particles in the bainitic regions than the 2 $\frac{1}{4}$ CrV steel.

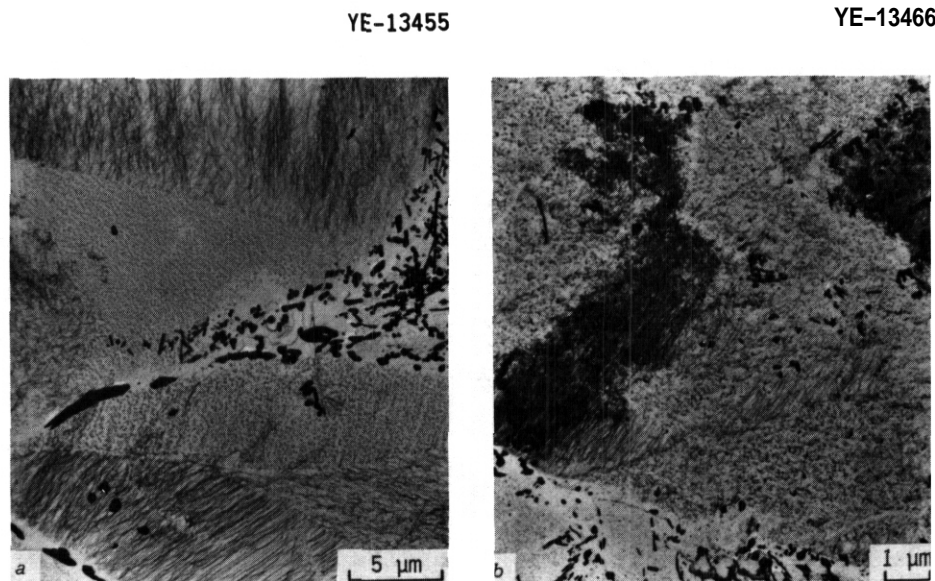
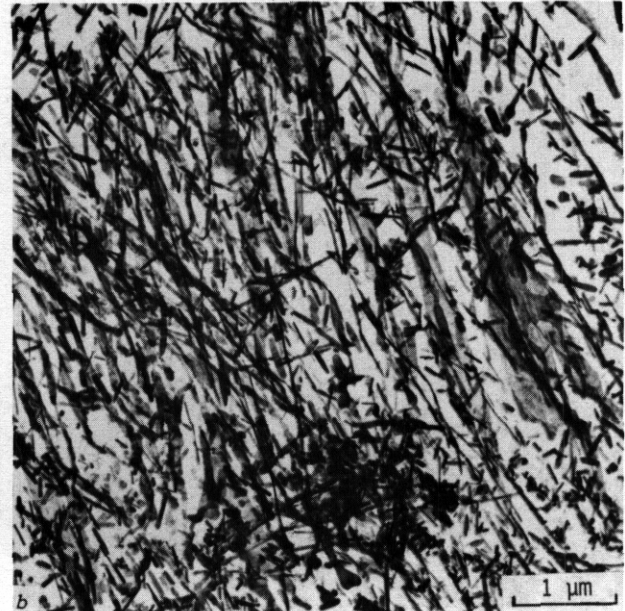
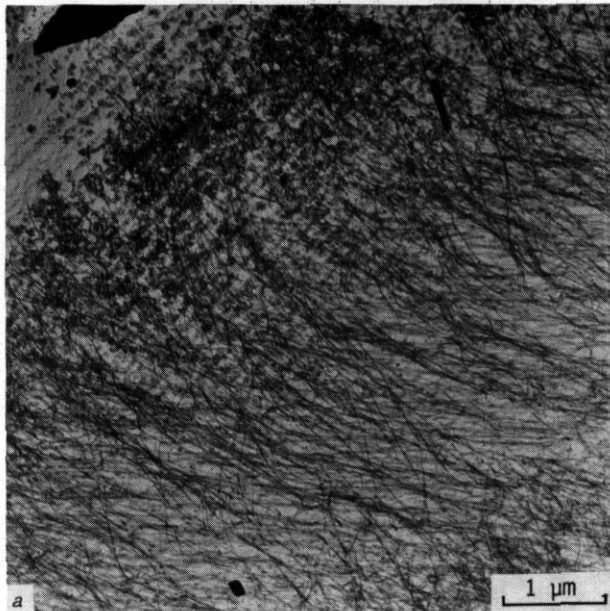


Fig. 1. Extraction replicas that show examples of the different precipitates that occur in (a) 2 $\frac{1}{4}$ CrV and (b) 2 $\frac{1}{4}$ Cr-1WV steels.

YE-13456

YE-13453



YE-13456

YE-13459

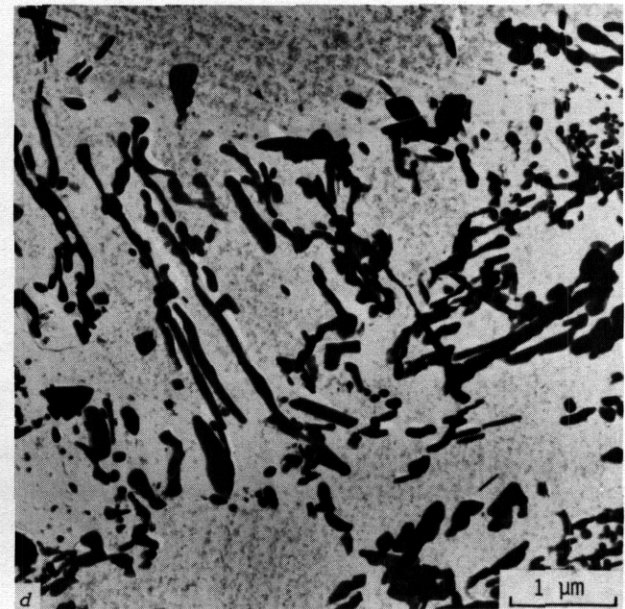
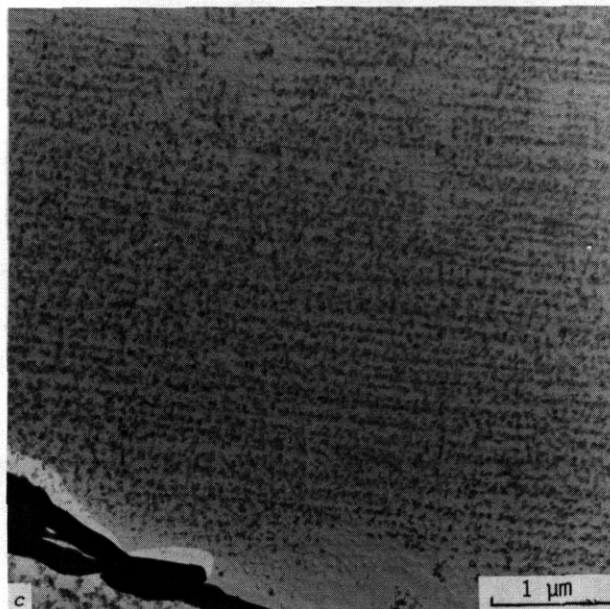


Fig. 2 Examples of different precipitate types on the extraction replica of $2\frac{1}{4}\text{CrV}$ steel: (a) fine fibers, (b) coarse fibers or "ribbons," (c) interphase precipitates, and (d) blocky precipitates.

Because the $2\frac{1}{4}\text{Cr-2W}$ steel contained no polygonal ferrite, no fibrous or ribbon precipitates were observed. The steel contained two types of precipitate: fine needlelike particles and large blocky particles (Fig. 3).

A few fibrous precipitates were observed in the $2\frac{1}{4}\text{Cr-2WV}$ steel, which contained 15-20% polygonal ferrite. Some interphase precipitate regions were also detected, but the precipitate particles were much smaller than they were in the $2\frac{1}{4}\text{CrV}$ and $2\frac{1}{4}\text{Cr-1WV}$ steels. The bainite of the $2\frac{1}{4}\text{Cr-2WV}$ steel, like that of the $2\frac{1}{4}\text{Cr-2W}$ steel, contained two types of precipitate: large blocky particles and a high density of fine particles (Fig. 4). The blocky particles in the $2\frac{1}{4}\text{Cr-2WV}$ were similar in appearance to those in the $2\frac{1}{4}\text{Cr-2W}$ steel, but the fine particles were different. There was a higher density of the fine, randomly distributed particles in the $2\frac{1}{4}\text{Cr-2WV}$ steel, and they did not appear to have the needlelike morphology. At high magnification [Fig. 4(b)], it was possible to distinguish a polygonal shape that often appeared to be square in two dimensions. Because of the small size of the interphase precipitates, the regions containing them were difficult to distinguish from the fine precipitates in the bainitic regions.

YE-13457

YE-13458

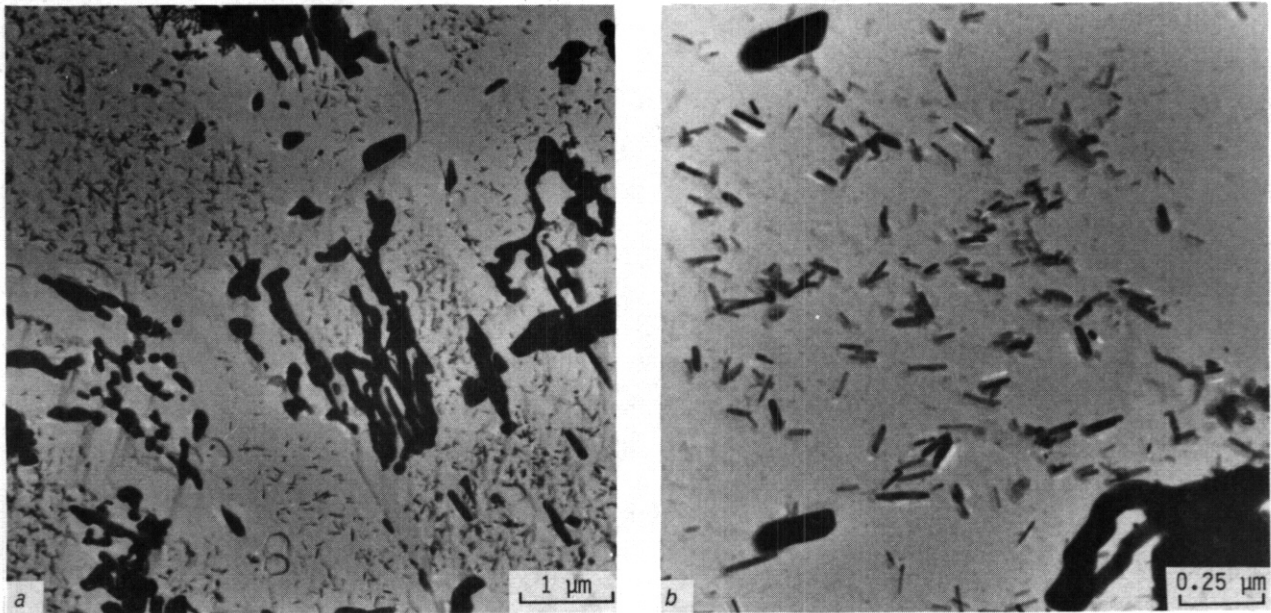


Fig. 3. Extraction replica of 2%Cr-2W steel showing (a) the general precipitate distribution and (b) the fine distribution of precipitates at higher magnification.

YE-13457

YE-13461

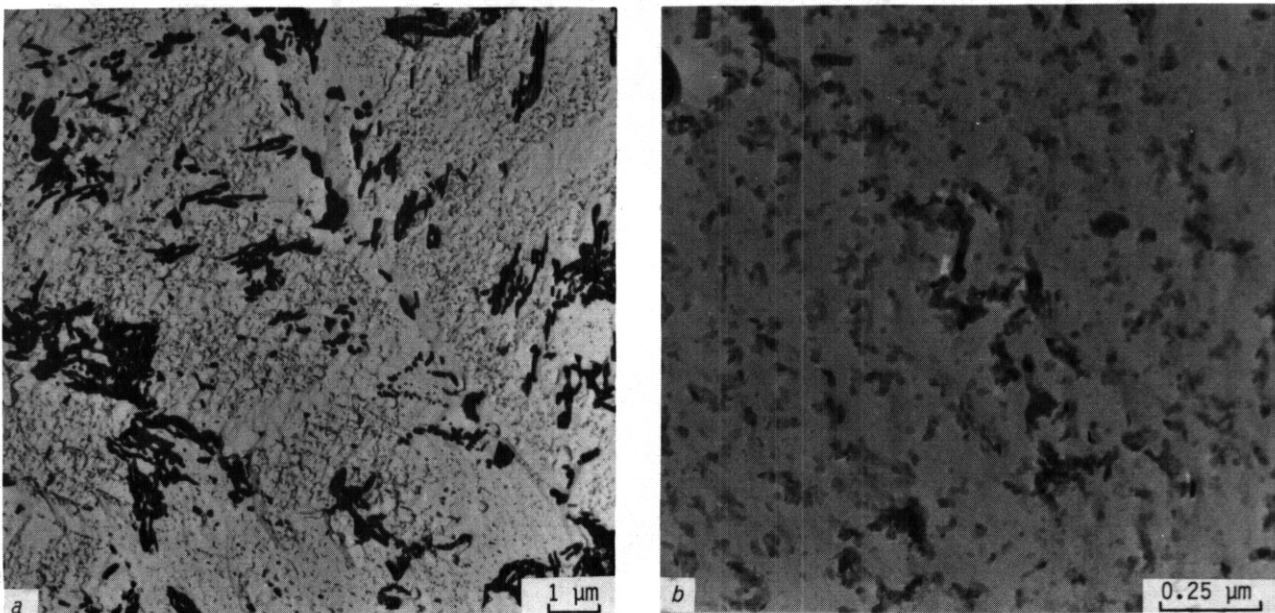


Fig. 4. Extraction replica of 2%Cr-2W steel showing (a) general precipitate distribution and (b) the distribution of fine precipitates at higher magnification.

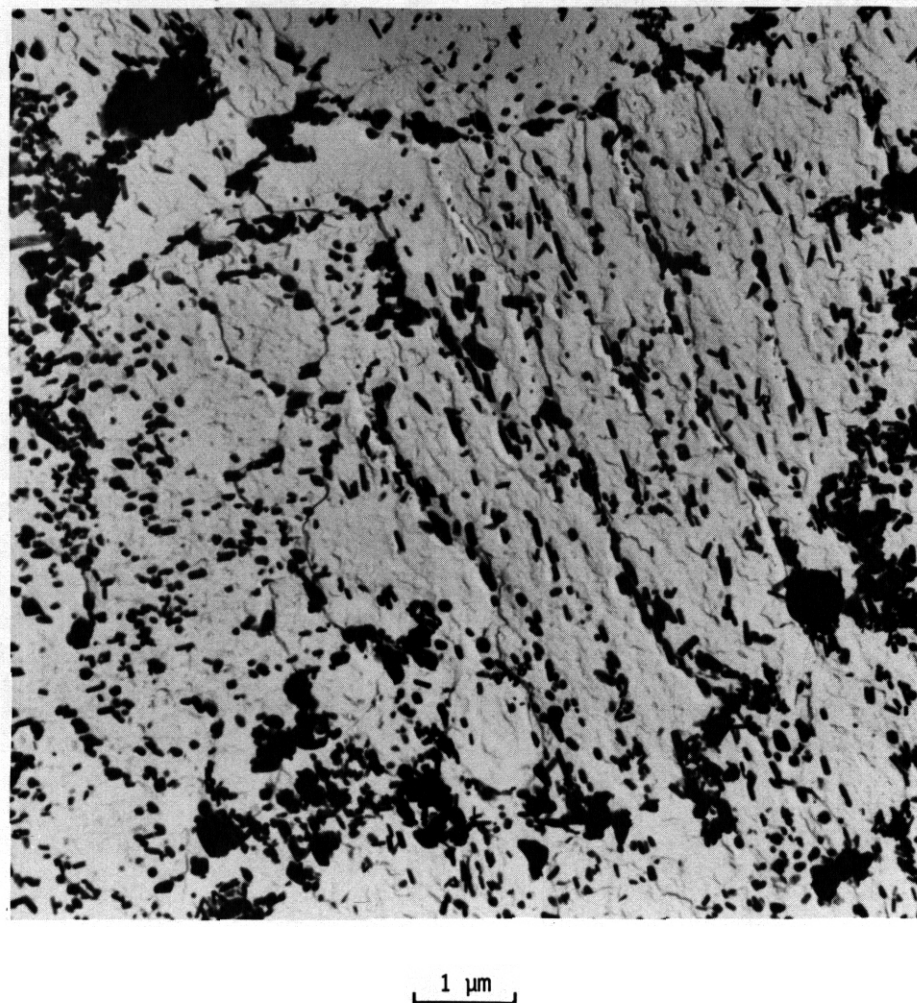


Fig. 5. Extraction replica of 5Cr-2WV steel.

As seen in Fig. 5, the general distribution of precipitate particles in the 5Cr-2WV steel was different from the distributions in the 2 $\frac{1}{4}$ -Cr steels. Most of the particles have a blocky morphology. Although there appeared to be two types of precipitates, most of them had a rectangular appearance of quite uniform size. There were a few particles of somewhat larger size. Many of these apparently formed on prior austenite grain boundaries, while others lay in fairly straight lines, indicating that they had formed on lath boundaries. Although not easily seen on the micrograph in Fig. 5, there was also a distribution of fine particles that could be detected at higher magnification.

The 9Cr-2WV and 9Cr-2WVTa steels had a precipitate distribution of fairly large blocky precipitates (Fig. 6). Most of these precipitates appeared to have formed on lath boundaries or on prior austenite grain boundaries. The matrix regions often appeared free of precipitates, although at higher magnification a distribution of fine precipitate could be detected. The 12Cr-2WV steel had a similar microstructure, with the exception that some of the grains did not contain the large precipitates that appeared in the majority of the microstructure (Fig. 7). These grains are the delta-ferrite that constitutes about 25% of the microstructure. It appeared that these grains may also contain a very fine precipitate.

Foil specimens were also examined by TEM. Such specimens are generally not as useful to study the precipitates as the replicas are. However, they do show the dislocation structures. For the low-chromium steels, the polygonal ferrite regions contained very few dislocations. Therefore, these regions did not appear significantly different in the foils than they did in the replicas. The bainitic regions contained a high dislocation density -- even after the tempering treatments. As tempering proceeds, subgrains should begin to form, and the high dislocation density would be expected to decrease.

YE-13463

YE-13464

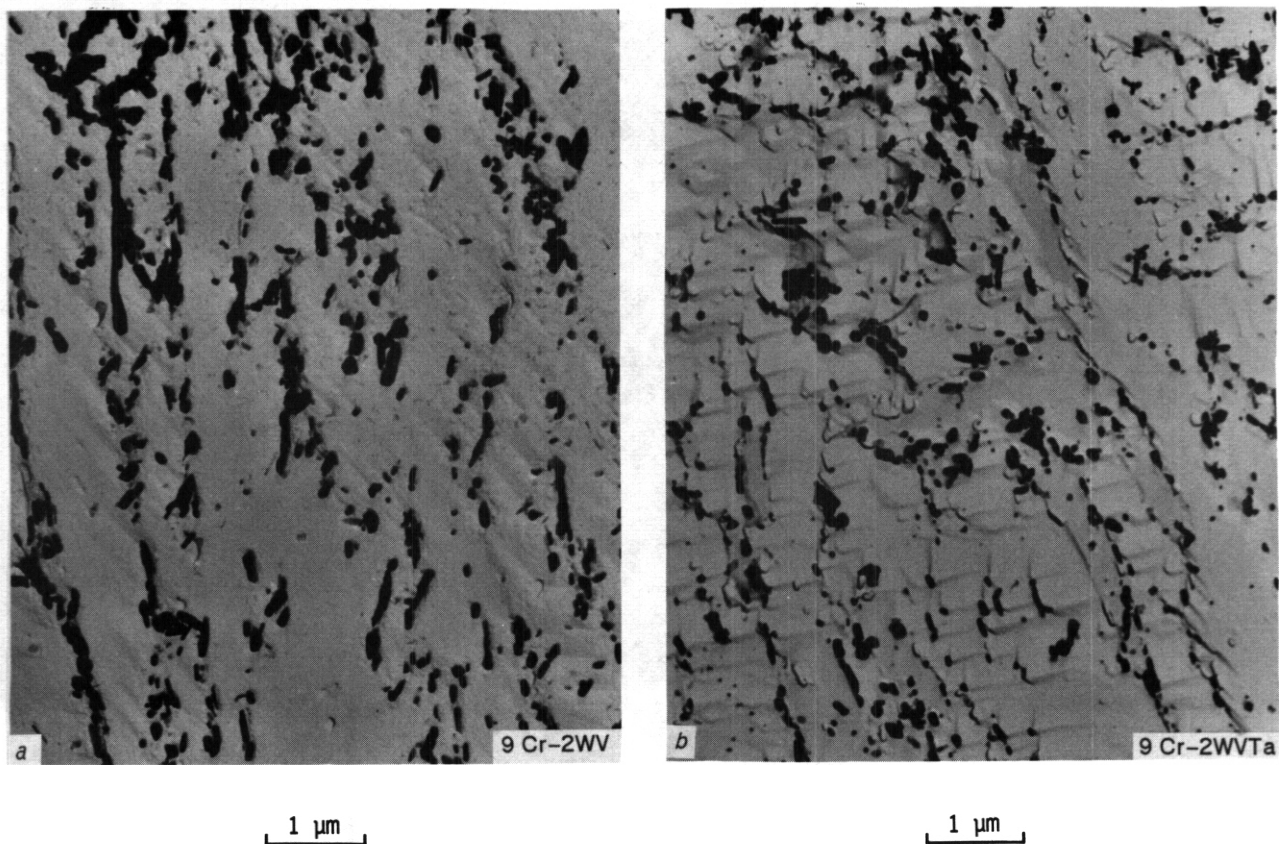


Fig. 6. Extraction replicas of (a) 9Cr-2WV and (b) 9Cr-2WVTa steels.

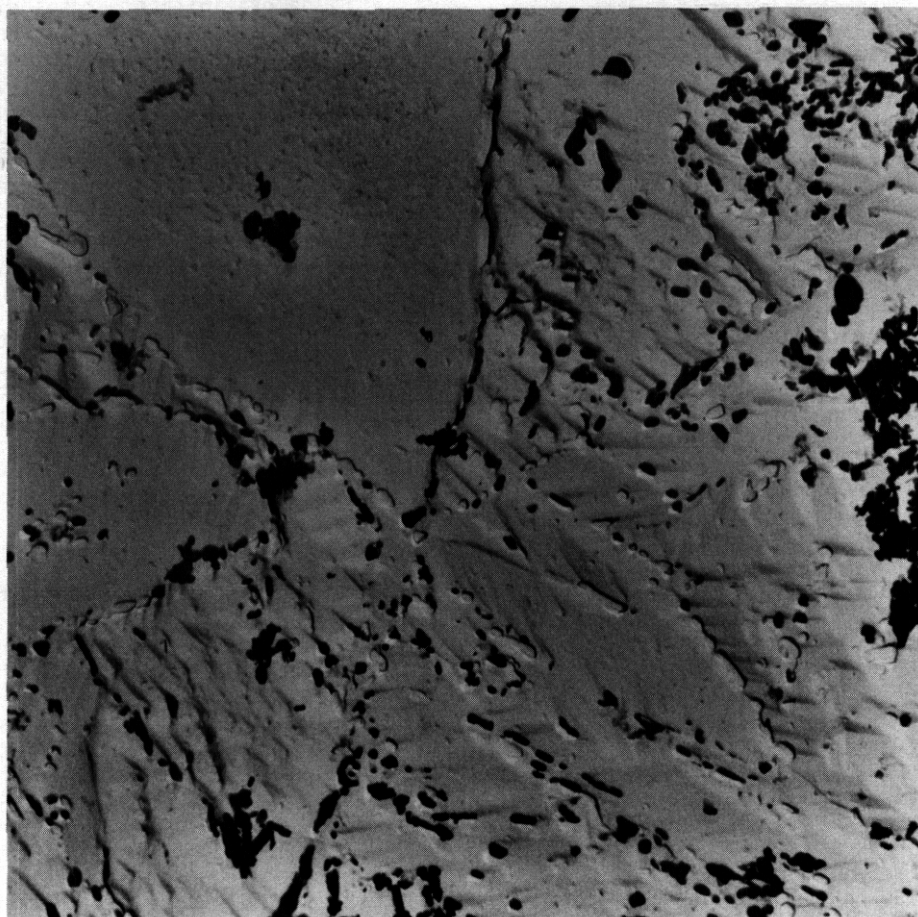
The **high-chromium** steels had a tempered martensite structure, which consisted of laths containing a relatively high dislocation density. Again, prolonged tempering would be expected to lower the dislocation density and lead to the development of subgrains. Because of the high dislocation density, the precipitates were not as easily observed as they were on the replicas.

2. Precipitate Identification

To help identify the precipitates, they were extracted electrolytically. The amount of precipitate was determined by weighing, and the extracted precipitates were analyzed by X-ray diffraction. The type of precipitate observed appeared to depend on the chromium concentration. For the 9-Cr and 12-Cr steels, only $M_{23}C_6$ was positively identified. In the $2\frac{1}{4}$ -Cr steels, the precipitate detected appeared to depend on the vanadium and tungsten composition. When vanadium was present, the steels contained MC; M_7C_3 and M_6C were the other compounds detected. The $2\frac{1}{4}$ -Cr-2W steel contained M_3C and $M_{23}C_6$. The 5Cr-2WV steel, which has a chromium concentration between the high and low concentrations, contained $M_{23}C_6$ and M_7C_3 , which is a combination of the compounds found for the high- and the low-chromium concentrations.

One problem with X-ray diffraction for identifying the carbides is that the fine particle size of the extracted carbides often makes it difficult to obtain a positive identification. This gave rise to unidentified X-ray diffraction lines for several of the extracted specimens. Further, the overlap of lines for different compounds complicates the positive identification of the carbides. Therefore, it is possible that several of these specimens may contain carbides in addition to those that were positively identified.

To further identify the precipitates and to correlate them with morphology, the carbide-extraction replicas were examined by XEOS (x-ray energy-dispersive spectroscopy). Analysis of the complicated microstructures of the $2\frac{1}{4}$ CrV and $2\frac{1}{4}$ Cr-1WV steels (Figs. 1 and 2) indicated that both the fine fibers and interphase precipitates were vanadium rich and are presumably MC. Both types of precipitate contained considerable amounts of chromium, with the fine fibers containing the most chromium. The coarse fibers or ribbons were iron and chromium rich, with slightly more iron than chromium. Presumably, these are M_7C_3 , since



1 μm

Fig. 7. Extraction replica of 12Cr-2WV steel.

this carbide can contain both large amounts of iron and chromium. The large precipitates that formed in the bainite were mainly of two types: chromium rich and iron rich. A broad beam analysis over a field of these precipitates revealed that on the average they were chromium rich. These are probably the M_7C_3 found by x-ray diffraction. A few large precipitates were found to be vanadium rich, presumably MC particles.

The large precipitates in the bainite of the 2 $\frac{1}{4}$ Cr-2W and 2 $\frac{1}{4}$ Cr-2WV steels were similar to those in the 2 $\frac{1}{4}$ CrV and 2 $\frac{1}{4}$ Cr-1WV: M_7C_3 and M_3C . No $M_{23}C_6$ was detected in the 2 $\frac{1}{4}$ Cr-2W, as was observed by X-ray diffraction. The fine precipitates in these two steels were different. In the 2 $\frac{1}{4}$ Cr-2W steel, the fine needlelike precipitates were chromium and tungsten rich and are probably M_2C or M_2X . The fine precipitates in the 2 $\frac{1}{4}$ Cr-2WV steel were MC particles. However, instead of being only vanadium rich, as was true for the 2 $\frac{1}{4}$ CrV and 2 $\frac{1}{4}$ Cr-1WV steels, the fine MC in this steel was rich in tungsten. Some of the larger particles in this steel were also found to be vanadium- and tungsten-rich MC, and some were vanadium rich.

The large precipitates in the 5Cr-2WV steel were mainly M_7C_3 , while the very small particles were vanadium-rich MC. For the 9Cr-2WV, 9Cr-2WVTa, and 12Cr-2WV, the precipitates were either $M_{23}C_6$ -- large particles -- or MC -- small particles and a few of the large particles. In the 9Cr-2WV and 12Cr-2WV steels, the MC was vanadium rich with considerable chromium present (no large amount of tungsten as was true for the 2 $\frac{1}{4}$ Cr-2WV steel). The 9Cr-2WVTa contained two types of MC: vanadium rich and tantalum rich, both of which contained considerable chromium.

Table 2 summarizes the precipitates that were found.

Table 2. Identification of precipitates by X-ray diffraction^a and analytical electron microscopy^b

Steel	Precipitate ^c (wt %)	Tentative Identification
2 1/4CrV	0.926	M ₃ C + M ₇ C ₃ + MC
2 1/4Cr-1WV	1.059	M ₃ C + M ₇ C ₃ + MC
2 1/4Cr-2W	1.797	M ₃ C + M ₇ C ₃ + M ₂₃ C ₆
2 1/4Cr-2WV	1.946	M ₃ C + M ₇ C ₃ + MC
5Cr-2WV	2.299	M ₂₃ C ₆ + M ₇ C ₃ + MC
9Cr-2WV	2.520	M ₂₃ C ₆ + MC
9Cr-2WVTa	2.033	M ₂₃ C ₆ + MC
12Cr-2WV	2.037	M ₂₃ C ₆ + MC

^aX-ray diffraction of the extracted precipitates.

^bX-ray energy dispersive spectroscopy (XEDS) on extraction replicas.

^cObtained by weighing the extracted precipitates.

higher transformation temperature and a slower moving interface. Interphase precipitates form at a low-energy interface by the movement of steps along the boundary.⁴

Considerable research has been conducted on Fe-V-C alloys in an effort to use the interphase precipitates for dispersion strengthening. (The effect of the fibrous precipitates on strength is unknown, although the properties are not expected to be as favorable as are those of a fine interphase precipitate.) Steels containing a dispersion of interphase precipitates have been developed to have properties superior to those of tempered martensite.⁵ However, an isothermal transformation is the easiest way to form uniform distributions of interphase precipitates.^{4,5} An isothermal heat treatment is generally not practical in commercial practice. Studies have been made to determine how interphase precipitates could be developed during a continuous cool from the austenitizing temperature. One proposal to accomplish this (and maintain the FIRD characteristics of the steel) is by adding manganese to the steel.⁵ Considerable research would be required to develop such alloys for commercial production, and at present Only continuous cooling of FIRD steels is being investigated.

The observations on the fibrous and interphase precipitates in the 2 1/4CrV and 2 1/4Cr-1WV steels are in accordance with the above discussion. Both the chromium and vanadium carbides were observed to form as fibers, although the chromium-rich fibers were much coarser and appeared ribbonlike. This observation agrees with previous work that showed that the chromium carbides form coarser fibers than vanadium carbides.⁴ The observation that fibers and interphase precipitates form in a finer distribution in the 2 1/4Cr-1WV can be attributed to the difference in the transformation characteristics for these two steels. Because of the higher hardenability of the steel with tungsten, the transformation in this steel occurs at a lower temperature. A much finer precipitate distribution was evident for all of the carbide morphologies in the steel with 1%W. Also, in the 2 1/4Cr-1WV steel, none of the ribbon structure was evident. In a similar way, the small amount of fibrous and interphase precipitate that formed in the 2 1/4Cr-2WV steel was finer than that in the 2 1/4Cr-1WV steel.

The synergistic effect of tungsten and vanadium was evident in the tensile properties of the 2 1/4-Cr steels, where the 2 1/4Cr-2W steel was generally the weakest or had properties similar to those of the 2 1/4CrV.⁶ The overall carbide distribution of the 2 1/4Cr-2W steel was coarser than the distributions in the steels containing vanadium -- even the steel without tungsten.

With the exception of the MC, the carbides in the 2 1/4-Cr steels were similar to those observed in 2 1/4Cr-1Mo steel.⁷ The carbides detected by x-ray diffraction -- M₃C, M₇C₃, and M₂₃C₆ -- are observed in 2 1/4Cr-1Mo steel; M₂C and M₆C are also seen.⁷ Which of the carbides is present in the 2 1/4Cr-1Mo depends on the heat treatment the steel is given.⁷ Although M₂C was not detected by x-ray diffraction, the XEDS analysis indicated that the needles in the 2 1/4Cr-2W steel are probably M₂C (or M₂X). Those needles were tungsten rich, which is what is expected; in 2 1/4Cr-1Mo steel, molybdenum-rich M₂C forms.

For the 9- and 12-Cr steels, the carbides were primarily M₂₃C₆, although from the XEDS analysis most of the finer precipitates were concluded to be MC. Similar carbides were found in the 9Cr-1MoVNb and 12Cr1MoVW steel.^{8,9} The carbides in the 5Cr-2WV steel contained the chromium-rich carbides found in both the low- and high-chromium steels: both M₇C₃ and M₂₃C₆ were observed, indicating how the chromium concentration determines the carbides that occur.

The large amount of precipitation that occurred on prior austenite grain boundaries and lath boundaries in the microstructures of the 5-, 9-, and 12-Cr steels was similar to observations in the 9Cr-1MoVNb steel.⁸ Much more precipitate was observed in the 12Cr-1MoVW steel;⁸ however, this steel contained 0.2% C, twice as much carbon as the 9Cr-1MoVNb steel and the steels of the present study.

Discussion

The precipitate morphologies observed in these steels are related to the characteristics of the austenite to polygonal ferrite transformation in alloy steels. Because the eutectoid composition in such steels occurs at lower carbon concentrations and higher temperatures than in the Fe-C system, classical pearlite does not appear in the microstructure.⁴ Three different types of ferrite-carbide microstructures are observed:⁴ fibrous carbides, interphase precipitates, and carbides that form in supersaturated ferrite during tempering, often forming on dislocations.⁴ The first two types of precipitation occur at a moving austenite-ferrite interface. The fibers are analogous to pearlite and occur at an incoherent phase boundary; they are much closer to equilibrium than the interphase precipitates. Fibers are associated with a

CONCLUSIONS

The results of transmission electron microscopy observations on eight experimental heats of Cr-W steel with chromium composition varying between 2 1/4 and 12% indicate that these steels develop microstructures similar to the Cr-Mo steels (2 1/4Cr-1Mo, 9Cr-1MoVNb, and 12Cr-1MoVW) presently being considered for fusion-reactor applications. Precipitate types in the alloys varied, depending on the chromium content. For the 2 1/4-Cr steels, M_3C and M_7C_3 were the primary precipitates; for the 9- and 12-Cr steels, $M_{23}C_6$ was the primary precipitate. The 5-Cr steel contained M_7C_3 and $M_{23}C_6$. The steels with vanadium contained MC.

REFERENCES

1. R. L. Klueh and E. E. Bloom, "The Development of Ferritic Steels for Fast Induced-Radioactivity Decay for Fusion Reactor Applications," Nucl. Eng. Design/Fusion 2, 383-389 (1985).
2. R. L. Klueh, "The Development of Ferritic Steels for Fast Induced-Radioactivity Decay," pp. 117-123 in ADIP Semiannu. Prog. Rep., Sept. 30, 1985, DOE/ER-0045/15, U.S. DOE, Office of Fusion Energy.
3. R. L. Klueh, "The Development of Ferritic Steels for Fast Induced-Radioactivity Decay," pp. 109-113 in ADIP Semiannu. Prog. Rep., Mar. 31, 1986, DOE/ER-0045/16, U.S. DOE, Office of Fusion Energy.
4. RWK Honeycombe, "Ferrite," Met. Sci. 14, 201-214 (1980).
5. P. R. Wilyman and RWK Honeycombe. "Relation Between Transformation Kinetics and Mechanical Properties of Vanadium Steels," Met. Sci. 16, 295-303 (1982).
6. R. L. Klueh. "The Development of Ferritic Steels for Fast Induced-Radioactivity Decay," pp. 151-161 in Fusion Reactor Materials Semiannu. Prog. Rep., Mar. 31, 1987, DOE/ER-0313/2, U.S. DOE, Office of Fusion Energy.
7. R. G. Baker and J. Nutting, "The Tempering of 2 1/4%Cr-1%Mo steel After Quenching and Normalizing," J. Iron Steel Inst. (London) 192, 257-268 (1959).
8. J. M. Vitek and R. L. Klueh, "Precipitation Reactions During the Heat Treatment of Ferritic Steels," Met. Trans. 14A, 1047-1055 (1983).
9. P. J. Maziasz, R. L. Klueh, and J. M. Vitek, "Helium Effects on the Void Formation in 9 Cr-1MoVNb and 12 Cr-1MoVW Irradiated in HFIR." J. Nucl. Mater. 141-143, 929-937 (198).

THE INFLUENCE OF SPECIMEN SIZE ON CHARPY IMPACT TESTING OF UNIRRADIATED HT-9- B.S. Loudon and A. S. Kumar (University of Missouri-Rolla). F. A. Garner and M. L. Hamilton (Pacific Northwest Laboratory) and W. L. Hu (Westinghouse Hanford Company)

OBJECTIVE

The object of this effort is to determine the impact of using **sub-size** specimens in the study of mechanical properties and their dependence on irradiation and material variables.

SUMMARY

The effect of specimen size on the impact properties of HT-9 has been studied. The data from the precracked and notched-only specimens of HT-9 were used along with previously published data on other steels to develop correlations that predict from subsized specimen data the ductile-brittle transition temperature (DBTT) and upper shelf energy (USE) anticipated for full-size specimens. Each correlation is based on physical insight and can be applied equally well to both precracked and notched-only specimens. The correlation for USE works best for fracture energy in a range characteristic of irradiated materials, while a previously published correlation works better for more ductile materials. The DBTT correlation, however, works well on all materials for which sufficient data have been published.

Introduction

The development of alloys for structural applications in fusion reactors requires that the influence of environmental factors on their mechanical properties be determined. Such factors include stress, temperature and neutron irradiation. Current irradiation studies involve the ferritic **12Cr-1Mo-VW** steel designated HT-9. **It** has been found that neutron irradiation of ferritic alloys causes an upward shift in the ductile-brittle transition temperature (DBTT), while at the same time lowering the upper shelf energy (USE) for fracture [1,2].

The Charpy impact test is a qualitative method of testing mechanical properties. **It** involves delivering an impact to a notched rectangular bar, which may or may not be precracked. The energy needed to fracture the bar **is** not only a function of the specimen dimensions and test **geometry** but also the test temperature and the prior history of the bar, including the radiation environment.

The standard specimen is a rectangular V-notched bar, 55 mm long with a 1.0 mm square cross-section as defined by ASTM Standard E23-86. These dimensions are too large, however, for inclusion of a comprehensive test matrix in currently available high flux reactors. **Subsize** specimens have therefore been developed to assess the effect of radiation on impact behavior [3].

The major drawback in using subsized Charpy specimens is that they yield a lower DBTT than that derived from full size specimens. This is largely due to a change in the stress state which exists at the notch or crack front. For full size specimens the stress state is mainly one of plane strain, which tends to **promote** brittle fracture. Decreasing the specimen size increases the percentage of the specimen cross-section which is under plane stress, a condition which promotes ductile failure by minimizing constraint. The shift from plane strain to plane stress makes the material appear to be more ductile at a given temperature and therefore decreases the DBTT. In addition, the USE in a Charpy impact test is reduced when specimen size is reduced due to the smaller volume involved in the fracture process.

The purpose of this study was to develop estimates of the corrections needed to apply data generated from irradiated subsized specimens to design applications which require data from full size specimens. Although irradiated specimens were not included in this study, precracked specimens were included and were used to assess the validity of a new Correlation for test conditions which tend to produce lower ductility levels, such as those generated in irradiation environments.

Experimental Procedure

All specimens used in this study were machined from HT-9 plate material of heat **9607R2**, which was manufactured by Electralloy Corporation for the US-DOE Fusion Materials Program. The chemical composition and tensile properties of this heat are given elsewhere [4]. A series of heat treatments was performed on the plate stock to produce a tempered martensitic structure with a hardness of 255 OPH and a prior austenite grain size of ASTM 5 to 6. All specimens were taken from the base material in the transverse (T-L) orientation, in which the long axis of the specimen lies perpendicular to the rolling direction and the direction of elongation of the grains is the same as the direction in which the crack propagates. Specimens in this orientation will have the least resistance to fracture and will therefore provide a minimum estimate of fracture energy.

Dimensions for both full size and subsized specimens are given in Fig. 1. The full size specimen dimensions are in accordance with ASTM Standard E23-86. While there are no standards available for subsized specimens, the dimensions used in this study for half-size and third-size specimens are similar to those used in other investigations [5,6].

Precracked specimens were prepared by loading the notched specimen in a three-point bend arrangement and subjecting it to an oscillating load in a closed loop hydraulic system. The minimum and maximum loads for the oscillations were determined in advance according to ASTM Standard E399 modified for miniature specimens.

Adjustable anvils and interchangeable crossheads made possible the testing of different size specimens on the same instrumented drop tower. Data from each test were recorded on a digital oscilloscope and transferred to a desktop computer for storage and analysis.

Calibration of the instrumented hammer was performed by adjusting the load signal gain so that the maximum load obtained during dynamic testing was the same as the maximum load determined during the slow bend testing of a strain-rate insensitive alloy (6061 aluminum in the T651 heat-treatment) [1]. In addition, a static calibration of the load cell was performed to ensure that its response was linear over the desired range.

The impact velocity of the crosshead was calibrated by attaching a 1 m long flag to the crosshead positioned so that the flag passed an infrared sensor just prior to impact, causing a change in voltage during interruption by the flag. The duration of this change was measured on the oscilloscope and the velocity calculated. Velocity was calculated as the average of at least ten calibration runs.

Temperature control for full-size specimens was accomplished in a conditioning chamber where high temperatures were attained with a heated stream of air and low temperatures were reached by using cold nitrogen gas. Temperature control was achieved by adjusting the rate of gas flow into the conditioning chamber. Each specimen was kept at the test temperature for five to ten minutes prior to testing to ensure temperature stabilization to within two degrees Celsius. Temperature control for the subsize specimens used the same sources of heated or cooled gas, but because the conditioning chamber was designed specifically for full-size Charpy specimens, the miniature specimens were manually placed and aligned in the testing position and the gas was directed across the specimen surface. A thermocouple spot-welded across from the notch (opposite the surface being impacted) was used to monitor the temperature for each test.

Specimen placement for full-size specimens was achieved by air-driven pistons that moved the specimen from its initial position, into and out of the conditioning chamber, and finally into the testing position using a rotary positioning arm. ASTM Standard E23-86 provides for a maximum five second delay between obtaining the desired temperature and impacting the specimen. For full-size specimens, the elapsed time between the exit of the sample from the conditioning chamber and the impact was approximately 0.2 seconds. For subsize specimens, no specimen transfer was involved.

Results

Definitions of the DBTT are numerous. It is defined here as the temperature at the midpoint between the upper and lower shelf energies. The relationship between the apparent absorbed energy, E_a , and the actual absorbed energy, ΔE , in a Charpy test is given as [7]:

$$AE = E_a (1 - E_a / 4E_0), \quad (1)$$

where E_a is the energy integrated from the load-time curve ($V_0 \int_0^{\tau} P(t) dt$), $P(t)$ is the load at time t during the impact test, τ is the duration of the test, V_0 is the initial impact velocity, E_0 is the available impact energy, given by $1/2 m V_0^2$ and m is the mass of the crosshead.

The test results for both the notched-only and precracked conditions for all three specimen sizes are tabulated in Tables 1 and 2 and shown in Fig. 2 with a Gaussian integral fit through the data points [8]. In the notched condition the DBTT decreases from 271 K for full-size specimens to 226 K and 209 K for half-size and third-size specimens, respectively. In the precracked condition the DBTT decreases from 275 K for full-size specimens to 246 K and 239 K for half-size and third-size specimens, respectively. The DBTT values obtained in the precracked specimens are consistently higher than those observed in the notched specimens, with the difference between notched and precracked DBTT increasing as specimen size is decreased. In addition, the observed changes in DBTT with specimen size are smaller for precracked than for notched specimens due to the increased stress concentration at the crack tip.

Table 2 demonstrates that a substantial reduction occurs in USE with both decreasing size and precracking of the specimen. Precracking reduces the USE by roughly a factor of three, regardless of specimen size. Reduction in specimen size causes a drop in USE of roughly a factor of six for half-size specimens and a factor of about twenty for third-size specimens, regardless of whether the specimens are precracked or notched.

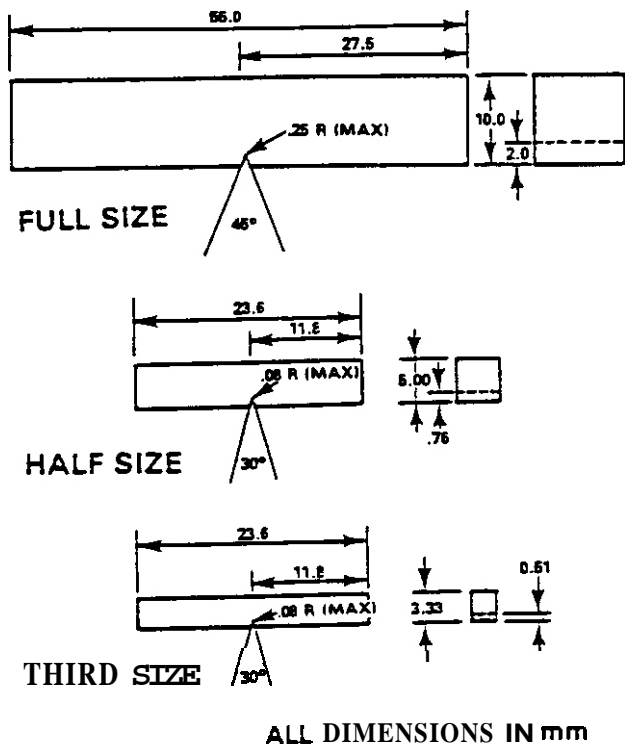


Fig. 1 Dimensions of full and subsize Charpy specimens.

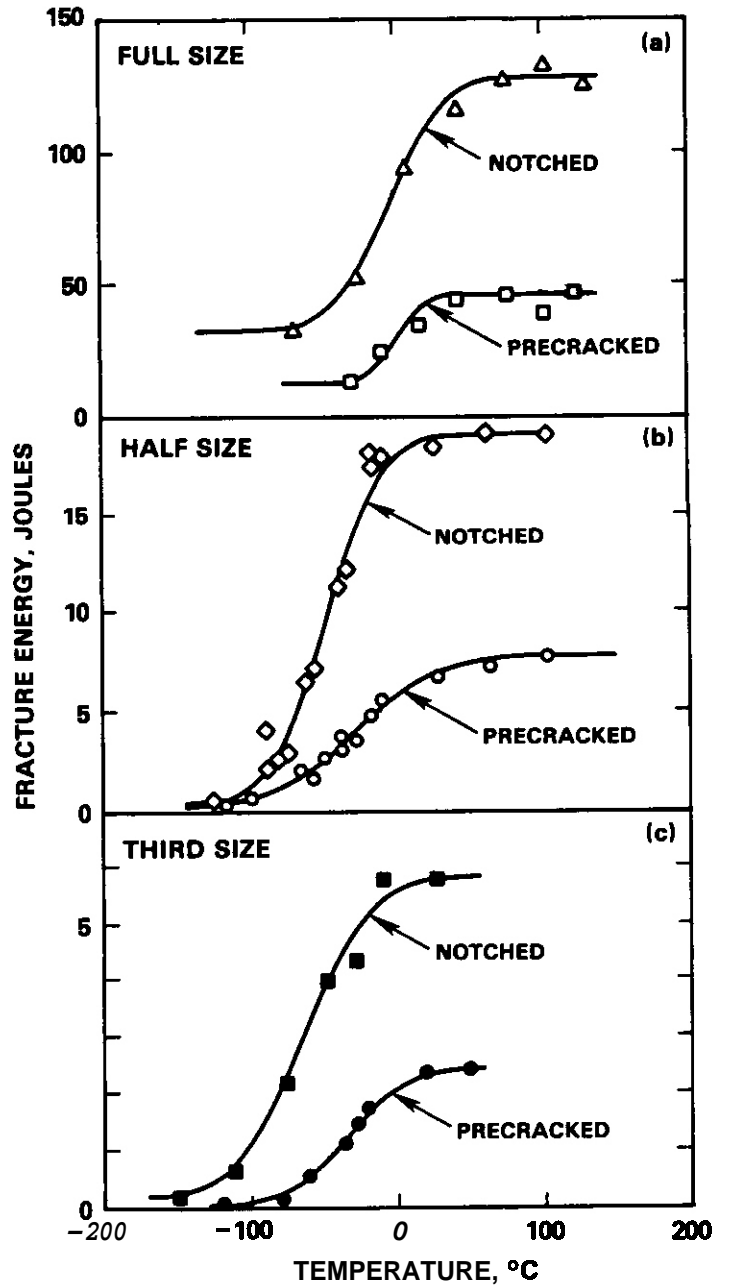


Fig. 2 Dependence of fracture energy on temperature for both notched-only and precracked specimens for (a) full size, (b) half size, (c) third size.

TABLE 1

HT-9 Charpy Data - DBTT

DBTT			
	Notched-Only (K)	Precracked (K)	DBTT * (K)
Full Size	271	275	4
Half Size	226	246	20
Third Size	209	239	30

$$\text{DBTT} = \text{Precracked OBTT} - \text{Notched DBTT}$$

TABLE 2

HT-9 Charpy Data - USE

USE			
	Notched-Only (K)	Precracked (K)	Ratio * (K)
Full Size	129	44	2.9
Half Size	19	8	2.4
Third Size	6	2	3

$$* \text{ Ratio} = \frac{\text{Notched USE}}{\text{Precracked USE}}$$

Correlation Development

A methodology is presented below that will permit an estimation from subsized specimen data of the shifts in OBTT (ΔDBTT) and upper shelf energy (ΔUSE) which would be observed in full-size specimens following neutron irradiation. The methodology invokes a hypothesis also considered by others [9], namely that fracture is controlled by the maximum tensile stress ahead of the crack tip normal to the crack plane. When this stress exceeds a critical value σ^* the crack propagates causing fracture. According to Lucas et al [10], σ^* is a material property unaffected by specimen size or notch geometry. Note that the published data employed in this study for the analysis of DBTT and USE are not from identical studies due to the lack of sufficiently complete published information on fracture stress.

DBTT Shift Due to Irradiation or Other Variables

It is anticipated that the neutron-induced ΔDBTT will be a function of the specimen size, particularly for the small sizes investigated in this study. For larger size specimens typical of nil ductility tests, however, the correlation between DBTT as measured in the Charpy V-notch test and nil ductility transition temperature as measured in a drop weight test remains the same after irradiation, indicating that size effects are not as important at larger sizes [11]. In order to estimate ΔDBTT for full-size specimens based on subsized specimen data, a normalized DETT (DETT_n) is defined in the present work. The shift in DBTT due to irradiation or any other environmental variable is postulated to be independent of specimen size or notch geometry. DETT_n is defined as the ratio of the measured DBTT to the normalization factor, σ^* , which is equal to the maximum normal elastic stress at the notch root. The expression used to calculate σ^* was:

$$\sigma^* = K_t 3P_m L / (2B(W-A)^2) \quad (2)$$

where K_t is the stress concentration factor. The formulae to calculate K_t are given in reference 12. The values of K_t for full-, half- and third-size notched specimens used in the present study are 4.8, 7.6, and 6.2, respectively. L , E , W and A are the span, thickness, width and notch depth, respectively (Fig. 1). P_m is the maximum load observed in a Charpy test at the point of general yielding. The value of P_m was not measured in the present study and therefore an alternative approach was employed to calculate

it. In order to calculate σ_f , a value of σ_f^t estimated by Lucas et al [10] for HT-9 is used. In related work of Lucas et al [13], fracture stress was given by:

$$\sigma_f^t = 6.52 P_m / B(W-A) \quad (3)$$

Therefore,

$$P_m = \sigma_f^t * B(W-A) / 6.52 \quad (4)$$

Since σ_f^t is constant for a given material appropriate values of B, W and A give values of P_m for both full-size and subsize specimens. For precracked specimens the value of σ_f^t is assumed to be the same as that of notched specimens. since in this study σ_f^t is hypothesized to control fracture.

To validate the starting hypothesis, the full-size OETT is plotted as a function of subsize DBTT in Fig. 3 for the notched-only as well as the precracked specimens tested in both our study and that of Lucas et al [13]. The study of Lucas et al involved only full- and third-size specimens. Compositions of all steels in Fig. 3 are given in reference 13. It is evident that, for a given material, heat treatments or precracking change the DBTT_n such that they all lie on a straight line with a slope of approximate unity. Considering the data of Lucas et al, the A508 steel and the re-austenitized A508 steel data can be connected with a straight line of slope close to unity. Similar behavior is shown in the DBTT_n data from the A710 steel in the as-received, peak aged, overaged and underaged conditions. The A302 DBTT_n data were available for only one alloy condition, as is shown in the figure. For the HT-9 specimens tested in the current study, it can be seen that the OETT for notched-only and precracked conditions could also be connected by a line with slope of approximately unity for both the half- and third-size specimens. However, more widely spaced or additional data are needed to support the validity of this statement. The DBTT_n data suggest the following relationship between full-size and subsize data for a given material:

$$(DBTT_n)_{full\ size} = (DBTT_n)_{subsize} + constant \quad (5)$$

As shown in Fig. 3, the constant is both size and material dependent, but is independent of alloy condition. Shifts in OETT can therefore be calculated by subtracting equation 5 for alloy condition 1 from equation 5 for alloy condition 2, causing the constant to disappear for a given subsize specimen and a particular steel, yielding:

$$\Delta(DBTT_n)_{full\ size} = \Delta(DBTT_n)_{subsize} \quad (6)$$

$\Delta DBTT_n$ is the shift in DBTT_n due to a change in alloy condition such as that induced by heat treatment, precracking or irradiation. Hence, shifts in OETT values due to irradiation for full-size specimens can be obtained from subsize data.

Although irradiated specimens were not included in the present study, precracked specimens were included and were used to assess validity of the correlation for test conditions producing lower levels of ductility, such as are generated in irradiation environments. The shifts in DBTT_n for full-, half- and third-size specimens due to precracking are shown in Fig. 3 to be approximately equal. Thus, this experiment provides validity for equation 6, as does that of Lucas et al. Based on these results it is believed that the shifts in DBTT_n for full-size and subsize specimens due to irradiation-induced embrittlement will also be equal.

Upper Shelf Energy

Other investigators have used various normalization factors that incorporate the thickness E and ligament size, (W-A), to correlate the USE values for full- and subsize specimens C6.101. Corwin and coworkers C61 used $(B(W-A))^{3/2}$ as a normalization factor, which is related to the extent of plastic deformation below the notch root. One shortcoming of this approach is that only two of the specimen dimensions are used, while the third dimension and the notch geometry are not taken into account.

In the present study, the following normalization factor was used, incorporating all specimen dimensions as well as the notch geometry:

$$B(W-A)^2 / LK_t \quad (7)$$

where K_t , L, E, W and A are the stress concentration factor, span, thickness, width, and notch depth, respectively. The stress concentration factor is a function of the ligament size (W-A) and the radius of the notch root. The normalized USE is the ratio of the measured USE to the normalization factor.

The insight underlying this combination of parameters can be seen by examining their individual effect on USE. For instance, as the span L is increased, the strain rate at the notch is decreased and the USE is lowered [6]. A high value of K_t will also lower the USE by causing brittle fracture. Finally, the product $B(W-A)^2$ is an approximation of the volume of plastic deformation at the crack tip [10]. As this volume decreases, the USE also decreases.

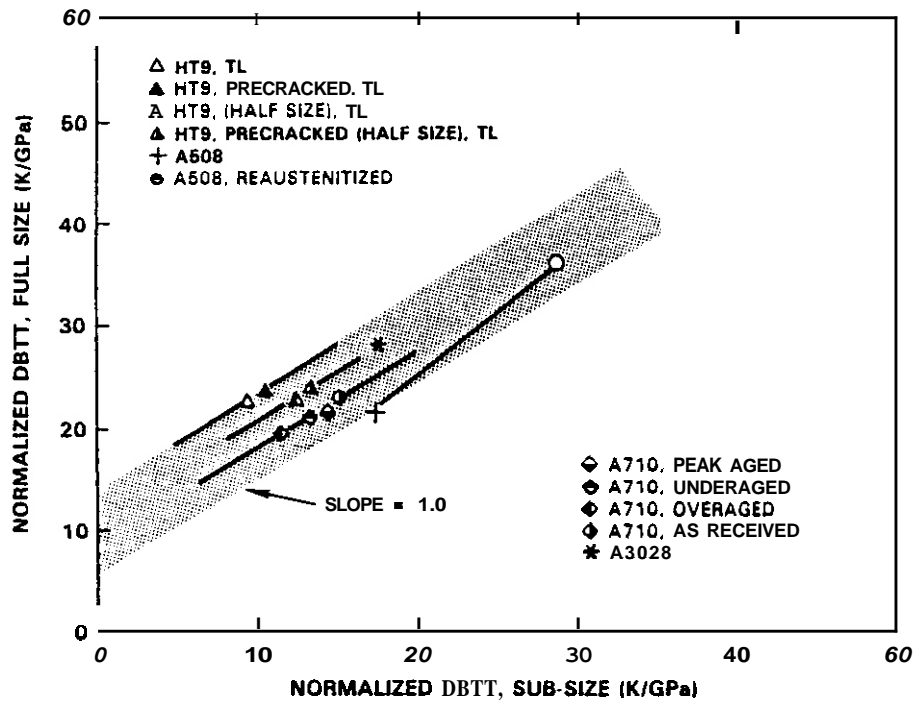


Fig. 3 Comparison of normalized DBTTs for various materials. All subsize specimen data points correspond to third size specimens except those marked half size. The dimensions for the HT-9 specimens are given in Fig. 1; the third size specimens used by Lucas et al [12] were $3.3 \times 3.3 \times 18.3$ mm with a 0.67 mm deep notch, and a root radius of 0.076 mm. Note that for specimen groups of one size and one material, the data points can be connected with a line of slope near unity.

The normalization was applied to the results of the present work as well as to data for ten other materials from Corwin and coworkers [5,6] and to one data set from the work of Ferguson [14]. Fig. 4a shows a graph of normalized USE, divided by the average of the normalized values of full-, half- and third-size specimens obtained for each material, against full-size USE. If the current normalization factor is indeed valid, the normalized energies for full-, half- and third-size would be equal and the points in Fig. 4a would fall on the horizontal line with ordinate equal to 1.00. It is clear from Fig. 4a that the normalization is most accurate (within $\pm 10\%$) for materials with relatively low values of USE, i.e., for full-size values less than 150 J. Such low USEs are characteristic of irradiated materials. Given the large range of USE values observed in HT-9 specimens, the normalization factor does an excellent job of collapsing these data.

Discussion

Fig. 4b shows that the normalization factor of Corwin et al [6], used to analyze the same USE data field, failed to correlate materials exhibiting low USEs. The success of Corwin's model at high USE values is thought to be somewhat fortuitous, but it would be expected to work best under conditions where notch geometry is relatively unimportant, i.e., in those alloys with a greater degree of substantial work-hardening. At lower levels of ductility, the influence of work-hardening is relatively small compared to stress concentration considerations and the proposed model is more successful. This is particularly demonstrated by the success of the current correlation for precracked specimens. It is obvious, however, that some measure of the fracture energy's dependence on work-hardening must be incorporated in order to extend the range of validity over which our correlation is valid. Note in Figs. 4a and 4b that there is a persistent bias with respect to the placement of the normalized data as a function of specimen size, and that the sense of this bias is reversed in the two correlations. This also implies that the full dependence on size effects has not been incorporated in either model. It should be noted, however, that the bias in both models is minimized in the range of fracture energies where each correlation is most successful.

Compared to the USE correlation, the more general validity of the current correlation for DBTT is thought to arise from the fact that the DBTT is associated with fracture energies lower than that of the USE, thereby minimizing the impact of work-hardening considerations.

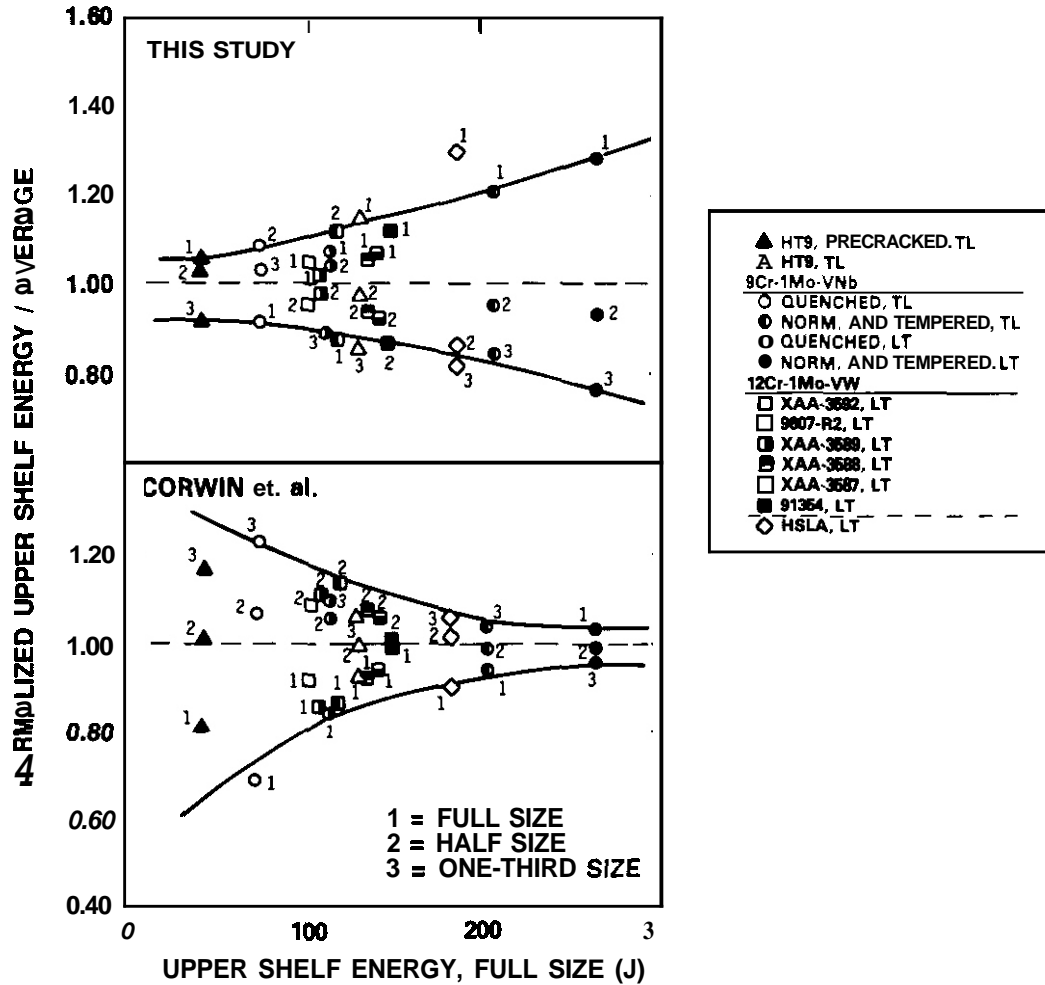


Fig. 4 Comparison of normalized USEs of various materials. Superscripts 1, 2 and 3 on data points refer to full, half and third size specimens. All specimens are notched-only, except those labeled precracked. TL means that the specimen axis is perpendicular to the rolling direction. LT means that the axis of the specimen is parallel to the rolling direction. The specimen geometries for all specimens are shown in Fig. 1.

- (a) Normalization of the present study
(b) Normalization of Corwin et al C61

CONCLUSIONS

A normalization factor for the DBTT has been proposed. It is related to the maximum elastic normal stress at the notch root. The normalized DBTT is the ratio of the measured DBTT to the normalization factor. The shift in the normalized DBTT for full-size specimens has been shown to equal that for subsized specimens over a wide range of materials. The normalization correlates data for both notched-only and precracked specimens.

A new normalization factor for upper shelf energy was also proposed that takes all specimen dimensions and notch geometry into account, thereby including the stress concentration at the notch root. The normalized USE equals the ratio of USE to the normalization factor. Normalized USEs for full-size specimens were approximately equal to those of subsized specimens for full-size USEs below approximately 150 J, the range of values characteristic of irradiated materials.

FUTURE WORK

This work will continue, incorporating other data fields and developing correlations which span materials having a wide range of upper shelf energies.

REFERENCES

1. W. L. Hu and D. S. Gelles. Proc. Conf. on Ferritic Alloys for Use in Nuclear Energy Technologies, Snowbird, UT, (June 1983) p. 631.
2. R. W. Powell, G. D. Johnson, M. L. Hamilton and F. A. Garner. in the Proc. of the ANS International Conf. on Reliable Fuels for Liquid Metal Reactors ■ Tucson, AZ, (September 1986) p. 4-17.
3. P. McConnell, J. W. Sheckherd, J. S. Perrin and R. A. Willaert. ASTM STP 888, eds., W. R. Corwin and G. E. Lucas. (American Society for Testing and Materials. 1986) p. 353.
4. T. A. Lechtenberg. ADIP Semiannual Progress Report, DOE/ER-0045/8 (March 1983) p. 363.
5. W. R. Corwin, R. L. Kleuh and J. M. Vitek. J. Nucl. Mater. 122-123 (1984) 343.
6. W. R. Corwin and A. M. Hougland. ASTM STP 888, eds., W. R. Corwin and G. E. Lucas. (American Society for Testing and Materials. 1986) p.325.
7. D. R. Ireland. ASTM STP 563, (American Society for Testing and Materials. 1974) p. 3.
8. G. Hofsr and C. C. Hung. Nuc. Tech. 49 (1980) 492.
9. R. A. Willaert, O. R. Ireland and A. S. Tetelman. ASTM STP 484, (American Society for Testing and Materials, 1970) p. 20.
10. G. E. Lucas, G. R. Odette, J. W. Sheckherd, P. McConnell and J. S. Perrin, ASTM STP 888, eds., W. R. Corwin and G. E. Lucas. (American Society for Testing and Materials. 1986) p. 305.
11. R. Hawthorne and L. E. Steele, ISI Special Report No. 69, 1961.
12. H. Neuber, Theory of Notch Stresses, Springer Publishers. Berlin. 1958, 2nd Ed. p. 71.
13. G. E. Lucas, G. R. Odette, J. W. Sheckherd and M. R. Krishnadev. Fusion Tech., 10 (1986) 728.
14. B. L. Ferguson. In: Proc. of a Symposium held at the Annual Meeting of the American Institute of Mining, Metallurgical and Petroleum Engineers, Denver. CO, (February 1978) p. 90.

TEMPERATURE DEPENDENCE OF YOUNG'S MODULUS OF LOW-ACTIVATION FERRITIC ALLOYS — H. T. Lin and B. A. Chin
(Department of Mechanical Engineering, Auburn University, Auburn, AL 36849)

OBJECTIVE

To investigate the Young's modulus of low-activation ferritic alloys as a function of temperature.

SUMMARY

Measurements of Young's modulus of low-activation ferritic alloys have been performed using a dynamic mechanical technique over the temperature range from -150 to 350°C . The results indicate that the moduli of alloys investigated decrease approximately linearly with test temperature. Also, the constant is independent of chromium content and its corresponding microstructure. Based on a comparison with the literature, good agreement was found between data obtained in this study and those reported by various investigators.

PROGRESS AND STATUS

Introduction

Because of their good mechanical properties and excellent resistance to radiation-induced swelling and creep, ferritic alloys have been chosen for investigation as candidates for the structural components of fusion reactors. However, these alloys will become highly radioactive during service, imposing waste disposal problems after service. This issue has led to the development of a series of low-activation ferritic alloys by Hanford Engineering Development Laboratory (HEDL).

No research has been conducted to investigate the tensile elastic constant, E , of low-activation ferritic alloys as a function of temperature. In an effort to provide physical property data on candidate alloys for use in concept evaluation, design, safety analysis and performance/verification studies of various fusion energy systems, measurements were performed to provide values of Young's modulus as a function of test temperatures from -150 to 300°C . Also, agreement between data obtained in this investigation and results reported by various investigators was evaluated.

Experimental Procedures

Eleven heats of low-activation ferritic alloys patterned on $2\frac{1}{4}\text{Cr-1Mo}$, 9Cr-1Mo , and 12Cr-1Mo steels were fabricated by HEDL. The nominal chemical compositions of these alloys are listed in Table 1.

Table 1. Chemical Composition of Low-Activation Ferritic Alloys

Heat No.	Composition, wt %					
	Cr	V	W	C	Mn	Ta
V02262	2 $\frac{1}{4}$	0.5		0.1		
V02263	2 $\frac{1}{4}$	1.0		0.1		
V02264	9.0	0.5		0.1		
V02265	9.0	1.3		0.2	1.0	
V02266	9.0	0.5		0.1	2.0	
V02268	9.0	0.3	1.0	0.1	2.5	
V02267	12.0	1.0		0.1	6.5	
V02269	12.0	0.3	1.0	0.1	6.5	
V02702	12.0	0.3	1.0	0.1	6.5	0.1
V02734	12.0	0.3	1.0	0.1	6.5	0.25
V02735	12.0	1.0	0.3	0.1	8.0	0.25

All heats were hot-rolled with an intermediate heat treatment at 700°C for 30 min to a final thickness of 2.54 mm. All sheets were homogenized for 20 h at 1000°C followed by air-cooling. The materials were solution annealed for 1 h at 1150°C , air-cooled, then given a tempering treatment at 700°C for 2 h followed by air-cooling. A small section of material was cut from each sheet and cold-rolled to the final thickness of 0.25 mm.

The elastic constant measurements were performed using a dynamic mechanical thermal analyzer (DMTA) which is a microprocessor-based instrument capable of measuring the dynamic modulus of different geometries through a variety of clamping configurations. Materials in the present study were evaluated in a single cantilever arrangement on the DMTA and were tested at a temperature range from -150 to 300°C at intervals of 50°C at a frequency of 1 Hz.

Results and Discussion

Tensile elastic constant measurements of low-activation ferritic alloys are summarized in Table 2. Each value of the constant reported is the average of three determinations with an error of 1%. The

Table 2. Temperature Dependence of Young's Modulus, 10^{11} Pa

	-150°C	-100°C	-50°C	0°C	50°C	100°C	150°C	200°C	250°C	300°C
2 1/4 Cr										
V02262	2.290	2.240	2.188	2.140	2.110	2.089	2.042	1.995	1.905	1.820
V02263	1.930	1.905	1.862	1.862	1.820	1.820	1.820	1.778	1.738	1.698
9 Cr										
V02264	2.188	2.188	2.140	2.042	1.995	1.950	1.950	1.950	1.905	1.905
V02265	2.089	2.089	2.042	2.042	1.995	1.950	1.950	1.950	1.905	1.698
V02266	1.950	1.928	1.905	1.862	1.820	1.778	1.778	1.778	1.738	1.698
V02268	2.140	2.140	2.089	2.042	1.995	1.995	1.995	1.972	1.950	1.905
12 Cr										
yo2267	2.089	2.042	2.042	1.995	1.950	1.905	1.905	1.862	1.820	1.738
V02269	2.140	2.089	2.089	2.065	2.042	1.995	1.995	1.950	1.905	1.862
V02702	1.905	1.862	1.862	1.820	1.778	1.778	1.738	1.738	1.660	1.621
V02734	1.995	1.950	1.950	1.905	1.862	1.820	1.820	1.738	1.698	1.660
V02735	2.042	1.995	1.995	1.950	1.905	1.862	1.862	1.820	1.820	1.738

results in Figs. 1 through 3 show moduli of 2 1/4-, 9- and 12-Cr alloys as a function of test temperatures. The observations indicate that elastic modulus decreases approximately linearly with increasing test temperature. The decrease in modulus is due to the decrease in cohesive force between atoms with increasing temperature, which consequently leads to an increase in degrees of freedom of atomic motion.

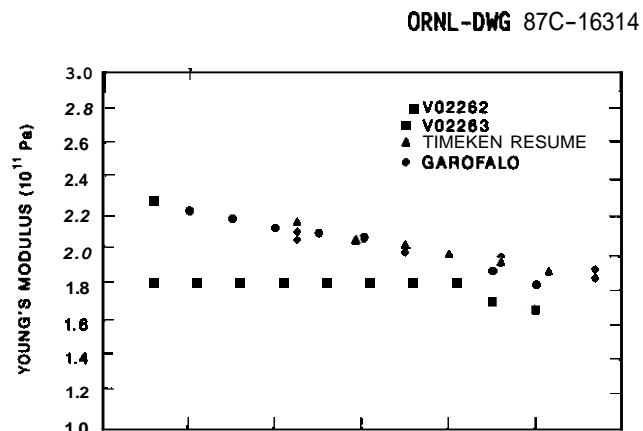


Fig. 1. Temperature dependence of Young's modulus of 2 1/4-Cr alloys.

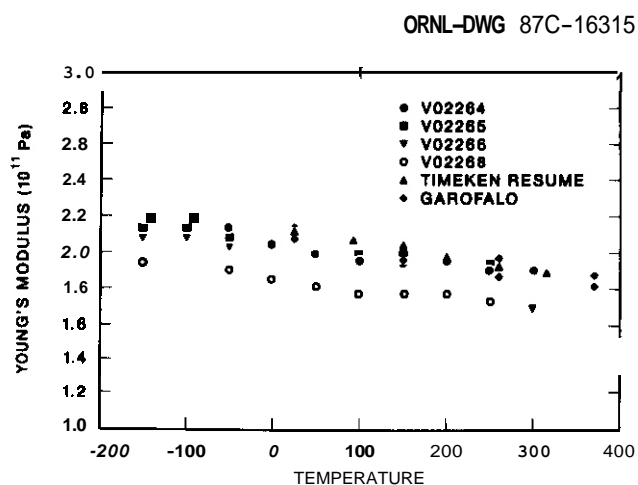
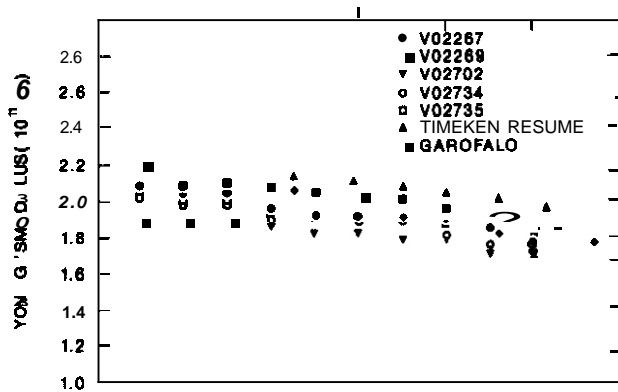


Fig. 2. Temperature dependence of Young's modulus of 9-Cr alloys.

By comparing the results obtained from specimens with different chromium content, as shown in Figs. 1 through 3, it was observed that a good agreement exists. At any test temperature, the variation in constant E among test specimens, with the same chromium content but with different alloying composition, is 7×10^9 Pa (1×10^6 psi). It was known that the elastic constant of metals and alloys is governed by the cohesive energy between the atoms.⁴ However, the nature of cohesive energy in metals, and particularly in alloys, is not well understood. It is suggested that the variation in elastic constant is due to the difference in the effect of alloying elements on the charge distribution and Fermi energy level, which are dominant factors affecting the cohesive energy, in turn affecting the elastic constant. Additionally, it is of interest to note that measurement of E is approximately independent of chromium concentration. The standard variation is found to vary between 2×10^9 Pa (0.29×10^6 psi) and 4×10^9 Pa (0.58×10^6 psi) for all the low-activation alloys studied.



in Figs. 1 through 3 for purposes of comparison. These additional data were determined by static as well as dynamic measurements. A reasonable agreement is observed among the results of various investigators. The variation is in the range of 5×10^9 Pa (0.73×10^6 psi) and 23.8×10^9 Pa (3.45×10^6 psi).

In spite of different chromium contents and minor alloying elements, it is revealed from Figs. 1 through 3 that there is essential agreement on the rate of decrease in the Young's modulus with temperature, dE/dT . A statistical analysis indicates that the slope of dE/dT is

CONCLUSIONS

The results of this study lead to the following conclusions:

- Tests at various temperatures on low-activation alloys with minor variation in alloying elements, but with a significant difference in chromium content, show that Young's modulus is independent of chromium concentration.
- Elastic modulus E of ferritic steels decreases approximately linearly with increasing test temperatures.
- The rate of decrease in elastic modulus E with temperature, dE/dT , is essentially the same for all ferritic steels.

REFERENCES

1. D. S. Gelles and M. L. Hamilton, p. 128 in AOIP Semiannu. Progr. Rep. Sept. 30, 1984, DOE/ER-0045/13, USDOE Office of Fusion Energy.
2. F. Garofalo, P. R. Malenock, and G. V. Smith, p. 10 in Symposium on Determination of Elastic Constants, June 25, 1952. ASTM 129.
3. "Resume' of High-Temperature Investigations Conducted During 1948-50," The Timeken Roller Bearing Co., Steel and Tube Division, Canton, Ohio.
4. M. A. Jaswon, The Theory of Cohesion, Pergamon Press, Ltd., London, 1954.
5. P. Chevenard, Revue de Metallurgie 40, 289 (1943).
6. G. E. Bennett and R. M. Davies, J. Inst. Metals 75, 759 (1948-49).
7. C. Zener, Phys. Rev. 60, 906 (1941).
8. T. S. Ke, Phys. Rev. 71, 533 (1947).
9. T. S. Ke, J. Appl. Phys. 19, 285 (1948).
10. T. S. Ke, Phys. Rev. 72, 41 (1947).
11. T. S. Ke, Trans. AIME 176, 448 (1948).

6.2 Austenitic Stainless Steels

IRRADIATION CREEP AND SWELLING OF AISI 316 TO EXPOSURES OF 130 dpa AT 385-400°C - F. A. Garner (Pacific Northwest Laboratory) and D. L. Porter (EBR-II Project, Argonne National Laboratory)

OBJECTIVE

The object of this effort is to determine the parametric sensitivity of void swelling and irradiation creep for structural materials proposed for fusion service.

SUMMARY

The creep and swelling of AISI 316 stainless steel have been studied at 385 to 400°C in EBR-II to doses of 130 dpa. Most creep capsules were operated at constant stress and temperature but mid-life changes in these variables were also made. This paper concentrates on the behavior of the 20% cold-worked condition but five other conditions were also studied. Swelling at <400°C was found to lose the sensitivity to stress exhibited at higher temperatures while the creep rate was found to retain linear dependencies on both stress and swelling rate. The creep coefficients extracted at 400°C agree with those found in other experiments conducted at higher temperatures. In the temperature range of <400°C, swelling is in the recombination-dominated regime and the swelling rate falls strongly away from the ~1%/dpa rate observed at higher temperatures. These lower rates of creep and swelling, coupled with the attainment of high damage levels without failure, encourage the use of AISI 316 in the construction of water-cooled fusion first walls operating at temperatures below 400°C.

PROGRESS AND STATUS

Introduction

Type 316 stainless steel is sometimes considered as a candidate structural material for the first wall and other components of proposed fusion devices. While the use of this steel will be limited by its large rates of swelling and creep above ~450°C, the potential exists for its use in devices in which the first wall runs at lower temperatures, particularly for water-cooled devices. Based on available data, the incubation period of swelling is much longer at lower temperatures and creep will also be delayed.^{1,2} It is also expected that below some temperature on the order of 400°C, the steady-state swelling rate will fall from the temperature-independent value of ~1%/dpa and eventually vanish as recombination-dominated point defect kinetics comes into play.^{3,4} In that event, the design limitations imposed on swelling-related allowable exposure can be relaxed considerably.

The lowest temperature attainable in the US. fast reactors employed to test fusion candidate materials is ~370°C. Data on this steel at this temperature do not extend beyond 50 displacements per atom (dpa) and are not being collected at higher fluence levels.² Data at 400°C are available to ~70 dpa but are insufficient to determine whether the steady-state swelling rate has begun to decline below the rate of 1%/dpa. The possibility that both creep and steady-state swelling rates are reduced at ~400°C has now been addressed by examining a very comprehensive irradiation creep experiment recently completed in EBR II, in which many creep tubes reached exposures on the order of 130 dpa. The data from these tubes represent the highest exposure level ever reported for an irradiation creep experiment. A previous experiment in this series was conducted at 550°C but was terminated at ~80 dpa.^{5,6} The steel employed in both of these experiments was the N-lot heat 87210, previously used as a reference heat in the US. breeder reactor program.

Experimental details

Four cold-work levels (0, 5, 10, 20%) as well as two separate aging conditions were employed. These latter were 20% cold-worked followed by aging at 482°C for 24 hours (Heat Treat C), and Heat Treat C followed by another aging at 704°C for 216 hours (Heat Treat D). This report will concentrate on the 20% cold-worked condition as the most likely fusion candidate material and will examine the other conditions only to the depth required to determine whether the major conclusions are dependent on the starting condition of the material. The larger body of data on all conditions and test histories will be presented elsewhere.

Hoop stress levels of 0, 206, 276 and 343 MPa (0, 30, 40, 50 ksi) were attained with pressurized helium. Most tubes were irradiated at constant stress and temperature but some were deliberately subjected to abrupt changes in stress level and/or temperature.

The pressurized section of the capsules was 0.98 m in length but the bottom 0.71 m contained a loosely fitting stainless steel rod designed to reduce the pressure pulse that could result from a sudden failure. The outer diameter of the capsule was 0.584 cm with a wall thickness of 0.038 cm. Irradiation was conducted in Row 7 of EBR-II in two thirty-seven pin subassemblies designated X101 and X133. Approximately 5 dpa ($\pm 10\%$) are produced in this reactor for each 1.0×10^{22} n/cm² ($E > 0.1$ MeV) depending on the position in reactor. The dpa levels cited for each datum in this paper incorporate the position dependence of this parameter.

To minimize the effect of swelling-induced axial growth on the experiment, only the section at or below the capsule center was used in the analysis. At the end of each irradiation period, a contact profilometer was used to measure the capsule diameter on a spiral trace along the entire length of the capsule. The majority of capsules were measured as many as twenty-two times during the irradiation, averaging between examinations approximately 6 dpa at capsule center. As shown in Fig. 1, the temperature over the region of interest rose from 385 to 400°C at capsule center.

When the experiment was terminated, selected capsules were sectioned into 25 cm increments and density changes were measured in order to separate the swelling and creep strains. The effects of displacement rate on creep and swelling were determined by comparing the strain at different positions along the capsule.

Results

Fig. 2 shows the diameter changes observed in four selected 20% cold-worked capsules at the capsule center position. Each capsule operated at a different level of pressurization and the total center line strain increased with increasing stress. The diameter change ΔD of the unstressed capsule is assumed to be due only to isotropic swelling where $\Delta D/D = \Delta V/3V$, an assumption that has been verified many times previously. The diameter change of pressurized capsules is due to both irradiation creep and swelling, with the latter possibly enhanced by applied stresses. Based on previous studies of this steel, the enhancement of swelling by stress at 400°C is expected to be very small, however.^{7,8}

The dependence of swelling on stress can be checked by comparing the density changes of each of these capsules. Fig. 3 shows that in the three pressurized capsules, there was no observable effect of stress at any position along the capsule. Whereas the data in Fig. 2 were taken all at one position and displacement rate, the data in Fig. 3 were derived at different axial locations and incorporate relatively large differences in displacement rate and relatively small differences in temperature. Fig. 3 does not contain any density data for the unstressed capsule but does contain the last four measurements of swelling deduced from diameter change at capsule center. These data also confirm the insensitivity of swelling to stress at 400°C. No density data were available for this capsule because the filler rod (which exists at a slightly higher temperature) had swelled into contact with the capsule wall at -80 dpa, binding with and distorting it. Normally this does not occur at lower fluences or when gas-driven creep is operating on the capsule wall.

The swelling rate implied by the data in Fig. 3 is on the order of 0.05 to 0.07%/dpa, much lower than 1%/dpa. This rate is derived over a considerable range of displacement rate, however, and one would expect a dependence on displacement rate whenever a strong dependence on temperature is observed.⁹ The effect of the flux and temperature variations on total deformation can be observed in Fig. 4. One can deduce from Fig. 4 that the swelling rate derived from Fig. 3 might be an underestimate. The average stress-free swelling rate under isoflux conditions can be derived from Fig. 2 and is indeed somewhat larger at $S = 0.11\%/dpa$ over the range 70 to 130 dpa.

Fig. 5b shows that one cannot place too much confidence in the reproducibility of such estimates under conditions where the swelling rate is changing so strongly. Note that at -20 dpa, one capsule at 343 MPa (50 ksi) lost its pressure and thereafter swelled stress-free at a relatively constant rate of $S \approx 0.04\%/dpa$. A similar event occurred at -60 dpa in a 10% cold-worked capsule initially at 343 MPa and yielded a post-depressurization swelling rate of $S \approx 0.05\%/dpa$. Another occurred at -6 dpa in one of the aged (Heat Treat D) capsules at 276 MPa and thereafter yielded a remarkably constant swelling rate of $S \approx 0.09\%/dpa$ over the range of 10 to 107 dpa.

Figs. 5a and 5b show that the overall strain behavior of nominally identical capsules is quite reproducible. The small differences seen probably reflect minor differences in irradiation conditions at various positions across the subassembly.

One would expect the strain rate to increase if the stress level and/or the temperature were to be increased. Figs. 6a and 6b show that this indeed occurs in experiments where deliberate increases were made in these variables. Note in Fig. 6b that the combination of higher stress and an increase to 550°C yielded a total deformation rate that approaches the $\Delta D = 0.33\%/dpa$ limit observed as an upper limit of similar capsules irradiated isothermally at 550°C.^{5,6} During isothermal irradiation at 400°C, the total strain rate of 20% cold-worked 316 at 343 MPa (50 ksi) only reached $\Delta D \approx 0.14\%/dpa$ at 125 dpa.

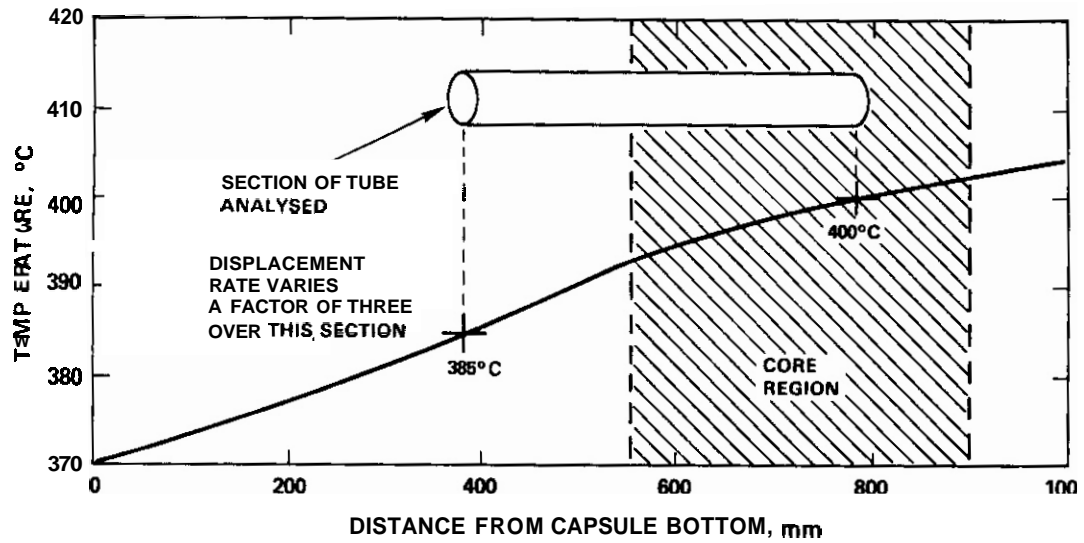


Fig. 1. Temperature profile along creep capsule.

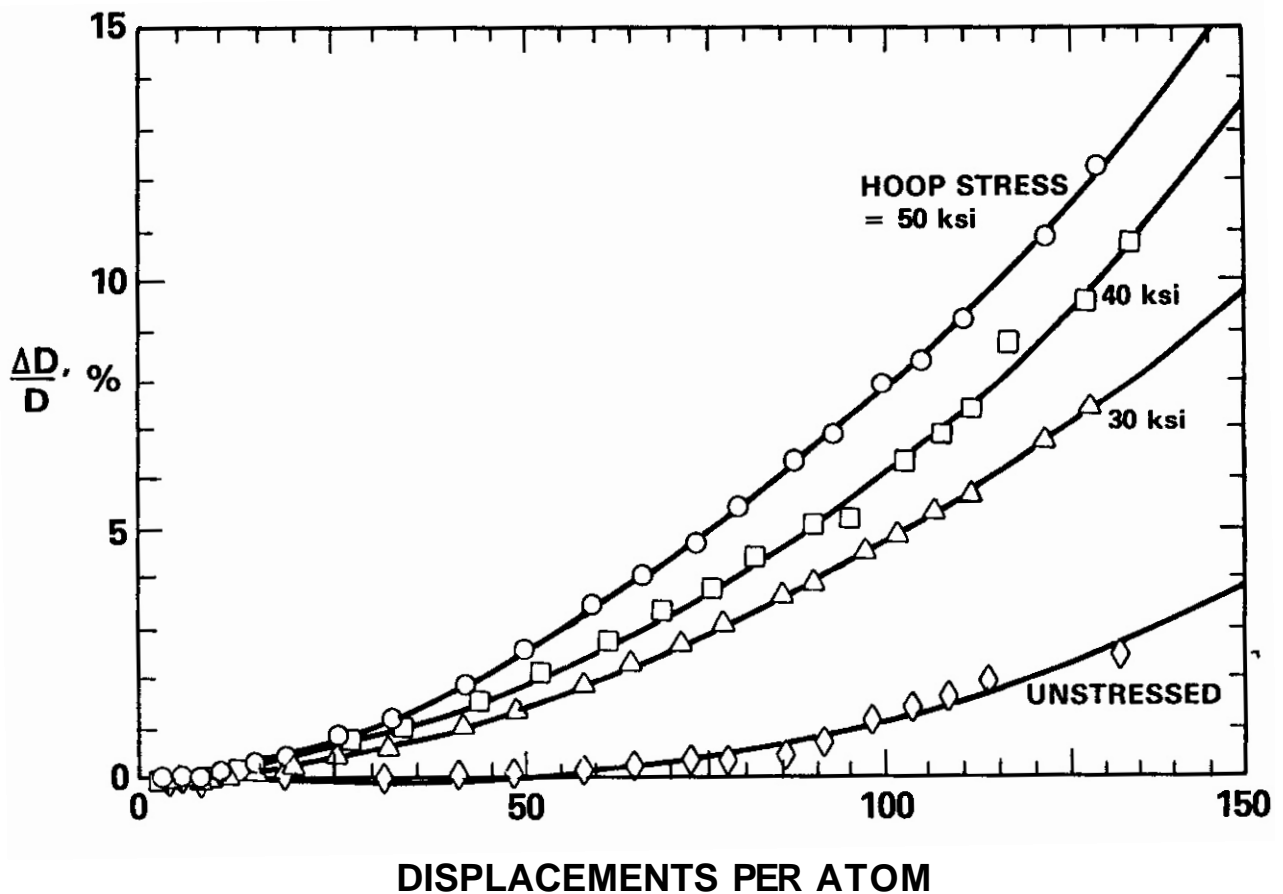


Fig 2. Diameter changes induced at capsule center in four selected creep capsules constructed from 20% cold-worked AISI 316 stainless steel and irradiated in EBR-II. The hoop stresses ranged from 0 to 343 MPa (0-50 ksi).

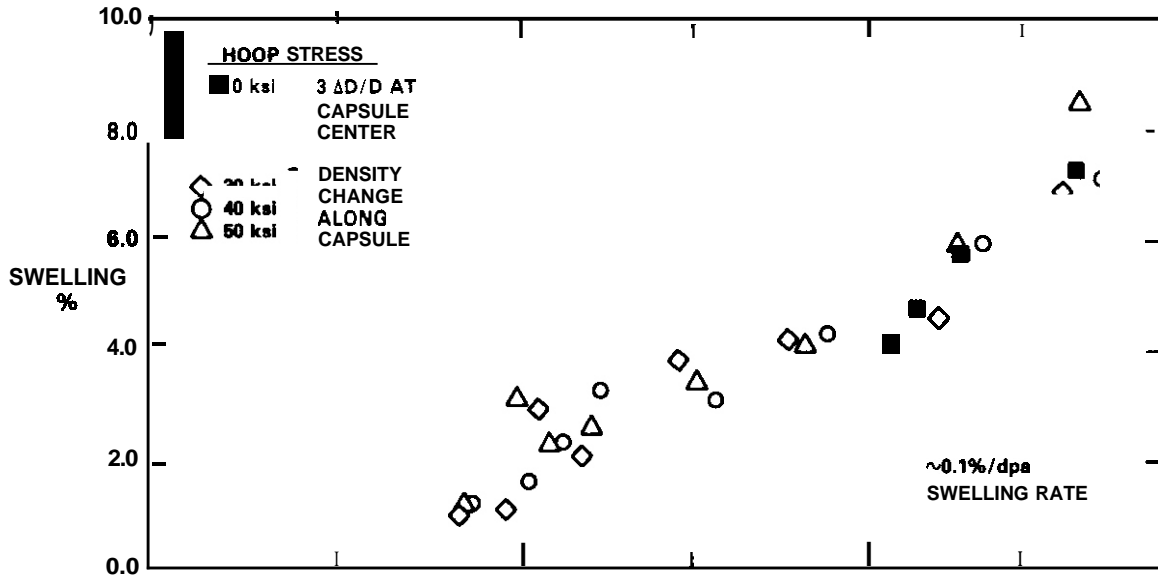


Fig. 3. Swelling measured along the length of the three pressurized creep capsules shown in Fig. 2. Also shown are the swelling values inferred from time-dependent diameter change measurements at the center of the unstressed capsule.

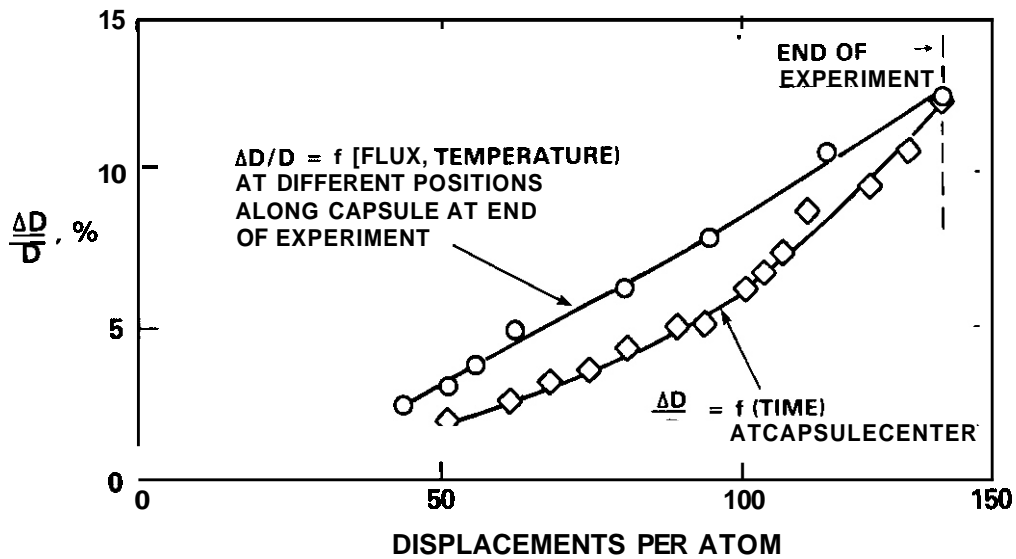


Fig. 4. Influence of displacement rate and temperature variations on total strain observed in a 20% cold-worked capsule with a hoop stress of 276 MPa (40 ksi).

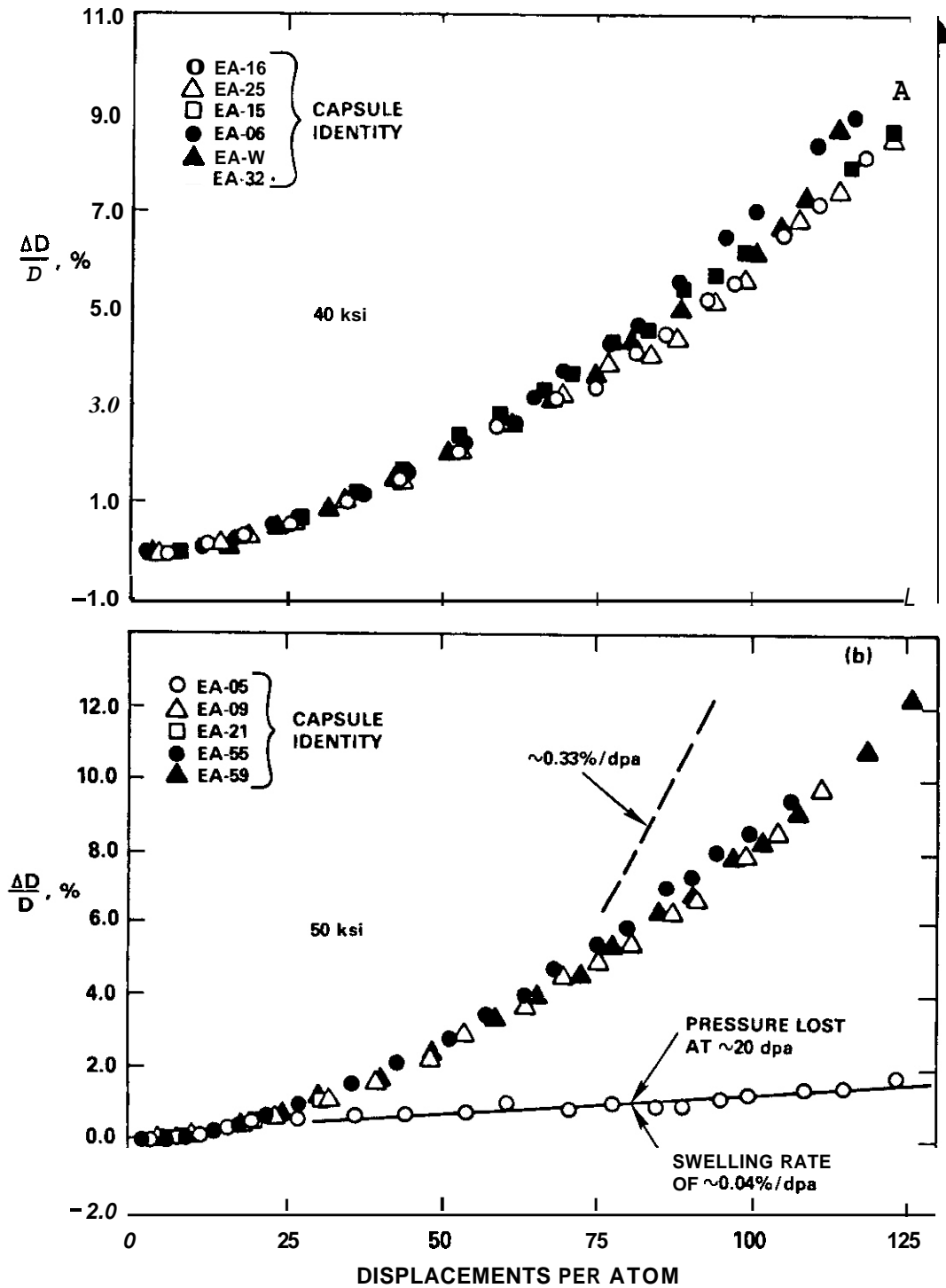


Fig. 5. Diameter changes observed in 20% cold-worked steel for (a) six nominally identical creep capsules at 276 MPa (40 ksi) and (b) five nominally identical capsules at 343 MPa (50 ksi). Note that one capsule failed at 20 dpa and swelled without stress thereafter.

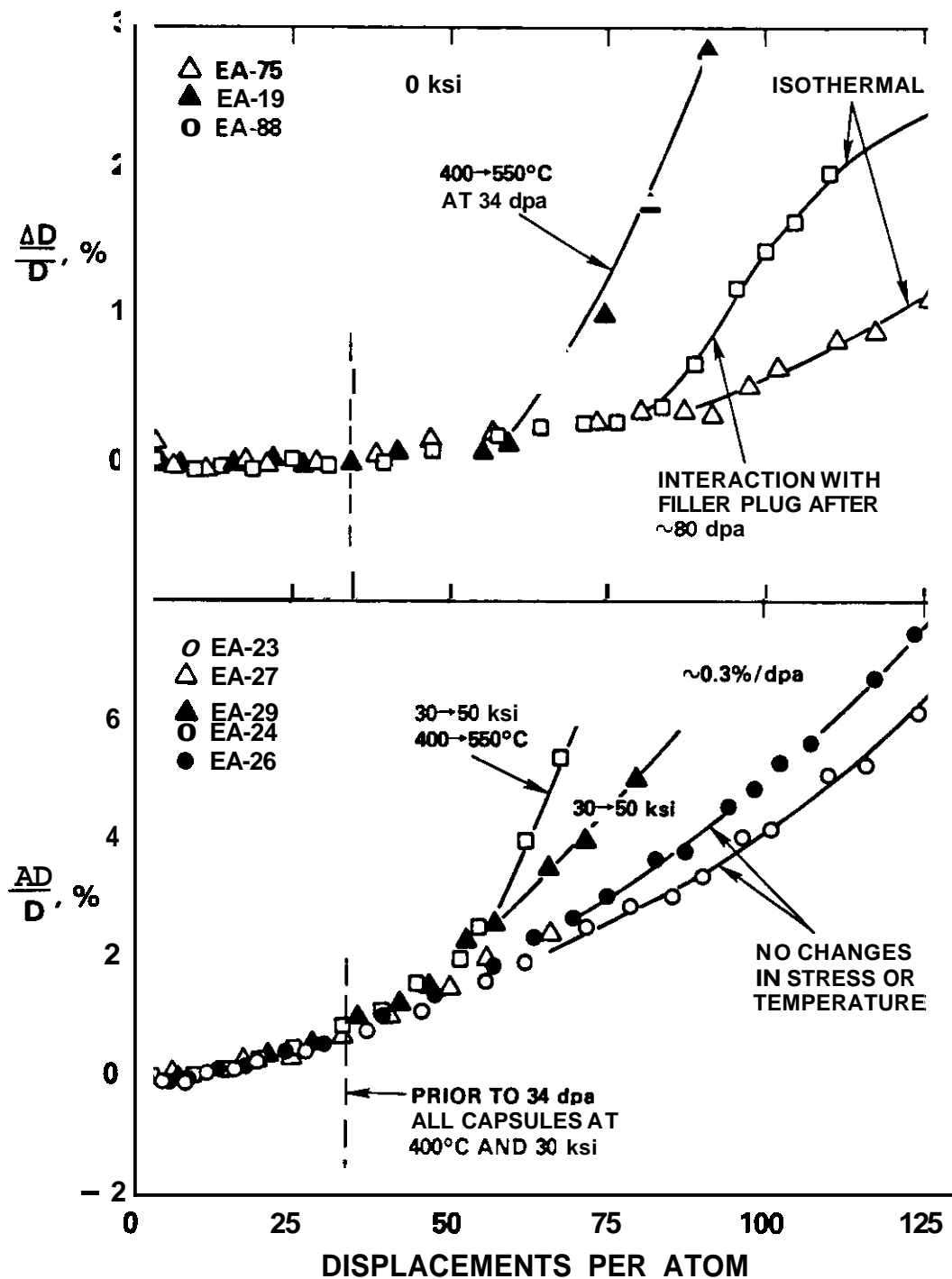


Fig. 6. Influence of radiation history on strain behavior of 20% cold-worked steel at 400°C. Increasing the stress level accelerates the deformation rate but increasing both the stress and the temperature causes a more pronounced increase in deformation rate.

The strain rates of AISI 316 are somewhat sensitive to material condition as well as environmental variables as demonstrated by looking at other conditions in this experiment. In the heat treat D condition the total strain rate ΔD at 400°C reached 0.22%/dpa at 276 MPa (40 ksi), but when the temperature was changed from 400 to 550°C at 32 dpa, the total creep rate of Heat Treat D at 276 MPa immediately went to the 0.33%/dpa limit.

Fig. 7 shows the diameter changes of five nominally similar capsules initially irradiated at 550°C. (The experimental details of these irradiations were described in references 5 and 6). At -30 dpa two of these capsules were subjected to an abrupt decrease in temperature to 400°C. Prior to the changes these capsules were just beginning to exhibit accelerated swelling and creep rates but these quickly subsided from the increasing rates observed in the three capsules maintained at 550°C. The swelling rate of the unstressed capsule was found to be $S = 0.10\%/dpa$. This reduction in swelling rate tends to confirm that at 400°C the swelling rate is dominated by the kinetics of point defect recombination.

Discussion

The data presented in this paper show that at 400°C the N-lot heat of AISI 316 stainless steel is right on the steep slope of the recombination-dominated regime of swelling. In this regime, the swelling rate is falling away with decreasing temperature from the 1%/dpa value observed over a large range of temperatures (425 to 725°C).¹⁻³ One would expect to see in this regime a sensitivity to displacement rate, thermal-mechanical condition and prior irradiation history. All of these sensitivities were indeed observed. If we confine the study to isothermal irradiation of cold-worked steel, the swelling rate has fallen at 400°C to a level on the order of 5 to 10% of the 1%/dpa value. At the lower temperatures expected in a water-cooled fusion first wall, the swelling should be vanishingly small. Since the largest component of the creep rate is thought to be proportional to the swelling rate, creep should also decline in importance.

It has been proposed that the creep rate $\dot{\epsilon}$ at any relevant temperature is linearly dependent on stress σ and related to the swelling rate S by the following relation.^{1,10-12}

$$\frac{\dot{\epsilon}}{\sigma} = B_0 + D_0 \dot{S}$$

The creep compliance B_0 has been shown to be approximately equal to $1 \times 10^{-6} \text{ MPa}^{-1} \text{ dpa}^{-1}$ for a wide range of austenitic steels.^{1,12} The swelling-enhanced creep coefficient D_0 is likewise thought to be relatively constant at $\sim 10^{-2} \text{ MPa}^{-1}$ over a wide range of steels and temperatures.

Using the insight gained in this study of stress-independent swelling at 400°C to analyze the data in Fig. 2, the values of B_0 and D_0 can be calculated. Note in Fig. 8 that the instantaneous creep coefficient ($B_0 + D_0 S$) is independent of stress level as predicted and appears to saturate at higher exposures. At zero dpa and therefore zero swelling rate, B_0 is indeed $-1 \times 10^{-6} \text{ MPa}^{-1} \text{ dpa}^{-1}$. Assuming a swelling rate of $\sim 0.04\%/dpa$ and using the 40 ksi curve at 130 dpa, D_0 is calculated to be $-0.6 \times 10^{-2} \text{ MPa}^{-1}$. Both estimates of B_0 and D_0 thus appear to be in good agreement with the anticipated values.

The attainment of these results was facilitated by the lack of stress effects on swelling at this temperature. At higher temperatures stress indeed enhances swelling and complicates the analysis somewhat.^{6,7} A somewhat surprising recent insight is that the sign of the stress is not important but only its magnitude. Compressive stress states are equally as effective as those of tension in accelerating the onset of swelling.^{13,14} In a previous model compressive stresses were assumed to delay the onset of swelling.^{13,14}

It was shown in earlier papers that rate theory considerations alone are insufficient to explain the swelling behavior of AISI 316 and other austenitic stainless steels, particularly in the incubation period of swelling where variables such as stress, gas content, displacement rate and temperature history exert their greatest influence.^{1,3,15-17} One must also invoke the time-dependent composition of the alloy matrix as the alloy undergoes a radiation-induced microchemical evolution involving precipitation of elements such as silicon, nickel and phosphorus. These three elements in particular have been shown to have a large effect on void nucleation rates¹⁸⁻²¹ and the precipitation sequences are known to be sensitive to irradiation variables such as stress, displacement rate and temperature history.^{1,16,17,22}

One would therefore expect to find that the independence of swelling on stress in 20% cold-worked AISI 316 at 400°C would be mirrored in a similar independence of the precipitate evolution and microchemical evolution of the alloy matrix. This supposition is confirmed by the results of an earlier study involving analysis of precipitation in this heat of steel.²² The experiment was conducted on creep capsules from this same experiment but which were removed at 50 to 70 dpa for destructive examination. Indeed the precipitate evolution of the steel was found to be insensitive to the stress level.

There is an interplay, however, between the effects of the various variables affecting precipitation that precludes confident predictions applicable to all steels and irradiation conditions. Although 20%

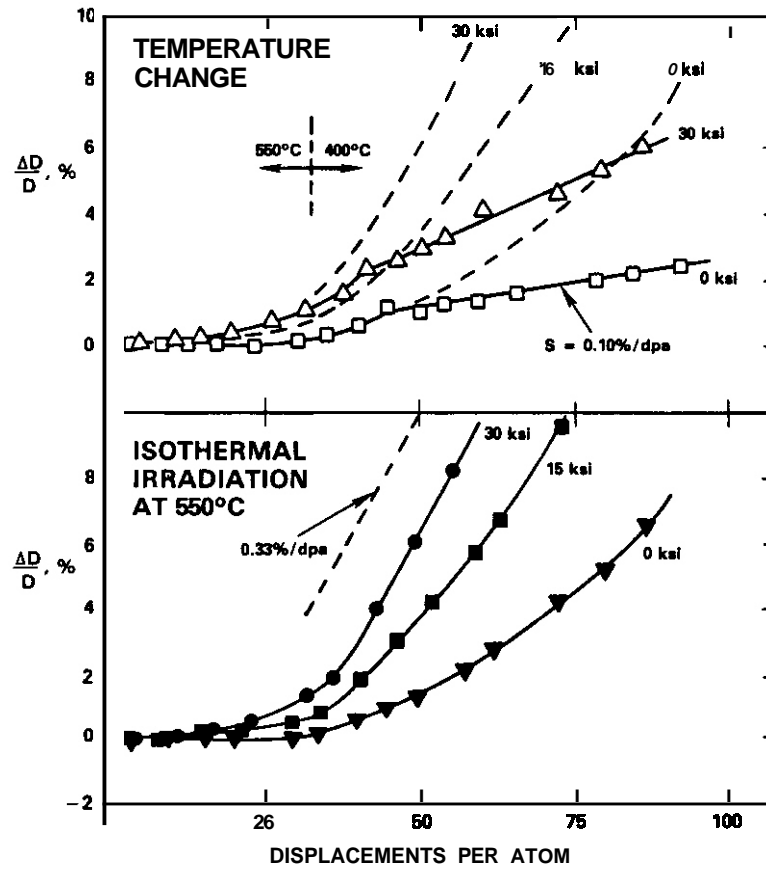


Fig. 7. Diameter changes of (a) two 20% cold-worked capsules at 0 and 206 MPa (30 ksi), subjected to an abrupt decrease in temperature and (b) three others irradiated only at 550°C at 0, 103 and 206 MPa (0, 15, 30 ksi).

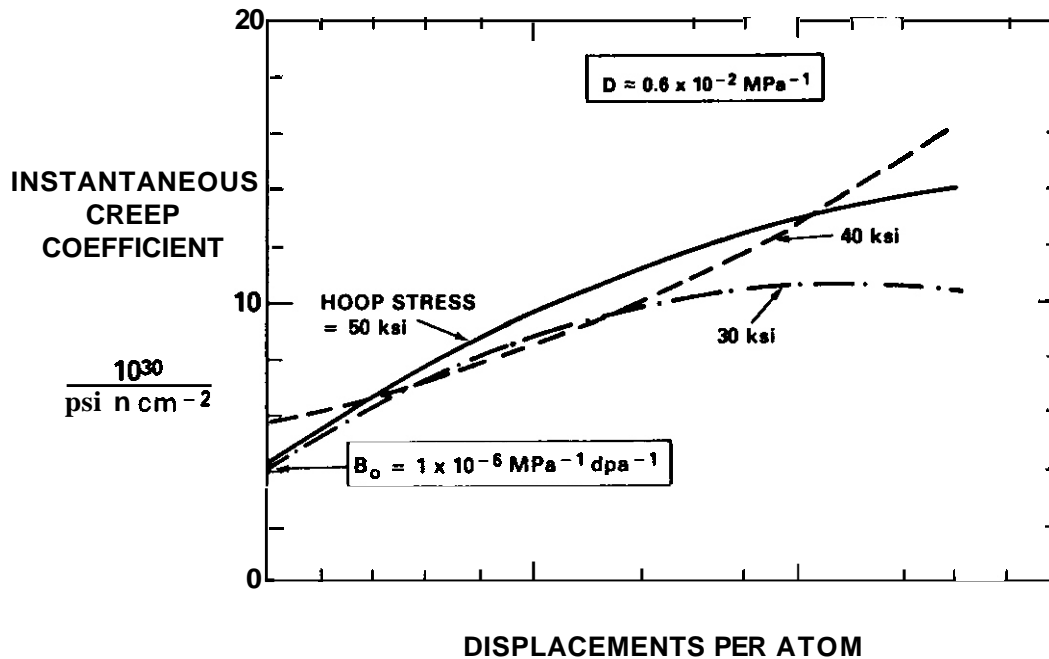


Fig. 8. Determination of instantaneous creep coefficients from the data shown in Fig. 2. The creep rate is linear with stress and increases as the swelling rate increases.

cold-worked **AISI 316** demonstrated an independence of stress at this temperature. a similar study on annealed **AISI 304** exhibited stress-affected swelling at core center positions but not at lower displacement rates found toward the bottom of the creep capsule.²³

CONCLUSIONS

In the region around 400°C and below, the neutron-induced swelling rate of **AISI 316** declines rapidly from the temperature-independent value of ~1%/dpa observed over a wide range of higher temperatures. The irradiation creep rate decreases correspondingly. While swelling loses its sensitivity to stress in this temperature range, the irradiation creep rate retains its linear dependence on stress and its linear dependence on swelling rate. Creep coefficients derived from higher temperature experiments are found to be applicable at 400°C as well. The cold-worked form of this steel is capable at 400°C of reaching neutron exposures causing damage well in excess of 100 dpa without failure. This capability, coupled with the low rates of swelling and creep, encourage the use of **AISI 316** in the construction of water-cooled first walls of fusion devices.

FUTURE WORK

The analysis of the data for conditions other than 20% cold-worked will be continued.

REFERENCES

1. F. A. Garner, J. Nucl. Mater., 1226123, 459 (1984).
2. F. A. Garner, p. 111 in Optimizing Materials for Nuclear Applications, Eds. F. A. Garner, D. S. Gelles, and F. W. Wiffen, (The Metallurgical Society, Warrendale, PA, 1985).
3. F. A. Garner and W. G. Wolfer, J. Nucl. Mater., 1226123, 201 (1984).
4. W. G. Wolfer, J. Nucl. Mater., 122 & 123, 367 (1984).
5. F. A. Garner, D. L. Porter and B. J. Makenas, J. Nucl. Mater., 279 (1987).
6. D. L. Porter and F. A. Garner, p. 11 in Influence of Radiation on Material Properties, ASTM STP 956, Eds. F. A. Garner, C. H. Henager, Jr. and N. Igata (1987).
7. F. A. Garner, E. R. Gilbert and D. L. Porter, p. 680 in Effects of Radiation on Materials: Tenth Conference, ASTM STP 725, Eds. D. Kramer, H. R. Brager and J. S. Perrin, (1981).
8. D. L. Porter, M. L. Takata and E. L. Wood, J. Nucl. Mater., 116, 272 (1983).
9. F. A. Garner and J. J. Laidler, p. 177 in Proc. Workshop on Correlation of Neutron and Charged Particle Damage, CONF-760673, (Oak Ridge, TN 1976).
10. J. P. Foster, W. G. Wolfer, A. Biancheria and A. Boltax, p. 213 in Proc. BNES Conf. on Irradiation Embrittlement and Creep in Fuel Cladding and Core Components, (London, England, 1972).
11. K. Ehrlich, J. Nucl. Mater., 100, 149 (1981).
12. J. L. Boutard, Y. Carteret, R. Cauvin, Y. Guerin and A. Maillard, Vol. 1, p. 109 in Proc. BNES Conf. on Dimensional Stability and Mechanical Behavior of Irradiated Metals and Alloys, (Brighton, England, 1983).
13. T. Lauritzen, S. Vaidyanathan, W. L. Bell and W. J. S. Vang, p. 101 in Radiation-Induced Changes in Microstructure, ASTM STP 955, Eds., F. A. Garner, N. H. Packan and A. S. Kumar (1987).
14. H. Ullmaier, Rad. Effs., 101, 147 (1986).
15. F. A. Garner, p. 165 in Phase Stability During Irradiation, Eds., J. R. Holland, L. K. Mansur and O. I. Potter, (The Metallurgical Society, Warrendale, PA 1981).
16. H. R. Brager and F. A. Garner, J. Nucl. Mater., 117, 159 (1983).
17. W. J. S. Yang and F. A. Garner, p. 186 in Effects of Radiation on Materials: Eleventh International Symposium, ASTM STP 782, Eds., H. R. Brager and J. S. Perrin (1982).
18. F. A. Garner and W. G. Wolfer, J. Nucl. Mater., 102, 143 (1981).

19. B. Esmailzadeh and A. S. Kumar, p. 468 in Effects of Radiation on Materials: Twelfth International Symposium. ASTM STP 870, Eds. F. A. Garner and J. S. Perrin (1985).
20. F. A. Garner and A. S. Kumar, in Ref. 13, p. 289.
21. W. A. Coghlan and F. A. Garner, in Ref. 13, p. 315.
22. F. A. Garner and D. L. Porter, in Ref. 17, p. 186.
23. D. L. Porter and F. A. Garner, in Ref. 19, p. 212.

THE INFLUENCE OF Mo, Si, P, C, Ti, Cr, Zr AND VARIOUS TRACE ELEMENTS ON THE NEUTRON-INDUCED SWELLING OF AISI 316 STAINLESS STEEL - F. A. Garner (Pacific Northwest Laboratory) and H. R. Brager (Westinghouse Hanford Company)

OBJECTIVE

The object of this effort is to determine the dependence of neutron-induced swelling on compositional variations.

SUMMARY

The individual and synergistic influences of seven major and eleven minor solutes on the swelling of 316 stainless steel were investigated in an irradiation experiment conducted in EBR-II. All elements exert their influence on the duration of the transient regime of swelling, through their effect on both vacancy diffusivity and precipitate evolution, often causing a complex response with increasing solute level. On a per atom basis, phosphorus is the most effective and consistent suppressor of swelling. Trace elements were found to have no significant effect. No combination of these elements appears to suppress the tendency of this steel to swell at $\sim 1\%/dpa$ following the transient regime.

PROGRESS AND STATUS

Introduction

In the development of advanced steels for service in breeder or fusion reactors, one approach has been to modify the composition of AISI 316 stainless steel from that employed in early breeder reactor construction. [1-5] This was done in the hope that solute additions would lower the large swelling rate found in austenitic steels and simple Fe-Cr-Ni ternary austenitic alloys C6-91. It has become obvious, however, that the addition of solutes such as phosphorus, silicon and titanium lead only to a modification of the incubation period of swelling [9-13].

While some results on the separate effects of phosphorus and titanium on neutron-induced swelling have been published [10-12], the individual and synergistic effects of other important solutes have not been addressed in detail, nor have the synergies between solute additions and thermomechanical treatment been thoroughly examined. To aid in the development of an optimized fusion candidate alloy, swelling measurements have been obtained on specimens irradiated in an early liquid metal reactor program experiment designated the third material variables experiment. MV-III.

Experimental Details

The MV-III experiment involved 150 heats of steel, all of which contained approximately 14 weight percent (w/o) nickel and silicon levels greater than or equal to 0.7 w/o. Many of these compositional variations on AISI 316 existed in more than one thermomechanical condition, and were irradiated at as many as six temperatures. This ambitious experiment thus involved over two thousand combinations of specimen/irradiation conditions. There were two major and several minor categories of specimens. The largest portion comprised alloys having variations in seven major solute elements (Ti, Si, P, Zr, Cr, C, Mo), with each element having at least two and sometimes as many as five different concentration levels. The second category of alloys was chosen to explore the influence of minor trace impurities. In this series alloys designated as "high purity" were made from high purity ingredients and had a nominal alloy composition of Fe-16Cr-14Ni-2.5Mo-2.0Mn-0.8Si-0.2Ti-0.04C-0.01Zr. The "trace" impurity alloys had the same base composition but contained small and typical amounts (0.01 to 0.05 w/o) of ten minor elements (Al, As, Co, Cu, N, Nb, Sn, Ta, V and W) normally found in AISI 316. At these levels, phosphorus is also considered to be a trace element but it had already been included as a major solute in the more extensive alloy series at levels ranging from 0.01 to 0.08 w/o. For a number of base alloys including that of the high purity, a minor category of alloys studied the effect of boron additions at 0.005%.

The specimens were in the form of microscopy disks (3 mm diameter by 0.3 mm thick) and were contained in sodium filled subcapsules. The irradiation was conducted in row two of the EBR-II fast reactor at displacement rates ranging from 0.6 to 1.1×10^{-6} dpasec. Each 1.0×10^{22} n/cm² ($E > 0.1$ MeV) in this reactor produces approximately 5 dpa of displacement damage. Displacement levels as large as 75 dpa were reached at some irradiation temperatures. After removal and cleaning, the radiation induced changes in density were measured using an immersion density technique accurate to 0.16% swelling. Due to the large size of the specimen matrix, only selected subsets of specimens were chosen for measurement. These were the solution annealed and 20% cold worked subsets irradiated at 425°C to 7.6 and 11.3×10^{22} n/cm² ($E > 0.1$ MeV) or at 540°C to 6.3, 10.0 and 14.9×10^{22} n/cm² ($E > 0.1$ MeV).

Results

Earlier studies had shown that phosphorus, silicon and titanium, in that order, had the greatest influence per atom on modifying the duration of the transient regime of swelling [9-13]. The results of the MV-III experiment confirm this earlier conclusion and provide insight on the synergisms of these elements with those of Zr, Cr, Mo and C. The data base is too large to present in its entirety, but certain trends persist throughout. Regardless of the individual combinations of solutes, cold worked alloys always swelled less than their annealed counterparts and swelling at 425°C was always less than at 540°C, although the difference could be either large or small. In all alloys, the swelling rate increased continually with fluence, frequently reaching the ~1%/dpa limit found to be characteristic of austenitic alloys. In alloy series where all solutes but one were held constant, the swelling curves appeared to be nested, with only the incubation period showing a strong influence on solute content. The degree of solute influence could be large or small, and was frequently not monotonic with increasing solute content. Boron was a good example of a solute with no perceptible or consistent impact on swelling.

The action of phosphorus in this alloy series was always monotonic, however, leading to extensions in the incubation period as shown in Fig. 1. When the influence of phosphorus is compared to that of other "trace" elements, it is obvious that phosphorus is the only minor solute of significance, as shown in Fig. 2 and 3. Also shown in these and other figures is the relatively weak influence of zirconium to increase swelling in the range 0.01 - 0.3 w/o.

There were synergisms found between zirconium, titanium and carbon as would be expected for these carbide-forming elements. An example is shown in Fig. 4 which demonstrates that increased titanium levels do not always lead to lower swelling. The influence of carbon sometimes, but not always, leads to a peak in swelling at 0.04 w/o. Increases in chromium (10.4 to 16.2 w/o) and molybdenum (1.5 to 3.5 w/o) usually caused an increase in swelling, although there were occasionally peaks in swelling near 14 w/o chromium. The effect of molybdenum was most pronounced at 540°C as shown in Fig. 5. The somewhat variable influence of chromium on swelling is shown in Fig. 6.

The MV-III experiment concentrated on rather high silicon levels compared to that of conventional steels. While it is usually expected that silicon additions will decrease swelling, both increases and decreases were observed, depending on the level of other solutes, the temperature and the thermomechanical condition. Typical examples of silicon's influence are shown in Fig. 7.

Discussion and Conclusions

It appears from this and earlier studies that no combination of conventional solutes can suppress permanently the tendency of AISI 316 to swell at about 1%/dpa. The effect of all solute combinations studied appears to lie only in the duration of the transient regime and is not always monotonic in nature. There does appear to be some limited benefit to reducing the levels of chromium and molybdenum from standard levels of 16 - 18 w/o and 2.2 - 2.6 w/o, respectively, and with maintaining relatively low carbon levels (less than or equal to 0.04 w/o). It appears that addition of too much titanium and zirconium becomes counterproductive but the upper limit is hard to specify using only the subsets of material and irradiation conditions chosen for measurement.

Silicon additions are known to suppress swelling but at high concentrations are associated with large levels of phase instability [14]. Further reductions in swelling at one temperature may thus be balanced by increases at other temperatures where the phase evolution proceeds at a different rate or with a different balance of precipitates. Increases in phosphorus appear to be much more effective in reducing swelling and with much less detrimental forms of precipitation C11.12.16.171. Other minor solutes typically found in steels appear to be insignificant and there is no need to control their levels.

The swelling of this alloy has been shown to be related to the microchemical evolution of the alloy matrix [18-22] as precipitates remove elements known to have a strong effect on vacancy diffusivity [12, 13, 23-26]. This evolution is very complex and is quite sensitive to solute combinations and levels, thermo-mechanical treatment and environmental history C6.9.13.21.221. It thus appears that the synergistic effects of various elements on precipitate formation often outweigh the initial influence of these elements on vacancy diffusivity.

FUTURE WORK

This effort is complete.

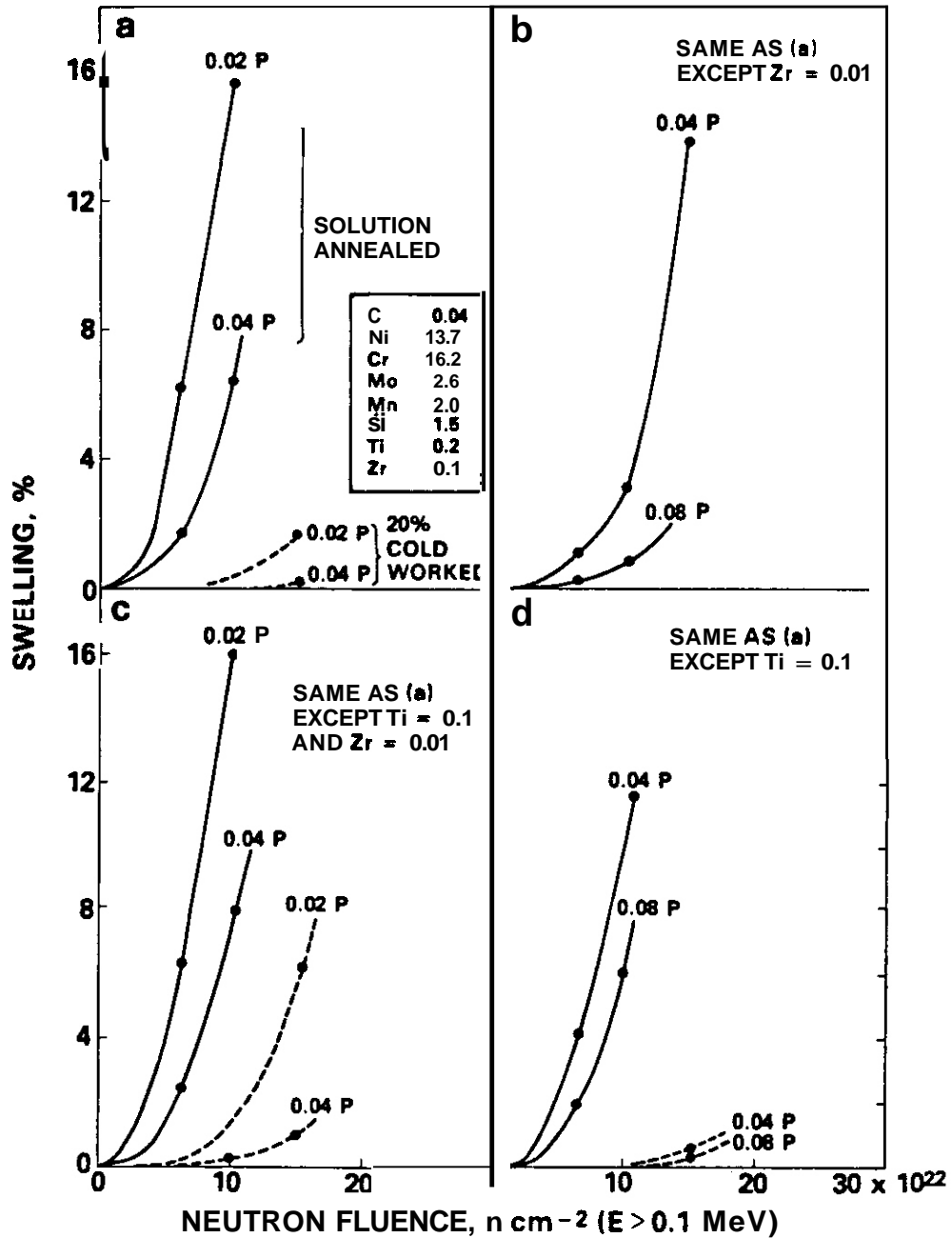


Fig 1. Effect of phosphorus, titanium, zirconium and cold work on the swelling of solute-modified AISI 316 after irradiation at 540°C in EBR-II. The composition of each alloy series is shown in the upper right hand corner.

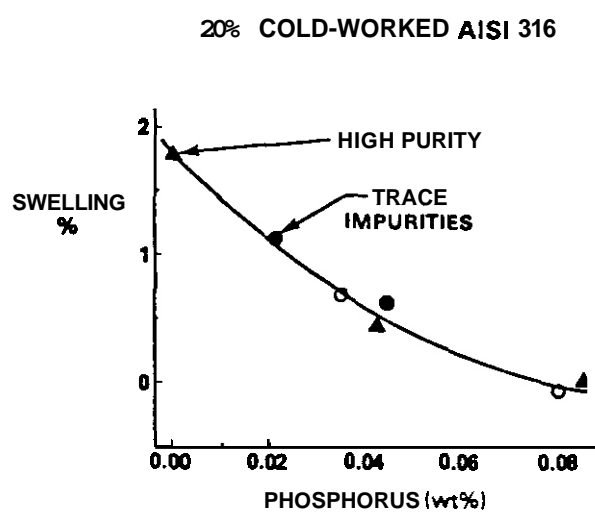


Fig 2. The relative influence of phosphorus and trace impurities on the swelling of "high purity" alloys in the 20% cold worked condition after irradiation at 425°C to $11.0 \times 10^{22} \text{ n cm}^{-2}$ ($E > 0.1 \text{ MeV}$) or 55 dpa. The open circles denote alloys with 0.1 w/o zirconium instead of 0.01 w/o zirconium.

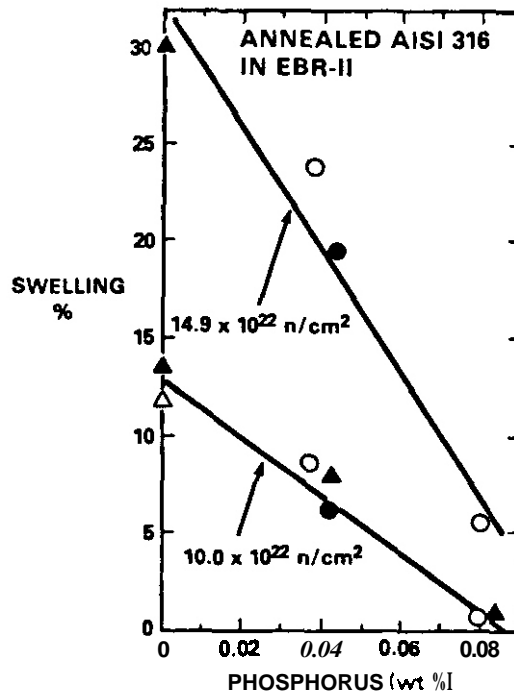


Fig 3. The relative influence of phosphorus and trace impurities for annealed "high purity" alloys irradiated at 540°C . The open circles denote alloys with 0.1 w/o zirconium.

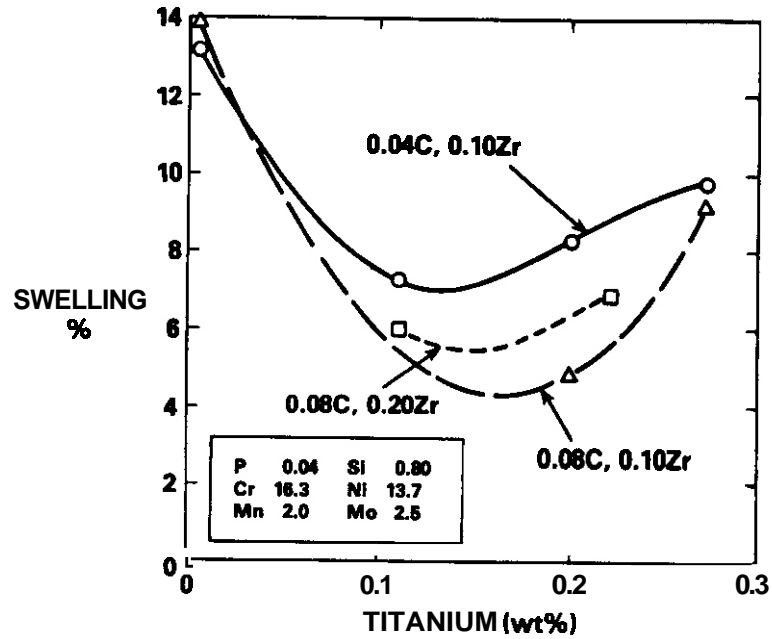


Fig 4. Influence of Ti, Zr and C on swelling of annealed alloys irradiated at 540°C to $10.0 \times 10^{22} \text{ n cm}^{-2}$ ($E > 0.1 \text{ meV}$) or -50 dpa.

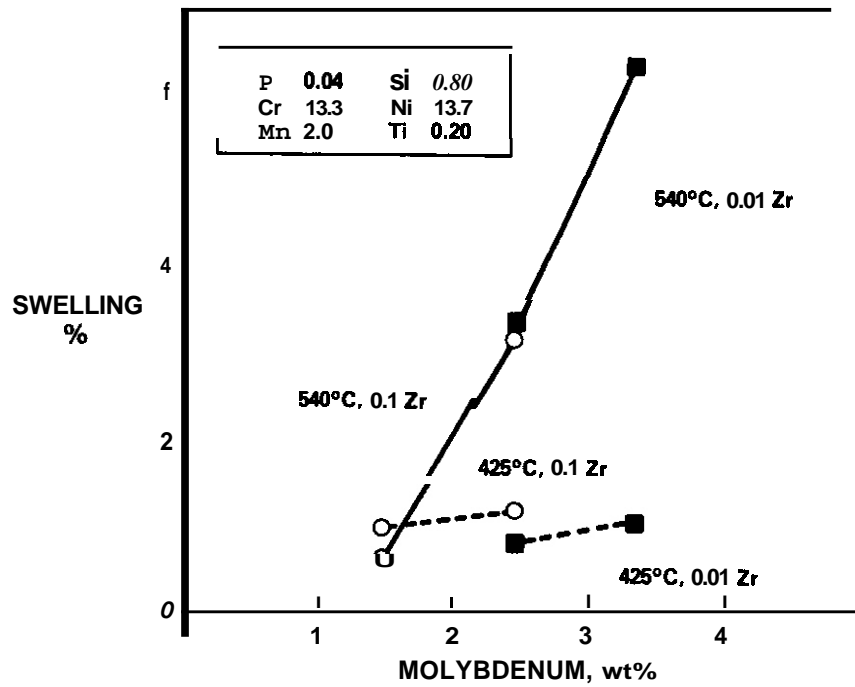


Fig 5. Effect of molybdenum on swelling of annealed alloys at 425°C (55 dpa) and 525°C (-50 dpa). Data for zirconium levels of 0.01 and 0.10 w/o are shown.

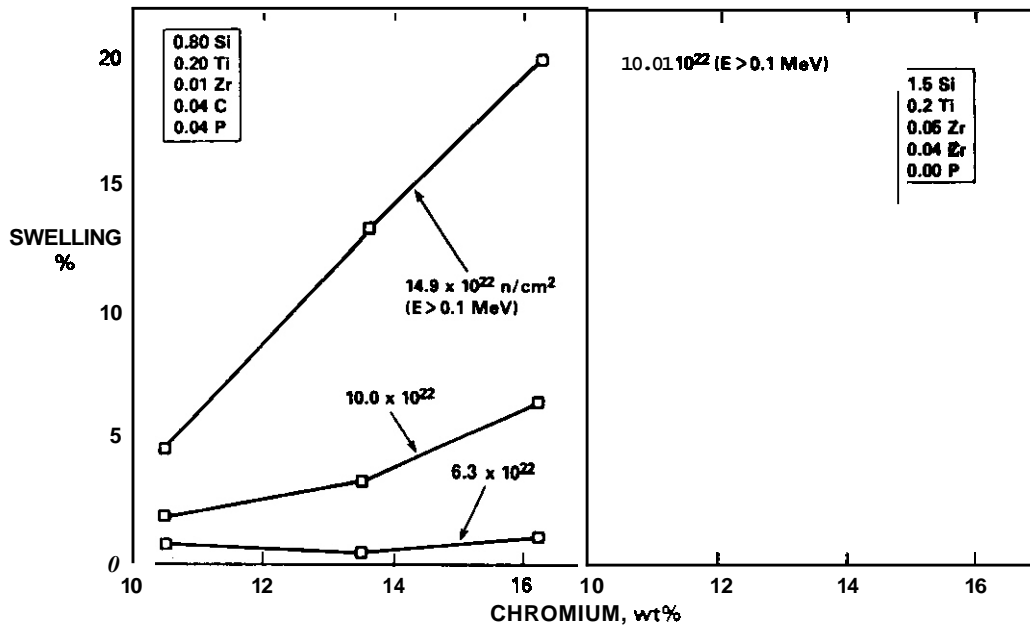


Fig 6. Effect of chromium on swelling at 540°C of Fe-14.0Ni-2.5Mo-2.0Mn steels in the annealed condition.

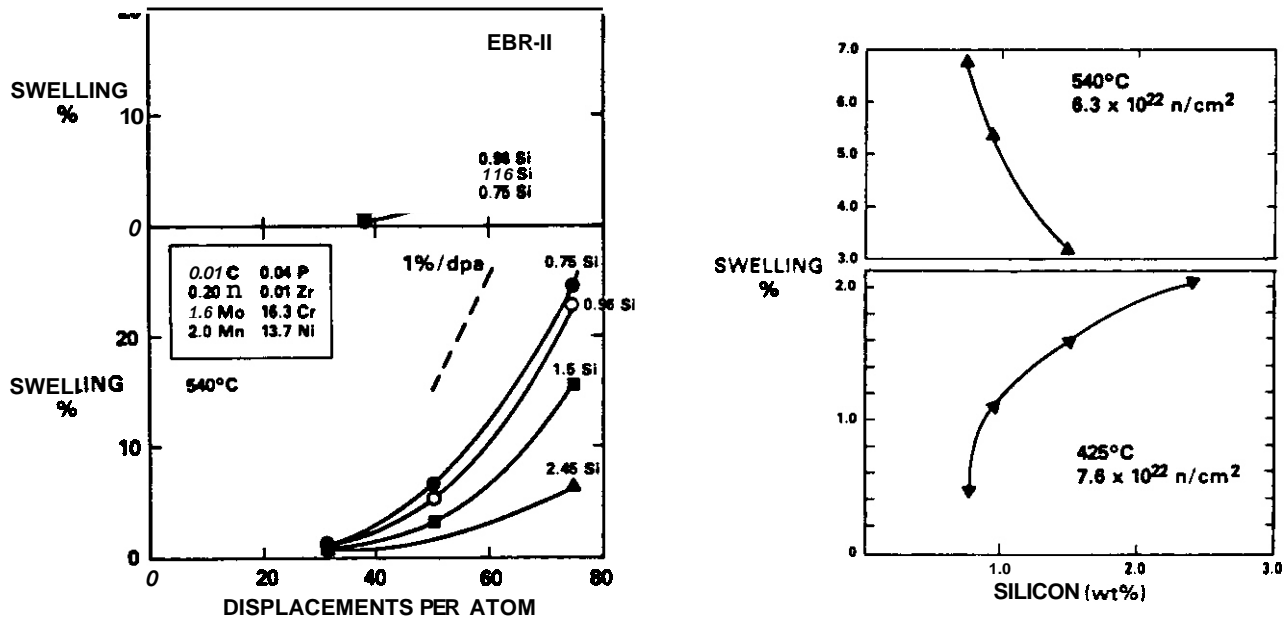


Fig 7. Effect of silicon on transient regime of annealed solute modified alloys (left). Influence of silicon on swelling of these annealed alloys at two temperatures (right).

REFERENCES

- 1 J. M. Dupouy in Effects of Radiation on Materials. ASTM STP 782, Eds. H. R. Brager and J. S. Perrin (American Society for Testing and Materials. Philadelphia. 1982) p. 1179.
- 2 W. Schneider. K. Herschbach and K. Ehrlich, *ibid*, p. 30.
- 3 D. R. Harries in Radiation Effects In Breeder Reactor Structural Materials, Eds. M. L. Bleiberg and J. W. Bennett (The Metallurgical Society of AIME, New York. 1977) p. 27.
- 4 J. J. Laidler. J. J. Holmes and J. W. Bennett. *ibid*. p. 41.
- 5 J. Bramman, C. Brown. J. S. Watkin, C. Cawthorne. E. J. Fulton. P. J. Barton and E. A. Little, *ibid*, p. 429.
- 6 F. A. Garner. J. Nucl. Mater., 122 6 123 (1984) 459.
- 7 F. A. Garner and H. R. Brager. in Symp. on Effects of Radiation on Materials, ASTM STP 870, Eds. F. A. Garner and J. S. Perrin (American Society for Testing and Materials. Philadelphia. 1985) p. 187.
- 8 B. J. Makenas. *ibid*, p. 202.
- 9 F. A. Garner, in Optimizing Materials for Nuclear Applications. Eds. F. A. Garner. O. S. Gelles and F. W. Wiffen (The Metallurgical Society. Warrendale, 1985) p. 111.
- 10 F. A. Garner. H. R. Brager and R. J. Puigh, J. Nucl. Mater.. 133 6 134 (1985) 535.
- 11 F. A. Garner and H. R. Brager. J. Nucl. Mater.. 133 6 134 (1985) 511.
- 12 F. A. Garner and A. S. Kumar. in Radiation Induced Changes in Microstructure. ASTM STP 955, Eds. F. A. Garner. N. F. Packan and A. S. Kumar (American Society for Testing and Materials. Philadelphia. 1987) p. 289.
- 13 F. A. Garner and W. G. Wolfer. J. Nucl. Mater.. 122 6 123 (1984) 201.
- 14 H. R. Brager and F. A. Garner. *ibid*. ref. 9, p. 219.
- 15 W. J. S. Yang. *ibid*. ref. 12, p. 888.
- 16 E. H. Lee. P. J. Maziasz and A. F. Rowcliffe. *ibid*. ref. 9, p. 191.
- 17 E. H. Lee. L. K. Mansur and A. F. Rowcliffe. J. Nucl. Mater.. 122 6 123 (1984) 299.
- 18 H. R. Brager and F. A. Garner, J. Nucl. Mater.. 73 (1978) 9.
- 19 F. A. Garner. *ibid*. ref. 9, p. 165.
- 20 H. R. Brager and F. A. Garner, J. Nucl. Mater.. 117 (1983) 159.
- 21 W. J. S. Yang and F. A. Garner. in Effects of Radiation on Materials, ASTM STP 782. Eds. H. R. Brager and J. S. Perrin (American Society for Testing and Materials. Philadelphia. 1982) p. 186.
- 22 F. A. Garner and D. L. Porter, *ibid*. p. 295.
- 23 F. A. Garner and W. G. Wolfer. J. Nucl. Mater.. 102 (1981) 143.
- 24 B. Esmailzadeh. A. S. Kumar and F. A. Garner. J. Nucl. Mater.. 133 6 134 (1985) 590.
- 25 B. Esmailzadeh and A. S. Kumar. *ibid*, ref 7, p. 468.
- 26 W. A. Coghlan and F. A. Garner. *ibid*. ref. 12, p. 315.

SWELLING BEHAVIOR OF AUSTENITIC STAINLESS STEELS IN A SPECTRALLY TAILORED REACTOR EXPERIMENT; IMPLICATIONS FOR NEAR-TERM FUSION MACHINES — R. E. Stoller, P. J. Maziasz, A. F. Rowcliffe (Oak Ridge National Laboratory) and M. P. Tanaka (Japan Atomic Energy Research Institute)

OBJECTIVE

The objective of this work is to analyze relevant data from fission reactor irradiation experiments in order to provide guidance for fusion reactor design.

SUMMARY

Current designs for engineering test reactors such as the International Thermonuclear Experimental Reactor propose to use an austenitic stainless steel for the first wall. Most of the available swelling data have been derived from neutron-irradiation experiments in which helium generation rates are very low (fast breeder reactors) or very high (mixed spectrum reactors). Recently a spectrally tailored experiment was concluded in the Oak Ridge Research Reactor in which the helium generation rate and damage rate were maintained at values typical of a fusion reactor operating at $\sim 1 \text{ MW/m}^2$. It was found that the swelling behavior of a titanium-modified stainless steel (PCA) in both the cold-worked and solution-annealed conditions differed significantly from the behavior observed in earlier experiments in which the He/dpa ratio was either ~ 0.5 or ~ 50 . The results suggest that there is a strong dependence of microstructural evolution on the He/dpa ratio. The data are shown to be consistent with earlier theoretical predictions of swelling behavior that is a non-monotonic function of the He/dpa ratio. Finally, both the present data set and a larger collection of low-temperature swelling data are discussed in the context of near-term machines.

PROGRESS AND STATUS

Introduction

During the Third Topical Meeting on Fusion Reactor Materials, a panel discussion was convened to discuss the suitability of austenitic stainless steels for first-wall and blanket structural applications.¹ The subject of void swelling in austenitic steels was summarized in papers presented by F. A. Garner² and by P. J. Maziasz.³ The general picture emerged that the initial low-swelling transient regime (LSTR) inevitably gives way to a more rapid linear swelling regime with increasing neutron fluence. Linear swelling rates are generally in the range $(0.5\text{--}1.0)\%/dpa$ (displacements per atom) — leading to levels of swelling that cannot be accommodated in large engineering structures. Component lifetimes are thus limited by the extent of the LSTR, which in turn depends upon temperature, stress, composition, initial microstructure, and damage rate. The observation that transient regimes for titanium-modified alloys could be extended up to 75 dpa in Fast Breeder Reactor (FBR) irradiations was regarded as encouraging. It was pointed out, however, that the FBR environment is atypical of fusion since the helium generation rate is so low (He/dpa $\sim 0.4 \text{ appm/dpa}$) and helium is known to have a powerful influence on cavity nucleation. Data from irradiation experiments conducted in the High Flux Isotope Reactor (HFIR), in which the helium generation rate is very high (He/dpa ~ 70), and also atypical of fusion, showed that helium could influence microstructural evolution in two distinct modes.³ In solution-annealed (SA) AISI 316, for example, helium production accelerated the development of bias-driven voids and shortened the LSTR relative to the FBR case. In cold-worked (CW) AISI 316, the microstructure was dominated by a very high concentration of helium bubbles which effectively suppressed both radiation-induced segregation (RIS) and the development of bias-driven voids. However, neutron data at the fusion He/dpa ratio were not available, and there was no consensus on how to predict behavior in a fusion environment using data obtained at other He/dpa ratios. A model-based analysis by Stoller and Odette⁴ of the behavior observed in FBR and HFIR irradiations showed that the effect of He/dpa ratio on swelling was non-monotonic and that the transient regime could actually be a minimum for helium generation rates characteristic of fusion.

A spectrally tailored experiment in the Oak Ridge Research Reactor (ORR) was recently concluded after reaching fluences in the range of 11 to 13 dpa. The He/dpa ratio was maintained at ~ 18 throughout the experiment by periodically altering the local neutron spectrum by means of removable neutron shields. In this report, we compare the swelling behavior of an austenitic steel (PCA), irradiated in the ORR experiment, with the swelling behavior of the same material irradiated in both the Fast Flux Test Facility (FFTF) at Hanford and in the HFIR. The results are discussed in terms of the modeling predictions of Stoller and Odette. The implications of the results for the performance of the first wall of the proposed International Thermonuclear Experimental Reactor (ITER) are also considered.

Experimental

The composition of the titanium-modified austenitic stainless steel used in this study is shown in Table 1. Specimens were irradiated in the form of disks 3 mm in diameter and 0.25 mm thick. After punching disks from 25% CW sheet, annealing was carried out at 1175°C for 1 h in a helium back-filled capsule. Neutron irradiations were carried out in the FFTF MOTA-1B experiment, in the HFIR experiments CTR-31 and -32, and in the ORR experiments MFE-4A and -4B. In both the FFTF and ORR experiments, temperatures were continuously monitored and controlled during irradiation. Uncertainties in temperature and dose for these experiments are 25 and $\pm 10\%$, respectively. Temperatures in the HFIR CTR-32 experiments were not measured. Recent measurements⁵ on a similar instrumented capsule in HFIR indicate that the temperature uncertainty is 215%. Following irradiation and prior to electrothinning for TEM examination, bulk density determinations were carried out with a precision of 0.005 g/cm³. The temperatures, fluences, helium generation rates, and swelling determinations by density measurement are shown in Table 2.

Table 1. Composition of PCA, Heat No. K280 (weight percent)

Fe	Ni	Cr	Ti	C	Mn	Mn	Si	P	S	B	N
Bal	16.2	14.0	0.24	0.05	2.3	1.8	0.4	0.01	0.003	0.001	0.01

Results

The experiments listed in Table 2 included both SA and 25% CW material. The results presented here focus on the SA material in order to provide the most complete comparison of the

three reactor environments and to establish the major data trends. A more detailed presentation of the complete data set will be given elsewhere.⁶ The SA data at -10 dpa, summarized in Table 2, is plotted in Fig. 1. The cavity microstructures observed at 400 and 500°C are shown in Fig. 2. These data indicate a significant reduction in the LSTR for the SA material irradiated in the spectral tailoring experiment in the ORR. Irradiation at near the fusion He/dpa ratio has led to a lower total cavity density (bubbles plus voids) than is observed in the HFIR; however, void formation is enhanced. Compared to the FFTF, irradiation at the fusion He/dpa ratio has resulted in both a higher total cavity density and a higher void density. The swelling of 25% CW material irradiated at the fusion He/dpa ratio was similarly enhanced.

Table 2. Irradiation Conditions and Swelling Data for PCA

Experiment	Dose Rate (dpa/s) ($\times 10^{-7}$)	He/dpa (appm/dpa)	Dose (dpa)	Temperature (°C)	Swelling, %	
					SA	25% CW
HFIR CTR-32	11	47	11	400	0.0	
	11	47	11	500	0.05	
	11	41	11	600	0.66	
FFTF MOTA-18	9	0.4	9	420	0.07, 0.16	-0.02
	16	0.4	15	520	-0.06, -0.1	-0.02, 0.01
ORR MFE-4A	1.4	18	13	400	0.33, 0.38	0.01, 0.02
ORR MFE-4B	1.4	18	12	500	2.5, 28	0.74, 1.1
	1.4	18	12	600	0.0, 0.1	-0.08, 0.11

The evolution of the dislocation microstructure and the precipitation behavior also vary strongly with reactor environment. Faulted loop formation was enhanced and a higher network dislocation density was observed in specimens irradiated in the ORR. This was particularly true for the 25% CW material as shown in Fig. 3. In earlier work, swelling suppression under high He/dpa conditions was correlated with a high bubble density that formed in the presence of a fine dispersion of MC particles.³ This correlation seems to hold in the present data set. In the ORR-irradiated material, MC was observed at both 400 and 600°C where swelling is low. However, at 500°C, where swelling occurs rapidly, little or no MC could be observed. In the HFIR-irradiated material, the rapid onset of swelling at 600°C also correlated with the absence of the MC phase.

Discussion

These swelling data are the first obtained under neutron irradiation in the United States program at the He/dpa ratio typical of a DT fusion reactor first wall. As such, they can be useful in beginning to

ORNL-DWG 87-15255

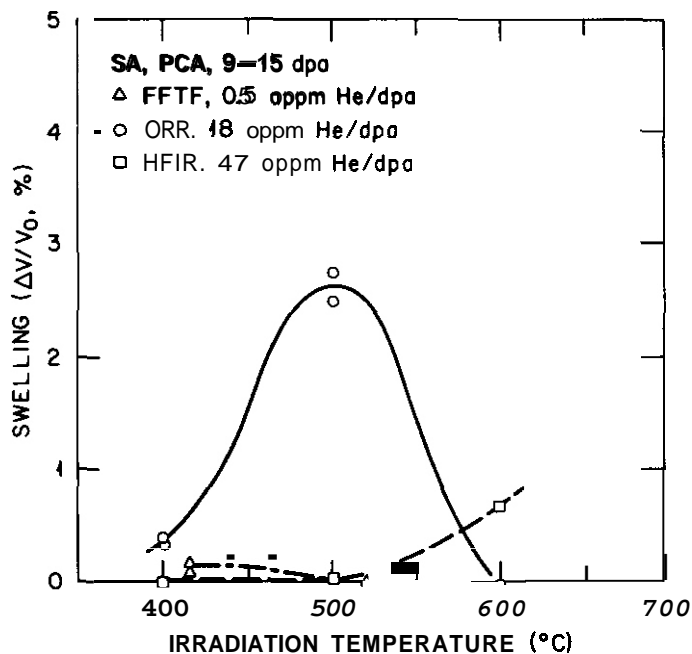


Fig. 1. Temperature dependence of swelling of SA PCA at 9 to 15 dpa in the HFIR, FFTF, and ORR. Data from Table 2, this report.

the dislocation structure that evolves.' At the higher dose rates, a higher density of faulted loops is observed. This leads to a higher total dislocation density which reduces the vacancy supersaturation; hence, the void nucleation rate is reduced. This situation has been reproduced in the comprehensive microstructural model of Stoller and Odette.¹⁰ For a fixed He/dpa ratio, their model predicts that the LSTR will be shorter at lower damage rates. Figure 4 shows the influence of the damage rate at 500°C using the theoretical model and the nominal model parameters of ref. 12. The reduced incubation time is the result of a lower total dislocation density leading to a higher vacancy supersaturation.

The observation of a reduced LSTR in the spectrally tailored experiment is superficially consistent with the trends in the fuel pin data discussed above. However, several differences between the fuel pin data and the present data suggest that damage rate is not the variable that is primarily responsible for the enhanced swelling observed in the ORR experiment. In the first place, the temperature dependence of the effect is different in the two sets of data. In the fuel pin data, the maximum effect of damage rate occurs at the higher temperatures with the magnitude of the effect decreasing steadily with decreasing temperature. Below 450°C, the effect is either nonexistent or possibly reversed.⁷⁻⁹ In the present instance, a comparison of the HFIR and ORR data at 600°C shows that swelling is actually higher at the higher damage rate. At 500°C, the situation is reversed and is similar to the fuel pin case (i.e., swelling is more rapid at the lower damage rate). Contrary to the fuel pin data, this situation still holds strongly at 400°C.

The second major difference is that the material irradiated in the low-damage-rate ORR experiment exhibited higher loop and dislocation densities than that irradiated in the higher-damage-rate experiments in HFIR and in FFTF. The opposite is observed in the fuel pin experiments. These experimental observations strongly suggest that, although there may be some influence of damage rate, the microstructural evolution in the three reactor environments is controlled primarily by the He/dpa ratio.

The earlier theoretical work of Stoller and Odette⁴ provides a framework for the interpretation of these results. Using a simple, rate-theory-based model of cavity evolution, these authors predicted that swelling would not be a monotonic function of the He/dpa ratio and that a swelling peak could exist near the fusion He/dpa ratio. The predicted swelling at 550°C after 75 dpa is reproduced from ref. 4 in Figure 5, along with the swelling data from Table 2 plotted as a function of He/dpa ratio. Although the model predictions were at a much higher dose, the predicted non-monotonic behavior is quite similar to the observed behavior. The physical basis for this effect of helium on swelling was first discussed by Odette and Langley¹³ and has been described in more detail by Mansur et al.¹⁴ The swelling enhancement at the intermediate He/dpa ratio is due to the influence of helium on the total cavity density. The cavity density is known to be dependent on the He/dpa ratio.¹⁵ For small increases in the He/dpa ratio,

answer the questions that have been raised regarding the influence of helium.¹⁻³ A definitive answer is not yet possible because of the relatively low doses obtained in these three irradiations, and because the dose rate in the spectral tailoring experiment was a factor of 7 to 10 lower than in the HFIR or the FFTF. Because the influence of the dose rate is potentially significant, this issue will be examined before proceeding to discuss the results further.

Swelling data obtained from fuel pin cladding from the French reactors RAPSODIE and PHENIX provide the best comparison of the influence of dose rate in a fast reactor irradiation.¹⁶ These data indicate that the LSTR is reduced at lower dose rates for temperatures above about 500°C. Below 500°C, the data are somewhat inconclusive. The ambiguity at lower temperatures may in part be due to how the duration of the transient is determined. For example, the data at 430°C from ref. 8 indicate that swelling begins at a lower dose for fuel pin cladding in the periphery of the PHENIX core (lower dose rate), but that the swelling rate is subsequently lower. Hence, for low doses the peripheral fuel pins appear to swell more while at higher doses the pins nearer the core center exhibit more swelling. The swelling curves for the two positions cross over at about 1% swelling. The interpretation of these data is also clouded by the fact that it is obtained from fuel pin cladding. Such irradiations are not isothermal,¹⁷ and temperature changes during irradiation are known to have a marked influence on swelling.^{10,11} The reduced LSTR at the lower dose rates in SA material irradiated at 500°C and above has been explained on the basis of differences in

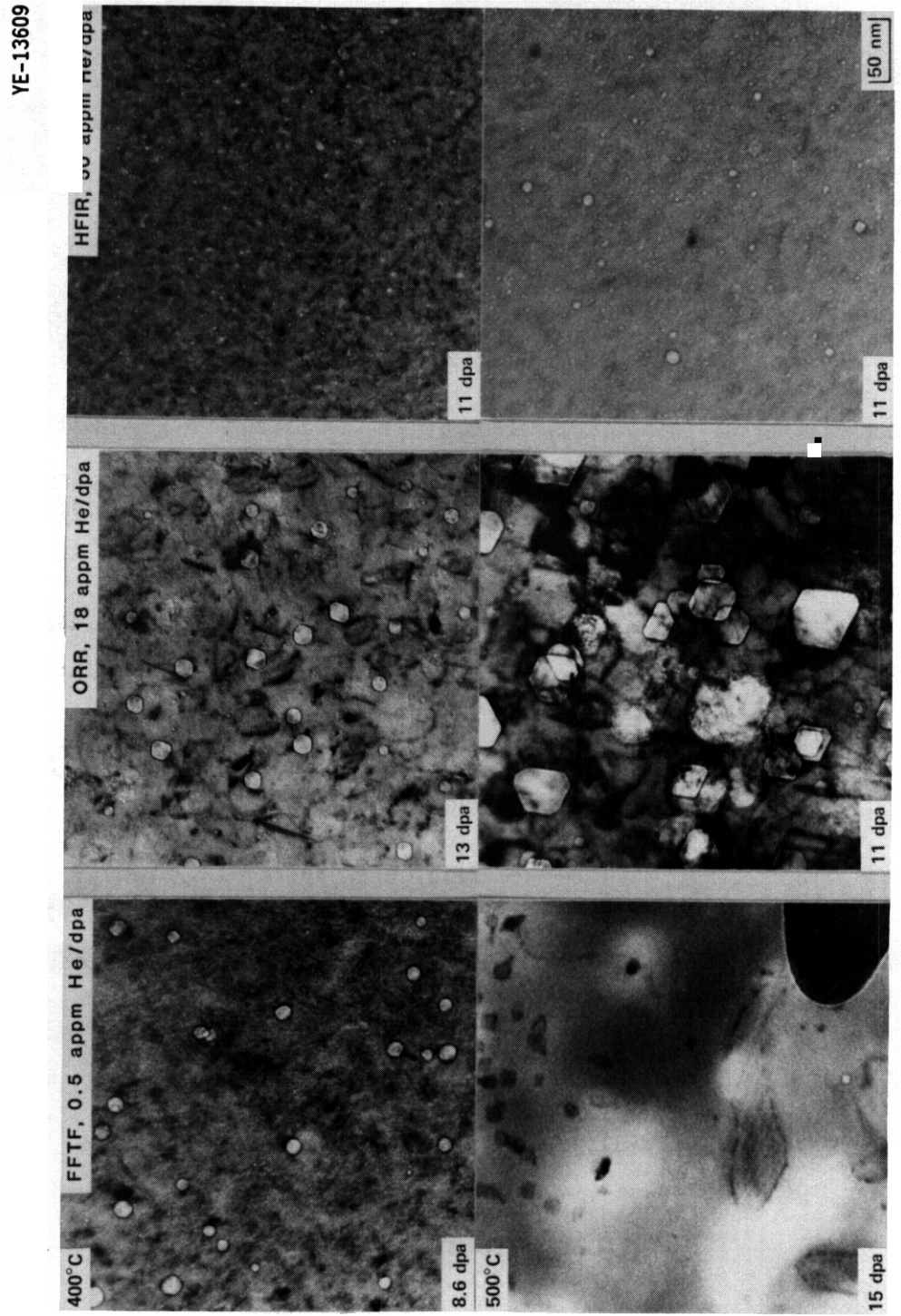


Fig Z Cavity microstructure observed in SA PCA at 400 and 500°C at 9 to 15 dpa in the HFIR, FFTF, and ORR.

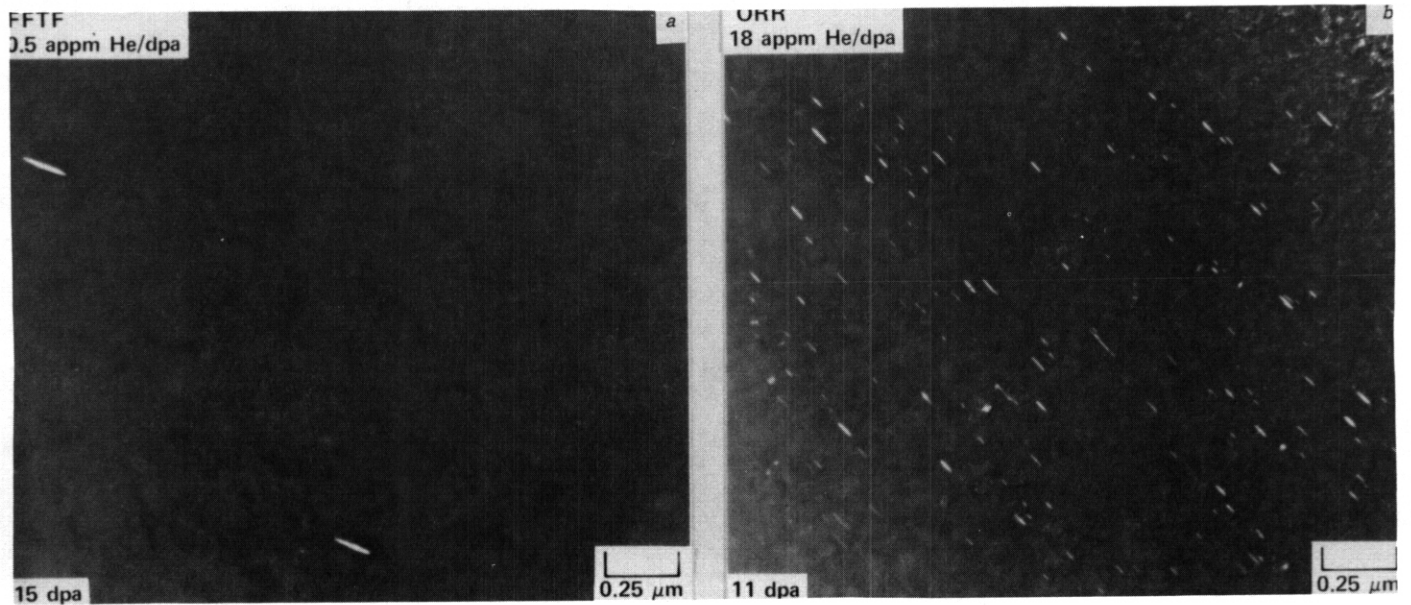


Fig. 3. Comparison of the dislocation structure observed in 25% CW PCA after irradiation to 15 dpa in the FFTF (a) and 11 dpa in the ORR (b). Weak-beam micrographs using stacking fault streaks in material irradiated at 500°C.

ORNL-DWG 87-15253

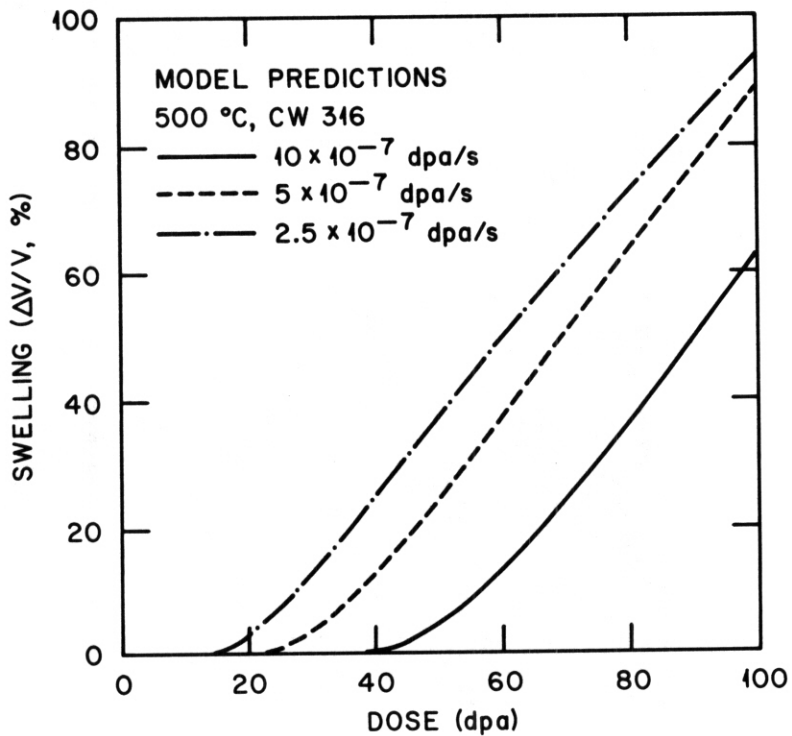


Fig. 4. Predicted swelling as a function of dose rate for 20% CW material.

the LSTR is reduced since more helium is available to drive bubble growth to the critical size for void formation.¹⁶ For higher Heldpa ratios, a regime can be reached in which the cavity density is so high that it begins to suppress the vacancy supersaturation. This leads to a larger critical number of gas atoms for void formation and a longer LSTR. This type of behavior has been observed in another heat of AISI 316 stainless steel (DO heat) that was irradiated in the HFIR and in the EBR-II.¹⁵ Because the swelling rate is dependent on the sink densities that evolve in the "steady-state" regime, the Heldpa ratio can also affect the swelling rate.⁴

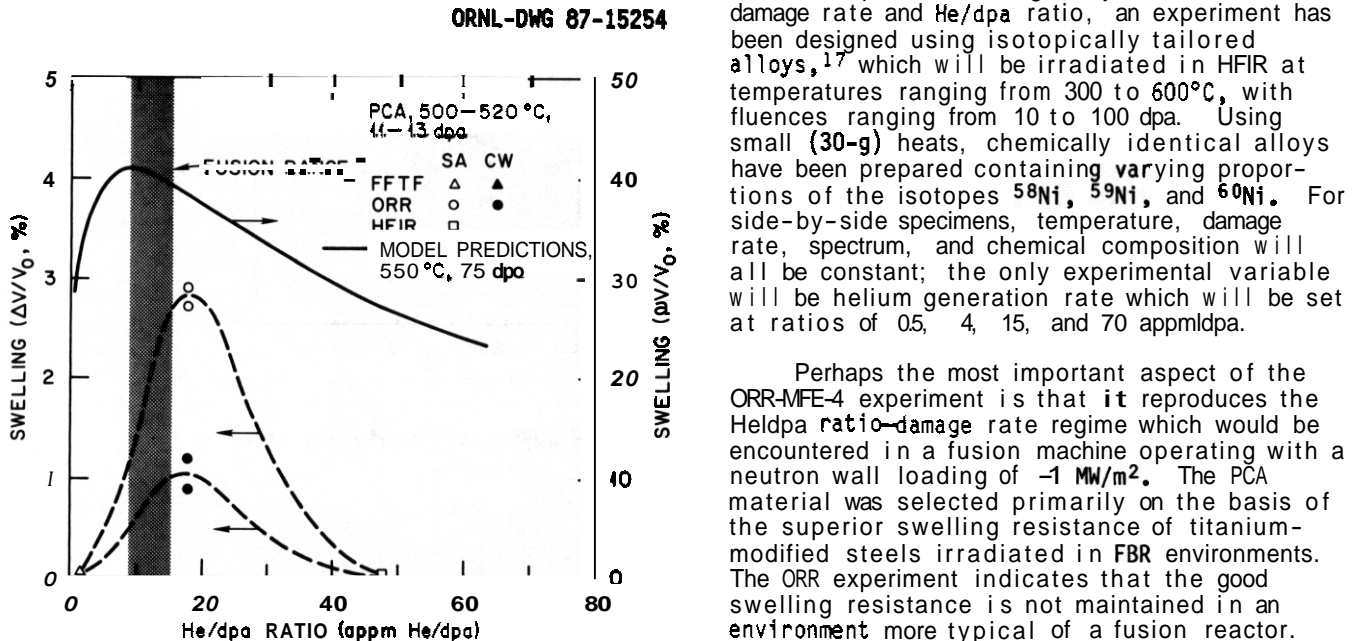


Fig. 5. Comparison of observed and predicted swelling as a function of Heldpa ratio. Data from MFE-4A and -4B experiment and model predictions from ref. 4.

To separate unambiguously the effects of damage rate and He/dpa ratio, an experiment has been designed using isotopically tailored alloys,¹⁷ which will be irradiated in HFIR at temperatures ranging from 300 to 600°C, with fluences ranging from 10 to 100 dpa. Using small (30-g) heats, chemically identical alloys have been prepared containing varying proportions of the isotopes ⁵⁸Ni, ⁵⁹Ni, and ⁶⁰Ni. For side-by-side specimens, temperature, damage rate, spectrum, and chemical composition will all be constant; the only experimental variable will be helium generation rate which will be set at ratios of 0.5, 4, 15, and 70 appm/dpa.

Perhaps the most important aspect of the ORR-MFE-4 experiment is that it reproduces the Heldpa ratio-damage rate regime which would be encountered in a fusion machine operating with a neutron wall loading of ~ 1 MW/m². The PCA material was selected primarily on the basis of the superior swelling resistance of titanium-modified steels irradiated in FBR environments. The ORR experiment indicates that the good swelling resistance is not maintained in an environment more typical of a fusion reactor. Another objective of the isotopically tailored experiment is to determine the behavior of several modified PCA compositions which are designed for improved phase stability in the fusion He/dpa-damage rate-temperature regime.

Recommendations

The proposed International Thermonuclear Experimental Reactor (ITER) will probably employ a water-cooled, austenitic stainless steel first wall structure. The extent to which swelling will have to be accommodated in the design is an important question. Figure 6 presents data illustrating the swelling behavior of several heats of AISI 316, both cold worked and annealed, irradiated in an FBR environment at 370 to 405°C.¹⁸⁻²¹ In this environment, swelling is accelerating very slowly out of the transient regime, and swelling remains below 2% up to a dose of ~ 50 dpa. Most of the cold-worked data are for the FFTF first core heats;¹⁸ even with a constant specification, heat-to-heat variations in swelling are a factor of approximately 2 to 3. The ORR data for the SA PCA lie on the upper bound of these FBR data sets. However, there is a strong possibility that because of the continued generation of helium at a Heldpa ratio of ~ 18 , the swelling of the PCA could accelerate further. A prudent approach toward ITER would be to limit maximum temperatures to 300 to 350°C, particularly if it is important for reasons associated with stress corrosion cracking to use solution-annealed material. Swelling data at 300°C from the ORR-MFE-4 spectrally tailored experiment will become available in 1988 together with data at 60, 200, 300, and 400°C from a second ORR spectrally tailored experiment (6J/7J) carried out under a U.S./Japan collaborative program.²²

The data shown in Figs. 1, 2, and 6 also draw attention to the fact that the interpretation of experimental results is not simple. An experiment such as the MFE-4 that is designed to examine a single variable can expose fundamental differences in behavior that are lost in experiments designed to generate engineering data. Conversely, it may be inappropriate to use an engineering data base to draw conclusions about fundamental mechanisms. A large data set such as that shown in Fig. 6 can be used in a conservative fashion for design purposes; however, the results of extrapolating to other irradiation environments are uncertain. While the judicious use of theoretical models and well-designed, fundamental experiments can increase the level of confidence in such extrapolations, the results discussed here emphasize the need for the fusion materials community to obtain engineering data in an irradiation environment that is typical of the ultimate application.

12. R. E. Stoller and G. R. Odette, pp. 371-392 in Radiation Induced Changes in Microstructure: Thirteenth Conf. ASTM STP 955, ed. F. A. Garner, N. H. Packan, and A. S. Kumar, ASTM, Philadelphia, 1987.
13. G. R. Odette and S. J. Langley, pp. 395-416 in Radiation Effects and Tritium Technology for Fusion Reactors, (Proc. of Int. Conf.) ed. J. S. Watson and F. W. Wiffen, CONF-750989, Vol. 1, 1976.
14. L. K. Mansur, E. H. Lee, P. J. Maziasz, and A. F. Rowcliffe, J. Nucl. Mater. 141-143 (1986) 633-646.
15. G. R. Odette, P. J. Maziasz, and J. A. Spitznagel, J. Nucl. Mater. 10311104 (1981) 1361-1365.
16. R. E. Stoller and G. R. Odette, pp. 358-370 in Radiation Induced Changes in Microstructure: Thirteenth Conf. ASTM STP 955, ed. F. A. Garner, N. H. Packan, and A. S. Kumar, ASTM, Philadelphia, 1987.
17. L. K. Mansur, A. F. Rowcliffe, M. L. Grossbeck, and R. E. Stoller, J. Nucl. Mater. 139 (1986) 228-236.
18. J. F. Bates and M. K. Korenko, Nucl. Technol. 48 (1980) 303-314.
19. T. A. Kenfield, W. L. Bell, H. J. Busboom, G. C. McClellan, and W. K. Appleby, Reactor Swelling of Types 304, 316 and 321 Stainless Steels at High Fluences in EBR-II, GEF-000-62, General Electric Company, 1977.
20. J. F. Bates and J. L. Straalsund, A Compilation of Data and Empirical Representation of Irradiation-Induced Swelling of Solution Treated Types 304 and 316 Stainless Steels, HEDL-TME 78-3, Hanford Engineering Development Laboratory, 1971.
21. F. A. Garner, private communication, 1987.
22. J. L. Scott et al., pp. 6-11 in AOIP Semiann. Prog. Rep. Mar 31, 1985. DOE/ER-0045/14, US DOE Office of Fusion Energy.

PRECIPITATE IDENTIFICATION IN TITANIUM-MODIFIED AUSTENITIC STAINLESS STEELS AFTER IRRADIATION AT 500°C IN HFIR TO ~57 dpa — M. Suzuki and S. Hamada (Japan Atomic Energy Research Institute, assigned to ORNL) and P. J. Maziasz (Oak Ridge National Laboratory)

OBJECTIVE

The objective of this study is to determine the microstructural development of JPCA irradiated to 57 dpa in HFIR.

SUMMARY

Irradiation-enhanced and -induced precipitates were identified in the Japanese prime candidate alloy (JPCA) which was irradiated to 57 dpa at 500°C in HFIR. Comparison was made between the solution annealed (SA) and the 20% cold-worked (CW) JPCA. The SA material had higher swelling and also had a higher volume fraction of irradiation-induced precipitates. Precipitation in the SA JPCA was primarily M_6C with small amounts of titanium-rich MC and still smaller amounts of 6-phase. By contrast, the CW JPCA contained much more MC and less M_6C .

PROGRESS AND STATUS

Introduction

Although JPCA has shown good performance after irradiation in HFIR up to 34 dpa at 300 to 600°C,¹ recent results at 500°C to higher dose (57 dpa, 4260 appm He) show considerable void swelling in SA JPCA. Swelling was about 7% by immersion density measurement. On the other hand, JPCA that had been cold worked or cold worked and aged prior to irradiation showed about 1% swelling after similar irradiation. Fine distributions of titanium-rich MC precipitates usually provide the swelling resistance advantage of the JPCA type of alloy. Swelling resistance should therefore be strongly dependent on the MC stability. The purpose of the present paper is to describe the precipitate evolution in JPCA after high dose irradiation in HFIR, and correlate it with void formation and swelling behavior.

Experimental procedure

The materials used in the present experiment were SA and 20% CW JPCA. Chemical composition of JPCA is shown in Table 1. After irradiation at 500°C to 57 dpa and an estimated helium content of 4260 appm in HFIR, microstructural data were obtained from examination of thin foils and carbon replicas using a JEM 2000FX analytical electron microscope (AEM) with X-ray energy dispersive spectroscopy (XEOS). Because the reactor-irradiated steels were highly radioactive, microchemical analysis was performed on precipitates extracted on carbon replicas.

Table 1. Chemical compositions and heat treatments of JPCA used (Heat treatment: SA at 1100°C)

Alloy	Content, wt %												
	C	Si	Mn	P	S	Ni	Cr	Mo	Ti	Nb	B	N	Co
JPCA	0.06	0.50	1.77	0.027	0.005	15.60	14.22	2.28	0.24		0.0031	0.0039	0.002

Results and discussion

Microstructures of the SA and the CW JPCA are shown in Fig. 1. The SA material has much higher void swelling and a larger volume fraction of coarse irradiation-produced precipitates than the CW. Typical micrographs of extracted carbon replicas which were used for microchemical analysis are shown in Fig. 2. By comparing the precipitate distributions observed on the carbon replica with those in thin foils [cf Fig. 1(a) with Fig. 2(b), or Fig. 1(b) with Fig. 2(c)], one can see that the carbon extraction replicas have the same distribution of precipitates as in the thin foils, so that representative phase analysis can be conducted on the replicas.

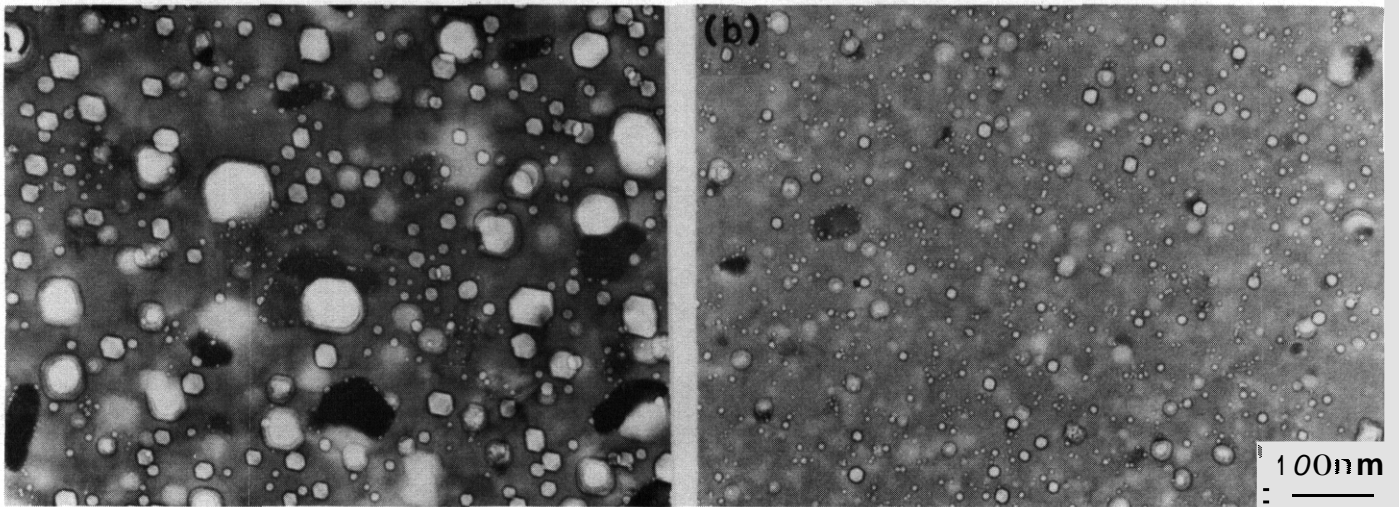


Fig. 1. Microstructure of (a) solution annealed and (b) 20% cold-worked JPCA after irradiation to 57 dpa at 500°C in HFIR.

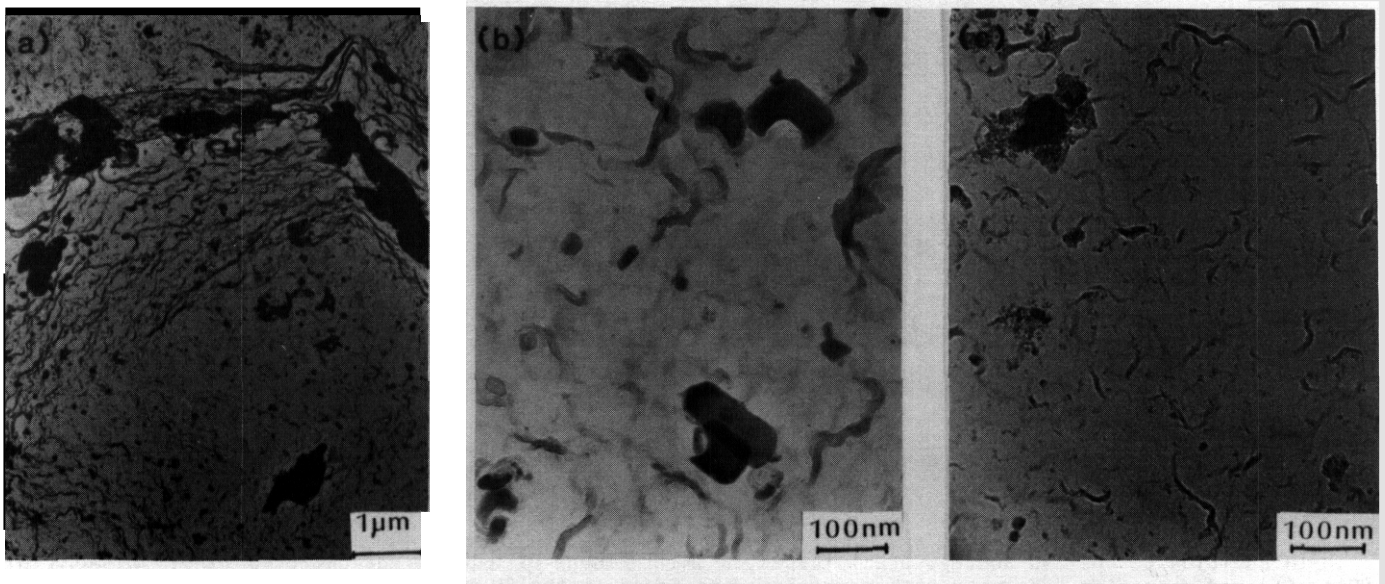


Fig. 2. Precipitates on extracted carbon replica after irradiation to 57 dpa at 500°C in HFIR (a) SA, around the grain boundary region; (b) SA within the grain interior, (c) CW, within the grain interior.

For the SA, coarse precipitates up to 1 μm were formed along the grain boundaries, and relatively small precipitates ranging from less than 10 to 500 nm were formed within the grains. The relative difference between matrix and grain boundary precipitation was similar for the CW, but precipitates were much smaller. In both materials, the coarse precipitates along the grain boundaries were mostly identified as M_6C , although there was also some TiC in the CW. The M_{23}C_6 phase was also found in both materials; however, there were only a few of these particles. In the grain interior, most of the large precipitates were M_6C or titanium-rich MC (TiC). Typical morphologies and representative XEDS spectra are shown in Fig. 3. By careful observation, large MC particles could be distinguished from M_6C by the fact that almost all TiC contained internal contrast structure regardless of size, whereas M_6C appeared clear inside with the exception of very small internal cavities² (Fig. 4).

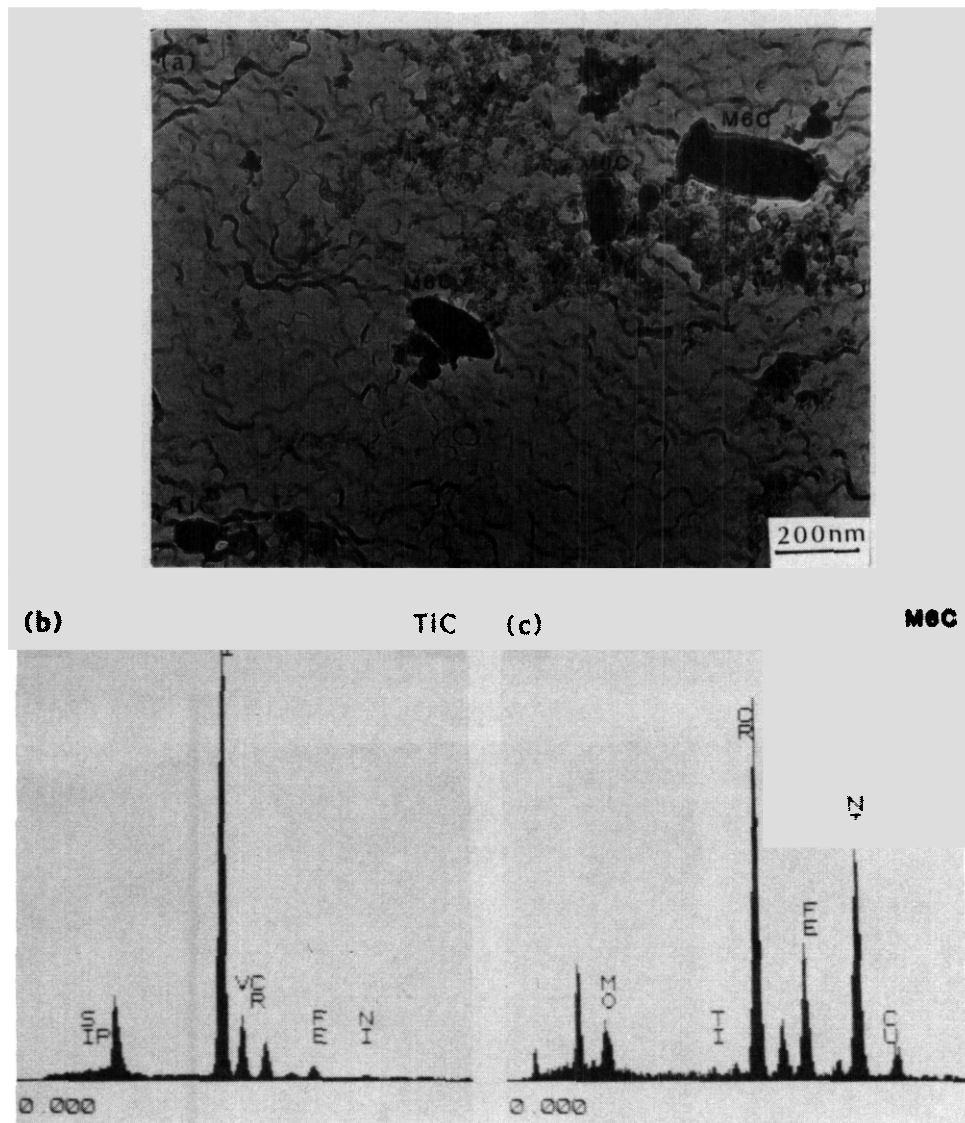


Fig. 3. Precipitates on extracted carbon replica from CW JPCA after irradiation to 57 dpa at 500°C in HFIR.

In addition to the TiC and M_6C precipitates, a small amount of G-phase was detected in the SA material (Fig. 5) and many fine, chromium-rich particles were found in the CW material (Fig. 6). Some of these fine, chromium-rich particles were also found in the SA but much less than observed in the CW material. The chromium-rich precipitate had a face-centered-cubic structure with a lattice parameter of around 42 nm, although diffraction was very difficult for particles smaller than 10 nm in diameter. This lattice parameter is nearly that of TiC . Therefore, these chromium-rich precipitates may be related to the titanium-rich MC observed at lower dose and found to be very rich in chromium when formed during irradiation.) If the replacement of titanium by chromium continues during irradiation, it could produce the strange, chromium-rich particles observed after 57 dpa.

Relative volume fractions of these precipitates can be estimated via analysis of broad-beam XEOS spectra obtained from a large area of the replica containing many precipitates. Figure 7 shows the spectra obtained from (a) grain boundary of the SA JPCA, (b) grain boundary of the CW JPCA, (c) grain interior of the SA JPCA and (d) grain interior of the CW JPCA. The differences in spectra reflect changes in the distribution of phases in the overall precipitate. For example, the spectrum of the grain boundary of the SA material indicates that M_6C is the major grain boundary phase. This is also the case for the grain interior of the SA JPCA, although a little more TiC is detected there as well. By contrast, the titanium peak for the CW material is much higher than that of the SA material, indicating that much more titanium-rich MC is present.

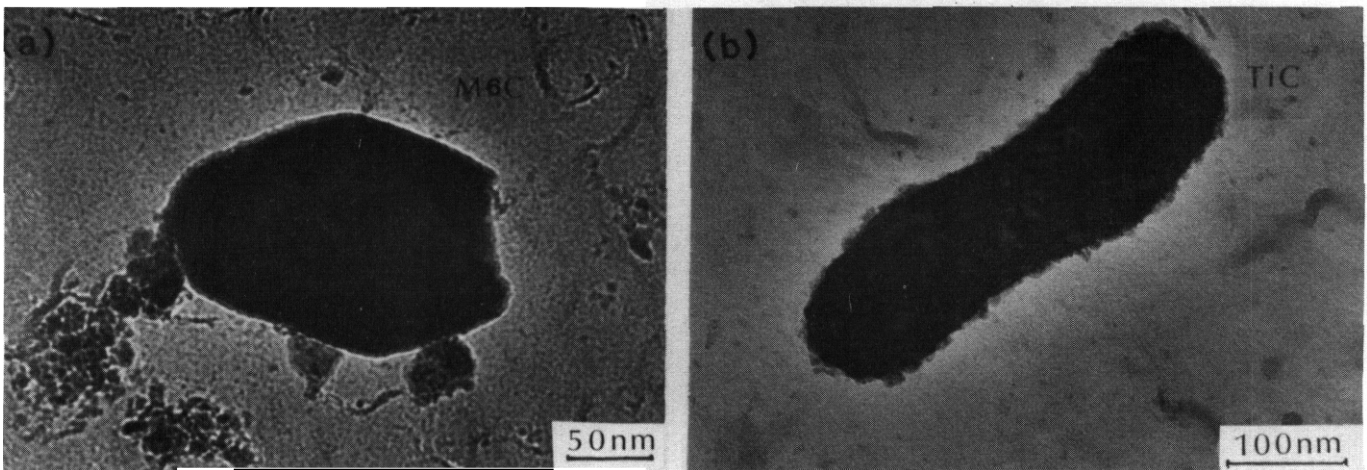


Fig. 4. Precipitates on extracted carbon replica after irradiation to 57 dpa at 500°C in HFIR. (a) M_6C , (b) TiC .

YP4771

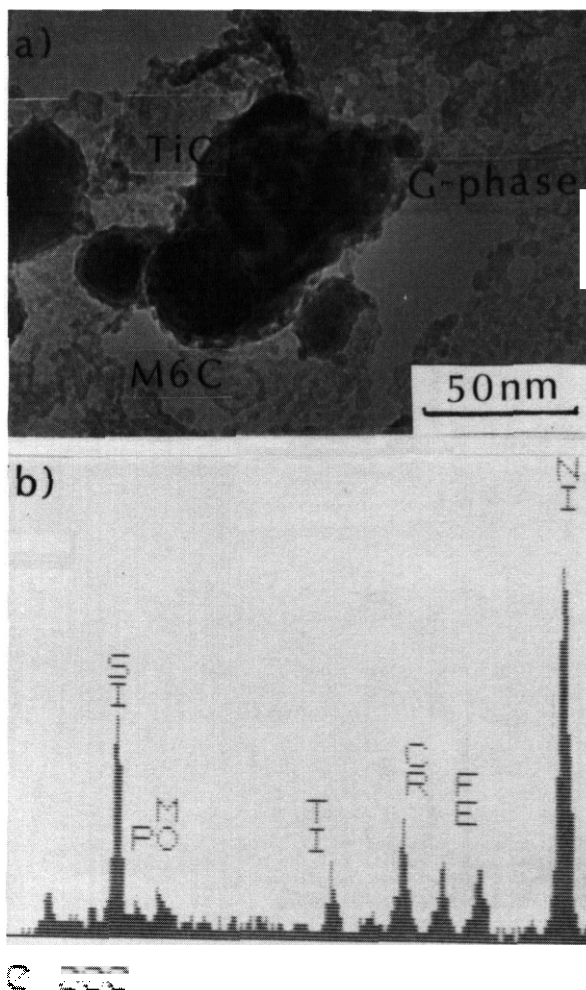


Fig. 5. Precipitates on extracted carbon replica from SA JPCA after irradiation to 51 dpa at 50°C in HFIR.

In addition, the ratio of chromium to nickel suggests that there is very little M_6C in the CW relative to the SA material. This behavior is also consistent with the many chromium-rich fine precipitates in the matrix. Rough estimates of the volume fractions of the various phases are shown in Table 2.

Table 2. Precipitates observed in JPCA after irradiation to 57 dpa at 500°C in HFIR

	Grain Boundary	Grain Interior
SA JPCA	M_6C	M_6C ~ 70% TiC ~ 20%
	$(M_{23}C_6)$	(Chromium-rich phase) (G-phase)
CW JPCA	M_6C	M_6C = 40% TiC = 40%
	$(M_{23}C_6)$	Chromium-rich phase

CONCLUSIONS

Analysis of the precipitates in JPCA irradiated to 57 dpa at 500°C in HFIR revealed the following:

1. Irradiation of the SA JPCA produces primarily M_6C precipitation, with small amounts of titanium-rich MC. Besides these, a few fine $M_{23}C_6$ and G-phase particles were also detected.

2. By contrast, irradiation of the CW JPCA produced much more fine titanium-rich MC and fine chromium-rich precipitates, much less M_6C , and no detectable G-phase.

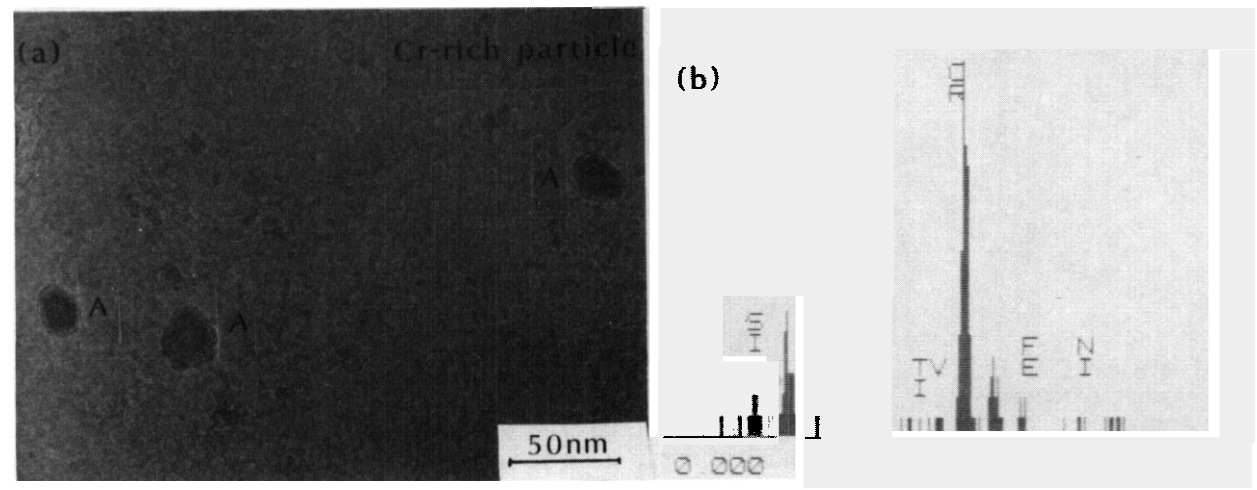


Fig. 6. Chromium-rich particle observed in CW JPCA after irradiation to 57 dpa at 500°C in HFIR.

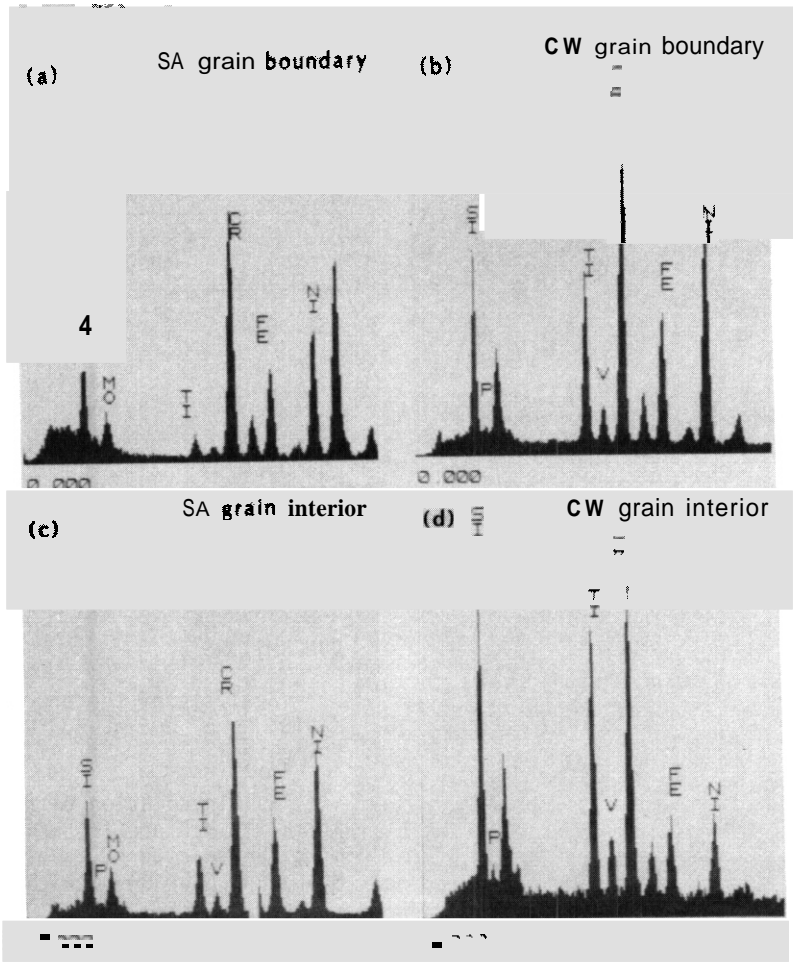


Fig. 7. XEDS spectrum obtained using broad beam to average the composition of many precipitate particles. (a) SA, along the grain boundary; (b) CW, along the grain boundary; (c) SA, within the grain interior; (d) CW, within the grain interior.

FUTURE WORK

Future work will focus on the processes which control the disappearance of titanium-rich MC-type precipitates and the concurrent development of M_6C phase. The strange chromium-rich precipitate produced during irradiation will also be studied in more detail, as it may be a key factor in the degradation of fine MC.

REFERENCES

1. M. P. Tanaka, S. Hamada, A. Hishinuma, and P. J. Maziasz, to appear in Journal of Nuclear Materials.
2. S. Hamada, M. P. Tanaka, and P. J. Maziasz, in Fusion Reactor Materials Semiannual Prog. Rep. Sept. 30, 1986. DOE/ER-0313/1.
3. M. Suzuki, S. Hamada, and M. P. Tanaka, in Fusion Reactor Materials Semiannual Prog. Rep. March 31, 1987, DOE/ER-0313/2.

SWELLING BEHAVIOR AND MICROSTRUCTURAL EVOLUTION IN TYPE 316 STAINLESS STEEL IRRADIATED IN HFIR — S. Hamada, M. Suzuki (Japan Atomic Energy Research, assigned to ORNL), P. J. Maziasz (Oak Ridge National Laboratory), M. P. Tanaka, and A. Hishinuma (Japan Atomic Energy Research)

OBJECTIVE

The objective of this work is to define the microstructural changes and swelling behavior in type 316 stainless steel irradiated in HFIR to 30 dpa at 300 to 600°C. This work has been performed under the U.S./Japan collaborative program for fusion materials research.

SUMMARY

Swelling behavior and microstructures were investigated in solution-annealed (SA) and 20% cold-worked (CW) type 316 stainless steel irradiated to 30 dpa at 300 to 600°C in the High Flux Isotope Reactor (HFIR). At irradiation temperatures <400°C, a high concentration (2 to $4 \times 10^{23} \text{ m}^{-3}$) of small bubbles (1.5 to 4.5 μm diam) were formed uniformly in the matrix. Swelling was low (<0.2%) in both SA and CW materials irradiated to 30 dpa. In SA 316, cavity size increased, but the number density decreased with increasing irradiation temperature above 500°C. At 500°C, there was a mixture of bubbles and voids, but at 600°C, most of the cavities were voids. Maximum swelling (-5%) occurred at 500°C. By contrast, cavities in 20% CW specimens were much smaller, with diameters of 6 and 9 μm at 500 and 600°C, respectively, suggesting that they were primarily bubbles. The cavity number density in CW 316 at both 500 and 600°C ($\sim 1 \times 10^{22} \text{ m}^{-3}$) was about one order of magnitude less than at 400°C. Swelling increased slightly as irradiation temperature increased, peaking at 600°C (0.3%). These results indicate that SA 316 swells more than CW 316 at 500 and 600°C, but both SA and CW 316 are resistant to void swelling in HFIR at 400°C and below to 30 dpa.

PROGRESS AND STATUS

Introduction

The radiation resistance of structural materials is a crucial factor in the development of fusion reactors. The irradiation damage caused by fusion neutrons is characterized by atomic displacement-damage and helium produced by transmutation reactions. The displacement-damage effects in type 316 stainless steel have been extensively studied by irradiating the steels in fast breeder reactors. The effects of transmuted helium have been investigated by irradiation in HFIR (High Flux Isotope Reactor), a mixed-spectrum reactor in which thermal neutrons react with ^{58}Ni to produce helium.¹⁻³ However, most of these data have been obtained at temperatures which are much higher (>500°C) than those expected in the proposed FER (Fusion Experimental Reactor). Swelling in the presence of helium has not yet been examined for the low temperature operating range of the FER.

Experimental

The chemical composition of the type 316 stainless steel used in this experiment is given in Table 1. After 3-mm-diam transmission electron microscopy (TEM) disks were punched from the cold-rolled 0.27-mm-thick sheet, they were solution annealed for 30 min at 1050°C. To produce 20% CW materials, the steel (0.34 mm in thickness) was annealed for 30 min at 1050°C prior to a final 20% reduction by cold rolling, after which the disks were punched from the sheet. The surfaces of the disk were lightly mechanically polished to 0.25-mm-thick sheet to prevent strain prior to irradiation.

Table 1. Chemical Composition of Type 316 Stainless Steel

Content, wt %												
C	Si	Mn	P	S	Ni	Cr	Mb	Ti	Nb	B	N	Co
0.058	0.61	1.80	0.028	0.003	13.52	16.75	2.46	0.005	<0.1			<0.1

The disks were irradiated in the JP-1, -3, -6, and -7 capsules of HFIR at 300 to 600°C up to 36 dpa (2327 appm He). After irradiation, disks were electropolished in a twin-jet Tenupol unit and examined with a JEM 2000FX high-resolution electron microscope operating at 200 kV. Carbon-extraction replica films were also prepared from the TEM disks to analyze the composition of precipitates. These analyses were made using x-ray energy dispersive spectroscopy (XEDS) and a TN 5500 computer to obtain quantitative compositions.

Experimental Results

Cavity Distribution – The cavities and cavity size distributions observed in SA and CW specimens irradiated at 300 to 600°C in HFIR are shown in Figs. 1 and 2, respectively. At 300°C, a uniform distribution of fine cavities (1 to 5 nm in diameter) was observed in the matrix of both CW and SA steels; densities were $\sim 10^{23} \text{ m}^{-3}$. The sharp, narrow peaks in the size distributions suggest that most of these fine cavities are Subcritical bubbles [Fig. 2(a) and (b)]. The swelling in both materials at 300°C was less than about 0.14%. Cavity distributions in the matrix of SA and CW steels at 400°C are similar to those observed at 300°C, except that some larger cavities (4 to 8 nm in diameter) are also present. The larger faceted cavities are probably evolving into supercritical voids. The size-distribution histograms show a broadening toward larger sizes, suggestive of an incipient bimodal distribution. These size distributions suggest a critical size of 4 to 5 nm.⁴ The swelling in SA and CW at 400°C was 0.22 and 0.14%, respectively.

As the irradiation temperature increased to 500°C, cavity evolution became significantly different between SA and CW material. Cavity sizes in SA material irradiated at 500°C are much larger than at 400°C, while those in CW material are only slightly larger than at 400°C [Fig. 1(e) and (f)]. Both size distributions of SA and CW material at this temperature show sharp, narrow peaks at smaller sizes (<5 nm) that suggest these are subcritical bubbles [Fig. 2(e) and (f)]. However, SA material develops a broad tail toward larger sizes that suggests a significant number of subcritical bubbles have converted to bias-driven voids. The concentration of cavities in SA and CW decreases by about one order of magnitude compared to 400°C. The swelling in SA and CW was 1.09 and 0.16%, respectively. In SA material at 500°C, cavity appearance suggests that the largest ones are being affected by the electropolishing and therefore are eliminated from swelling estimates. This would lead to an underestimate of the swelling determined by TEM. Swelling values obtained by immersion density measurements were larger than those obtained by TEM; swelling in SA and CW was 5.1 and 0.87%, respectively.

At 600°C, large, faceted voids (10 to 65 nm in diameter) were observed in SA 316, whereas a uniform distribution of much smaller cavities (5 to 10 nm in diameter) was found in the matrix of CW 316 [Fig. 1(g) and (h)]. The cavity size distribution of SA 316 shows a broad distribution with a tail toward larger sizes, with the peak at about 30 nm, whereas the cavity size distribution in CW is sharp and narrow with a peak at 10 nm [Fig. 2(g) and (h)]. The concentration of voids decreased by three orders of magnitude in SA, but decreased only slightly in CW. The swelling decreases to 1% in SA but slightly increases in CW (0.29%) at 600°C compared to 500°C. However, polishing effects could also cause many large voids to be missed in TEM estimates of swelling at 500°C.

Dislocation Loop Evolution – The dislocation structure in all specimens consisted of network and Frank faulted loops. Loops are a particularly important factor in assessing the effect of point defects produced by irradiation. The faulted Frank loops were therefore imaged separately from the network, using a high-resolution dark-field method suggested by Okamoto and Harkness.⁵

A high concentration of dislocation loops was found in SA and CW at 300°C. The dislocation loop density increased slightly at 400°C, but then decreased dramatically at 500°C. Loop growth was greater at irradiation temperatures of 500°C and higher, and many apparently have unfaulted to form a network. At 600°C, only a loose tangle of dislocation network was found; no loops were observed by using the high-resolution dark-field method. Figure 3 shows the dislocation development at 300 to 600°C in SA and 20% CW 316.

Precipitation – The precipitates formed in type 316 stainless steel during HFIR irradiation were quite sensitive to the irradiation temperature. No precipitation was observed in either SA or CW at 300°C. Precipitates did develop at 400, 500, and 600°C, as shown in Fig. 4. A low concentration of small intragranular particles were observed at 400°C via Moiré fringes [see Fig. 4(a)]. These particles were found to be the chromium-rich M_{23}C_6 type phase, as shown via XEDS analysis on an extraction replica in Fig. 4(b); Moiré fringe spacing was also consistent with the crystal structure information for M_{23}C_6 (refs. 6,7). Some precipitates were also observed along grain boundaries, and there was no difference in precipitation between SA and CW materials. None of these M_{23}C_6 precipitates showed any association with cavities.

At 500 and 600°C, there was a large difference in precipitation between SA and CW 316. Many precipitates at 500°C were observed throughout the matrix in SA 316 and were associated with voids of similar size. The average diameter and number density of precipitates were 37 nm (15- to 65-nm range) and $24 \times 10^{21} \text{ m}^{-3}$, respectively. By contrast, precipitates formed in CW specimens at 500°C were similar to those observed at 400°C. The XEDS spectrum of an extracted particle from SA 316 irradiated at 500°C is presented in Fig. 4(e) and the composition is listed in Table 2. This precipitate was identified as the M_6C type phase whose major components are Ni, Cr, Fe, Si, and Mo. The composition agrees well with the characteristic M_6C composition reported by Lee et al. and others.⁸⁻¹⁰ The precipitate microstructural evolution in CW 316 at 600°C is similar to that found at 500°C. However, for the same comparison, precipitates in SA 316 coarsened considerably with increased temperature [cf. Fig. 4(b) and (c)]. These precipitates

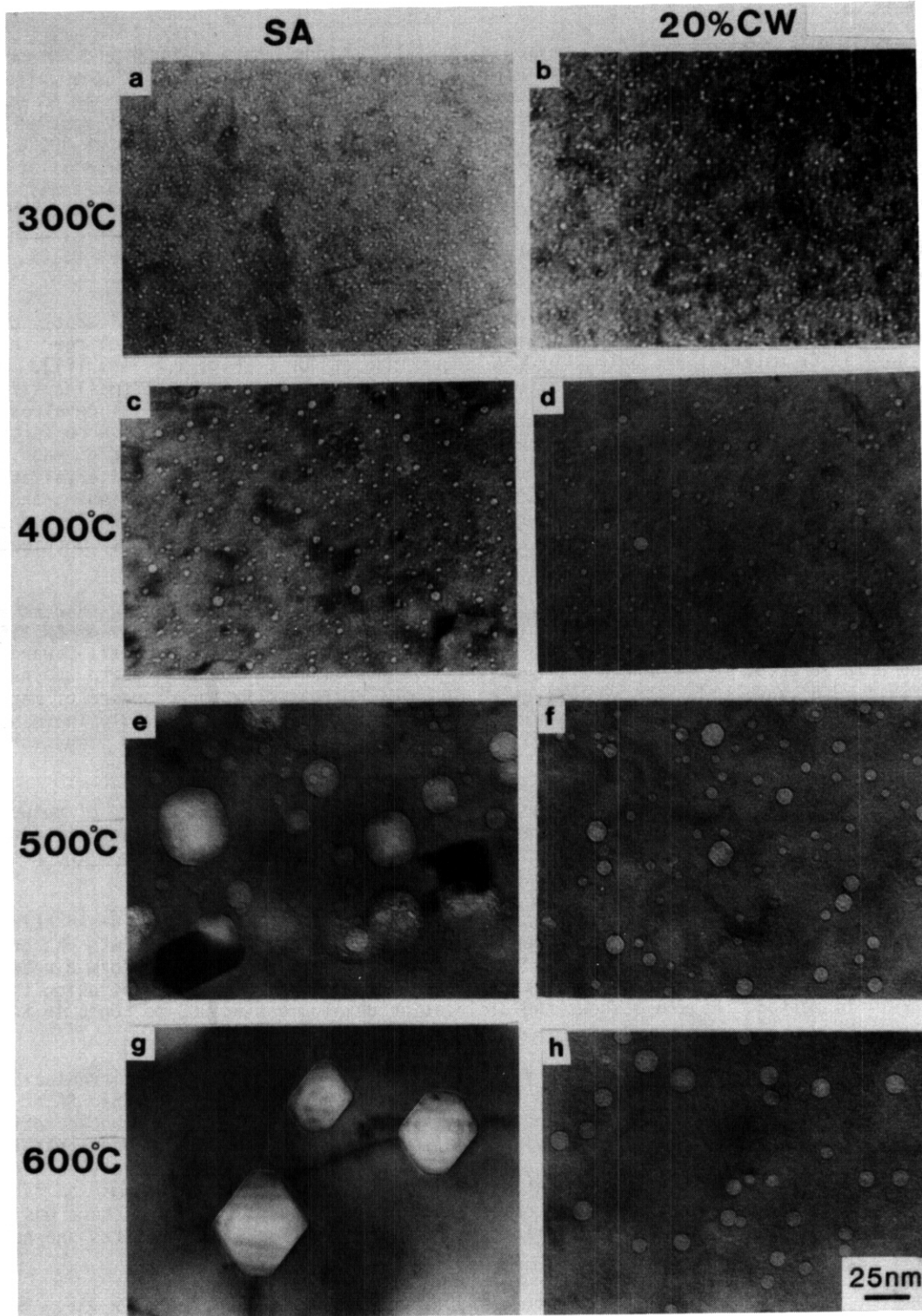


Fig. 1. A comparison of cavities for SA (a,c,e,g) and 20% CW (b,d,f,h) type 316 stainless steel irradiated in HFIR at 300 to 600°C up to 36 dpa and to 2327 appm He.

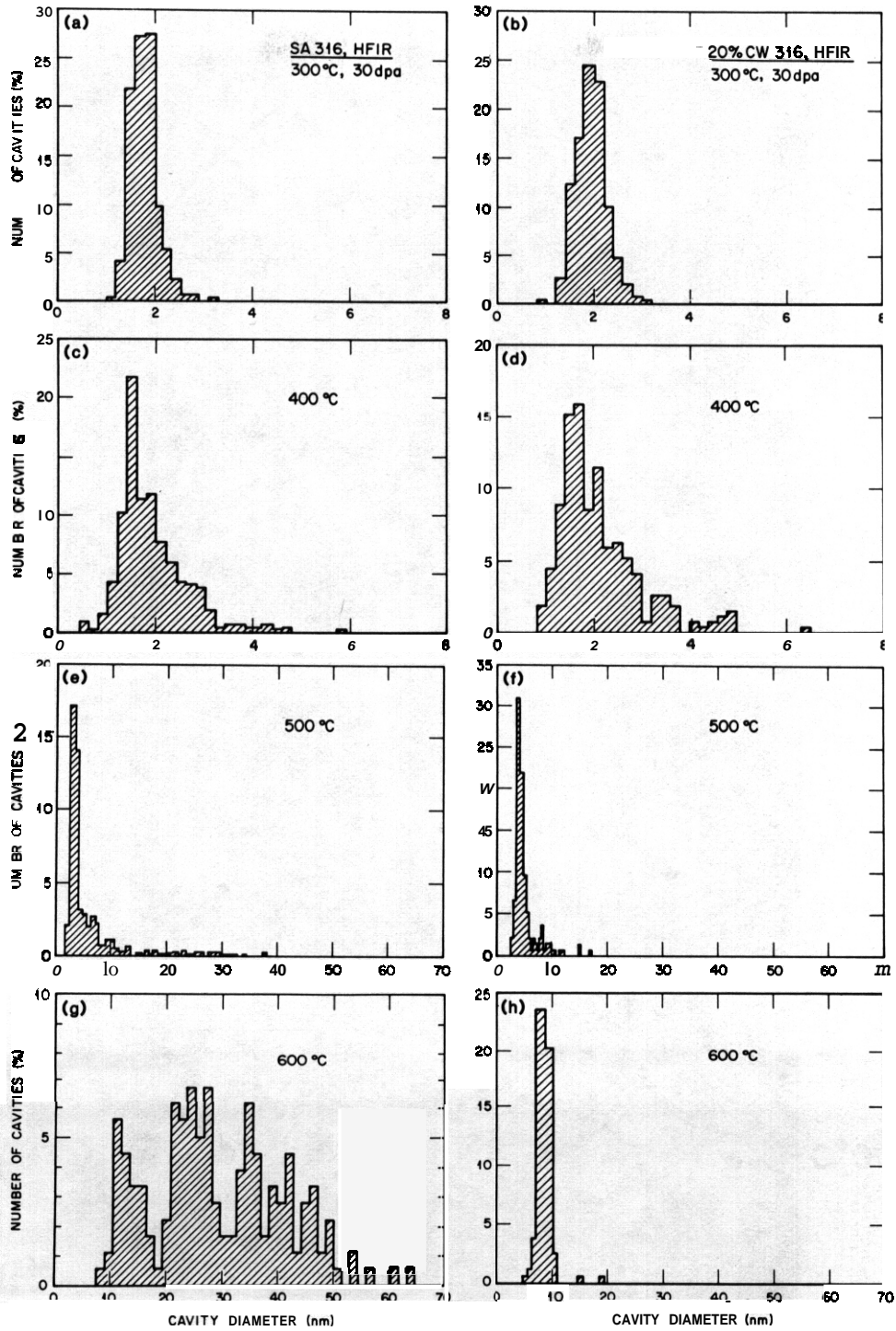


Fig. 2. Histograms of cavity size distribution in SA (a,c,e,g) and 20%CW (b,d,f,h) type 316 stainless steel irradiated up to 36 dpa in HFIR at 300 to 600°C.

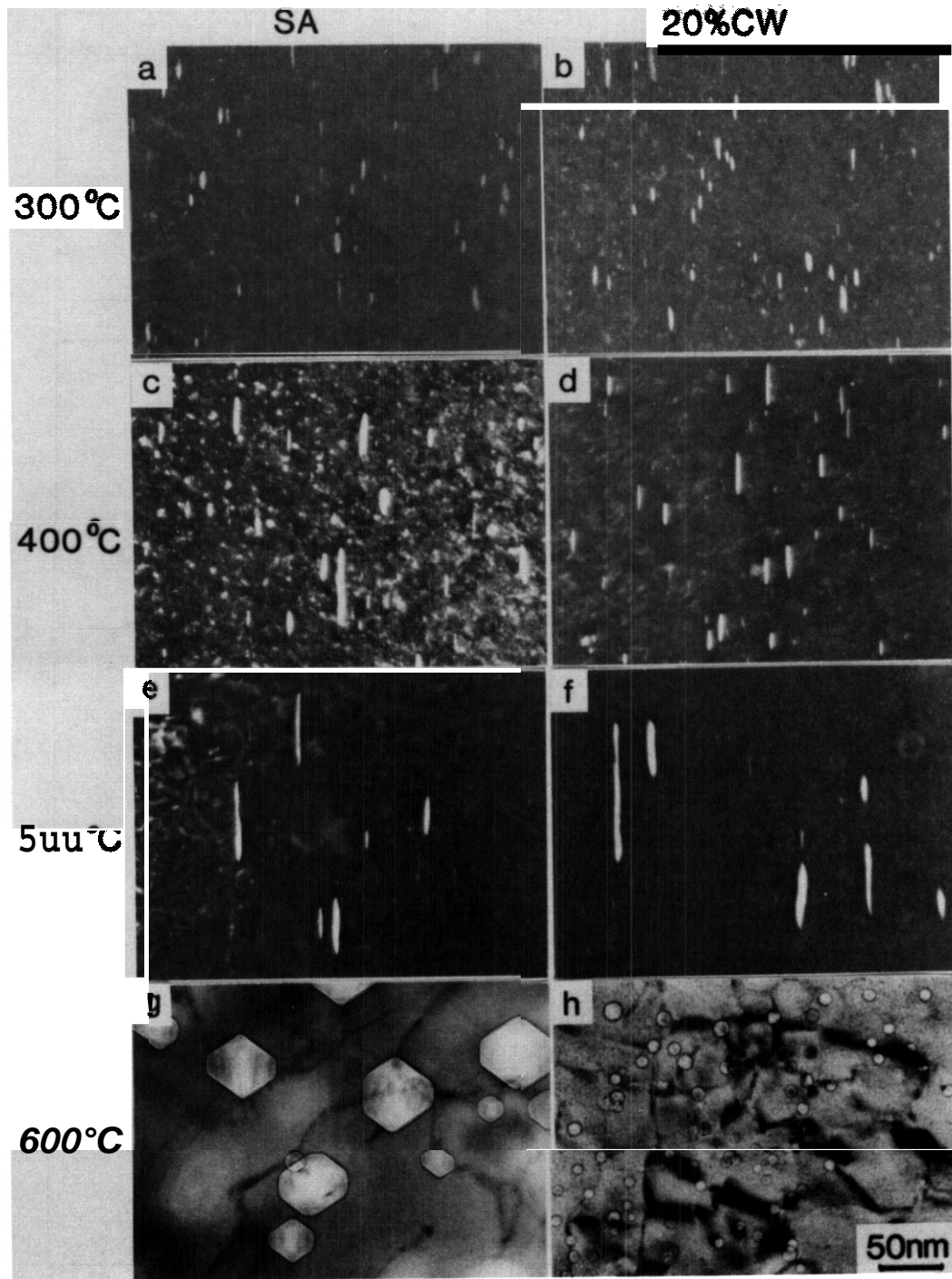


Fig. 3. Dislocation microstructures in SA and 20% CW 316 irradiated in HFIR at 300 to 600°C up to 36 dpa and to 2327 appm He.

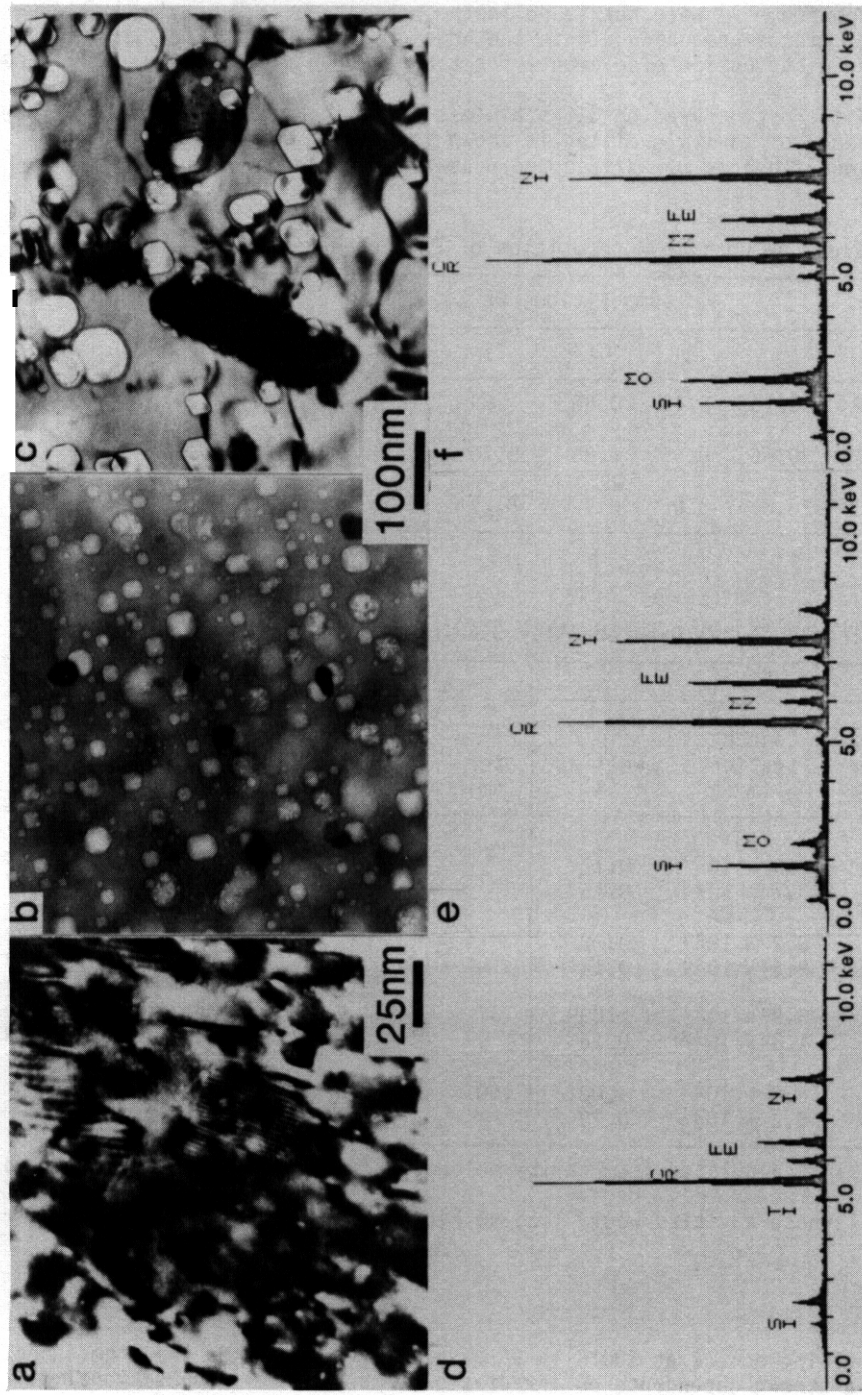


Fig. 4. Precipitates and X-ray spectrum from extracted particles in SA 316 irradiated in HFIR. (a,d) 400°C, 33.4 dpa; (b,e) 500°C, 34.0 dpa; and (c,f) 600°C, 36.1 dpa.

had an average diameter of 160 nm (100- to 270-nm range) and number density of $23 \times 10^{19} \text{ m}^{-3}$. Despite increased precipitate sizes, the associated voids were not much larger than those found at 500°C, which means that at 600°C, voids are smaller than their associated precipitates. Figure 4(f) shows an XEDS spectrum from a typical extracted particle and from SA 316 at 600°C, and again, the phase is identified as M_6C . Compositionally, this phase contains about 30 wt % each of Cr and Ni, 17% Mo, and 1% Si, and the lattice parameter is $a_0 = 1.10 \text{ nm}$. Comparison of the M_6C composition at 500 and 600°C (Table 2 and Fig. 4) shows that the molybdenum content of the phase has increased considerably with irradiation temperature. Most of the precipitates observed on this replica were identified as M_6C phase. Other phases like γ' , G, and Laves, which have been reported elsewhere,⁸⁻¹¹ were not found in the present work; M_{23}C_6 (τ) phase was found only at 400°C. The probability of microsegregation within the huge precipitates on the replica was examined, but results indicate a uniform distribution of elements for the electron probe size used (~65 nm).

Data on irradiation conditions and microstructures on 316 stainless steel irradiated in HFIR are summarized in Table 3. Temperature dependence of cavity swelling is shown in Fig. 5; swelling data for 20% CW DO-heat and N-lot determined at various fluences by Maziasz and Braski⁴ are also included.

Table 2. Data on the Chemical Composition of Extracted Particles

Position Analyzed	Composition, wt %								
	Fe	Ni	Cr	Mn	Ti	Si	P	Mo	V
400°C (4d) ^a	15.61	2.09	63.15	2.40	0.05	1.64	0.52	6.24	1.97
500°C (4e) ^a	18.29	31.51	30.56	0.55	0.05	9.75	1.03	6.84	1.05
600°C (4f) ^a	10.37	28.61	28.81	0.02	0.12	8.27	1.07	20.37	2.01

^aSee Fig. 4.

Table 3. Microstructural Data on Alloy 316 Irradiated in HFIR

Heat Treatment	Irradiation Condition			Data						
	Temperature (°C)	Damage (dpa) ^a	Helium Content (appm)	Cavity			Diameter (nm)	Concentration (m ⁻³)	Loop	
				Diameter (nm)	Concentration (m ⁻³)	Swelling ^b (%)			Diameter (nm)	Concentration (m ⁻³)
SAC CW ^d	300	33.0	2116	1.9	3.9×10^{23}	0.13			10.3	13×10^{22}
	300			2.0	3.7×10^{23}	0.15			10.4	15×10^{22}
SA CW	400	33.4	2142	2.3	3.2×10^{23}	0.22			16.0	25×10^{22}
	400			2.3	2.3×10^{23}	0.14			11.6	45×10^{22}
SA CW	500	34.0	2187	13.3	8.9×10^{21}	1.09 ^e	37	2.4×10^{21}	21.1	12×10^{20}
	500			6.1	1.3×10^{22}	0.16			29.3	3.5×10^{20}
SA CW	600	36.1	2327	33.9	48×10^{20}	1.00	160	23×10^{19}		
	600			8.8	82×10^{21}	0.29				

^aDisplacements per atom, ^bSwelling calculated from cavity volume fraction, ^cSolution annealed.

^dCold worked, ^eEstimation of all these cavities would lead to higher swelling of 5 to 10%.

Discussion

In the present work, a peak in swelling occurs at 500°C in SA material (Fig. 5). On the other hand, swelling in CW material does not show a strong dependence on irradiation temperature. Compositional differences in precipitate phases also suggest that maximum radiation induced segregation (RIS) of solute elements correlates with the swelling maximum observed in SA 316 at 500°C.

SA Material — At temperatures below 400°C, swelling is low in SA 316 because the cavity size is small and the cavity concentration is high. Calculations of gas atom accommodation by the cavity structure suggest that most of the fine cavities are equilibrium bubbles. The high concentration of helium bubbles and loops increases the critical cavity size so that conversion of bubbles to voids is suppressed.¹²

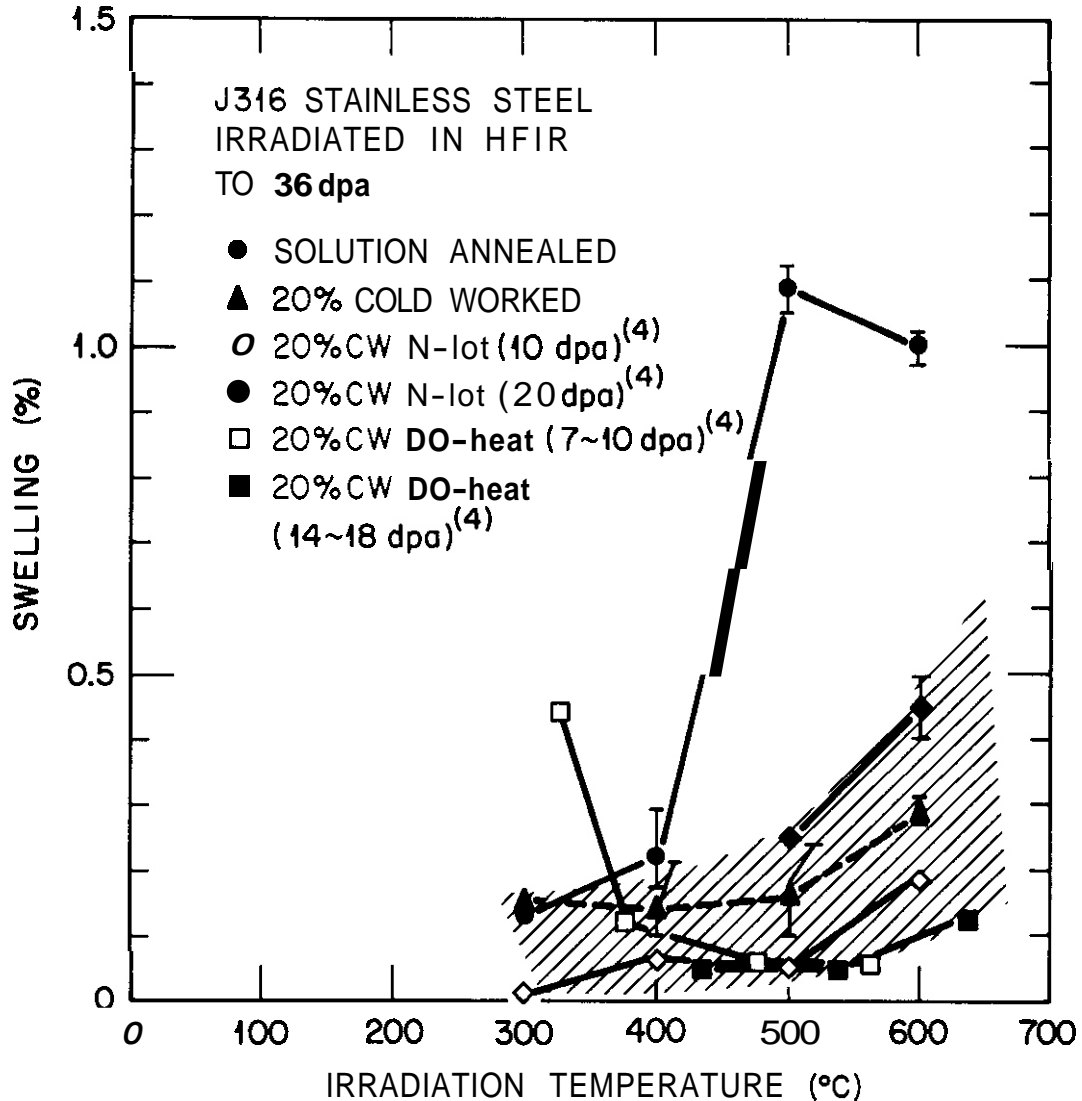


Fig. 5. Cavity swelling plotted as functions of irradiation temperature for SA and 20% CW type 316 stainless steel irradiated in HFIR at 300 to 600°C up to 36 dpa and to 2327 appm He. Data indicated with ref. 4 were reported by Maziasz and Braski.

At 500°C, the average cavity size is about five times that at 400°C, while the cavity number density is about one order of magnitude less than at 400°C. More than half of the cavities present appear to be larger than their critical size and thus have converted into bias-driven voids.^{4,13} Bubble growth and/or coalescence are more likely at higher temperatures. Coalescence/coarsening of cavities with increasing temperature could contribute to a reduction in the critical cavity size as well as make bubbles suddenly larger than their critical size, both of which would increase conversion of bubbles to voids. The coarse M_6C phase particles which develop at 500°C should also directly enhance the growth rate of attached voids by acting as point defect collectors.^{14,15} Furthermore, these M_6C particles in SA 316 may preferentially absorb interstitials to increase the net bias of the material, further increasing swelling. The XEDS shows that the M_6C at 500°C is modified by RIS, with slightly more Ni and Si, and much less Mo than at 600°C. An interstitial bias for these particles has been suggested on the basis of their strong chemical affinity for Si and Ni which migrate interstitially when RIS is intense.^{**} The microstructure observed in SA 316 at 500°C after ~30 dpa suggests that swelling will continue to increase at higher dose.

At 600°C, few Frank loops remain in the SA 316 matrix, and some of the largest voids are found at climbing dislocations. Increased bulk recombination with temperature would reduce long-range migration of interstitials and reduce loop nucleation. Moreover, bubble nucleation decreases and growth increases at higher temperatures, leading to a coarser microstructure, particularly if bubbles nucleate along the

reduced concentration of network dislocations. Together, these changes in bubble density would lead to a large decrease in void density. Even though voids are larger at 600°C, there are so few that swelling is less at 500°C.

CW Material - Swelling in CW 316 is low and does not depend much on temperature. At 300 and 400°C, cavity behavior is similar in SA and CW material [Fig. 1(a-d)]. Both have a high concentration of fine helium bubbles in the matrix, and swelling is minimal. However, SA and CW materials behave differently at 500 and 600°C. Many small cavities (below 10 nm in diameter) are uniformly dispersed along the dislocation lines in CW 316. The high density of dislocations from cold work provide more bubble nucleation sites, since most subcritical bubbles are observed to be attached to dislocations. Calculations to account for partitioning of helium atoms suggest that most of these small cavities are equilibrium bubbles, not voids. The high concentration of helium bubbles could then act as strong sinks to increase the critical cavity size and thus suppress their conversion into voids. These same bubble sinks would also dilute RIS¹⁴ to produce enhanced thermal M₆C rather than the modified M₆C observed in SA 316 at 500°C. This change may further contribute to reduced swelling in CW 316.

Finally, data in Fig. 5 show that swelling varies from heat to heat for 20% CW 316 stainless steels irradiated in HFIR to below 30 dpa (cross-hatched region). The data suggest, however, that for a swelling-resistant heat of 316 stainless steel, 20% CW can effectively suppress swelling to below 0.5% during HFIR irradiation at 600°C to 36 dpa.

CONCLUSIONS

Solution-annealed and 20% CW type 316 stainless steels have been irradiated in HFIR to 36 dpa and 2327 appm He at temperatures of 300 to 600°C. Cavity development was examined by transmission electron microscopy. The conclusions are as follows:

1. Swelling in solution-annealed 316 stainless steel depends strongly on temperature, with a maximum at 500°C.
2. Swelling in 20% CW material, increases slightly with increasing irradiation temperature, but is much lower than solution-annealed material, particularly at 500 and 600°C.
3. 20% CW is more effective at extending the incubation time for swelling resistance at temperatures at 500°C and above.
4. The temperature dependence of void swelling in both SA and CW 316 correlates well with differences observed in cavity, precipitate, and dislocation microstructures.
5. Swelling data on heat-to-heat variations of type 316 stainless steel suggest that swelling in 20% CW type 316 stainless steel is less than 0.5% when irradiated in HFIR to 36 dpa at 600°C and below. Both SA and CW 316 are resistant to void swelling at 400°C and below.

ACKNOWLEDGMENT

The authors wish to thank N. H. Rouse, L. T. Gibson, and E. L. Ryan for excellent sample preparation. The authors are very grateful to R. L. Klueh for many helpful discussions. The assistance of Frances Scarborough in typing the manuscript is also gratefully acknowledged.

REFERENCES

1. P. J. Maziasz, F. W. Wiffen, and E. E. Bloom, p. 259 in Proc. Conf. Radiation Effects and Tritium Technology for Fusion Reactors, CONF-750989, Vol. 1, 1976.
2. P. J. Maziasz and D. N. Braski, J. Nucl. Mater. **122&123** (1984) 311.
3. P. J. Maziasz, J. Nucl. Mater. **122&123** (1984) 236.
4. P. J. Maziasz and D. N. Braski, p. 98 in ADIP Semiann. Prog. Rept., DOE/ER-0045/8, Office of Fusion Energy, Washington, DC, 1982.
5. P. R. Okamoto and S. D. Harkness, J. Nucl. Mater. **48** (1973) 204
6. P. H. Pumphrey and J. W. Edington, Acta Met. 22 (1974) 89.
7. P. D. Southwick and R. W. Honeycombe, Metal Sci. 16 (1982) 475.

8. E. H. Lee, P. J. Maziasz, and A. F. Rowcliffe, p. 191 in Conf. Proc. on Phase Stability During Irradiation, eds. J. R. Holland et al., The Metallurgical Society of AIME, Warrendale, PA, 1981.
9. H. R. Brager and F. A. Garner, J. Nucl. Mater. 73 (1978) 9.
10. L. E. Thomas, Trans. ANS 28 (1978) 151.
11. P. J. Maziasz, J. A. Horak, and B. L. Cox, p. 271 in Conf. Proc. on Phase Stability During Irradiation, eds., J. R. Holland et al., The Metallurgical Society of AIME, Warrendale, PA, 1981.
12. M. P. Tanaka, P. J. Maziasz, A. Hishinuma, and S. Hamada, J. Nucl. Mater. 141-143 (1986) 943.
13. E. H. Lee and L. K. Mansur, Phil. Mag. A No. 4 (1985) 493.
14. P. J. Maziasz, J. Nucl. Mater. 1088109 (1982) 359.
15. L. K. Mansur, Phil. Mag. A 44 (1981) 867.

6.3 Vanadium Alloys

GRAIN BOUNDARY CHEMISTRY OF A V-15%Cr-5%Ti ALLOY -- E.R. Bradley and R.H. Jones (Pacific Northwest Laboratory^a)

OBJECTIVE

The objective of this study is to evaluate the segregation of impurities to grain boundaries of candidate vanadium-base alloys and determine the combined effects of impurity segregation and hydrogen on mechanical properties. The results of the investigations will be used to identify potential impurity limits required in vanadium alloys for structural applications in fusion reactors.

SUMMARY

Phosphorus and sulfur grain boundary segregation has been measured in V-15%Cr-5%Ti using a high-resolution (50 nm) Auger electron spectrometer (AES). Surface coverages as high as 0.31 monolayers of phosphorus and 0.13 monolayers of sulfur were observed. A larger titanium concentration on the intergranular surfaces relative to cleavage surfaces could be explained by precipitates of titanium oxide or nitride observed by transmission electron microscopy (TEM). Also, a combined impurity segregation-hydrogen embrittlement was suggested by the percentage of intergranular fracture observed in the hydrogen-charged AES fracture samples.

PROGRESS AND STATUS

Introduction

Vanadium-base alloys are being considered for structural applications in fusion reactors. Candidate alloys are being tested to evaluate the effects of composition, thermomechanical treatment, impurity concentration, irradiation, and chemical environment on the mechanical and corrosion properties. Results of these tests have shown embrittlement under a variety of conditions, but the cause of the embrittlement is uncertain.

Hydrogen embrittlement is a potential degradation mechanism for all structural materials in a fusion environment. Hydrogen will be present in fusion materials from direct injection from the plasma, nuclear (n,p) reactions, tritium gas in the breeding blanket, and cathodic reduction in water-cooled reactors. Hydrogen has been shown to cause subcritical crack growth in a wide variety of materials including vanadium, ferritic steels, austenitic steels, nickel-base alloys and aluminum alloys. The collection of hydrogen at particle-matrix interfaces, grain boundaries, or other defects ahead of the crack tip is thought to be a primary factor in the subcritical crack growth, although hydride precipitation may also be important in vanadium alloys.

Segregation of impurities such as phosphorus and sulfur to grain boundaries has been shown to accelerate hydrogen-induced subcritical crack growth and intergranular stress corrosion cracking of ferritic steels and may also be an important factor in vanadium alloys. Evidence for substantial sulfur segregation to grain boundaries of V-15%Cr-5%Ti has been presented by Diercks and Smith (1). Also clear evidence that segregation of impurities such as sulfur, phosphorus, and antimony accelerate hydrogen-induced subcritical crack growth in iron and nickel has been demonstrated by Jones et al. (2,3). Therefore, an evaluation of impurity segregation and its effect on hydrogen-induced subcritical crack growth of vanadium alloys has been initiated. The results of AES analysis of intergranular and cleavage fracture surfaces produced by in situ fracture of hydrogen-charged V-15%Cr-5%Ti samples are presented in this report.

Experimental Procedures

The V-15%Cr-5%Ti alloy used in this study was from the fusion reactor materials stockpile, Heat No. CAM-835. Three heat treatments were used to evaluate the effects of temperature and annealing time on grain boundary segregation. All samples were first annealed at 1473°K for 1 h in quartz capsules under an inert atmosphere and water quenched. Additional annealing treatments consisted of: 1) 1233°K for 2.5 h, furnace cool; or 2) 1233°K for 2.5 h, furnace cool plus 973°K for 250 h, furnace cool. Heat treatments at 1233 and 973°K were conducted in a vacuum furnace with the pressure being less than 1×10^{-7} torr.

^(a) Operated for the U.S. Department of Energy by Battelle Memorial Institute under Contract DE-AC06-76RL01830.

Chemical analysis of the fracture surfaces were performed using a high-resolution (50 nm) Physical Electronics 660 scanning AES. Samples were fractured in situ at ambient temperature using the impact fracture unit supplied with the instrument. A saw cut across one face of the **3.3-mm-square** cross section provided the necessary stress concentration for fracture at the desired location. The samples were also electrolytically charged with hydrogen to promote intergranular fracture. Hydrogen charging was accomplished at room temperature in a **1 N H₂SO₄** solution at cathodic potential of **-0.65 V (SCE)**. Current density was **-5 mA/cm²** and total charging time was 2.5 h. The samples were loaded in the Physical Electronics 660 scanning AES immediately after hydrogen charging and examined as soon-as possible to minimize hydrogen loss. Samples were fractured when the system pressure was below **7 x 10¹⁰ torr**.

The Auger spectra were taken with an electron accelerating voltage of **10 kV** and an electron current of about **55 nA**. Under these conditions, the resolution was estimated to be about **0.1 μm**. This resolution enabled the intergranular and transgranular fracture regions to be clearly identified. Large precipitates on the intergranular faces were also visible and these regions were avoided in the analysis. At least eight intergranular faces and two transgranular cleavage faces for each sample were analyzed. An Auger spectrum was obtained by scanning the electron beam over a small area on each face, taking care to avoid regions with obvious precipitates. Spectra from focused spots within the area were also taken to check inhomogeneities. With few exceptions, no significant differences were seen between the area and spot analysis.

The Auger peak amplitudes and elemental sensitivities were used to estimate the atom fraction of V, Cr, Ti, S, and P in the near-surface region of the intergranular and transgranular fracture faces. The atom fraction was calculated by the relation:

$$\text{Atom Fraction (x)} = \frac{\frac{I_X}{S_X}}{\frac{I_{Cr}}{S_{Cr}} + \frac{I_V}{S_V} + \frac{I_{Ti}}{S_{Ti}} + \frac{I_S}{S_S} + \frac{I_P}{S_P}} \quad [1]$$

where I_X = observed peak-to-peak Auger signal for element X and S_X = relative Auger sensitivity for element X. The elemental sensitivities were obtained from the Handbook of Auger Electron Spectroscopy (4) and the following Auger peaks were used in the analysis: V (473 eV), Cr (571 eV), Ti (418 eV), P (120 eV), and S (152 eV). The calculation assumes the elements are distributed uniformly throughout the region of analysis, which extends 1 to 2 nm below the surface depending on the escape depth of the Auger electrons. Segregated elements such as sulfur and phosphorus are expected to be concentrated at the grain boundary and thus, the above calculation would underestimate the grain boundary concentration because of the assumed uniform distribution.

The grain boundary surface coverage for sulfur and phosphorus was estimated using a modified form of the approximation developed by Hondros and Seah (5). For grain boundary coverages of one-half of a monolayer or less, the coverage C_X of element X on a V-Cr-Ti substrate was calculated by the relation:

$$C_X = \lambda_X \frac{\frac{I_X}{S_X}}{\frac{I_{Cr}}{S_{Cr}} + \frac{I_V}{S_V} + \frac{I_{Ti}}{S_{Ti}}} \quad [2]$$

where λ_X = electron escape depth in monolayers. The peak intensities, I, and the elemental sensitivities, S, were the same as those used previously in calculating atom fractions. The electron escape depth was calculated by:

$$\lambda_X = 0.18 \sqrt{E_X} \quad [3]$$

where E_X is the energy of the Auger electron in eV and the constant, which has units of monolayers per $eV^{1/2}$, was obtained by averaging electron escape depth data.

Following scanning AES analysis, the fracture surfaces were examined by SEM to determine the relative amount and distribution of intergranular fracture. Samples for TEM examination were then prepared from the ends of the fracture sample by conventional techniques. The microstructures were examined to evaluate differences in precipitation which occurred during annealing.

Results and Discussion

Results from Auger analysis of the fracture surfaces showed significant concentrations of sulfur, phosphorus, and titanium on the intergranular surfaces compared to the transgranular cleavage surfaces as can be seen from the data in Table 1. The Auger spectra from the cleavage surfaces exhibit strong Auger peaks for vanadium with smaller peaks corresponding to chromium and titanium, Figure 1. No evidence of sulfur or

Table 1. Average Values from AES Analysis of Fracture Surfaces

Heat Treatment	Analysis(a) Region	Atom Fraction(b)					Surface(c) Coverage		% IG (d) Fracture
		Chromium	Vanadium	Titanium	Phosphorus	Sulfur	Phosphorus	Sulfur	
Time, h/ °K/cool									
1.0/1473/Quench	IG	0.11±0.02	0.66i0.04	0.09i0.03	0.09±0.01	0.05±0.01	0.22±0.04	0.13±0.04	18
1.0/1473/Quench 2.5/1233/FC	IG	0.08i0.04	0.57i0.05	0.18±0.03	0.13±0.02	0.03±0.01	0.31±0.05	0.08i0.03	73
1.0/1473/Quench 2.5/1233/FC 2501 973/FC	IG	0.09±0.07	0.57±0.09	0.19±0.10	0.12i0.03	0.03±0.02	0.28i0.07	0.09i0.04	76
1.0/1473/Quench	TG	0.16i0.03	0.79±0.04	0.05i0.01	0.00	0.00	0.00	0.00	
1.0/1473/Quench	TG	0.14±0.02	0.81±0.02	0.05±0.01	0.00	0.00	0.00	0.00	
1.0/1473/Quench 2.5/1233/FC 2501 973/FC	TG	0.14±0.01	0.79±0.01	0.07i0.00	0.00	0.00	0.00	0.00	

- (a) IG = intergranular, TG = transgranular
 (b) Calculated from Equation 1
 (c) Calculated from Equation 2
 (d) at 0.3 mm below notch

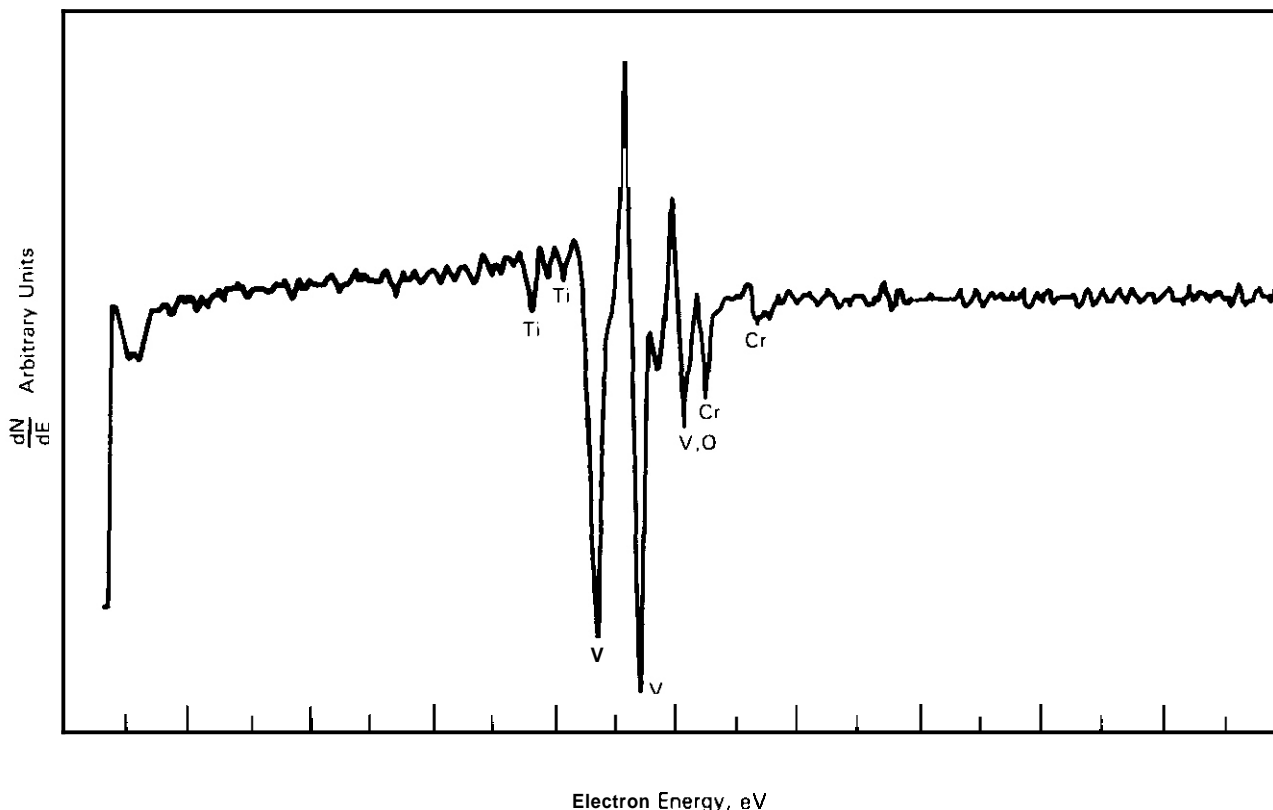


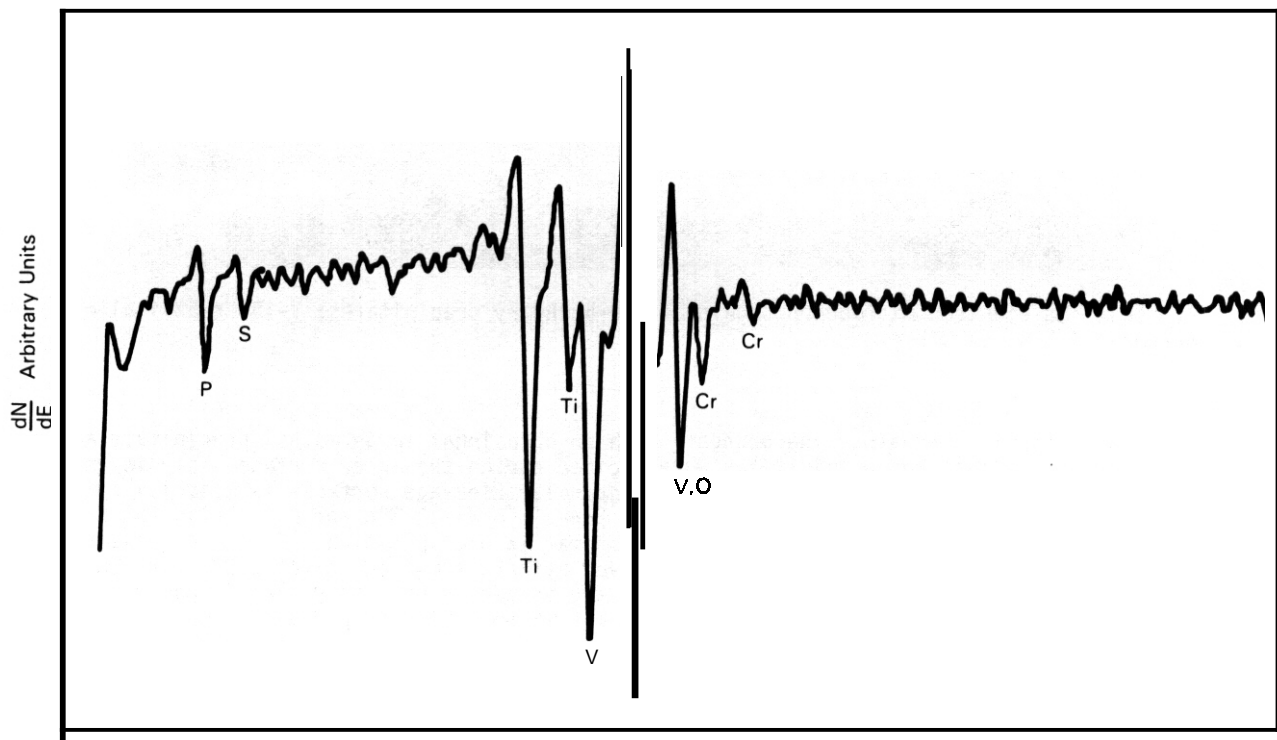
Fig. 1. Typical Auger spectra from a transgranular cleavage face; V-15Cr-5Ti alloy annealed 1 h at 1473°K plus 2.5 h at 1233°K.

phosphorus was observed on the transgranular cleavage surfaces, which indicates the areas analyzed did not contain large sulfur- or phosphorus-containing precipitates. Also, segregation of impurities to precipitate surfaces is commonly observed and provides another possible source for elevated sulfur or phosphorus concentrations on transgranular cleavage faces. The composition of the cleavage surfaces calculated from Equation 1 is in good agreement with the nominal composition of the alloy and did not vary significantly with heat treatment. The observed variations in the calculated atom fractions, 0.02, are well within the uncertainty of measuring the peak amplitudes of the small chromium and titanium peaks.

Diercks and Smith (1) reported sulfur and phosphorus on cleavage surfaces of V-15%Cr-5%Ti while none was observed in the present study. This difference would have resulted from either a difference in sulfur and phosphorus containing inclusions in the various studies or from a difference in spatial resolution or percent intergranular fracture of the Diercks and Smith, and present AES analysis. Since Diercks and Smith reported phosphorus segregation on cleavage surfaces of the same heat of material CAM 835, differences in the inclusion chemistry is not the likely explanation. In the present study, the V-15%Cr-5%Ti was hydrogen-charged to produce a significant percentage of intergranular fracture and the AES was high resolution. Therefore, cleavage and intergranular surfaces were clearly distinguishable in the present study, while small intergranular areas may have been analyzed unknowingly in the Diercks and Smith study (1).

In contrast, Auger spectra from intergranular faces exhibited significant peaks corresponding to sulfur and phosphorus and a major increase in amplitude for the titanium peaks. These features are illustrated in Figure 2 by a typical spectra from the sample whose final annealing temperature was 1233°K. Similar spectra were obtained for all of the intergranular faces examined, although the relative peak amplitudes varied somewhat between intergranular faces within the same sample and also with heat treatment. The peaks for sulfur and phosphorus are well defined and consistent with elemental segregation to grain boundaries. However, the relative intensities of the two major titanium peaks suggest that the titanium is present in the form of a precipitate rather than as elemental titanium. For titanium metal, the amplitude of the 418 eV peak should be 1.3 times greater than the 387 eV peak (5), whereas the present data show the opposite trend in relative peak intensities; the 387 eV peak amplitude was 1.5 to 2.2 times greater than for the 418 eV peak. Similar changes in the relative titanium peak amplitudes have been reported for titanium oxides (6). Nitrides could also produce a similar response with an additional contribution to the amplitude of the 387 eV peak from the 379 eV peak of nitrogen. Precipitates containing sulfur or phosphorus are not considered likely because direct correlations between the concentration of these elements and titanium were not observed in the Auger data.

Microstructures of the annealed alloys also suggest grain boundary precipitation to be responsible for the increased titanium concentration on the intergranular surfaces. Precipitates were observed at the grain boundaries in the sample annealed at 1473°K, as shown by a typical micrograph in Figure 3. Fine precipi-



00

Fig. 2. Typical Auger spectra from an intergranular face; V-15%Cr-5%Ti alloy annealed 1 h at 1473°K plus 2.5 h at 1233°K.



Fig. 3. Transmission electron micrograph showing grain boundary precipitates; V-15%Cr-5%Ti alloy annealed 1 h at 1473°K.

tates, 30 nm, were distributed along the boundary with an occasional large matrix precipitate adjacent to the boundary. Regions with large precipitates were avoided during the Auger surface analysis and the increased titanium concentration relative to the transgranular cleavage surfaces is most likely associated with the fine grain boundary precipitates. Additional annealing at 1233°K for 2.5 h plus 250 h at 973°K produced increased grain boundary precipitation and also matrix precipitation. Figure 4 shows a bimodal size distribution of grain boundary precipitates observed after a final anneal at 973°K for 250 h. The larger precipitates have a maximum dimension of 130 nm and appear to be thin plates lying in the grain boundary; maximum dimension for the small precipitates was 15 nm. Disc shaped matrix precipitates are also seen in Figure 4 under weakly diffracting conditions. These precipitates were distributed throughout the matrix but were more heavily concentrated near the grain boundaries. Matrix precipitates would not significantly influence the intergranular surface Auger analysis because of the shallow surface region being analyzed. Therefore, the increase in the grain boundary titanium concentration with decreasing annealing temperature and increasing annealing time is thought to result from continual precipitation of fine titanium oxides and/or nitrides at the grain boundaries, although these precipitates have not yet been identified.

The data in Table 1 show significant concentrations of phosphorus and sulfur on the intergranular surfaces regardless of the calculational method employed. The atom fraction calculations provide a lower limit to the **estimated** concentrations because of the assumed uniform distribution within the analysis volume. Conversely, the surface coverage calculation assumes **complete** segregation to the surface which represents **an** upper bound to the estimated concentrations. Because thermal segregation would be expected to concentrate the impurities at the grain boundary, the surface coverage calculations are considered the more appropriate for estimating and comparing segregation levels. The grain boundary coverage in monolayers would be twice that reported in Table 1 because of partitioning of segregated elements between the two fracture surfaces.

Only weak temperature dependences for segregation of phosphorus and sulfur to grain boundaries were observed. The average surface coverage for phosphorus increased from 0.22 to 0.31 monolayers when the annealing temperature decreased from 1473 to 1233°K but remained relatively constant, 0.28 monolayers, with further decreases in annealing temperature. The surface coverage for sulfur showed the opposite temperature dependence with the average coverage decreasing from 0.13 monolayers at the highest annealing temperature, 1473°K, to 0.08 and 0.09 monolayers, respectively, for annealing at 1223 and 973°K. The small decrease in sulfur segregation at lower temperatures is thought to be due to a competitive segregation process between

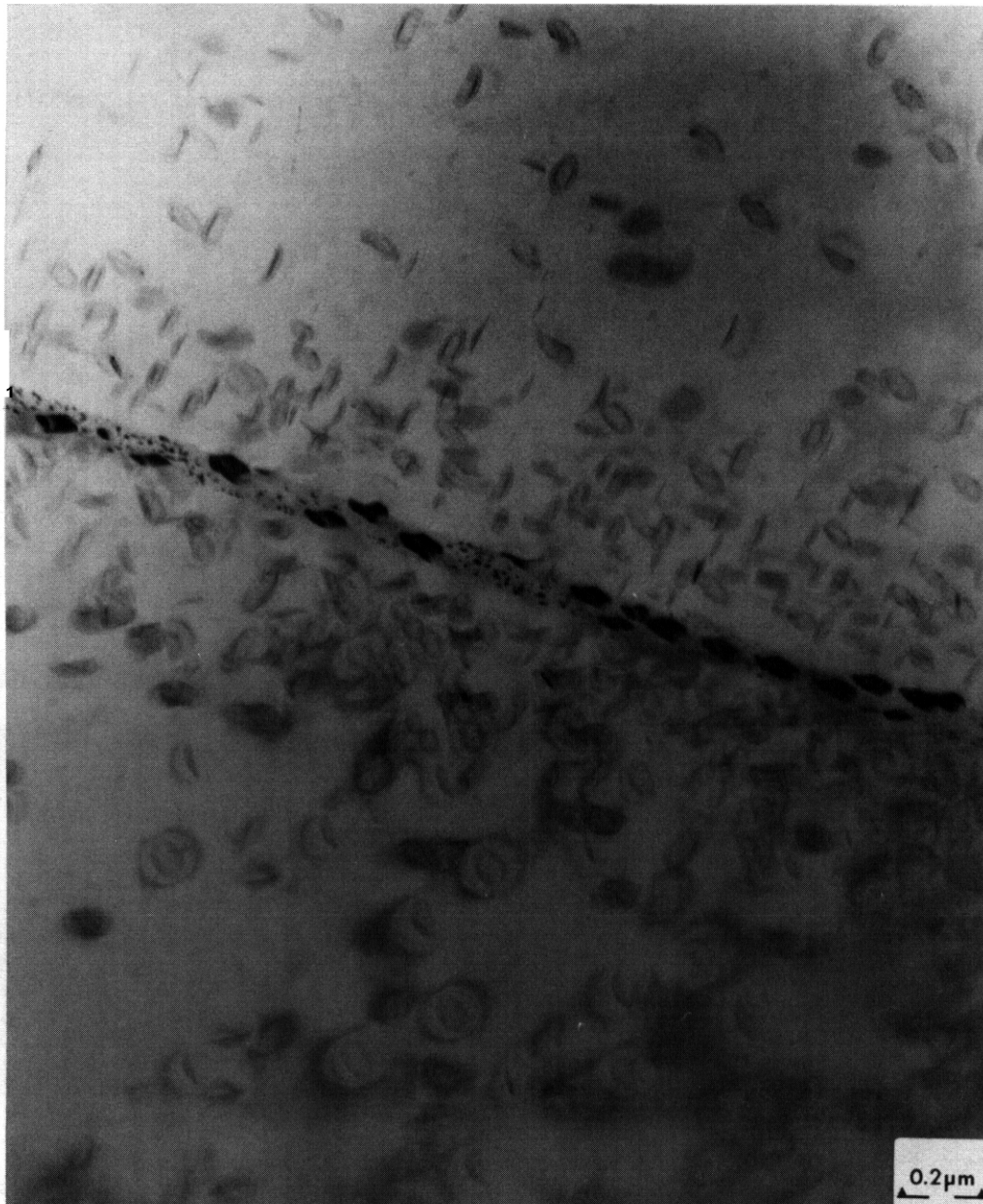


Fig. 4. Transmission electron micrograph showing grain boundary precipitates; V-15Cr-5Ti alloy annealed 1 h at 1473°K plus 25 h at 1233°K plus 250 h at 973°K.

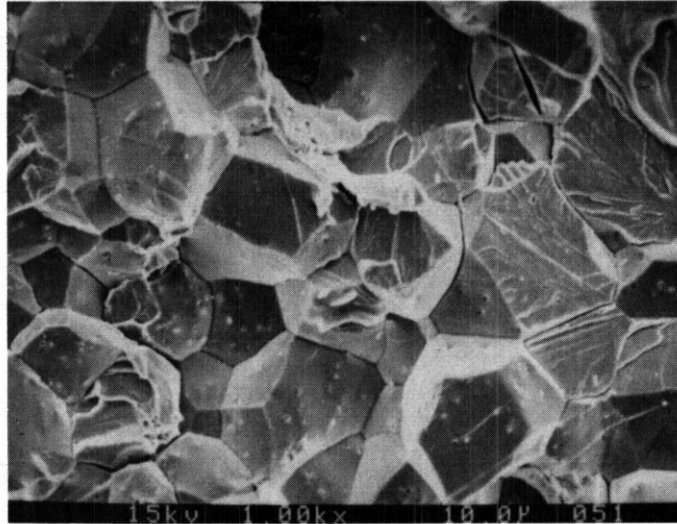


Fig. 5. Scanning electron micrograph of fracture surface at 0.33 mm from notch; V-15Cr-5Ti alloy annealed 1 h at 1473°K plus 25 h at 1233°K plus 250 h at 973°K.

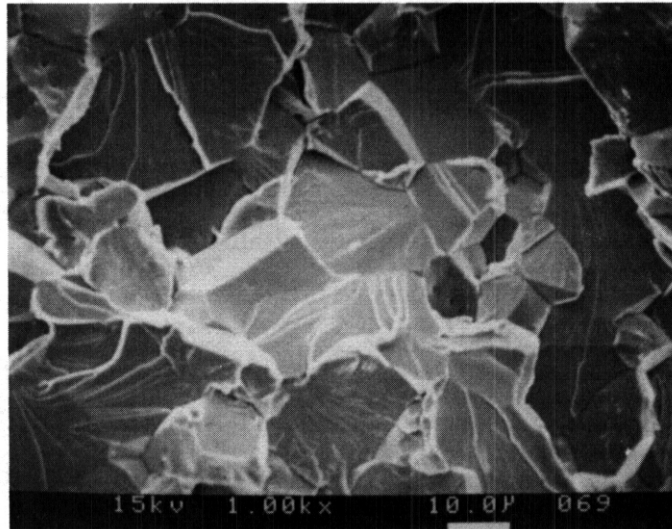


Fig. 6. Scanning electron micrograph of fracture surface at 0.33 mm from notch; V-15Cr-5Ti alloy annealed 1 h at 1473°K.

sulfur and phosphorus. Displacement of sulfur by phosphorus from grain boundaries has been previously observed in ferritic alloys. The weak temperature dependence for segregation suggests that the phosphorus and sulfur concentrations are near to or below the solubility limit at the 1473°K. Thermal segregation models show a strong temperature dependence on segregation when the segregant concentration is below the solubility limit and the temperature dependence is small when the solubility limit is exceeded (5). Chemical analysis of the alloy showed the phosphorus and sulfur concentrations to be 260 and 110 at.ppm respectively. Solubility data for these elements in vanadium or vanadium alloys are not available but the segregation data suggest the solubility limit was exceeded below ~1250°K.

Some qualitative information regarding the combined effects of hydrogen and segregation on the fracture mode was obtained by examining the fracture surfaces after AES examination. Fracture in all samples occurred by a mixture of intergranular and transgranular crack propagation, with isolated regions showing ductile tearing. However, differences in the amount of intergranular fracture were observed. This was especially

evident immediately below the notch where fracture initiated. Intergranular fracture was predominant in this region for samples with final annealing temperatures of **1233°K** and **973°K**, while transgranular cleavage was the primary fracture mode for the sample annealed only at **1473°K**. These differences in fracture mode at 0.3 mm below the notch are shown in Figures 5 and 6 for samples with final annealing temperatures of **973°K** and **1473°K**, respectively. The fracture surface for the sample annealed at 1233°K was similar to that of the **973°K** heat treated sample. Measurements from micrographs taken 0.3 mm below the base of the notch show 18, 73, and 76% intergranular fracture for final annealing temperatures of 1473, 1223, and **973°K**, respectively. The amount of intergranular fracture decreased with increasing distance from the notch for the two samples annealed at the lower temperatures and the fracture characteristics of all three samples were similar at locations far from the notch. The fracture characteristics from the central regions of the samples were very similar to those of the as-received material, which had not been hydrogen charged.

The observation that phosphorus segregation resulted in more intergranular fracture in the hydrogen-charged AES fracture samples than did sulfur segregation is contrary to observations in other materials. Jones et al. (7) and Bruemmer et al. (8) have shown in iron and nickel, respectively, that sulfur is far more effective than phosphorus in promoting intergranular fracture in the presence of hydrogen. Either the present **V-15%Cr-5%Ti** results, which are preliminary, are incorrect or else combined impurity segregation-hydrogen embrittlement effects are reversed in vanadium alloys. Further research is needed to help clarify this observation.

FUTURE DIRECTION

An evaluation of the effect of hydrogen on the subcritical crack growth of vanadium alloys is planned. Stress intensity thresholds and crack growth rates under static and cyclic load conditions will be determined. Also, the temperature dependence of the crack growth rate will be measured for either external cathodic hydrogen or for internal hydrogen. The purpose of these tests is to lead to a model of hydrogen induced subcritical crack growth of vanadium alloys and to help identify critical issues regarding their application.

REFERENCES

1. D. R. Diercks and D. L. Smith, "Environmental Effects on the Properties of Vanadium-Base Alloys." pp. 177-181, in Alloy Development for Irradiation Performance: Semiannual Progress Report for Period Ending March 31, 1985, DOE/ER-0045, Oak Ridge National Laboratory, Oak Ridge, Tennessee, July 1985.
2. R. H. Jones, M. T. Thomas and D. R. Baer, Scripta Metall. 18, p. 47, (1984).
3. R. H. Jones, S. M. Bruemner, M. T. Thomas and O. R. Baer, Metall. Trans. 14A, p. 1749, (1983).
4. L. E. Davis et al., Handbook of Auger Electron Spectroscopy, Physical Electronics Industries, Eden Prairie, Minnesota, 1976.
5. E. D. Hondros and M. P. Seah, International Metals Review, 222, pp. 263-301, (1977).
6. G. D. Davis, M. Nathan and K. A. Anderson, "A Study of Titanium Oxides Using Auger Line Shapes," Applications of Surface Science 15, pp. 321-333, (1983).
7. R. H. Jones, S. M. Bruemner, M. T. Thomas and D. R. Baer, Scripta Metall. 16, p. 615, (1982).
8. S. M. Bruemner, R. H. Jones, M. T. Thomas and D. R. Baer, Metall. Trans. 14A, p. 223, (1983).

THE MICROSTRUCTURE OF ANNEALED V-15Cr-5Ti — T. Schober (visiting scientist from IFF, KFA Jülich, F. R. of Germany) and O. N. Braski (Oak Ridge National Laboratory)

OBJECTIVE

The goal of this study is to analyze the microstructure of V-15Cr-5Ti using analytical TEM and X-ray diffraction techniques. The V-15Cr-5Ti alloy is being considered for use as a first-wall material for a fusion reactor.

SUMMARY

The V-15Cr-5Ti has a bcc structure with a lattice parameter $a_0 = 0.301573 \pm 0.0001071$ nm. Numerous small faceted precipitates were observed that are fcc with a composition $Ti_{0.98}V_{0.02}Ni_{0.6}Co_{0.4}$. A smaller number of fcc, $M_{23}C_6$ -type, particles were also identified with a composition $(Cr_{0.6}Fe_{0.4})_{23}C_6$ and $a_0 \approx 1.0621$ nm. Occasionally, Ti-V phosphides and sulfides (approximate $Ti_{0.5}V_{0.25}S_{0.25}$) were found in the matrix. Some of the particles, especially those containing titanium, may also contain oxygen.

PROGRESS AND STATUS

Introduction

V-15Cr-5Ti is one of several vanadium alloys that are candidates for the first wall of prospective fusion reactors. In this work, we present a study on the reference, annealed state of that alloy prior to any neutron irradiation. Such knowledge is essential for interpreting results on the mechanical properties or radiation effects. A potential weakness of V-15Cr-5Ti lies in its strong tendency to interact with light interstitial elements such as C, N, and O. These interstitials are expected to form precipitate phases with the major elements in the alloy.

Experimental

Disks of 3 mm diameter were punched from 0.25-mm-thick V-15Cr-5Ti foil (CAM 834). The composition of this heat in wt % is 14.5 Cr, 6.2 Ti and in wt ppm — 276 C, 180 O, and 281 Ni. The disks were wrapped in clean tantalum foil, and vacuum annealed for 1 h in a vacuum $<10^{-4}$ Pa. The gettering action of the tantalum foil minimized the pickup of interstitial contaminants. The disks were electropolished for TEM using a H_2SO_4 -methanol electrolyte (1:7) at $-20^\circ C$ and a specimen current of 120 mA. TEM observations were performed using the foils as well as carbon extraction replicas. The experimental techniques included energy-dispersive spectroscopy (EDS), electron energy loss spectrometry (EELS) for the light elements, and convergent beam diffraction (CBED). Relativistic corrections were used in the analyses of the spectra. Electrolytic extractions of bulk V-15Cr-5Ti produced fine powders of the embedded precipitates which were not readily attacked by the electrolyte. These were used to determine X-ray lattice parameters of the precipitate phases. Finally, bulk alloy specimens were used to determine the bcc lattice parameter of the matrix proper.

Results

The following results were reproduced in three independent annealing runs.

The grain size resulting from the anneal at $1200^\circ C$ was $\approx 20 \mu m$ and the dislocation density was estimated to be about 10^5 cm^{-2} . The X-ray lattice parameter of the bcc matrix was determined to be 0.301573 ± 0.0001071 nm. An in-foil check on the matrix composition using EOS gave results within the accuracy of the technique in a V-15Cr-5Ti composition. Conceivably chromium depletion could occur on account of its high vapor pressure.

A high concentration of small faceted precipitates (Fig. 1) was observed in all samples. EOS analysis on such particles extracted from the alloy on carbon replicas yielded a metal atom composition of Ti:V = 98:2. In view of the inherent errors, we estimate that the titanium concentrations in these particles may range from 95 to 100%. Selected area diffraction (SAO) experiments confirmed that the particles had a fcc structure and a lattice parameter close to that for TiN. Table 1 summarizes the results of our SAD work. In X-ray work on electrolytic extractions from bulk specimens, a lattice parameter of 0.4256 ± 0.00051 nm was obtained. (The powder diffraction file lattice parameters for TiN and TiC are: 0.424 and 0.43285, respectively.) In these extractions, a value of 1.3% was obtained for the weight percentage of all precipitates combined. This percentage is several times greater than that calculated

Table 1. Identification of TiN using SAD

Experimentally observed lattice spacing (nm)	Literature value for TiN (powder diffraction file 6-0642) (nm)	fcc indices
0.2442	0.244	111
0.2119	0.212	200
0.149	0.1496	220
0.12695	0.1277	311
0.12164	0.1223	222

using the reported carbon and nitrogen contents in the alloy and assuming that only a TiN(C) phase was extracted. EELS spectra taken from such particles under conditions of negligible carbon contamination showed the presence of comparable amounts of carbon and nitrogen in these particles. Integration of the 55-eV-wide peak windows (using peak counts $>10^4$ and relativistic corrections) yielded the following carbon and nitrogen compositions for the above particles: C (40 ± 4) at. %, N (60 ± 4) at. %. We thus identify the main precipitate fraction as: fcc $Ti_{0.98}V_{0.02}N_{0.6}C_{0.4}$ with $a_0 = 0.4256$ nm. CBE0 results support these conclusions.

Aside from the above titanium carbonitrides, quite large precipitates were occasionally observed; a typical example is shown on a replica in Fig. 2. EOS gave the following metal atom composition: (60 ± 5) at. % Cr and (40 ± 5) at. % Fe. EELS experiments on these particles were inconclusive in view of their extreme thickness. Precision SAD experiments, however, allowed these particles to be unambiguously identified as fcc $M_{23}C_6$. Table 2 summarizes the SAD data. Within experimental limits the lattice parameter of the above particles is identical to the 1.0621 nm value quoted by Andrews et al.¹ Thus, it is concluded that the second most frequent precipitates have the composition $(Cr_{0.6}Fe_{0.4})_{23}C_6$ and have a fcc structure with $a_0 = 1.0621$ nm.

Table 2. Identification of $M_{23}C_6$

hkℓ	Present results (averaged) (nm)	$M_{23}C_6$ d spacings (after ref. 1) (nm)
111	0.6095	0.6132
002	0.533	0.5311
022	0.3735	0.3755
113	0.3183	0.3203
222	Not observed	0.3066
004	Not observed	0.2655
133	0.242	0.2437
024	Not observed	0.2375
224	0.216	0.2168
333/115	Not observed	0.2044
044	Not observed	0.1878
135	0.180	0.1795

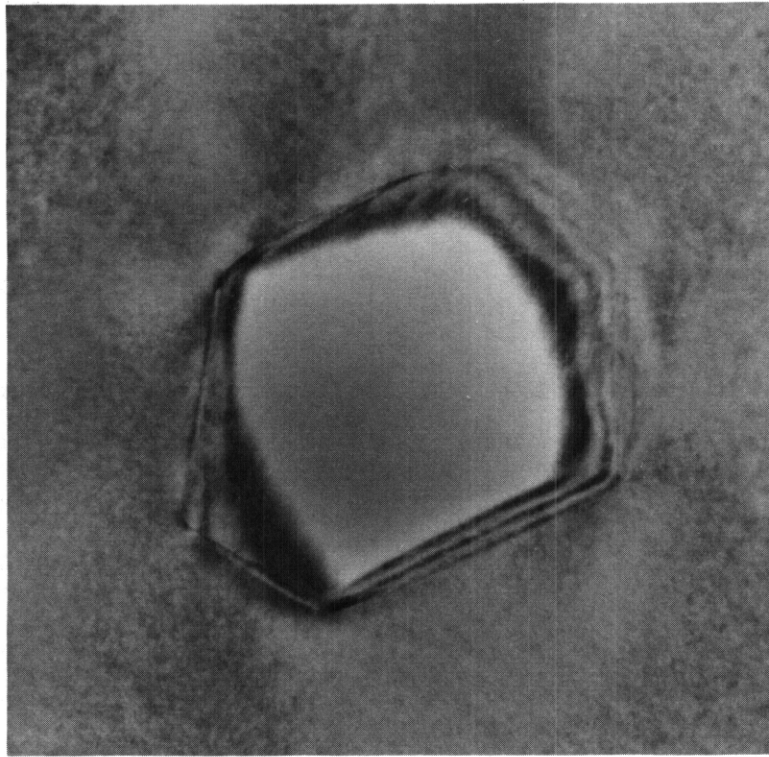
Occasionally, phosphides and also sulfides were observed which had metal compositions in the vicinity of the matrix. Given the very low frequency of these particles, no attempt was made to identify them. Similarly, occasional sulfides were seen with the approximate composition $Ti_{0.5}V_{0.25}S_{0.25}$. As shown in Fig. 3 grain boundaries were decorated with very small precipitates. These were shown to be TiN(C) as identified above.

Discussion

As in many other systems, titanium functions as an internal getter for nitrogen and carbon. Noteworthy is the absence of precipitated oxides. We note that oxygen is very difficult to observe by EELS when vanadium is present given the overlapping K and L edges. Thus, oxygen may have been observed in these precipitates. Presumably, a portion of the oxygen in the alloy is in solid solution.

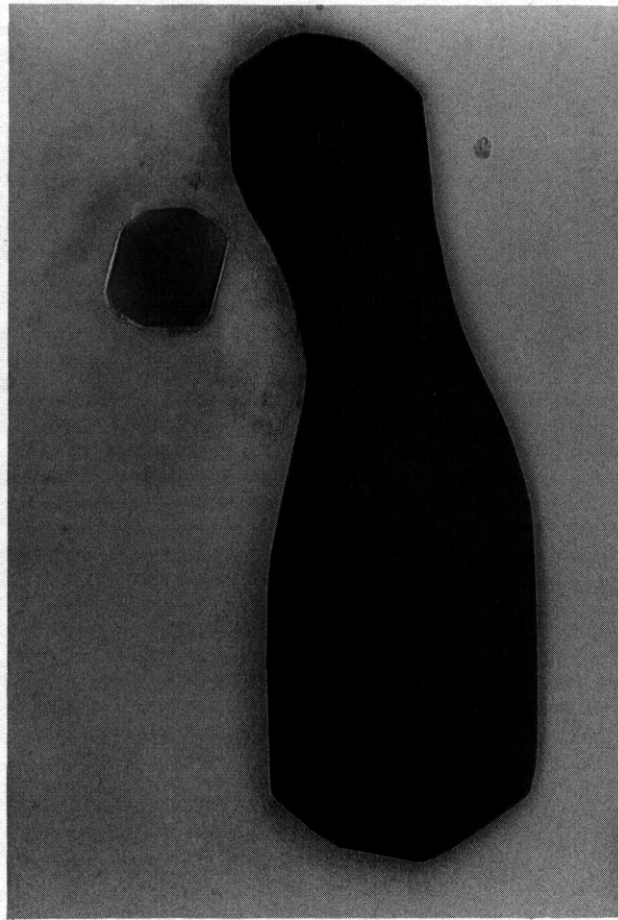
REFERENCE

1. K. W. Andrews, D. J. Dyson, and S. R. Keown. The Interpretation of Electron Diffraction Patterns, Plenum Press, New York, 1967.



0.1 μm

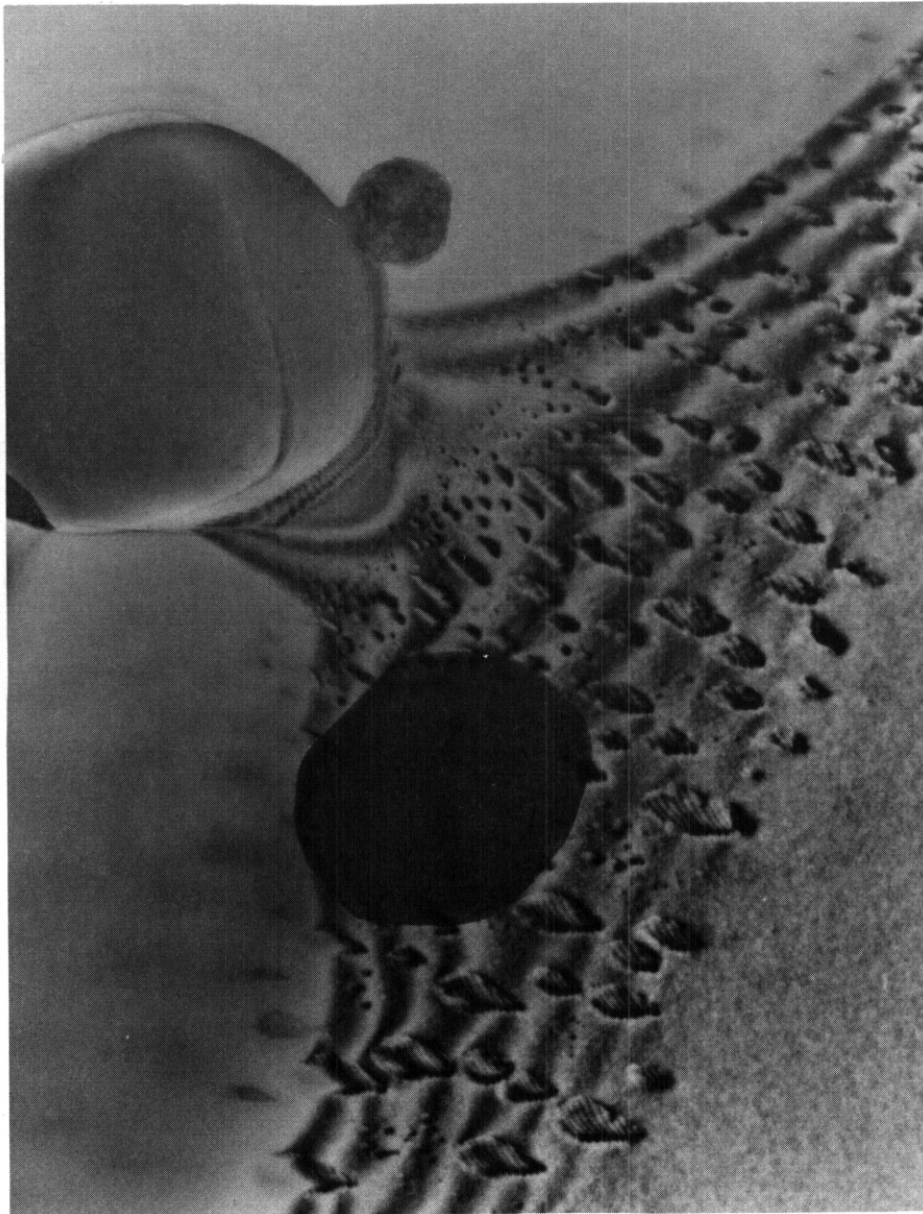
Fig. 1. TiN(C) particle in vacuum-annealed V-15CR-5Ti.



, 0.2 μm ,

Fig. 2. Extraction replica of vacuum-annealed V-15Cr-5Ti particle.
(a) M_{23}C_6 ($\text{M} = \text{Cr}_{0.6}\text{Fe}_{0.4}$) (b) $\text{TiN}(\text{C})$.

YE-13677



, 0.2 μm ,

Fig. 3. TiN(C)-type precipitates on grain boundaries of vacuum-annealed V-15Cr-5Ti. Note the net of interfacial misfit dislocations on each particle.

THE TENSILE PROPERTIES OF SEVERAL VANADIUM ALLOYS AFTER IRRADIATION TO 90 dpa IN FFTF - Q N Braski (Oak Ridge National Laboratory)

OBJECTIVE

The goal of this research is to investigate the effects of displacement damage and helium generation on the tensile properties of vanadium alloys.

SUMMARY

The tensile properties of three vanadium alloys have been measured after they were irradiated in the FFTF at 420°C to 90 dpa. The results showed that irradiation hardening saturated in the V-3Ti-1Si alloy after less than 10 dpa and after about 40 dpa for VANSTAR-7 and V-15Cr-5Ti. Implanted helium produced further slight increases in the yield strength after 90 dpa in VANSTAR-7 and V-3Ti-1Si, and caused further embrittlement of V-15Cr-5Ti. The fact that the total elongations for all three alloys were about the same as those measured earlier for 40 dpa was encouraging.

PROGRESS AND STATUS

Experimental

The alloy sources, heat numbers, chemistry, and final annealing treatments for V-15Cr-5Ti, VANSTAR-7, and V-3Ti-1Si have been published earlier.¹ Disks (3 mm in diameter) and miniature tensile specimens (SS-3 type)² were sealed in ⁷Li-filled TZM capsules and irradiated to 90 dpa in the Fast Flux Facility (FFTF) MOTA 10 experiment. The irradiation temperatures were 420, 520, and 600°C. Some of the specimens were preimplanted with helium to levels ranging from 14 to 480 appm using the tritium trick.³ The amounts of helium were measured by Or. B. M. Oliver, of Rockwell International Corporation, Canoga Park, California. A duplicate set of specimens were encapsulated in a similar fashion and thermally aged at the respective irradiation temperatures for 730 days. These specimens served as control specimens. Both irradiated and aged control specimens were tested in tension, under vacuum (<10⁻⁴ Pa), and at their respective irradiation temperatures. A crosshead speed of 85 μm/s (strain rate equal to 1.1 × 10⁻³ s⁻¹) was employed. The specimens irradiated at 520 and 600°C were not evaluated because they experienced inadvertent temperature excursions in the reactor of several hundred degrees above their intended values.

RESULTS

The results of the postirradiation tensile tests are given in Table 1. The left side of the table lists the results for the thermally aged control specimens while the right side presents those for the irradiated ones. Note that specimens with no ductility (elongation) were unable to produce values for the yield strength and only an ultimate strength (when failure occurred) is given. However, if a specimen exhibited even small amounts of plastic strain, a yield strength was measured.

The effect of irradiation on the yield strength of the vanadium alloys is shown in Fig. 1. Yield strength is plotted against the damage level so that the most recent results can be compared with the results obtained at lower damage levels. In general, neutron irradiation hardens metal alloys by inducing or accelerating precipitation processes and creating dislocations and other lattice defects, all of which tend to restrict the flow of dislocations. As shown in Fig. 1, irradiation effectively doubled the yield strength of all three alloys, but the damage level needed to cause saturation of the hardening depended on the alloy. Apparent saturation occurred in the V-3Ti-1Si alloy after less than 10 dpa, but approximately 40 dpa was required for V-15Cr-5Ti and VANSTAR-7. By referring to Table 1, the reader can verify that, after 90 dpa, implanted helium produced further increases in yield strength for the VANSTAR-7 and V-3Ti-1Si. Irradiation hardening caused the V-15Cr-5Ti specimens, without helium, to fail before a yield point was reached; the addition of helium weakened the grain boundaries, and failure occurred even sooner.

The effect of neutron irradiation on the ductility or total elongation of the vanadium alloys is summarized in Fig. 2. After 90 dpa, VANSTAR-7 retained the highest ductility followed by V-3Ti-1Si, with V-15Cr-5Ti showing nil ductility. Although these results are virtually the same as those measured after 40 dpa at 420°C, the V-3Ti-1Si had demonstrated better ductilities than either VANSTAR-7 or V-15Cr-5Ti at 520 and 600°C at that damage level.¹ Based on those earlier results, it is probably reasonable to speculate that the ductilities of all three alloys would also have been greater at the two higher temperatures after 90 dpa. At these higher temperatures the effects of irradiation hardening are attenuated.

Table 1. Vanadium Alloy Tensile Data – Unirradiated Controls and Specimens Irradiated to 90 dpa

Unirradiated Controls (Aged 420°C for 730 days)					Irradiated (90 dpa = 552 EFPD ^a)						
Specimen No.	³ He Level (appm)	Strength, MPa		Elongation, %		Specimen No.	³ He Level (appm)	Strength, MPa		Elongation, %	
		Yield	Ulti- mate	Uniform	Total			Yield	Ulti- mate	Uniform	Total
V-15Cr-5Ti						V-15Cr-5Ti					
RA155	0	417	541	14.1	24.6	RA109	0		725		
RA51	0	397	556	12.4	20.3	RA179	0		721		
RA70	0	379	550	13.5	22.3	RA80	14		754		
RA142	80	375	539	12.6	21.7	RA52	80		577		
RA173	80	397	556	12.4	20.3	RA168	300		465		
RA167	300		359			RA32	300		465		
RA12	300	373	401		0.5	VANSTAR-7					
VANSTAR-7						QA72	0	839	849	0.5	6.2
QA99	0	302	459	10.6	22.5	QA35	42	844	844	0.3	3.3
QA72	0	311	465	12.3	23.8	QA13	42	867	881	0.6	5.2
QA117	0	271	434	10.3	19.6	QA46	150	865	890	0.3	0.6
QA05	42	312	447	13.8	22.2	QA51	150	894	897	0.5	3.3
QA42	150	330	471	13.3	22.5	V-3Ti-1Si					
V-3Ti-1Si						RB25	0	790	874	32	4.6
RB36	0	313	461	8.3	12.6	R858	135	968	1023	1.5	2.0
RB60	135	456	554	9.2	14.6	RB02	135	823	904	3.1	5.6
RB49	480	464	597	8.6	10.6	RB18	480	963	1022	2.0	2.2

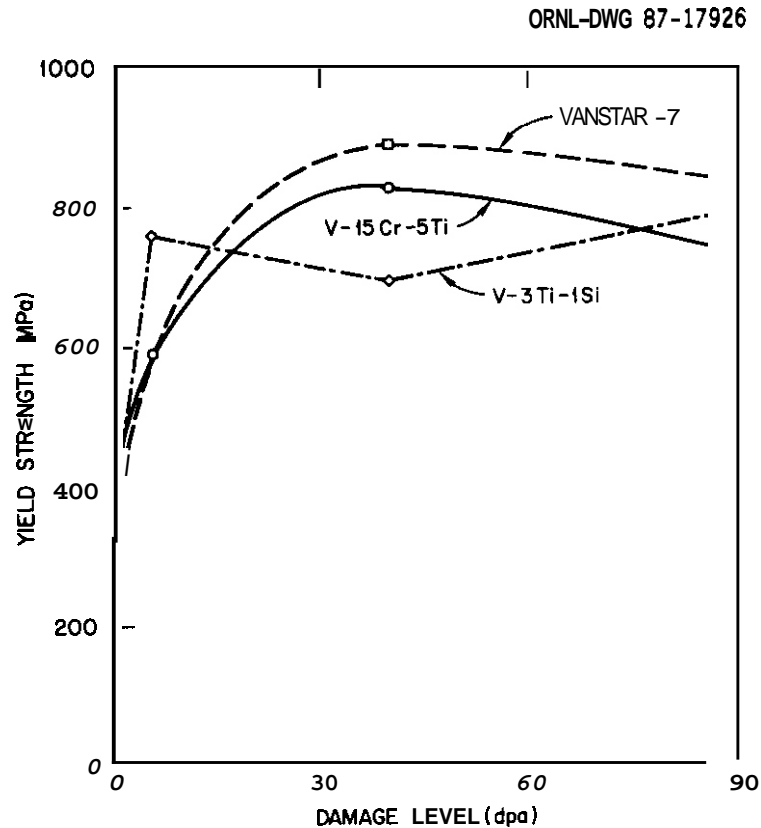
^aEffective full power days.

Fig. 1. Yield strength as a function of damage level.

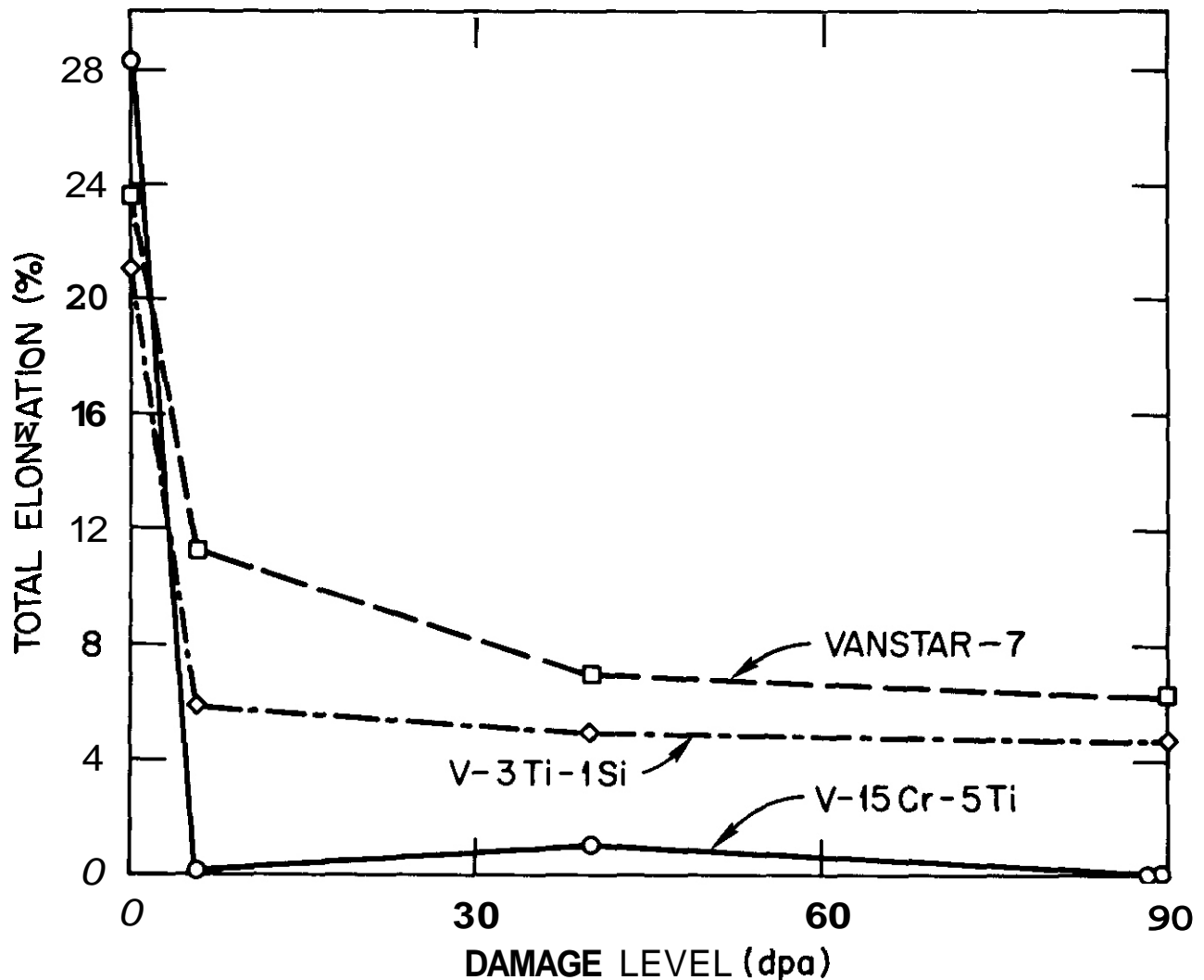


Fig. 2 Total elongation as a function of damage level.

CONCLUSIONS AND FUTURE WORK

Although the V-15Cr-5Ti alloy performed quite poorly, the results for the V-3Ti-1Si and VANSTAR-7 are encouraging: both alloys exhibited some usable remaining ductility after irradiation to the relatively high damage level of 90 dpa, with helium present. The continued development of vanadium alloys is expected to substantially improve their radiation resistance.

A number of the fracture surfaces of the tested tensile specimens will be examined by SEM to determine their fracture mode. The microstructures of all three alloys, with various helium contents, have been examined by TEM but the micrographs need to be evaluated with regard to radiation-produced precipitation, defects, and swelling.

REFERENCES

1. O. N. Braski, pp. 60-64 in ADIP Semiannu. Prog. Rep. Mar. 31, 1986, DOE/ER-0045/16, U.S. DOE, Office of Fusion Energy.
2. R. L. Klueh, p. 54 in ADIP Semiannu. Prog. Rep. Sept. 30, 1984, DOE/ER-0045/13, U.S. DOE, Office of Fusion Energy.
3. O. N. Braski and D. W. Ramey, Effects of Radiation on Materials: Twelfth International Symposium, ASTM STP 870, F. A. Garner and J. S. Perrin, Eds., American Society for Testing and Materials, Philadelphia, 1985, pp. 1211-1224.

INFLUENCE OF NEUTRON IRRADIATION ON THE CHARPY IMPACT PROPERTIES OF V-15Cr-5Ti - N. S. Cannon,
M. L. Hamilton², A. M. Ermi¹, D. S. Gelles², and W. L. Hu¹

- ¹ Westinghouse Hanford Company
² Pacific Northwest Laboratory

OBJECTIVE

The object of this effort is to determine the influence of composition, heat treatment and irradiation conditions on the impact properties of vanadium-based lox activation alloys.

SUMMARY

Vanadium alloys are being evaluated for fusion reactor first wall and blanket applications to achieve both low neutron activation and operating temperatures above those suitable for ferritic steels. Both pre- and postirradiation impact tests have been completed on miniature Charpy specimens of the alloy V-15Cr-5Ti in the annealed condition (1200°C/1 hr/air cool). Irradiation was conducted in lithium-filled TZM capsules at 365, 404, 520 and 600°C to doses ranging from 6 to 30 dpa. The ductile-to-brittle transition temperature was unexpectedly high in the unirradiated condition, on the order of 130°C. Impact tests demonstrate that irradiation induces a large upward shift in DBTT in this alloy. Fracture occurred primarily by transgranular cleavage in irradiated specimens at test temperatures as high as 240°C.

PROGRESS AND STATUS

Introduction

Vanadium alloys are being considered for structural applications in a fusion reactor due to their low neutron activation level and to the relatively high operating temperatures which can be achieved as a result of their high melting points. It is well known, however, that body centered cubic alloys are susceptible to brittle failure at low temperature. The temperature at which such alloys undergo a transition in fracture mode from ductile to brittle (DBTT) is known to shift toward higher temperature under neutron irradiation. The magnitude of this change in DBTT, which is sensitive to irradiation temperature, is an important factor in the selection of alloys for fusion reactor applications.

The V-15Cr-5Ti alloy was selected as a reference material for the evaluation of vanadium alloys based on what is known about its generally attractive mechanical, corrosion, fabrication and irradiation performance properties [1]. Recent tensile data, however, have demonstrated that this alloy is significantly embrittled during neutron irradiation to doses as low as 30 dpa [2,3]. Examination of the fracture surfaces revealed that a transition in fracture mode from transgranular cleavage to ductile rupture appeared at temperatures as high as 500 or 600°C.

In this work, impact tests were performed on miniature Charpy specimens of V-15Cr-5Ti to determine the effect of neutron irradiation on the DBTT. Scanning electron fractography was utilized to determine the fracture mode as a function of test temperature in both irradiated and unirradiated specimens.

Experimental Procedures

One-third size Charpy samples (3.3 x 3.3 x 23.6 mm, with a 0.5 mm deep notch) of V-15Cr-5Ti (heat CAM-835B) were irradiated in the Materials Open Test Assembly (MOTA) in the Fast Flux Test Facility (FFTF). The specimens were given an anneal at 1200°C for 1 hour in 0.2 atm argon prior to irradiation, resulting in an average grain size of ASTM 7 (~30 μm). Vanadium has a high affinity for interstitial elements such as carbon, oxygen and nitrogen which are present at low levels in the FFTF sodium coolant. Specimens were therefore irradiated in lithium-filled RM capsules to prevent significant contamination by these elements. The lithium was enriched to 99.99% ⁷Li to prevent the formation of unacceptable levels of helium and tritium from ⁶Li (present at 7.5% in natural lithium) [4].

Irradiations were conducted at 365, 404, 520 and 601°C to 6, 30, 18 and 14 dpa, respectively, with the temperature actively controlled to ±5°C. After having accumulated one-third of their total irradiation exposure, the specimens irradiated at 520 and 601°C were subjected to a short, unplanned overtemperature transient, rising to 676 and 806°C, respectively, for approximately one hour. This short temperature excursion should not affect the behavior of the alloy since the temperatures in question are low relative to the capability of the alloy.

Following irradiation, the specimens were removed from the subcapsules and cleaned using anhydrous ammonia, ethyl alcohol and water prior to testing. Specimen handling problems during testing indicated that a sticky residue remained on the specimens after the cleaning operations. A number of shallow cut marks were also observed on the specimens at locations far from the notch. These appear to have originated from the tube cutter operations used to open the capsules. Neither of these phenomena are believed to have affected the impact tests.

A detailed description of the test system is given elsewhere [5] so only a brief summary of the system is given here. Impact tests were performed in an instrumented drop tower which incorporated a temperature conditioning chamber and a remotely operated specimen transfer mechanism. Specimens were either heated using direct electrical resistance or cooled by flowing nitrogen vapor. The test temperature was maintained for five to ten minutes prior to initiating the test. The temperature change associated with specimen transfer has been demonstrated to be insignificant because the specimen transfer and test occur very rapidly [5]. Calibrations showed that the temperature was uniform across the middle of the specimen to within $\pm 2^\circ\text{C}$. The impact velocity was calculated from an average of ten determinations of the time interval required for a flag to pass through an infrared sensor of known height during an unobstructed drop. The load cell was calibrated dynamically using strain-rate-insensitive aluminum specimens supplied by the National Bureau of Standards. The load-time data were integrated by computer to calculate the fracture energy. The true energy, E , absorbed in the impact test was determined by compensating for the change in velocity during energy absorption. The final relationship is given as

$$E = E_a (1 - E_a/4E_0). \quad (1)$$

The apparent energy, E_a , absorbed by the specimen during the impact is calculated as the area under the load-time trace by $E_a = \int V_0 P dt$, where V_0 is the initial impact velocity. P is the load and t is time. The total available energy, E_0 , at the moment of impact is determined by $E_0 = mV_0^2/2$, where m is the mass of the crosshead.

The control samples tested were both unirradiated and unaged. The use of unaged controls is supported by a study in which it was shown that the tensile behavior of V-15Cr-5Ti is virtually identical in the aged and the unaged conditions C61. This same study also validated the technique of irradiating vanadium alloys in lithium, since aging of the thermal controls in lithium did not affect tensile properties.

Room temperature hardness tests were conducted on the ends of several specimens in a Rockwell C tester prior to impact testing. Fractographic examinations were conducted following impact tests using standard procedures [5].

Results

Tests were performed at temperatures ranging from -110 to 240°C , the latter being the maximum temperature for which the test system was designed. The data are listed in Table 1. The maximum load and the energy absorbed at maximum load are related to crack initiation and are included in the table for completeness.

Fracture energy is shown as a function of temperature in Figure 1 with a hyperbolic tangent curve fit to the data obtained C71 on unirradiated specimens. While the upper shelf is not well defined for the unirradiated condition, it is evident that the DBTT is on the order of 130°C . Fractography revealed that lower shelf fracture occurred primarily by transgranular cleavage. Figure 2 shows a typical cleavage fracture surface for specimen RH46 tested at 70°C .

The fracture energy of the irradiated samples is also shown in Figure 1. At the upper testing limit of 240°C the alloy is still on the lower shelf. Therefore, the DBTT appears to have shifted a minimum of 170°C , to at least 300°C . Fractography on specimen RH05, irradiated at 365°C to 8 dpa, is shown in Figure 3, where it is demonstrated that transgranular cleavage dominates in the irradiated material on the lower shelf as well as in unirradiated material.

Discussion

The DBTT of 130°C in the unirradiated condition was unexpectedly high, initially leading to the speculation that there was a hitherto undetected error in the composition or preparation of the specimens. No explanation for such unanticipated results has been found, however. Fracture on the lower shelf was dominated by transgranular cleavage in both the irradiated and unirradiated conditions. Since intergranular failure does not occur to a significant extent in either the irradiated or unirradiated conditions, the possibility that fabrication- or radiation-induced grain boundary solute segregation is responsible for the high DBTT is eliminated.

The vanadium specimens tested on the lower shelf produced load-time traces which oscillated repeatedly about zero load following crack initiation; this "ringing" effect is typical of brittle failure. The nonphysical negative value of fracture energy calculated for specimen RH05 indicates that the ringing was not perfectly symmetrical about zero load. The actual failure energy is probably very close to zero.

TABLE 1
IMPACT DATA ON V-15CR-5Ti

Specimen ID	Test Temp. (°C)	Irrad. Temp. (°C)	Dose (dpa)	Total Fracture Energy (J)	Energy to Max. Load (J)	Maximum Load (kN)
<u>CONTROL SPECIMENS</u>						
RH49	-110	---	---	0.036	0.053	0.697
RH48	-84	---	---	0.119	0.052	0.673
RH50	-65	---	---	0.131	0.087	0.888
RH47	-50	---	---	0.160	0.091	0.933
RH51	-20	---	---	0.010	0.094	0.896
RH45	21	---	---	0.197	0.133	1.061
RH46	**70	---	---	0.198	0.170	0.931
RH80	89	---	---	1.222	0.343	1.153
RH56	95	---	---	0.774	0.346	1.182
RH52	**105	---	---	1.240	1.107	1.158
RH53	105	---	---	3.282	3.274	1.222
RH54	105	---	---	0.195	0.221	1.315
RH57	130	---	---	1.399	1.429	1.168
RH67	130	---	---	5.180	3.107	1.067
RH55	150	---	---	7.883	3.319	1.134
RH58	180	---	---	10.701	9.475	1.779
RH74	241	---	---	8.180	2.710	0.979
<u>IRRADIATED SPECIMENS</u>						
RH05**	240	365	6	-0.077	0.016	0.350
RH04	242	365	6	0.028	0.014	0.398
RH14	225	404	30	0.012	0.010	0.210
RH27	242	520	18	0.018	0.009	0.268
RH35	240	601	14	0.015	0.030	0.545

*

The negative value of fracture energy is due to the fact that the brittle vanadium specimens produced load-time traces which oscillated repeatedly about zero load following crack initiation. The negative value is the result of the integration of the areas under both positive and negative loads. The actual failure energy is probably very close to zero.

**

Fracture surface examined by SEM

The comparison shown in Figure 1 between irradiated and unirradiated fracture energies does not completely describe the degree of embrittlement induced in V-15Cr-5Ti during irradiation. In fact, the irradiated vanadium is even more brittle at 240°C than was the unirradiated material at -110°C, as shown by two observations. First, the average lower shelf energy of the irradiated specimens is almost a factor of ten lower than that of the unirradiated lower shelf specimens, despite the expected drop in fracture energy with decreasing temperature. The average fracture energy of the four non-negative values for the irradiated specimens is 0.018 J, whereas the average fracture energy for the eight unirradiated specimens which are clearly on the lower shelf is 0.131 J. In addition, the maximum load to fracture is almost a factor of two lower in the irradiated samples than in the most brittle of the unirradiated samples, as shown in Figure 4. No consistent trend with irradiation temperature was observed in the maximum load.

The conclusions drawn from the impact tests are supported by the hardness data. The Rockwell C hardness of the specimens went from a value of 15 in the unirradiated condition, comparable to unirradiated 9Cr-1Mo, to a value of 35, comparable to HT-9 following low temperature (-365°C) irradiation. One specimen fractured as the indenter was applied. In addition, one of the irradiated samples was already broken when it was removed from the capsule, verifying indirectly the embrittled nature of the alloy.

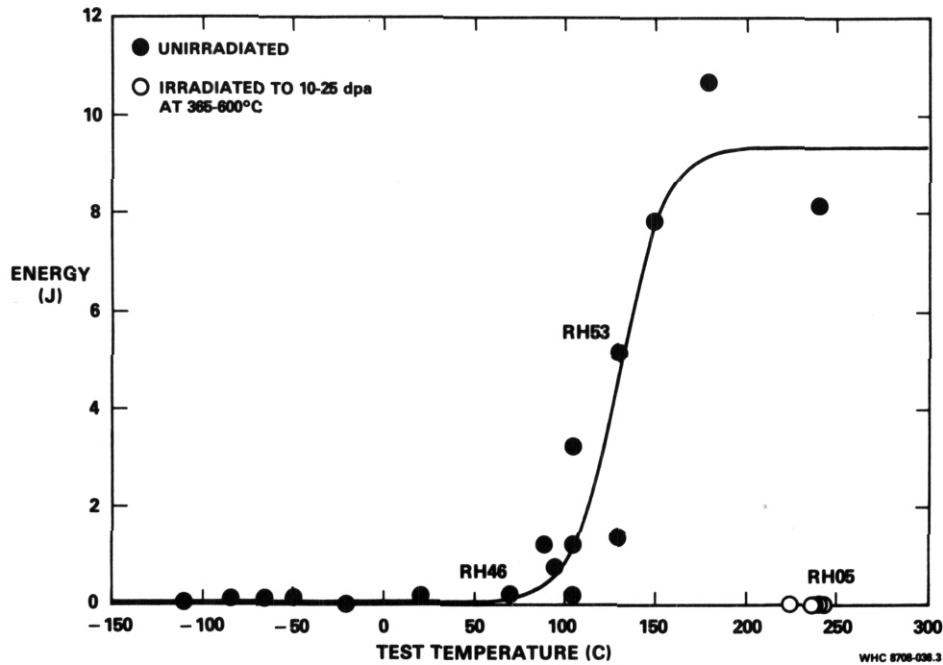


Figure 1. Impact test results on V-5Cr-5Ti. Specimen identification numbers are given next to specimens examined fractographically.

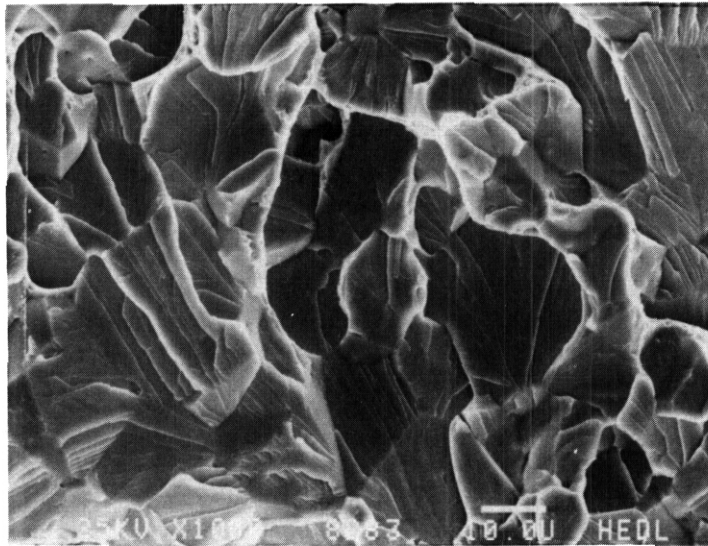


Figure 2. Fracture surface of control specimen RH46 tested at 70°C. The surface exhibits a transgranular cleavage failure typical of lower shelf fracture. (1000x)

It can be inferred from the fractography that the tearing modulus of irradiated V-15Cr-5Ti is extremely low. Specimens tested on the lower shelf exhibited virtually no deformation. There were no shear lips at the edge of the specimen as are typically observed in brittle failure, nor was there any macroscopic change in the shape of the cross section at the notch. Such a shape change was observed, however, in an unirradiated specimen tested near the DBTT (RH53, 105°C), as shown in Figure 5. Note, however, that this change occurred without the appearance of shear lips at the edges of the specimen, indicating that all the deformation occurred during bending, prior to crack initiation. This suggests that once a crack has been initiated in V-15Cr-5Ti, it propagates extremely easily without promoting plastic deformation even under plane stress near specimen surfaces. One would therefore expect that standard fracture toughness tests on this material would yield a valid linear elastic K_{Ic} .

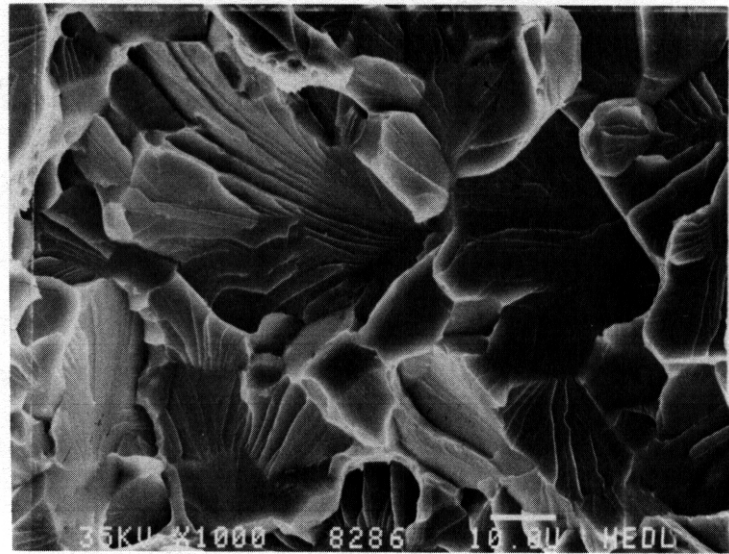


Figure 3. Fracture surface of specimen RH05 irradiated at 365°C to 8 dpa and tested at 225°C. (1000x)

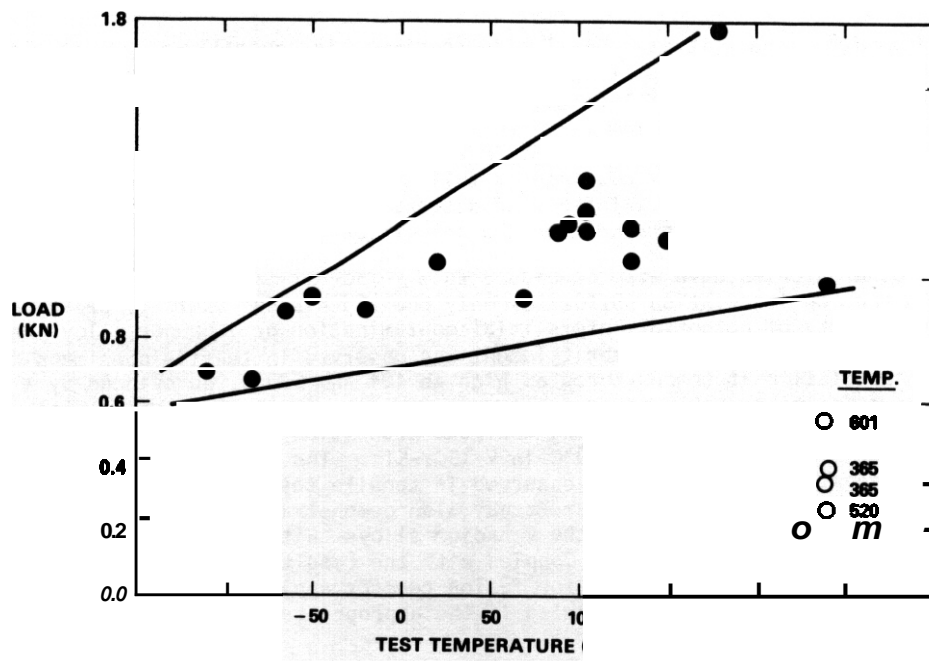


Figure 4. Maximum load observed in impact tests on V-15Cr-5Ti.

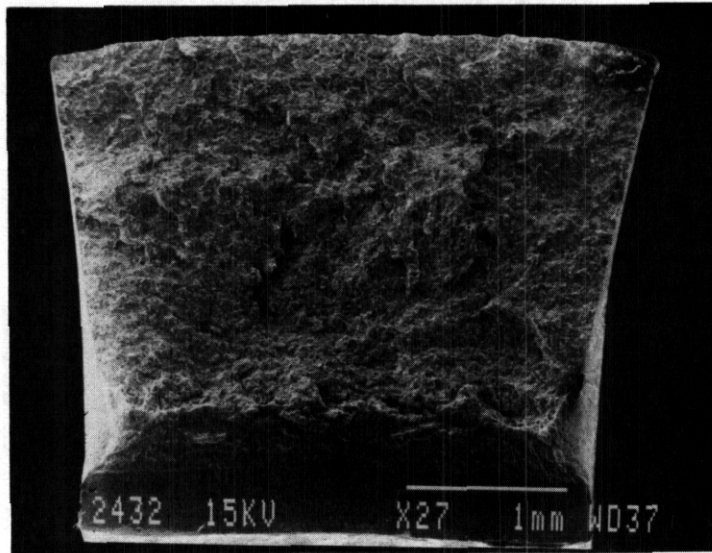


Figure 5. Fracture surface of control specimen RH53 tested at 105°C. Note the deformation in the overall shape of the specimen despite the total absence of shear lips at the specimen surface. (27x)

The DBTT determined from impact tests on full size specimens is generally higher than that determined from miniature specimens, due to the fact that brittle behavior will generally persist to higher temperatures as the degree of constraint increases [8,9]. The low apparent tearing modulus and the absence of plane stress deformation in the vanadium specimens implies that the difference in the DBTTs determined from full size and miniature specimens would be minimized. In the absence of other data, it is impossible to estimate how far above 300°C the DBTT obtained on full size impact specimens might be. There are, however, tensile data which support the existence of a transition temperature in excess of 500°C C61. These data will be summarized in the remainder of the discussion.

Although several other studies have also concluded that V-15Cr-5Ti is extremely susceptible to embrittlement during neutron irradiation [6,10,11], only one [6] has successfully separated the effects of irradiation from the effects of potential interstitial contamination or improper alloy preparation C61. That study demonstrated that significant embrittlement was observed in tensile specimens of another heat of V-15Cr-5Ti after irradiation at temperatures as high as 404 and 520°C, as evinced by a significant loss of ductility and a fracture wholly or partially due to transgranular cleavage. Both ductile and brittle failure were observed at 520°C, implying that the transition from ductile to brittle fracture in uniaxial tension occurs in the vicinity of 500°C in V-15Cr-5Ti. The transition temperatures observed in impact tests are invariably higher than those observed in tensile tests [8], implying that the true DBTT for the alloy is probably above 520°C. The same study also demonstrated that there is a large degree of variability in the embrittlement observed in the vanadium alloys, with several alloys exhibiting good resistance to radiation-induced degradation. Coupled with the results of the current effort it appears that while V-15Cr-5Ti is probably unsuitable for fusion reactor applications in the current heat treatment condition, the alloy system may still hold promise if the appropriate compositional and thermomechanical modifications are made.

CONCLUSIONS

Alloy V-15Cr-5Ti appears to be unsuitable for fusion reactor structural applications in the heat treatment condition used for this study. It exhibits an unacceptably high DBTT in the unirradiated condition and a large shift in DBTT following moderate levels of neutron irradiation as well as a decrease in lower shelf energy. No evidence of solute segregation was observed in either the irradiated or unirradiated conditions. The tearing modulus of irradiated V-15Cr-5Ti appears to be much lower than is typical of ferritic steels proposed for fusion service.

References

1. O. R. Oiercks and E. A. Loomis, J. Nucl. Mater. 141-143 (1986) 1117.
2. M. L. Grossbeck and J. A. Horak. Rad. Eff. 101 (1986) 169.
3. O. N. Braski, J. Nucl. Mater. 141-143 (1986) 1125.
4. A. M. Ermi. ADIP Semfann. Prog. Rep.. DOE/ER-0045/13, Sept. 30, 1984, p. 21.
5. W. L. Hu and D. S. Gelles, in: Proc. Topical Conf. on Ferritic Alloys for Use in Nuclear Energy Technologies. Snowbird. 1983, Eds. J. W. Davis and O. J. Michel (AIME. New York. 1984) p. 631.
6. D. N. Eraski. in: Effects of Radiation on Materials: Thirteenth Int. Symp. in press.
7. N. S. Cannon. M. L. Hamilton and A. M. Ermi. Fusion Reactor Materials Semfann. Prog. Rep.. DOE/ER-0313/2, Mar. 31, 1987. pp. 245-246.
8. S. T. Rolfe and J. M. Barsom, Fracture and Fatigue Control in Structures: Applications of Fracture Mechanics. Prentice-Hall Inc., Englewood Cliffs, NJ (1977).
9. G. E. Lucas, G. R. Odette. J. W. Sheckherd. P. McConnell. and J. Perrin. In The Use of Small-Scale Specimens for Testing Irradiated Material. ASTM STP 888, Eds. W. R. Corwin and G. E. Lucas (1984) p. 305.
10. R. Bajaj and R. E. Gold. Phase I Final Report, Westinghouse Electric Corp. (1983).
11. M. L. Grossbeck and J. A. Horak, in: Effects of Radiation on Materials: Thirteenth Int. Symp. In press.

Acknowledgments

The authors are grateful to D. N. Eraski at the Oak Ridge National Laboratory for providing the Charpy specimens and to E. A. Loomis of the Argonne National Laboratory for removing the specimens from the T2M capsules. cleaning and shipping them back to Hanford for testing.

STRENGTH, DUCTILITY, AND DUCTILE-BRITTLE TRANSITION TEMPERATURE FOR MFR CANDIDATE VANADIUM ALLOYS -
B. A. Loomis, R. H. Lee, and D. L. Smith (Argonne National Laboratory)

OBJECTIVE

The objective of this research is to determine the composition of a vanadium-base alloy with the optimum combination of swelling resistance, corrosion resistance, and mechanical properties in the environment of a magnetic fusion reactor.

SUMMARY

The dependence of the yield strength, tensile strength, elongation, and reduction in area on temperature for the V-15Ti-7.5Cr, V-20Ti, V-15Cr-5Ti, V-12Cr-5Ti, V-10Cr-5Ti, and V-3Ti-1Si alloys was determined from tensile tests at temperatures ranging from 25 to 700°C. The strength of the alloys increased with an increase of the combined Cr and Ti concentration. The total elongation for the alloys ranged between 20% and 38%. The reduction in area ranged from 30% to 90%. The ductile-to-brittle transition temperature (DBTT), which was determined from the temperature dependence of the reduction in area, was less than 25°C for the V-15Ti-7.5Cr, V-20Ti, and V-3Ti-1Si alloys. The DBTT for the V-10Cr-5Ti, V-12Cr-5Ti, and V-15Cr-5Ti alloys was also less than 25°C if these alloys were annealed to reduce the hydrogen concentration prior to the tensile test. If these latter alloys were not annealed prior to the tensile test, the DBTT ranged from 40°C to 90°C and the DBTT increased with an increase of the Cr concentration. Alloys with a Cr/Ti concentration ratio of <0.5 were less susceptible to hydrogen embrittlement.

PROGRESS AND STATUS

Introduction

Experimental results obtained recently on the tensile properties of neutron-irradiated vanadium alloys have shown that some vanadium alloys, e.g., the V-15Cr-5Ti alloy, are embrittled during moderate fluence (40 dpa) neutron irradiation while other alloys are not embrittled, e.g., the V-2Ti and V-3Ti-1Si alloys. These results suggest that optimization of the vanadium alloy composition for acceptable mechanical properties in the environment of a magnetic fusion reactor (MFR) may not yet be complete. To optimize the use of available reactor space for neutron irradiation of mechanical property specimens of candidate vanadium alloys, it was considered expedient to evaluate some of the alloys on the basis of the tensile properties for the materials in the unirradiated condition. This report presents the results of evaluations of the tensile properties of several candidate vanadium alloys. The results indicate that certain V-Cr-Ti alloys may be more susceptible to hydrogen embrittlement as structural materials for a MFR.

Materials and procedure

Vanadium alloys with nominal compositions of V-15Ti-7.5Cr, V-20Ti, V-15Cr-5Ti, V-12Cr-5Ti, V-10Cr-5Ti, and V-3Ti-1Si were obtained in the form of 50% cold-worked sheet with an approximate thickness of 0.9 mm. Chemical analyses of the materials, that were performed by the Analytical Department of the Teledyne Wah Chang Albany Company, are presented in Table 1. Tensile specimens with the dimensions shown in Fig. 1 were machined from the as-received sheet. Specimens were machined with the tensile axis orientation either parallel to the rolling direction or perpendicular to the rolling direction of the as-received sheet. Since the tensile properties were not significantly different for the two orientations, an orientation distinction will not be considered in this report. The tensile specimens of the 50% cold-worked alloy were recrystallized by annealing for 1 h in a vacuum of 2×10^{-5} Pa. The V-15Ti-7.5Cr, V-15Cr-5Ti, V-12Cr-5Ti, and V-10Cr-5Ti alloys were annealed at 1125°C. The annealing temperatures for the V-20Ti and V-3Ti-1Si alloys were 1100°C and 1050°C, respectively. These annealing temperatures resulted in an average, recrystallized grain diameter of 0.020 μm. The surfaces of the tensile specimens were mechanically ground and polished to a surface finish of 0.3 μm. During the surface preparation, the specimens were exposed to water, ethylene glycol, acetone, ethyl alcohol, and methyl alcohol. The as-machined tensile specimens were either annealed and then mechanically polished (AP) or mechanically polished and subsequently annealed (PA) prior to tensile testing. In this study, the majority of the specimens were strained to fracture after using the (AP) procedure. The (AP) procedure was believed to more closely simulate the exposure of vanadium alloys to various environments, e.g., liquid ammonia, ethyl alcohol, and water, after corrosion testing or irradiation in liquid alkali metals. The release of hydrogen from the tensile specimens during annealing was determined by use of a quadrupole, partial-pressure gas analyzer mounted in the ion-pumped vacuum system.

The tensile specimens were tested at a tensile strain rate of 0.0011 s^{-1} for a crosshead speed of $0.008 \text{ mm} \cdot \text{s}^{-1}$. All of the tensile tests were conducted in an environment of flowing ($3 \times 10^{-5} \text{ m}^3 \cdot \text{s}^{-1}$) argon of 99.9999% purity. The temperature of the specimens was determined by use of a chromel-alumel thermocouple that was arc-welded to the edge of the specimen, and the temperature of the specimen during the tensile test was controlled to $\pm 1^\circ\text{C}$. The tensile specimens were heated to the test temperature at a rate of $0.2^\circ\text{C} \cdot \text{s}^{-1}$,

Table 1 Alloy compositions

Nominal Composition	Melt Number	Concentration (wt %)		Concentration (ppm)									
		Cr	Ti	O	N	C	Si	H	S	Nb	Mo	Fe	Al
V-15Ti-7.5Cr	ANL 94	7.2	14.5	1110	250	400	400	<5	20	110	160	910	30
V-20Ti	CAM 832	-	17.7	830	160	380	480	<5	<10	44	200	390	33
V-15Cr-5Ti	CAM 834	12.9	5.9	400	490	280	1230	9	50	50	320	420	150
V-15Cr-5Ti	ANL 204	14.5	5.0	330	96	120	400	<5	20	33	87	180	210
V-15Cr-5Ti	ANL 101	13.5	5.2	1190	360	500	390	<5	<30	100	540	520	40
V-12Cr-5Ti	TWC 040	10.9	5.0	470	80	90	270	<5	20	28	140	350	140
V-10Cr-5Ti	ANL 206	9.2	4.9	230	31	100	340	<5	20	160	<20	170	140
V-3Ti-1Si	ORNL 10837	-	3.1	210	310	310	2500	8	120	55	270	380	160

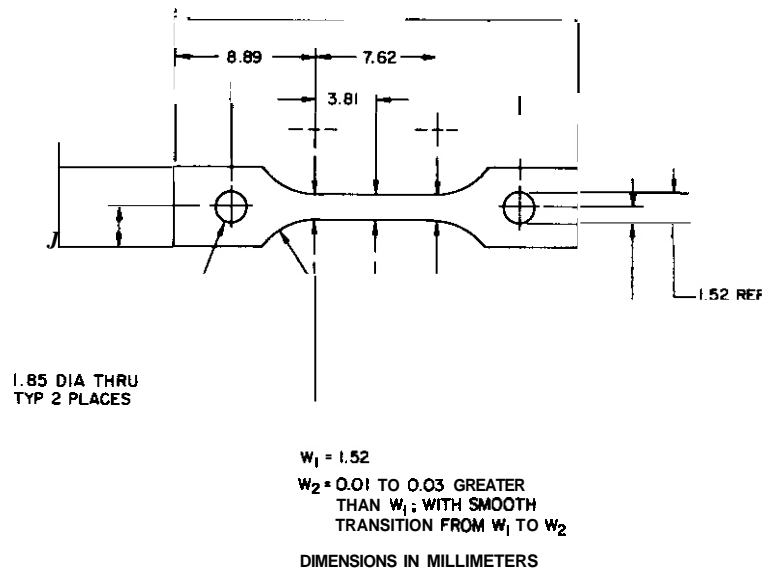


Fig. 1. Dimensions for vanadium alloy tensile specimens.

Experimental results

The yield strength (Y.S.) evaluated at 0.2% offset or the yield point, the ultimate tensile strength (U.T.S.), uniform elongation (E_u), total elongation (E_t), and reduction in cross-sectional area (R.A.) for the alloys at 25°C to 700°C are listed in Table 2. The temperature dependence of the Y.S., U.T.S., and R.A. is shown in Figs. 2, 3, and 4, respectively. For clarity in Figs. 2, 3, and 4, data are only shown for the V-15Ti-7.5Cr (ANL 94), V-15Cr-5Ti (ANL 101), and V-3Ti-1Si (ORNL 10837) alloys. In the case of the V-20Ti alloy, a curve in Figs. 2 and 3 for the temperature dependence of the strength would be displaced -50 MPa below the curve for the V-15Ti-7.5Cr alloy. In the case of the V-10,12Cr-5Ti alloys and the V-15Cr-5Ti (CAM 834 and ANL 204) alloys, curves for their temperature dependence of the strength would be 150 MPa from the curve for the V-15Cr-5Ti (ANL 101) alloy. The dependence of the ratio of the hydrogen partial pressure (P_H) to the total gas pressure (P_T) in the vacuum system on temperature during heating ($0.2^\circ\text{C}\cdot\text{s}^{-1}$) of the as-polished V-12Cr-5Ti tensile specimens is also shown in Figs. 2, 3, and 4. The peak in the P_H/P_T spectrum was lower by approximately one order of magnitude for alloy specimens that were annealed in the as-received condition.

The yield strength and tensile strength for the alloys increased with an increase of the combined Cr and Ti concentration (Figs. 2 and 3), and the strength of the alloys decreased with an increase of the test temperature from 25°C to 225°C for both the (AP) and (PA) procedures. The yield and tensile strength for an alloy with the (PA) procedure was significantly lower than the yield and tensile strength for an alloy with the (AP) procedure for test temperatures of 25°C and 100°C. The yield strength of the alloys was essentially constant at test temperatures between 225°C and 600°C; however, the tensile strength for the alloys

Table 2 Temperature dependence of tensile properties for vanadium alloys

Alloy	T (°C)	Y.S. (MPa)	U.T.S. (MPa)	E _u (%)	E _t (%)	R.A. (%)
V-15Ti-7.5Cr (ANL 94)	25 ^a	636	717	19.9	28.3	75.4
	25	643	718	21.0	29.7	63.7
	100 ^a	556	647	20.5	28.2	77.1
	100	602	688	20.7	27.3	66.4
	225	490	618	19.7	24.7	73.5
	325	493	682	20.7	25.2	69.3
	420	485	730	22.0	29.0	66.5
	520	484	730	24.1	27.6	61.5
	600	469	738	25.7	27.1	51.0
	650	441	661	23.1	27.6	52.8
	700	350	584	18.1	30.3	52.8
V-20Ti (CAM 832)	25	599	655	27.8	30.7	74.7
	25	628	692	21.9	32.1	67.5
	100 ^a	525	640	22.0	30.1	76.0
	225	437	588	19.9	24.5	65.8
	325	436	636	23.9	28.5	68.9
	420	443	658	24.4	29.7	59.5
	520	445	678	28.6	33.1	58.5
	600	417	667	20.2	28.0	55.1
	650	400	554	20.2	29.4	71.7
	700	331	496	13.4	22.7	66.8
V-15Cr-5Ti (CAM 834)	25	533	627	24.9	31.0	85.4
	25	588	688	25.5	27.8	32.2
	100	483	589	24.9	36.6	58.5
	225	407	548	22.6	29.1	81.7
	325	368	522	23.2	29.7	85.4
	420	379	571	21.4	26.6	77.7
	520	359	567	20.2	26.8	72.3
	600	384	610	25.3	31.1	71.3
	650	373	573	17.6	30.2	70.3
	700	355	519	20.6	32.4	72.8
V-15Cr-5Ti (ANL 204)	25	520	624	24.5	31.5	82.5
	25	570	674	25.8	32.3	40.3
	100	495	599	22.8	28.6	61.2
	225	399	525	22.0	27.3	82.2
	325	348	500	18.8	25.6	81.4
	420	346	524	20.4	26.0	79.8
	520	350	538	19.2	24.5	69.9
	600	335	560	20.9	24.8	66.2 ¹
	650	356	575	22.3	27.4	63.0
	700	339	564	21.5	28.1	61.6
V-15Cr-5Ti (ANL 101)	25 ^a	532	632	23.3	32.1	80.2
	25	579	682	24.7	32.9	43.3
	100 ^a	439	545	22.0	31.1	85.9
	100	485	593	24.1	32.0	65.4
	225 ^a	365	470	22.1	28.1	85.0
	225	370	478	17.1	24.9	86.4
	325	317	449	16.7	23.2	80.9
	420	341	518	20.7	26.6	83.2
	520	326	502	16.9	22.6	74.6
	600	342	555	20.7	26.0	71.6
	650	342	559	24.8	30.3	61.2
	700	337	544	20.9	25.7	60.4

Table 2. (Contd.)

Alloy	T (°C)	Y. S. (MPa)	U.T.S. (MPa)	E _u (%)	ε _t (%)	R.A. (%)
V-12Cr-5Ti (TWC 040)	25 ^a	491	573	23.1	31.0	84.6
	25	519	613	26.4	31.1	40.5
	100 ^a	402	500	21.2	27.0	91.4
	100	442	539	21.0	28.9	66.5
	225	358	476	16.5	20.7	84.0
	225 ^a	347	464	20.7	25.7	79.9
	325	304	448	17.3	23.9	82.0
	420	321	501	18.4	24.3	77.6
	520	303	486	11.2	22.0	71.5
	600	299	519	22.3	26.0	71.7
	650	310	529	20.2	24.5	65.6
	700	248	425	21.2	25.5	63.7
V-10Cr-5Ti (ANL 206)	25 ^a	440	541	22.6	33.3	91.3
	25	521	617	26.5	32.3	47.5
	100 ^a	387	482	20.3	31.5	90.8
	100	431	533	23.1	33.5	74.1
	225	334	448	21.5	28.7	82.4
	325	300	452	21.4	30.1	85.8
	420	300	467	19.7	25.2	83.2
	520	297	463	18.4	23.3	83.5
	600	297	502	21.3	24.5	78.1
	700	251	488	21.3	26.6	62.1
V-3Ti-1Si (ORNL 10837)	25 ^a	360	468	29.1	22.3	87.2
	25	446	518	24.9	34.7	72.1
	100	352	464	21.9	27.4	80.2
	225	235	344	22.3	27.6	89.6
	325	227	386	17.2	24.0	90.4
	420	238	437	19.8	25.6	84.3
	520	228	424	19.2	23.0	87.4
	600	230	435	20.9	24.9	77.4
	700	160	330	21.5	26.5	67.5

^aAlloy specimen underwent procedure (PA). Specimens without the superscript underwent the (AP) procedure.

increased on increasing the test temperature from ~225°C to 420°C. The experimental results suggest that the yield and tensile strength for an alloy were not dependent on the (AP) or (PA) procedure at temperatures above 225°C. The yield and tensile strength for the V-15Ti-7.5Cr, V-20Ti, V-10,12Cr-5Ti, and V-3Ti-1Si alloys decreased significantly above 600°C whereas the yield and tensile strength for the V-15Cr-5Ti alloys did not decrease above 600°C. The onset of the temperature-independent yield stress regime at 225°C was also the temperature for the onset of a significant release of hydrogen during annealing of an alloy with the (AP) or (PA) procedure. It should be noted that, with the exception of a V-12Cr-5Ti and V-15Cr-5Ti (ANL 101) specimens at 225°C, tensile specimens with the (AP) procedure were tested at temperatures ranging from 225°C to 700°C. Moreover, the heating rate to the tensile test temperature was approximately the same as the heating rate for the generation of the data on the release of hydrogen. The increase of the tensile strength for the alloys at test temperatures above 225°C can also be correlated with a pronounced increase in the release of hydrogen. A yield point of varying magnitude was evident in the load-elongation curve for each of the alloys on testing at temperatures below 425°C. For test temperatures of 425°C and above, the yield point was replaced by a serrated yielding. The onset of serrated yielding can be correlated with the abrupt decline of ρ_H/ρ_T at 425°C (Fig. 2). Serrations in the load-elongation curves for deformation beyond the initial yielding were evident for the alloys on testing at temperatures ranging from 325°C to 600°C (Fig. 3).

The total elongation for the alloys ranged from 20% to 38%, and the values were not strongly dependent on the test temperature (Table 2). In contrast, the reduction in cross-sectional area (R.A.), which ranged from 32% to 90%, was strongly dependent on the test temperature (Fig. 3) and also on the (AP) and (PA) procedure. In Fig. 3, an R.A. curve for the V-20Ti alloy would closely parallel the curve for the V-15Ti-7.5Cr alloy. Also, R.A. curves for the V-10,12Cr-5Ti alloys and the V-15Cr-5Ti (CAM 834 and ANL 204) alloys would parallel the curve for the V-15Cr-5Ti (ANL 101) alloy. The R.A. for the alloys with the (AP) procedure increased with an increase of test temperature from 25°C to 225°C. For test temperatures above

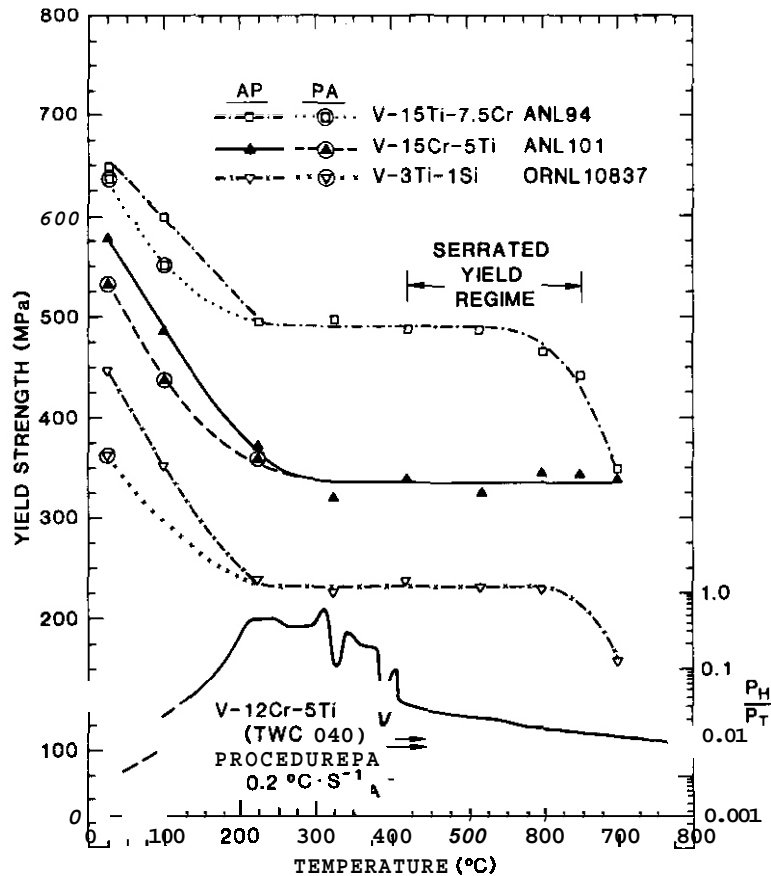


Fig. 2 Temperature dependence of the yield strength and hydrogen evolution for vanadium alloys.

225°C, the RA for alloys with the (AP) procedure either decreased as the test temperature was increased to 600°C, viz., the V-20Ti and V-15Ti-7.5Cr alloys, or remained essentially constant to ~520°C and then decreased with an increase of test temperature, viz., V-10,12,15Cr-5Ti and V-3Ti-1Si alloys. The experimental results suggest that the RA for an alloy was not dependent on the (AP) or (PA) procedure for test temperatures above 225°C. The RA for the alloys at 25°C increased substantially with a change of the procedure from (AP) to (PA). The increase of the R.A. at 25°C was especially pronounced (30-40% to 80-90%) for the V-10,12,15Cr-5Ti alloys. In contrast, the increase of the RA at 25°C for the V-15Ti-7.5Cr, V-20Ti, and V-3Ti-1Si alloys was substantially less. e.g., 64% to 75% for the V-15Ti-7.5Cr alloy.

Optical microscopy of the fracture surfaces of the tensile specimens suggested that the eventual fracture of the tensile specimens was determined by the dominance of either transgranular cleavage or ductile elongation (tearing). The RA was considered to be the most accurate parameter determined from the tensile tests for a quantitative evaluation of the dominance of transgranular cleavage and ductile elongation. We have arbitrarily taken the 55% RA as the transition from a dominance of the transgranular cleavage to a dominance of ductile elongation. On this basis, the ductile-brittle transition temperatures (DBTT) for the alloys that underwent the (AP) or (PA) procedure are listed in Table 3. All of the alloys with the (PA) procedure had a DBTT below 25°C. In the case of the alloys that underwent the (AP) procedure, the DBTT for the V-15Ti-7.5Cr, V-20Ti, and V-3Ti-1Si alloys was less than 25°C, whereas the DBTT for the V-10,12,15Cr-5Ti alloys ranged from 40 to 90°C. The DBTT for the V-10,12,15Cr-5Ti alloys with the (AP) procedure increased with an increase of the Cr concentration in the alloy.

Discussion of results

The addition of either chromium, titanium, hydrogen, oxygen, nitrogen, or carbon to pure vanadium, in general, produces solid solution strengthening, i.e., an increase of the yield and tensile strength and a decrease of ductility.²⁻⁴ The results of the present study show that the strength of the V-15Ti-7.5Cr, V-20Ti, V-15Cr-5Ti, V-12Cr-5Ti, V-10Cr-5Ti, and V-3Ti-1Si alloys at temperatures from 25°C to 700°C increased with an increase of the combined Cr and Ti concentration.

Table 3. Ductile-brittle transition temperatures (DBTT)

Alloy	Melt Number	DBTT (°C)	
		(PA)	(AP)
V-15Ti-7.5Cr	ANL 94	<25	<25
V-20Ti	CAM 032	<25	<25
V-15Cr-5Ti	CAM 034	<25	90
V-15Cr-5Ti	ANL 204	<25	80
V-15Cr-5Ti	ANL 101	<25	60
V-12Cr-5Ti	TWC 040	<25	70
V-10Cr-5Ti	ANL 206	<25	40
V-3Ti-1Si	ORNL 10837	<25	<25

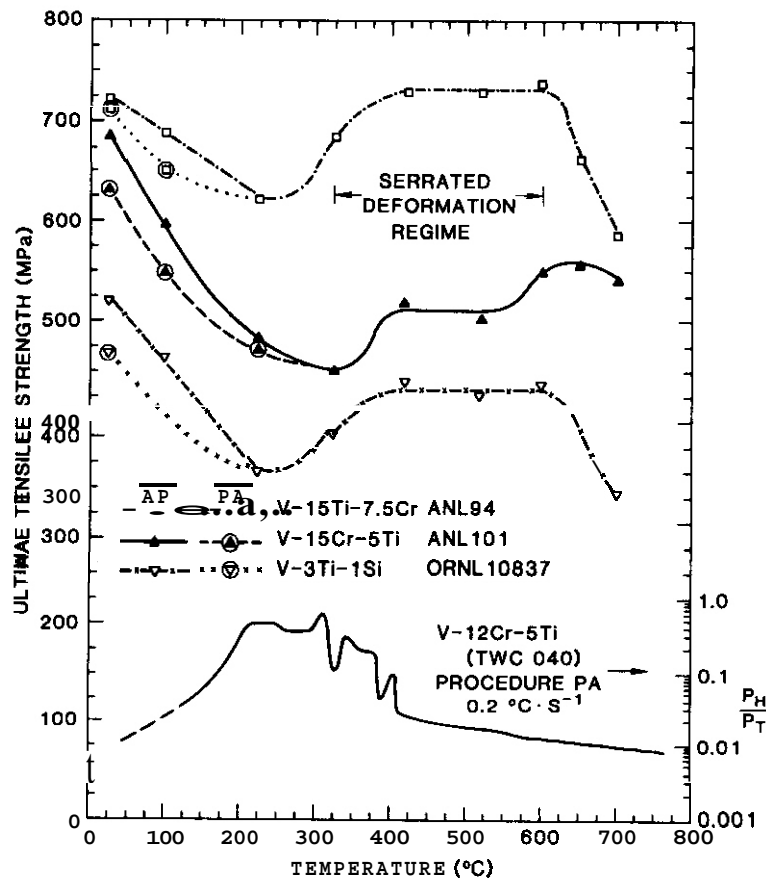


Fig. 3. Temperature dependence of the tensile strength for vanadium alloys.

The presence of hydrogen impurity in the alloys had an especially significant effect on the tensile properties of the alloys. The increase in the yield and tensile strength, the decrease in the reduction of the cross-sectional area, and the increase of the DBTT for the alloys on changing the procedure for the preparation of the tensile specimens from (PA) to (AP) can be attributed to an increase of the hydrogen concentration in the tensile specimens during the (AP) procedure. It was not established if the hydrogen was introduced into the tensile specimens by mechanical abrasion during grinding and polishing and/or by contact with water and organic media. The embrittlement of vanadium upon contact with water and organic media has been attributed to an increase in hydrogen concentration.^{5,6}

Crack initiation and propagation in a vanadium alloy containing hydrogen impurity can be related to the hydrogen solubility and diffusivity in the alloy.⁷ A decrease in the hydrogen solubility and/or an increase in the hydrogen diffusivity in vanadium by the addition of alloying elements can be expected to increase the tendency for crack propagation and embrittlement.⁶ Titanium increases the solubility of hydrogen in

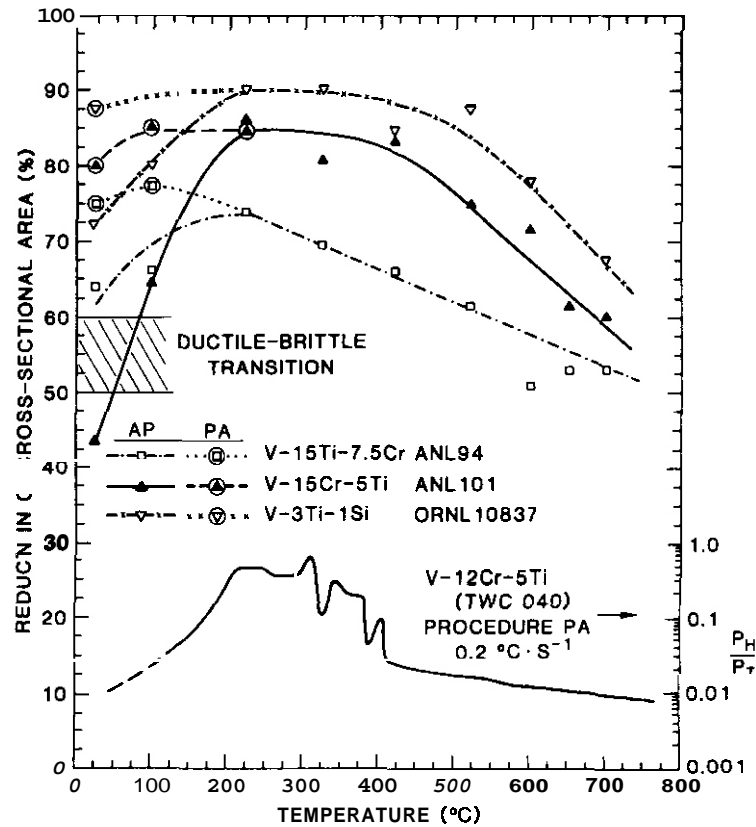


Fig. 4. Temperature dependence of the reduction in cross-sectional area for vanadium alloys.

vanadium and chromium decreases the solubility.^{7,8} The diffusivity of hydrogen in vanadium decreases with the addition of titanium.⁷ Therefore, the greater susceptibility of the V-10,12,15Cr-5Ti alloys to hydrogen embrittlement in comparison with the V-15Ti-7.5Cr, V-20Ti, V-3Ti-1Si alloys with the (AP) procedure can be correlated with the higher Cr/Ti concentration ratio for the former group in comparison with the latter group, i.e., a Cr/Ti ratio of 2-3 for the former group and 0-0.5 for the latter group.

The presence of oxygen (nitrogen and carbon) impurity in the alloys also had a significant effect on the strength of the alloys. The onset of serrations in the load-elongation curves was clearly correlated with either the decrease of the yield strength to a plateau value (Fig. 2) or the significant increase of the tensile strength (Fig. 3). Serrated yielding and deformation is generally attributed to the diffusion of impurity atoms, e.g., oxygen, nitrogen, and carbon, to moving dislocations which, in turn, repeatedly break away from their impurity atmospheres. Alternatively, the dislocations formed during the deformation collect solute atmospheres and remain locked in position so that additional dislocation sources are activated with the resultant formation of repeated minute yield points. The onset of serrations in the load-elongation curves obtained in this study may also be correlated with the removal of hydrogen from the tensile specimens. This correlation suggests that oxygen (nitrogen and carbon) impurity atoms may be strong traps for hydrogen atoms.¹⁰ Therefore, the concentration of oxygen (nitrogen and carbon) impurity in an alloy may have been an additional factor that determined the susceptibility of an alloy to hydrogen embrittlement.

CONCLUSIONS

The yield and tensile strength for the V-15Ti-7.5Cr, V-20Ti, V-15Cr-5Ti, V-12Cr-5Ti, V-10Cr-5Ti, and V-3Ti-1Si alloys increases with an increase of the combined Cr and Ti concentration. The total elongation, that is determined from tensile tests on these alloys at 25°C to 700°C, ranges from 20% to 38%. The V-Cr-Ti alloys with a Cr/Ti concentration ratio of 2-3, i.e., the V-10,12,15Cr-5Ti alloys, are more susceptible to hydrogen embrittlement than V-Cr-Ti alloys with a Cr/Ti concentration ratio of 0-0.5, i.e., the V-15Ti-7.5Cr, V-20Ti, and V-3Ti-1Si alloys. The DBTT, which is determined from the temperature dependence of the reduction in area, is less than 25°C for the V-15Ti-7.5Cr, V-20Ti, and V-3Ti-1Si alloys. The DBTT for the V-10Cr-5Ti, V-12Cr-5Ti, and V-15Cr-5Ti alloy is also less than 25°C if these alloys are annealed to reduce the hydrogen concentration prior to the tensile test. If these latter alloys are not annealed prior to the

tensile test, the DBTT ranges from 40°C to 90°C and the DBTT increases with an increase of the Cr concentration. The exposure of vanadium-base alloys to hydrogenous media during specimen preparation and/or after exposure to other environments (e.g., liquid alkali metals) can have a significant effect on the mechanical properties because of hydrogen pickup by the materials. The mechanical testing environment (e.g., vacuum or inert gas) as well as the test conditions (i.e., temperature, heating rate), which influence hydrogen egress from the material, are also important parameters in the subsequent mechanical behavior.

REFERENCES

1. D. N. Braski, "The Effect of Neutron Irradiation on Vanadium Alloys," J. Nucl. Mater. 141-143, 1125 (1986).
2. N. Iwao, T. Kainuma, T. Suzuki, and R. Watanabe, "Mechanical Properties of High Strength Vanadium-Base Ternary Alloys," J. Less-Common Met. 83, 205 (1982).
3. T. Kainuma, N. Iwao, T. Suzuki, and R. Watanabe, "Effects of Oxygen, Nitrogen, and Carbon Additions on the Mechanical Properties of Vanadium and V/Mo Alloys," J. Nucl. Mater. 80, 339 (1979).
4. B. A. Loomis and O. N. Carlson, "Investigation of the Brittle-Ductile Transition in Vanadium," in: Reactive Metals, Vol. 2, ed. W. R. Clough, Interscience Pub., 1958, p. 221.
5. D. G. Westlake, "Problems in the Preparation of Vanadium-Hydrogen Alloys for Transmission Electron Microscopy," Trans. Met. Soc. AIME 239, 1106 (1967).
6. S. Takano and T. Suzuki, "An Electron-Optical Study of E-Hydride and Hydrogen Embrittlement of Vanadium," Acta. Met. 22, 265 (1974).
7. S. Tanaka and H. Kimura, "Solubility and Diffusivity of Hydrogen in Vanadium and Its Alloys Around Room Temperature," Trans. Japan Inst. Met. 20, 647 (1979).
8. D. T. Peterson and S. O. Nelson, "Isopiestic Solubility of Hydrogen in Vanadium Alloys at Low Temperatures," Met. Trans. 16A, 367 (1985).
9. R. W. K. Honeycombe, The Plastic Deformation of Metals (St. Martins Press, New York, 1968) p. 144.
10. A. I. Shirley, C. K. Hall and N. J. Prince, "Trapping of Hydrogen by Oxygen and Nitrogen Impurities in Niobium, Vanadium, and Tantalum," Acta. Met. 31, 985 (1983).

64 Copper Alloys

NEUTRON INDUCED SWELLING OF COPPER ALLOYS AT 98 DPA AM) 450°C - H. R. Brager (Westinghouse Hanford Company) and F. A. Garner (Pacific Northwest Laboratory)

OBJECTIVE

The object of this effort is to provide data on the swelling of high conductivity alloys in response to fast neutron irradiation and to use these data to help in predicting material behavior in anticipated fusion environments.

SUMMARY

An irradiation series on copper alloys in FFTF-MOTA at about 450°C has been completed. Four exposure levels were reached with the maximum at 98 dpa. Immersion density measurements of various copper alloys show swelling values ranging from 1 to 64% at 98 dpa. Copper dispersion-hardened with 0.25% Al₂O₃ (designated A125) and the precipitation-strengthened alloy MZC appear to be the most swelling resistant high conductivity alloys.

PROGRESS AND STATUS

Introduction

In earlier reports, the swelling of pure copper, and six commercial copper alloys irradiated in FFTF-MOTA at 450°C was described for fast neutron damage levels of 16, 47, and 63 dpa⁽¹⁻²⁾. Data were also published for Cu-5wt% Al and Cu-5wt% Ni at these same fluence levels⁽³⁾. Additional data are now available for these same materials irradiated to $1.6 \times 10^{23} \text{ n cm}^{-2}$ ($E > 0.1 \text{ MeV}$), the highest fluence planned for this series, which for pure copper corresponds to 98 dpa in the FFTF spectrum. The irradiation conditions were described in the earlier reports. The alloy compositions and thermal-mechanical conditions are presented in Table 1 along with a summary of the swelling data.

Results

Fig. 1 shows the swelling of those alloys which exhibit the largest amounts of swelling. Pure zone-refined copper reaches 56% after 98 dpa. Consistent with its swelling behavior at lower fluences^(1,2), copper with 0.1 wt% silver exhibits a greater amount of swelling than pure copper. The swelling rate of Cu-0.1Ag is compared in Fig. 1 with the 1%/dpa line. This line represents the peak swelling rate reported for reactor irradiated Fe-Cr-Ni fcc alloys⁽⁴⁾ and pure nickel⁽⁵⁾. For fluences greater than the initial 16 dpa data, the swelling rate of the Cu-0.1Ag decreased to the 0.5%/dpa rate observed in pure copper. Specimens of specially prepared (not commercially obtained) Cu-5Al exhibited swelling behavior very similar to that of the Cu-0.1Ag material.

The swelling of specially prepared Cu-5Ni closely followed that of zone-refined pure copper. The Cu-1.8Ni-0.3Be alloys in the cold-worked and aged and in the annealed and aged conditions swell less than pure copper and may be approaching a lower swelling rate. A lower swelling rate is also exhibited in CuAgP at fluences greater than 50 dpa (See Fig. 21).

The lowest swelling copper alloys that were investigated included MZC, Cu-Be and Cu-A125. The swelling of these alloys with different pre-irradiation conditions is shown in Figs. 3 and 4. At 98 dpa, all of the specimens exhibit measurable swelling (~1%), indicating that the incubation fluence at this irradiation temperature has been exceeded. Note the apparent reversal in swelling of MZC between 63 and 98 dpa, which will be discussed in the next section.

Discussion

There are two interesting aspects of these irradiation experiments. The first is concerned with the performance of the commercial alloys and the possibility that such alloys may serve as structural components for plasma limiters and possibly other high heat flux applications in fusion reactors. The most promising material in this irradiation series is the oxide dispersion-hardened alloy A125. This material consists of commercial grade pure copper with a high density of small and essentially inert particles of Al₂O₃ [1,6]. It was previously shown that the changes in electrical resistivity and mechanical properties of copper alloys could be explained in terms of the transmutation products (largely Ni and Zn), void and dislocation formation and precipitation sequences [2,7]. The earlier onset of swelling in the cold-worked and aged condition of A125 (compared to the cold-worked condition) may represent a reduction in the preirradiation dislocation density upon aging, but this possibility has not yet been explored using microscopy.

oys ted FTF 450

Alloy	Alloy Composition (wt%)	Condition	Swelling (%)		
			dpa: 16	47	63
			> 0.1MeV: 2.5x10 ²² 7.7x10 ²² 1.0x10 ²³ 1.6x10 ²³		
Cu (MARZ)	Cu(99.999)	annealed	6.5	22.2,23.3	30.1,31.3,33.2
Cu-5Ni	Cu-5Ni	annealed	2.15	—	27.7,31.8
Cu-5Al	Cu-5Al	annealed	—	—	46.8,45.8,39.4
CuAg	Cu-0.1 Ag	20% CW	16.6	35.4,38.2	47.4
CuAgP	Cu-0.3Ag-0.06P-0.08Mg	20% CW	7.9	16.0,16.2	17.1
CuNiBe (1/2 HT) a)	Cu-1.8Ni-0.3Be	20% CW and aged (3 h at 480°C)	1.70	13.9,14.6	22.3,24.6
CuNiBe (AT) a)	Cu-1.8Ni-0.3Be	20% CW and aged (3 h at 480°C)	0.29	3.05	5.73,6.59
CuBe (1/2 HT)	Cu-2.0Be	20% CW and aged (2 h at 320°C)	- 0.18	0.18,1.11,1.71	1.09,1.61
CuBe(AT)	Cu-2.0Be	annealed and aged (2 h at 320°C)	- 0.66	-0.45,-0.24,+0.12	-0.43,-0.25
MZC	Cu-0.9Cr-0.1Zr-0.05Mg	90% CW, aged (0.5 h at 470°C)	1.03	0.79	5.15,7.90
Cu-Al25 (CW)	Cu-0.25 Al(asAl203)	20% CW	0.13	0.23,0.36,0.86	0.28
Cu-Al25 (CWA)	Cu-0.25 Al(asAl203)	20% CW + aged (1 h at 550°C)	—	-0.18,0.05,0.52	0.04,1.45,1.85

a)

pect

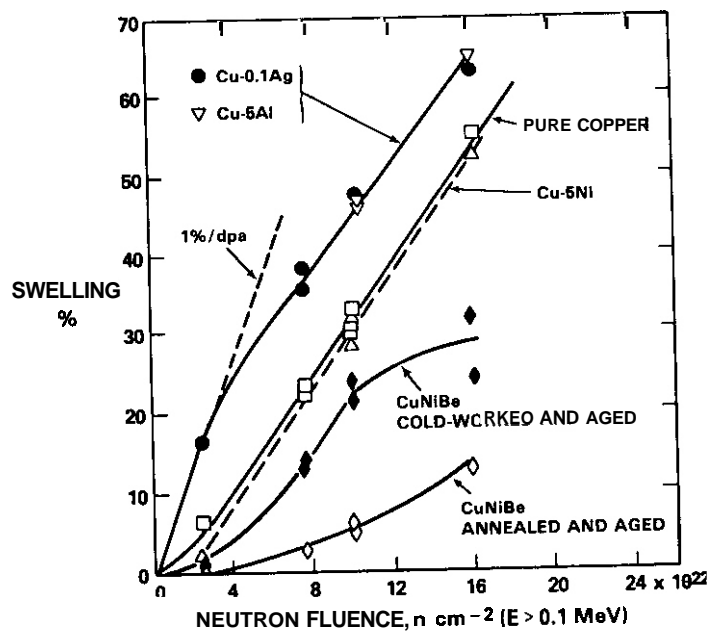


Fig. 1. Swelling Observed in a Variety of Copper Alloys at 450°C in FFTF-MOTA.

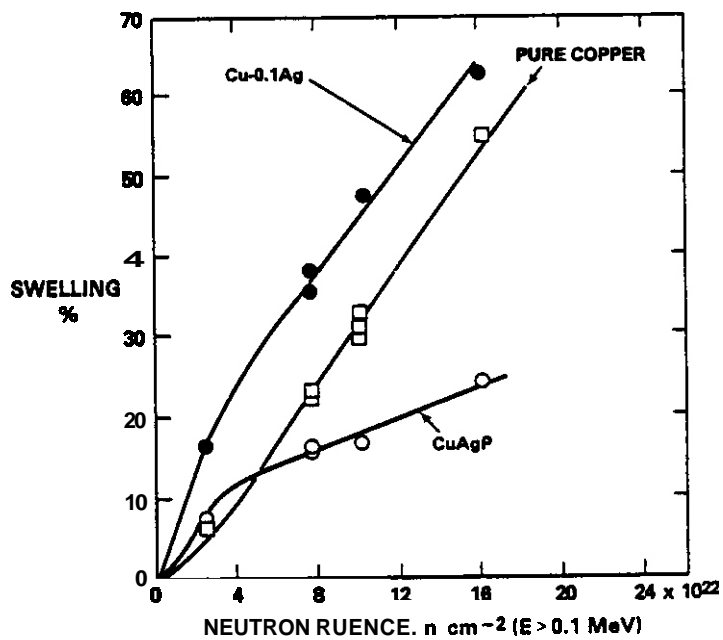


Fig. 2. Influence of Silver and Phosphorus on the Swelling of Copper at 450°C .

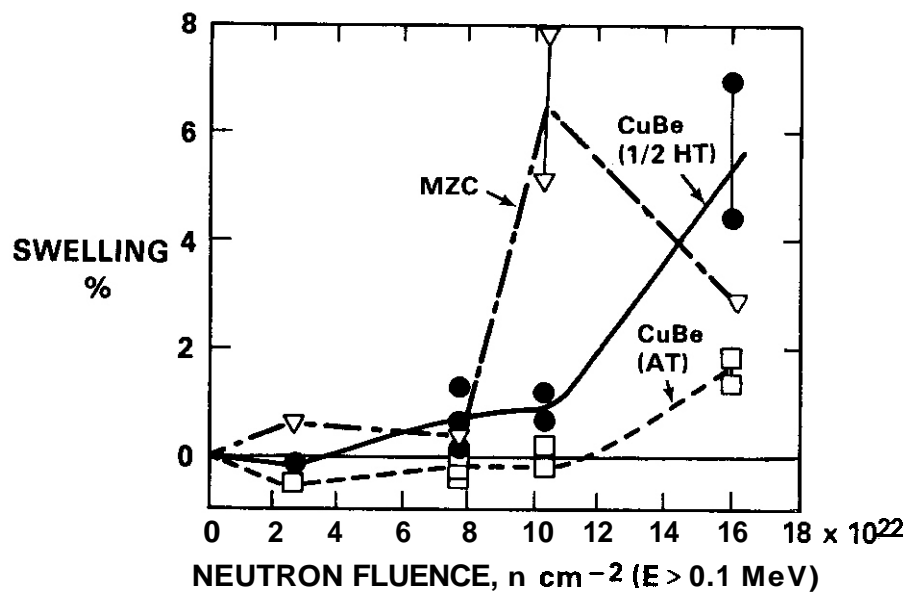


Fig. 3. Swelling of MZC and CuBe Alloys Observed in FFTF-MOTA at 450°C

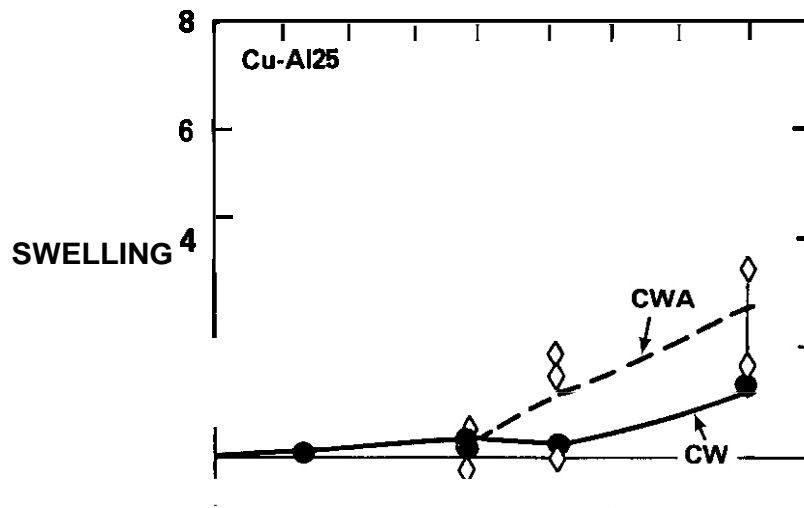


Fig. 4. Swelling of Cu-Al25 in FFTF-MOTA at 450°C.

The difference in swelling of the **CuBe** alloys having different pre-irradiation treatments is consistent with the microstructures observed after irradiation to 16 dpa **C61**. At that low fluence, the pre-irradiation aging of the annealed material (condition AT) induced a high density of small precipitates that were only slightly influenced by the irradiation. This microstructure inhibited the nucleation of voids at 16 dpa **relative** to the cold worked and aged material (designated 1/2 HT) in which significant swelling occurred in regions that had recrystallized.

The apparent decrease in swelling with increasing exposure for the **MZC** alloy is thought to be an artifact in view of an inconsistency in the data reported for the irradiation after 63 dpa [2]. While the immersion density measurements of the **MZC** at 63 dpa indicated swelling of 5 to 8%, the electron microscopy results showed no significant void formation. This difference was thought to have been produced by not **completely** removing an aluminum coating found to be attached to the **MZC** specimen surface after 63 dpa irradiation. The aluminum had been included as spacer material to prevent self-welding between adjacent copper **specimens** during irradiation. While some small amount of aluminum may have remained on the copper specimen irradiated to 98 dpa also, this would result in "apparent" swelling values that are larger than the "correct" measurements. This would suggest that the current **MZC** swelling data are best treated as maximum estimates with the datum at 98 dpa more reliable than those at 63 dpa. Previously reported electrical resistance measurements of **MZC** after 63 dpa irradiation were in the same range as that of A125 as well as for zone-refined copper [1].

The second aspect of these irradiations involves the simpler alloys and eventually may provide sane insight on the fundamental processes involved in the radiation-induced evolution of these alloys. In the Fe-Cr-Ni austenitic system, it was shown earlier that the simple solute-free alloys provide an early indication of the maximum swelling rate to be expected in more complicated alloys in that alloy system(4) .

It now appears that both the nickel(5) and copper alloy systems exhibit the possibility of swelling at the $\sim 1\%/dpa$ rate observed in the Fe-Cr-Ni austenitic system but this occurs only at lower fluence levels. At higher fluence levels these systems relax to a lower swelling rate of $\sim 0.5\%/dpa$ which is not exceeded for any solute additions or thermal-mechanical treatments investigated in this study. In the copper system, however, solute additions (such as silver and possibly aluminum) are necessary to **reach the** higher but **short-lived swelling** rate, while no solute additions are necessary in the nickel system(5). Both Makin(8) and Leister(9) have observed that the swelling of copper during charged particle irradiation is increased by the addition of silver. Unfortunately the role of silver cannot be examined by microscopy and EDX analysis due to the very large swelling levels achieved in this experiment . The effect of combined phosphorus and silver additions to reduce the swelling rate even further has not been previously observed and may involve precipitation sequences. This possibility may be addressed in future studies.

Conclusions

Minor solute additions have a pronounced influence on the irradiation resistance of the high-conductivity copper alloys. Swelling of pure copper and the various alloys of copper **varied** over a range from 1 to more than 60% for material irradiated near 450°C to about 98 dpa. Based on swelling data and **previously** published electrical conductivity and microstructure results, the most **promising** materials of those examined are oxide dispersion-strengthened copper (alloy A125) and precipitation-strengthened **MZC** and, to a lesser extent, the **CuBe** alloy.

Future Work

This report completes the work planned on this experimental series. A second generation **experimental** series [10], now being irradiated in the FFTF/MOTA , is designed to further explore variations of the swelling-resistant alloys identified in the first series.

REFERENCES

1. H. R. Brager, H. L. Helnisch and F. A. Garner. J. Nucl. Matl., 133 6 134, 676-679, 1985.
2. H. R. Brager. J. Nucl. Matl., 141-143, 79-86. 1986.
3. F. A. Garner and H. R. Brager. pp. 110-113 in Damage Analysis and Fundamental Studies Quarterly Progress Report DOE/ER-0046/25, May 1986.
4. F. A. Garner. J. Nucl. Matl., 122 6 123, 459-471, 1984.
5. F. A. Garner, J. Nucl. Matl., 148, 288-293.
6. H. R. Brager. J. Nucl. Matl., 141-143, 163-168, 1986.
7. F. M. Mann. Damage Analysis and Fundamental Studies Quarterly Progress Report, DOE/ER_0046/24, February 1986.
8. M. J. Makin, p. 269 in Voids Formed by Irradiation of Reactor Materials. S. F. Pugh, Ed.; British Nuclear Energy Society. 1971.
9. K. H. Leister, Kernforschungszentrum Karlsruhe Report No. KFK-3499 (In German). May 1983.
10. H. R. Brager, pp. 307-308, In Fusion Reactor Materials Semi-annual Progress Report, DOE/ER-0313/1, June 1987.

6.5 Environmental Effects on Structural Alloys

CORROSION AND MASS TRANSFER IN LITHIUM 12Cr-1MoVW STEEL SYSTEMS - G. E. Bell (University of California, Los Angeles), P. F. Tortorelli (Oak Ridge National Laboratory), and M. A. Abdou (University of California, Los Angeles)

OBJECTIVE

The objective of this research is to provide experimental data for development of, and comparison with, an analytical model of the mass transport processes of 12Cr-1MoVW steel in the presence of thermally convective lithium. Measurements of chemical and metallurgical changes are used to understand mechanisms and kinetics of the relevant reactions.

SUMMARY

Data from weight change and surface analyses of 12Cr-1MoVW steel exposed to lithium in two modified (TCLs) showed the importance of chromium depletion and chromium-containing nodule formation over certain temperature ranges. These reactions strongly affected the resulting mass transfer profile and the dependence of such on temperature.

PROGRESS AND STATUS

As reported previously,¹ a mass transfer modeling study was undertaken using thermal convection loops (TCLs) of a modified ORNL design. The weight change and surface composition data taken from these loop experiments are being used to develop a quantitative model of mass transfer in the subject system.¹ The two TCLs operated at maximum temperatures (T_{max}) of 500 and 655°C with temperature differentials of approximately 150 and 140°C, respectively. During the current reporting period, the $T_{max} = 500^\circ\text{C}$ loop reached 3000 h of operation with specimens inserted in the lithium, while specimens in the second TCL accumulated about 1500 h of specimen exposure. Weight change data as a function of time for selected specimens from these two loops are shown in Figs. 1 and 2. Weight changes in the $T_{max} = 500^\circ\text{C}$ loop are approximately an order of magnitude smaller than those in the $T_{max} = 655^\circ\text{C}$ experiment. Note also that, in both loops, the magnitude of the initial weight change rates (the slope of the weight change versus time curve for times less than 500 h) are large in comparison with the subsequent steady-state rates. Weight loss is occurring for almost all specimens in the $T_{max} = 500^\circ\text{C}$ loop with the exception of the highest temperature hot leg specimen (498°C). In general, weight loss is not a monotonic function of temperature in this loop. Additionally, "traditional" solubility-driven thermal gradient mass transfer (that is, mass removal in the hot zone and deposition in the cold zone) does not appear to be occurring in the $T_{max} = 500^\circ\text{C}$ experiment. The weight change data in Fig. 2 for the $T_{max} = 655^\circ\text{C}$ loop shows both mass removal and deposition occurring throughout the loop. Thermal gradient mass transfer does appear significant at these higher temperatures. Similar behavior had been earlier observed in loop experiments with 12Cr-1MoVW steel using a standard ORNL TCL characterized by lower lithium mass flow rate, Reynolds number, and nitrogen content.^{2,3} Assuming linear kinetics at times greater than 500 h, maximum "steady-state" corrosion rates were approximately 30 times higher for the $T_{max} = 655^\circ\text{C}$ experiment (7.4 mg/m²·h) than for the $T_{max} = 500^\circ\text{C}$ one (0.24 mg/m²·h). Significant weight gains can be found in the temperature range 490 to 530°C for both loops with maximum deposition rates of 0.07 and 4.5 mg/m²·h for $T_{max} = 500$ and 655°C, respectively.

Scanning electron microscope (SEM) examinations of selected surfaces from the hot and cold legs of both loops after 990 and 1230 h in the $T_{max} = 500$ and 655°C loops, respectively, showed "pebble-like" structures on all the underlying surfaces exposed to lithium (Fig. 3). Energy dispersive x-ray analysis (EOX) of these surfaces revealed depletion in chromium to between 7 and 10% from the original 11.5%. The amount of chromium depletion from the underlying base material increases with temperature. The size of the surface pebbles was also seen to increase with increasing temperature [Figs. 3(a)-(d)]. It is not clear whether the observations of chromium depletion and surface "pebbling" are related, and further investigation is needed. Chromium-rich, faceted-nodule deposits on some specimens were found in both the $T_{max} = 500$ and 655°C loops in the temperature range 490 to 530°C [Figs. 3(b) and (c)]. Note that the "pebbled" base material surface beneath the faceted nodules still persists. The nodules first appear at the grain boundaries in the $T_{max} = 500^\circ\text{C}$ loop [Fig. 3(b)], probably because of the presence of chromium in the carbide phase ($M_{23}C_6$) which may act as a precursor for growth of these nodules. More nodules were present on the $T_{max} = 655^\circ\text{C}$ specimens exposed at 530°C. The nodules were not present on the highest (655°C) and lowest (360°C) temperature specimens. The similarity of such features to those observed in independent loop experiments^{2,3} emphasizes the importance of chromium transport (possibly via ternary nitride corrosion product formation) in the temperature range of interest for ferrous alloy-lithium systems.

Weight Change Versus Time: GEB-1

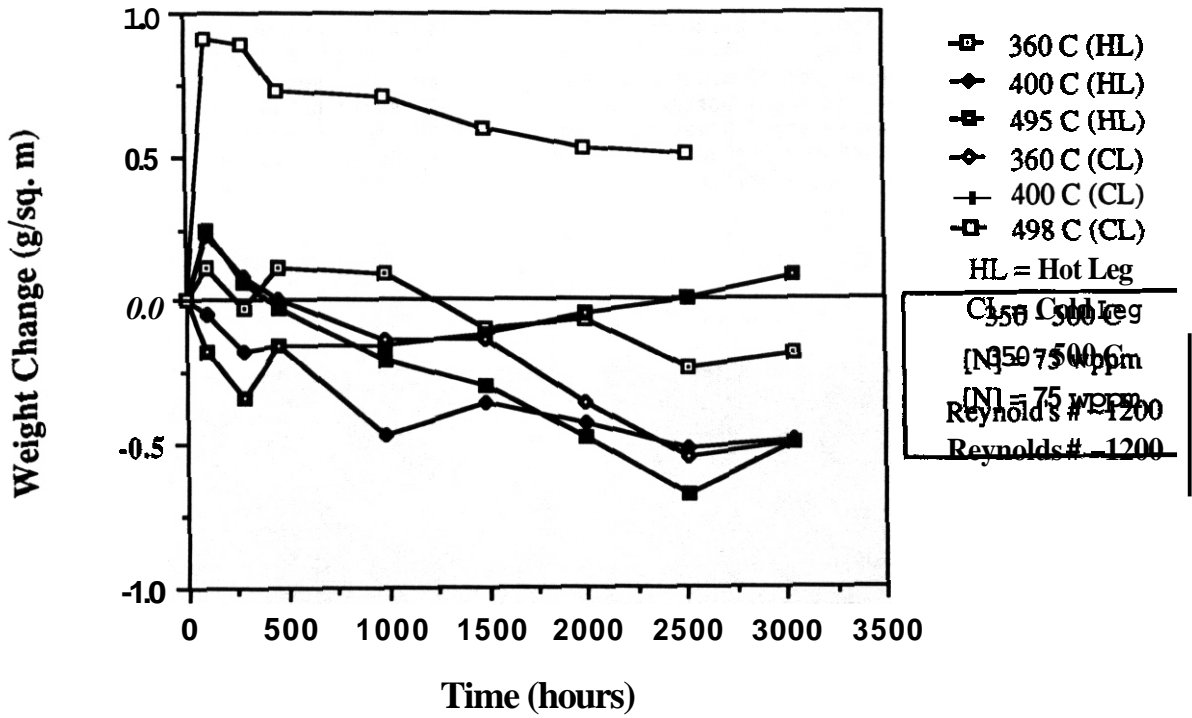


Fig. 1. Weight change versus time for 12Cr-1MoVW specimens in thermally convective lithium (350-500°C).

Weight Change Versus Time: GEB-2

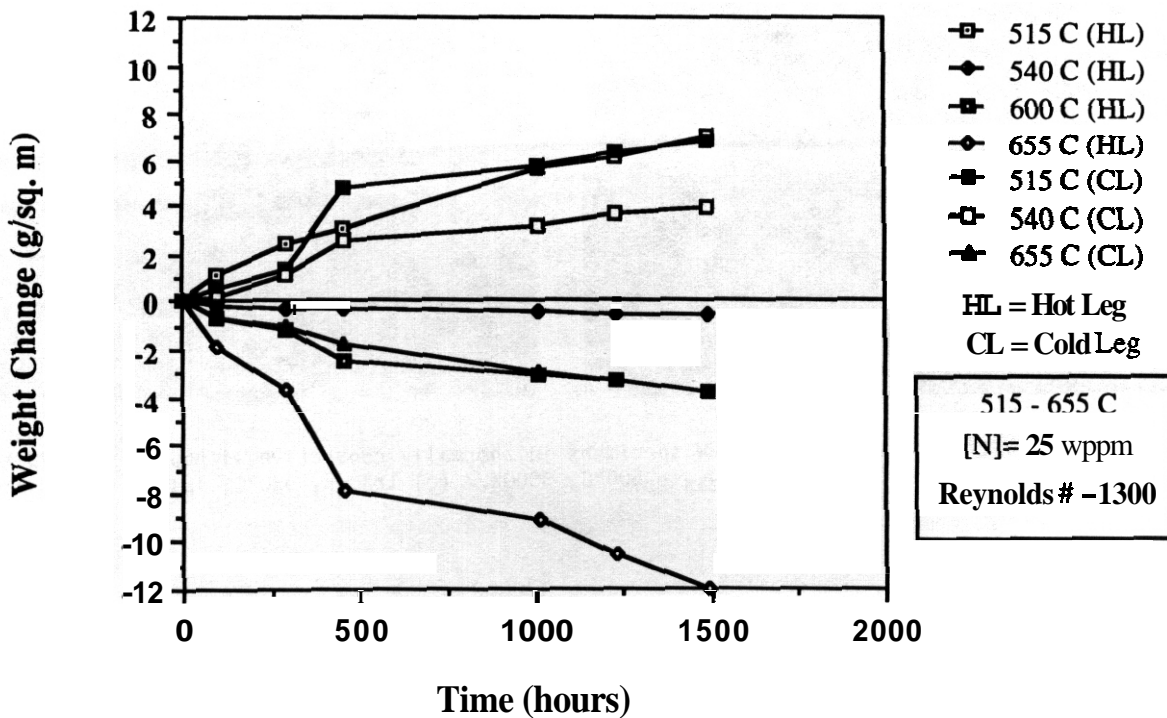


Fig. 2. Weight change versus time for 12Cr-1MoVW specimens in thermally convective lithium (515-655°C).

As discussed elsewhere, the formation of chromium-rich deposits may be related to surface products involving reactions with nitrogen⁴⁻⁷ and may involve coexistence (or pre-existence) of carbides.⁸ The occurrence of the nodules over a specific temperature range (~490 to 530°C) coincides with the 520°C solidus on the Fe-Cr equilibrium phase diagram.³ This phase boundary may help explain the nodule formation by surface equilibrium partitioning in this temperature range. However, the existence of these nodules does not preclude surface product reactions; the presence of lithium and/or a corrosion product with lithium nitride may affect the kinetics of the phase transformation. More nodules appear in higher T_{max} systems because there is more chromium available from dissolution. Further surface analyses of specimens from the higher temperature TCL may help determine the importance of Fe-Cr surface solid phase formation in lithium system and its relation to weight change data. However, regardless of the mechanism by which such nodules form, it is apparent that the formation of the surface nodules must be considered in any mass transfer model of lithium Fe-Cr (-Ni, Mn) systems and, specifically, in the design of heat transport systems utilizing Fe-Cr alloys with lithium.

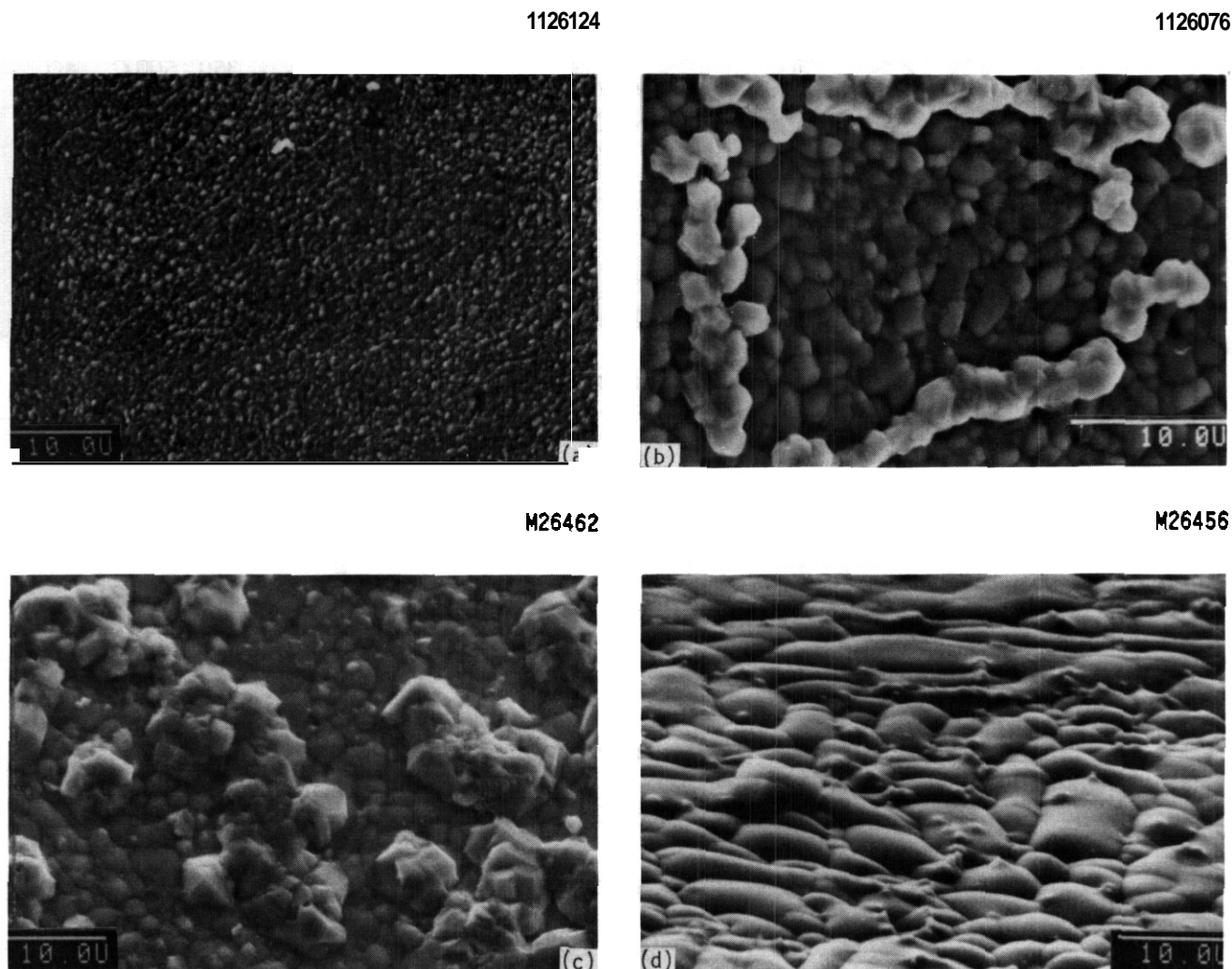


Fig. 3 SEM micrographs of 12Cr-1MoVW specimens in thermally convective lithium. (a) 990 h, 360°C, $T_{max} = 500^\circ\text{C}$, 2000X. (b) 990 h, 498°C, $T_{max} = 500^\circ\text{C}$, 3000X. (c) 1230 h, 530°C, $T_{max} = 655^\circ\text{C}$, 2000X. (d) 1230 h, 655°C, $T_{max} = 655^\circ\text{C}$, 2000X.

CONCLUSIONS

1. Weight changes in 12Cr-1MoVW steel systems can be correlated with chromium depletion and/or formation of nodules containing significant amounts of chromium.

2. Solubility-driven mass transfer makes a greater contribution to mass transport at higher temperatures. Formation of chromium-containing nodules occurs over a restricted temperature range (470-550°C) and strongly influences the net mass transfer profile.

3. Formation of surface nodules must be considered in any mass transfer model and, specifically, in the design of heat transport systems utilizing Fe-Cr alloys with lithium.

FUTURE WORK

During the next reporting period, the loop experiments for the mass transfer modeling, the associated weight change and surface analyses, and the postexposure analysis of the specimens will be completed. Final incorporation of the findings into the analytical model will begin. The standard ORNL TCLs will be used to examine low activation ferrous alloys in Pb-17 at. % Li and to initiate studies of modified ferritic alloys (lower Cr) in lithium. A comprehensive mass transfer analysis of results from TCL studies of austenitic and ferritic steels exposed to Pb-17 at. % Li for 10,000 h will be undertaken.

REFERENCES

1. G. E. Bell, M. A. Abdou, and P. F. Tortorelli, "Thermal Convection Loop Studies in Support of Mass Transport Modeling of Lithium/12Cr-1MoVW Steel Systems," pp. 275-78 in *Fusion Reactor Materials Semiannu. Pmg. Rep. Mar. 82*, 1987, DOE/ER-0313/2, U.S. DOE, Office of Fusion Energy.
2. P. F. Tortorelli and J. H. DeVan, "Corrosion of an Fe-12Cr-1MoVW Steel in Thermally Convective Lithium," pp. 215-21 in *Pmc. Topical Conf. on Ferritic Alloys for Use in Nuclear Energy Applications, Snowbird, Utah, June 1983*, ed. J. W. Davis and D. J. Michel, AIME, Warrendale, PA, 1984.
3. P. F. Tortorelli, "Corrosion Studies in Thermally Convective Lithium: 12Cr-1MoVW Steel and Low Activation Austenitic and Ferritic Alloys," pp. 331-36 in *Fusion Reactor Materials Semiannu. Pmg. Rep. Sept. 80*, 1986, DOE/ER-0313/1, U.S. DOE, Office of Fusion Energy.
4. P. F. Tortorelli, "Corrosion of Ferritic Steels by Molten Lithium: Influence of Competing Thermal Gradient Mass Transfer and Surface Product Reactions," presented at the Third International Conference on Fusion Reactor Materials, Karlsruhe, West Germany, Oct. 4-8, 1987; to be published in the proceedings.
5. P. F. Tortorelli and J. H. DeVan, "Corrosion of Fe-Cr-Mn Alloys in Thermally Convective Lithium," *J. Nucl. Mater.* 141-143, 579-83 (1986).
6. M. G. Barker et al., "The Interaction of Chromium with Nitrogen Dissolved in Liquid Lithium," *J. Nucl. Mater.* 114, 143-49 (1983).
7. W. F. Calaway, "The Reaction of Chromium with Lithium Nitride in Liquid Lithium," pp. 18-18 - 18-26 in *Proc. 2nd International Conf. on Liquid Metal Technology in Energy Production, Richland, Washington, April 1980*, ed. J. M. Dahlke, U.S. DOE, CONF-800401P2, 1980.
8. E. Ruedl et al., "Phase Stability and Corrosion of Cr-Mn Austenitic Steels Exposed to Pure Lithium," *J. Nucl. Mater.* 122&123, 1247-1251 (1984).
9. R. P. Elliot, *Constitution of Binary Alloys, First Supplement*, McGraw-Hill Book Company, Inc., New York, 1965.

CORROSION AND NONMETALLIC ELEMENT TRANSFER OF VANADIUM ALLOYS IN LITHIUM - O. K. Chopra and D. L. Smith
(Argonne National Laboratory)

OBJECTIVE

The objective of this program is to investigate the influence of a flowing lithium environment on the corrosion behavior and mechanical properties of structural alloys under conditions of interest for fusion reactors. Corrosion rates are determined by measuring the weight change and depth of internal corrosive penetration as a function of time and temperature. These measurements, coupled with metallographic evaluation of the alloy surface, are used to establish the mechanism and rate-controlling processes for the corrosion reactions. Initial effort on mechanical properties is focused on fatigue and tensile tests in flowing lithium environment of controlled purity.

SUMMARY

Corrosion data are presented on nonmetallic element transfer and dissolution behavior of several vanadium alloys exposed to flowing lithium at 427, 482, and 538°C. The results indicate that chemical interactions between alloy elements and nitrogen and/or carbon in lithium play an important role in the corrosion behavior of these alloys. The influence of alloy composition and exposure conditions on corrosion of vanadium alloys is discussed.

PROGRESS AND STATUS

The corrosion behavior of several vanadium alloys is being investigated in a flowing lithium environment. A detailed description of the lithium loop and the test procedure has been presented earlier.^{1,2} Three corrosion test runs of 1500- to 2500-h duration were conducted at temperatures between 538 and 371°C. For these tests, the concentrations of carbon and nitrogen in lithium were -10 and 120 wppm, respectively, and the nitrogen content varied between 100 and 20 wppm for the different tests. The corrosion data and results from metallographic examination of the lithium-exposed specimens of several vanadium alloys have been reported previously.^{3,4} The results indicated that pure vanadium has the highest dissolution rate and the alloys with 15 or 20% Ti have the lowest rates. Chemical interaction plays an important role in the corrosion behavior of these alloys. During this reporting period, the lithium-exposed specimens were analyzed chemically to determine the changes in nonmetallic elements after exposure to lithium. To determine the depth of the diffusion zone over which these compositional changes occurred, microhardness measurements were also performed.

The weight losses of several vanadium alloys exposed to flowing lithium at 482 and 427°C (run 8) are shown in Fig. 1. At both temperatures, the weight losses of all alloys increased linearly with time after an incubation period of up to 700 h. The incubation period increased with an increase in the titanium content of the alloy. Alloys containing 15 or 20% Ti, in fact, showed a weight gain during the initial 700-h exposure to lithium. The weight losses of vanadium alloys with time were somewhat different than the weight losses of ferritic or austenitic steels, which show rapid dissolution during the initial transient period. The weight change for vanadium alloys represents two competing processes, viz., weight loss due to dissolution of alloy elements and weight gain from pickup of nonmetallic elements, particularly nitrogen, from lithium. The latter process is dominant during the initial period of lithium exposure.

The steady-state dissolution rates for the various vanadium alloys exposed to lithium are given in Table 1. At 482°C, the dissolution rates decreased in the following order: pure V, V-3Ti-15Cr, V-5Ti-(10 to 15Cr), V-12 to 15Cr-(3Fe-1Zr), and V-15 to 20Ti-(7.5Cr). A similar trend was also seen at 427°C; however, all alloys that contained titanium showed low dissolution rates. The data also indicate that under the lithium exposure conditions used, the dissolution rates of all vanadium alloys were greater than those of ferritic steels. For example, steady-state dissolution rates of ferritic AT-9 and Fe-9Cr-1Mo steel at 482 and 427°C (run 8) were 0.2 mg/m²·h and 0.07 mg/m²·h, respectively.²

Metallographic examination of cross sections of the various lithium-exposed specimens revealed that alloys containing >15% Ti developed a uniform reaction scale after exposure to lithium. Micrographs of the cross sections of V-20Ti and V-15Cr-5Ti specimens exposed to lithium are shown in Fig. 2. The V-20Ti specimens developed a uniform surface scale during the initial ~700 h of exposure and the thickness of the scale increased with increasing temperature, e.g., ~1.5, 2.5, and 6.0 μm at 427, 482, and 538°C, respectively. However, the scale thickness did not change significantly with time, i.e., the rate of movement of the alloy/scale interface was approximately the same as recession of the specimen surface. The formation of the reaction scale accounts for the weight gain of the V-20Ti specimens during the initial ~700-h exposure. The micrographs of the V-15Cr-5Ti specimens show patches of surface layer (~2 μm thick) which appear to be breaking off from the specimen, Fig. 2. This spalling of reaction scale from the specimen surface may account for the large weight loss of V-15Cr-5Ti alloy. A similar behavior was observed for pure vanadium and the various vanadium alloys that contained ≤5% Ti.

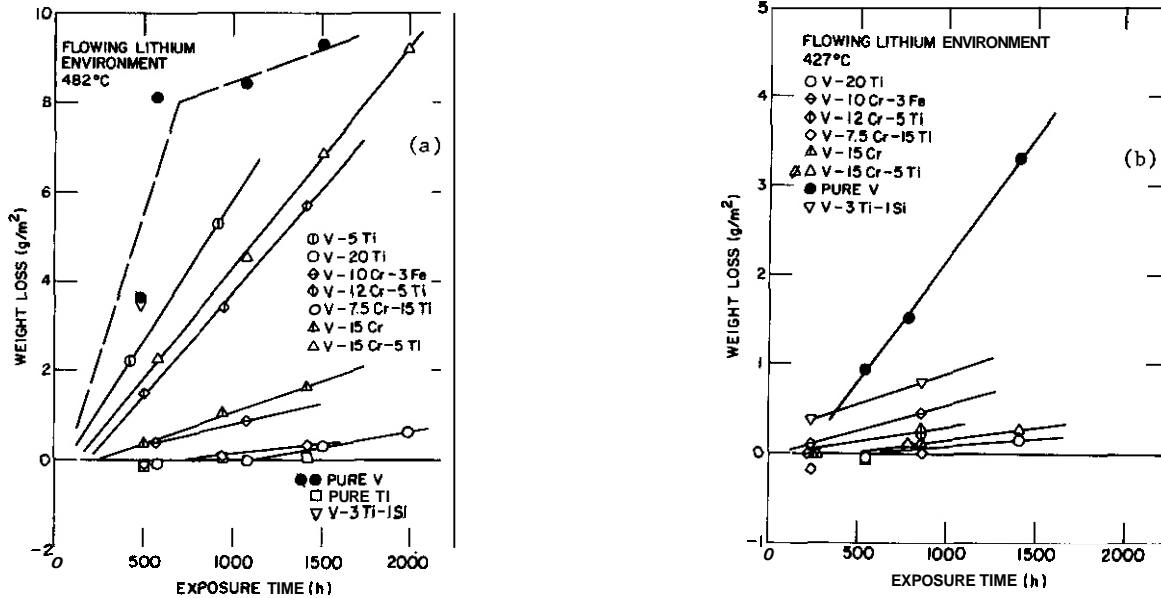


Fig. 1. Weight loss versus exposure time for vanadium alloys exposed to flowing lithium at (a) 482°C and (b) 427°C. Each symbol type represents weight loss for a single specimen after various exposure times.

Table 1. Dissolution rates for vanadium alloys exposed to flowing lithium

Alloy	Dissolution Rate (mg/m ² ·h) ^a					
	Run 6 (~50 wppm N) ^b		Run 8 (-20 wppm N) ^b		Run 5 (-100 wppm N) ^b	
	538°C	482°C	482°C	427°C	427°C	372°C
Pure V	-	-	c	2.76	-	-
V-10Cr-3Fe-1Zr	-	-	0.86	0.73	-	-
V-15Cr	-	-	1.38	0.47	-	-
V-5Ti	-	-	6.34	-	-	-
V-12Cr-5Ti	-	-	4.64	0.17	-	-
V-15Cr-5Ti	2.66	2.95	4.97	0.27	0.54	0.036
V-20Ti	-	0.22	0.72	0.24	-	-
V-7.5Cr-15Ti	-	-	0.48	d	-	-
V-3Ti-1Si	-	-	7.15 ^e	0.75	-	-

^aDissolution rates based on net weight loss. The values are not corrected for weight change due to nonmetallic element transfer.

^bRepresents the average nitrogen content in lithium during the different test runs.

^cDissolution rates change with time, i.e., the rates are -13 mg/m²·h during the initial 500-h exposure and decrease to -2 mg/m²·h for longer times.

^dThe specimen showed weight gain for times up to -800 h.

^eCalculated from a single exposure time.



Fig. 2. Weight loss versus exposure time for V-15Cr-5Ti alloy exposed to flowing lithium at various temperatures. Each symbol type represents weight loss for a single specimen after various exposure times.

The concentrations of nitrogen, oxygen, and carbon in pure V, V-10Cr-3Fe-1Zr, V-20Ti, and two heats of V-15Cr-5Ti specimens exposed to lithium at 421, 482, and 538°C are given in Table 2. All alloys showed a significant increase in the nitrogen content. The gain in nitrogen increases with exposure time and temperature. Analyses of the specimens with and without the surface reaction scale indicate that the increase in nitrogen content is associated with the surface reaction scale as well as with the bulk material. The solubility of nitrogen in vanadium is 3600 and 4700 wppm at 482 and 538°C, respectively.

The V-10Cr-3Fe-1Zr and V-15Cr-5Ti alloys also showed an increase in carbon whereas pure vanadium showed little or no change in carbon content. The solubility of carbon in vanadium is 366 and 265 wppm at 482 and 427°C, respectively. Consequently, the carbon content measured in the pure V specimens represents the saturation value. The vanadium alloys have carburized and should contain carbides of titanium, chromium, or zirconium. Under the present conditions of lithium exposure (1.2, -10 wppm C), all vanadium alloys, including pure vanadium, should carburize. It is likely that the V_2C which forms on pure vanadium specimens is not adherent and spalls during lithium exposure. This may be the dominant contribution to the weight loss of pure vanadium.

The oxygen content of pure vanadium and of V-15Cr-5Ti alloy decreased after exposure to lithium; however, the V-10Cr-3Fe-1Zr and V-20Ti alloys showed only minor changes in oxygen. For a cold-trap temperature between 200 and 220°C, the concentration of oxygen in lithium is estimated to be between 35 and 50 wppm. Under these conditions, since the equilibrium concentration of oxygen in vanadium will be extremely low (<1 ppb), decreases in the oxygen concentrations are predicted. The results indicate that the loss of oxygen from vanadium alloys is very slow.

The depth of the diffusion zone for the nonmetallic elements in the lithium-exposed specimens was determined by measuring microhardness. The results for V-15Cr-5Ti and V-10Cr-3Fe-1Zr alloys are shown in Figs. 3 and 4, respectively. Both alloys showed an increase in hardness after lithium exposure; however, the hardness profiles for the two alloys are distinctly different. The V-15Cr-5Ti alloy showed a sharp increase in hardness of the surface region (10 to 20- μ m deep) of the specimen, whereas the V-10Cr-3Fe-1Zr alloy exhibited a more uniform increase in hardness. The results indicate that the increase in hardness was caused primarily by the increase in the nitrogen content of the alloys; the hardness profiles for V-10Cr-3Fe-1Zr alloy show good agreement with computed diffusion profiles for nitrogen. Also, the microhardness results agree very well with changes in nitrogen concentration. For example, the difference in the nitrogen content of Cam and ANL heats of V-15Cr-5Ti alloy (2361 and 2808 wppm N, respectively) is reflected in their hardness profiles, shown in Fig. 3. Also, the V-10Cr-3Fe-1Zr alloy exposed for 687 h at 482°C showed a hardness increase to a depth of >30 μ m and contained 4570 wppm N while the two heats of V-15Cr-5Ti exposed for 1600 to 2000 h at 482°C showed an ~10- μ m hardened region and contained 2400 to 2800 wppm N.

The difference in the hardness profiles for V-10Cr-3Fe-1Zr and V-15Cr-5Ti alloys can be attributed to the precipitation of TiN in the latter. The formation of TiN in V-15Cr-5Ti alloy decreases the diffusion of nitrogen into the alloy and hence, produces a thinner hardened layer relative to the V-10Cr-3Fe-1Zr alloy which shows a flat hardness profile. The microhardness of three alloys with 5Ti and different amounts of chromium, exposed to lithium at 482°C, is shown in Fig. 5. All alloys had identical hardness profiles.

The effect of carbon on the hardness profiles of vanadium alloys cannot be estimated from the present results. Diffusion of carbon in vanadium is more than an order of magnitude faster than nitrogen diffusion. The pickup of carbon may also contribute to the increase in hardness. Additional data are needed to evaluate the carburization behavior of vanadium alloys in lithium.

Table 2 Composition of nonmetallic elements in several vanadium alloys exposed to lithium

Alloy	Specimen ID	Test Run	Exposure Condition		Composition ^a (wppm)		
			Temp. (°C)	Time (h)	N	O	C
Pure V	-	-	Unexposed		161 ± 41	1,101 ± 73	360
	V-70	8	427	1405	565 ± 71	889 ± 107	320
	V-84	8	482	484	681 ± 65	986 ± 97	340 [330]
	V-64	8	482	1508	3,404 ± 187	737 ± 122	270
					12,720 ± 1461	[828 ± 911	[-]
V-10Cr-3Fe-1Zr	-	-	Unexposed		271 ± 66	607 ± 100	890
	V-52	6	482	687	4,570 ± 250	724 ± 157	990
	v-57	6	482	619	-	-	1270
	V-66	8	482	1080	-	-	1070
	v-51	6	538	590	12,418 ± 621	524 ± 140	-
	v-55	6	538	794	-	-	1190
V-15Cr-5Ti (Cam)	-	-	Unexposed		527 ± 109	1,291 ± 168	390
	V-71	8	427	1405	607 ± 84	422 ± 119	500 16101
	V-65	8	482	1992	2,361 ± 114	505 ± 119	570
	v-59	6	482	619	11,536 ± 911	1443 ± 771	[-]
					-	530	
V-15Cr-5Ti (ANL)	-	-	Unexposed		299 ± 68	1,384 ± 112	390
	v-53	6	482	1618	2,808 ± 177	537 ± 163	700
	V-50	6	538	1384	10,925 ± 565	1,174 ± 165 ^b	-
					[10,022 ± 5051	[562 ± 981	16701
V-20Ti	-	-	Unexposed		566 ± 168	1,163 ± 254	-
	v-49	6	538	1384	8,224 ± 433	2,687 ± 244 ^b	-
					15,735 ± 2951	11,416 ± 124]	[-]

^aValues within brackets represent concentrations for specimens which were mechanically polished to remove the surface reaction scale. The concentration of H ranged between 3 and 8 wppm for the various specimens with or without lithium exposure.

^bThese specimens contain 50 to 70 wppm H. The increased O and H content is most likely due to hydroxides which form after the specimens were cleaned.

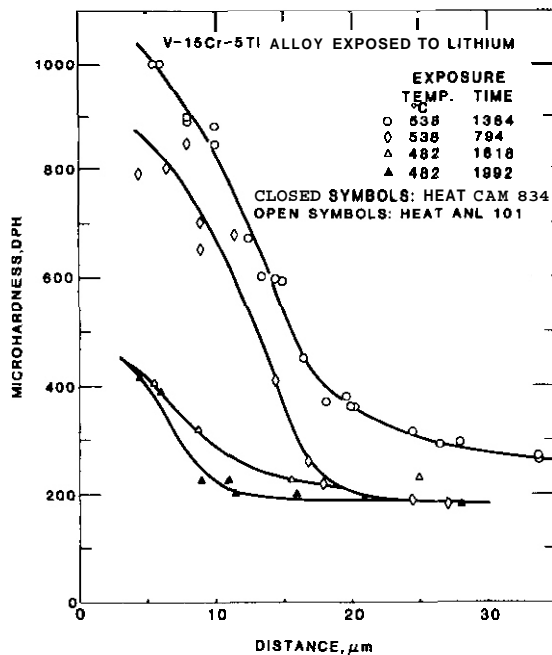


Fig. 3. Microhardness of the surface region of V-15Cr-5Ti alloy exposed to lithium.

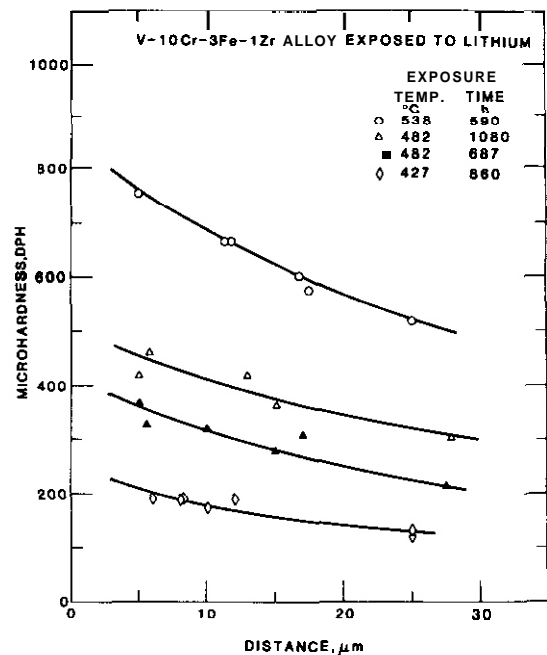


Fig. 4. Microhardness of the surface region of V-10Cr-3Fe-1Zr alloy exposed to lithium.

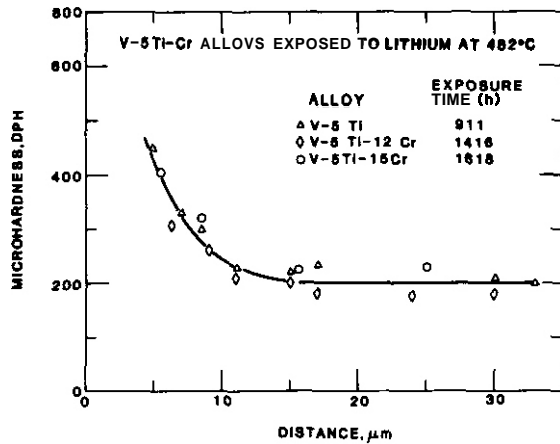


Fig. 5. Microhardness of vanadium alloys containing 5%Ti and different amounts of chromium exposed to lithium.

DISCUSSION

The temperature dependence of the equilibrium values of nitrogen and carbon concentrations in lithium for which metal nitrides and carbides are stable^{5,6} is shown in Fig. 6. The equilibrium nitrogen concentration in lithium for the formation of Li_3CrN_5 is also plotted. The results indicate that for the exposure conditions used in runs 5, 6, and 8, the carbides of titanium, vanadium, and chromium, ternary nitride of chromium, and nitrides of vanadium and titanium are expected to be stable (the nitrogen content during run 8 is slightly lower than the equilibrium value required for the formation of V_2N ; however, the difference is insignificant). Consequently, the chemical interactions to form these compounds have a dominant role in the corrosion behavior of vanadium alloys in lithium.

Metallographic results indicate that the low dissolution rates of the alloys containing $\geq 15\% \text{Ti}$, e.g., V-20Ti and V-7.5Cr-15Ti, are due to the formation of a protective surface scale. Chemical analyses of the specimens indicate that the scale is primarily composed of mixed nitrides. The composition of metallic elements in the scale is approximately the same as that in the bulk alloy. This nitride scale, however, is quite brittle and can spall when exposed to thermal stresses. Alloys containing 5%Ti or less do not develop a uniform surface scale. The reaction products easily break off from the alloy surfaces, resulting in high dissolution rates. The dissolution rates for V-15Cr-1Ti in lithium at 482 and 538°C (viz., 3 to 5 $\text{mg}/\text{m}^2 \cdot \text{h}$) agree fairly well with the rate ($\sim 3 \text{ mg}/\text{m}^2 \cdot \text{h}$) obtained at 550°C in flowing lithium containing -10 wppm nitrogen. The scales on these alloys are also primarily nitrides. However, the contribution of carbide formation to the dissolution behavior of the alloys cannot be evaluated from the existing data. A similar behavior is observed for pure vanadium, i.e., high dissolution rates due to chemical interactions between vanadium and nonmetallic elements such as nitrogen and/or carbon.

The addition of chromium to vanadium seems to influence the chemical interactions and reduce dissolution rates. However, the chromium-containing alloys exhibit significant embrittlement after exposure to lithium. The cause of embrittlement has not been determined, but it could arise from the pickup of hydrogen from lithium. However, significant changes in the measured hydrogen content were not observed in the lithium-exposed specimens. The V-15Cr-5Ti and V-10Cr-3Fe-1Zr alloys show significant increases in carbon concentration, which may contribute to the observed embrittlement. The influence of carburization on the tensile properties of vanadium alloys needs further investigation.

SUMMARY

The corrosion data for several vanadium alloys indicate that during the present tests, the concentrations of nitrogen and possibly carbon in lithium were above acceptable limits, and chemical interactions between alloy elements and nitrogen and/or carbon in lithium played an important role in the corrosion behavior of these alloys. When exposed at 482°C to lithium containing 20 to 50 wppm N and 8 to 12 wppm C, the dissolution rates of the various vanadium alloys decreased in the following order: pure V, V-3Ti-15Ti, V-5Ti-(12 to 15Cr), V-10 to 15Cr-(3Fe-1Zr), and V-15 to 20Ti-(7.5Cr). The alloys containing 15 to 20% Ti developed a protective nitride scale. Under the present exposure conditions, all vanadium alloys picked up nitrogen and carbon from lithium and lost oxygen. The chromium-containing alloys became embrittled after exposure to lithium.

FUTURE WORK

Corrosion tests are planned in lithium containing -1 wppm nitrogen to evaluate the dissolution behavior of vanadium alloys under conditions where vanadium nitride does not form. X-ray diffraction and electron microprobe analyses will be performed to evaluate the nature of the reaction products on the alloy surfaces.

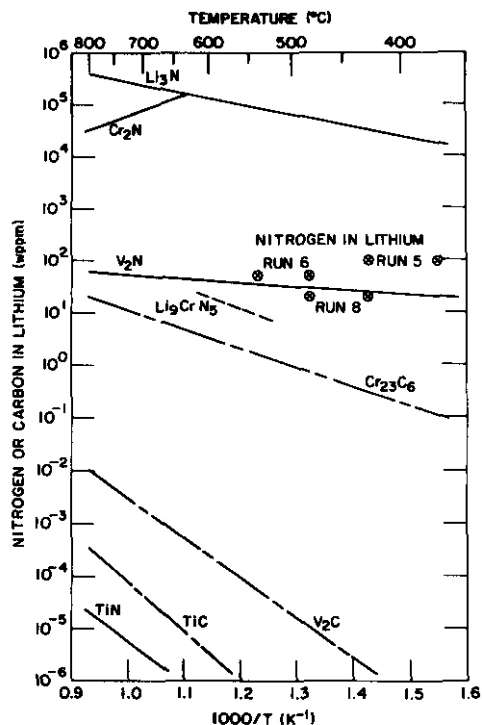


Fig. 6. Temperature dependence of the nitrogen and carbon concentrations in lithium at which selected structural metal nitrides and carbides are stable.

REFERENCES

1. O. K. Chopra and D. L. Smith, "Corrosion of Ferrous Alloys in a Flowing Lithium Environment," J. Nucl. Mater. 133 & 134, 861-866 (1985).
2. O. K. Chopra and D. L. Smith, "Influence of Temperature and Lithium Purity on Corrosion of Ferrous Alloys in a Flowing Lithium Environment," J. Nucl. Mater. 141-143, 584 (1986).
3. O. K. Chopra and D. L. Smith, "Corrosion of Ferritic Steels and V-15Cr-5Ti Alloy in Flowing Lithium," pp. 328-333 in Fusion Structural Materials Semiannual Progress Report for the Period Ending September 30, 1986, DOE/ER-0313/1, Oak Ridge National Laboratory, Oak Ridge, Tenn., June 1987.
4. O. K. Chopra and D. L. Smith, "Corrosion of Vanadium Alloys in Flowing Lithium," pp. 269-274 in Fusion Structural Materials Semiannual Progress Report for the Period Ending March 31, 1987, DOE/ER-0313/2, Oak Ridge National Laboratory, Oak Ridge, Tenn., September 1987.
5. D. L. Smith and K. Natesan, "Influence of Nonmetallic Impurity Elements on the Compatibility of Liquid Lithium with Potential CTR Containment Materials," Nucl. Technol. 22, 392 (1974).
6. K. Natesan, "Influence of Nonmetallic Elements on the Compatibility of Structural Materials with Liquid Alkali Metals," J. Nucl. Mater. 115, 251 (1983).
7. M. G. Barker, J. A. Lees, and L. E. Schreinlechner, "The Corrosion of Type 316 Stainless Steels in Static and Dynamic Liquid Lithium," in: Proc. 14th Symp. on Fusion Technology, Avignon, France, September 1986.
8. H. V. Borgstedt and J. Konys, "Lithium Corrosion of the Alloys V15Cr5Ti and V3Ti15Si," presented at the Workshop on Lithium and Pb17Li Eutectic. Kernforschungszentrum, Karlsruhe, IMF II, May 1986.

7. SOLID BREEDING MATERIALS

EEATRIX-I IRRADIATION EXPERIMENT - G. W. Hollenberg (Pacific Northwest Laboratory)

OBJECTIVE

The objective of this experiment is to irradiate solid breeder materials from participating IEA countries in a fast neutron reactor environment.

SUMMARY

A tritium solid breeder irradiation experiment was designed and fabricated to reach a goal exposure of 600 full power days in the fast neutron flux of the EBR-II reactor in order to obtain swelling, tritium retention, and stability data. Lithium ceramic pellets, spheres and single crystals from Europe, Japan and the USA are contained within 19 closed capsules. Burn-up levels from 10 to 35×10^{20} captures/cc will be obtained during this irradiation at "isothermal" temperatures on 1 cm diameter pellets from approximately 500 to 900°C. Larger diameter pellets (1.6 to 2.3 cm) will produce large temperature gradients and centerline temperatures of over 1200°C. Characterization of these materials provided an assessment of current fabrication capabilities which exist for these materials.

STATUS AND PROGRESS

Introduction

The investigation of solid breeder materials for tritium production to support DT fusion has increased significantly in the past decade with major fabrication and mixed-spectrum irradiations occurring in Europe, Canada, Japan and the US. As a part of EEATRIX-I test program (Breeder Exchange Matrix), International Energy Agency (IEA) members were invited to contribute samples of state-of-the-art solid breeder materials to a fast reactor irradiation which allows more homogeneous, higher ${}^6\text{Li}$ burn-ups. Closed capsules were used without in situ recovery. This paper provides a description of the irradiation conditions and a summary of the characteristics of the materials.

This experiment is contrasted with previous irradiations¹⁻³ in the EBR-II reactor which have been totally devoted to U.S. fabricated lithium ceramics. Those experiments allowed the observation of several fusion blanket relevant phenomena, such as swelling and lithium transport in Li_2O and tritium release which agreed with trends found in mixed-spectrum in situ recovery tests. The FUBR-1B experiment will provide a high burn-up comparison of materials made by a variety of fabrication routes and will also allow much higher temperatures in large diameter pellets with large temperature gradients.

Experimental Design

Two EBR-II subassemblies were used in this experiment in row 7 reactor positions which are at the edge of the core with a flux of 1×10^{15} n/cm²/sec. One subassembly consisted of 7 pins (2.04 cm OD) with 3 subcapsules per pin while the other contained three larger diameter pins (2.60 cm OD) with 2 subcapsules per pin. Each of the subcapsules contained a 5.08 or 5.71 cm long column of solid breeder material, a cerium getter tab for reduction of T_2O , and a plenum for helium gas build up. All lithium ceramic spheres and pellets were ${}^6\text{Li}$ enriched. For thermal insulation and compatibility, large diameter pellet columns were contained between two discs of depleted Li ceramics with the same chemical composition. Tritium generated within the capsule can diffuse through the stainless steel subcapsule walls into the reactor sodium where it is subsequently removed in the cold traps.

The materials being irradiated in this experiment are listed in Table I along with the site of fabrication. The measured ${}^6\text{Li}$ enrichment of oxide, aluminate, zirconate, and silicate pellets are listed along with densities that vary from 73% (CEN-Saclay- LiAlO_2) to 93% (KfK-Karlsruhe- Li_4SiO_4). Also, spheres of Li_2O (4 m 77.5% T.D.) and Li_4SiO_4 are included with measured densities based upon the weight of the spheres loaded into the subcapsule and the volume of the cavity that was filled. Finally, Li_2O single crystals of natural and depleted ${}^6\text{Li}$ content were included.

The irradiation began in May 1987 for a goal exposure of 600 full power days (4×10^{22} n/cm²). Predicted burn-up levels in Table I were obtained by extrapolating the measured burn-up levels from previous lithium ceramic pins in these same positions³. Heat generation rates were based on these burn-up rates and kerma factors obtained from dosimetry runs near these positions and reactor supplied gamma heating rates. Because of the low neutron cross section the self-shielding was predicted to be less than 5%.

In Table I it can be seen that the heat generation rates of pellets vary from 27 to over 60 W/cc as a result of the effects of ${}^6\text{Li}$ enrichment, position-dependent flux and composition. Similarly, the burn-up varies from 12 to 35×10^{20} atoms/cc for the enriched materials. For Li_2O pellets, burn-up levels of 19×10^{20} atoms/cc represent an end-of-life peak burn-up while for the ternary ceramics, which might be used in conjunction with neutron multipliers, a burn-up of 70×10^{20} atoms/cc may be more representative¹. Hence, the predicted burn-up levels in this test are between 50 and 200% of end-of-life blanket designs.

Thermal analysis was conducted with the axisymmetric HEATING-5 computer code⁴. Unirradiated thermal conductivity values for Li_2O were taken from Takahashi and Kikuchi⁵, for Li_2SiO_3 and LiAlO_2 from Schulz⁶, and for Li_4SiO_4 and Li_2ZrO_3 from Hollenberg⁷. Mizuno⁸ recently reported that the temperature independent thermal conductivity of an Li_2O pebble bed was $0.016 \text{ W/cm}^\circ\text{C}$. This value was adopted for both the Li_2O and the Li_4SiO_4 pebbles. The predicted temperatures in Table I are for the centerline of the pellet. Small diameter pellets are essentially isothermal compared to the 2.3 to 1.0 cm pellets. In Fig. 1 the predicted radial temperature profiles are presented for the large diameter pellets. The large temperature range present in the Li_2O pellets exceeds the upper limits suggested earlier by Johnson and Hollenberg⁹ for Li_2O in order to test the upper limit (which is thought to be associated with mass transfer). In addition, the centerline temperatures for Li_2ZrO_3 and LiAlO_2 are the highest ever tested for ternary solid breeder materials. Higher operating temperatures are typically associated with the enhancement of tritium breeding ratios in actual fusion blankets since less structural material for coolant channels is required.

TABLE I
TEST MATRIX OF SOLID BREEDER MATERIALS

MATERIAL	^6Li ENRICHMENT (%)	COLUMN LENGTH (cm)	COLUMN DIAMETER (cm)	THEORETICAL DENSITY (%)	PREDICTED CENTERLINE TEMPERATURE ($^\circ\text{C}$)	LITHIUM BURN-UP (10^{20} atom/cc)	TOTAL HEATING (W/cc)	TRITIUM PRODUCTION (Ci)
LARGE DIAMETER PELLETS								
LiAlO_2 -Saclay	95	5.08	2.32	73	1124	15	32	1520
Li_4SiO_4 -Karlsruhe	81	5.08	1.64	89	793	24	48	1257
Li_2ZrO_3 -HEDL	95	5.08	1.98	88	1226	24	51	1806
Li_2O -JAERI	56	5.08	1.67	86	905	35	66	1867
SMALL DIAMETER PELLETS								
Li_2O JAERI	56	5.71	.97	82	503	31	60	634
Li_2O JAERI	56	5.71	.97	82	733	27	52	552
Li_2O JAERI	56	5.71	.97	82	970	34	64	680
Li_2O Springfield	56	5.71	.96	80	730	26	51	522
Li_4SiO_4 -Karlsruhe	81	5.71	.95	93	552	27	54	536
Li_2SiO_3 -Karlsruhe	95	5.71	.95	80	758	19	39	368
Li_2ZrO_3 -Springfield	95	5.71	.94	81	758	18	54	349
LiAlO_2 Saclay	95	5.71	.95	73	460	13	30	265
LiAlO_2 Saclay	95	5.71	.95	73	736	12	27	235
LiAlO_2 Saclay	95	5.71	.95	73	959	15	32	289
LiAlO_2 -I Casaccia	95	5.71	.95	80	733	16	35	314
LiAlO_2 -II Casaccia	95	5.71	.95	80	741	16	35	313
SPHERES								
Li_2O MAPI (4 mm Dia)	56	5.71	1.04	45	791	18	35	424
Li_4SiO_4 Karlsruhe (1 mm Dia.)	68	5.71	.98	36	452	10	20	199
SINGLE CRYSTALS								
Li_2O -JAERI	7.5	2.7	.72	--	528	5	21	26
Li_2O -JAERI	0.07	3.0	.72	--	477	.04	14	-

Materials Preparation

Materials in this experiment were fabricated by a variety of routes from enriched lithium carbonate at each of the sites:

Li_2O powder was fabricated at JAERI by the decomposition of Li_2CO_3 under a vacuum of 1×10^{-6} torr for 90 hrs at 795°C . Pellets were then pressed and vacuum sintered at temperatures from 1120 to 1180°C .

Li_2O single crystals were formed at JAERI by zone melting Li_2O rods in an infrared imaging furnace. The rods were formed by isostatically pressing and sintering at 1000°C for 10 hours.

Li_2O spheres were fabricated at Mitsubishi Atomic Power Industries (MAPI) from powder which also was synthesized from Li_2CO_3 decomposition. The powder was pressed into a small sphere by a pair of hemispherical dies and then sintered at 1100°C for four hours.

Li_2O pellets were fabricated at Springfields Laboratory by the vacuum decomposition of Li_2O_2 and then hot pressing the powder. (10)

LiAlO_2 powders were synthesized in Casaccia by two techniques. In both cases a sol gel was prepared from an aluminum nitrate solution and enriched lithium carbonate. The one technique was based upon the microwave heating of the sol for drying (type I) while the other technique required the spray drying of the sol (type II). Pellets were then fabricated by cold pressing and sintering. (11)

LiAlO_2 powders were synthesized at Saclay by the reaction of Li_2CO_3 with fine Al_2O_3 powder. The pellets were then isostatically pressed and sintered. (9)

Li_2SiO_3 powder was synthesized at KfK-Karlsruhe by addition of amorphous SiO_2 to LiOH and precipitation of a hydroxide which was then spray dried and heat treated at 250°C . Pellets were then fabricated by cold pressing and sintering. (12)

Li_4SiO_4 powder was synthesized at Karlsruhe by addition of amorphous SiO_2 to LiOH in methanol which was then spray dried and heat treated at 250°C . Pellets were then fabricated by cold pressing and sintering while spheres were made by extruding rods and rolling into spheres prior to firing. (12)

Li_2ZrO_3 powder was synthesized at ANL by the spray drying of a slurry of Li_2CO_3 and ZrO_2 powder. The slurry was calcined at 650°C for over 72 hours in air. Chlorine free ZrO_2 powder was derived from zirconium nitrate by vacuum decomposition. Pellets were hot pressed at HEDL in graphite dies and annealed in oxygen.

Li_2ZrO_3 powder was synthesized at Springfields Laboratory by the solid-state reaction of Li_2O_2 and ZrO_2 . This powder was then hot pressed into pellets. (10)

Materials Characterization

Characterization of the materials was conducted prior to finish grinding, final vacuum outgassing and pin loading. Microstructural and chemical characteristics of the materials are listed in Table II.

The characteristic grain sizes appeared to be related to the various solid breeder compositions as shown in Table II and Figure 2. The high lithium content ceramics, i.e., Li_2O and Li_4SiO_4 , possessed larger grain sizes than the more refractory Li_2ZrO_3 and LiAlO_2 pellets which possessed submicron grain sizes. From a diffusional tritium release point of view the stable submicron grain sizes are attractive but must be coupled with an adequate diffusion coefficient. The specific surface areas were measured by BET analysis with krypton. The specific surface area values appear to be roughly consistent with the observed grain sizes in that large grained samples (Li_4SiO_4 and Li_2O) possessed surface areas less than $0.1 \text{ m}^2/\text{cm}^3$ while the fine grained Li_2ZrO_3 and LiAlO_2 materials possessed greater than $0.5 \text{ m}^2/\text{cm}^3$ surface areas.

The average density of the materials in Table I was not constant but ranged from 73% to over 90% of theoretical depending on the source; demonstrating density to still be a major fabrication variable. In Table II the open and closed porosity of individual samples as measured by a gas pycnometer are listed. Less than 3% of the porosity was in the form of closed porosity which indicates that tritium release can occur through the pore channels from the central regions of the pellet even for materials of 90% TD.

The X-ray diffraction analysis of these materials indicated that almost all of these materials were phase pure. The major exception to this was the presence of approximately 5% Li_2SiO_3 in the Li_4SiO_4 pellets. A lithium assay analysis was conducted by acid dissolution and inductively coupled plasma spectroscopy. The values for Li_2SiO_3 , Li_2ZrO_3 , and LiAlO_2 agree with the stoichiometric values considering the errors present in this analysis. The lithium assay for the Li_4SiO_4 pellets was approximately 4% lower than what would be calculated from the stoichiometric composition. This reinforces the belief that high lithium compounds, i.e., Li_4SiO_4 , Li_8ZrO_6 , etc., are generally less stable and more difficult to process without phase separation. The low values for the lithium content of the Li_2O may be caused by absorbed water in the samples prior to measurement. Isotopic ratios were preselected on the basis of lithium reaction rates and heat generation rates. For the most part, material fabricators were able to obtain isotopic ratios, as measured by spark source mass spectroscopy, to within 2% of the prescribed amount even with the very small batches used for this testing.

Individual metallic impurity levels in these samples were measured by spark source mass spectrographic analysis and the total impurities are included in Table II. Levels of total impurities below 2000 ppm were found in all materials and in most materials it was possible to obtain less than 1000 ppm. The zone-melted Li_2O single crystals were found to have total impurity levels as low as 96 ppm.

Metallic impurities will be important in actual blankets because of their contribution to radioactivity, a concern during decommissioning. Only chlorine and fluorine anionic impurities were measured because of their importance in stress corrosion cracking but were found to be less than 20 ppm for each sample examined.

Table II

Characterization Data on Lithium Ceramics

Material	Grain Size(um)	Surface Area (m ² /cc)	Porosity (%) Open/ Closed	XRD Phases	Li Content (%) Measured/ Stoichiometric	Total Impurities
Li ₄ SiO ₄ Spheres Karlsruhe	8	0.10	--- 2.8	-----	-	457 ppm
Li ₄ SiO ₄ Pellets Karlsruhe	33	0.04	7.8 / 2.0	95% Li ₄ SiO ₄	16.7 / 21/2	783 ppm
Li ₂ SiO ₃ Pellets Karlsruhe	24	0.10	18.5 / 0.1	100% Li ₂ SiO ₃	15.0 / 13.7	944 ppm
Li ₂ O Pellets JAERI	13	0.01	15.2 / 2.1	100% Li ₂ O	38.4 / 44.6	503 ppm
Li ₂ O Pellets Springfield	7	0.037	19.3 / 2.7	100% Li ₂ O	38.0 / 44.6	1304 ppm
Li ₂ O Spheres MAPI	7	0.017	--- / 0.0	100% Li ₂ O	37.7 / 44.6	318 ppm
Li ₂ ZrO ₃ Pellets Springfield	1.4	0.561	18.4 / 0.1	100% Li ₂ ZrO ₃	8.3 / 8.0	1950 ppm
Li ₂ ZrO ₃ Pellets HEDL	0.3	-----	11.2 / ---	100% Li ₂ ZrO ₃	8.7 / 8.0	353 ppm
LiAlO ₂ Pellets Casaccia I	0.4	0.58	17.9 / 1.8	100% LiAlO ₂	9.7 / 9.3	159 ppm
LiAlO ₂ Pellets Casaccia II	0.4	3.1	17.4 / 2.2	100% LiAlO ₂	9.3 / 9.3	783 ppm
LiAlO ₂ Pellets Saclay	0.3	0.51	26.5 / 0.1	100% LiAlO ₂	8.8 / 9.3	1464 ppm

CONCLUSIONS

An international effort has resulted in a fast neutron irradiation experiment which will evaluate the stability and performance of a variety of solid breeder single crystals, spheres and pellets. In addition to achieving moderate to high lithium burn-up levels, large diameter pins were found to be capable of simulating or exceeding the large temperature differences used for design purposes.

FIGURES

1. Predicted Temperature Distribution in the Large Diameter Pellets. Large Temperature Differences Typical of Blanket Operating Conditions Exist in These Pellets.
2. Photomicrograph of Lithium Ceramic Microstructures Reveal the Large Grain Size of Li₂O and Li₄SiO₄ in Comparison to the Submicron Grain Size of Li₂ZrO₃ and LiAlO₂.

TABLES

- I. Test Matrix of Solid Breeder Materials
- II. Characterization Data on Lithium Ceramics

REFERENCES

1. G. W. Hollenberg, R. C. Knight, et. al., J. Nucl. Mater. 141-143 (1986) 271-274.
2. D. L. Porter, et. al., J. Nucl. Mater. 122 & 123 (1984) 929-933
3. D. L. Baldwin, G. W. Hollenberg, J. Nucl. Mater. 141-143 (1986) 305-310
4. W. D. Turner, D. C. Elrod, and I. I. Siman-Tov, ORNL/CSD/TM-15, 1977
5. T. Takahashi and T. Kikuchi, J. Nucl. Mater. 91 (1980) 93-102

REFERENCES - Continued

6. B. Schulz, Proc. Fus. Reactor Blanket & Fuel Cycle Tech. Symp., Tokai-mura, 1986, Eds. Takahashi and Tanaka
7. G. W. Hollenberg and D. E. Baker. HEDL-SA-2674 (1982)
8. M. Mizuno, H. Akiyama. and M. Katou. Proc. Japan Nucl. Soc., Kyoto (1986)
9. C. E. Johnson and G. W. Hollenberg. J. Nucl. Mater. 122 6123 (1984) 871-881
10. P. Kennedy, R. Conrad. H. Hevast and E. Brauns, "Exotic Development of Ceramic Tritium Breeding Materials." Nov. 1986 Studlecentrum voor Kernenergie (SCK/CFN), Brussels. Belgium.
11. C. Alvanf, C. Ciavola, S. Casadio and A. DiBartolomeo, Fusion Technology (In Press).
12. D. Vollath and H. Wedemeyer. in Advances In Ceramics Vol 25 (1988) (to be published). "Fabrication and Properties of Lithium Ceramics." I. Hastings and G. Hollenberg. editors.

SOLID BREEDER MATERIALS FABRICATION AND MECHANICAL PROPERTIES - R. B. Poeppel, K. Štr, and C. Y. Chu
(Argonne National Laboratory)

OBJECTIVE

The objectives of this program are to synthesize ceramic powders and/or fabricate samples of candidate solid breeder materials for various international cooperative irradiation test programs, and to characterize the mechanical properties of selected lithium ceramics.

SUMMARY

Samples of lithium orthosilicate were fabricated for mechanical properties tests. Ceramic-grade powder was synthesized from stoichiometric mixtures of lithium carbonate and amorphous silica. Samples were pressed from the powder and sintered in air at temperatures between 950 and 1100°C. Compression tests were conducted at constant crosshead speed in a furnace filled with argon. Temperatures ranged from 750 to 1000°C and strain rates were between 10^{-6} and 10^{-4} s⁻¹. A steady-state stress was obtained as a function of strain rate at each of three temperatures. The stress exponent was found to range from a value of -6.5 at 850°C to -3.3 at 950°C. Two manuscripts^{1,2} were prepared for the Proceedings of the American Ceramic Society Special Symposium on "Fabrication and Properties of Lithium Ceramics." Abstracts have been prepared for the 90th Annual Meeting of the American Ceramic Society, Nuclear Division, to be held in Cincinnati on May 1-5, 1988.

PROGRESS AND STATUS

Lithium orthosilicate (Li₄SiO₄) is being considered as a potential breeder blanket material for fusion reactors because of its high lithium atom density (520 x 10²⁰ atoms/cm³) and high stability. Although lithium oxide has the highest lithium atom density of any of the lithium materials (816 x 10²⁰ atoms/cm³), it reacts with H₂O and CO₂ and has to be handled in a dry inert atmosphere. Besides, water exposure during operation could be detrimental to the use of lithium oxide as blanket material. Room-temperature strength and toughness are important properties relative to handling and installation of breeder blankets. Once in service, the blanket would be subjected to stress at high temperature because of thermal expansion or helium-induced swelling. Swelling of the solid breeder material can directly impact the design lifetime of the blanket. Therefore, knowledge of both room temperature and high-temperature mechanical properties is essential for designing an efficient blanket.

Preparation and fabrication procedures for lithium orthosilicate have been developed. Various synthesis routes for Li₄SiO₄ powder have been proposed. During this reporting period, ceramic-grade Li₄SiO₄ powder was prepared from suspensions of stoichiometric amounts of lithium carbonate and amorphous silica in isopropanol. The intimate mixture of 2Li₂CO₃·SiO₂ in the suspension was first pan dried in air. The pan-dried powder then underwent calcination and reaction at 650°C:



A Li/Si ratio of 3.94 was measured by chemical analysis (induction-coupled-plasma/atomic-emission spectroscopy); the value for stoichiometric lithium orthosilicate is 4.00. X-ray diffraction analysis revealed that a minor second phase of lithium metasilicate (Li₂SiO₃) was present. Li₂ZrO₃, which was introduced during ball milling, was identified by energy dispersive x-ray spectroscopy as the principal impurity. Additive (polyethylene glycol) was ball milled with the calcined powder in isopropanol. The suspension was then spray dried. An average particle size as small as 1 μm was obtained. The powder was cold pressed into cylindrical pellets and rectangular bars at selected pressures in the range of 124 MPa (18,000 psi) to 193 MPa (28,000 psi). A green density as high as 68% of theoretical was achieved. The pellets and bars were sintered at temperatures between 950°C and 1100°C. Densities between 70 and 95% of theoretical have been achieved. These sintered pellets and bars were later used for mechanical-properties studies.

Chemical analysis and x-ray diffraction data indicated that the wearing rate of alumina media during the ball milling stage was higher than for zirconia media. Hence, ZrO₂ media were used for all ball milling. Two drying techniques, pan drying and spray drying, were practiced. Powder produced by the pan-dried technique had irregular particle shapes with a smaller surface area and broader particle size distribution. However, this technique is required to dry the intimate mixtures of 2Li₂CO₃·SiO₂ suspension. Because the initial particle size of amorphous silica powder (0.014 μm) is much smaller than that of lithium carbonate powder (12 μm), the silica tends to be ventilated away during spray drying. On the contrary, spray-dried powder has a spherical particle shape with a larger surface area and a narrower particle size distribution. So the spray-dried technique was applied to the Li₄SiO₄ suspension just before pressing. Calcination time tests suggested that at 650°C, 48 h is not sufficient for complete calcination; residual Li₂CO₃ and amorphous SiO₂ were detected by x-ray diffraction. A longer time of about 72 h is required to complete the reaction. Calcination at higher temperature reduces the calcination time, but also produces larger particle sizes.

Pressing with and without binder and at different pressures has also been investigated. Pressing without binder resulted in lower green and sintered densities, and sometimes collapse of the green body. Pressing at higher pressure produced higher green density. However, excessive pressure also led to cracking. An optimizing pressure should be obtained in order to achieve the optimum density without cracking. Sintering temperature had a larger effect than sintering time on the final density. Sintering time had a larger effect on grain growth than on density. Thus, grain-size variations at the same density can be achieved for a given temperature by changing the sintering time.

Compression tests were conducted at constant crosshead speed in a furnace filled with argon. Temperatures ranged from 750 to 1000°C (0.67 to $0.8 T_m$, where T_m is the melting temperature of Li_4SiO_4 in Kelvin) and strain rates were between 10^{-6} and 10^{-4} s^{-1} . The data were recorded as load vs time. Final specimen dimensions were used to convert the load/time data to stress vs strain. Scanning electron microscopy was used to determine grain sizes before and after testing. Stress exponents were obtained and possible rate-controlling deformation mechanisms were determined from these values.

In all tests in which fracturing did not occur, a steady-state stress, σ_s , was obtained. Values of σ_s vs $\dot{\epsilon}$ at three different temperatures are plotted in Fig. 1. Values of n (stress exponent) obtained in these tests are plotted in Fig. 2. A monotonic decrease in n with increasing temperature is apparent for temperatures from 850 to 950°C. At 950°C, n is approximately 3.3, which is within the range predicted by theory and found for many materials. Li_4SiO_4 exhibited extensive plasticity at high temperatures, with strain of greater than 50% achieved.

Comparison with other lithium compounds at a given temperature reveals that Li_4SiO_4 requires greater stress to deform plastically than did Li_2O , and less than Li_2ZrO_3 or LiAlO_2 . Data on the effect of aspect ratio (length/diameter ratio of the pellet) on the steady-state stress are shown in Fig. 1 (top panel). A higher aspect ratio results in lower steady-state stress, which is thought to be due to the inhomogeneity of the material in pellets with a higher aspect ratio.

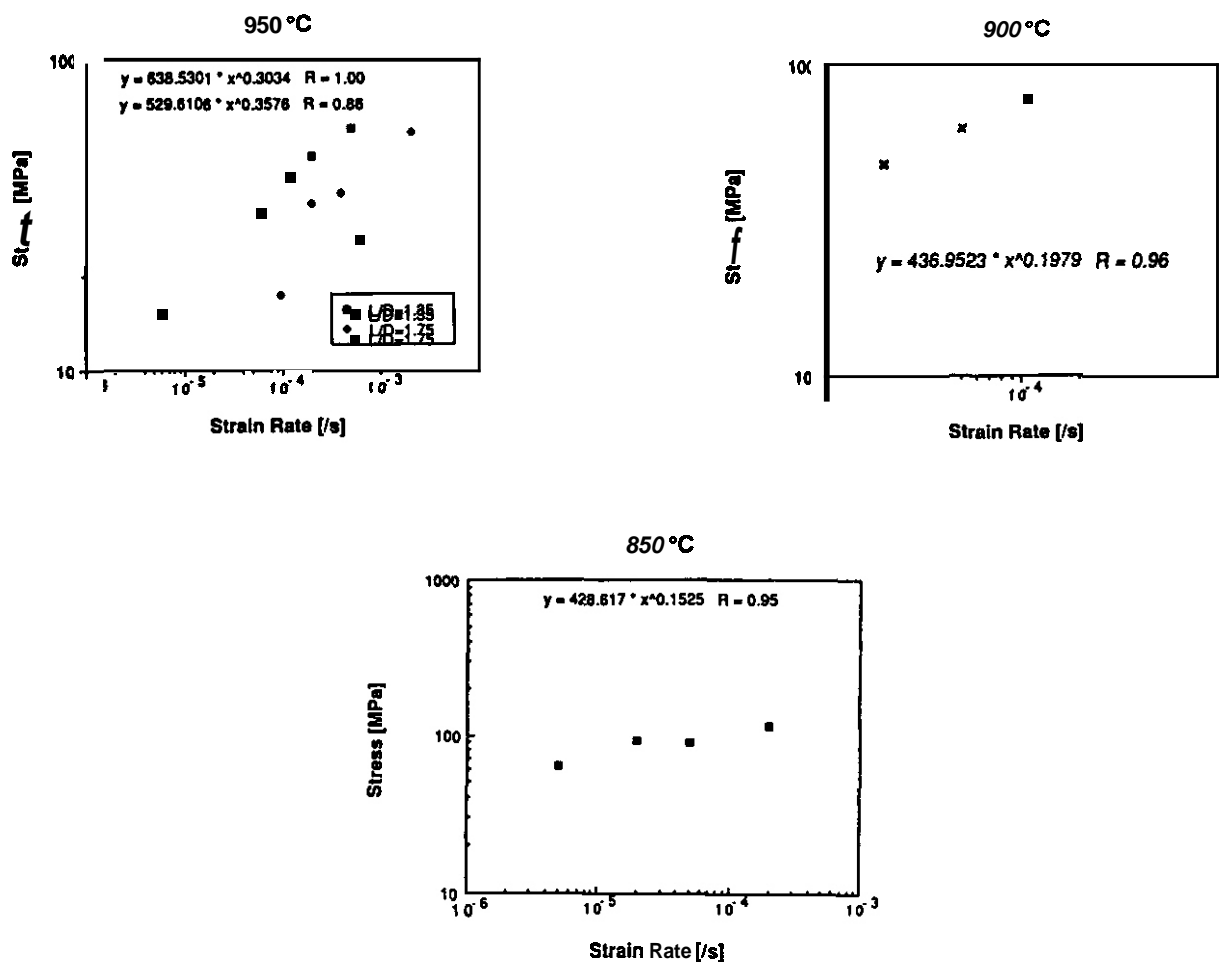


Fig. 1 Steady-state stress vs strain rate for three temperatures: 950, 900, and 850°C.

Stress Exponent vs T

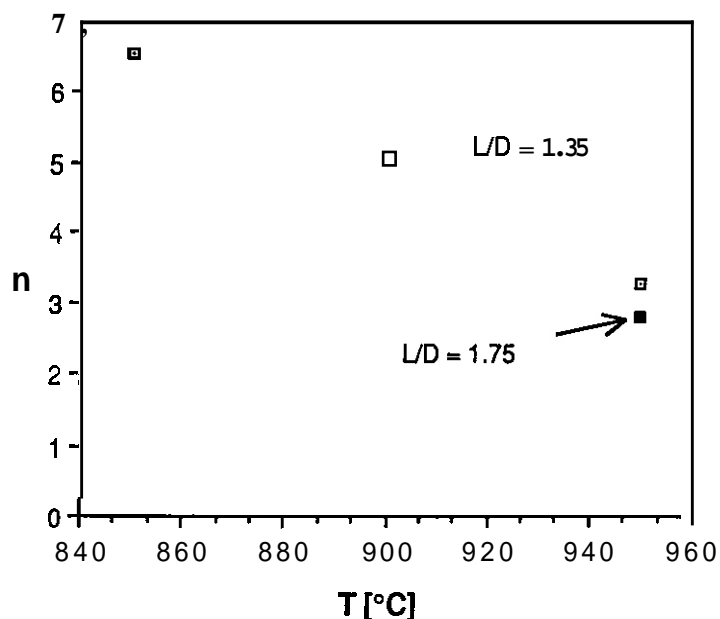


Fig. 2. Dependence of stress exponent on temperature.

FUTURE WORK

This task will be closed out early in FY 1988. A paper describing the results will be prepared for the International Symposium on Fusion Nuclear Technology to be held in Tokyo, Japan, on April 10-15, 1988.

The sintered volume shrinkage of the pellets and bars will be discussed in terms of the fundamental shrinkage equation. Addition of an excess amount of silica enhanced sintering. The possible mechanisms of this phenomenon will be identified. Since the grain size of the breeder material influences its tritium recovery and, to some extent, its mechanical properties, the effect of MgO addition on grain growth will also be explored.

Effects of porosity and grain size on the steady-state stress will be examined. Activation energy will be calculated when sufficient data have been collected. Transmission electron microscopy will be used to examine dislocation structures and thus confirm the mechanism of high-temperature deformation.

REFERENCES

1. D. S. Applegate and R. B. Poeppel, "CRITIC-I Instrumented Lithium Oxide Irradiation Part 1 - Lithium Oxide Fabrication and Characteristics," to be published in Proc. Symp. on Fabrication and Properties of Lithium Ceramics, 89th Ann. Mtg. of Am. Ceram. Soc., Pittsburgh, Pa., April 26-30, 1987.
2. R. B. Poeppel, J. L. Routbort, E. Buchmann, S. Lonschien, D. S. Applegate, and M. C. Billone, "Steady-State Deformation of Some Lithium Ceramics," *ibid.*

ADSORPTION, DISSOLUTION, AND DESORPTION CHARACTERISTICS OF THE $\text{LiAlO}_2\text{-H}_2\text{O}$ SYSTEM, Albert K. Fischer and Carl E. Johnson (Argonne National Laboratory)

OBJECTIVE

The objective of this work is to provide measured thermodynamic and kinetic data related to tritium retention and release from ceramic tritium breeder materials. Such data relate to issues of tritium retention and release, and, hence, to concerns about tritium inventory. The information will enable (1) comparison of candidate breeder materials, (2) calculation of operating conditions, and (3) elucidation of the phenomena underlying the behavior of tritium in breeder materials.

SUMMARY

Isotherms at 673 and 773 K are presented for surface adsorption of $\text{H}_2\text{O}(\text{g})$ and for solubility of OH^- in LiAlO_2 as a function of $\text{H}_2\text{O}(\text{g})$ partial pressure. The Freundlich adsorption isotherms for 673 and 773 K, respectively, are:

$$\log(\theta) = (-1.590 \pm 0.691) + (0.497 \pm 0.064) \log(p_{\text{H}_2\text{O}})$$

and

$$\log(\theta) = (-1.112 \pm 0.061) + (0.497 \pm 0.052) \log(p_{\text{H}_2\text{O}})$$

where θ is the fraction of surface covered, and $p_{\text{H}_2\text{O}}$ is the partial pressure $\text{H}_2\text{O}(\text{g})$ in Pascals. Hydroxide dissolution is exothermic. Depending on conditions, LiAl_5O_8 can be a second phase or a solute to give isotherms with slopes of 0.5 or 0.4, respectively. The hydroxide solubility isotherms for 673 and 773 K, respectively, are:

$$\log(x_{\text{OH}}) = (-4.667 \pm 0.096) + (0.399 \pm 0.088) \log(p_{\text{H}_2\text{O}})$$

and

$$\log(x_{\text{OH}}) = (-4.899 \pm 0.079) + (0.499 \pm 0.063) \log(p_{\text{H}_2\text{O}})$$

where x_{OH} is the mole fraction OH^- . The rate of $\text{H}_2\text{O}(\text{g})$ evolution from LiAlO_2 showed the kinetics of the process to be second order in hydroxide with an activation energy of 14.7 ± 1.9 kcal (61.5 ± 7.9 kJ), a value less than that reported for $\text{H}_2\text{O}(\text{g})$ evolution from Li_2O or from LiOH .

PROGRESS AND STATUS

INTRODUCTION

Accounting for the tritium inventory in the tritium breeding blanket of a fusion reactor requires, among other things, knowledge of: (1) the adsorption-desorption characteristics of tritium-containing species on the breeder surface, (2) the solubility of tritoxide and tritide in the bulk breeder, and (3) the kinetics of various processes that transport tritium out of the breeder. An experimental study on LiAlO_2 is presented that provides information for the thermodynamics of adsorption of $\text{H}_2\text{O}(\text{g})$ and dissolution of OH^- , and for the kinetics of the evolution of $\text{H}_2\text{O}(\text{g})$. Detailed thermodynamic calculations performed earlier [1] indicated that the solubility of hydroxide in a breeder is, in general, dependent on the oxygen activity. For low oxygen activities (below about 10^{-15}) the dependence is significant, but for the oxygen activities above this level, such as in high purity helium, the dependence is slight. Although the effect of low oxygen activity on the measured values was not addressed, the question will be examined experimentally by the use of gases with fixed ratios of $\text{H}_2\text{O}:\text{H}_2$. Effects related to low oxygen activities are the subject of future reports.

EXPERIMENTAL

Adsorption measurements were made by the frontal analysis technique of gas chromatography [2], also known as the breakthrough technique. The method is to introduce a gas stream with a known flow rate and partial pressure of $\text{H}_2\text{O}(\text{g})$ into the inlet of a packed column of the sample at a known time. A Beckman H_2O analyzer measures the $\text{H}_2\text{O}(\text{g})$ level in the effluent gas. Because the adsorption process is rapid, the response of the analyzer remains at the preinjection baseline level until the surface of the sample reaches the degree of coverage that is thermodynamically required by the prevailing temperature and partial pressure of $\text{H}_2\text{O}(\text{g})$. At that time, water vapor emerges at the end of the column (breakthrough occurs) and the analyzer records a sharp rise in water level in the effluent gas. A similar technique was used by Yoshida et al [3] to study surface adsorption of H_2O on Li_2O .

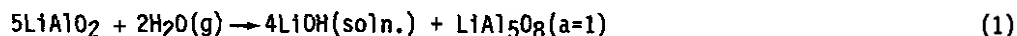
Figure 1 is a schematic representation of typical data from an experimental run. The area "ADS" indicates the amount of water vapor adsorbed on the surface. Reaction and dissolution of hydroxide is a slower process than adsorption and was recorded in the next part of the curve measuring the uptake of $H_2O(g)$. In this region of increasing H_2O content in the effluent gas, the area after the breakthrough point and before the level of the plateau is a measure of the solubility of hydroxide and is labeled "SOL" in Fig. 1. Establishment of the plateau level of the water concentration in the gas phase indicates equilibrium of the solid with the hydroxide reaction product at an activity corresponding to p_{H_2O} . After this plateau, the gas phase composition was switched back to pure helium and evolution of $H_2O(g)$ was recorded. Integration under this curve, area "EV" in Fig. 1, provided data for the kinetic analysis of the water evolution process.

The γ - $LiAlO_2$ particles were used as purchased from CERAC. They had a particle size range of 150 to 300 μm and a surface area of 0.16 ± 0.02 m^2/g (BET analysis). A sample column was loaded with 0.333 mol of this material. Its purity was 99.9%, with Na, Fe, Ca, Mg, Cu, and Si accounting for the 0.1% impurity content.

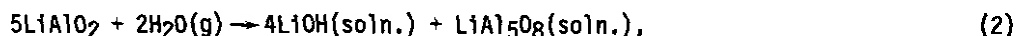
RESULTS

Baseline corrections. Because the baseline conditions always involve a small partial pressure of $H_2O(g)$, there will always exist some residual hydroxide, both on the surface and in the bulk. These amounts of residual hydroxide must be added to the amounts measured on the surface and in the bulk in order to obtain corrected data. The amount of this residual hydroxide was estimated for the adsorption and the solubility measurements to provide the necessary corrections. The estimate involved an experiment and a calculational part. Experimentally, after the water evolution had run its course and the baseline was reestablished, the sample was heated to 939 K (666°C). This temperature was selected to avoid sintering of the surface and thereby altering its area. Under these conditions, the additional $H_2O(g)$ evolution provided a partial measure of the amount of residual hydroxide remaining in the sample in equilibrium with the partial pressure of $H_2O(g)$ in the helium sweep gas. The difference between the amounts of water evolved in the heatings from 673 to 939 K and from 773 to 939 K was $(8.32 \pm 4.6) \times 10^{-7}$ mol (one standard deviation).

The total amount of residual hydroxide had to be estimated and apportioned between that to be ascribed to the surface and that to be ascribed to the bulk. This estimation was approached in the following way. The slope of $\log(\theta)$ or $\log(x_{OH})$ vs. $\log(p)$ curves obtained from the raw data for adsorption and solubility had values greater than 0.5. (θ is the fraction of surface covered, x_{OH} is the mole fraction of hydroxide in the bulk, and p is the partial pressure of $H_2O(g)$.) At 673 K the raw values of the slopes were 0.550 and 1.032 for the adsorption and solubility curves, respectively. These values were 0.673 and 0.606, respectively, for 773 K. However, a value 0.5 would be expected for the slope of the adsorption isotherm for dissociative adsorption of H_2O . Furthermore, a value of 0.5 would be expected for the hydroxide dissolution process if it produces insoluble $LiAl_5O_8$ (activity, a , is equal to 1) according to the reaction,



However, if $LiAl_5O_8$ is soluble in $LiAlO_2$ so that the reaction is



the slope would be 0.4. Applying additive corrections for the residual quantities to each measured value of θ or x_{OH} would reduce the slopes of the respective curves. By an iterative process, the incremental values needed to produce curves with slopes of 0.5 were determined. The values of 673 K are 7×10^{-3} for θ and 1.95×10^{-5} for x_{OH} . At 773 K they are 6×10^{-2} for θ and 8.4×10^{-6} for x_{OH} . The incremental values of mol fraction hydroxide needed to produce curves with slopes of 0.4 for the solubility data were also determined. They are 3.0×10^{-5} and 2.0×10^{-5} for 673 and 773 K, respectively. The selection of these values is explained in the discussion section.

Surface adsorption. Figure 2 presents the surface adsorption isotherms for adsorption of $H_2O(g)$ on $LiAlO_2$ at 673 K and 773 K. The value of θ is based on the measured surface area and on the approximation that the size of one adsorption site is 10^{-15} cm^2 . This assumption is based on observations by DeBoer et al. [4] that the water monolayer capacity on alumina corresponds to 1.1×10^{15} sites/ cm^2 . Also, the crystallographic surface density of aluminum atoms on alumina has been reported to be $1.02 \times 10^{15}/cm^2$ [5]. Possibly, a maximum value for site density could be set because there are 1.7×10^{15} oxide ions in a close-packed sheet [6]. However, all exposed faces of the $LiAlO_2$ sample are not necessarily such crystallographic planes.

Both isotherms are of the Freundlich type and include the additive corrections for residual surface OH groups to produce a slope of 0.5. The linear regression equations representing the adsorption isotherms,

$$\log(\theta) = (-1.590 \pm 0.691) + (0.497 \pm 0.064) \log(p_{H_2O}) \quad (3)$$

and

$$\log(\theta) = (-1.112 \pm 0.061) + (0.497 \pm 0.052) \log(p_{H_2O}) \quad (4)$$

where p_{H_2O} is the partial pressure of $H_2O(g)$ in Pascals.

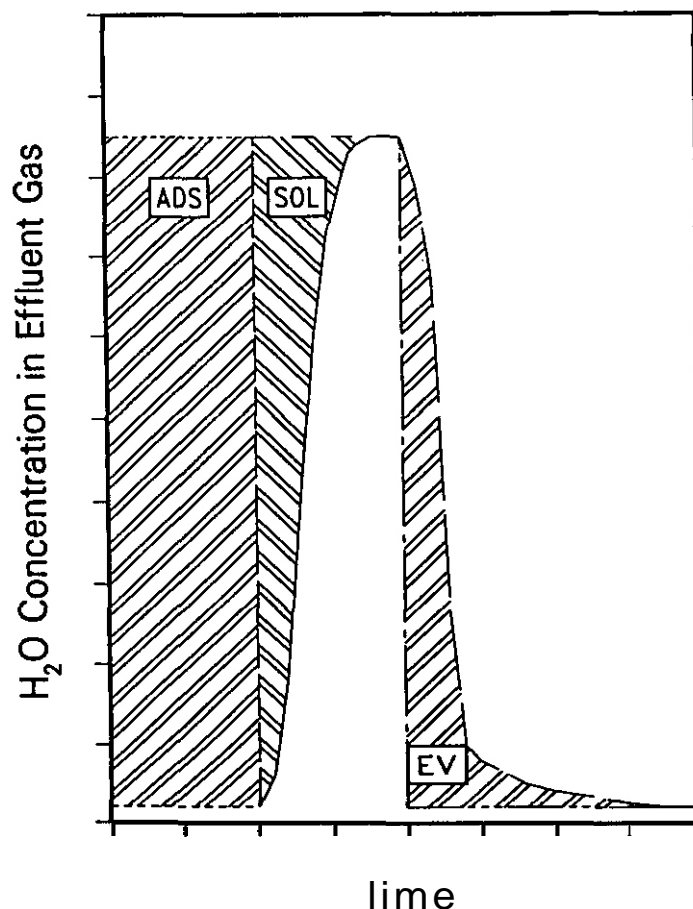


Fig. 1. General form of data from an experimental run showing the regions characterizing adsorption of $\text{H}_2\text{O}(\text{g})$ (ADS), solubility of OH^- in LiAlO_2 (SOL), and rate of evolution of $\text{H}_2\text{O}(\text{g})$ (EV).

Solubility. Figure 3 presents the isotherms for the solubility of OH^- in LiAlO_2 at 673 K and 773 K. These isotherms include the additive corrections for residual hydroxide and give a slope of 0.4 for 673 K and 0.5 for 773 K. The reasons for these values of slopes are presented in the discussion section. The linear regression equations for 673 K and 773 K, respectively, are:

$$\log(x_{\text{OH}}) = (-4.667 \pm 0.096) + (0.399 \pm 0.088) \log(p_{\text{H}_2\text{O}}) \quad (5)$$

and

$$\log(x_{\text{OH}}) = (-4.899 \pm 0.079) + (0.499 \pm 0.063) \log(p_{\text{H}_2\text{O}}) \quad (6)$$

Based on a reference state of LiOH for unit activity at the temperatures of the measurements and with Tetenbaum and Johnson's data [7] for the $\text{LiOH-Li}_2\text{O-H}_2\text{O}(\text{g})$ equilibrium, activity coefficients were calculated for LiOH as a solute in LiAlO_2 . Within the precision and range of the measurements, the activity coefficients are independent of composition and are $1.4 \times 10^4 \pm 2 \times 10^3$ and $4.3 \times 10^3 \pm 3 \times 10^2$ at 673 and 773 K, respectively.

Kinetics of $\text{H}_2\text{O}(\text{g})$ evolution. Kinetic data for the $\text{H}_2\text{O}(\text{g})$ evolution process were obtained by stepwise integration under the curves corresponding to the EV area of Fig. 1. To determine the reaction order, a generalized rate equation was used:

$$dx_{\text{OH}}/dt = k_g(a - m_{\text{OH}})^n \quad (7)$$

where dx_{OH}/dt is the rate of water loss expressed in terms of hydroxide, k_g is the generalized rate constant, a is the amount of hydroxide present in the system at the zero time for the start of the kinetic analysis, m_{OH} is the amount of hydroxide that has been lost (as H_2O) at time, t , and n is the kinetic order of the process. The values of a and m_{OH} were also corrected for residual hydroxide by the same amounts as discussed above. The reaction order was found to be 2.22 ± 0.17 for 673 K and 1.95 ± 0.17 for 773 K. The reaction appears to be essentially second order. This result justified plotting the data as $m/a(a-m)$ vs. kt , for which a linear fit is characteristic of second-order kinetics. General conformance to linear

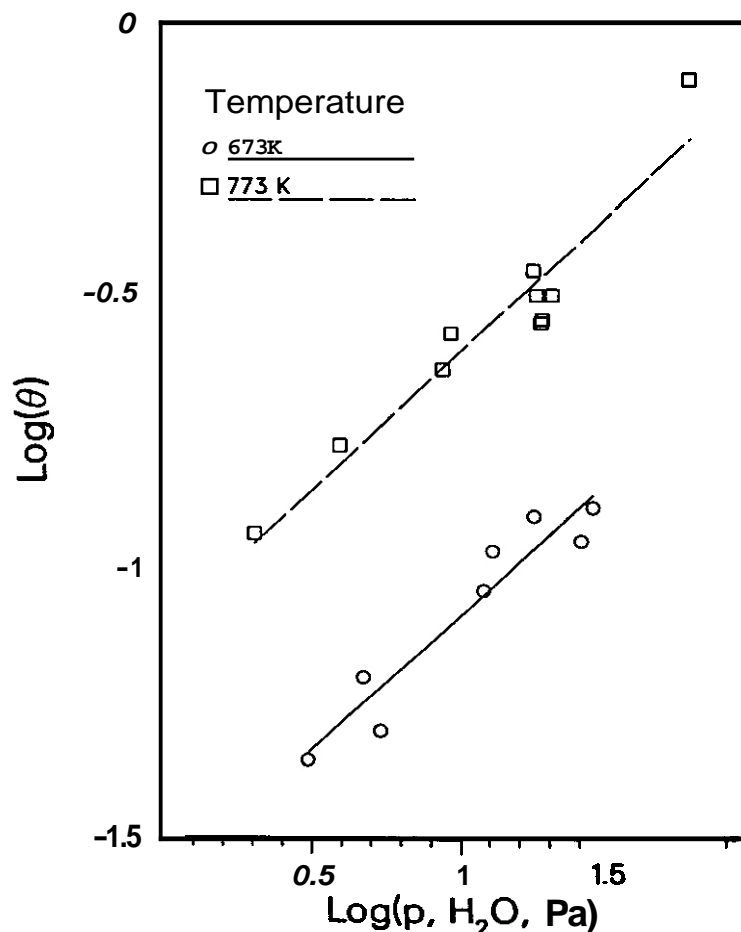


Fig. 2. Surface adsorption isotherms for the $\text{LiAlO}_2\text{-H}_2\text{O}(\text{g})$ system at 673 and 773 K.

behavior was found. The second-order rate constants derived in terms of evolved $\text{H}_2\text{O}(\text{g})$ in units of $(\text{mol min})^{-1}$ were $995+130$ for 673 K and $4118+538$ for 773 K. The activation energy derived from these second-order rate constants is $14.7+1.9$ kcal ($61.5+7.9$ kJ).

Post-run heatup results. For several cases, following completion of $\text{H}_2\text{O}(\text{g})$ evolution at the temperature of a run, the temperature was raised to about 923 K. The curve for the subsequent $\text{H}_2\text{O}(\text{g})$ evolution under these conditions often showed up to three peaks. The relative heights of these peaks were variable. A detailed interpretation of them has not been made yet. However, their occurrence is consistent with the Freundlich view that the absorption process involves sites of different properties and energies.

DISCUSSIONS AND CONCLUSIONS

The choice of increments of mole fraction hydroxide needed to correct the raw data for residual hydroxide to give slopes of 0.4 or 0.5 for the $\log(x_{\text{OH}})$ vs. $\log(p_{\text{H}_2\text{O}})$ curves was based on the following considerations. First, in heating the sample under a constant low partial pressure of $\text{H}_2\text{O}(\text{g})$, the baseline helium flow conditions, evolution of $\text{H}_2\text{O}(\text{g})$ was observed. On cooling, uptake of $\text{H}_2\text{O}(\text{g})$ was observed. This is a direct observation that, under conditions of constant partial pressure of $\text{H}_2\text{O}(\text{g})$, the overall adsorption/solubility decreases as temperature rises. The overall process is, therefore, exothermic. (Endothermic behavior for solubility was observed for Li_2O by Tetenbaum et al [8] and by Norman and Hightower [9]. If the solubility data points had been adjusted so that both isotherms had slopes of either 0.4 or 0.5, the isotherms would have been essentially identical. This would indicate that solubility is independent of temperature, which is not consistent with the observations made when the samples were heated. The assignment of slope to the isotherms was thus based on a comparison between (1) the observed difference in evolved H_2O on heating to 939 K from 673 and from 773 K and (2) the difference between the total moles of H_2O equivalent to the

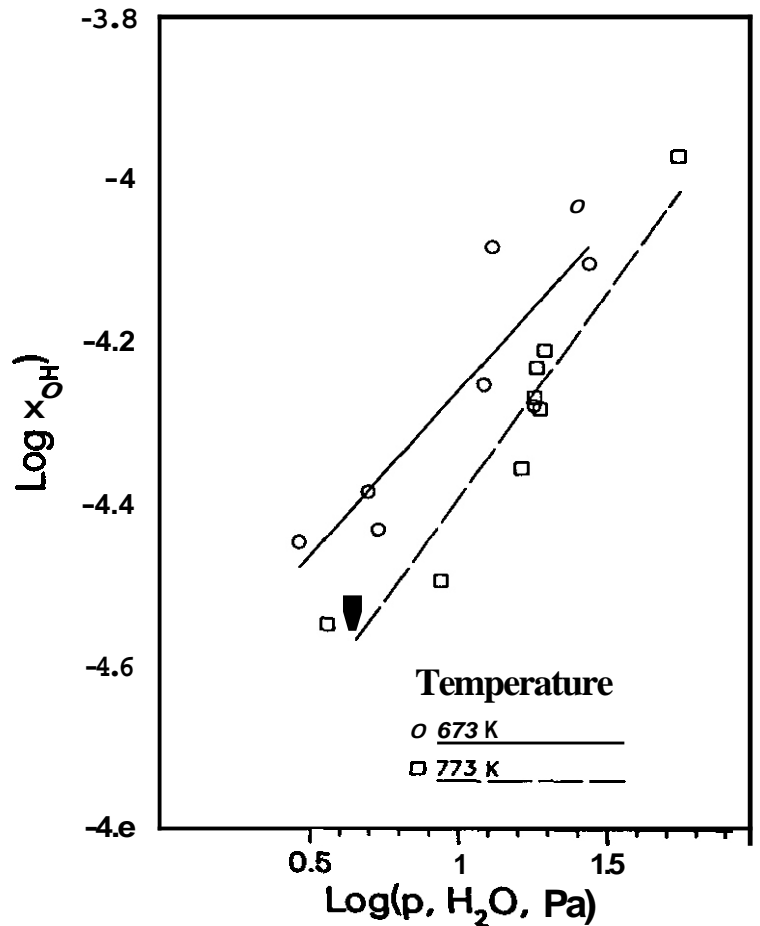


Fig. 3. Isotherms for the solubility of hydroxide in LiAlO_2 at 673 and 773 K.

increments of hydroxide required to produce the 0.4 and 0.5 slopes for the two temperatures. Within experimental error, the slope assignment of 0.4 to the 673 K isotherm and 0.5 to the 773 K isotherm was consistent with the difference in water evolved in the heating from these temperatures to 939 K.

For the $\text{H}_2\text{O}(\text{g})$ partial pressure range of these measurements, the comparison of the slopes of the solubility curves suggests that LiAl_5O_8 is soluble in LiAlO_2 at 673 K but not at 773 K, an example of retrograde solubility. In terms of the ternary phase diagram for the LiAlO_2 - LiOH - LiAl_5O_8 system, the relevant portion is a minute region around the LiAlO_2 corner. In general, one would expect a single-phase region of solubility at the corner. Adjacent to it, there would be two-phase regions, one involving LiOH as a second phase, and one involving LiAl_5O_8 as a second phase. The latter is the one under consideration. The $p_{\text{H}_2\text{O}}$ values in the measurements are below the values that would be required for a LiOH phase to exist, namely 30 Pa at 673 K and 376 Pa at 773 K [10]. Also, the two temperatures, 673 and 773 K, bracket the melting point of LiOH, 744 K. It is possible that the behavior of OH^- would be different below and above this temperature. If so, then isotherms for both adsorption and solubility would reflect different processes. It becomes necessary, therefore, to measure additional, more closely spaced isotherms to separate the effects clearly.

To provide a benchmark for reactor blanket conditions, the solubility of tritium as tritons in the form of tritoxide is: $\text{wppm T} = 4.5 \times 10^4 x_{\text{OH}}$, assuming no isotope effect. Extrapolation to 1 wppm $\text{H}_2\text{O}(\text{g})$ in the sweep gas at 10^5 Pa total pressure gives 0.39 and 0.18 wppm T in LiAlO_2 at 673 and 773 K, respectively.

For the Li_2O system, the hydroxide activity coefficients in the present $p_{\text{H}_2\text{O}}$ range are 3.2×10^5 and 3.0×10^4 for 673 and 773 K, respectively [8]. The ratio of hydroxide activity coefficient in Li_2O to that in LiAlO_2 is about 23 and 7 for 673 and 773 K, respectively. Non-ideal behavior appears to be stronger in Li_2O than in LiAlO_2 .

Freundlich adsorption isotherms are generally indicative of surface heterogeneity, such as the presence of more than one kind of surface site for adsorption [11]. This heterogeneity arises from differences among

O^{2-} , Li^+ , and Al^{3+} sites as well as from dislocations, ledges, etc. on the surface. Different energies of adsorption are expected from such chemical and physical differences. Different kinds of sites can dominate in different measurements involving different ranges of surface coverage. Evidence for this was found in the heatings that were performed after some of the runs.

Although the hydroxide solubility for a given p_{H_2O} appears to decrease at higher temperature, the fractional surface coverage between 673 and 773 K appears to increase. However, preliminary results from a few measurements at 873 K indicate that the degree of surface adsorption decreases at this higher temperature. Low temperature chemisorption that becomes reversed at higher temperature is one way to understand the results. Without more closely spaced isotherms, it is impossible to determine at which temperature the maximum adsorption occurs. It is, therefore, premature to attempt calculations of heats of adsorption.

If the equations for θ are nevertheless extrapolated to a p_{H_2O} value corresponding to a condition of 1 vppm $H_2O(g)$ in a sweep gas of 10^5 Pa total pressure, then $\theta = 0.0082$ and 0.025 for 673 and 773 K, respectively. Reactor blanket conditions might fall into such a range.

Adherence to a rate equation that is second-order in the hydroxide content of the system is consistent with a rate-determining bimolecular process. This process is taken to be the combination of two surface OH^- groups to split out a molecule of $H_2O(g)$ with an activation energy of 14.7 kcal (61.5 kJ). (An intervening, but faster, desorption step, $H_2O(ads) \rightarrow H_2O(g)$, is possible.) For a system containing small amounts of tritium and relatively large amounts of protium, as in a reactor, the kinetic behavior would be pseudo-first order in tritoxide. A report by Kudo [12] on the kinetics of thermal decomposition of $LiOH(H_2O(g)$ evolution) indicated that the rate-limiting step follows first-order kinetics and that the activation energy is 29.5 ± 1.1 kcal (123.4 ± 4.6 kJ). Kudo suggested that desorption of H_2O molecules was the first-order rate-limiting step in that system. An alternative view is that the first-order rate-limiting step is proton diffusion through the bulk to the surface [13].

Removal of H_2O from $LiOH$ results in a two-phase system of $LiOH-Li_2O$. If the main processes to consider for the surface are desorption from the surface and surface combination of OH^- , then a comparison of the present results for $LiAlO_2$ with those of Kudo for $LiOH-Li_2O$ suggests some differences for the two systems. Because the slow step on $LiAlO_2$ is bimolecular combination of OH^- , it appears that unimolecular desorption is faster than combination of OH^- groups on $LiAlO_2$. For $LiOH-Li_2O$, the reverse relationship between the two processes is suggested by Kudo's results. Furthermore, the overall evolution process is easier from $LiAlO_2$ because the activation energy is lower. Kudo et al. also reported [14] that the evolution of HTO from neutron irradiated followed first-order kinetics with an activation energy of 18.8 ± 1.3 kcal (78.7 ± 5.4 kJ). A conclusive explanation for the difference in his values was not given. However, the activation energy for $H_2O(g)$ release from $LiAlO_2$ from the present work is lower than either of the values for the Li_2O or $LiOH^-$ systems. On this basis, tritium release from $LiAlO_2$ would be expected to be easier than from Li_2O .

FUTURE WORK

An additional isotherm (for $600^\circ C$) is being measured. This will be followed by measurements of the effect of $H_2(g)$ in the gas stream. There are indications that the rate of release of $H_2O(g)$ is accelerated under these conditions, and earlier calculations [11] had indicated that lower oxygen activities affect hydroxide solubility. Concurrent efforts will commence to start measurements on the Li_2ZrO_3 system analogous to those on $LiAlO_2$.

REFERENCES

- [1] A. K. Fischer, J. A. McDaniel, and C. E. Johnson, J. Nucl. Mater. 141-143 (1986) 344 and references therein.
- [2] J. R. Conder and C. L. Young, Physicochemical Measurement by Gas Chromatography (John Wiley & Sons, 1979) pp. 6, 124, 354.
- [3] H. Yoshida, S. Konishi, H. Takeshita, T. Kurasawa, H. Watanabe, and Y. Naruse, J. Nucl. Mater. 122-123 (1984) 934.
- [4] J. H. OeBoer, J. M. H. Fortuin, B. C. Lippens, and W. H. Meijjs, J. Catalysis 2 (1963) 1.
- [5] T. Morimoto, M. Nagao, and J. Imai, Bull. Chem. Soc. Japan 44 (1971) 1282.
- [6] W. S. Millman, F. H. Van Cauwelaert, and W. K. Hall, J. Phys. Chem. 83 (1979) 2764.
- [7] M. Tetenbaum and C. E. Johnson, J. Nucl. Mat. 126 (1984) 25.
- [8] M. Tetenbaum, A. K. Fischer, and C. E. Johnson, Fusion Technology 7 (1985) 53.
- [9] J. H. Norman and G. R. Hightower, J. Nucl. Mater. 122-123 (1984) 913.

- [10] M. Tetenbaum and C. E. Johnson, *J. Nucl. Mat.* 126 (1984) 25.
- [11] D. O. Hayward and S. M. W. Trapnell. *Chemisorption (Butterworths, 1964)* p. 174.
- [12] H. Kudo, *J. Nucl. Mat.* 87 (1979) 185.
- [13] A. K. Fischer and C. E. Johnson, *Proceedings on Properties of Lithium Ceramics, American Ceramic Society Meeting, April 1987, Pittsburgh, PA, in press.*
- [14] H. Kudo, K. Tanaka, and H. Amano, *J. Inorg. Nucl. Chem.* 40 (1978) 363.

MODELING OF TRITIUM TRANSPORT IN CERAMIC BREEDER MATERIALS J. P. Kopasz and C.E. Johnson (Argonne National Laboratory)

OBJECTIVE

The objective of this work is to develop a computer model that will describe tritium behavior in ceramic breeder materials. The model will enable one to compare the relative contributions of the different transport processes; such as bulk diffusion, grain boundary diffusion, desorption, permeation and trapping, to the total tritium inventory and to the tritium release kinetics.

SUMMARY

A computer model to predict tritium release from a ceramic breeder was developed which considers diffusion and desorption as the rate controlling mechanisms. This model performed much better than a pure diffusion model when predicting the tritium release under pure helium purge gas for Li_2SiO_3 samples from the LISA tritium release experiment. Work is now in progress to develop a more sophisticated model which will also include transport in the gas phase. Plans have also been made to investigate the effects of processes which currently are regarded as secondary in nature: These include grain boundary diffusion, trapping, etc.. in order to determine their importance in developing an overall model for tritium transport and release.

PROGRESS AND STATUS

Until recently the tritium release from ceramic breeder materials was interpreted as either diffusion controlled^{1,2,3} or desorption controlled.^{4,5} These models were unable to satisfactorily describe much of the data obtained in tritium release experiments. In addition, the inappropriate use of the simple diffusional release model has resulted in a large variation in tritium diffusivities which appear in the literature especially for materials such as LiAlO_2 . We have developed a diffusion-desorption model which is a significant improvement over previous models. The details of the model are presented in the proceedings of the ICFRM-3 conference⁶ and only the results will be discussed in this report.

The diffusion-desorption model leads to the following expression for the tritium flux as a function of time for a spherical grain after a temperature change occurs.

$$R_t = \left(1 - \frac{3}{\pi} \frac{K_d C_1}{G a}\right) \left(\frac{G a}{3} - 2h^2 \sum_{n=1}^{\infty} \frac{\exp(-D a_n^2 t)}{a_n^2 [a^2 a_n^2 + ah(ah-1)]}\right) + K_d C_1$$

R_t = tritium flux

G = generation rate/unit volume

a = grain radius

K_d = effective desorption rate constant

C_1 = concentration of tritium at the surface prior to the temperature change

D = tritium diffusivity

$h = K_d/D$

are the roots of $a \cot a = 1 - ah$

Using this equation and previously determined values of the diffusion preexponential term and activation energy⁷ and assuming an activation energy of desorption of HTO from Li_2SiO_3 of approximately 105 kJ/mol the in situ tritium release from a sample of lithium metasilicate was calculated. The results are in good agreement with the experimentally observed release for the LISA experiment under conditions of pure helium purge gas. In order to compare this model with a pure diffusion model the tritium release was calculated using the temperature profile of a second Li_2SiO_3 sample from the LISA experiment using both a pure diffusional release model and the diffusion-desorption model. The diffusion model did a very poor job of predicting the observed tritium release behavior when the diffusion coefficients calculated by Werle⁷ were used (Fig. 2). When the diffusion coefficients were optimized to fit the data the fit was fair but not as good as that for the diffusion-desorption model. In addition in order to get a fair fit to the experimental data using a pure diffusion model for this sample a diffusion activation energy of 75 kJ/mol was needed, a value twice that calculated by Werle.⁷

The diffusion-desorption model did a good job of predicting the tritium release profile for the metasilicate sample (Fig. 1). The fit to the observed data could be improved further by increasing the diffusion preexponential term slightly from that calculated by Werle⁷. Predictions of the tritium release for two other samples of Li_2SiO_3 calculated using this model were also in good agreement with the experimental data. There were some regions in the observed tritium release profiles where the diffusion-desorption model did not accurately predict the tritium release rate. This may be an indication that the values used for the diffusivity and the desorption rate constant used in the calculations are in error or that a third mechanism is important in determining tritium release in these regions.

In order to add the effects of grain boundary diffusion, surface reactions or permeation to the model it becomes necessary to move away from an analytical solution and look toward a numerical approximation to the solution of the coupled differential equations. We chose to use the OISPL software package⁹ to solve the system of differential equations which control tritium transport in a ceramic breeder. Work is currently under way in adapting this program to the problem of diffusion, desorption and permeation.

FUTURE WORK

The importance of grain boundary diffusion, trapping, and permeation on the tritium release from ceramic breeders will be studied by modeling these effects individually and in conjunction with diffusion and desorption. If any of these processes are found to be important in determining tritium release they will be addressed, along with diffusion and desorption, in the main code which will calculate the dynamic tritium release and inventory.

REFERENCES

1. R.G. Clemmer et al. "The TRIO Experiment", ANL-84-55, Argonne National Laboratory (1984).
2. K. Okuno and H. Kudo, J. Nucl. Mater. 138 (1986) 210.
3. T. Kurasawa, H. Watanabe, G. W. Hollenberg, Y. Ishi, A. Nishimura, H. Yoshida, Y. Naruse, M. Aizawa, H. Ohno, S. Konishi J. Nucl. Mater. 141-3 (1986) 265.
4. M. Dalle Donne, Fusion Tech. 9 (1986) 503.
5. T. Tanifuji, K. Noda, S. Nasu, and K. Uchida J. Nucl. Mater. 95 (1980) 108.
6. J. P. Kopasz, S. W. Tam, and C.E. Johnson, Proceedings of ICFRM-3, Karlsruhe, F.R.Germany Oct.4-10.1987.
7. H. Werle, J.J. Abassin, M. Briec, R. G. Clemmer, H. Elbel, H. F. Hafner, N. Mason, P. Sciens, H. Wedemeyer, "The LISA-1 Experiment" J. Nucl. Mater. 141-143 (1986) 321 and unpublished data.
8. G.K. Leaf and M. Minkoff "DISPL1: A Software Package for One and Two Spatially Dimensioned Kinetics-diffusion Problems" ANL-84-56

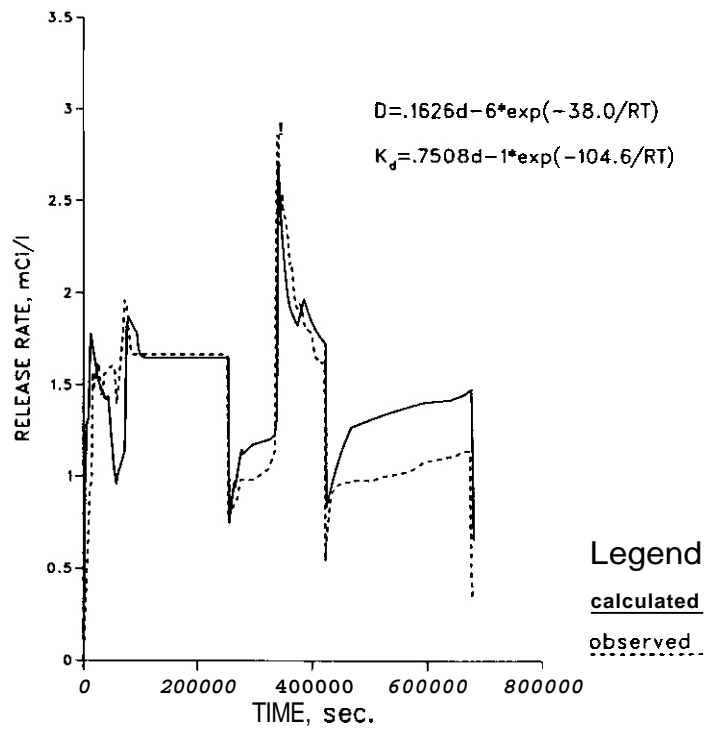


Fig. 1. Calculated and observed tritium release diffusion-desorption model

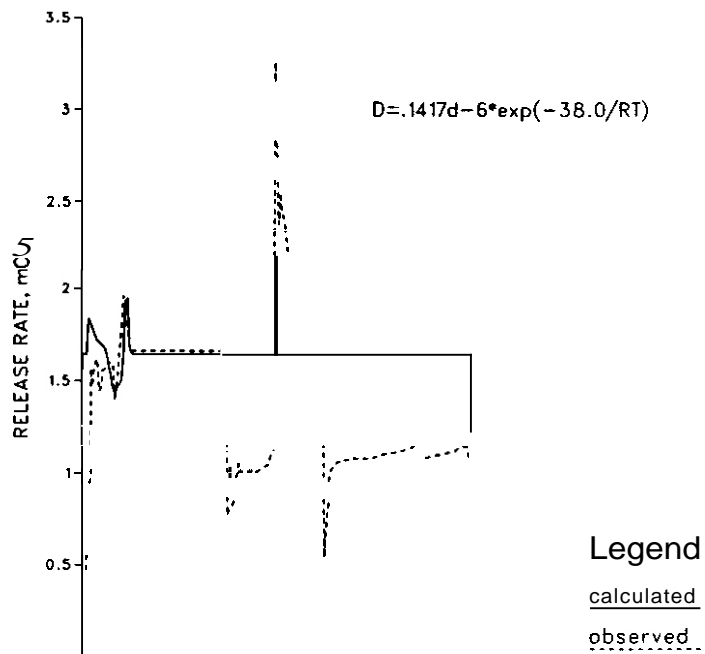


Fig. 2. Calculated and observed tritium release pure diffusion model.

8. CERAMICS

NEUTRON IRRADIATION TESTING OF CERAMIC-TO-METAL SEALS • H. N. Barr and F. Hittman (Hittman Materials and Medical Components, Inc.) and H. Martinez, F. W. Clinard, Jr., R. O. Brown and J. Cook (Los Alamos National Laboratory)

OBJECTIVE

The goal of this work is to determine the leak tightness and structural integrity of a selection of ceramic-to-metal seals after irradiation to a fluence of 4×10^{23} fast n/m^2 at room temperature.

SUMMARY

Butt-type ceramic-to-metal seals made from (1) niobium bonded to alumina, alon, spinel, or an aluminasilicon nitride ceramic and (2) MACOR bonded to titanium were irradiated to a dose of 4×10^{23} n/m^2 at room temperature. The neutron source was the beam stop area of the Los Alamos Meson Physics Facility (LAMPF). Post-irradiation testing showed that hermeticity of all but the MACOR/Ti samples was retained, even after application of 6.9×10^6 Pa (1000 psi) of hydraulic pressure. Pressurization to failure showed that all seals were capable of withstanding much higher pressures without structural failure. All ceramic-to-niobium seals appear qualified for use near the first wall of the Compact Ignition Torus (CIT) for the full lifetime of that machine while MACOR/Ti seals should be usable for lower fluences, or the full fluence where leak tightness is not required.

PROGRESS AND STATUS

Introduction

Ceramic-to-metal seals are required for a number of applications in fusion devices. Up to now, problems associated with neutron irradiation damage have been minimal due to the very low fluxes generated. However, next-generation D-1-burning machines will change all that. Of particular importance is the survival of various ceramic-metal bonded components near the first wall of the CIT, a machine with an expected lifetime first-wall dose of 3×10^{23} fusion n/m^2 . Examples of applications for seals there are feedthroughs for diagnostic systems and antenna standoffs for RF heating systems.

When considering which ceramic-metal systems are good candidates for use in a neutron environment, it is necessary to take into account both known radiation resistance and ease of fabrication. Earlier work has shown that spinel ($MgAl_2O_4$), ALON ($Al_2O_3-N_3$) and an Al_2O_3/Si_3N_4 mixture all exhibit good resistance to neutron damage. Alumina (Al_2O_3) is relatively damage-sensitive, but is known to survive doses up to $\approx 10^{23}$ n/m^2 (ref. 4). At the time that MACOR was selected for this test it was known that this easily-fabricated machinable glass-ceramic was essentially unaffected by a dose of 10^{22} 14 MeV n/m^2 . Thus these five ceramics were selected for evaluation. The companion metals (Ti for MACOR, Nb for the other ceramics) were chosen on the basis of compatibility of thermal expansion coefficients; their radiation resistance was considered adequate for the target dose. In this progress report we describe the resistance of these ceramic-to-metal seals to neutron fluxes approximating those expected for lifetime exposure near the first wall of the CIT.

Experimental procedure and results

Sources for the ceramics used were: for the alumina, Wesgo (Al 995); for the ALON, Coors; for the aluminasilicon nitride, Greenleaf Technical Ceramics (GEM-4); for the spinel, Trans-Tech Inc.; and for the MACOR, Corning (9658).

Ceramic disks of diameter 6.35 mm and thicknesses from ≈ 1 to 3 mm were metallized by an active-metal thin film sputtering technique and vacuum-brazed to the ends of niobium or titanium tubes. The tubes had a diameter the same as that for the disks and wall thickness of ≈ 1 to 2 mm. The braze metal was a silver-copper eutectic alloy. A total of 15 seals (3 of each of the 5 materials systems) were made. All assemblies were helium leak tested and found vacuum-tight, both before and after five thermal cycles between $-65^\circ C$ and $200^\circ C$.

The test seals were placed in a double-walled metal container in the beam stop area of LAMPF⁶ and irradiated with spallation neutrons over several months to a fluence of 4×10^{23} n/m^2 at room temperature. The neutron spectrum at that facility resembles a fission spectrum with the addition of neutrons in the MeV energy range (high-energy tail). After irradiation the container was transported to the hot-cell facility at Los Alamos and the seals removed for testing.

The 15 test assemblies were inspected, photographed, and leak tested. All samples were intact except for some chipping of the edges of the ceramic disks. Helium leak testing showed that all seals were tight with the exception of the MACOR/Ti samples, which showed slight leaks.

Ten of the 15 samples (two of the three from each materials family) were pressurized with oil to 6.9×10^6 Pa (1000 psi); all held the pressure with no signs of damage. These 10 samples were then leak tested as before. All tested leak-tight, including the two MACOR/Ti seals that had shown slight leaks as-irradiated.

The reason for this change is not known, but may be associated with the presence of the oil (although the samples had been degreased after the pressure tests].

These 10 samples were then re-pressurized, this time to failure where possible. All withstood high pressures, rupturing between 3.5×10^7 Pa (5000 psi) for a MACOR-Ti seal and 1.3×10^8 Pa (18,600 psi) for an alumina/Nb seal. The other alumina/Nb seal could not be ruptured at the highest attainable pressure of 1.7×10^8 Pa (24,000 psi).

Discussion

All ceramic-to-metal seals tested here with the exception of the MACOR/Ti samples performed well after irradiation. There seems to be no question that seals made of alumina, alon, spinel, or alumina/silicon nitride and bonded to niobium by the technique described above can tolerate neutron damage levels similar to those expected at the first wall of the CIT, unless unexpected problems develop as a result of the generation of transmutation products that are known to accompany 14 MeV neutron irradiation. It will be necessary, of course, to keep other sources of damage (e.g., thermal shock from direct deposition of plasma energy) under control to assure satisfactory performance.

The poorer performance of the MACOR/Ti samples casts doubt as to their reliability when used at the first wall of CIT. There are two possible explanations for the observed leaks in the irradiated seals: (1) swelling of the MACOR, and (2) inherent problems with the seal interface. With respect to the first, recent work has shown that this glass-ceramic suffers significant swelling after irradiation to 4×10^{22} and 10×10^{22} 14 MeV n/m^2 (2.05 and 0.93 vol%, respectively). This unusual dose-dependence has been postulated to result from different swelling rates for the glass matrix and the precipitated mica flakes that in equal proportions make up the two-phase microstructure of this material.

The second explanation has to do with the nature of the machined surface of the MACOR. Peel tests have shown that a thin layer of glass-ceramic is removed, implying that machining causes microcracks that weaken the near-surface region. As demonstrated here a successful seal can still be made, but the presence of the damaged layer may indicate a weakened assembly. It would therefore seem that MACOR/Ti seals are not the best choice for CIT first wall use unless the neutron dose is reduced by periodic replacement of the component. However, after the irradiation dose employed here strength of the bonded joint remained reasonably high, so that for applications where leak tightness is not required a bonded MACOR/Ti system may still be satisfactory.

CONCLUSIONS

Ceramic-to-metal seals made of alumina, alon, spinel or alumina/silicon nitride bonded to niobium have been demonstrated to hold up well to an irradiation dose of 4×10^{23} fast n/m^2 , and appear appropriate for lifetime first-wall applications in CIT. Seals made of MACOR and titanium are reasonably strong but show signs of leakage after such irradiation, and so where hermeticity is required irradiation doses for that materials system should be held to lower levels.

FUTURE WORK

Samples are currently being prepared for metallographic examination to determine whether microscopic flaws, especially in the bonded joints, can be detected.

REFERENCES

1. K. M. Young, L-P Ku and S-L Liew, "CIT Radiation Levels and TFTR Observations", presented at Planning Meeting on Neutron Irradiation Effects and Materials Research and Development, Livermore, California, April 7, 1987.
2. F. W. Clinard, Jr., G. F. Hurley and R. W. Klaffky, "Ceramics for Fusion Reactor Applications", *Res Mechanica* 8, 207-34 (1983).
3. C. A. Parker, L. W. Hobbs, K. C. Russell and F. W. Clinard, Jr., "Damage Structures in Fast Neutron Irradiated Magnesium Aluminate and Electron Irradiated Aluminum Oxynitride Spinel", *J. Nucl. Mater.* 133&134, 741-4 (1985).
4. R. S. Wilks, J. A. Desport and J. A. G. Smith, "The Irradiation-Induced Macroscopic Growth of $\alpha\text{-Al}_2\text{O}_3$ Single Crystals", *J. Nucl. Mater.* 24, 80-86 (1967).
5. J. O. Fowler, Jr., G. F. Hurley, J. C. Kennedy and F. W. Clinard, Jr., "14 MeV Neutron Irradiation Effects in MACOR Glass-Ceramic", *J. Nucl. Mater.* 103&104, 755-9 (1981).
6. M. S. Wechsler and W. F. Sommer, "The Radiation Damage Facility at the LAMPF A-6 Target Station", *J. Nucl. Mater.* 122&123, 1078-84 (1984). See also W. F. Sommer, W. Lohmann, K. Graf, I. K. Taylor and R. M. Chavez. "Operating Experience at the Los Alamos Scallation Radiation Effects Facility at LAMPF". Los Alamos National Laboratory Report LA-UR 85-3917.
7. F. W. Clinard, Jr., "Ceramics for Fusion Applications", *Ceramics International* 13, 69-75 (1987)
8. W. A. Coghlan and F. W. Clinard, Jr., "Damage to MACOR Glass-Ceramic from High-Dose 14 MeV Neutrons", this volume.

DAMAGE TO MACOR GLASS-CERAMIC FROM HIGH-DOSE 14 MeV NEUTRONS - W. A. Coghlan and F. W. Clinard, Jr. (Los Alamos National Laboratory)

OBJECTIVE

The goal of this work is to assess changes in MACOR machinable glass-ceramic after irradiation to neutron fluences up to the applications-relevant dose of 1×10^{23} n/m² at RTNS-II.

SUMMARY

Eight samples of MACOR machinable glass-ceramic were irradiated at room temperature to fluences between 4 and 10×10^{22} 14 MeV n/m² at RTNS-II. Post-irradiation measurements showed that electrical resistivity was little changed, but that swelling was significant. The latter results are interpreted in terms of differential swelling between the glassy and crystalline phases, implying a possible loss of strength in this dose range. These findings raise a question as to whether MACOR can retain its structural properties at neutron doses characteristic of lifetime exposure at the first wall of the Compact Ignition Torus. Further work on these samples, in progress, will help to answer that question.

PROGRESS AND STATUS

Introduction

MACOR machinable glass-ceramic (a product of Corning Glass Works, Corning, NY) is a material of great usefulness for fusion applications where the need for a small number of insulator components can make grinding to shape prohibitively expensive. Examples of applications are ion source insulators for neutral beam injectors and insulating spacers for diagnostic coils.

The microstructure of MACOR consists of a borosilicate glass matrix containing 1-10 μ m flakes of crystalline mica that were precipitated from the matrix by heat treatment. In its final form the material consists of about 50 vol% of each phase. It can be anticipated, based on general knowledge of radiation resistance of glasses and crystalline silicates, that MACOR will be damaged by relatively low doses of neutrons compared with the behavior of conventional ceramics such as alumina.

In earlier work² we evaluated changes in MACOR after irradiation to 1×10^{22} 14 MeV n/m² at room temperature. It was found that density and thermal diffusivity were unchanged, while strength and electrical conductivity increased slightly. It was apparent at that time that higher-fluence data were needed to duplicate damage doses to applications such as those described above. In this progress report^{2,3} we present results to date on physical property measurements of MACOR after irradiation to doses up to 1×10^{23} 14 MeV n/m².

Experimental procedure

Samples of MACOR were submitted to the RTNS-II neutron source at Lawrence Livermore National Laboratory for irradiation. Eight disk-shaped specimens were stacked and irradiated so that those nearest the neutron source received a fluence of 1×10^{23} n/m², while those at the rear received a dose of 4×10^{22} n/m². These are doses at the center of each sample. The specimens, of dimensions 16 mm dia by 0.55 mm thick, were irradiated at room temperature. The end samples of the stack of eight were received from RTNS-II in a broken condition.

To date, measurements have been made of post-irradiation electrical conductivity and density changes. Electrical conductivity was measured over the frequency range of 5×10^4 to 5×10^6 Hz using a Hewlett Packard Model 4342A Q-meter. Density was determined by use of an immersion technique² in which samples are levitated in an aqueous solution of thallium salts and the density of the liquid subsequently measured in a Mettler DMA 45 density meter. At this writing electrical conductivity of four samples plus a control have been measured, while density of the two end samples along with a control has been determined.

Results and discussion

Room-temperature electrical conductivity of the samples is shown in Fig. 1, along with the data reported earlier by Fowler et al.² Doses for the tested samples ranged from 6×10^{22} n/m² (MACOR-6) to 8×10^{22} n/m² (MACOR-31). These results show a slight increase in conductivity after irradiation, of a level that should have little technological significance. These findings are in good agreement with those reported earlier² after a dose of 1×10^{22} n/m², implying that this is not a property that changes readily with neutron irradiation. Thus a modest extrapolation of this good behavior to somewhat higher fluences (perhaps to the dose of 3×10^{23} n/m² that is characteristic of lifetime at the first wall of the Compact Ignition Torus)³ would be justified. However, it should be pointed out that much larger increases in electrical conductivity can be expected during irradiation (see for example ref. 4), especially considering that during a burn the ionizing component of the irradiation flux in that machine will be on the order of 10^4 Gy/s (ref. 3).

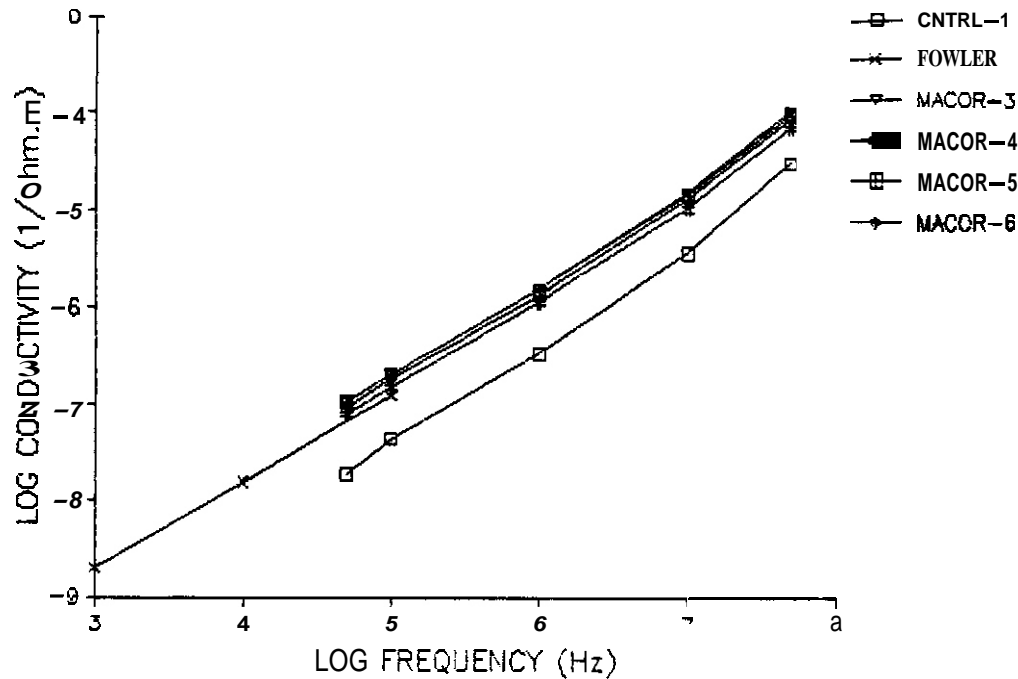


Fig. 1. Electrical conductivity vs. test frequency for irradiated and control MACOR.

Swelling values for the two samples measured here are shown in Table 1, along with results from earlier, lower-dose studies. Our interpretation of this unusual dose-dependence is that the measured response results from simultaneous swelling of the mica phase and densification of the glassy phase, neither of which is unusual in itself. It would be expected that dose-dependencies of swelling would differ for the two phases, so that one might dominate at a particular damage level. Thus at 1×10^{22} n/m² densification of the glass appears to dominate, at 4×10^{22} n/m² dilation of the mica phase is predominant, and at 1×10^{23} n/m² shrinkage of glass once again becomes important. These arguments imply a possible degradation of strength resulting from internal strains.

Table 1. Swelling of irradiated MACOR. A negative value refers to densification.

Dose, 14 MeV n/m ²	Swelling, vol%
1×10^{20}	0 (ref. 2)
1×10^{22}	-0.08 (ref. 2)
4×10^{22}	2.05
1×10^{23}	0.93

CONCLUSIONS

Measurements of electrical conductivity of MACOR after irradiation to fluences up to 1×10^{23} 14 MeV n/m² show a slight but technologically unimportant increase. Much greater degradation is expected during a fusion reactor burn phase, as a consequence of absorption of an intense flux of ionizing radiation. Swelling up to this dose shows a complex dependence on fluence, which is attributed to different swelling rates for the glass and mica phases. An accompanying degradation of strength may result from this behavior. At this point in the analysis of these samples some question exists as to whether MACOR will retain its structural integrity when exposed to a lifetime neutron dose at the first wall of the Compact Ignition Torus.

FUTURE WORK

Further work is planned to determine density changes at intermediate doses and to analyze the electrical conductivity results Presented here. Additional studies, some to be conducted in cooperation with colleagues in Japan, will include measurements of strength and assessment of damage-induced microstructural changes using transmission electron microscopy.

REFERENCES

1. G. H. Beall, K. Chyung, D. G. Grossman and G. P. Smith, "Machinable Glass-Ceramics: New Materials for Electrotechnical Applications", presented at the World Electrotechnical Congress, Moscow, **USSR**, June **1977**.
2. J. D. Fowler Jr., G. F. Hurley, J. C. Kennedy and F. W. Clinard, Jr., "14 MeV Neutron Irradiation Effects in MACOR Glass-Ceramic", *J. Nucl. Mater.* **103&104**, 755-9 (1981).
3. K. M. Young, L-P. Ku and S-L. Liew, "CIT Radiation Levels and TFTR Observations", presented at Planning Meeting on Neutron Irradiation Effects and Materials Research and Development, Livermore, California, April 7, 1987.
4. R. W. Klaffky, B. H. Rose, A. N. Goland and G. J. Dienes, "Radiation-Induced Conductivity of Al_2O_3 : Experiment and Theory", *Phys. Rev. B* **21**, 3610-34 (1980).

IMPROVED COMPUTATION OF DIELECTRIC CONSTANTS MEASURED BY IN-WAVEGUIDE TECHNIQUES
H. M. Frost (Los Alamos National Laboratory)

OBJECTIVE

To provide more accurate reduction of 'raw' data into the associated dielectric constants, k , and loss tangents, $\tan\delta$ when the measurements are performed by in-waveguide techniques.

SUMMARY

Brief details **are** presented for the derivation of a formula for calculating k from the frequency difference $\Delta f_n = f_{n+1} - f_n$ measured via the channel spectrum ('raw' data) for the transmission loss of a rectangular parallelepiped inserted within waveguide. Comparison is made in terms of the previously used formula adapted from 'free-space' theory. Implications for fusion ceramics for 'rf' windows **are** presented.

PROGRESS AND STATUS

Calculations

The frequencies f_n for the peaks in a microwave transmission channel spectrum of a waveguide specimen of length L can be used to calculate k when f_n satisfies the condition

$$L = nc_0 / \{2f_n / (k - p_n)\} \quad \text{Eq. (1)}$$

In this expression, adapted from the free-space case, n is an integer, c_0 is the speed of light in free-space vacuum, and $p_n = \sin^2(\theta_n) = (f_c/f_n)^2$, with θ_n the effective angle for the constant-phase wavefront at $f = f_n$ within the waveguide and f_c the cut-off frequency. Recursion relations were developed from Eq. (1) to second order in $\{f_c/(f_n/k)\}^2$ for f_n via calculation of the sum and difference quantities $(n+1)f_n$. The resulting two equations were combined and simplified, retaining terms to first order in $\Delta f_n/f_n$ to give the result

$$k = (f_r/\Delta f_n)^2 \{1 - [(f_c/f)^2 k^{-1} + (1/2)(f_c/f)^4 k^{-2}]\}, \quad \text{Eq. (2)}$$

where $f_r = c_0/(2L)$ has the form of a fundamental resonant frequency. Recognition of the smallness of the second order term on the right hand side of Eq. (2) leads to a quadratic equation in k . (For $k=9$, $L=5\text{cm}$, $f=100\text{GHz}$, and $f_c=60\text{GHz}$, that term's value is 0.007.) The resulting expression for k is

$$k \approx (f_r/\Delta f_n)^2 - p_n, \quad \text{Eq. (3)}$$

where $p_n = \sin^2(\theta_n) = (f_c/f_n)^2$ and $f^2 = f_{n+1}f_n$. Compare this with

$$k \approx (f_r/\Delta f_n)^2 + p_n, \quad \text{Eq. (4)}$$

erroneously assuming .. for the waveguide case .. that f_n equals $n\Delta f_n$, as applicable to free-space measurements. 'Old' values of k measured in waveguide but calculated via Eq. (4) are easily corrected via

$$k_{\text{new}} = k_{\text{old}} - 2p_n. \quad \text{Eq. (5)}$$

At 100 GHz, the correction term, $-2p_n$, equals -0.8 .. which is of the order of 10% of the k -value for alumina. 'New' values of $\tan\delta$ are calculated as before, but with the corrected values of k inserted into the appropriate formula.

Discussion

The preceding correction decreases the estimate of k . In contrast and in comparison,

correction for the clearance or gap in the 'thin' transverse dimension (i.e., E-field direction for a field in the TE₀₁ mode) between the 'wide' transverse surface of the test specimen and the wide waveguide-wall surface has the effect of increasing this estimate. Based on a standard correction formula, a gap-error contribution of +0.8 to the estimate of k corresponds to a gap of 0.5 mil (13 μm) within the thin dimension of the W-band waveguide's internal cross-section of 50x100 mils (1.3x2.5 mm). For the quantities $\tan\delta$ and $k\tan\delta$, the same trend of '+' & '-' compensating errors applies.

From the standpoint of fusion ceramics for rf-window applications, removal of systematic errors from determinations of the values of the dielectric properties of corresponding candidate materials is crucial to predicting their mechanical reliability under a stressful radiation environment. This follows from published models for Weibull statistics for fracture and static fatigue within a reactive environment. These models indicate that predictions of service lifetimes to failure, t_f , depend sensitively on the specific estimates of the loss factor, $k\tan\delta$. In the case of WESGO AL-995 alumina (99.5%) with $k_{\text{true}} = 9.7$, an absolute error of +0.1 means that t_f is underestimated as 78% of the true value. Worse, if an error of +0.8 applies (as in the preceding paragraph), then the t_f estimate is only 15% of the true value -- 'not good' from the standpoint of window design. If the total measurement errors are negative instead, i.e., -0.1 and -0.8, then the corresponding t_f values are overestimated by factors of 1.3 and 3.0, respectively -- 'dangerous' from the design standpoint.

Acknowledgments

Detailed calculations leading to Eq.(2) were checked by W. Beyermann

CONCLUSIONS

In rf-window research at fusion-ceramics centers such as Los Alamos, the microwave experimentalist needs to take an integrated view of the topic so that the accuracy (and precision) of dielectric measurements made is sufficient for subsequent reliable predictions of service lifetime. Because the thermo-mechanical stress due to dielectric heating can be proportional to the quantity $k\tan\delta P/K$ where P is the in situ microwave power and K the thermal conductivity of the window ceramic, accurate determination of these latter quantities is also crucial.

FUTURE WORK

Plans include quantification of systematic errors due to specimen-waveguide gaps and to wall losses not 'calibrated out' via the normalization techniques routinely used in our dielectric measurements at 90-100 GHz.

REFERENCES

- ¹W. W. Ho, "Millimeter Wave Dielectric Property Measurements of Gyrotron Window Materials," Technical Report for 1/83-2/84, ORNL/SUB/83-51926/1, Rockwell Int. Sci. Ctr., Thousand Oaks, CA, April 1984.
- ²H. M. Altschuler, "Dielectric Constant," Ch. IX in "Handbook of Microwave Measurements" (eds., M. Sucher and J. Fox), Interscience Publishers (distributors), New York, 1963.
- ³M. K. Ferber, H. D. Kimrey, and P. F. Becher, J. Mat. Sci. 19, 3767-3777 (1984); P. F. Becher and M. K. Becher, J. Mat. Sci. 19, 3778-3785 (1984).
- ⁴H. M. Frost and F. W. Clinard, Jr., J. Nucl. Mat. (in press).

MODEL FOR DEFECT AGGREGATION AND SWELLING IN NEUTRON-IRRADIATED SPINEL - W. A. Coghlan* and R. J. Livak
(Los Alamos National Laboratory)

OBJECTIVE

This goal of this work is to model the continued swelling of spinel after low levels of neutron damage in order to better understand defect behavior in ~~theis~~ candidate fusion reactor material.

SUMMARY

Samples of single-crystal spinel ($MgAl_2O_4$) were irradiated to neutron fluences up to 8×10^{22} n/m² ($E \geq 0.1$ MeV) at $\approx 50^\circ\text{C}$ in the Omega West Reactor. All the irradiated samples showed continued swelling out of reactor during storage at ambient room temperature. A model based on interstitial clustering has been developed that describes this post-irradiation swelling of spinel.

PROGRESS AND STATUS

Introduction

When exposed to high dose neutron irradiation, spinel exhibits low swelling^{1,2}, and enhanced strength^{1,3} and fracture toughness. This behavior has been explained in terms of recombination and aggregation of irradiation-induced defects.^{1,5} As reported previously for low dose neutron irradiation at 50°C ,⁶ swelling of spinel increases rapidly to 0.03 vol% followed by saturation. A model based on the interaction of irradiation-induced defects is able to account for the saturation of swelling. Subsequent measurements made after removal from the reactor showed that spinel continued to swell. This report describes the modeling done to explain the continued swelling after irradiation.

Results and Discussion

The saturation of swelling in reactor is attributed to maintaining a quasi-steady state concentration of excess oxygen vacancies and interstitials by recombination with no effective interstitial sinks operative. If interstitials were lost to sinks, then the vacancy concentration would continue to increase giving more swelling. Interstitials may not aggregate because of the large gamma radiation field in the reactor that keeps the interstitials ionized and thus repelled from each other by coulomb forces.

The irradiated spinel samples continued to swell out of reactor an additional -0.012 vol% when stored for 260 days at ambient temperature ($\approx 20^\circ\text{C}$). Transmission electron microscopy utilizing weak beam, dark-field imaging revealed small defect clusters in the irradiated samples after storage as shown in Figure 1. The measured cluster density was 1×10^{17} cm⁻³ with a typical diameter of 1.5 nm. These small defect clusters are presumably of interstitial nature because interstitial loops have been observed in spinel at higher damage levels of 30 dpa.

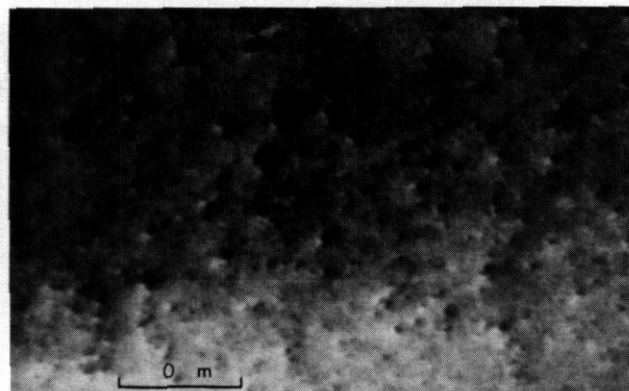


Figure 1. Weak beam, dark-field image showing small defect clusters in spinel irradiated to a fluence of 8×10^{22} n/m² at $\approx 50^\circ\text{C}$.

* Permanent address: Department of Chemical, Biological, and Materials Engineering, Arizona State University, Tempe, AZ 85287.

A model based on chemical rate equations has been used to explain these observations of continued swelling after irradiation. One assumption made is that oxygen interstitial clusters form by diffusion during room temperature storage. Furthermore, the recombination of oxygen vacancy-interstitial pairs is assumed to be negligible such that the excess vacancy concentration is maintained in the crystal. To achieve an increase in specific volume when oxygen interstitials cluster, it is necessary to assume that the relaxation volume of an oxygen interstitial is less than the ionic volume of oxygen in either a normal atom site or an interstitial loop.

In spine there are 6.09×10^{22} oxygen atoms/cm³ corresponding to an oxygen anionic volume (V_o) of 1.64×10^{-23} cm³. The smaller metallic cations are assumed to be within the oxygen interstices. The swelling in reactor saturated at about 0.03 vol% because of excess point defects. This swelling is equivalent to 1.83×10^{19} V_o . Based on the calculations of L.R. Greenwood, the neutron fluence to saturate swelling created 1.22×10^{20} cm⁻³ Frenkel pairs, assuming a 30% survival rate from the cascades. Based on the argument that the defect concentrations on the oxygen sublattice are controlled by the faster diffusing oxygen interstitial species, the oxygen vacancy and interstitial concentrations will be given by $\sqrt{(G/R)} = 2.63 \times 10^{19}$ cm⁻³ where G equals the generation rate of point defects and $R = 4\pi r'D/\Omega$ (r' = vacancy-interstitial recombination radius, D = diffusion coefficient of oxygen interstitial, and Ω = atomic volume). Many of the point defects created during the irradiation will have recombined. Dividing the equivalent swelling volume by the remaining defect concentration gives $0.694 V_o$ as the necessary volume of each remaining Frenkel pair to obtain the measured value of swelling.

Based on the assumption that negligible interstitial clustering occurs during irradiation due to the ionizing gamma field in reactor, then the calculated value of $0.694 V_o$ for each remaining Frenkel pair gives the observed swelling when used with the rate equations. Taking $V_v = 0.2 V_o$ and $V_i = 0.494 V_o$ where V_v and V_i are the relaxation volumes of oxygen vacancies and interstitials respectively, the calculated swelling as a function of irradiation time is shown in Figure 2.

The electron microscope observations revealed a cluster density of 1×10^{17} cm⁻³ with a typical diameter of 1.5 nm. A dislocation loop with $b = a/4$ [110] and diameter 1.5 nm will contain 30 oxygen interstitials. Thus, the total number of interstitials in the visible loops is about 3×10^{18} cm⁻³. After irradiation, the samples continued to swell about 0.01 vol% corresponding to an additional volume of 6.09×10^{18} V_o . Since the relaxation volume of an oxygen interstitial is taken to be $0.494 V_o$, swelling will occur when an interstitial joins a dislocation loop and its volume becomes V_o . The increase in volume for such an event equals $V_o - V_i$. Thus, the continued swelling after irradiation can be explained for the case where $(6.09 \times 10^{18} V_o)/(V_o - V_i)$ interstitials are absorbed at dislocation loops. For $V_i = 0.494$, the number of interstitials joining loops is 1.2×10^{19} cm⁻³ which is four times the approximate number of interstitials in the observed loops. This discrepancy may be attributed to smaller interstitial clusters that are not visible in the electron microscope images.

The calculated number of interstitials in loops is only a factor of two less than the expected total number of interstitials produced by irradiation. If any recombination of interstitials and vacancies occurred, then the amount of swelling would be reduced. Thus, it may be possible that in the absence of the ionizing gamma field of the reactor the vacancy-interstitial recombination rate is greatly diminished. Figure 3 is a plot of expected swelling as a function of storage time. The capture parameters in the model were chosen to match approximately the observed time dependence. The calculated swelling curve shows an incubation period that would be expected since smaller interstitial clusters would form first and then grow.

The model for continued swelling after irradiation accounts for interstitial clusters containing from one to six interstitial atoms. Clusters with more than six atoms are assumed to collapse into dislocation loops. The relaxation volume of each larger cluster slowly approaches that of 1 V_o for each interstitial in the loop. Only single interstitials are assumed to diffuse. Figure 4 gives the cluster concentration as a function of storage time with two different scales used in (a) and (b) to show the concentrations of the larger clusters. As the final interstitials aggregate, the calculated loop density becomes 6.4×10^{17} cm⁻³ with an average radius of 0.7 nm. These results do not account for loop growth so the final size distribution is not known. Thus, the number of loops that would be large enough to be seen in the electron microscope is not given by these calculations.

CONCLUSIONS

In support of the assumptions made in this model, swelling saturated at a damage level of 0.002 dpa indicating a saturation of point defect concentration with the absence of growing interstitial loops. Growing loops would have given increasing swelling in reactor because of the steadily increasing vacancy concentration. However, interstitial clustering did occur since defect clusters are observed by TEM after storage of the irradiated crystals. The presence of these clusters would be consistent with observed continued swelling out of reactor if the relaxation volume of an oxygen interstitial was less than an atomic volume.

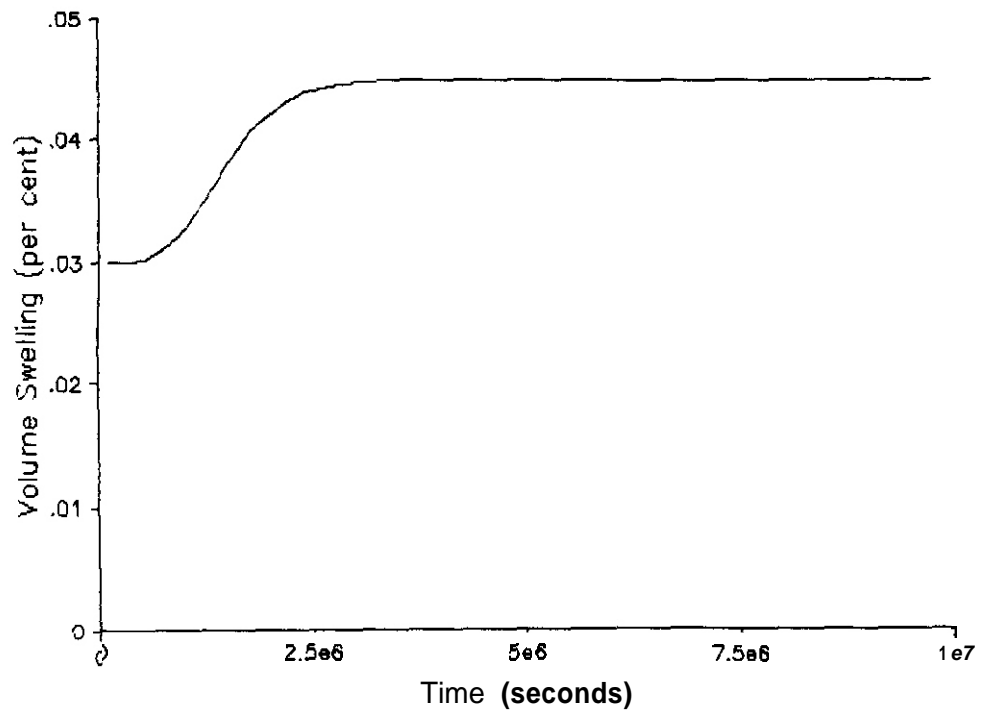
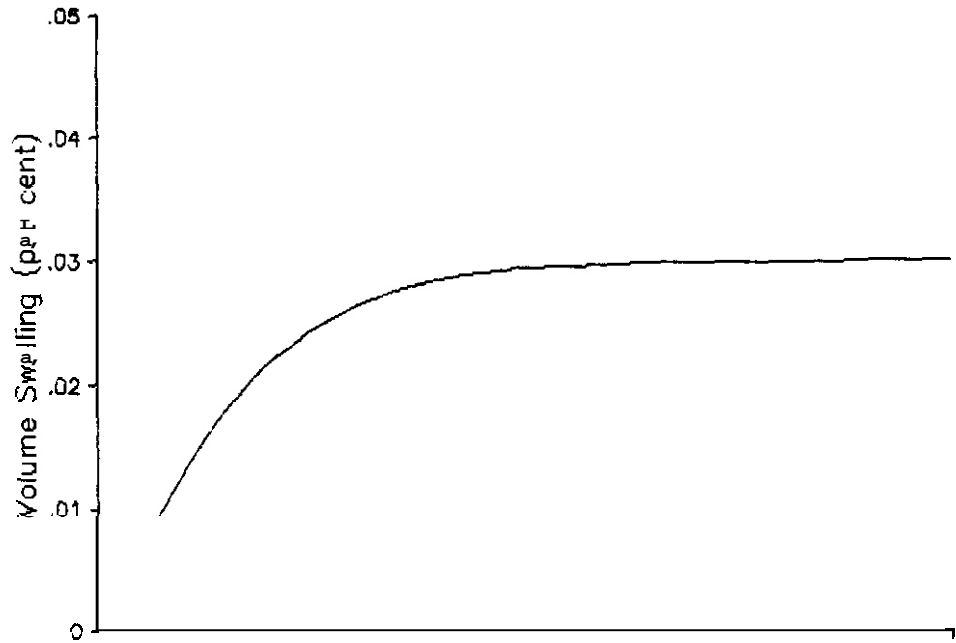


Figure 3. Calculated swelling of spinel during post-irradiation storage at room temperature for the case $V_v = 0.2 V_o$ and $V_i = 0.494 V_o$.

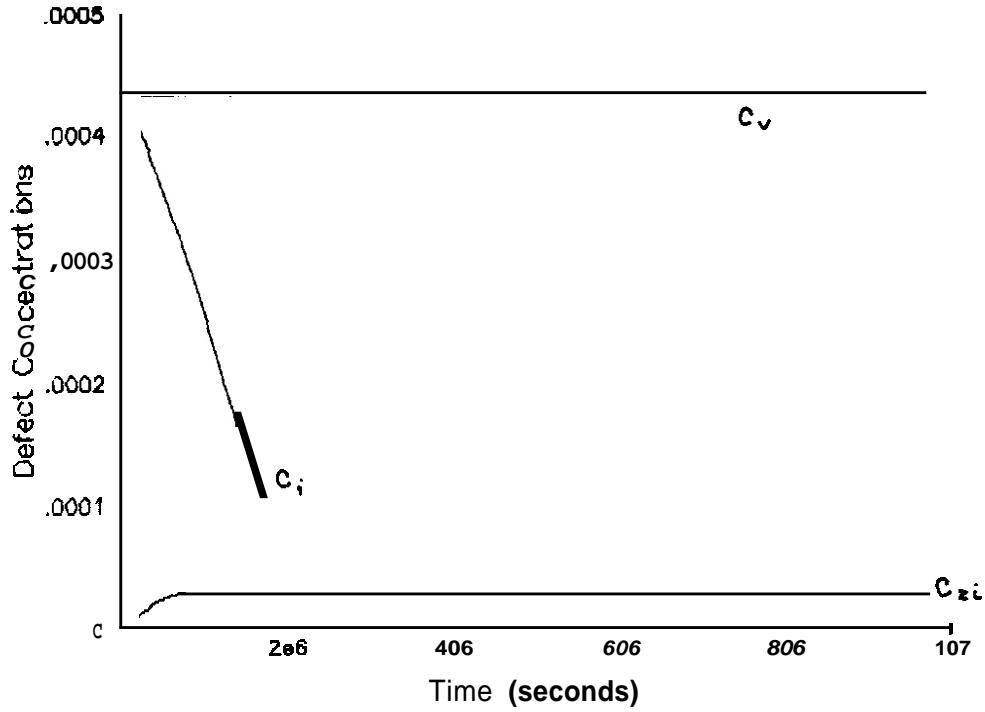


Figure 4a. Calculated defect concentrations (atom fraction) as a function of post-irradiation storage time (C_v and C_i equal vacancy and interstitial concentrations respectively).

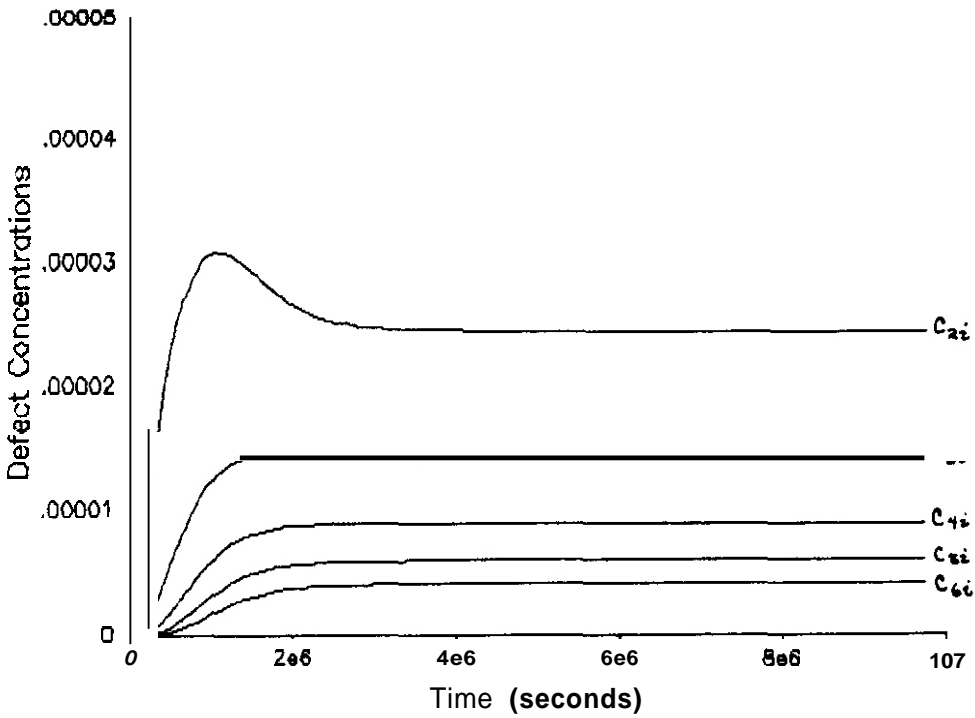


Figure 4b. Calculated interstitial defect cluster concentrations (atom fraction) as a function of post-irradiation storage time.

FUTURE WORK

After refining these calculations, this model for continued swelling after irradiation will be published in the literature.

REFERENCES

1. G.F. Hurley et al., "Structural Properties of MgO and $MgAl_2O_4$ after Neutron Irradiation near Room Temperature," J. Nucl. Mater. **103 & 104**, 761-766 (1981).
2. F.W. Clinard, Jr., G.F. Hurley and L.W. Hobbs, "Neutron Irradiation Damage in MgO, Al_2O_3 and $MgAl_2O_4$ Ceramics," J. Nucl. Mater. **108 & 109**, 655-670 (1982).
3. F.W. Clinard, Jr. et al., "Structural Performance of Ceramics in a High-Fluence Fusion Environment," J. Nucl. Mater. **122 & 123**, 1386-1392 (1984).
4. F.W. Clinard, Jr. et al., "The Effect of Elevated-Temperature Neutron Irradiation on Fracture Toughness of Ceramics," J. Nucl. Mater. **133 & 134**, 701-704 (1985).
5. L.W. Hobbs and F.W. Clinard, Jr., "Faulted Defect Aggregates in Neutron-Irradiated $MgAl_2O_4$ Spinel," J. de Physique **41**, C6-232--C6-236 (1980).
6. W.A. Coghlan et al., "Swelling of Spinel after Low-Dose Neutron Irradiation," pp. **33-35** in Seventh Annual Progress Report on Special Purpose Materials for Magnetically-Confined Fusion Reactors, DOE/ER-0113/4, U.S. Department of Energy, May, 1985.
7. W.A. Coghlan et al., "Swelling of Spinel after **Low-Dose** Neutron Irradiation." J. Nucl. Mater. **141-143**, 382-386 (1986).
8. L.K. Mansur, "Void Swelling in Irradiated Materials: Assessment of Theory," Nucl. Technol. **40**, 5-34 (1978).

9. SUPERCONDUCTING MAGNET MATERIALS

No contributions received this period.

DISTRIBUTION

- 1-13. Argonne National Laboratory, 9700 South Cass Avenue, Argonne, IL 60439
M. C. Billone
O. K. Chopra
R. G. Clemmer
D. R. Diercks
P. A. Finn
A. K. Fischer
Y. Y. Liu
B. A. Loomis
R. F. Mattas
L. A. Niemark
S. W. Tam
E. R. Van Deventer
H. Wiedersich
14. Argonne National Laboratory, EBR-II Division, Reactor Materials Section, P.D. Box 2528, Idaho Falls, ID 83403-2528
D. L. Porter
15. Arizona State University, Department of Mechanical and Aerospace Engineering, Tempe, AZ 85281
W. A. Coghlan
16. Auburn University, Department of Mechanical Engineering, Auburn, AL 36849
B. A. Chin
- 17-30. Battelle-Pacific Northwest Laboratory, P.D. Box 999, Richland, WA 99352
J. L. Brimhall
D. G. Doran (5)
M. D. Freshley
F. A. Garner
D. G. Gelles
M. L. Hamilton
H. L. Heinisch
G. W. Hollenberg
B. D. Shipp
O. D. Slagle
- 31-32. Carnegie Institute of Technology, Carnegie-Mellon University, Schenley Park, Pittsburgh, PA 15213
W. M. Garrison, Jr.
J. C. Williams
- 33-36. GA Technologies, Inc., P.D. Box 85608, San Diego, CA 92138
J. Baur
G. R. Hopkins
T. A. Lechtenberg
D. I. Roberts
- 37-38. General Dynamics Corporation, 5001 Kearny Villa Road, San Diego, CA 92138
T. L. Cookson
V. Stegar
39. General Electric, Advanced Nuclear Technology Operation, 310 Deguine Drive, Sunnyvale, CA 94088
S. Vaidyanathan
40. Georgia Institute of Technology, School of Textile Engineering, Atlanta, GA 30332
D. s. Tucker
41. Grumman Aerospace Corporation, c/o TFTR Project, Princeton Plasma Physics Laboratory, Princeton University, A. Site, Building 1-E, Princeton, NJ 08540
R. G. Micich
- 42-44. Lawrence Livermore National Laboratory, P.O. Box 808, Livermore, CA 94550
E.N.C. Oalder
M. Guinan
J. Perkins
- 45-53. Los Alamos National Laboratory, P.O. Box 1663, Los Alamos, NM 87545
J. L. Andersen
L. D. Caudill
D. J. Dudziak
H. M. Frost
G. Hurley
C. D. Kise
R. Liepens
R. J. Livak
T. Zocco

54. Manlabs, Inc., 231 Erie Street, Cambridge, MA 02139
O. Tognarelli
55. Massachusetts Institute of Technology, Department of Metallurgy and Materials Science, Cambridge, MA 02139
L. W. Hobbs
56. Massachusetts Institute of Technology, 138 Albany Street, Cambridge, MA 02139
O. K. Harling
- 57-58. Massachusetts Institute of Technology, 77 Massachusetts Avenue, Cambridge, MA 02139
I-Wei Chen N. J. Grant
- 59-60. Massachusetts Institute of Technology, Plasma Fusion Center Headquarters, Cambridge, MA 02139
H. O. Becker D. B. Montgomery
61. McDonnell-Douglas Astronautics Company, East, P.O. Box 516, Bldg. 92, St. Louis, MO 63166
J. W. Oavis
- 62-63. National Bureau of Standards, Boulder, CO 80302
F. R. Fickett M. B. Kasen
64. National Materials Advisory Board, 2101 Constitution Avenue, Washington, DC 20418
K. M. Zwilsky
65. Naval Research Laboratory, Washington, DC 20375
J. A. Sprague
- 66-131. Oak Ridge National Laboratory, P.O. BOX X, Oak Ridge, TN 37831
Central Research Library A. W. Longest
Document Reference Section L. K. Mansur
Laboratory Records Department (2) P. J. Maziasz
Laboratory Records - RC T. K. Roche
Patent Section A. F. Rowcliffe (35)
J. Bentley R. L. Senn
L. A. Berry I. Siman-Tov
E. E. Bloom R. E. Stoller
O. N. Braski M. S. Suzuki
W. P. Eatherly K. R. Thoms
M. L. Grossbeck P. T. Thornton (3)
S. Hamada P. F. Tortorelli
R. L. Klueh F. W. Wiffen
R. A. Lillie S. J. Zinkle
K. C. Liu
- 132-134. Princeton Plasma Physics Laboratory, Princeton University, P.O. Box 451, Princeton, NJ 08540
J.P.F. Conrads Long-Poe Ku
H. Furth
135. Rensselaer Polytechnic Institute, Troy, NY 12181
D. Steiner
136. Rockwell International Corporation, NA02, Rocketdyne Division, 6633 Canoga Avenue, Canoga Park, CA 91304
D. W. Kneff
- 137-138. Sandia National Laboratories, P.O. Box 5800, Albuquerque, NM 87185
M. J. Davis W. 8. Gauster
- 139-140. Sandia National Laboratories, Livermore Division 8316, Livermore, CA 94550
W. Bauer W. G. Wolfer

141. University of California, Department of Chemical and Nuclear Engineering, Santa Barbara, CA 93106
G. R. Lucas
- 142-144. University of California, Department of Chemical, Nuclear and Thermal Engineering, Los Angeles, CA 90024
M. A. Abdou
R. W. Conn
N. M. Ghoniem
145. University of California, Los Alamos National Laboratory, P.O. Box 1663, Los Alamos, NM 87545
T. Zocco
146. University of Missouri, Department of Nuclear Engineering, Rolla, MO 65401
A. Kumar
147. University of Michigan, Department of Nuclear Engineering, Ann Arbor, MI 48109
T. Kammash
- 148-152. Westinghouse Hanford Company, P.O. Box 1970, Richland, WA 99352
A. M. Ermi
G. D. Johnson
F. M. Mann
R. J. Puigh
R. L. Simons
153. Department of Energy, Oak Ridge Operations Office, P.O. Box E, Oak Ridge, TN 37831
Assistant Manager for Energy Research and Development
- 154-157. Department of Energy, Department of Fusion Energy, Washington, DC 20545
S. E. Berk
J. F. Clarke
M. M. Cohen
T. C. Reuther
- 158-207. Department of Energy, Office of Scientific and Technical Information, Office of Information Services, P.O. Box 62, Oak Ridge, TN 37831
For distribution as shown in DOE/TIC-4500, Distribution Categories UC-423 (Magnetic Fusion Reactor Materials) and UC-424 (Magnetic Fusion Energy Systems)

